UNIVERSIDAD NACIONAL AUTÓNOMA DE MÉXICO
PROGRAMA DE POSGRADO EN ASTROFÍSICA
INSTITUTO DE RADIOASTRONOMÍA Y ASTROFÍSICA

ON THE OBSCURATION OF THE ACTIVE GALACTIC NUCLEI

TESIS
QUE PARA OPTAR POR EL GRADO DE:
DOCTOR EN CIENCIAS (ASTROFÍSICA)

PRESENTA
DONAJI CATALINA ALEJANDRA ESPARZA ARREDONDO

TUTORES
DRA. OMAIRA GONZÁLEZ MARTÍN
INSTITUTO DE RADIOASTRONOMÍA Y ASTROFÍSICA
DRA. DEBORAH DULTZIN KESSLER
INSTITUTO DE ASTRONOMÍA

MORELIA, MICHOACÁN, JUNIO 2021

On the Obscuration of the Active Galactic Nuclei

by

Donaji Catalina Alejandra Esparza Arredondo

A thesis submitted for the degree of doctor of philosophy

in

Astrophysics Science

in the

Instituto de Radioastronomía y Astrofísica

of the

Universidad Nacional Autónoma de México

Supervisors

Dra. Omaira González Martín

&

Dra. Deborah Dultzin Kessler

Morelia, Michoacán, 2021

To my ancestors who sacrificed their dreams to give me an opportunity to make my dreams come true...

... And to my fellow women who burned at the stake for trying to live them.

Acknowledgments

Esta tesis es una gran y reconfortante historia de poco más de cuatro años. Cada pequeña parte me recuerda una historia, una aventura y/o una lección aprendida. La culminación de este trabajo representa el que espero sea mi inicio como futura investigadora.

Personal

Agradezco con gran amor a mis padres Imelda y Jorge por los sacrificios y el apoyo dado siempre en cada pequeño paso hasta llegar hasta esta meta.

A mi querida hermana por entenderme y motivarme. Eres mi orgullo!

A mi amado amigo y novio Gustavo por compartir y apoyarme durante este largo proceso. Infinitas gracias por siempre estar a mi lado y motivarme en los momentos más oscuros. Por las charlas increíbles sobre ciencia, donde recordé porque seguí este camino.

A mis queridas y maravillosas jefas Omaira y Deborah. Este trabajo no hubiera sido posible sin ustedes. Mi querida Deborah muchas gracias por haberme recibido en tu oficina hace 7 años siendo apenas una pequeña pupila recién entrada a la maestría. Gracias por compartir tus conocimientos y tus consejos para iniciar mi recorrido por este mundo de la astronomía. Gracias por introducirme al feminismo y enseñarme que mi carácter no sobraba en esta carrera. Mi querida Omaira muchas gracias por haber llegado en el momento correcto. Gracias por haberme dado la confianza como tu primera estudiante en un nuevo país. Muchas gracias por nunca dejarme sola, por tomarme de la mano y caminar a mi lado mientras aprendía. Gracias por cada consejo tanto académico como personal. Por buscar y proveer los recursos económicos para poder compartir mi trabajo y conocer otros ambientes. Mil gracias a ambas por las palabras de aliento, por los abrazos y por los jalones de oreja que necesitaba. Gracias por preocuparse por mí durante todos estos años. Espero algún día tener la oportunidad de ser tan buena asesora, investigadora y mujer como ustedes.

A mi grupo de AGNs del IRyA: Omaira, Natalia, Cesar, Alice, Sinhué, Jafet y Ulises. Gracias por dar lugar a este maravilloso espacio de trabajo. Como he disfrutado cada reunión, desde aquellas para poner en mesa un nuevo proyecto hasta donde no teníamos idea por donde seguir. Espero pronto poder festejar la llegada a nuestro décimo artículo aceptado.

A mis colaboradores Dra. Josefa Masegosa (pepa), Dra. Cristina Ramos Almeida, Dr. Jacopo Fritz, Dr. Ismael García Bernete, Dra. Mariela Martínez Paredes. Muchas gracias por aceptar trabajar conmigo, aconsejarme y compartirme sus conocimientos.

A mi comité tutor: Dra. Itziar Artexaga, Dr. Luis Felipe Rodriguez y Dr. Jacopo Fritz.

Gracias por estar al pendiente de mis avances cada semestre durantes estos años.

A mis amigos Andy, Rubén y Ezequiel por estar allí en los días buenos y malos. Por las tazas de café y por las cervezas. Mil gracias por compartir este camino llamado posgrado.

A mi pequeña cachorra Peta por su compañía durante todos estos años, especialmente en el último.

Institucional

Agradezco al Instituto de Radioastronomía y Astrofísica (IRyA) por haberme recibido tan amablemente. Sin duda extrañaré el ameno ambiente del instituto.

A la Universidad Nacional Autónoma de México (UNAM) por haberme dado la oportunidad de ser parte de esta maravillosa comunidad y darme las herramientas para convertirme en Astrofísica.

A CONACYT por darme el apoyo financiero para realizar mis estudios de posgrado, sin duda este apoyo fue fundamental para mi formación.

Al programa de apoyo a proyectos de investigación e Innovación tecnológica (PAPIIT) por su apoyo financiero a través de los proyectos *IN105720* e *IA103118* cuya responsable es la Dra. Omaira González Martín. Estos apoyos fueron vitales para pagar las publicaciones de los trabajos presentados y financiar la culminación de esta tesis.

Abstract

The growth of the supermassive black holes depends on the availability of material close to them. Several works point out that the feeding mechanism of these sources is an accretion disk. The nuclei where this feeding process occurs are known as Active Galactic Nuclei (AGN). Both the theoretical and observational studies of these sources are complicated due to their small sizes and distances. Previous studies have found that there are observational differences between AGN, which leads to the construction of diverse classes.

To understand the diversity of classes observed among AGN, it is necessary to postulate the existence of a material capable of obscuring the internal parts with a geometrically and optically thick torus of gas and dust for some lines of sight. However, this torus is not spatially resolved even for the nearest AGN. Several techniques have been developed to study its geometry and physical properties. For example, spectroscopic studies have been broadly used to characterize the main properties of the torus. Still, the torus has many parameters, including its geometry, composition, and inner structure, which have not been constrained yet.

Spectroscopy studies employ two ranges of the electromagnetic spectrum to study the torus: X-ray and mid-infrared (mid-IR). X-rays show signs of the torus emission throughout the reflection component peaking at $\sim$ 20 keV. The X-ray spectral shape depends on the geometry of this emission. The mid-IR emission is another powerful tool to study the torus' properties because the continuum emission in this range is dominated by dust heated by the AGN. Meanwhile, the mid-IR wavelengths have been used to establish the torus properties, X-ray wavelengths have been less explored. The main difference between these two wavelengths is that X-rays trace the neutral or less ionized gas, and mid-IR traces the dust properties of the AGN torus.

In this work, we explore the complexity of this torus and its role in AGN activity. First, we present the results obtained from comparing the dust and gas distributions in a sample of nearby AGN (Esparza-Arredondo et al., 2021). For this, we study a sample of 36 AGN with observations from *NuSTAR* and *Spitzer* spectra available. We analyze the spectra individually using current models. In particular, we study in-depth whether a smooth or clumpy distribution can explain gas distribution at X-rays and dust at the mid-IR. The main result is that 80% of the objects can be fitted with smooth gas and clumpy dust distributions. However, a more detailed analysis, including information such as the variability of the density column of the obscuring material in the line of sight and derived parameters (e.g., covering

factor), shows three scenarios regarding gas and dust distribution: (1) gas and dust are distributed in clouds; (2) gas is distributed smoothly, and dust is distributed in clouds; (3) gas and dust are in a smooth distribution, although this scenario is the one that least objects prefer.

Furthermore, a comparison of the attenuation obtained by the dust and the hydrogen column density of the gas shows that the dust-to-gas ratio of the obscuring structure is much lower than that of the interstellar medium, reaching as low as 0.01. These results point to the fact that there is much more gas than dust in the vicinity of the accretion disk of these sources. We think that this can be explained if the gas is occupying the dust-free regions, either between the dust clouds or in the internal part of the dust torus, where the dust does not survive the radiation field of the AGN.

Then, we present a new technique capable of simultaneously fitting the spectra of these two wavelengths, combining the torus models developed at mid-IR and X-ray wavelengths. The data resulting from the application of this technique to IC 5063 are presented and discussed (Esparza-Arredondo et al., 2019). This object is used as a test for this simultaneous fitting technique that allows us to restrict for the first time all the observational parameters of the dust torus of an AGN. We find that the gaseous torus observed through the X-ray reflection component and the dust torus studied through infrared emission can be explained with the same geometry. After testing different combinations of models, we find that a smooth torus model can explain the emission at X-rays and mid-IR wavelengths at the same time. In the future, we aim to apply this technique to a complete sample of AGN.

Finally, we also study the possible evolution of the AGN components when they are in a rising or fading activity phase. For this, we compiled our catalog of AGN candidates that show hints of the fading and rising of their activity in the last decades, where we analyzed the role of this torus component (Esparza-Arredondo et al., 2020). This is the first time such an extensive compilation of fading AGN candidates is presented. For this, we use well-known scaling relationships between the infrared continuum, the intrinsic continuum at X-rays, and the [OIII] emission line. The fundamental hypothesis of this analysis lies in the fact that each component traces the emission from the nucleus at different time scales. We start from a sample of almost 900 sources, of which we find about 90 candidates to be changing their current level of activity. 96 % of them are fading while 4 % are in the rising activity phase. Significantly, 50 % of these candidates are found in galaxy mergers, and 30 % have relativistic jets seen in radio frequencies (much higher than in the general AGN population where the jets are found in less than 10 % of them). In almost all of the sources where we have analyzed the dust through the mid-IR spectrum, we found that its properties are best fitted a to toroidal geometry. This contrasts with most of the AGN, where a wind model is preferred over the torus model. This suggests that they are in a stage where the wind is no longer relevant. Therefore, the existence of jets and the lack of winds in the fading and rising stages are consistent with the switching off and on of the AGN duty cycle.

The results presented in this thesis contribute to the solution of broad questions of astrophysical research, such as *How do the gas and dust contribute to the obscuration of the AGN?*, *What is the connection between the AGN and their host galaxies?*, and *How could the AGN help us to understand the history of our universe?*

This thesis is a compilation of three papers, of which two are published in "Astrophysical Journal" (Esparza-Arredondo et al., 2019, 2020) and one is currently accepted for publication in "Astronomy & Astrophysics Journal" (Esparza-Arredondo et al. 2021). Note that I am the first author of these three works.

Resumen

El crecimiento de los agujeros negros supermasivos depende de la disponibilidad de material cercano a ellos. Varios trabajos señalan que el mecanismo de alimentación de estas fuentes es un disco de acreción. Los núcleos donde ocurre este proceso de alimentación se conocen como núcleos galácticos activos (AGNs). Tanto el estudio teórico como observacional de estas fuentes es complicado por sus pequeños tamaños y sus distancias a nosotros. Estudios previos han encontrado que existen diferencias observacionales entre AGNs, lo que lleva a la construcción de diversas clases.

Para comprender la diversidad de clases observadas entre AGNs, es necesario postular la existencia de un material capaz de oscurecer las partes internas con un toro geométricamente y ópticamente grueso de gas y polvo para algunas líneas de visión. Sin embargo, este toro no se resuelve espacialmente ni siquiera para los AGNs más cercanos. Diferentes técnicas se han desarrollado para estudiar su geometría y propiedades físicas. Por ejemplo, los estudios espectroscópicos se han utilizado ampliamente para caracterizar las principales propiedades del toro. Aún así, el toro tiene una gran cantidad de parámetros, tanto geométricos como de composición y estructura interna, que aún no se han restringido.

Los estudios espectroscópicos emplean dos rangos del espectro electromagnético para estudiar el toro: los rayos X y el infrarrojo medio. Los rayos X muestran señales de la emisión del toro a través de la componente de reflexión que pica alrededor de ~ 20 keV. La forma del espectro en rayos X depende de la geometría de esta emisión. Mientras tanto, la emisión en el infrarrojo medio de los AGNs es otra herramienta poderosa para estudiar las propiedades del toro, debido a que el continuo de emisión en este rango está dominado por el calentamiento del polvo debido al AGN. Mientras que el infrarrojo ha sido más utilizado para establecer las propiedades del toro, los rayos X han sido poco explorados (ver introducción). La diferencia principal es que los rayos X nos trazan las propiedades del gas neutro o poco ionizado, el infrarrojo traza las propiedades del polvo.

En este trabajo, exploramos la complejidad de este toro y su papel en la actividad de los AGNs. Primero, presentaremos los resultados obtenidos al comparar individualmente las distribuciones de polvo y gas en una muestra de AGNs (Esparza-Arredondo et al. 2021). Para ello hemos estudiado una muestra de 36 AGNs con observaciones del satélite de rayos X *NuSTAR* y el satélite de infrarrojo medio *Spitzer*. Hemos hecho el análisis de los espectros de manera individual, utilizando los modelos más aceptados hasta la fecha en ambas longitudes de onda. En concreto hemos estudiado en profundidad si la distribución de gas en rayos X y

de polvo en el infrarrojo medio se puede explicar con una distribución suave o grumosa. El resultado principal es que 80% de los objetos pueden ajustarse con una distribución suave del gas y una distribución grumosa del polvo. Sin embargo, un análisis más en detallado, incluyendo información como la variabilidad de la columna de densidad del material oscurecedor en la línea de visión y los parámetros derivados (p.e. covering factor), muestra tres escenarios en cuanto a la distribución del gas y polvo: (1) gas y polvo distribuídos en nubes; (2) gas distribuído de manera suave y polvo distribuido en nubes; (3) gas y polvo en una distribución suave, aunque este escensario es el que menos objetos prefieren. Además una comparación de la atenuación obtenida por el polvo y la columna de densidad del hidrógeno del polvo muestra que el cociente polvo-a-gas de la estructura oscurecedora es mucho menor al del medio interestelar, llegando a ser tan bajo como 0.01. Todo esto apunta a que hay mucho más gas que polvo en las inmediaciones del disco de acrecimiento de estas fuentes. Creemos que esto puede ser explicado si el gas está ocupando las regiones libres de polvo, bien sea entre las nubes de polvo o en la parte interna del toro de polvo, donde el polvo no sobrevive al campo de radiación del AGN.

A continuación, presentaremos una nueva técnica capaz de ajustar simultáneamente los espectros de estos dos telescopios combinando los modelos de toro desarrollados en rayos X e infrarojo. Se presentarán y discutirán los datos resultantes de la aplicación de esta técnica a la fuente IC 5063 (Esparza-Arredondo et al. 2019). Este objeto ha servido como prueba para esta técnica de ajuste simultáneo que nos ha permitido restringir por primera vez todos los parámetros observacionales del toro de polvo de un AGN, utilizando el método de ajuste espectral. Encontramos que el toro gaseoso observado a través de la componente de reflexión en rayos X y el toro de polvo que se estudia a través de la emisión infrarroja pueden ser explicados con una misma geometría. Después de probar varias combinaciones de modelos hemos encontrado que un modelo de toro suave es capaz de explicar la emisión en rayos X y en infrarrojo medio al mismo tiempo. En el futuro pretendemos aplicar esta técnica a una muestra completa de AGNs.

Finalmente, estudiamos también la posible evolución de las componentes de los AGNs cuando se encuentran en una fase de crecimiento o decrecimiento de la actividad. Para ello recompilamos nuestro propio catálogo de AGNs candidatos al desvanecimiento o aumento de su actividad en las últimas décadas, donde analizamos el papel de este componente toroidal (Esparza-Arredondo et al. 2020). Esta es la primera vez que una gran compilación de AGNs candidatos a desvanecimiento son presentados. Esto lo hemos hecho utilizando relaciones de escala bien conocidas entre el contínuo en infrarrojo medio, el contínuo intrínseco de los rayos X y la emisión en la línea de [OIII]. La hipótesis clave de este análisis recae en el hecho de que cada componente traza la emisión del núcleo en escalas de tiempo diferentes. Hemos partido de una muestra casi 900 fuentes de las que hemos encontrado unas 90 fuentes candidatas a estar cambiando su nivel de actividad actual. El 96% de ellas está decayendo mientras que el 4% se encuentra en fase de activación del núcleo. De manera relevante, el 50% de estos candidatos se encuentran en mergers de galaxias y 30% tienen chorros relativistas vistos en

radio-frecuencias (mucho más alto que en muestras generales de AGN donde el chorro se encuentra en entorno al 10% de los AGNs). En casi todas las fuentes donde hemos podido analizar el polvo a través del espectro infrarrojo medio, sus propiedades son mejor ajustadas a una geometría toroidal. Esto contrasta con muchos AGNs donde el modelo de viento es preferido sobre el modelo de toro. Esto sugiere que se encuentran en una etapa donde el viento ya no es relevante. Por lo tanto, la existencia de jets y la falta de vientos en las etapas de desvanecimiento y encendido son consistentes con el apagado y encendido del ciclo de trabajo de los AGNs.

Los resultados presentados en esta tesis contribuyen a la resolución de grandes preguntas de investigación en astrofísica, e.g.: *¿Cómo contribuyen el gas y el polvo al oscurecimiento de un AGN?*, *¿Cuál es la conexión entre los AGNs y sus galaxias anfitrionas?* y *¿Cómo podría ayudarnos el AGN a comprender la historia de nuestro universo?*

Esta tesis es una compilación de tres artículos, de los cuales dos están publicados en la revista "Astrophysical Journal" (Esparza-Arredondo et al. 2019, Esparza-Arredondo et al. 2020) y otro se encuentra aceptado para ser publicado en la revista "Astronomy and Astrophysics" (Esparza-Arredondo et al. 2021). Nótese también que en los tres trabajos soy autora principal.

Contents

Chapter 1

Introduction and Background

1.1 The active galactic nuclei

Black holes (BHs) are objects in space whose large gravitational field does not even let the light escape. Theoretically, the existence of these objects ("non-luminous bodies") was proposed since the XVIII century by John Michael (1784) and Pierre-Simon Laplace (1796). In 1916, after the publication of the theory of general relativity, Schwarzschild found a solution to Einstein's equations and, for the first time, obtained the mathematical solution for a BH (Schwarzschild, 1916). At the end of the 30's, Oppenheimer and Snyder suggested that the massive stars could collapse into BHs when reaching a critical gravitational radius (Oppenheimer & Volkoff, 1939). However, the "black hole" term was used for the first time in 1968 in a scientific conference by John Wheeler. In the following years was found the observational proof of their existence.

BHs of different sizes have been found, including those with masses ranging from $3 - 30$ $M_{\odot}$, remnants of stellar nuclei merger in a type II supernova, and even supermassive black holes (SMBHs) with masses of the order of $10^6 - 10^9$ $M_{\odot}$, located in the central part of galaxies. SMBHs with a gaseous disk capable of producing enormous amounts of energy around them are known as "Active Galactic Nuclei" (AGN). Currently, it is estimated that in the local Universe, at $z \leq 0.1$, about 1 out of 50 galaxies contains an optically thick, geometrically thick accretion disk around SMBH, and about one over three contains an optically thick, geometrically thin accretion disk around the SMBH (Netzer, 2013).

Fath's work in 1909 marked the beginning of the study of AGN . With the goal of testing the claim that spiral nebulae showed a continuous spectrum consistent with a collection of stars, Fath observed several of these sources, among them the famous NGC 1068 (see below). He found that this source showed a spectrum with strong lines in absorption. In the next years, NGC 1068, together with other sources, were studied by several astronomers and noted the presence of nuclear emission lines in their spectra (Slipher, 1917; Hubble, 1926). In fact, a systematic study of galaxies with nuclear emission lines was presented by Seyfert (1943). For the first time, he classified the so-called Seyfert galaxies which host active galactic nuclei, based on characteristics of optical spectra such as broad Balmer emission lines or

certain asymmetric emissions. Today, in his honor, the galaxies with high excitation nuclear emission lines are known as Seyfert galaxies. Although until then these works provided relevant information to understand AGN, they were not enough to put them in the spotlight of most astronomical studies.

The great interest in the AGN would begin with the development of radio astronomy at the end of the 50s. Edge et al. (1959) and Bennett (1962) presented the third Cambridge (3C) survey at 159 MHz and 178 MHz, respectively. In the next years, several of these sources were identified with optical (Zwicky, 1964) and ultraviolet (UV, Markarian, 1967) observations. The first quasi-stellar object (QSO) 3C48, was observed in 1960 and reported by Sandage (1964). He found that the spectrum of this source showed broad emission lines at 'unfamiliar wavelengths', and photometry showed the object to be variable and to have an excess of UV emission compared with normal stars. In 1963, Maarten Schmidt noticed that four emission lines in the optical spectrum of 3C 273 agreed with the expected wavelengths of Hβ, Hγ, Hδ, and Hϵ with a z = 0.16 (Schmidt, 1963). This redshift allowed him to identify a line in the UV part of the spectrum with MgII λ2798. This result was confirmed by Oke (1963), who found an emission-line in the infrared (IR) spectra of this source ($\lambda \sim 7600$ Å) which corresponded to Hα according to the redshift proposed by Schmidt. For 3C48, Greenstein obtained its spectrum and also observed the Mg II line, which supported a z =0.37 for this source (Greenstein, 1963).

Greenstein & Schmidt (1964) explored three possible involving explanations of the redshift of these sources 1) rapid motion of objects in or near the Milky Way, 2) the gravitational redshift[1], and 3) cosmological redshift[2]. They proposed a model in which a central source of the optical continuum was surrounded by the emission-line region and a still larger radio-emitting region. Through this model, they calculated several properties as mass and radii of the central sources of these galaxies. Also, they mentioned that the host galaxy could be hidden due to the brightness of the nuclear emission (confirmed later on by Kristian, 1973). At the end of the 60s, the cosmological redshift values of QSOs were accepted, and the idea of a common physical phenomenon between these objects and Seyfert galaxies arose (Gunn, 1971).

1.1.1 AGN optical classification

The sorting of AGN is important because it gives us information about the physical process, evolution, and properties of each galaxy. Currently, there are several AGN classes depending on the observed luminosity at different wavelengths. The most spread classification is driven from optical spectroscopy. In this work, we study "Seyfert galaxies" which have a low-to-moderate bolometric luminosity ($L_{bol} \sim 10^{42} - 10^{45}$ ergs^{-1})[3]. The Seyfert galaxies are

[1]The gravitational redshift corresponds to an increase in the wavelength and decrease in the frequency of the photon, which espends energy to escape from the gravitational well. See Einstein's theory of general relativity.

[2]The cosmological redshift is due to universe expansion. The wavelength of photons propagating through the expanding space is stretched.

[3]The AGN bolometric luminosity (L_{bol}) depends on the mass accretion rate and on the efficiency for the conversion of gravitational energy into radiation (**?**).

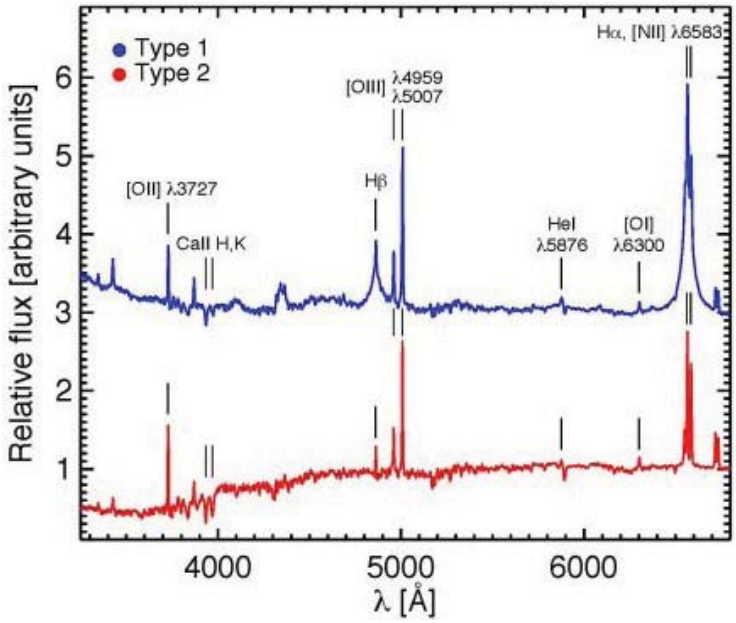

Figure 1.1: Typical spectra of Seyfert type I (top) and II (bottom). The prominent emission lines are highlighted. Figures modified from DiPompeo et al. (2018) Taken from: Hickox & Alexander (2018).

divided into type I and type II (see Fig. 1.1).

- **Type I Seyfert (Sy1):** These sources show broad and narrow permitted (e.g. H I, He I, and He II) and narrow forbidden (e.g. [O III], [N II], [O I]) emission lines in near-IR (NIR), optical, and UV wavelength ranges. Sometimes, they also show semi-forbidden emission lines (e.g. C III]).

- **Type II Seyfert (Sy2):** These sources only contain strong narrow forbidden emission lines (other lines are [O I], [S II], and [Fe VII]).

Other classification are 1) **Quasars** which have broad emission lines, high bolometric luminosities ($L_{bol} \sim 10^{45} - 10^{48}\,ergs^{-1}$), and are located at high redshift ($0.1 < z < 7.5$, see Falomo et al., 2014; Bañados et al., 2018); 2) **Blazars** which are radio loud and optically violent variable sources. These objects have a strong relativistic beamed jet pointing close to the line of sight to the observer; 3) **LINERs** which are common but are the faintest class, at optical wavelengths are dominated by emission lines of low ionization; and 4) **Radio galaxies** which are strong radio sources, with optical spectra similar to Seyfert galaxies. Fanaroff & Riley (1974) divided this last category into two groups; FRI and FRII according the ratio between nuclear and extended flux at radio frequencies. FRII are mostly extended showing radio lobes while FRI most of their emission comes from the unresolved nuclear source.

The discrimination between photoionization due to star formation (SF) or AGN is a hard task. Optical wavelengths offer a good opportunity to disentangle both using emission-line diagnostic diagrams. Baldwin et al. (1981) first proposed the diagnostic diagrams (now known as the BPT diagram, see Figure 1.2) to separate normal HII regions, planetary nebula,

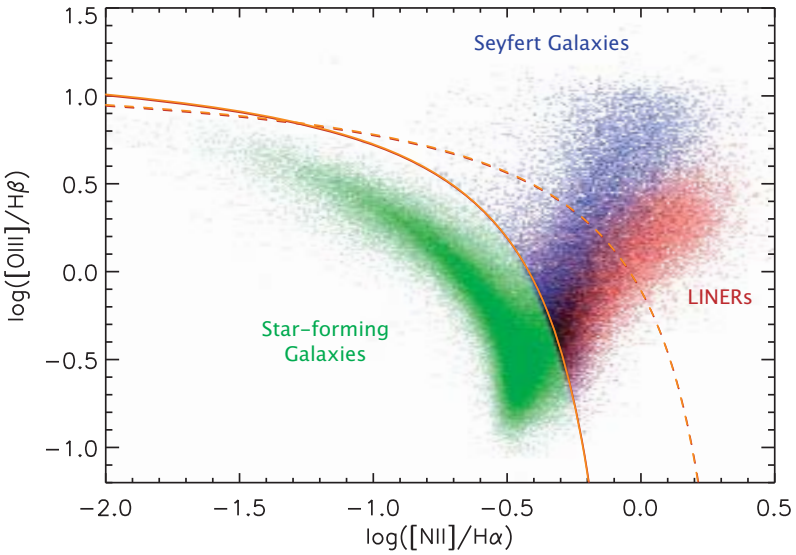

Figure 1.2: The BPT diagram used to classify the emission-line galaxies as: Seyfert, LINER, Composite and star-forming galaxies. The curves indicate empirical (solid) and theoretical (dashed) dividing lines between active galactic nuclei (AGN) and star-forming galaxies, based upon the SDSS observations (Kauffmann et al., 2003) and MAPPINGS III photoionization models (Kewley & Dopita, 2002). Taken from Fosbury et al. (2007).

and AGNs. The BPT diagram most frequently used consists in a comparison between the [NII] 6584Å/Hα 6563Å and [OIII] 5007Å/Hβ 4861Åratios. The next commonly-used BPT diagnostic diagrams are [SII] 6717Å, 6731 Å/Hα 6563 Å versus [OIII] 5007 Å/Hβ 4861 Å(BPT-SII) and [OI] 6300 Å/Hα 6563 Å versus [OIII] 5007 Å/Hβ 4861 Å(BPT-OI) (see also Veilleux & Osterbrock, 1987). Essentially, the BPT diagram consists in the combination of high and low excitation forbidden emission lines scaled to a permitted line. These diagrams are set to minimize reddening issues by using close-by emission lines in each ratio.

This BPT diagram has been extended and refined in diverse works through theoretical photoionization models and/or observations (e.g. Ho et al., 1997; Kewley et al., 2001; Kauffmann et al., 2003; Kewley et al., 2006, 2013). The theoretical photoionization models explore the shape of the classification line between SF and AGN galaxies. As we explain below, X-ray and mid-infrared wavelengths are also good spectral ranges to study the AGN nature of these sources thanks to the dominance of the AGN continuum at those wavelengths over other circumnuclear processes.

1.1.2 AGN components

The study of AGN is complex because they are compact unresolved sources (size $\sim$ 1 kpc). The majority of the components of these sources are located within 10 pc of the SMBH, which in most cases prevents from spatially resolving them with the current technology. Figure 1.3 shows an updated sketch of the main AGN structure presented by Ramos Almeida & Ricci (2017). Currently, the main components of AGN are:

- The **SMBH** is the central engine of AGN. The SMBH are defined as a small region

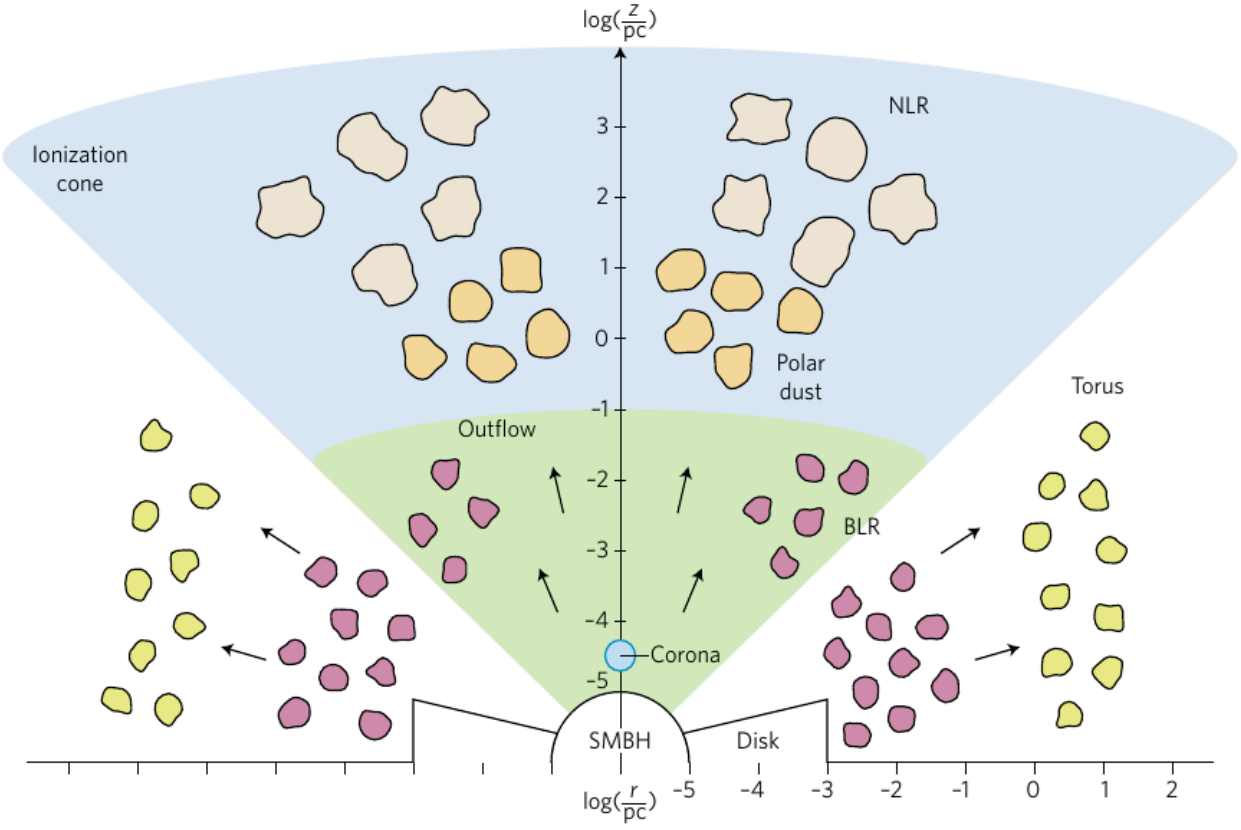

Figure 1.3: Main components of AGN structure seen along the equatorial and polar directions. Different colours indicate different compositions or densities. Taken from Ramos Almeida & Ricci (2017).

of space ($10^{-6} - 10^{-5}$ pc) within which the force of gravity is so strong that nothing, not even light, can escape. The SMBH are characterised by three parameters: mass (M_{BH}), charge, and angular moment (spin)[4].

The basic properties of a SMBH of mass M_{BH} are described using the gravitational radius r_g which is defined as:

$$r_g = \frac{GM}{c^2} \simeq 1.5 \times 10^{23} \frac{M_{BH}}{10^8} cm \tag{1.1}$$

where c is the speed of light and G is Newton's constant of gravitation.

There are several methods to measure the BH mass, which can be classified as direct or indirect according to Peterson (2014). The direct methods are those where the mass is obtained from stars dynamics or from the acceleration of the gas induced by the BH (e.g. stellar and gas dynamical modelling, see Miyoshi et al., 1995; Gültekin et al., 2009; McConnell & Ma, 2013). Meanwhile, the indirect methods are those where the BH mass is inferred from empirical relationships between it and the host-galaxy's properties, such as $M_{BH} - \sigma_*$ (Ferrarese & Merritt, 2000; Gebhardt et al., 2000; Tremaine et al., 2002), $M_{BH} - L_{bulge}$ (Kormendy & Richstone, 1995; Magorrian

[4]The idea of BH only have these three properties is known as "no hair theorem"(Heusler, 1996)

et al., 1998), and $R-L$ relationship (Kaspi et al., 2000; Bentz et al., 2013; Guerras et al., 2013). It is also possible to estimate the BH mass using the radius of the broad line region (BLR) approximated through the reverberation mapping method. This method is based on the principle that the emission-line fluxes vary strongly (reverberate) in response to changes in the continuum. Consequentially, the emission-line response is delayed with respect to changes in the continuum (Peterson, 1993; Pancoast et al., 2011). The measurement of the BH mass through this method also assumes bound Keplerian orbits, thus the mathematical form is:

$$M_{BH} = f(R_{BLR})\frac{R_{BLR}\nu_l^2}{G}[gr] \tag{1.2}$$

Where $\nu_{\rm I}$ is some measure of the velocity obtained from the line profile (e.g. FWHM), and $f(R_{BLR})$ is a geometrical-dynamic factor that depends on the distributions and inclination of the orbits to the line of sight (i.e., the shape of the BLR). See Chapter 7 in Netzer (2013) for more details. The latest review on this topic is presented by Peterson (2014).

Quantitatively, **the spin parameter (a)** of BH with mass $\rm M_{BH}$ and angular momentum $J \simeq M_{BH} r_g c$ is defined as:

$$a = \frac{cJ}{GM_{BH}^2} \tag{1.3}$$

Assuming that gravity is described by general relativity theory, in 1963 Roy Kerr found the mathematical description of an isolated and uncharged spinning BH (Kerr, 1963)[5]. According to this solution, the structure of the space-time around a spinning BH depends only on $\rm M_{BH}$ and a. Also, the Kerr solution shows that the space-time outside rotates around the BH like a vortex. The a parameter can take values between -1 and 1, where the plus and minus signs refer to the direction of the rotation. Several properties of SMBH depend on their spin since this determines the maximum energy that can be extracted from the hole during accretion[6].

In the last years, several techniques have been developed to measure the spin of SMBH. The method most used to date is based on the gravitational redshift of atomic features in the X-ray spectrum (such as the Fe emission line). The emission lines used in this technique are produced in the accretion disk due to photo-excited chemical elements in the surface layers by X-rays that come from the corona (see following bullets). These emission lines become highly broadened and asymmetric, with prominent blueshifted peaks and long redshifted tails for different reasons such as 1) the normal Doppler effect, 2) the time-dilation of Special Relativity, and 3) the gravitational redshifting of General Relativity. The spin of the black hole is encoded in these line profiles, e.g., as one considers BH of progressive higher spin, the innermost stable circular orbit

[5]The simple solution considers the case of a stationary BH and found that the event horizon radius is given by the Schwarzchild radius ($r_s = 2r_g$).

[6]In accretion thin disk, the difference in a between 0 and 1 translates to a factor about 10 in radiation conversion efficiency (see Chapter 4 in Netzer, 2013)

(ISCO) moves closer to the event horizon, the gravitational redshift of X-rays reflected from the ISCO increases, and the extend of the redshifted tail of the iron line grows. Therefore, the spin value is obtained through a carefully modeling of these emission lines (e.g., Laor, 1991; Brenneman & Reynolds, 2006; Reynolds, 2012; Risaliti et al., 2013). A second technique to measure the BH spin consists of comparing observations and thermal spectrum models of the disk. These thermal models take into account the detailed structure of the accretion disk as well as the influence of the Doppler effect and gravitational redshifting. Additionally, it requires extra information such as BH mass, the inclination of the accretion disk, and distance from the earth. This method assumes that most of the free energy to be radiated as thermal emission from the accretion disk surface. Therefore, a disk around a rapidly spinning BH has higher temperatures than a similar disk around a non-spinning black hole (e.g., Czerny et al., 2011; Done et al., 2013; Capellupo et al., 2017; Piotrovich et al., 2017).

Recently, two new techniques have been starting to develop that could help to measure the SMBH spin soon: the detection of the gravitational waves (Detweiler, 1980; Falcke & Markoff, 2013; Goddi et al., 2017) and the interferometry images with the event horizon telescope (Doeleman et al., 2008; Fish et al., 2011; Gralla et al., 2018). See Reynolds (2019) for a review on this topic.

The electric charge parameter of BH is usually set to zero. This assumption is supported by the argument that the presence of plasma around BH leads to prompt discharging. However, several theoretical works have been developed in order to estimate this value (e.g. Heusler, 1996). Recently, Zajaček et al. (2019) summarize the results concerning the observational constraints on the electric charge associated to the BH in our own Galaxy. This parameter remains unknown in other galaxies.

- Around the SMBH an **accretion disk** is located. This disk could be defined as subparsec-rotation-dominated accretion flow. Through this disk, the gravitational energy is transformed into heat and kinetic energy. The disk will have a differential rotation in the sense that the angular velocity depends on the radius (Abramowicz & Fragile, 2013).

  There are several fundamental quantities related with the accretion process:

  – Eddington luminosity (L_{edd}): It is the maximum luminosity that a body can have when there is a balance between the radiation and gravitation forces (Hydrostatic equilibrium):

  $$L_{Edd} = \frac{4\pi G c m_p}{\sigma_T} M_{BH} \simeq 1.5 \times 10^{38} \left(\frac{M_{BH}}{M_\odot} \right) \, erg/s \tag{1.4}$$

  where σ_T is the Thomson cross-section, m_p is the proton mass, G is gravitational constant, and c is the speed light velocity constant.

– Eddington accretion rate is the maximum accretion rate if isotropic emission is assumed, and it depends on the assumed efficiency ϵ ($= \frac{L}{\dot{M}_{BH}c^2}$). This quantity is defined as

$$\dot{m}_{Edd} = \frac{L_{Edd}}{\epsilon c^2} \approx \frac{1}{\epsilon} 2 \times 10^{-9} M_{\odot} yr^{-1} \tag{1.5}$$

– The accretion rate ($\dot{M}_{BH}$) depends of the efficiency to convert the infalling mass into energy. This quantity could be quantified as ratio between L_{Edd} and the bolometric luminosity of the source (L_{bol}) as

$$\dot{M}_{BH} = \frac{L_{bol}}{L_{Edd}} \left(\frac{1.5 \times 10^{38} erg/s}{\epsilon c^2} \right) \left(\frac{M_{BH}}{M_{\odot}} \right) \equiv \frac{L_{bol}}{L_{Edd}} \dot{m}_{Edd} \tag{1.6}$$

Using equation 1.5, the accretion rate is defined as:

$$\dot{M}_{BH} = \frac{L_{bol}}{\epsilon c^2} \tag{1.7}$$

– Growth rate of the SMBH mass (t_{BH}) is defined as a characteristic time in which the M_{BH} will significantly increases due to the accretion process.

$$t_{BH} = \frac{M_{BH}}{\dot{M}_{BH}} \approx \epsilon \left(\frac{L_{bol}}{L_{edd}} \right)^{-1} 5 \times 10^{8} yr \tag{1.8}$$

For a source accreting in the Eddington limit it is in the order of Myr.

The accretion disks are classified according to their geometry into thin, slim, and thick disks. Each one of these can be optically thin or thick, depending on the column density (or surface density) and the level of ionization of the gas.

Theoretically, the accretion disks could be classified according to their $\dot{M}_{BH}$ as very fast accretors ($0.5 \leq L_{bol}/L_{Edd}$), radiatively efficient ($0.01 \leq L_{bol}/L_{Edd} \leq 0.5$), and radiatively inefficient ($L_{Edd} \leq 0.001$). Efficient accretion disks were explored by Shakura & Sunyaev (1973) for the first time. Currently, the geometrically thin (but optically thick) accretion disks are the most accepted. These disks are in a balance between loosing angular momentum and increasing kinetic energy due to local viscosity (see also Netzer, 2013). Inside of this classification, the "two components" accretion disk models are also considered. These models propose either two disks with different temperatures or an accretion disk and an extra component known as the corona.

Inefficient accretion disks are modeled as geometrically thick (but optically thin). In these disks, the decrease of gas density lowers the cooling rate. This means that most of the heat is carried through advection, rather than irradiation. These models are known as "advection dominated accretion flows" (ADAF) and "radiative inefficient accretion flows" (RIAF) (Ichimaru, 1977; Esin et al., 1997; Narayan et al., 1998, 2012)[7].

[7]The RIAFs represents cases in which ions and electrons can have very different temperatures. The ADAF is used to describe such a process in the limit of very low density (advection dominates RIAFs) (see caption

- The **Corona** was defined as a plasma of hot electrons close to the accretion disk, which scatters the energy in the X-ray band (Haardt et al., 1994). The emission mechanism of such X-ray component together with other AGN X-ray components is discussed in detail in Section 1.5.

- The **Broad Line Region (BLR)** is defined as a dust-free region of subparsec-scale ($0.1 - 10\,\mathrm{pc}$). Classically, it is assumed that this region contains gas-clouds with high rotational velocities ($\sim 1,000 - 10,000$ km/s, Padovani et al., 2017). Due to these high velocities, the emission lines associated to the BLR, e.g, Hα, MgII, CIV, and [OIV], are broadened due to Doppler effect. The column density of this region is expected to be high $\sim 10^{23}\,\mathrm{cm}^{-2}$ (Netzer, 2013).

  The nature of the BLR is not well understand yet. An early explanation suggested that the origin of the BLR was "the bloated stars" scenario by Alexander & Netzer (1997). This scenario proposed that the winds or envelopes of bloated stars origin this broad line emissions. Nowadays these clouds are thought to be a radiatively driven wind from the disk. An updated scenario will be explained in Section 1.3.

- A dusty axisymmetric structure with a radius between $\sim 0.1 - 10\,\mathrm{pc}$ that is classically called **torus** is located around the component mentioned above (BLR, accretion disc, etc). Currently, the physical parameters (as geometry and composition) of this structure are controversial. Recently, this component was resolved at radio wavelengths for a few objects. These studies used ALMA (Atacama Large Millimeter Array) high-resolution images of the emission of molecular gas and dust using the CO(3-2) and HCO^+(4-3) lines (García-Burillo et al., 2019; Garcia-Burillo et al., 2021). Unfortunately, this technique is restricted to the brightest AGN. The spectroscopy fitting technique has been used more frequently to study this component since more data is available. This work is focused on understanding this component through this last technique, so detailed information is given in Sections 1.4 and 1.5.

- The **Narrow Line Region (NLR)** is located outside of the torus at $100 - 1000\,pc$ along the direction of the opening angle of the torus (ionization cones). This region has a lower-density ($10^4\,cm^{-3}$) and lower-velocity ($\sim 100 - 500$ km/s, Padovani et al., 2017) ionized gas compared to the BLR. The gas contains dust except in most central parts Netzer (2015). The column density of this region ($10^{20-21}\,\mathrm{cm}^{-2}$) is smaller than that assumed for the BLR (Netzer, 2013).

- The **relativistic jets** are observed on scales from few parsecs to Mpc along perpendicular direction of the accretion disk. The jets emerge from the nuclei in a relativistic, supersonic, and proton-dominated state, and they terminate in strong, hot spot shocks. The most accepted theory about their origin explains that a jet is formed when the BH spins and the accretion disk is strongly magnetized (due to gas accretion at high

4 in the book by Netzer, 2013).

latitude beyond the BH sphere of influence). Although this component is out of the scope of this work, see Blandford et al. (2019) for a review on this component.

1.1.3 The unified model

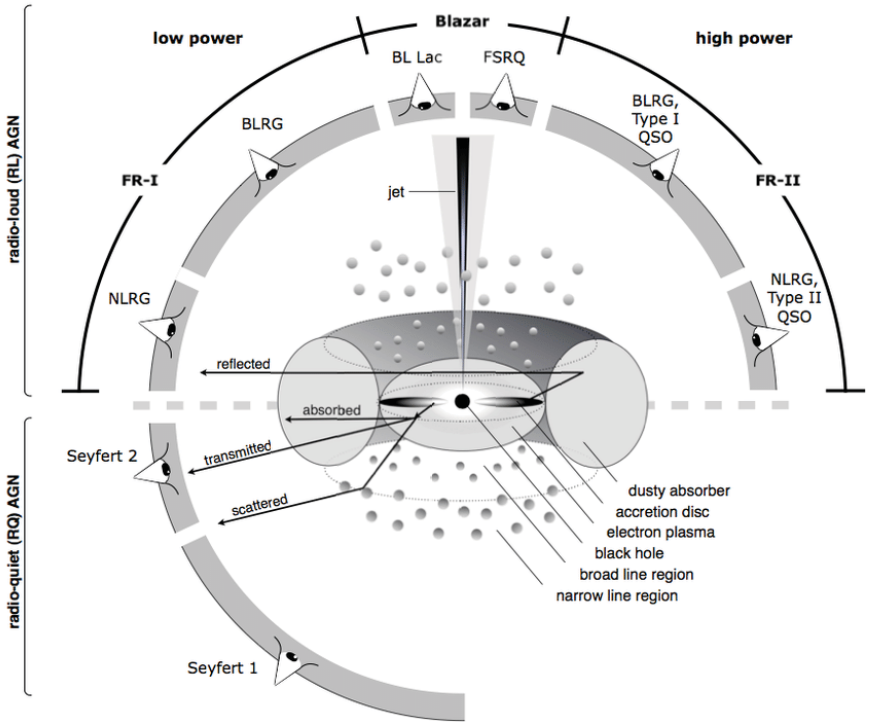

Figure 1.4: Unification model presented by Urry & Padovani (1995). Figure from Beckmann & Shrader (2012).

The location of each component of AGN has given rise to several models trying to explain the different types. Currently, the most accepted model is known as the unified model, and it was proposed by Antonucci & Miller (1985) and Urry & Padovani (1995). This model proposes that all AGN are mainly the same object. Still, the observational differences depend only on some physical parameters, such as 1) the torus position relative to the observed line of sight, 2) the luminosity of the source, and 3) the presence of the jet. Figure 1.4 shows the classical sketch of this model presented by Beckmann & Shrader (2012). Inside of this classification, we can found several subclasses, for example:

- Type I (Sy1) and type II (Sy2): The key for the unification between type I and II is the existence of an optically thick dust torus obscuring the inner parts for some line of sights; the BLR is blocked up by they dusty torus for these viewing angles, and therefore, the spectrum of type II only shows narrow lines from the NLR. When the line of sight do not intercept the dusty torus, a direct view of the BLR shows a type I spectrum.

- Quasar (QSO) and Seyfert: The key to unifying these two kinds of sources is their luminosities. The stellar absorption features of QSO are very weak compared to the

Seyfert. Also, in the case of Seyferts, the narrow lines are generally weaker, therefore, relative to the broad lines. The Seyferts have relatively low luminosities and are seen only nearby, where the host galaxy can be resolved. Meanwhile, the QSO is typically seen at greater distances because they are bright enough to be observed at the high redshift Universe.

- Radio loud (RL) and radio-quiet (RQ) AGN: This classification is obtained from radio wavelengths. The radio-loud sources show a relativistic jet emanating from the nucleus. Meanwhile, in the radio-quiet sources, the jet is lacking. Therefore both families are unified by the existence or not of a relativistic jet. Another way to distinguish between these two kinds of sources is through the "radio loudness parameter (R)"[8]. According with Kellermann et al. (1994) the boundary between the two populations is set at $R \sim 10$ ($\mathrm{R_{RL}} > 10$ and $\mathrm{R_{RQ}} < 10$).

This model was firstly supported by the idea that the BLR of Sy2 was obscured by dust (Rowan-Robinson, 1977). Several years later, this was confirmed through observations of NGC 1068, a prototype Sy2, with the spectropolarimeter or the Shane telescope at Lick Observatory by Antonucci & Miller (1985). These observations revealed that the polarized flux of this source had the appearance of a Sy1 spectrum. This was interpreted as a polarization process of nuclear light due to material above the nucleus near the axis. They concluded that this source, viewed face-on, would be a Sy1. Two years later, several toroidal geometries were also proposed (e.g. Osterbrock, 1978), and this idea received support from the discovery of ionization cones in the nuclei of some AGN (e.g. Pogge, 1988). Finally, this model was also supported by early X-ray studies, which showed that Sy2s are usually obscured while Sy1s show, on average, lower obscuration (Awaki et al., 1991). In particular, X-ray studies of NGC 1068 also found that nuclear emission is obscured by optically thick material (Matt et al., 1997; Bauer et al., 2015). In Section 1.3, we will discuss the issues of the unification model.

1.2 Spectral Energy Distribution of AGN

The energy released by the AGN is in the range of $10^{38} - 10^{48}\,\mathrm{erg\ s^{-1}}$ and it emits at all wavelengths. Each wavelength range is dominated by emission originated in the different components of the AGN structure. Therefore, each wavelength regimen gives us information about some of the AGN physical processes. Figure 1.5 shows the AGN spectral energy distribution (SED) from radio to γ-rays with the main physical components identified with different colors.

The AGN SED shows several features that are unique from them. One of these features is a bump that dominates the sub-millimeter (sub-mm) to NIR wavelengths. This bump is broad, generally peaks between $25-60\mu m$, and slowly decreases toward sub-mm wavelengths

[8]The radio loudness parameter is defined as the ratio of monochromatic luminosities (5GHz) and optical B band at 4400 Å.

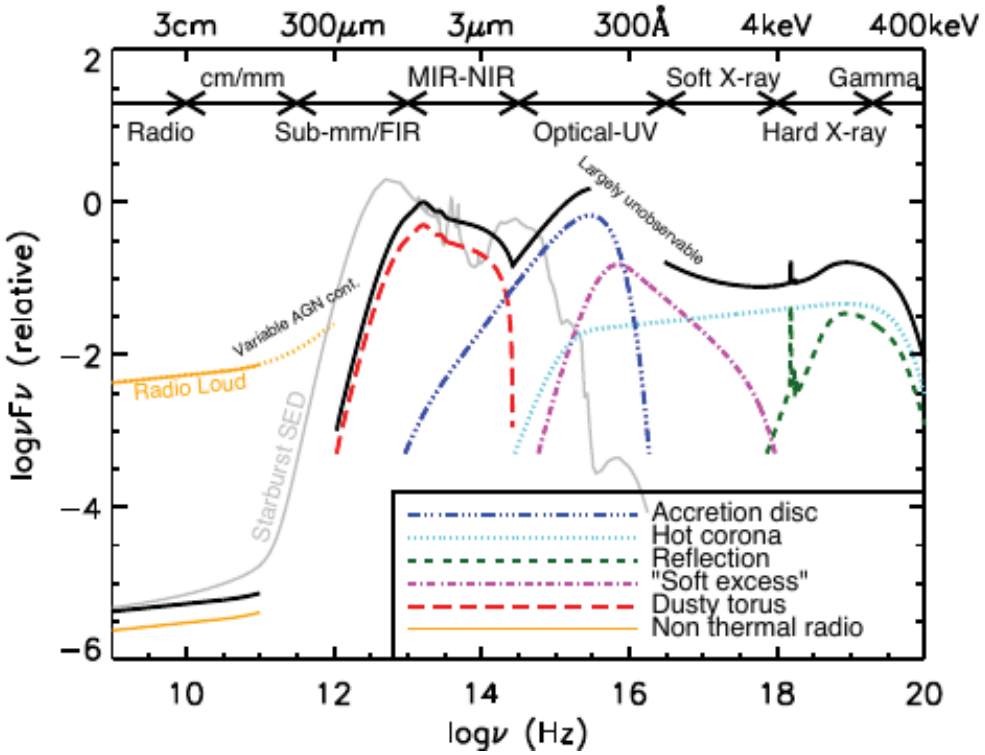

Figure 1.5: Spectral energy distribution of an AGN, loosely based on the observed SEDs of radio-quiet quasars (non-jetted quasars). The black solid curve represents the total SED and the various coloured curves (with and arbitrary offset) represent the individual components. They grey curve shows an example radio-UV SED of starburst galaxy (M82). Figure from Harrison (2014).

($> 100\mu m$ Wilkes, 1999). The AGN SED at radio wavelengths is dominated by non-thermal emission (associated with a jet) or thermal emission (associated with the accretion disk) for radio-loud and radio-quiet AGN, respectively (Padovani et al., 2017). Currently, the sub-mm/FIR emission is controversial. Some works suggest that this range, except in the most luminous quasars or powerful radio-loud AGN, has a great contribution from the host galaxy process, such as star formation (Harrison, 2014). Rodriguez Espinosa et al. (1987) analyzed the IRAS data of a sample of classical Seyfert galaxies. They found that SF produces the bulk of the far-IR ($> 30\,\mu$m) emission in these galaxies. Recently, some authors analyzed the possibility that the dusty torus could also be contributing at sub-mm wavelengths in some sources (Pasetto et al., 2019). This is certainly the case for the emission at infrared bands originated from hot dust in the torus. This thesis is partially focused on this wavelength range, so we further discuss it in the next Section 1.4.

A second bump is observed at optical/UV wavelengths, which peak around 1000Å(extreme-UV) and is classically known as "the big blue bump". The origin of this second bump is the accretion disk (Wilkes, 1999). As a first approximation, it can be described as a power law of the form:

$$L_\nu \propto \nu^{-\alpha} \text{ or } \mathrm{L}_\lambda \propto \lambda^{\beta} \tag{1.9}$$

where α is the frequency spectral index (between zero and one), β is the wavelength spectral index, and $\beta = 2 - \alpha$. Note that the UV wavelengths are very difficult to observe from the earth.

Most X-ray emission is associated with three main components: the soft excess, the corona, and the reflection component. In Section 1.5, these three components are further explained due to the importance of this wavelength range for this thesis work. Only a small fraction of the AGN population are strong γ-ray emitters (Netzer, 2013, e.g., Blazars). The origin of this emission is non-thermal (jet or associated to the lobes, see Padovani et al., 2017).

1.3 Issues of the unified model and other scenarios

Since the unified model was proposed, large samples of AGN and specific sources have been studied in detail. These studies have left several open questions for which the classical unified model cannot provide an answer. For example, initially, Nicastro et al. (2003) postulated the existence of "True Seyferts 2s", i.e., sources optically classified as Sy2, without any evidence of X-ray obscuration. These sources show no evidence of the presence of the BLR, even in polarized light (see Veilleux et al., 1997; Tran, 2001, 2003). Most of these Sy2 are currently classified as changing-look sources, which is a class of objects further discussed below in this section.

Furthermore, the unified model assumes that the geometry of the circumnuclear matter in AGN is coaxial with the spin of the BH, which might not be true in several complex scenarios[9] (see Bianchi et al., 2012). Raban et al. (2009) found that the nuclear components of NGC 1068 are misaligned: the orientation of the dust is tilted with respect to the jet. Moreover, the position angle (PA) of the visible ionization cone does not match the PA of the inner dust cone.

In recent years, several works found an anti-correlation between the AGN luminosity and the covering factor[10] (Cf) of the obscuring medium, indicating an evolution on the inner properties of the dusty/gaseous medium not easily explained as a single unified scenario (see Ueda et al., 2003; Steffen et al., 2003; Simpson, 2005). In fact, recently, Ricci et al. (2017), using X-ray data, found the evolution of the Cf with the Eddington ratio for Compton-thin sources. They found that AGN with $L_{Edd} < 10^{-1.5}$ (low Eddington ratio) have been obscured with a large Cf ($\sim$ 85%), while those with $L_{Edd} > 10^{-1.5}$ show outflowing material and a smaller covering factor ($\sim$ 40%), half of which is associated with Compton-thick material. Previously, Ramos Almeida et al. (2011) found that Cfs of Sy2 are larger than those found in Sy1 using IR SED fitting (see also Ichikawa et al., 2015; Alonso-Herrero et al., 2011; Mateos

[9]Examples of complex scenarios are: the actual BH spin may not reflect the rotation axis of the accretion disk if the BH growth is due to multiple, unrelated accretion events; or the obscuring material is not within the gravitational sphere of influence of the BH.

[10]The covering factor is the fraction of sky covered by the obscuring material, as seen from the accretion disk. It is one of the main elements that regulates the intensity of the reprocessed X-ray and IR radiation Ramos Almeida & Ricci (2017).

et al., 2016). This result implies that the observed differences between Sy1 and Sy2 are not only due to orientation effects and that the torus is not identical for all AGNs of the same luminosity (Ramos Almeida & Ricci, 2017). In fact, the classification between Sy1 and Sy2 could be probabilistic (Elitzur, 2012).

Another case is the disappearance of the dust torus in AGNs at low luminosities, both from theoretical (e.g. Elitzur et al., 2014) and observational (González-Martín et al., 2017) point of views, which implies some evolutionary track on this obscuring medium. Furthermore, even some type-1 AGN lack signatures of the circumnuclear dusty obscurer (Jiang et al., 2010; Hao et al., 2010). The Unified model does not predict the lack of these components. To explain these sources without dust, several explanations/scenarios have been proposed: 1) Since the ignition of the AGN was created, the time could not be enough to form dust, yet (in the case of quasars at z = 2)[11], 2) dust destruction (dynamically or by radiation), or 3) the AGN is not centered in the SMBH (due to merger events)[12]. But it is not only the lack of dust. Even when dust exists, several works have found that dust geometry could be different. Sometimes appears not as a single component but as two or three: some of them claimed to be disk-like or polar elongated as well (e.g. Tristram et al., 2014).

These differences are also found for the NLR. Several works found nuclei unambiguously hosting a relatively powerful AGN based on their X-ray or mid-IR properties. Still, their optical spectra do not show lines associated with the NLR in their optical spectra (e.g. Marconi et al., 2000; Ballo et al., 2004). The NLR of these objects could be heavily obscured by the absorbing medium of the host galaxy, or it may not have been formed yet (e.g Goulding & Alexander, 2009; Pérez-Beaupuits et al., 2011).

The observations at different epochs of the same AGN opened new questions about a real unification theory of these sources. Matt et al. (2003) analyzed the properties of a sample of Sy2 galaxies whose X-ray spectra changed appearance from Compton-thick to Compton-thin and viceversa on time-scales of years. They argued that these changes could be due to the switching-off of the nucleus. Later, several authors found that the broad part of some optical emission lines (e.g. Hβ, Hα) appear and disappear in these kind of sources (e.g. Osterbrock, 1977; Antonucci & Cohen, 1983; Lyutyj et al., 1984; Penston & Perez, 1984; Shapovalova et al., 2010). Currently, the "changing-look AGN" term is used to describe an object that shows X-ray and/or optical spectral changes that modify its classification. These spectral changes are observed on astrophysical short timescales ($\leq 1yr$ to few decades, Guo et al., 2019).

LaMassa et al. (2015) discovered, through optical and X-ray observations, the first changing look quasar that transitioned from a type 1 to a type 1.9 quasar in one decade. Nowadays, three possible physical mechanisms could explain this rapid changing look behavior: 1) dust reddening (variable obscuration due to obscuring material, Tran et al., 1992); 2) accretion rate change (compatible with an evolutionary scenario of AGN, Elitzur et al., 2014); 3) tidal

[11] 1 Gyr to form a torus (Hao et al., 2011).

[12] In merging events, an SMBH can be kicked out (or be recoil), and it brings along the accretion disk, and BLR, but not the dusty torus due is less tightly bound to it (Loeb, 2007; Civano et al., 2010).

disruption events (e.g. a star disrupted by the SMBH, Merloni et al., 2015). The dust reddening mechanism has been discarded for most of the sources (see, e.g. Hutsemékers et al., 2020). Meanwhile, the accretion rate and the tidal disrupt events mechanisms are still in debate (e.g. Zhang, 2021; Nagoshi et al., 2021).

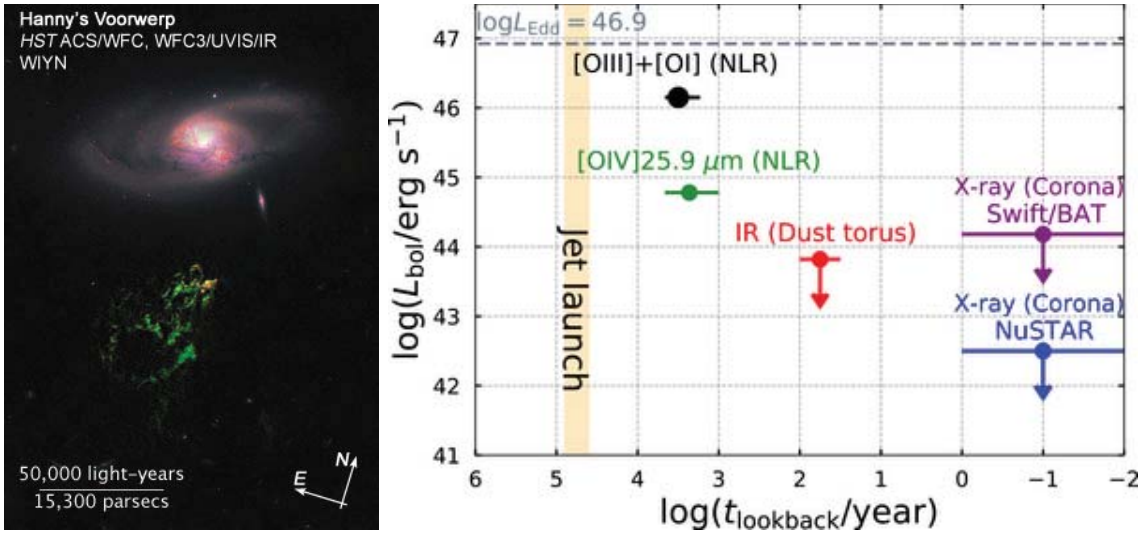

Figure 1.6: Left: Hannys Voorwerp object. Illustration from NASA, ESA, and Z. Levay. Right: Long-timescale light curve of Arp 187 based on the AGN indicators with multiple physical scales. The estimated look back time is based on the light crossing time of each emission region. Figure from: Ichikawa et al. (2019b).

Currently, it is clear that AGN have activity cycles. However, it is not clear how and why they initiate or finish. Marconi et al. (2004) suggested that the active phase should last $10^7 - 10^9$ yr spread in small duty cycles of 10^5 yr each (see also Novak et al., 2011; Schawinski et al., 2015; Shulevski et al., 2015). Additionally, these duty cycles could be a key factor in understanding the relationship between the AGN and the host galaxy. Several physical processes are associated with these duty cycles, such as reignition, enhancement, and fading of AGN. These processes are studied through the differences in the energy budget between the accretion disk, the NLR (optical ionizing echoes), and torus (mid-IR dust echoes).

The Hanny's Voorwerp object near the spiral galaxy IC 2497 is a clear example of a fading AGN and was found through of study of optical ionization echoes (see Figure 1.6 Lintott et al., 2009). See the right panel of Figure 1.6, which is taken from Ichikawa et al. (2019b). This object shows an NLR spanning a projected range from 15 to 35 kpc from the galaxy nucleus that should have been produced by an AGN at least 2 orders of magnitude higher in bolometric luminosity than the current nuclear luminosity. This indicates that the nucleus faded from a QSO-like luminosity to a modest Seyfert/LINER level within 10^5 yr. The nucleus of the galaxy Arp 187 is another case of fading an AGN and was found through mid-IR dust echoes. This source showed a clear decline of nuclear activity (with over 1000 times lower luminosity) in an estimated time-lapse of 10^4yr (Ichikawa et al., 2017, 2019a,b). Recently, Ichikawa et al. (2019b) claimed that the nucleus of Arp 187 has already ceased its activity, with its NLR and jet being evidence of the past activity (see Figure 1.6, right).

Currently, it is well known that the unified model needs several major modifications (see Netzer, 2015, for a review). Other models have been proposed implying a connection between AGN classes through an evolution induced by the perturbations of the near environment due to the fall of gas to the nucleus (e.g. Krongold et al., 2003a; Koulouridis, 2014). Several authors propose that AGN components should be modified. For example, the accretion disk may not exist, being replaced by an inefficient corona (Liu & Meyer-Hofmeister, 2001). These models search for an analogy between the accretion states of the X-ray binary system (XRBs) and AGN. It is known that XRBs on the active period go through phases when their accretion disk evolves in different states (Done et al., 2007). At high Eddington ratios, the accretion flow in XRBs forms a geometrically thin disk as proposed by (Shakura & Sunyaev, 1973). Eventually, this thin disk evolves to a radiatively inefficient accretion disk (Narayan et al., 1998) because the inner region is progressively evaporated as the Eddington ratio drops down (Ruan et al., 2019). This idea of similarity between accretion disks in AGN and XRBs is supported by observational evidence of similar characteristics between both systems (e.g., the fundamental plane of BH activity, Merloni et al., 2003; Falcke et al., 2004; McHardy et al., 2006).

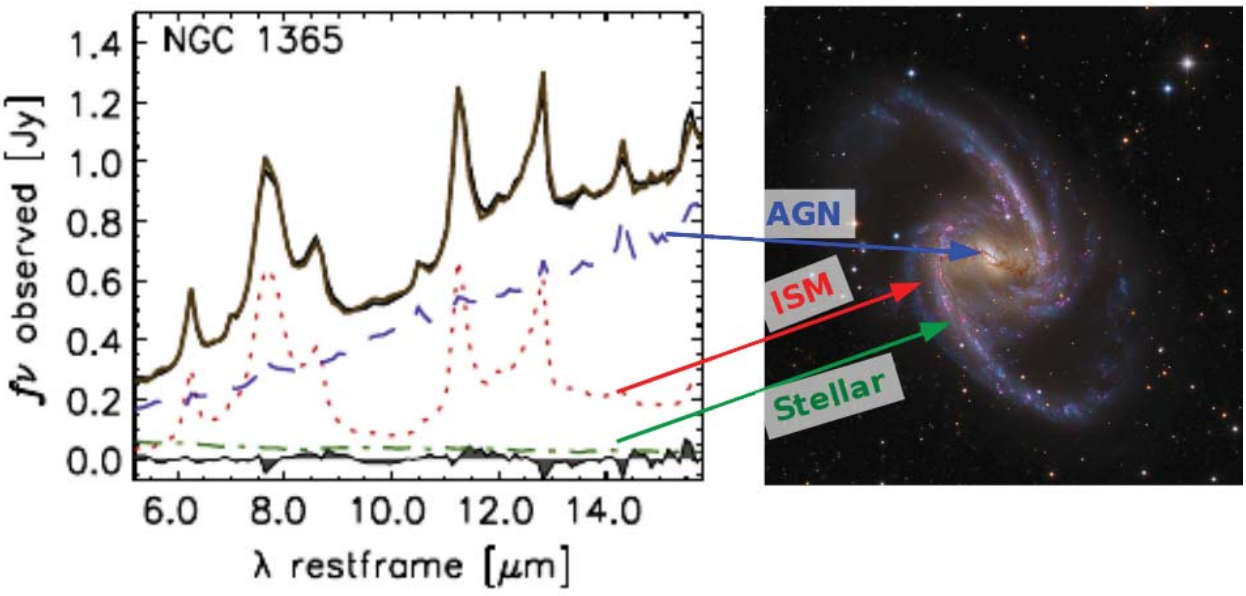

Figure 1.7: Right: IRS spectrum of NGC 1365 (black solid line). The dotted, dashed, and dotted-dashed lines show the ISM (PAHs), AGN, and stellar components, respectively. The shaded area at the bottom represents the residuals. Figure adapted from Hernán-Caballero et al. (2015). Left: Optical image of this source. Figure from Mike Selby and Leonardo Orazi (right, taken from *Astronomy Picture Of the Day*: *https* : *//apod.nasa.gov/apod/ap*210108.*html*).

1.4 AGN at mid-IR wavelengths

The infrared wavelengths are a powerful tool to study some properties of AGNs, even detecting those that are highly obscured which are not detectable to optical or X-ray wavelengths

(Netzer, 2013). The AGN mid-IR spectrum has several components that allow us to study the circumnuclear star formation and the dusty structure associated with the AGN.

Figure 1.7 shows a decomposition of an AGN spectrum at these wavelengths using the three main physical components (Hernán-Caballero et al., 2015): Interstellar medium (ISM), stellar emission, and AGN. This spectrum shows several emission lines at 6.2, 7.7, 8.6, 11.3, and 12.7 μm associated with the polycyclic aromatic hydrocarbon (PAH) features which can be used as star-formation tracers (e.g. Esquej et al., 2014). The PAHs are molecules in space that contain 20-100 carbon and hydrogen atoms, which are heated at high temperatures by young B stars (Peeters et al., 2004). The PAHs emission has been observed in the nuclear regions close to the AGN (e.g. González-Martín et al., 2013; Alonso-Herrero et al., 2014; Esparza-Arredondo et al., 2018). Other mid-IR spectral lines observed at this wavelengths provide important information about the AGN power, components, and environment. For example, the [OIV] $\lambda\,25\mu$m, the [SIV] $\lambda\,10.5\mu$m, [NeV] $\lambda\,14.32\mu$m, and [NeIII] $\lambda\,15.56\mu$m are used to identify AGN and study their NLR (e.g. Diamond-Stanic et al., 2009; LaMassa et al., 2010; Dasyra et al., 2011; Dicken et al., 2014).

Through photometric data from WISE and *Spitzer*, the color-magnitude and color-color diagrams have been created to use mid-IR wavelengths to identify AGN systematically. These diagrams use observations at four mid-infrared bands, 3.4, 4.6, 12, and 22 μm to study galactic and extragalactic sources (Stern et al., 2012; İkiz et al., 2020). In this way, it is possible to separate different emissions in the galaxies and, therefore, distinguish normal galaxies from AGN (Jarrett et al., 2011).

Other relevant signatures observed in this regime are the broad absorption/emission features around $10\mu m$ and 18μm, which are known as the silicate features. Like the mid-IR continuum, these silicates are a feature of the dust properties in the AGN. They have also been observed mostly in emission in type 1 AGN while in absorption in type 2 AGN (e.g. Hao et al., 2005; Siebenmorgen et al., 2005; Hatziminaoglou et al., 2015). Several works suggest that observational differences such as the width and shift of their peaks of these silicates emissions are correlated with a different fraction on the composition and/or size of the dust grains (e.g. Shi et al., 2006; Li et al., 2008; Xie et al., 2017; Martínez-Paredes et al., 2020). This thesis is focused mostly on the analysis of the mid-IR continuum to infer the properties of the dust in AGN.

1.5 AGN at X-ray wavelengths

The primary X-ray emission in AGN is produced by an optically thin corona of hot electrons plasma close to the accretion disk that scatters its energy due to inverse Compton (see Netzer, 2015; Ramos Almeida & Ricci, 2017, and references therein). This Comptonization produces one of the main components of X-ray spectra known as the intrinsic continuum (primary X-ray radiation). This component is modeled through a power-law[13] characterized

[13]The intrinsic continuum is usually modeled with a power-law for simplicity, although a Comptonization model would be a more physically motivated description.

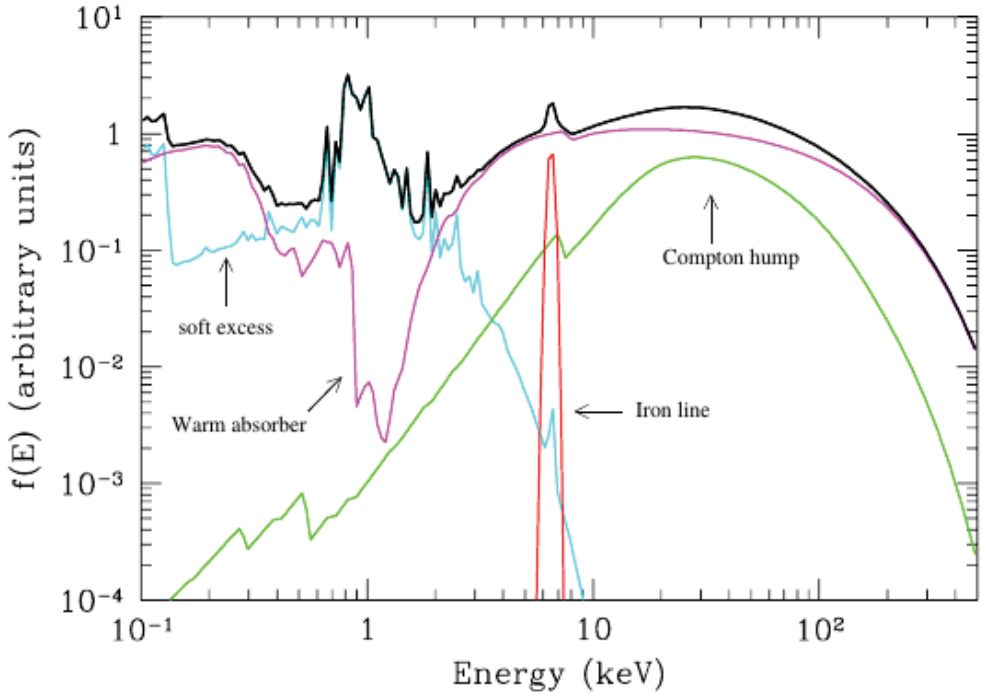

Figure 1.8: Average total spectrum and main components in the X-ray spectrum of a type I AGN. Figure from (Risaliti & Elvis, 2004).

by the photon index (Γ), and it dominates the spectral emission above 2 keV when not severely obscured. This emission is also a function of the high energy cutoff, E_{cut}, (Haardt & Maraschi, 1991; Marinucci et al., 2015), and the normalization. One part of this emission is reprocessed by the inner parts (accretion disk, BLR, and/or dust torus) to produce the two other components: 1) the Compton hump that shows a broad bump with its energy peak at $\sim$ 30keV and 2) the iron Kα emission line at 6.4 keV (Fe Kα, see Figure 1.8).

The Compton hump depends on the geometry of the reflecting medium (covering factor of the torus, Cf, and the average column density, N_H) of the reflector (Ghisellini et al., 1994). The shape of Fe Kα line depends on the chemical composition of reflector and its origin: 1) if it is produced in the surface of the accretion disc, the line is broad due to relativistic effects, while 2) if the origin is the cold neutral gas in the torus then the line is narrow. Although this line has been claimed to come from the accretion disk for a few objects (e.g., early works by Tanaka et al., 1995), the narrow line has been largely considered a signature of the cold neutral gas in the torus. Indeed, where the X-ray continuum is unobscured, the equivalent width (EW) of Fe Kα narrow line depends on the number of photons absorbed. Then, the EW of this feature is a clear signal of the torus in AGNs (Guainazzi et al., 2005). In obscured sources, large EWs are expected because most of the radiation of the intrinsic continuum is blocked by obscuring clouds (Ghisellini et al., 1994). Therefore, the X-ray reflected emission is a good tool for the diagnostic of the torus properties (Bassani et al., 1999; Panessa et al., 2006).

At wavelengths below 2 keV, two less understood components are observed: the soft excess and the warm absorber. The soft excess is commonly observed in Sy1 AGN as an

excess of X-ray emission below 1 keV (e.g. Halpern, 1984; Turner & Pounds, 1989; Scott et al., 2012). Several explanations have been explored, some of these are: 1) the warm Comptonization scenario[14], 2) the blurred ionized reflection[15], 3) the signature of strong, relativistically smeared, partially ionized absorption in the wind from the inner disk (see Boissay et al., 2016, and reference therein). The warm absorber is constituted by narrow absorption features at $\sim 0.7 - 0.8$ KeV observed in several numbers of Sy1s (e.g. Reynolds, 1997; Crenshaw & Kraemer, 1999; Monier et al., 2001; Ebrero et al., 2016). This feature is a blend of various absorption lines and absorption edges. It has been studied for many AGNs thanks to the high-resolution data. Krongold et al. (2003b), and Netzer et al. (2003) proposed that the matching of several absorption lines is due to the presence of two or three phases of the absorbing medium, at different temperatures and ionization stages.

This work is focused on the study of the neutral and distant reflection component observed at hard X-rays in AGN due to its potential use as a tracer of the torus properties.

1.6 Aim of this work

The unification model requires substantial revision. The cornerstone of the unified model is the obscuring structure, which is classically simplified as a torus. As explained above, both mid-IR and X-ray wavelengths can give information on this structure's composition, distribution, and geometry. However, although somehow accepted, the link between the dust-producing mid-IR continuum and the gas-producing X-ray reflection is unclear yet. The mid-IR continuum and the reflection components at X-rays are key to understanding the AGN obscuring component because both depend on the shape of the reprocessing material. There are several models developed for each wavelength range that attempts to reproduce the observed spectra (see Chapter 2). However, at both wavelengths, the observations cannot fully constrain all the parameters associated with these models and return a clear idea of the distribution of the material in the inner regions.

Furthermore, there are several possible hypotheses to understand the complexity of the AGN. There is a lot of evidence in favor of an evolutionary scenario whose timescale span is beyond the reach of human life. Nevertheless, several techniques have been developed to understand the AGN cycles through multi-wavelength approaches in the last years. The ignition and fading processes and their duration are fundamental to understanding the AGN evolution and its link to their host-galaxy coevolution. In this context, the obscuration component is key to distinguish between the early and late phases of AGN activity.

Based on the above open questions, three are the objectives of this thesis:

[14]This scenario proposes that UV photons from the accretion disk are up-scattered by a second Comptonizing corona cooler and optically thicker than the corona responsible for the primary emission.

[15]This scenario proposes that the emission lines produced in the inner part of the ionized disk are blurred by the proximity of the SMBH.

Objective 1

The first goal of this thesis is to investigate the complexity of the obscuring structure in AGN. We aim to understand whether the same structure that produces the reflection component at X-rays emits at mid-IR through dust heating in AGN.

Objective 2

This work explores the possibility that a simultaneous fitting of mid-IR and X-ray data can better restrict the dusty-gas torus parameters of AGN.

Objective 3

This work searches for a sample of fading and rising AGN to ponder the role of this obscuration component in the evolution of AGN activity.

Chapter 2

Methodology

This chapter includes information on the observations and catalogs used along this thesis. Furthermore, it also includes the models, assumptions, and statistical methods most relevant to this work.

2.1 Observations

2.1.1 Infrared observations

Infrared radiation[1] was discovered by the astronomer William Herschel in the 1800s while studying the sunlight (E. Scott Barr, 1961). For more than a century the infrared radiation was used to explore objects of the solar system as the moon, the sun, and some planets (see references in Walker, 2000). Modern infrared astronomy started around 1950 with the crucial advantage of the development of cryogenic detectors, which allowed the detection of fainter sources (Bond, 2000). In 1960, the first infrared magnitude system, which covers the wavebands R, I, J, K, L, and Johnson bands defined by Harold L Johnson (Johnson, 1960). At the end of this decade, the first observations of AGNs at mid-IR wavelengths were obtained through ground-based telescopes (Becklin & Neugebauer, 1969; Kleinmann & Low, 1970).

Another step forward was achieved thanks to the first infrared space-based observatories. In 1983 the Infrared Astronomy Satellite (IRAS) was launched with the mission to create the first all-sky survey from 10 to 100 μm. IRAS was a great step forward in the identification of new AGN because it demonstrated that these sources had an excess of mid-IR emission compared with normal galaxies, even showing distinct colors among them in the IRAS bands (see Keel et al., 2005, and reference there). The idea of the evolutionary scenario to explain the origin of AGNs (see Section 1.3) arose from these observations for the first time (Sanders et al., 1988). Twelve years after, the Infrared Space Observatory (ISO) was launched with four instruments onboard that covered the range between 2 and 240 μm. The resolution of

[1] infrared radiation is the emission due to the conversion of thermal energy into electromagnetic energy, i.e., it is due to photons emitted due to changes in the energy states of orbital electrons in the atoms or vibrational states and rotational of the molecular bonds.

observations from ISO allowed understanding how the mid-IR spectrum depends on different interstellar media and their heating mechanisms. These results allowed us better discrimination of infrared emission from AGN versus star formation at their host galaxy (e.g. Sturm et al., 2000).

A particularly difficult issue of mid-IR observations is that the background at mid-IR wavelength is larger than most astronomical sources' flux. Therefore, several observational techniques such as "chopping-and-nodding" are needed to subtract this background with a high precision[2].

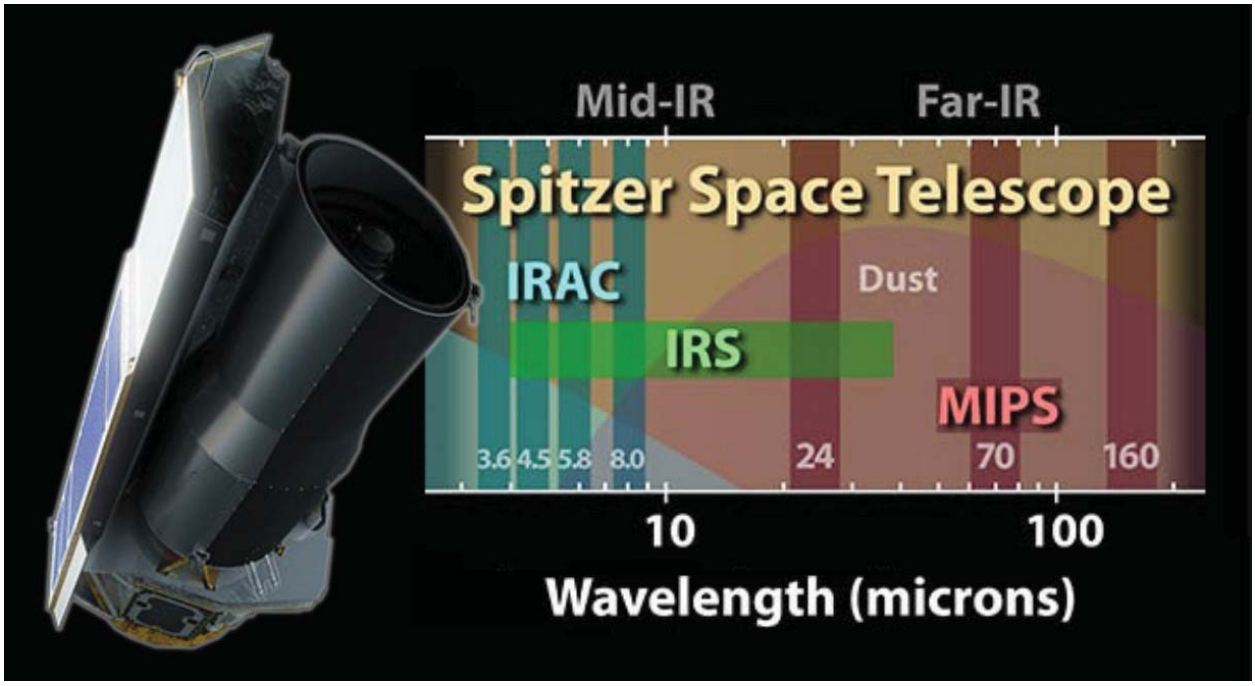

Figure 2.1: Illustration of the *Spitzer* telescope and diagram of the wavelength coverage for each of its instruments. The red and blue colors in the background of the image show the contribution due to dust and starlight, respectively. The blue vertical bands show the four IRAC filters. The red/brown vertical bands mark the three MIPS bands. MIPS is also capable of obtaining spectra in the range of 50 to 100 μm (red/brown horizontal band). The green horizontal band shows the range where the IRS instrument takes four spectra which together cover the range between 5.3 to 40 μm. IRS is the main instrument used in this thesis. Images courtesy of NASA/JPL-Caltech.

At the beginning of this century (2003), the *Spitzer* space telescope was launched with three different instruments onboard: the Infrared Array Camera (IRAC), the Multiband Imaging Photometer for *Spitzer* (MIPS), and InfraRed Spectrograph (IRS). Figure 2.1 shows the spectral range covered by each of these instruments. *Spitzer* was able to obtain spectral and photometric observations between 3 and 180 μm during 5.5 years. Then, it continued to get imaging at 3.6 and 4.5 μm until its deactivation on January 30, 2020. *Spitzer* had several advantages from their predecessors, such as its superior resolution, sensitivity, and spectroscopic capability. It helped to answer several questions related to the AGN and their environment. For instance, the connection between star-formation (SF) and AGN

[2]http://www.gemini.edu/sciops/instruments/mir/MIRChopNod.html

activity or the nature of the material that produces the obscuration on AGN (see Lacy & Sajina, 2020, for a complete review of AGN's works using *Spitzer* and references therein). A substantial part of this thesis work was developed using *Spitzer* spectra obtained with the IRS instrument, covering the spectral range between 5-30 μm with a spatial resolution ($\sim$3.6" at 5 μm and $\sim$7" at 30μm).

After *Spitzer*, several telescopes have been launched, as the Herschel Space Observatory, with instruments that cover the range between 55-671 μm, the Wide-field Infrared Survey Explorer (WISE) that produced an all-sky survey in four infrared bands (3.4, 4.6, 12, and 22 μm), and the Stratospheric Observatory For Infrared Astronomy (SOFIA) that is a Boeing 747SP airplane modified to carry a telescope with a diameter of 2.7 meters which carries observations are concentrating on the far-IR and sub-mm wavelengths. Unlike these telescopes, *Spitzer* is the only one able to obtain spectra that cover a broad range of mid-IR wavelengths where the dusty-torus emission dominates.

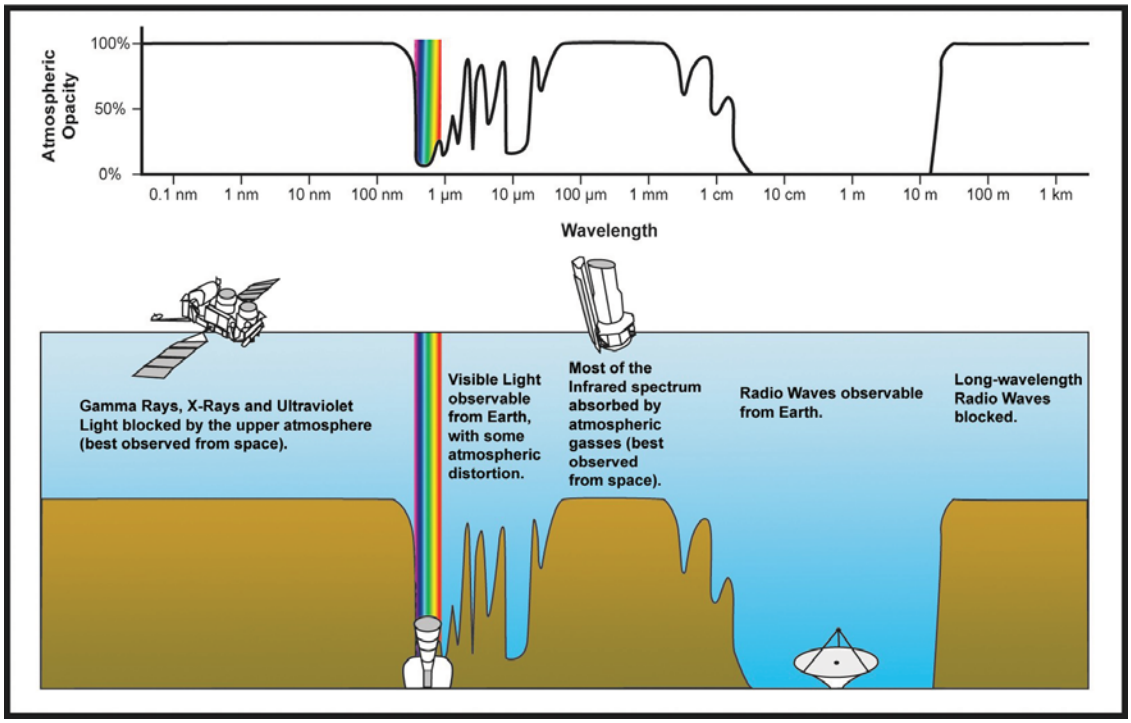

Figure 2.2: Atmospheric absorption percentages of the electromagnetic spectrum. Image credit: NASA

In the last 10 years, several infrared instruments have been developed and installed in ground-based telescopes which are also capable to produce high-resolution observations at these wavelengths. Particularly, in the case of AGN's studies, some of the instruments used are: VLT spectrometer and imager for the mid-IR (VISIR at VLT), Thermal-Region Camera Spectrograph (T-ReCS at Gemini), and CanariCam and EMIR at GTC (Gran Telescopio Canarias). These ground-based telescopes have better spatial resolution compared with that of space-based telescopes, which allow us to isolate the AGN contribution at a few tenths of parsecs from the nucleus. However, at infrared wavelengths, the earth's atmosphere only has some narrow windows allowing this radiation to be observed through ground-based telescopes

(see Figure 2.2). Furthermore, considering that the water vapor is one of the main absorbers of infrared radiation, these kind of telescopes must be sited in dry regions (mainly at high mountains) where the effect of water vapor is reduced and/or the atmosphere is thinner. Due to these complications, the number of observed AGN with a good quality, to study the inner regions of these sources, is limited.

The spectral resolution of *Spitzer*/IRS is similar to that obtained by ground-based observations and does not have these problems due to the atmosphere. The CASSIS[3] catalog provides a large number of reduced AGN observations (Cornell Atlas of *Spitzer*/IRS Sources, Lebouteiller et al., 2011), allowing to study large samples of AGN with uniform observations. All the above reasons explain why we use *Spitzer* spectra in this thesis work.

Certainly, the James Webb Space Telescope (*JWST*) will be the next great step in developing infrared astronomy and open a new way to explore the AGN. The *JWST* will cover the near- and mid-IR range (0.6-28.3 μm) with high sensitivity and resolution through four instruments: NIRCam, MIRI, NIRISS, and NIRSpec. *JWST* will be able to obtain high-resolution ($\sim$0.11 arcsec/pixel between $5-12\,\mu$m) mid-IR spectra of nearby AGN. The *JWST* sensitivity could, for instance, identify obscured AGN at the low luminosity range and/or at high redshift.

2.1.2 X-ray observations

The X-ray radiation was discovered by the physicist Wilhelm Konrad Röntgen in 1895 while studying the effects of cathode rays (electron beams) in electric discharges through low-pressure gases (Rontgen, 1896). He observed that a screen coated with a fluorescent material placed outside a discharge tube would glow even when this screen was shielded it from the direct visible and ultraviolet light of the gaseous discharge. He deduced this phenomenon was due to a new kind of radiation invisible that could cross the tube and caused the fluorescence of the screen. He also observed that opaque objects placed between the tube and the screen are transparent to this radiation. The first human radiography was obtained that day.

Unlike other wavelengths, such as optical, the earth's atmosphere absorbs most X-rays. Therefore, the observation of the universe through this wavelength is impossible from ground-based observatories. Because of these observations of cosmic sources through X-ray needed great technological efforts. The X-ray astronomy began in the early 1960s when the first X-ray telescope was launched under the direction of Riccardo Giacconi (Giacconi et al., 1962). The first two sources observed through the X-ray detectors of this telescope were Scorpius X-1 and Sagittarius (Giacconi et al., 1964).

The X-ray telescopes are very different from optical telescopes because X-rays do not reflect light in the same way that visible mirrors. The X-ray telescopes use grazing incident mirrors to focus X-ray emission. These mirrors have to be aligned nearly parallel to the incoming X-ray photons. The mirrors of these telescopes have paraboloids and hyperboloid shapes, which make these telescopes look more like a set of nested barrels (see Figure 2.3).

[3]http://cassis.astro.cornell.edu/atlas/

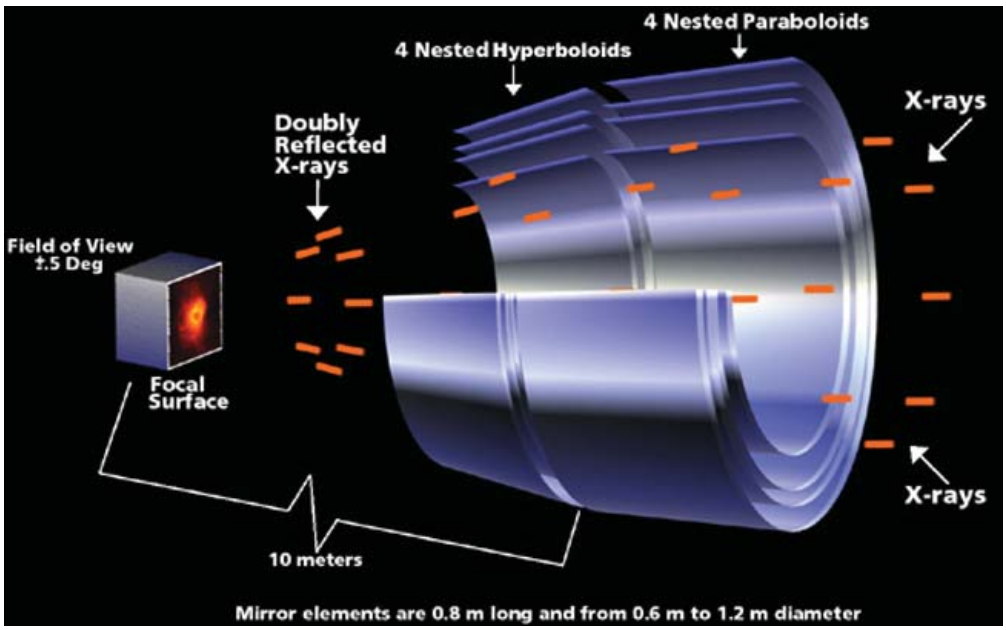

Figure 2.3: Schematic of grazing incidence (Wolter-I geometry). This cutaway illustrates the design and functioning of the High Resolution Mirror Assembly (HRMA) on Chandra. Illustration: NASA/CXC/D.Berry.

The number of coaxial surfaces increases the collection area of the telescope (i.e., the sensitivity), while the characterization of these surfaces places constraints on the spatial resolution (e.g., the better-polished surfaces give better spatial resolution).

During the 70s some X-ray missions were launched as: Small Astronomical Satellite 1 (*SAS-1, Uhuru* Giacconi et al., 1971), *Ariel V* (Smith & Courtier, 1976), the Third Small Astronomy Satellite (*SAS-3* Marshall & Clark, 1984), Orbiting Solar Observatory 8 (*OSO-8* Serlemitsos et al., 1976), and the Einstein Observatory (*HEAO-2* Giacconi et al., 1979). Particularly, the Ariel V satellite found that Sy1 galaxies are a class of X-ray emitters (Hayes et al., 1980) and discovered the existence of the iron emission line at 6.4 keV in extragalactic sources (Mitchell & Culhane, 1977). From 1980 to the early 2000s several X-ray satellites were active and studied the universe such as: the Rossi X-ray Timing Explorer (*RXTE*, Bradt et al., 1990), the Roentgen Satellite (*ROSAT*, Truemper, 1982), the Astro-C (Ginga) (Makino & ASTRO-C Team, 1987) , the Advanced Satellite for Cosmology and Astrophysics (*ASCA*, Tanaka et al., 1994), and the BeppoSAX (Boella et al., 1997). Through these satellites, several features of the AGN X-ray spectrum, such as variability and the existence of broad components for some of the iron emission lines, were discovered (e.g. Inoue, 1989; Brandt et al., 1994; Page, 1998; Madejski et al., 2001). Furthermore, these satellites provided for the first time all-sky surveys at X-rays. A wonderful result coming from the all-sky survey of the recently launched *eRosita* satellite is the existence of two very hot bubbles emitting at X-rays below and above the galactic plane of our galaxy. These bubbles wrap the two previously found smaller bubbles at gamma rays (Predehl et al., 2020). These bubbles may be the relics of former AGN activity in SgrA*.

In the last two decades, several X-ray missions were launched and continued active today.

Among these missions are the *Chandra* X-ray observatory (*AXAF* or *CXO*, Weisskopf et al., 2003) and the X-ray Multi-Mirror Mission (*XMM-Newton*, Jansen et al., 2001) both launched in 1999. These telescopes cover the energy range between $\sim 0.5 - 10\,\mathrm{keV}$ and $0.2 - 10\,\mathrm{keV}$, respectively. The advantage of the *Chandra* observatory is its high spatial resolution ($\sim$ 0.5-1.0 arcsec) thanks the unprecedented polishment and calibration of the four coaxial mirrors. Meanwhile, the advantage of the *XMM*-Newton observatory is its high sensibility (1227 cm^2 @ 1KeV) thanks to the collecting power of its 58 nested mirrors a poor spatial resolution ($\sim$15 arcsec). Then, other missions were launched as *Swift* (Burrows et al., 2005) and *Suzaku* (Mitsuda et al., 2007) which cover the energy range between $0.2 - 150\,\mathrm{KeV}$ and $0.2 - 600\,\mathrm{KeV}$, respectively, with lower spatial resolution (several arcmin).

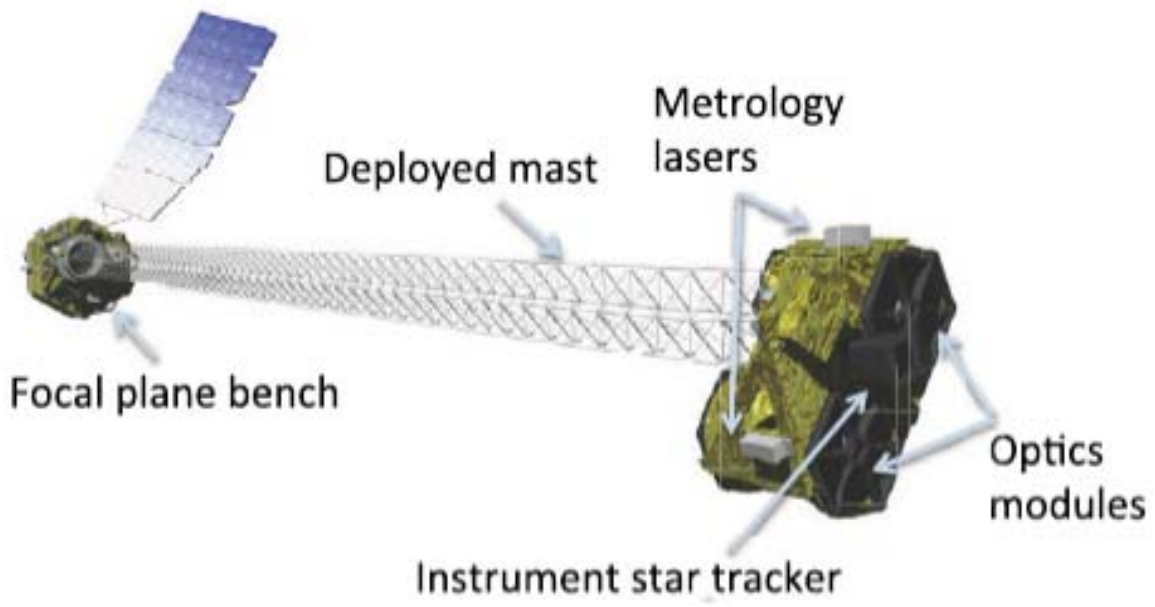

Figure 2.4: Diagram of the *NuSTAR* observatory in deployed configuration. Figure from (Harrison et al., 2013).

Parameter	Value
Energy range (KeV)	$3 - 79$
FoV at 10 KeV	10'
FoV at 68 KeV	6'
Angular resolution	18"
Energy resolution at 10 KeV	400 eV
Energy resolution at 68 KeV	900 eV

Table 2.1: Summary of performance parameters of NuSTAR telescope

The **Nuclear Spectroscopic Telescope Array** (***NuSTAR***, Harrison et al., 2013) is one of the most recent X-ray missions. After Swift, Suzaku, and BeppoSAX, it is the fourth mission dedicated to observing the hard X-rays ($3 - 79\,\mathrm{KeV}$), albeit with enough sensitivity to observe faint and distant AGN. *NuSTAR* has two co-aligned grazing incidence

telescopes (optics modules), focusing X-rays onto two Focal plane module detectors (FPMA and FPMB) located in an aluminum structure. The optics modules and focal plane are separated by a mast which provides a focal length of 10 meters. Metrology lasers are used to measure the varying translation, tilt, and rotation of the optics relative to the detectors. These changes are due to the thermal conditions, which vary over an orbit and with aspect angle relative to the Sun. These measurements are used during data processing to remove image blurring. Each optical module contains 133 nested multilayer-coated grazing incidence shells in a conical approximation to a Wolter-I geometry (see Figure 2.4). *NuSTAR* is ideal for studying the obscuration of the AGN due to its unprecedented combination of sensitivity and spatial and spectral resolution (see Table 2.1). This thesis used this satellite because, thanks to its unprecedented spectral coverage above 3 keV and sensibility, this satellite is ideal for characterizing the reflection component in AGN, which is one of the main subjects of this thesis work.

In the following years, several X-ray upcoming missions such as X-ray Imaging and Spectroscopy Mission (*XRISM* XRISM Science Team, 2020), *Athena* (Barcons & Athena Science Study Team, 2011), and the enhanced X-ray Timing and Polarimetry mission (*eXTP* In't Zand et al., 2019) promise great scientific advances due to improving technology. These missions will determine key details of the universe, such as SMBH growth and even the spin of BH, thanks to X-ray observations.

2.1.3 Ancillary multi-wavelength observations

To search for fading or rising AGN candidates (objective 3, see Section 1.6) we have compiled multi-wavelength information from the following catalogs:

Sloan Digital Sky Survey

The SDSS is a survey that started operations in 2000 through two telescopes located at the 2.5-m f/5 modified Ritchey-Chrétien altitude-azimuth telescope located at the Apache point observatory in southeast New Mexico and the Irénée du Pont Telescope at Las Campanas Observatory in northern Chile (Gunn et al., 2006). The data obtained through these telescopes are available through different data releases: SDSS-I (2000-2005), SDSS-II (2005-2008), SDSS-III (2008-2014), and SDSS-IV (2014-2020).

The SDSS-IV includes the data from three surveys: 1) Surveying galaxies and quasars to measure the Universe (Wavelength: $360 - 1000$ nm, resolution R ~ 2000, eBOSS, PI: Kyle Dawson), 2) Exploring the Milky Way from both hemispheres (APOGEE-2, PI: Steve Majewski, Wavelength Range: $1.51 - 1.70\mu$m. Spectral Resolution: R$\sim 22,500$), and 3) Mapping the inner workings of thousands of nearby galaxies (MANGA, Wavelength: $360 - 1000$ nm, resolution R ~ 2000, Bundy et al., 2015). The data are available through the web page: https://dr16.sdss.org. The SDSS archive contains infrared and optical spectra, imaging fields, and image mosaic creation. In this thesis, we use reddening-corrected emission line fluxes from SDSS (Berney et al., 2015).

Subarcsecond mid-infrared atlas of local AGN (Sasmirala)

This catalog is the first sub-arcsecond mid-infrared atlas of local AGN ($\langle z \rangle = 0.016$). It includes all publicly available N- and Q-band images obtained at ground-based 8-meter class telescopes (Gemini/Michelle, Gemini/T-ReCS, Subaru/COMICS, and VLT/VISIR). In total, it contains information on 253 AGN. The uniformly processed and calibrated images and nuclear photometry obtained through Gaussian and PSF fitting for all the objects and filters is contained in this atlas Asmus et al. (2014). The electronic access to the data is through the Virtual Observatory host at the German Virtual Observatory (GAVO): http://dc.g-vo.org/sasmirala. The nuclear 12 μm luminosities derived from this catalog are used in our work.

Swift-BAT AGN Spectroscopic Survey-II (BASS-II)

This catalog was created using the Burst Alert Telescope (BAT) instrument located on the *Swift* satellite. The goal of the BAT AGN Spectroscopic Survey (BASS) is to complete the first large ($>$ 1000AGN) survey of hard X-ray selected AGN with optical spectroscopy.

In this work, we used the multi-wavelength information compiled by the BASS-II catalog presented by Berney et al. (2015). This catalog considered the BASS data release 1 (Koss et al., 2017) which collected 559 optical spectra from targeted spectroscopic campaigns on BAT sources and public optical surveys (SDSS and 6DF Jones et al., 2009; Alam et al., 2015). The BASS-II catalog only considers the optical spectra of 340 AGN with a $z \sim 0.05$.

2.2 SED Models

2.2.1 Mid-IR AGN dust models

The AGN continuum emission at mid-IR wavelengths is dominated by the heating of the AGN dust component due to the AGN source (Prieto et al., 2001). Thus, the study of these wavelengths is crucial to study the AGN unification theories throughout the characteristics of this dust component. Several interferometric works at these wavelengths have been capable of resolving the nuclear dust distribution (e.g. Burtscher et al., 2013; Tristram et al., 2014; López-Gonzaga et al., 2016). Particularly, Tristram et al. (2014) studied the dust structure of the Circinus galaxy through this technique using MIDI/VLT observations. They found that its emission is distributed in two distinct components: a disk-like and extended component. This extended component is responsible for 80% of the mid-IR emission, and they associated this component with the dusty torus. However, López-Gonzaga et al. (2016) used this technique to studied the elongated mid-IR emission of 23 AGN and found that this emission in six of the sources is extended in a polar direction.

Unfortunately, this technique is restricted to the brightest and nearest AGN due to the high signal-to-noise required and spatial scales at play. Thus, these results might be biased to the most powerful and nearest AGN, which might not represent the entire AGN population.

Model	Dust distribution	Dust composition	N. SEDs	wv. range (μm) & N. bins	Parameters [range]
(1)	(2)	(3)	(4)	(5)	(6)
Fritz et al. (2006)	Smooth torus	Silicate & Graphite	24,000	0.001-1,000 178	i = [0 : 90] σ = [20 : 60] Γ = [0 : 6] β = [−1 : 0] Y = [10 : 150] $\tau_{9.7\mu m}$ = [0.1 : 10]
Nenkova et al. (2008a)	Clumpy torus	Standard ISM	1,247,400	0.001-1,000 119	i = [0 : 90] N_0 = [1 : 15] σ = [15:70] Y = [5 : 150] q = [0.0 : 3.0] τ_v = [10 : 300]
Hönig & Kishimoto (2010b)	Clumpy torus	Standard ISM ISM large Gr-dominated	1,680	0.01-36,000 105	i = [0 : 90] N_0 = [2.5 : 10.0] θ = [5 : 60] a = [−2.0 : 0] τ_{cl} = [30 : 80] (Y = 150)
Siebenmorgen et al. (2015)	Smooth & clumpy torus or/& outflow	Silicate & Amorphous carbon	3,600	0.0005-500 473	i = [19 : 86] R_{in} = [3 : 15.5] η = [1.5 : 77.7] τ_{cl} = [0 : 45] τ_{disk} = [0 : 1000] ($R_{out} = 170R_{in}$)
Stalevski et al. (2016)	Smooth & Clumpy torus	Silicate & Graphite	19,200	0.001-1,000 132	i = [0 : 90] σ = [10 : 80] p = [0 : 1.5] q = [0 : 1.5] Y = [10 : 30] $\tau_{9.7\mu m}$ = [3 : 11] (R_{in} = 0.5 pc)
Hönig & Kishimoto (2017)	Clumpy torus & outflow	Standard ISM ISM large	132,300	0.01-36,000 105	i = [0 : 90] N_0 = [5 : 10] a = [−3.0 : −0.5] θ = [30:45] σ = [7 : 15] a_w = [−2.5 : −0.5] h = [0.1 : 0.5] f_{wd} = [0.15 : 0.75] (Y = 500(large)/450(ISM)) ($R_{cl} = 0.035 \times R$) (τ_v = 50)

Table 2.2: Summary of the dusty models. Column(1): Author of the model. Column(2): Morphology and dusty distribution. Column(3): Dust chemical composition. Column(4): Number of SEDs produced. Column(5): Wavelength coverage and number of bins within the wavelength range. Column(6): Parameters and their range. Table showed by González-Martín et al. (2019a).

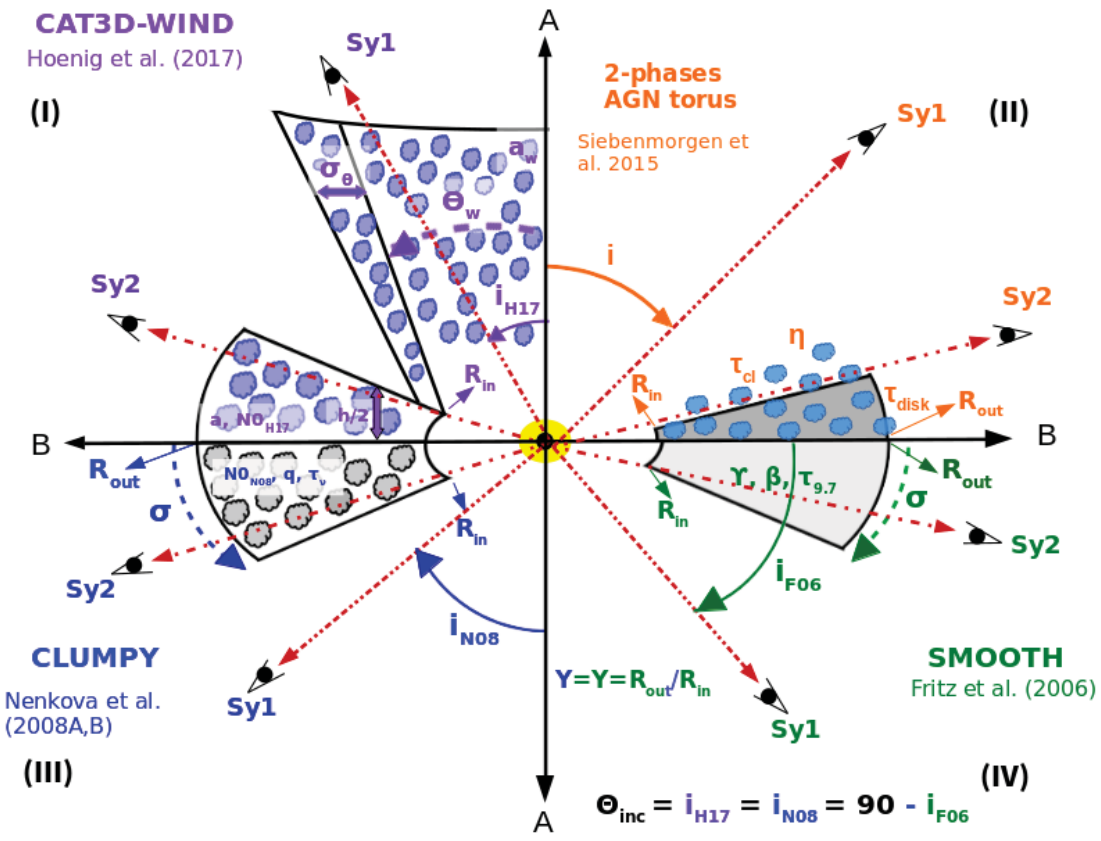

Figure 2.5: Sketch of the AGN dust structure proposed by different mid-IR models. The black and yellow circles show the BH and corona, respectively. The dust torus component is represented in each panel according to each mid-IR model. Sector (I): Disk-wind model (called CAT3D-WIND model) proposed by Hönig & Kishimoto (2017). Sector (II): 2-phases AGN torus model presented by Siebenmorgen et al. (2015). Sector (III): Clumpy model presented by Nenkova et al. (2008a,b). Sector (IV): Smooth model presented by Fritz et al. (2006). In panels I, II, and III, the blue and grey clouds represent clumpy dust distributions. In panels II and III, the grey shaded areas represent smooth dust distributions. According to each model, the dashed and dot-dashed lines mark the line-of-sights from which we observe Sy1 and Sy2. The respective parameters of each model are shown in the same color as its model name. See Table 2.2 for more details about each model.

Nonetheless, the spectroscopic technique does not have this limitation. Therefore, it is the best option to study this continuum emission on a large number of sources. The modeling of the spectral continuum at mid-IR allows us to study the properties of this structure.

During the last decades, several models that propose different distributions of this dust have been developed following the formalism of radiative transfer equations (e.g. Fritz et al., 2006; Nenkova et al., 2008b; Siebenmorgen et al., 2015; Stalevski et al., 2016; Hönig & Kishimoto, 2010b). These models assume different geometries, chemical properties, and dust distributions. According with their dust distributions they can be divided into three kinds: smooth (Fritz et al., 2006), clumpy (Nenkova et al., 2008a,b; Hönig & Kishimoto, 2010b, 2017), and smooth+clumpy (Stalevski et al., 2016; Siebenmorgen et al., 2015). Additionally, they can also be divided into two kinds of geometries: torus and torus+outflow. Table 2.2 compiles the properties of most of the models with broad SED libraries available in the literature. Furthermore, Figure 2.5 is a representation of some of these models. Through

these models, several parameters of the dusty structure can be derived, such as the torus angular width (σ), the relationship between the inner and the outer radius (Y), the number of clumps (N_0), among others. From these parameters, more complex quantities such as the covering factor, the total dust mass, and the outer radius of the structure can be derived (although this parameter sometimes is not restricted by the models, see Table 2.2).

Several works have used these models to fit spectra and photometry using high- and low-resolution observations of many AGN. Particularly, the smooth and clumpy models have been tested in large samples of AGN, finding differences in the torus parameters between type-1 and type-2 AGN (e.g. Ramos-Almeida et al., 2009; Ramos Almeida et al., 2011; Hönig et al., 2010a; García-Bernete et al., 2019) and even a dependency with the AGN luminosity (González-Martín et al., 2017, 2019b).

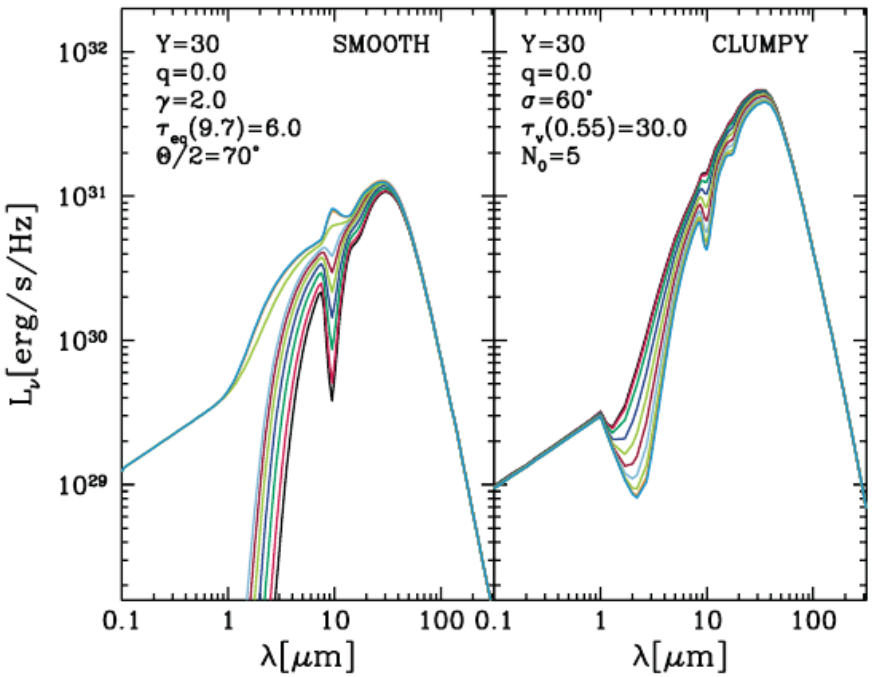

Figure 2.6: Examples of Smooth (left) and Clumpy (right) model SEDs with comparable model parameter values and different inclination angles. Figure from Feltre et al. (2012).

Issues of mid-IR dust models

The reasons why a clumpy rather than a smooth torus structure is preferred at mid-IR wavelengths are controversial. For example, clumpy models can explain the geometrical thickness of tori and the 10 μm silicate emission feature in the infrared spectra of Seyfert 2 galaxies. Feltre et al. (2012) performed a thorough comparison of these two models. They found that both models show very different behavior of the 10μm silicate emission feature (see Figure 2.6). However, this is due to both models' different chemical compositions rather than the actual dust distribution. They also concluded that there is not evidence of the dust being optically thin at 12.3μm for any of the two models, a characteristic which was reported to be typical of clumpy models but incompatible with the smooth model (Pier &

Krolik, 1992).

The disk-wind model is more recent. For this reason, it has been explored in fewer studies compared to the torus models discussed above. Indeed, it is capable of reproducing the recent interferometric observations of nearby AGN (López-Gonzaga et al., 2016). The NIR bump could be associated with the presence of nuclear hot dust linked to the wind component. Recently, González-Martín et al. (2019b) explored these dusty models with 110 available AGN SEDs drawn from the *Swift*/BAT survey with *Spitzer*/IRS spectroscopic data. They found that the disk-wind model by (Hönig & Kishimoto, 2017) is better at reproducing the mid-IR spectra of Sy1, while Sy2 galaxies are equally well fitted by both the clumpy torus and the disk-wind models. This result is also visible when dividing the AGN into high- and low-luminosity, the disk-wind model being better at reproducing high-luminosity AGN. However, they found large residuals for all models, indicating that the AGN continuum emission is more complex than predicted by the models or the space parameter is not well sampled.

None of these models is capable of constraining all torus parameters using only the mid-IR spectra. Ramos Almeida et al. (2014) found that to constrain all parameters is necessary to use the N-band spectrum together with the nuclear photometric data from near-IR. González-Martín et al. (2019a) found, using synthetic spectra, that *Spitzer* spectra in the range between $5 - 30\mu$m are enough to restrict all parameters. However, it is necessary to isolate the AGN emission from other emissions from star-formation and the interstellar medium. For this, high-resolution data are needed, which are not available yet for most of the objects. Although some objects have been observed from the ground in the 7-14μm range, full mid-IR coverage is not yet feasible from the ground. *JWST* will be key to solve this issue for large collections of sources. So far, we focus on objects where *Spitzer* can isolate the nuclear spectrum with a minor contribution from the circumnuclear contribution as suggested by González-Martín et al. (2019a).

2.2.2 X-ray reflection models

There are different models whose objective is to reproduce the X-ray reprocessing spectrum from a torus-shaped neutral medium, such as Mytorus (Murphy & Yaqoob, 2009), etorus (Ikeda et al., 2009), BNtorus (Brightman & Nandra, 2011), and ctorus (Liu & Li, 2015). These torus models are based on previous works that use Monte-Carlo simulations of photoelectric absorption, fluorescence, and Compton scattering to calculate X-ray spectra (e.g. Matt et al., 1991; Leahy & Creighton, 1993; Ghisellini et al., 1994; Nandra & George, 1994; Yaqoob, 1997). Among these models, there are several differences, such as the geometry of the torus and treatment of different components, e.g., the Compton scattering (Brightman et al., 2015). Table 2.3 shows a summary of the properties of the most common models used at X-rays for the distant neutral reflector, usually assuming a torus-like geometry. Note that these models return several parameters related to the reflecting material that they can compare directly with mid-IR models parameters, such as the viewing angle ($\theta_{\rm inc}$), the half-

Model Reference (1)	Gas distribution (2)	Lines (3)	Parameters [range] (4)
MYtorus Murphy & Yaqoob (2009)	uniform-density distribution	Fe Kα Ni Kα Compton shoulder	$\theta_{inc} = [0° - 90°]$ $\theta_{tor} = 60°$ $N_H = [10^{22} - 10^{25}]$ $\Gamma = [1.4 - 2.6]$ $E_{cut}/KeV = 200$ or 500 $A_{Fe}/A_{Fe,\odot} = 1$
etorus (Ikeda et al., 2009)	uniform-density sphere with polar cutouts and a central cavity	none	$\theta_{inc} = [1° - 89°]$ $\theta_{tor} = [0° - 70°]$ $N_H = [5 \times 10^{23} - 10^{25}]$ $\Gamma = [1.5 - 2.5]$ $E_{cut}/KeV = 360$ $A_{Fe}/A_{Fe,\odot} = 1$
ctorus (Liu & Li, 2015)	clumpy-density sphere with polar cutouts	Kα : Mg, Al, Si, S, Ar, Ca, Fe, Ni Kβ : Ca, Fe, Ni no compton shoulder	$\theta_{inc} = [19° - 89°]$ $\theta_{tor} = 60°$ $N_H = [10^{24}, 10^{25}]$ $\Gamma = [1.5 - 2.5]$ $E_{cut}/KeV = 500$ $A_{Fe}/A_{Fe,\odot} = 1$
BNtorus (Brightman & Nandra, 2011)			$\theta_{inc} = [18° - 87°]$ $\theta_{tor} = [26° - 80°]$ $N_H = [20.0 - 26.0]$ $\Gamma = [1 - 3]$ $E_{cut}/KeV = [0.1 - 320]$ $A_{Fe}/A_{Fe,\odot} = 1$
borus02 (Baloković et al., 2018)	uniform-density sphera with two conical polar cutouts	Kα : for all elements up to zinc Kβ : for all elements up to zinc Compton shoulder	$\theta_{inc} = [19° - 89°]$ $\theta_{tor} = [0° - 84°]$ $N_H = [22.0 - 25.5]$ $\Gamma = [1.4 - 2.6]$ $E_{cut}/KeV = [20 - 2000]$ $A_{Fe}/A_{Fe,\odot} = [0.01, 10.0]$
UXClumpy (Buchner et al., 2019)	clumpy distribution with the column density being decreasing toward the poles	Kα : C, O, Ne, Mg, Si, Ar, Ca, Cr, and Ni Fe Kβ	$\theta_{inc} = [0° - 90°]$ $\theta_{tor} = [6° - 90°]$ $N_H = [20.0 - 26.0]$ $\Gamma = [1.0 - 3.0]$ $E_{cut}/KeV = [60 - 400]$ $A_{Fe}/A_{Fe,\odot} = 1.0$ $CTkcover = [0. - 0.6]$

Table 2.3: Summary of the torus models used at X-rays to reproduce the X-ray reflection component. Column(1): Name of model and reference. Column(2): Morphology of the gas distribution. Column(3): Lines included by the treatment in the model. Column(4): Parameters and their range.

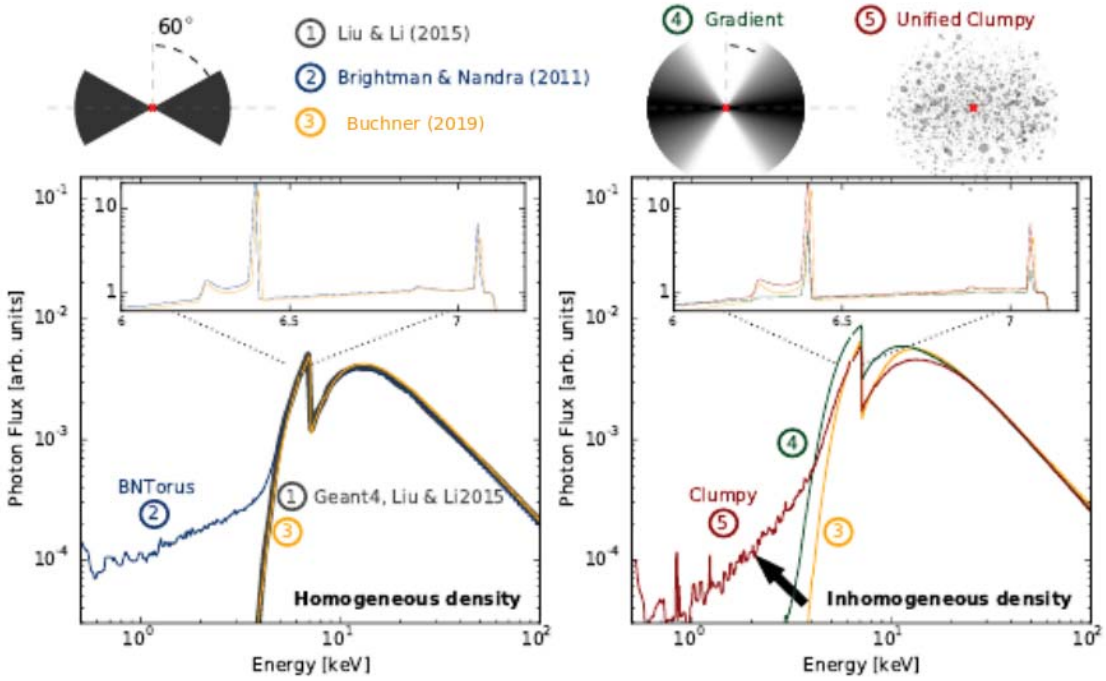

Figure 2.7: Simulated X-ray spectra with different geometries. Figure from Buchner et al. (2019).

opening angle $\theta_{\rm tor}$, and the average column density ($N_{\rm H}$, which can be compared with the optical depth).

In some works, these models together with the *NuSTAR* spectra have been used to study the strength and shape of the Compton reflection hump and, therefore, to determine the properties of the obscuring material (see Ramos Almeida & Ricci, 2017, and references therein). Particularly, these models have been used to study the covering factor since it is key to understand the diversity of AGN families (Brightman & Nandra, 2011).

The distribution of the gas has been explored already. Buchner et al. (2019) shows how the clumpy (i.e., non-homogeneous distribution of gas) could reflect into the spectral shape of the reflection component, including extended emission toward lower energies that is not visible in smooth models (see Figure 2.7).

In this work, we particularly use the smooth and clumpy models presented by Baloković et al. (2018) and Buchner et al. (2019), respectively. Figure 2.8 shows the illustrations of these two models as reported by their authors. The smooth model is known as "borus02" and proposes a smooth distribution of the gas around the inner parts of the AGN. One of the advantages of this model compared to the previous models is that it can independently calculate the column density of reprocessed material and that of the line-of-sight. Baloković et al. (2018) tested this model using four sources with available *NuSTAR* spectra: 3C 390.3, NGC 2110, IC 5063, and NGC 7582. Meanwhile, the clumpy model proposes a clumpy distribution of gas, and it is known as the "UXClumpy" model (Buchner et al., 2019). The geometry and parameters of this model were chosen to match the mid-IR clumpy model proposed by Nenkova et al. (2008b). This makes this model ideal to compare with the results

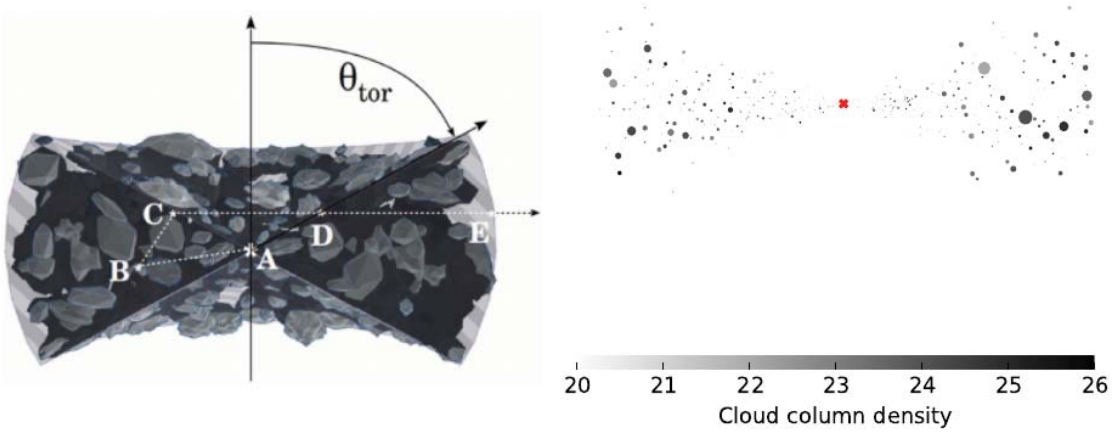

Figure 2.8: Sketches of the geometry and distribution of gas for the smooth torus (left) and clumpy torus (right) assumed at X-rays and presented by Baloković et al. (2018) and Buchner et al. (2019), respectively.

from mid-IR spectral fitting. Buchner et al. (2019) tested this model with *NuSTAR* spectra of several sources: Circinus, NGC 1068, NGC 424, NGC 3393, and ESO103-G035. Recently, Tanimoto et al. (2019) presented a new X-ray model that also assumes a clumpy distribution of gas. This model was also tested with *XMM-Newton*, *Suzaku*, and *NuSTAR* data from the Circinus galaxy. Unfortunately, this model is not publicly available yet.

Issues of X-ray reflection models

Most X-ray models are limited to torus-like geometries, which differ from observations. Although some effort has already been made to look for the X-ray signatures of a polar component, as assumed by disk-wind mid-IR models (e.g. Buchner, 2018; Liu et al., 2019), there are not available X-ray SED libraries of this type of models. For this reason, our analysis does not cover this geometry of the gas and dust.

Another issue is that some of the parameters of these models are linked together, e.g., the line-of-sight column densities and that of the reprocessed material, with a limited range of values. Currently, the X-ray spectra alone do not allow us to restrict the parameters of the models (e.g. Furui et al., 2016; Baloković et al., 2018). We overcome this issue by selecting reflection-dominated spectra to maximize the information on the shape of the reflection from the observations. Furthermore, we show that the simultaneous spectral fitting technique, combining mid-IR and X-ray spectra, can break the underlying degeneration among the parameters.

2.3 Scaling relations

2.3.1 Mid-IR versus X-ray luminosities

As already fully discussed in this thesis, the mid-IR and X-ray wavelengths are powerful tools to study the AGN. Both are key to understanding their nuclear regions and testing the

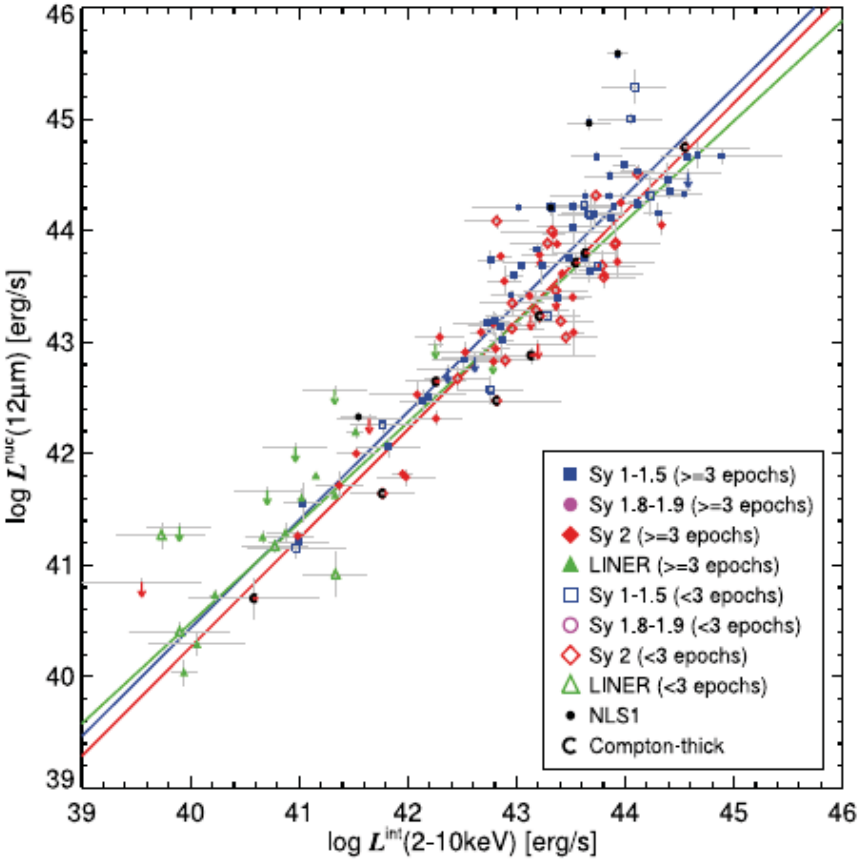

Figure 2.9: Relationship between the nuclear $12\,\mu$m and intrinsic $2-10\,$KeV luminosities for different AGN types. Figure taken from Asmus et al. (2015).

unification theories. Several works have investigated the relationship between the X-ray and mid-IR luminosity (e.g. Elvis et al., 1978; Glass et al., 1982; Krabbe et al., 2001; Lutz et al., 2004; Ramos Almeida et al., 2007). This relationship is interpreted as a connection between the accretion disk and the dusty torus, which mathematically has the form:

$$\log\nu\,\mathrm{L}(12\mu\mathrm{m}) \;=\; \alpha\log\mathrm{L}(2-10\,\mathrm{KeV}) \;+\beta$$

Where $\alpha = 1.11 \pm 0.07$ and $\beta = -4.37 \pm 3.08$ (Gandhi et al., 2009). This relationship heavily depends on the structure of obscuring dust. Obtaining the exact values of this relation is a hard task due to its requirement for nuclear isolation; therefore, high-angular-resolution data are required (e.g. Asmus et al., 2015). Sy1 and Sy2 follow the same relationship (see Figure 2.9), suggesting that they possess a similar dusty obscurer, following unification ideas. Outliers in this relationship might trace changes in shorter timescales of AGN activity because X-rays trace the current accretion disk emission while the mid-IR trace the echo of the past accretion disk emission processed by the distant dust emission.

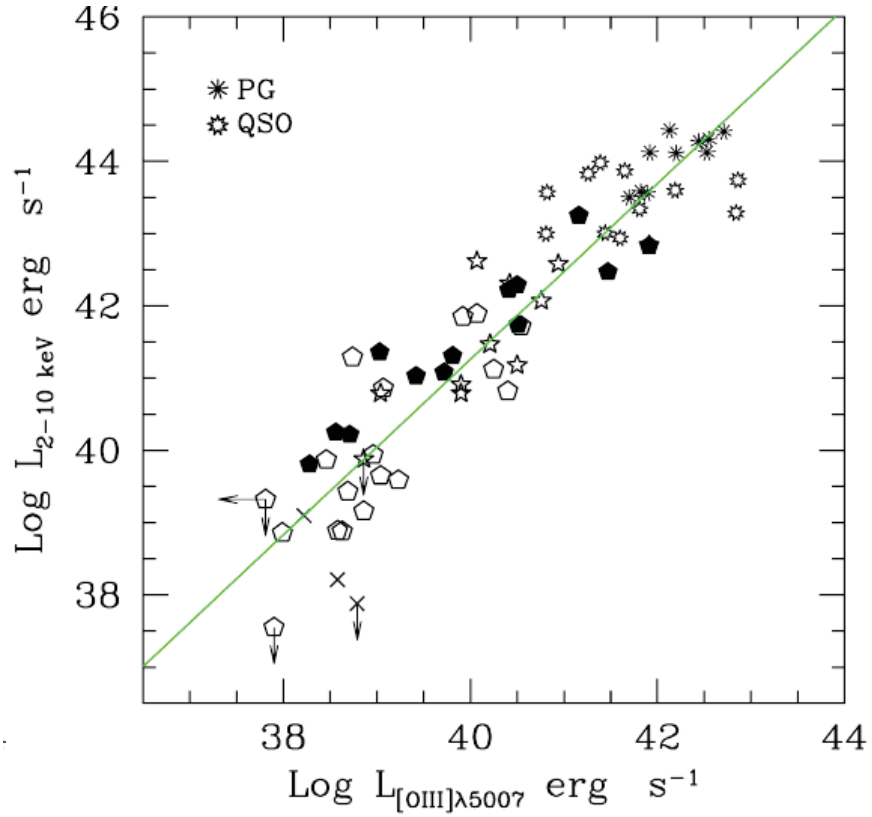

Figure 2.10: Relationship between the $2-10\,\mathrm{KeV}$ and [OIII] luminosities corrected for the Galactic and NLR extinction. The solid line shows the best fit linear regression line for a total sample of different AGNs. Filled polygons are Sy1, open polygons are Sy2, "mixed Seyfert" objects are indicated as crosses, Compton thick candidates are stars and low-z quasars are "rounded-stars". Figure from Panessa et al. (2006).

2.3.2 [OIII] versus X-ray luminosities

Several works have shown that a relationship between the [OIII] and hard X-ray luminosities that is a good option to study and complement the AGN search in surveys (see Figure 2.10 from Panessa et al. (2006)). This relationship can be interpreted as a connection between the accretion disk and the NLR, which mathematically have the form:

$$\log\nu\,\mathrm{L}(2-10\,\mathrm{KeV}) \;=\; \alpha\log\mathrm{L}([\mathrm{OIII}]) \;+\beta$$

Where $\alpha = 1.22 \pm 0.06$ and $\beta = -7.34 \pm 2.53$. (Panessa et al., 2006).

This relationship is well explored, showing a good behavior from high- to low-luminosity AGN (e.g. Ward et al., 1988; Panessa et al., 2006; González-Martín et al., 2009). Currently, this relationship is considered complementary to others for AGN selection in different surveys (e.g. Ueda et al., 2015). To minimize issues due to attenuation and/or obscuration, the slope and offset of this relationship are calculated using only unobscured AGN.

Although this relationship is well established, several issues arise from the nature of the different observations. A hard X-ray emission in the center of galaxies is considered a tell-tale sign of AGN. As mentioned in the previous sections, the X-ray luminosity can be used

as a tracer of the accretion disk. In fact, hard X-ray observations are able to provide one of the least biased AGN samples against obscuration (Ueda et al., 2015), although there are several problems to detect Compton-thick AGN only from X-rays (i.e. $\log(N_H[cm^{-2}]) > 24.3$, Tueller et al., 2008).

On the other hand, the [OIII] narrow emission line arises from gas located in NLR that is excited by the ionizing radiation escaping along the polar axis of the obscuring torus. This emission line is also used to infer the AGN bolometric luminosities and the accretion rates because it suffers only from moderate amounts of obscuration (Heckman et al., 2005).

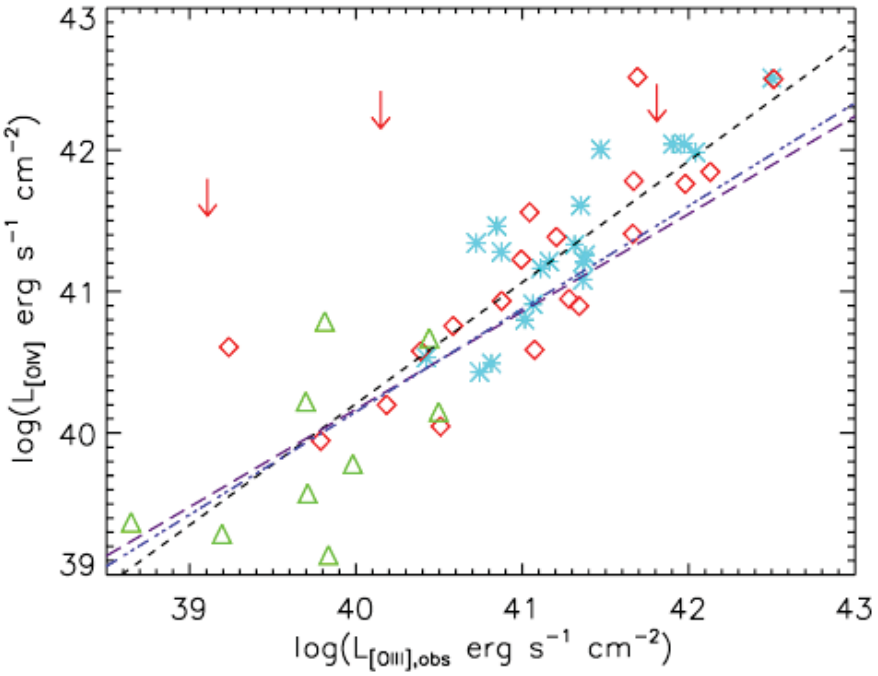

Figure 2.11: Relationship between $L_{[OIII]}$ and $L_{[OIV]}$. Cyan asterisk represents the [OIII] sample. The red diamonds and green triangles show the strong and weak PAH at 12 μm Sy2, respectively. Figure taken from LaMassa et al. (2010).

2.3.3 [OIII] versus [OIV] luminosities

In this work, we use the [OIII] emission line as a tracer of the NLR. However, this line could be affected by a large-scale extinction or contaminated by tidal tails seen after merging processes. To explore this, we compared [OIII] and [OIV] emission-line fluxes. The [OIV] emission line is classified as a good candidate for an isotropic tracer of AGN power in samples of Seyfert galaxies (e.g. Diamond-Stanic et al., 2009; LaMassa et al., 2010). This line is located at the longest wavelength end of the *Spitzer*/IRS window. This is fortunate because it is least likely to suffer from the effects of attenuation by the circumnuclear ISM (Dicken et al., 2014). According to Dicken et al. (2014), the relationship between these two emission lines has the following mathematical form:

$$\log L([OIV]) = 0.83 \log L([OIII]) + 7.5$$

Figure 2.11 shows the relationship between the [OIV] and [OIII] luminosities (LaMassa et al., 2010). The black dashed, purple dashed, and blue dot-dashed lines represent the relationships found by LaMassa et al. (2010), Diamond-Stanic et al. (2009), and Meléndez et al. (2008), respectively.

2.3.4 UV versus X-ray luminosities

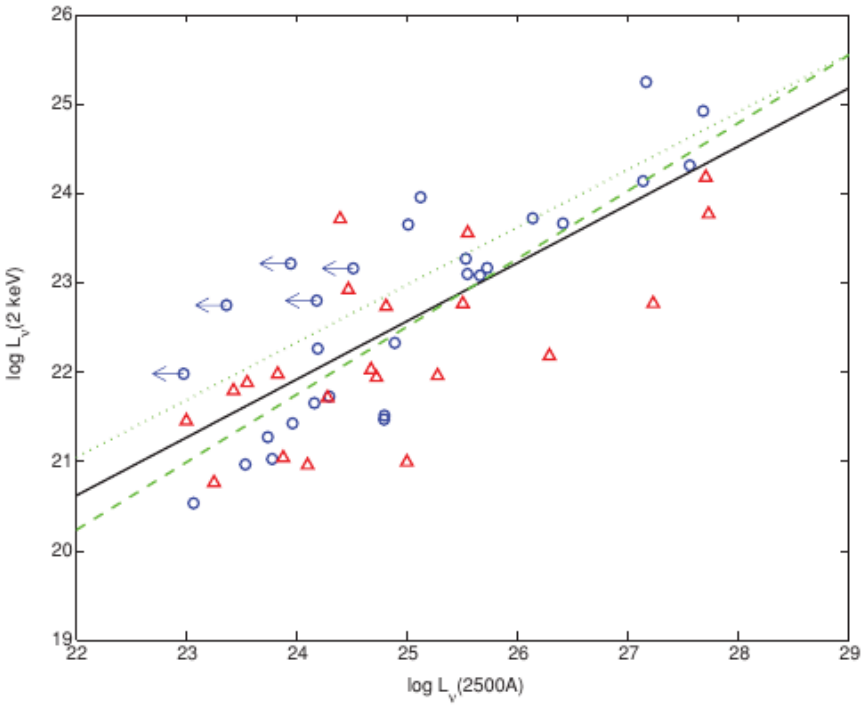

Figure 2.12: Optical/UV spectral luminosity at 2500 Å versus X-ray luminosity at 2 keV. Blue circles and red triangles refer to the Seyferts and LINERs sources, respectively. The black line corresponds to best-fitted found by Xu (2011). The green dashed and dotted lines correspond to the correlations found by Lusso et al. (2010) and Strateva et al. (2005), respectively. Figure is taken from Xu (2011).

The optical/UV continuum emission in AGN comes from the accretion disc; meanwhile, the X-ray emission is originated from the hot corona located above this disc. The X-ray can underestimate the disk emission if obscuration along the line of sight is not properly taken into account. Therefore, one way to explore whether the X-ray luminosity is a good tracer of the accretion disk luminosity is the comparison between X-rays and optical/UV luminosities. Figure 2.12 shows three correlations between these luminosities found in previous works. The general mathematical form of this relationship is:

$$\log \mathrm{L}_{\nu\,2\mathrm{KeV}} = \alpha \log \mathrm{L}_{\nu(2500\text{Å})} + \beta \tag{2.1}$$

Where $\alpha = (0.652 \pm 0.082)$, $= (0.760 \pm 0.022)$, or $= (0.648 \pm 0.021)$ and $\beta = (6.269 \pm 2.044)$, $= (3.508 \pm 0.641)$, or $= (6.734 \pm 0.643)$ according with Xu (2011), Lusso et al. (2010), and Strateva et al. (2005), respectively.

This relationship has been comprehensively studied in the last decades because it may provide a first hint about the nature of the energy generation mechanism in AGN and add to the understanding of the structure of the AGN accretion disk and X-ray corona (e.g. Strateva et al., 2005; Just et al., 2007; Young et al., 2010; Grupe et al., 2010; Lusso et al., 2010).

2.4 Simultaneous fitting technique

Developing a simultaneous fitting technique is required so the same tool can handle the spectral fitting at both X-ray and mid-IR wavelengths. The "X-Ray Spectral Fitting Package" (Xspec) can already handle x-ray spectra. Xspec is a command-driven, interactive, spectral fitting program within the HEASOFT software[4]. Classically, Xspec is used to analyze X-ray data from different satellites like *ROSAT*, *ASCA*, *Chandra*, *XMM-Newton*, *Suzaku*, *NuSTAR*, and *Hitomi*. Xspec already includes a large number of incorporated X-ray models (as mentioned in Section 2.2.2), and new models can be uploaded using the ATABLE and other tasks. Additionally, Xspec includes several statistical tests as introduced in Section 2.5.

Therefore, we chose to convert mid-IR data and models into Xspec format. For that purpose, we developed a code capable of converting mid-IR models and IRS/*Spitzer* spectra into Xspec format. This conversion processes is fully documented in González-Martín et al. (2019b). It consists in converting the SED libraries of each model to Xspec format in order to load each model as an additive table. To do so, we created a one-parameter table (in fits format) associated with all the SEDs using the FLX2TAB task within HEASOFT. We then wrote a python routine to change the headers associating each SED with a set of parameters. Each model has a number of free parameters plus redshift and normalization. Note that in the case of the clumpy model we were not able to obtain an Xspec model using the entire SED library owing to the unpractical size of the final model (over 100 GB). Instead, we slightly restricted the number of clouds and the angular width of the torus to the ranges $N_0 = [1, 3, 5, 7, 9, 11, 13, 15]$ and $\sigma = [15, 25, 35, 45, 55, 65, 70]$, respectively, to recover a more transferable model ($\sim$ 6 GB). The mid-IR spectra were converted through FLX2TAB task within HEASOFT which reads a text file that contains one or more spectra and errors and writes out a standard Xspec file and response file[5].

[4]https://heasarc.gsfc.nasa.gov/xanadu/xspec/

[5]The X-ray data are handled in event list in fits format that contain all positions, times, and energies of all the events detected. To analyze the X-ray data a file describing the calibration of the instrument is also needed called response matrix with the calibration of the instruments depending on the position and energy of each event recorded.

2.5 Statistical methods

2.5.1 Chi-square statistic

A chi-square (χ^2) statistic is a test that can be used to quantify how a model compares to observed data. This statistic compares the size of discrepancies between the expected results (e.g. observed spectrum) and the actual results (modeled spectrum), given the size of the sample and the number of variables in the relationship. This test considers the degrees of freedom to determine if a certain null hypothesis can be rejected based on the total number of variables and samples within the experiment. The equation to calculate the χ^2 is:

$$\chi^2 = \sum \frac{(O-e)^2}{e} \tag{2.2}$$

where O are observed values and e are expected values. The larger the value of χ^2 the less likely it is that null hypothesis (which assumes equality between both distributions data) is correct. In this work, we use the software Xspec which calculate the χ^2 value through the likelihood for Gaussian data, i.e.,

$$\chi^2 = \sum_{i=1}^{N} \frac{(y_i - m_i)^2}{\sigma_i^2} \tag{2.3}$$

where y_i are the observed data rates, σ_i their errors, and m_i the values of the predicted data rates based on the model[6]. Xspec also returns the reduced-χ^2 or $\chi^2_{\rm r}$ value, which is equal to χ^2/d.o.f. where d.o.f. is the number of degrees of freedom (number of data bins minus number of free parameters). The reduced-χ^2 value needs to be close to one, otherwise the observed data are likely not drawn from the model (χ^2/d.o.f. > 1) or the Gaussian sigma associated with the data are likely over-estimated (χ^2/d.o.f. < 1). Particularly, this work considers a good fit if χ^2/d.o.f. < 1.2. Additionally, Xspec returns the null hypothesis probability value which is the probability of the observed data being drawn from the model given the value of χ^2 and the number of degrees of freedom.

In this work, we use these statistics to test the goodness-of-fit between observed and simulated spectra through different models.

2.5.2 F-statistic

An f-test is a statistical test that compares the variance of two random independent samples. This test is used to identify the baseline model that best fits the data. The f-test require two regression models, one of which restrict one or more of the regression coefficients according to the null hypothesis. The classical formula to calculate this test is:

[6]https://heasarc.gsfc.nasa.gov/xanadu/xspec/manual/XSappendixStatistics.html

$$F = \frac{\left(\frac{RSS_0 - RSS_1}{p1 - p0}\right)}{\left(\frac{1 - RSS_0}{n - p1}\right)} \tag{2.4}$$

where RSS_i are the residual sums of squares of models i (0 or 1). Under the null hypothesis that model RSS_1 does not provide a significantly better fit than model 0, F will have an F distribution, with (p1 - p0, n - p1) degrees of freedom. The null hypothesis is rejected if the F calculated from the data is greater than the critical value of the F-distribution[7] for some desired false-rejection probability. In this work the critical value is 10^{-4}.

This f-test is contained in Xspec software and allows us to consider the values of χ^2 and number of degrees of freedom of two models[8]. In practise this test can be used only for nested models, where the new model adds complexity to the simpler one. Thus, it could be used to test if a parameter is needed to be untied or if a new component need to be included to significantly improve the fit. In this work, we consider several baseline models that assume different components for each wavelengths. We use this statistical test to choose the baseline model that best fit for our data among these.

2.5.3 Akaike method

The Akaike information criterion (AIC) is also a statistical test for evaluating how well a model fits the data. Emmanoulopoulos et al. (2016) re-calculated this criterion with a correction that considers the bias introduced by the finite size of the sample. The mathematical form is:

$$AIC_c = 2k - 2C_L + \chi^2 + \frac{2k(k+1)}{N - k - 1} \tag{2.5}$$

where C_L is the constant likelihood of the true hypothetical model, and does not depend on either the data or tested models, k is the number of free model parameters, and N is the number of data points. To compare two models, we need to calculate the difference between the criteria of both models like as:

$$\Delta[AIC_{c,2}] = AIC_{c,2} - AIC_{c,1} \tag{2.6}$$

where $AIC_{c,1}$ and $AIC_{c,2}$ are the AICs of *model1* and *model2* models, respectively. In general, the model with the lowest AIC is the 'most' preferred model among all models fitted to a given data set. The general rules to compare these model are:

- $\Delta[AIC_{c,2}] < 2$ values suggest 'substantial evidence' for the *model2* (in the sense that both models fit the data at least equally well).
- $3 < \Delta[AIC_{c,2}] < 7$ values indicates that the *model2* has considerably less support.
- $\Delta[AIC_{c,2}] > 10$ then the *model2* is highly unlikely.

[7] A F-distribution is a probability distribution continue.
[8] https://heasarc.gsfc.nasa.gov/xanadu/xspec/manual/node83.html

It is possible calculate the 'Akaike weight' of *model2* to estimate a quantitative measure of this statement, i.e. measure the the 'strength of evidence', following this equation

$$W[AIC]_{c,2} = \frac{e^{-\frac{\Delta[AIC_{c,2}]}{2}}}{e^{-\frac{\Delta[AIC_{c,1}]}{2}} + e^{-\frac{\Delta[AIC_{c,2}]}{2}}} \tag{2.7}$$

To compare the extent that one model is better than another one, we need to calculate the 'evidence ratio' following this equation:

$$\epsilon_2 = e^{-\frac{\Delta[AIC_{c,2}]}{2}} \tag{2.8}$$

where this value is calculated by the model with the largest difference (e.g. *model*2). These evidence ratio value is interpreted following these rules:

- If $\epsilon_2 \leq 0.01$ the *model2* is 100 times more likely than the *model1*.
- If $\epsilon_1 \geq 100$ the *model1* is 100 times more likely than the *model2*.

In this work, we use the AIC to compare different models (i.e. not nested) and determine which one statistically represents the best fit for the data.

Chapter 3

Torus properties for a sample of nearby AGN

In this chapter, we investigate the complexity of the obscuring structure in AGN. We chose a sample of 36 nearby AGN with available *NuSTAR* and *Spitzer* spectra. We chose these sources because they meet criteria that guarantee that mid-IR and X-ray spectra are dominated by the AGN dust and the reflection component, respectively. The mid-IR spectra of these sources have a stellar or interstellar contribution of less than 50%. Meanwhile, the reflection component of their X-ray spectra has at least 10% of contribution to the total spectra. We also discarded the sources where the reflection emission is due to ionized material in the disk.

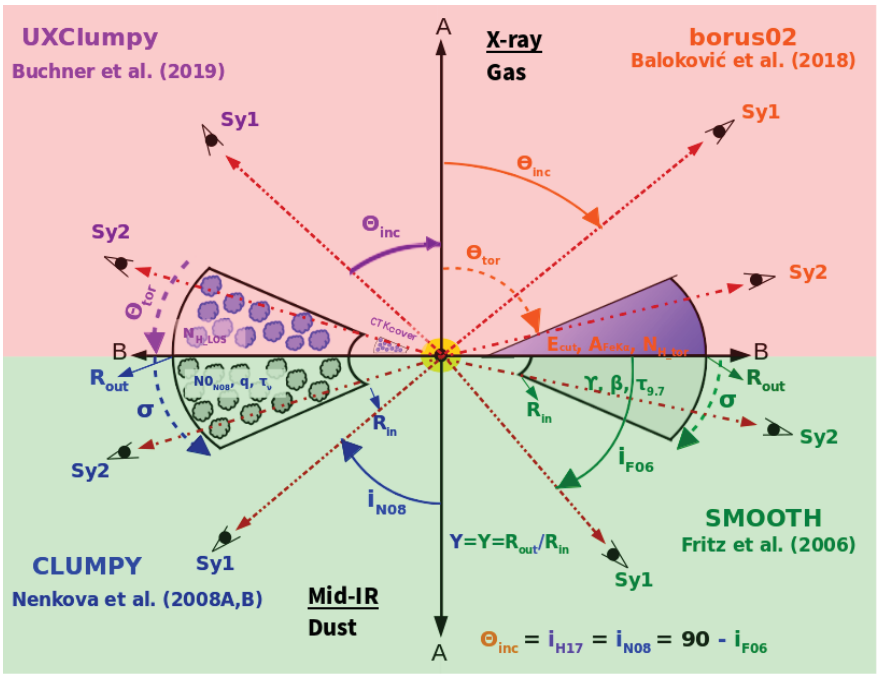

Figure 3.1: Illustration of the geometry of models used here. Top panel: X-ray models. Bottom panel: mid-IR models.

The disk reflection emission was studied through modeling relativistic reflection (*RELXILL* model[1] García et al., 2014; Dauser et al., 2014). *RELXILL* is an X-ray reflection model

[1]http://www.sternwarte.uni-erlangen.de/ dauser/research/relxill/

contained in XSPEC, which is used to constrain the properties of the accretion disk, such as the degree of ionization of the gas and the elemental abundances. The advantage of this model over its predecessors is that the radiative transfer is made to properly take into account the radiation of each point on the accretion disk to compute the resulting SED. We added this disk reflection model to the baseline model that returns the best fit for X-ray spectra.

We fitted these spectra with four mid-IR and X-ray baseline models (see Figure 3.1). These models assume a torus-like morphology with clumpy and smooth distributions of dust or gas (see Section 2.2 for their description). We only considered the mid-IR models that match in geometry and distribution with those available at X-rays. This is the reason why this analysis did not explore the disk-wind model. The resulting spectral fits using these models for each object in our sample are shown in Appendix B.

One of the main results of our investigation is that the distribution of gas and dust is complex if the gas-producing reflection at X-rays is associated with the dust responsible for the mid-IR dust continuum. We found at least six scenarios with different geometries and combinations of gas and dust distributions to explain our sample's observed properties. Moreover, it is worth highlighting that these scenarios are in agreement with the notion that gas could also be located in the dust-free region, which is also consistent with the large value for the gas-to-dust ratio found for the torus in our sample.

Author disclosure: This work was developed mostly on my own. Dra. Omaira González-Martín lead the analysis of the contribution of accretion disk reflection to the X-ray spectra. Dra. Omaira González-Martín and Dra. Deborah contributed to the review of the analysis, interpretation, and paper drafting. The other coauthors suggested changes and corrections to the final manuscript. This work was accepted in the Astronomy and Astrophysics Journal on April 20, 2021. The electronic version of this publication can be found in the following URL: https://arxiv.org/pdf/2104.11263.pdf

Astronomy & Astrophysics manuscript no. A_dust_gas_agn_torus
May 17, 2021

The dust-gas AGN torus as constrained from X-ray and mid-infrared observations

D. Esparza-Arredondo[1], O. Gonzalez-Martín[1], D. Dultzin[2], J. Masegosa[3], C. Ramos-Almeida[4,5], Ismael García-Bernete[6], Jacopo Fritz[1], and Natalia Osorio-Clavijo[1]

[1] Instituto de Radioastronomía y Astrofísica (IRyA-UNAM), 3-72 (Xangari), 8701, Morelia, Mexico
e-mail: d.esparza@irya.unam.mx
[2] Instituto de Astronomía (IA-UNAM), Mexico city, Mexico
[3] Instituto de Astrofísica de Andalucía (CSIC), Glorieta de la Astronomía s/n 18008, Granda, Spain
[4] Instituto de Astrofísica de Canarias (IAC), C/Vía Láctea, s/n, E-38205, La Laguna, Spain
[5] Departamento de Astrofísica, Universidad de La Laguna (ULL), E-38205 La Laguna, Spain
[6] Department of Physics, University of Oxford, Oxford OX1 3RH, UK

Received 03 December 2020; Accepted 27 April 2021

ABSTRACT

Context. In recent decades, several multiwavelength studies have been dedicated to exploring the properties of the obscuring material in active galactic nuclei (AGN). Various models have been developed to describe the structure and distribution of this material and constrain its physical and geometrical parameters through spectral fitting techniques. However, questions around the way in which torus mid-infrared (mid-IR) and X-ray emission are related remain unanswered.
Aims. In this work, we aim to study whether the dust continuum at mid-IR and gas reflection at X-rays have the same distribution in a sample of AGN.
Methods. We carefully selected a sample of 36 nearby AGN with *NuSTAR* and *Spitzer* spectra available that satisfy the following criteria: 1) the AGN component dominates the mid-IR spectra (i.e., the stellar and interstellar medium components contribute less than 50% to the spectrum), and 2) the reflection component contributes significantly to the X-ray spectrum. Furthermore, we discarded the sources whose reflection component could be produced by ionized material in the disk. We derived the properties of the nuclear dust and gas through a spectral fitting, using models developed for mid-IR and X-ray wavelengths assuming smooth and clumpy distributions for this structure.
Results. We find that a combination of smooth and clumpy distributions of gas and dust, respectively, is preferred for ∼ 80% of sources with good spectral fits according to the Akaike criterion. However, considering extra information about each individual source, such as the absorption variability, we find that ∼ 50% of our sources are best described by a clumpy distribution of both dust and gas. The remaining ∼50% of our sources can still be explained with a smooth distribution of gas and a clumpy distribution of dust. Furthermore, we explored the torus dust-to-gas ratio, finding that it is [0.01-1] times that of the interstellar medium.
Conclusions. The results presented in this paper suggest that the distribution of the gas and dust in AGN is complex. We find at least six scenarios to explain the observed properties of our sample. In these scenarios, three gas-dust distribution combinations are possible: clumpy-clumpy, smooth-smooth, and smooth-clumpy. Most of them are in agreement with the notion that gas could also be located in the dust-free region, which is consistent with the dust-to-gas ratio found.

Key words. Galaxies: active – Infrared: galaxies – X-rays: galaxies

1. Introduction

The term active galactic nuclei (AGN) is used to define the center of galaxies that contain a super-massive black hole (M_{BH} ∼ 10^6-10^9 $M_\odot$; SMBH) which is efficiently fed by material through an accretion disk (e.g., Kormendy & Richstone 1995; Kormendy & Ho 2013). The accretion disk, in turn, is embedded in a region of gas clouds with high-velocity dispersion known as the broad-line region (BLR; see e.g., Sulentic et al. 2000 and Marziani et al. 2010 for a review). These components are surrounded by an obscuring region composed of gas and dust that is traditionally referred to as the "torus" (Antonucci & Miller 1985; Urry & Padovani 1995). The classical unification model proposes that all classes of AGN observed are intrinsically the same but appear different merely due to the orientation effect (see Netzer 2015, for a review). However, the individual properties of the torus might also explain the AGN types, and they might be linked to changes in the accretion state ruled by the bolometric luminosity (L_{bol}) and/or the SMBH mass (Khim & Yi 2017).

Several techniques have been used to study the properties of the torus. They can be roughly divided into three categories: (1) interferometry (Tristram et al. 2009; Burtscher et al. 2013; Alonso-Herrero et al. 2018; García-Burillo et al. 2019; Impellizzeri et al. 2019; Combes et al. 2019); (2) reverberation (e.g., Suganuma et al. 2006; Koshida et al. 2014; Almeyda et al. 2017); and (3) spectral energy distribution (SED) fitting (e.g., Ramos-Almeida et al. 2009; Murphy & Yaqoob 2009; Ramos-Almeida et al. 2011; García-Bernete et al. 2019; Brightman & Nandra 2011; Liu & Li 2014; Furui et al. 2016; Yaqoob 2012; Esparza-Arredondo et al. 2019). Both interferometry and infrared (IR) reverberation are restricted to the brightest AGN due to the high signal-to-noise required and spatial scales at play. This work is based on the third technique, which allowed us to target larger AGN samples. Most of the AGN energy is produced in the ac-

cretion disk mainly by photons at ultraviolet (UV) and optical wavelengths. Dust absorbs part of this disk emission, which is then heated and reemitted as IR radiation (Rieke 1978). A portion of this UV and optical disk emission is also reprocessed by an optically thin corona of hot electrons' plasma above the accretion disk that scatters the energy in the X-ray bands due to inverse Compton scattering (Netzer 2015; Ramos Almeida & Ricci 2017, and references therein). This Comptonization produces one of the three main components seen in AGN at X-rays: the intrinsic continuum. The second and third components are the reflection of the intrinsic continuum, and the iron emission line at 6.4 keV (FeKα). These two components are produced due to the scattering of X-ray emission reflected by the inner walls of the torus or the BLR. While the FeKα line can be produced by material with column densities (N_H) as low as $N_H = 10^{21-23}\,cm^{-2}$, the Compton hump can only be seen by reprocessing X-ray photons in a Compton thick material $N_H > 10^{24}\,cm^{-2}$. The FeKα line and the Compton hump components might also be associated with the reprocessing of the intrinsic emission at the accretion disk (Fabian 1998; Laor 1991). Both the infrared continuum and the reflection components at X-rays depend on the shape (geometry and density) of the reprocessing material (e.g., Ghisellini et al. 1994; Nenkova et al. 2008a). Thus, comparing spectra and models helps to infer the properties of the AGN torus, which is otherwise unreachable for the vast majority of the AGN. Different sets of IR and X-ray torus models have been developed in attempts to reproduce the observed spectra (pioneering works by Krolik & Begelman 1988 and Granato & Danese 1994; see Ramos Almeida & Ricci 2017 for a review).

At mid-infrared (mid-IR) wavelengths, the stationary models that assume a smooth distribution of the dust were the first explored for computational reasons due to computational reasons (known as smooth models, e.g., Pier & Krolik 1992; Efstathiou et al. 1995; Manske & Henning 1998; Fritz et al. 2006). These smooth models were followed by models that adopt a clumpy distribution for the dust (e.g., Rowan-Robinson 1995; Nenkova et al. 2008a,b; Hönig et al. 2006; Schartmann et al. 2008; Hönig et al. 2010), a clumpy two-phase medium (Stalevski et al. 2012; Siebenmorgen et al. 2015), and more recently, a clumpy dusty disk with a polar outflow (Hönig & Kishimoto 2017). The smooth and clumpy models have been tested in large samples of AGN and have achieved to find differences in the torus parameters between type 1 and type 2 AGN (e.g., Ramos-Almeida et al. 2009, 2011; Hönig et al. 2010; Lira et al. 2013; García-Bernete et al. 2019) and even a dependency with the AGN luminosity (González-Martín et al. 2017, 2019B). However, obtaining the full set of parameters for the models has been difficult so far (Ramos Almeida et al. 2014; González-Martín et al. 2019B).

At X-ray wavelengths, several smooth and clumpy torus models have been developed to explore the reflection component produced by gas around the accretion disk (e.g., Murphy & Yaqoob 2009; Ikeda et al. 2009; Brightman & Nandra 2011). Although with slight differences in morphology, these models have made it possible to constrain several properties of the material that originates from the reprocessed emission. Only a few works have compared these models in an effort to constrain the model parameters (e.g., Liu & Li 2014; Furui et al. 2016; Baloković et al. 2018).

Although somehow accepted, the link between the dust-producing mid-IR continuum and the gas-producing X-ray reflection is not clear yet. Recently, a few works combine mid-IR and X-ray observations and models either by full spectral energy distribution (SED) fitting for a large collection of objects (e.g., Yang et al. 2020; Ogawa et al. 2020) or through the simultaneous fitting of both ranges for individual objects (see Esparza-Arredondo et al. 2019). The advantage of the simultaneous fitting technique is its capability to better constrain all the torus parameters. However, prior to performing the simultaneous fitting, the emission at both wavelengths needs to be confronted.

We present the results obtained from fitting a sample of AGN using the clumpy and smooth models to reproduce their mid-IR and X-ray emission. We discuss our results for each wavelength and how compatible they are with each other. Our goal is to understand if the same structure of material can produce both spectral components in AGN. A brief description of the models used in this work is shown in Sect. 2. The sample selection and spectral fitting methodology are described in Sect. 3.

The results for X-ray and mid-IR wavelengths are described in Sects. 4 and 5, respectively. The confidence range of error calculated here is 1 sigma. In Sect. 7 we discuss our results within the framework of our goals. Our conclusions are given in Sect. 8. Throughout this work, we assume a cosmology with $H_0 = 70\,km\,s^{-1}\,Mpc^{-1}$, $\Omega_M = 0.27$, and $\Omega_\lambda = 0.73$.

2. Description of the models

The models presented in this section were created through different radiative transfer codes and simulations, which include the physics required to account for mid-IR and X-ray main continuum features. All of them assume a torus-like morphology that obscures the accretion disk for certain inclination angles. Mid-IR models reproduce the continuum including re-emission due to dust outside the dust sublimation radius. X-ray models reproduce the reflection component and the FeKα emission line, assuming that both components come from a distant reflecting material composed by neutral gas. The X-ray models chosen here are more recent and flexible (more free parameters), and they solve some of the problems that affected their predecessors (see Liu & Li 2014). The mid-IR models are chosen to match those available at X-rays in geometry. Table 1 shows the parameters involved including coverage for each of them. Below we give a short description highlighting the main reasons why we chose them. We refer the reader to the primary papers for a complete description of them.

2.1. Mid-IR models

The two mid-IR models used to fit the mid-IR spectra in this work are presented below.

• Smooth model (by Fritz et al. 2006): This model considers a flared disk that is created as two concentric spheres with the polar cones removed and delimited by inner and outer radii. The model assumes a continuous/smooth distribution of dust with almost equal silicate and graphite proportions. The smooth model is a simple representation of the torus, but it is capable of giving a good approximation of the infrared SED of AGN (e.g., Esparza-Arredondo et al. 2019). This is the only mid-IR smooth torus model with a complete SED library in the literature to compare with the available X-ray models.

• Clumpy model (by Nenkova et al. 2008a,b): This model considers a toroidal distribution of dusty clumps with standard Galactic dust composition (53% silicates and 47% graphite). We favor this model over the other available clumpy torus models (in particular Hönig et al. 2010) because it provides the largest SED library, and it has been extensively used due to its probed

Model	Parameter	Range	Description
Smooth model	i	[0.01°, 90°]	Inclination angle respect to the equatorial plane
by Fritz et al. (2006)	σ	[20°, 60°]	Half-opening angle of the torus
	Y	[10, 150]	Ratio between the inner and outer radius
	γ	[0.01, 6]	Index of the logarithmic elevation density distribution
	β	[-1, -0.01]	Index of the radial profile of the density distribution
	$\tau_{9.7\mu m}$	[0.1, 10]	Equatorial optical depth at 9.7μ m
Clumpy model	i	[0.01°, 90°]	Inclination angle with respect to the polar plane
by Nenkova et al. (2008a,b)	σ	[15°, 70°]	Half-opening angle of the torus
	Y	[5, 100]	Ratio between the inner and outer radius
	N0	[1, 15]	Number of clouds in the equatorial plane of the torus
	q	[0.01, 2.5]	Slope of the radial distribution of clouds
	τ_ν	[10, 300]	Optical depth of each cloud
Smooth model (borus02)	θ_{inc}	[19°, 87°]	Inclination angle respect to the polar plane
by Baloković et al. (2018)	θ_{tor}	[0°, 84°]	Half-opening angle of the torus respect to the polar plane
	N_H	[22.0, 25.5]	Average column density of the torus [cm^{-2}]
	Γ	[1.4, 2.6]	Photon index of power law
	E_{cut}	[20,2000]	High-energy cut-off [KeV]
	$A_{Fe}/A_{Fe,\odot}$	[0.01,10.0]	Relative abundance of iron
Clumpy model (UXClumpy)	θ_{inc}	[0°,90°]	Inclination angle relative to the inner (flat) disk portion.
by Buchner et al. (2019)	θ_{tor}	[6°, 90°]	Cloud dispersion (half-opening angle of the torus)
	N_H	[20.0, 26.0]	Average column density of the line of sight [cm^{-2}]
	Γ	[1.0, 3.0]	Photon index of power law
	E_{cut}	[60,400]	High-energy cut-off [KeV]
	CTkcover	[0, 0.6]	Covering fraction of inner ring

Table 1. Summary of mid-IR and X-ray models used in this paper, including parameter range and description.

ability to explain the mid-IR emission of AGN at large range of luminosities (e.g., Ramos-Almeida et al. 2009; González-Martín et al. 2017; Martínez-Paredes et al. 2017; García-Bernete et al. 2019).

A comparison between these two mid-IR torus models is presented in Feltre et al. (2012). Recently, Hönig & Kishimoto (2017) presented a new radiative transfer model consisting of an inflowing disk dominating the near-IR emission and an outflowing wind emitting in the MIR (Hönig 2019). This model is motivated by the detection of a significant fraction of polar emission in the MIR in several nearby AGN (e.g., López-Gonzaga et al. 2016; Leftley et al. 2018). Although some effort has already been made to look for the X-ray signatures of this polar component (e.g., Buchner 2018; Liu et al. 2019), there are no available X-ray SED libraries for this type of model. For this reason, we did not explore disk+wind torus models here, in spite of their adequacy to reproduce IR spectra (e.g., González-Martín et al. 2019B).

2.2. X-ray models

The two X-ray models used to fit the X-ray spectra in this work are presented below.

- Smooth model (by Baloković et al. 2018): This smooth torus model is called borus02. The geometry of this model is a uniform-density sphere with two conical polar cutouts, where the opening angle is a free parameter. This geometry is fully compatible with the mid-IR smooth torus model by Fritz et al. (2006). We chose this model for its capability to separate the column density of the line of sight (LOS) and the reprocessing component that similar models lack (e.g., Brightman & Nandra 2011).
- Clumpy model (by Buchner et al. 2019): The so-called UXClumpy model assumes toroidal distribution with the column density being a monotonic function decreasing toward the poles. The geometry and parameters of this model were chosen to match the clumpy mid-IR model proposed by Nenkova et al. (2008a,b) (see Table 2 in Buchner et al. 2019), making this combination ideal for our work.

Baloković et al. (2018) and Buchner et al. (2019) compared the borus02 and UXClumpy models, respectively, with previous models (e.g., BNtorus by Brightman & Nandra 2011 and ctorus by Liu & Li 2014). They are the most recent among the available models with smooth and clumpy torus geometries. The inclination angle, θ_{inc}, photon index, Γ, and half-opening angle of the torus, θ_{tor}, cover similar ranges (see Table 1). In both models, the N_H parameter ranges are similar. However, the smooth model considers that the N_H from the torus and that of the LOS could be different (we test this possibility in Sect. 3).

3. Sample and spectral fitting

3.1. Mid-IR selection and spectral fitting

The initial sample included 169 AGN with available mid-IR IRS/*Spitzer* spectra within the CASSIS[1] archive (Lebouteiller et al. 2011) and X-ray *NuSTAR* (Harrison et al. 2013) observations. We only considered sources with more than 10 ksec of *NuSTAR*,

[1] https://cassis.sirtf.com

in order to have spectra with good signal-to-noise ratio, and full $\sim [5\mu m - 35\mu m]$ wavelength coverage for the IRS/*Spitzer* spectra. The final sample also included a minimum number of bins in the resulting X-ray spectrum (see below).

First, we converted IRS/*Spitzer* spectra into X-ray spectral fitting package XSPEC (Arnaud 1996) format using FLX2XSP task within HEASOFT[2]. Following the technique developed by González-Martín et al. (2019B), we fit each spectrum using four baseline models:

$$M1(IR) = zdust \times dust\,model \quad (1)$$
$$M2(IR) = zdust \times dust\,model + S\,tellar \quad (2)$$
$$M3(IR) = zdust \times dust\,model + IS\,M \quad (3)$$
$$M4(IR) = zdust \times dust\,model + IS\,M + S\,tellar \quad (4)$$

Where the "zdust" component is the foreground extinction by dust grains (Pei 1992). We found that the inclusion of zdust in "stellar" or "ISM" components or both is negligible since it returns similar results to those obtained when it is not considered. The ISM and stellar components are the interstellar medium and stellar population of 10^{10} years and solar metallicity. We note that a different choice of stellar population age does not affect the results. These components were taken from Smith et al. (2007) and Bruzual & Charlot (2003), respectively. Finally, the "dust model" corresponds to the smooth (Fritz et al. 2006) or clumpy (Nenkova et al. 2008a,b) torus models designed to describe the IR AGN emission. The initial parameters were set to the mean value over the parameter range. We computed the χ^2 statistic for the best fit by finding the absolute minimum within each parameter range. We then used f-statistics to test whether the inclusion of the stellar (eq. 2), ISM (eq. 3), or the stellar+ISM (eq. 4) components significantly improve the simpler model when f-test probability is below 10^{-4}.

We selected objects showing less than 50% of the stellar component compared to that of the torus component at 5μm and less than 50% of ISM component compared to that of the torus component at 30μm. González-Martín et al. (2019A) demonstrated that these restrictions are a good compromise to recover the model parameters using *Spitzer*/IRS spectra. We imposed that this condition be fulfilled when using both (clumpy and smooth) AGN dust models. In this way, we excluded 71 sources that are not AGN dominated at mid-IR wavelengths from our initial sample. This yielded a sample of 98 sources where the AGN dust dominates at mid-IR wavelengths that are sampled by *Spitzer*/IRS spectra.

3.2. X-ray selection

We used the High Energy Astrophysics Archive Research Center (HEASARC)[3] to download the data, and we processed the *NuSTAR* spectra of the 98 AGN with mid-IR *Spitzer* spectra dominated by the AGN dust. When multiple observations were available for a single object, we took the one with the longest exposure time to guarantee the best signal-to-noise ratio available.

The *NuSTAR* data processing was done using the data analysis software *NuSTARDAS* (v.1.4.4) distributed by HEASARC. The calibrated, cleaned, and screened event files were generated using the NUPIPELINE task (CALDB 20160502). We left the default pipeline option of not using any Atlantic anomaly (SAA) filtering. SAA high background periods do not significantly affect our observations, according to the *NuSTAR* SAA filtering reports. A circular region of $1' - 2'$ radius (depending on the brightness of the source) was taken to extract the source and background spectrum on the same detector and to compute the response files (RMF and ARF files) using the NUPRODUCTS package within *NuSTARDAS*. Finally, we used the GRPPHA task within the FTOOLS to group the spectra with at least 60 counts per bin. After reducing the data, we discarded 12 sources due to the low quality of the *NuSTAR* observations with fewer than 70 bins in the 3-70 keV range.

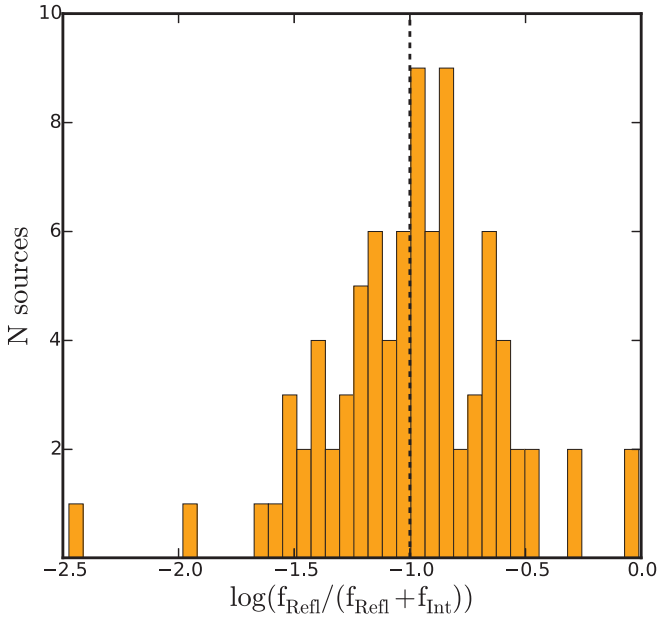

Fig. 1. Histogram of the reflection fraction in the 3-70 keV band for the sample of mid-IR AGN-dominated spectra (86 sources, see text).

We fit the remaining 86 *NuSTAR* spectra with a power-law model including neutral partial covering (modeled with *zpcfabs* within the XSPEC software) plus a reflection model. We are aware that attenuation from Compton scattering might have an impact at energies above 20-30 keV and is significant particularly when the column density of the gas in the LOS is larger than $\sim 10^{24}$ cm^{-2} (Maiolino et al. 2007). The only available model within XSPEC is CABS. Unfortunately, this model uses an inadequate approximation that results in a wrong spectral hardening, as reported by Murphy & Yaqoob (2009) and Yaqoob (2012). In fact, we carried out some tests, finding the inclusion of CABS results in unrealistically high luminosity (with intrinsic luminosity more than 10,000 times greater than the observed luminosity). Due to the lack of Compton-scattering models properly accounting for Compton scattering, we neglected this contribution. We note that many other works use the same approximation including only photoelectric absorption (e.g., Xu et al. 2017; Ronchini et al. 2019; Falocco et al. 2020; Wang et al. 2020). Therefore, the baseline model use in this work has the following form:

$$M(X-ray) = zpcfabs \times cutoffpl + reflection \quad (5)$$

The existence of the 6.7 and 6.96 keV emission lines was also tested by including Gaussian profiles at a fixed energy. For sample selection purposes, we chose the smooth torus model (borus02) for the reflection component (Baloković et al. 2018). We fixed the Ecut parameter from borus02 to 400 keV. We linked the photon index, high-energy cut-off, and column density parameters of the intrinsic and reflection components to the same

[2] https://heasarc.gsfc.nasa.gov/docs/software/heasoft/
[3] https://heasarc.gsfc.nasa.gov/docs/archive.html

Table 2. General properties of the sample

Object	Coordinates		Type*	z	L_X	M_{BH}[a]	Obsid	Exptime	NH
	RA	DEC			$\log(L_{2-10KeV})$	$\log(M/M_\odot)$		(k sec)	Variability
(1)	(2)	(3)	(4)	(5)	(6)	(7)	(8)	(9)	(10)
Mrk1018	02 06 15.98	-00 17 29.22	Sy1.8	0.0424	$42.89\pm^{0.03}_{0.03}$	8.03[1]	60301022003	43.3	N[1]
Mrk590	02 14 33.56	-00 46 00.18	Sy1.2	0.0213	$42.57\pm^{0.02}_{0.02}$	7.20[2]	90201043002	51.0	N[2]
PG0804+761	08 10 58.66	+76 02 42.45	Sy1	0.1000	$42.55\pm^{0.01}_{0.01}$	8.73[1]	60160322002	17.3	N[3]
RBS0770	09 23 43.00	+22 54 32.57	Sy1.2	0.0323	$43.80\pm^{0.01}_{0.01}$	7.34[1]	60061092002	18.8	-
I11119+3257	11 14 38.89	+32 41 33.48	Sy1	0.1890	$44.12\pm^{0.06}_{0.08}$	8.4[3]	60101045002	10.4	Y[4]
PG1211+143	12 14 17.67	+14 03 13.18	Sy1	0.0904	$43.85\pm^{0.01}_{0.01}$	7.49[2]	60001100007	74.8	N[5]
RBS1125	12 32 03.62	+20 09 29.49	Sy1	0.0630	$43.82\pm^{0.03}_{0.03}$	7.76[1]	60061229002	19.9	-
Mrk231	12 56 14.23	+56 52 25.24	Sy1	0.0422	$42.78\pm^{0.04}_{0.04}$	8.39[3]	80302608002	82.0	N[6]
Mrk1383	14 29 06.57	+01 17 06.15	Sy1	0.0866	$44.30\pm^{0.01}_{0.01}$	8.65[3]	60061254002	32.4	N[7]
Mrk1392	15 05 56.55	+03 42 26.34	Sy1.8	0.0361	$43.18\pm^{0.02}_{0.02}$	8.17[13]	60160605002	21.0	-
Mrk1393	15 08 53.95	-00 11 48.99	Sy1.5	0.0543	$43.88\pm^{0.01}_{0.01}$	7.87[1]	60376005002	30.8	Y[8]
PG1535+547	15 36 38.40	+54 33 33.21	Sy1	0.0451	$42.80\pm^{0.05}_{0.06}$	7.19[4]	60201023004	82.1	N[9]
ESO141-G055	19 21 14.15	-58 40 12.98	Sy1.2	0.0371	$43.94\pm^{0.01}_{0.01}$	–	60201042002	93.0	-
NGC7213	22 09 16.21	-47 10 00.08	Sy1.5	0.0051	$41.98\pm^{0.01}_{0.01}$	7.99[2]	60001031002	10.1	N[10]
MCG+01-57-016	22 40 17.06	+08 03 13.52	Sy1.8	0.0249	$42.79\pm^{0.02}_{0.02}$	7.20[13]	60061343002	21.3	-
UM146	01 55 22.02	+06 36 42.42	Sy2	0.0144	$41.84\pm^{0.06}_{0.07}$	6.23[13]	60465002002	28.4	-
NGC788	02 01 06.46	-06 48 57.15	Sy2	0.0136	$42.43\pm^{0.06}_{0.07}$	7.51[2]	60061018002	15.4	N[12]
NGC1052	02 41 04.79	-08 15 20.75	Sy2	0.0048	$41.74\pm^{0.01}_{0.01}$	8.19[2]	60201056002	59.6	Y[13]
NGC1358	03 33 39.68	-05 05 22.23	Sy2	0.0134	$42.38\pm^{0.02}_{0.03}$	7.88[2]	60301026002	49.8	-
J05081967+1721483	05 08 19.71	+17 21 48.09	Sy2	0.0175	$42.97\pm^{0.02}_{0.02}$	–	60006011002	15.5	-
Mrk3	06 15 36.45	+71 02 15.24	Sy2	0.0143	$43.53\pm^{0.01}_{0.01}$	8.65[2]	60002048004	33.4	N[14]
ESO428-G014	07 16 31.21	-29 19 28.89	Sy2	0.0054	$39.83\pm^{0.22}_{0.45}$	7.3[5]	60001152002	40.2	-
Mrk78	07 42 41.70	+65 10 37.43	Sy2	0.0371	$43.11\pm^{0.05}_{0.05}$	7.87[2]	60061336002	24.1	-
Mrk1210	08 04 05.86	+05 06 49.81	Sy2	0.0135	$44.63\pm^{0.02}_{0.02}$	7.1[6]	60061078002	15.4	Y[14]
J10594361+6504063	10 59 43.62	+65 04 06.37	Sy2	0.0836	$43.66\pm^{0.02}_{0.02}$	–	60061207002	25.9	-
NGC4388	12 25 46.82	+12 39 43.45	Sy2	0.0045	$41.87\pm^{0.02}_{0.02}$	8.54[7]	60061228002	21.3	N[11]
NGC4507	12 35 36.63	-39 54 33.66	Sy2	0.0118	$43.17\pm^{0.01}_{0.01}$	8.25[7]	60102051004	34.4	Y[11]
NGC4939	13 04 14.33	-10 20 22.32	Sy2	0.0085	$42.0\pm^{0.04}_{0.04}$	–	60002036002	22.0	Y[16]
ESO097-G013	14 13 09.91	-65 20 20.47	Sy2	0.0009	$40.78\pm^{0.02}_{0.02}$	7.95[8]	60002039002	53.8	N[14]
IC4518W	14 57 40.50	-43 07 54.00	Sy2	0.0162	$42.68\pm^{0.05}_{0.06}$	–	60061260002	7.78	-
ESO138-G1	16 51 20.27	-59 14 04.28	Sy2	0.0091	$42.43\pm^{0.04}_{0.04}$	6.7[9]	60201040002	45.6	N[14]
NGC6300	17 16 59.47	-62 49 13.98	Sy2	0.0029	$41.86\pm^{0.01}_{0.01}$	5.45[10]	60261001004	23.5	N[14]
ESO103-G35	18 38 20.32	-65 25 39.14	Sy2	0.0133	$43.23\pm^{0.01}_{0.01}$	7.0[11]	60301004002	43.7	-
MCG+07-41-03	19 59 28.36	+40 44 02.09	Sy2	0.0561	$44.61\pm^{0.01}_{0.01}$	–	60001083002	43.6	Y[15]
IC5063	20 52 02.33	-57 04 07.60	Sy2	0.0088	$42.55\pm^{0.01}_{0.02}$	7.74[2]	60061302002	18.4	Y[10]
PKS2356-61	23 59 04.36	-60 54 59.41	Sy2	0.0963	$43.96\pm^{0.04}_{0.04}$	8.96[12]	60061330002	23.0	N[17]

Notes. (*) Classification obtained from NASA/IPAC Extragalactic Database (NED)[a]. Note that UM 146 is classified as Sy2. However, its classification is controversial; It is also classified as Sy1.9 according to NED. The instrinsic (not absorbed) X-ray luminosity obtained through *clumin* tool from Xspec. References M_{BH}: (1) Kamraj et al. (2018); (2) Woo & Urry (2002); (3) Sani et al. (2010); (4) Vestergaard & Peterson (2006); (5) Fabbiano et al. (2019);(6) Clouse et al. (2011); (7) Nicastro et al. (2003); (8) Walton et al. (2013 b); (9) Piconcelli et al. (2011); (10) Awaki et al. (2005); (11) Wilkes et al. (2001); (12) Ursini et al. (2018); and (13) mass calculated using the $M_{BH} \propto \sigma$ relationship, using the σ values reported in the hyperleda database [b]. References for the N_H variability: (1) Krumpe et al. (2017); (2) Denney et al. (2014); (3) Papadakis et al. (2003); (4) Tombesi et al. (2017); (5) Reeves et al. (2018); (6) Teng et al. (2014); (7) Scott et al. (2004); (8) Wang et al. (2009); (9) Ballo et al. (2008); (10)Burtscher et al. (2016); (11)Risaliti et al. (2002); (12) Hernández-García et al. (2015); (13)Osorio-Clavijo et al. (2020); (14) Hernández-García et al. (2016); (15)Laha et al. (2020); (16)Guainazzi et al. (2005); and (17) Ursini et al. (2018).

[a] https://ned.ipac.caltech.edu/
[b] http : //leda.univ – lyon1.fr (Makarov et al. 2014).

value. In Sect. 3, we also discuss whether allowing different column densities along the LOS to the intrinsic continuum compared to that of the reflection component produced significantly improved results. The inclination angle cannot be constrained using this baseline model and data (see Sect. 3). Therefore, we fit each object to three fixed inclination angles (19°,45°, and 87°, which are the minimum, medium, and maximum values of this model, respectively). To choose the best fit for each source, we compared the χ^2/d.o.f. value obtained for each inclination angle. We followed this fit methodology for the clumpy torus model (UXClumpy) also considering three different inclination angles (1°,45°, and 90°, which are the minimum, medium, and maximum values of this model, respectively). These are slightly different due to the differences in the parameter space for these models (see Table 1).

We then computed the observed fluxes (i.e., absorbed) for intrinsic continuum (f_{intr}) and reflection component (f_{refl}) using cflux in XSPEC in an energy band between 3-70 KeV to both components. Additionally, we calculated the reflection fraction relative to the total flux as $f_{refl}/(f_{refl} + f_{intr})$. Figure 1 shows the histogram of the reflection fraction. We chose the 47 sources where the flux of the reflection component contributes at least 10% to the total flux (i.e., $f_{refl}/(f_{refl} + f_{intr}) > 0.1$, dashed vertical line in Fig. 1). This ensured that the reflection component had

a significant contribution to the X-ray spectrum to analyze its shape.

The purpose of this paper is to study the X-ray reflection produced by distant and neutral material to compare it with the results obtained from the dust emission at mid-IR. However, the X-ray reflection can also be produced by ionized material in the disk. If the latter is the case, comparison, which is one aim of this paper, is not possible. Therefore, we tested the need for this disk reflection component by adding the *relxill* component to the best fit obtained above. In this way, we identified 11 sources where disk reflection might be dominating the X-ray emission. Many of them are already reported by their disk reflection signatures, and all of them are type 1, as expected (see Appendix A for more details). We discarded these 11 sources from the analysis, so the final sample contains 36 AGN. Table 2 shows the main observational details of the sample. Twenty-one objects are type 2 Seyfert (Sy2), and fifteen are type 1 Seyfert (Sy1). Our sample covers four orders of magnitude in X-ray luminosities ($\mathrm{Log}(L_{2-10\mathrm{keV}}) \simeq 39.8 - 44.6$).

We fit the 36 *NuSTAR* spectra of our sample using the baseline model presented in Eq. 5. For the reflection component, we chose the two models discussed in Sect. 2: borus02 and UXClumpy, for the smooth and clumpy torus models, respectively. For each of them, we fit the spectra three times testing different inclination angles (see previous paragraphs). The average difference on χ^2/d.o.f. obtained between angles is $\Delta\chi^2(i_1 - i_2)$/d.o.f. ~ 0.3. Only five objects showed a significant improvement on the best fit (χ^2/d.o.f. < 1.2) by selecting an inclination angle $\theta_{\mathrm{inc}} = 90°$ for the smooth model and none when using the clumpy model. We explore how the other torus parameters are affected by the choice of fixing the inclination angle in Sect. 7.

Initially, we assumed that the column density along the LOS toward the intrinsic continuum and that of the medium producing the reflection component were the same. Thus, we used the one producing the minimum χ^2/d.o.f. value for each source as the best fit. We also fit the data to two baseline models where the column density of the LOS and the reprocessed material have different values (i.e., are not linked; $N_{H_{los}} \neq N_{H_{tor}}$). At first, we chose the values obtained from the previous analysis (i.e., with these two parameters linked; $N_{H_{los}} = N_{H_{tor}}$). We discuss the best scenario based on f-test statistics in the next sections.

4. X-ray results

4.1. Smooth versus clumpy baseline models

In order to understand if there is a preference for a smooth or a clumpy baseline model, we statistically compared the spectral fit obtained. Figure 2 shows the χ^2/d.o.f distribution obtained for both the smooth and clumpy torus models. In general, both models produce good results for above 86% of the sources. We tested to see if the iron lines at 6.70 keV and/or 6.97 keV could improve the spectral fitting of sources of our sample. Particularly, the use of the iron line at 6.70 keV, as an additional component to the total model, improves the fit of three sources: NGC 7213, ESO-097-G013, and MCG+07-41-03. Three AGN (Mrk 1018, PG 1535+547, and ESO 428-G014; two Sy1s and one Sy2s) show a significantly lower quality spectral fit with χ^2/d.o.f > 1.2 irrespective of the model used. Additionally, two sources (Mrk3 and ESO 097-G013; both Sy2s) have a χ^2/d.o.f > 1.2 when using the clumpy torus model (see bad spectral fits in Appendix B).

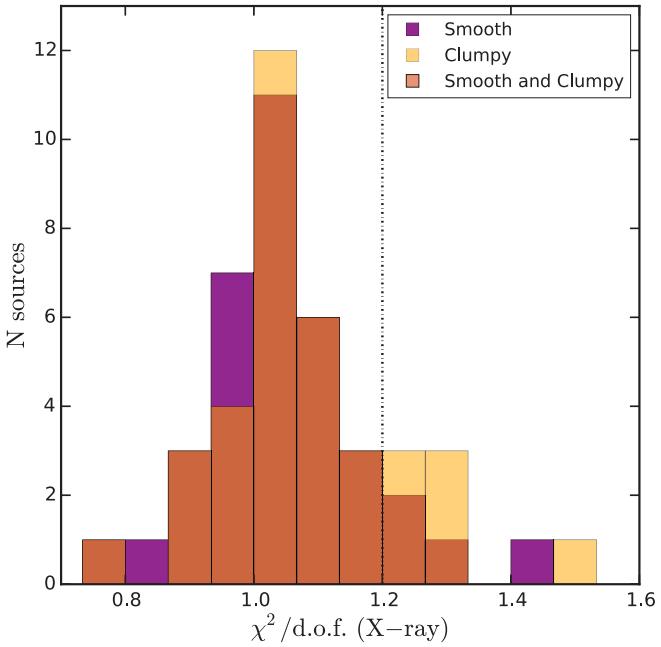

Fig. 2. Distribution of the best-fit statistics for the smooth (purple), clumpy (yellow), and both (dark salmon) baseline models in X-ray. The vertical dotted line shows the threshold of χ^2/d.o.f. = 1.2, where poorer fit are considered in this analysis (see text).

We estimated the "evidence ratio" using the Akaike information criterion (AIC) for both models. This evidence ratio allows us to compare if one model is better than another one using $\epsilon = \mathrm{W[AIC]_{clumpy}}/\ \mathrm{W[AIC]_{smooth}}$, where $\mathrm{W[AIC]_{clumpy}}$ and $\mathrm{W[AIC]_{smooth}}$ are the "Akaike weight" (see Eqs. 5-7 by Emmanoulopoulos et al. 2016). The clumpy baseline model is 100 times more likely to be appropriate than the smooth torus model when $\epsilon \leq 0.01$. The smooth baseline model is 100 times more likely to work than the clumpy torus model when $\epsilon \geq 100$. The results are shown in Table 3. For 16 sources ($\sim$ 44% of the sample), the smooth baseline model is preferred, while the clumpy baseline model is preferred for five sources ($\sim$ 14% of the sample). Both models fit the data similarly well in $\sim$ 42% of the sample (15 objects). There is no difference between Sy1 and Sy2; the smooth and clumpy torus models produce a better fit for five (11) and two (three) Sy1s (Sy2s), respectively. Similarly, we find no differences in the best model according to the X-ray luminosity.

The fit does not significantly improve when the LOS column density is allowed to vary with respect to the column density of the reflecting material (i.e., $N_{H_{tor}} \neq N_{H_{los}}$). Only the smooth baseline model allows us to test this option. We find that three sources are better fit when we free the column densities independently. We identify these sources with a white dot next to the model name in Table 7. Indeed, for these three sources the smooth torus model with $N_{H_{tor}} \neq N_{H_{los}}$ produces significantly better fits than those obtained with the clumpy one.

4.2. Smooth versus clumpy model parameters

Table 7 reports the results for the parameters obtained for the smooth and clumpy baseline models at X-rays. These models allow us to infer two parameters (column density of the reflecting material, $N_{H_{tor}}$, and half-opening angle of the torus, θ_{tor}), which are directly related to the reflection component and therefore can

Table 3. Best model results according to Akaike criterion

Seyfert 1					Seyfert 2				
Object	X-ray		mid-IR		Object	X-ray		mid-IR	
	ϵ	Model	ϵ	Model		ϵ	Model	ϵ	Model
Mrk1018	5.50E+00*	S/C	6.45E+05	Clumpy	UM146	6.71E-01	S/C	8.90E+08	Clumpy
Mrk590	2.55E-01	S/C	1.03E+27	Clumpy	NGC788	2.88E+04	Smooth	1.02E+45	Clumpy
PG0804+761	6.97E+02	Smooth	8.53E-24	Smooth	NGC1052	6.48E+00	S/C	3.49E+42	Clumpy
RBS0770	1.73E+00	S/C	1.24E-01	S/C	NGC1358	2.94E+00	S/C	8.06E-01	S/C
I11119+3257	7.65E-04	Clumpy	2.05E-38*	Smooth	J05081967+1721483	1.62E-03	Clumpy	1.68E+17	Clumpy
PG1211+143	2.25E+07	Smooth	3.31E-07	Smooth	Mrk3	1.54E+101	Smooth	6.44E+42*	Clumpy
RBS1125	5.59E+01	S/C	2.70E+29	Clumpy	ESO428-G014	4.90E+02*	Smooth	1.26E+11	Clumpy
Mrk231	2.07E+00	S/C	1.20E+03*	Clumpy	Mrk78	6.77E+01	S/C	1.76E+22	Clumpy
Mrk1383	2.55E+05	Smooth	4.93E+10	Clumpy	Mrk1210	1.26E-05	Clumpy	1.35E+29*	Clumpy
Mrk1392	1.21E-04	Clumpy	2.26E+26	Clumpy	J10594361+6504063	1.07E+02	Smooth	3.43E+00	S/C
Mrk1393	4.81E+00	S/C	4.84E+42	Clumpy	NGC4388	1.71E+21	Smooth	2.92E+14*	Clumpy
PG1535+547	1.15E-01*	S/C	1.06E-10	Smooth	NGC4507	1.51E+57	Smooth	6.31E+36	Clumpy
ESO141-G055	2.13E+16	Smooth	2.44E+00	S/C	NGC4939	3.06E+02	Smooth	7.53E+29	Clumpy
NGC7213	1.68E+05	Smooth	3.14E+177	Clumpy	ESO-097-G013	3.20E+129	Smooth	4.99E+120*	Clumpy
MCG+01-57-016	1.57E-02	S/C	3.61E+19	Clumpy	IC4518W	1.02E-02	S/C	2.15E+12	Clumpy
					ESO138-G1	7.01E-02	S•/C	1.13E+24	Clumpy
					NGC6300	5.92E+01	S•/C	1.13E+44*	Clumpy
					ESO103-G35	3.90E+09	Smooth•	8.36E+73	Clumpy
					MCG+07-41-03	1.02E+36	Smooth	2.57E+93*	Clumpy
					IC5063	5.16E-07	Clumpy	1.52E+34	Clumpy
					PKS2356-61	7.91E+03	Smooth	4.52E+00	S/C

Notes. Evidence ratio for the Akaike method and resulting model best to each source. S/C is included when either Smooth or Clumpy models provide an equally good fits. Bullets indicate that the best fit is obtained using the baseline model with $N_{H_{tor}}$ independent to the $N_{H_{los}}$. Asterisks indicate poor fits with χ^2/d.o.f. > 1.2 (see text).

Table 4. Mean and standard deviation values of X-ray parameters obtained for Sy1 and Sy2 when we used the smooth and clumpy baseline models to fit the *NuSTAR* spectra.

Parameter	baseline	Sy1			Sy2		
	model	#	mean	std	#	mean	std
(1)	(2)	(3)	(4)	(5)	(6)	(7)	(8)
$\log(N_H)$	smooth	14	23.9	0.6	21	23.8	0.6
	clumpy	15	23.4	0.6	21	23.4	0.7
Cf	smooth	6	0.4	0.2	16	0.8	0.2
	clumpy	12	0.4	0.2	12	0.8	0.1
Γ	smooth	15	1.9	0.2	18	1.8	0.3
	clumpy	15	2.1	0.2	21	1.8	0.2
θ_{tor}	smooth	4	33.5	11.5	5	34.3	22.3
	clumpy	8	10.6	10.3	11	16.0	11.1
$\log\left(\frac{f_{Refl}}{f_{Refl}+f_{Int}}\right)$	smooth	15	-0.8	0.2	21	-0.7	0.3
	clumpy	15	-0.8	0.3	21	-0.6	0.3

Notes. Col. (1): Parameter name. Col. (2): X-ray baseline model. Col. (3): number of sources considered to calculate the mean and standard values. We only considered AGN for which the parameters are well constrained. Cols. (4) and (7): Mean values to Sy1 and Sy2, respectively. Cols. (7) and (8): Standard deviation values to Sy1 and Sy2, respectively.

give us information on the reflecting material. Additionally, we obtain the reflection fraction at the 3-70 keV band, computed as the ratio between the flux of the reflection component (f_{Refl}) over the sum of the fluxes of the reflection component and the intrinsic emission component (f_{Int}), that is f_{Refl} / (f_{Refl} + f_{Int}). The errors of this relationship are computed through the method of propagation of uncertainties. We also computed the covering factor of the patchy obscurer, Cf, and the photon index, Γ, of the intrinsic continuum. Table 4 reports the mean and standard deviation for these parameters dividing the sample into Sy1 and Sy2 when we use the smooth and clumpy models.

Figures 3 show the comparison between the parameters obtained when using the smooth and the clumpy models at X-rays. In these figures, we include only source parameters restricted at least for one of the two models. Unfortunately, the half-opening angle of the torus, θ_{tor}, is restricted in very few objects preventing a direct comparison between models (see Table 4).

As explained in Sect. 3, we used the fraction of the reflection component to select sources where it is significant (at least 10% compared to the total flux of the source). Figure 3 (top left) allows us to investigate whether the selection criterion depends on the baseline model. Only for ESO 097-G013 do we find that the reflection fraction computed with the smooth model is larger than that obtained for the clumpy model. However, the χ^2/d.o.f. obtained when using the clumpy model for this source is above χ^2/d.o.f. > 1.2. This result confirms that, regardless of the baseline model used, the chosen criterion gives us the same result.

The covering factor, Cf, measures the scattered flux compared to the intrinsic flux through a patchy absorber. The Cf values come from a *zpcfabs* component. Figure 3 (top right) shows the comparison of the Cf obtained through the smooth and clumpy models. Sy2 galaxies have larger covering factors than Sy1 (see also Table 4). This result holds irrespective of the model used. By comparing two smooth torus models (MyTorus and borus02), Marchesi et al. (2019) found that the Cf at X-rays is recovered independently of the model used. However, see Sect. 6 for a comparison between the Cf obtained through X-ray and mid-IR observations.

Figure 3 (bottom left) compares the photon indices of the intrinsic continuum, Γ, for both baseline models. Roughly 83%

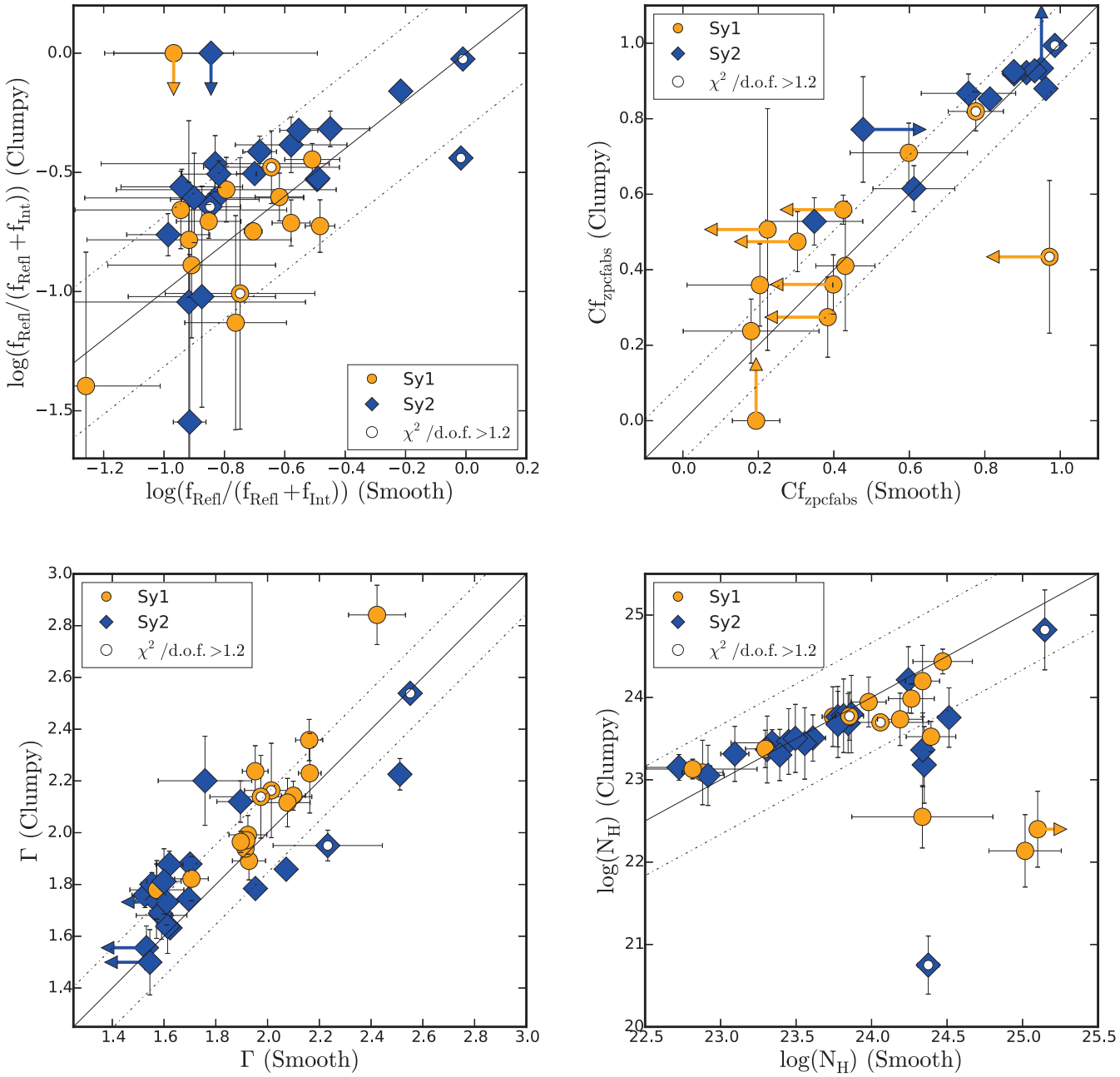

Fig. 3. Top-left: Fraction of the flux accounted for the reflection component relative to the total flux for the clumpy versus smooth baseline models. Top-right: Covering factors (i.e., ratio between the scattered and intrinsic emission, Cf) from the clumpy versus smooth baseline models. Bottom-left: Photon index (Γ) using the clumpy baseline model versus that using the smooth baseline model. Bottom-right: Column densities (N_H) using the clumpy baseline model versus that using the smooth baseline models. The Sy1 and Sy2 are shown as orange dots and blue diamonds, respectively. Arrows indicate lower and upper limits. The solid and dotted lines show the one-to-one relationship and 2σ dispersion according to the error bars of the data, respectively. The error bars were calculated through the propagation uncertainty method (see text).

of the sample is consistent with the one-to-one relation (six sources are outside, i.e. above 2-σ). We note that most of the sources show systematically larger photon indices when using the clumpy baseline model compared to the smooth baseline model. This is also visible in the mean values reported in Table 4.

Figure 3 (bottom right) shows the comparison of the column densities of the reflecting material obtained through the smooth and clumpy models. We find that $\sim$ 83% of the sources follow a linear relationship, indicating that for a large fraction of the sources the column density is independent of the model used. Six sources are significantly outside the one-to-one relation (i.e., above 2σ). Four of these six sources are Sy1 (RBS0770, Mrk1392, MCG +01-57-016, and ESO 141-G055) and two are Sy2 (ESO 428-G014 and NGC 6300). We find that the mean column density of the torus, $< N_{H_{tor}} >$, is larger for Sy1 than for Sy2 using the smooth model, while it is similar when using the clumpy model (see also Table 4). We ruled out that the selection

of the inclination angle affects these results (see Appendix C). Furui et al. (2016) compared the SED resulting from smooth and clumpy gas distribution in the torus models using the MONACO radiative transfer code. They found large differences between the SEDs produced by both models for large absorbing column densities ($N_H > 10^{24} cm^{-2}$). These differences are not found when two smooth gas torus models (MyTorus and borus02 models by Murphy & Yaqoob 2009 and Baloković et al. 2018, respectively) are compared (Marchesi et al. 2019). Our result is in good agreement with Furui et al. (2016), since both models show discrepant N_H values at the Compton-thick regime. In practice, while the smooth gas torus model infers $N_H > 10^{24} cm^{-2}$, the column density obtained with the clumpy gas torus model tends to be only mild ($N_H = 10^{22} - 10^{23}$ cm^{-2}).

We can use additional observational evidence to back up the smooth or clumpy distribution of the X-ray emitting material inferred from the modeling. Variability in the column density along the LOS has been reported for some objects (e.g., Risaliti et al. 2002; Markowitz et al. 2014; Laha et al. 2020). In Table 2, we indicate whether absorption variability (or lack thereof) has been reported for the sources in our sample. We find N_H variability information for 23 objects (see Col. 10 in Table 2). We consider a source as N_H non-variable or variable if multiple observations of the object have been published that analyze the long-term variability finding the presence or lack of changes on the N_H values, respectively. The sources (15 objects) without variable absorption are well fit with a smooth gas torus model at X-rays. On the other hand, five out of the eight sources with absorption variability are best fit with the clumpy gas torus model at X-ray (exceptions are NGC 4507, NGC 4939, and MCG+07-41-03). Thus, the detection or non-detection of variability in the column density along the LOS correlates quite well with the choice of a clumpy or smooth gas distribution at X-rays.

Therefore, we consider taking the non-variability and variability of LOS absorption as an indication for the smooth and clumpy distribution of the gas, respectively. Thus, this implies that we need to consider different baseline models for three sources, irrespective of the model obtained through statistical analysis as described in Sect. 4.1. We selected the clumpy distribution of the gas for NGC 4507, NGC 4939, and MCG+07-41-03, although they are best fit with a smooth distribution (see Sect. 4.1). Furthermore, we select the clumpy distribution at X-rays for Mrk 1392 and NGC 1052 and the smooth distribution for Mrk 1018, Mrk 590, Mrk 231, PG 1535+547, ESO 138-G1, and NGC 6300, although both models produce statistically similar results. This is highlighted in Table 6 with an asterisk next to the preferred model at X-rays.

We only constrain the angular width of the torus, θ_{tor}, for both models in six sources (~ 17%). The clumpy model is able to constrain this parameter in a larger number of sources (19 sources, i.e., ~ 53%) than the smooth model (eight sources, i.e., ~ 22%). This small number of constrained values prevent us from comparing this parameter. Although the X-ray inclination angle needs to be fixed and there are no statistically significant differences between the edge-on, face-on, or intermediate views (in fact this parameter is fixed in most of the previous works done at X-rays, e.g., Baloković et al. 2018), we find that the optical classification of the sources into Sy1 and Sy2 is consistent with the inclination angles (with the lowest χ^2/dof) obtain for the ~ 78% and 57% of the sample for the smooth and clumpy baseline models, respectively (i.e., Sy1s have $\theta_{inc} \leq 45°$ ($\theta_{inc} \geq 45°$) and Sy2s have $\theta_{inc} \geq 45°$ ($\theta_{inc} \leq 45°$) with smooth (clumpy) baseline model).

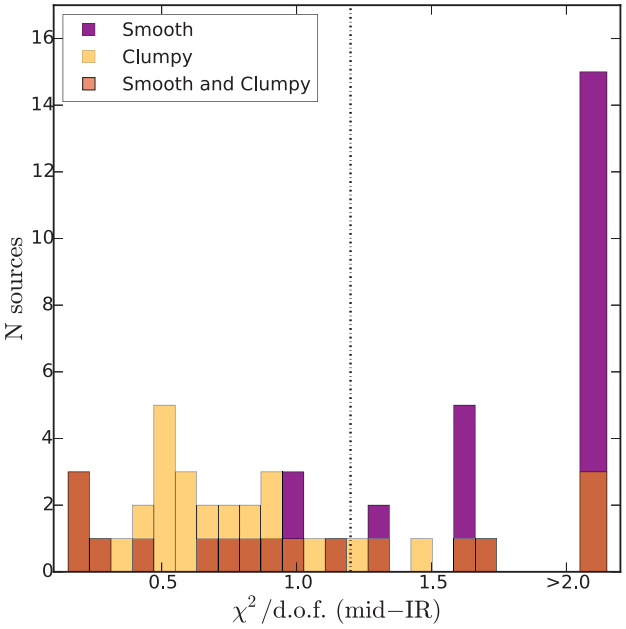

Fig. 4. Distribution of the best-fit statistics for the smooth (purple), clumpy (yellow) and both (dark-salmon) baseline models in mid-IR. The vertical dotted line shows the threshold of χ^2/d.o.f. = 1.2, where poorer fits are considered in this analysis (see text).

Tanimoto et al. (2018) found a correlation between the half-opening and inclination angles using the reflection model by Ikeda et al. (2009). According to Tanimoto et al. (2018), this means that along the LOS we are intercepting the outer edge of the torus, which seems unrealistic if done for all the objects. We compared the inclination and half-opening angles obtain from a smooth baseline model for 13 sources where the half-opening angle is completely or partially constrained. The difference between these two angles is large except for four objects (5° – 6° for ESO-097-G013, Mrk1386, ESO138-G1, and ESO428-G014). We do not find this correlation for the clumpy models either. Interestingly, the inclination and half-opening angles are consistent with the classification of each source under the unification scheme (except for NGC 1358) when using the smooth model. The vast majority of the objects do not show consistent inclination and half-opening angle values when using the clumpy model.

5. Mid-IR results

Table 8 shows the χ^2/d.o.f., contribution of the three components used at mid-IR (i.e., AGN dust, stellar, and ISM), and the parameter values that we obtain for the smooth and clumpy models. Figure 4 shows the distribution of χ^2/d.o.f. The smooth and clumpy models produce good spectral fittings (i.e., χ^2/d.o.f. < 1.2) for 33% (seven Sy1s and five Sy2s) and 72% (11 Sy1s and 15 Sy2s) of the sample, respectively. The smooth and clumpy models show a poor spectral fit with χ^2/d.o.f. > 1.2 for 67% of the sources (eight Sy1s and 16 Sy2s) and 28% of the sources (four Sy1s and six Sy2s), respectively. Objects showing bad fits using the clumpy model also show bad fits with the smooth model (exceptions are PG 0804+761 and PG 1211+143).

Table 3 shows the "evidence ratio" and preferred model when using the smooth and clumpy mid-IR models. For 20 sources with good spectral fits (~ 55%), we find that the clumpy model

Table 5. Mean and standard deviation values of the mid-IR parameters obtained for Sy1 and Sy2 when using the smooth and clumpy baseline models.

Parameter	baseline	Sy1			Sy2		
	model	#	mean	std	#	mean	std
(1)	(2)	(3)	(4)	(5)	(6)	(7)	(8)
i	smooth	3	23.4	18.3	3	36.4	27.7
	clumpy	2	81.6	2.3	2	42.8	7.0
σ	smooth	0	–	–	1	–	–
	clumpy	2	48.5	5.9	3	42.2	7.9
Y	smooth	3	11.7	0.5	5	33.5	15.8
	clumpy	9	14.5	4.3	9	17.8	8.33
$\tau_{9.7\mu m}$	smooth	5	4.9	2.3	1	–	–
τ_ν	clumpy	10	65.8	55.3	12	55.6	48.6
β	smooth	4	-0.51	0.19	1	–	–
γ	smooth	3	4.5	0.85	2	2.84	2.81
N_0	clumpy	8	4.35	1.45	10	6.19	2.34
q	clumpy	5	1.41	0.48	9	1.37	0.47

Notes. Col. (1): Parameter name. Col. (2): mid-IR baseline model. Col. (3): number of sources considered to calculate the mean and standard values. We only considered AGN for which the parameters are well constrained. Cols. (4) and (7): Mean values to Sy1 and Sy2, respectively. Cols. (7) and (8): Standard deviation values to Sy1 and Sy2, respectively.

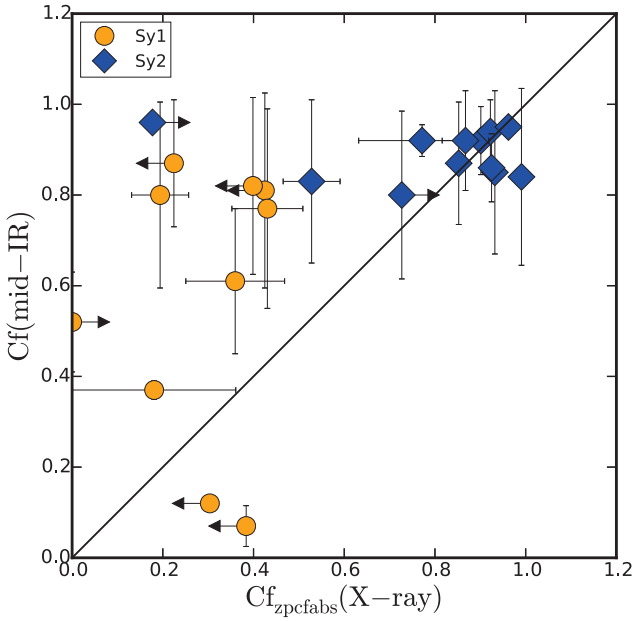

Fig. 5. Relationship between covering factors. The Sy1 and Sy2 are shown as dots and diamonds, respectively. The solid line shows the one-to-one relationship. The X-ray covering factor is obtained throughout the partial covering.

is preferred. Meanwhile, the smooth model is preferred for only three sources (∼ 8%). For the remaining five sources, both models produce statistically similar fits to the data. There are no significant differences between Sy1 and Sy2. Similarly, no differences for the best fits are found for different ranges of the X-ray luminosity.

Table 8 reports the best-fitting parameters obtained when using the mid-IR models. We explored the possibility of creating plots that compare parameters between models (as reported for the X-ray spectral fitting; see Sect. 4) but, unfortunately, many of them are not well restricted. Table 5 shows a summary of the number of sources with good fits (12 and 26 sources using smooth and clumpy models, respectively) where we can completely (Cols. 3 and 6) restrict each parameter.

In Table 5, we also show the mean and standard deviations per parameter, considering only restricted parameters (i.e., with an error bar well within the parameter space). We find that the parameters better restricted in both models are the ratio between the outer and the inner radius of the torus, Y, and the optical depth along the equator of the torus, (τ_ν or $\tau_{9.7\mu m}$, depending on the model used). The mean Y value for Sy2 is larger than that for Sy1 irrespective of the model used. Moreover, the mean τ_ν is similar for both Sy1 and Sy2. Meanwhile, the inclination angle (i) and the half-angular width of the torus (σ) are restricted only for a few objects. There are no differences between the number of parameters that are restricted in Sy1 and Sy2 for any of the two models. We find that the number of clouds in the equator of the torus (N_0) and the radial distribution of the clouds (q) are restricted to 18 and 14 sources, respectively, for the clumpy model. The mean N_0 for Sy2 is larger than that for Sy1, and the mean q is similar for both Sy1 and Sy2. These results are in good agreement with those obtained in previous works (e.g., García-Bernete et al. 2019, and references therein). The parameters associated with the vertical and radial dust distribution, β and γ, are restricted only for a few objects in the smooth model. In previous work (Esparza-Arredondo et al. 2019), we showed that the torus parameters are better restricted through mid-IR and X-ray simultaneous fits. This will be the subject of a forthcoming investigation (Esparza-Arredondo et al. in prep.).

6. X-ray versus mid-IR results

In this section, we present the results obtained from a direct comparison of the properties derived from mid-IR and X-ray parameters. First, we analyze whether the covering factor derived from X-rays through *zpcfabs* component can be compared with the one derived from the mid-IR data. Then, we explore the dust-to-gas ratio of the AGN torus through column density and optical depth.

6.1. Covering factor

The covering factor of the AGN is one of the key parameters to describe the AGN population. It might be different among AGN types (Ramos-Almeida et al. 2009; Mateos et al. 2016; García-Bernete et al. 2019) and it might also evolve along the AGN duty cycle of activity (Lawrence 1991; Krongold et al. 2003; Ricci et al. 2017b). This idea is supported by the decrease of the mid-IR-to-optical-luminosity ratio as the AGN bolometric luminosity increases (Maiolino et al. 2007). While Ramos Almeida et al. (2014) suggest that the covering factor is a robust estimate using a mid-IR SED fitting (although also model dependent, see González-Martín et al. 2019B), this might not be the case for the covering factors inferred from the partial covering applied to the intrinsic continuum at X-rays. To perform this comparison, we obtain the mid-IR Cf using the posterior distributions of the parameters. We compute the Cf for the clumpy and smooth models

at mid-IR wavelengths following these equations:

$$\mathrm{Cf}\,(Smooth) = \frac{ln(\tau_{9.7})}{\gamma} \quad (6)$$

$$\mathrm{Cf}\,(Clumpy) = 1 - \int_0^{\pi/2} cos\left(\beta e^{N_0 e^{-\beta^2/\sigma^2}}\right) d\beta \quad (7)$$

Figure 5 shows the mid-IR versus X-ray Cf for all the objects with good spectral fits at both wavelengths. We use for each source the best-fit model (either smooth or clumpy), taking into account if the source shows absorption variations (see Sect. 4). As it can be seen, no correlation is found between mid-IR and X-ray Cf. Most Sy2s show Cf > 0.7 at X-ray and are also consistent with large Cf at mid-IR wavelengths. Meanwhile, Sy1s with Cf < 0.7 at X-ray have larger Cf at mid-IR. If the covering factors at X-ray are dominated by the material at the host galaxy, we expect similar behaviors from both AGN types. However, we find that Sy2s AGN tend to have larger covering factors (irrespective of the baseline model used) than Sy1s AGN. This discrepancy in the Cf of Sy1s AGN could be explained if the soft emission is coming from nuclear X-ray radiation leaking through patchy obscuring gas in the LOS, which may not be associated with torus-scale gas. Alternatively, this emission might be due to the scattering of nuclear radiation in distant gas. Indeed, the soft X-ray emission of Sy1 is complex and additional components are usually required to fit them. For instance, Mrk 1018 was modeled by Noda & Done (2018) including a soft Comptonization component to reproduce the soft emission. This soft Comptonization component is suggested to have originated in the accretion disk. Thus, the Cf estimate at X-rays might be wrongly estimated due to the complexity of the soft X-ray emission of Sy1. Spectra below 3 keV (perhaps with *XMM*-Newton) are required to properly account for the complexity of the soft emission, obtaining a better determination of the X-ray Cf for Sy1. Therefore, we opted to focus the subsequent analysis and discussion on the Cf obtained at mid-IR.

6.2. Torus dust-to-gas ratio

The dust-to-gas ratio is found to be constant in our own Galaxy with a ratio between gas column density and optical extinction of $A_V/N_H \sim 2 \times 10^{-21} cm^{-2}$ (Draine 2003). However, this might not be the case for other galaxies (Draine 2009). Furthermore, the AGN might provide a source of production and/or destruction of dust (Sturm et al. 2005; Srinivasan et al. 2017) that might yield a significantly different dust-to-gas ratio near the AGN.

Figure 6 shows the column density versus the optical depth using the preferred combination of models at X-ray and mid-IR wavelengths. We include sources with a good spectral fitting (χ^2/d.o.f. < 1.2). The solid, dashed, and dashed-dotted lines show 1, 0.1, and 0.01 times the Galactic dust-to-gas ratio[4], respectively.

The dust-to-gas ratio in AGN is in the range between ~0.01 and slightly above one times the Galactic dust-to-gas ratio. Moreover, Sy2 seems to have a larger dust-to-gas ratio (> 0.1) than Sy1. Maiolino et al. (2001) showed consistent results with a ratio in the 0.3 – 0.01 range using optical dust measurements and X-ray LOS column densities. Burtscher et al. (2016) explored this relation using the absorption along the LOS measured by the BAT AGN spectroscopic survey (BASS Ricci et al. 2017)

[4] $N_H = 1.9 \times 10^{21} * 1.086 * \tau_\nu$ (Bohlin et al. 1978).

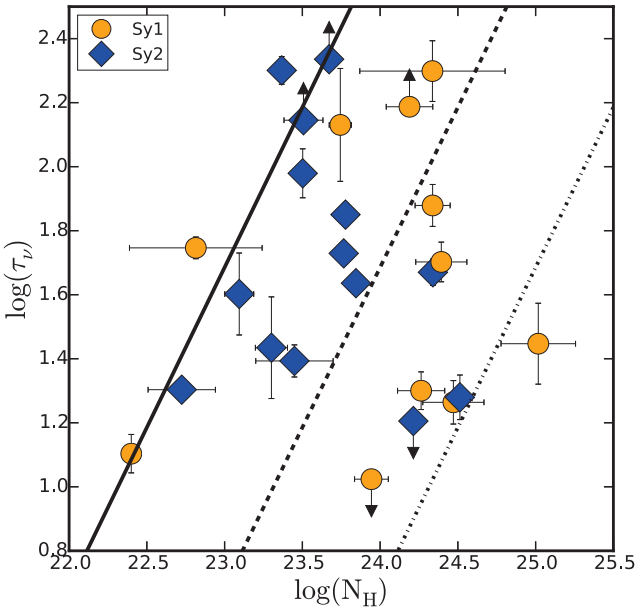

Fig. 6. Relationship between column density and optical depth. The Sy1 and Sy2 are shown as dots and diamonds, respectively. The solid, dashed, and dashed-dotted lines show 1, 0.1, and 0.01 times the galactic dust-to-gas ratio, respectively.

and the optical extinction[5]. They found a ratio consistent with the Galactic value or below in AGN, finding a minimum ratio of ~0.02.

This range for the dust-to-gas ratio is larger than that found in nearby galaxies (Draine 2009). There are several plausible explanations. One possibility discussed in the literature (Maiolino et al. 2001; Burtscher et al. 2016) is that absorbing column density along the LOS is variable. However, we report measurements of the density for the reflection component here, which is constant over the years. Furthermore, many of our sources show a lack of N_H variability (see Table 2). Gas at the dust-free inner region or at both the dust-free and dust torus regions are also possibilities to explain a smooth distribution at X-rays and a clumpy distribution at mid-IR wavelengths. These scenarios are further discussed below.

7. Discussion

Placing constraints on the geometry of the torus parameters from SED spectral fitting is possible from near-IR, mid-IR, and sub-millimeter observations (Gallimore et al. 2016; García-Burillo et al. 2016; Ramos Almeida & Ricci 2017; Lopez-Rodriguez et al. 2018). However, near-IR and sub-millimeter observations might be contaminated by stellar (Ramos Almeida et al. 2014) diffuse dust emission (Mason et al. 2006) and synchrotron emission (Pasetto et al. 2019), respectively.

Joining mid-IR and X-ray spectra of AGN might yield a better understanding of the obscuring structure (e.g., Liu & Li 2014; Tanimoto et al. 2019; Esparza-Arredondo et al. 2019). Some parameters (e.g., the outer radius of the torus) can be recovered using only mid-IR observations, but some others (e.g., inclination

[5] Optical extinctions are derived from near-IR color temperatures (using spectral fitting) against the offset from the near-to-mid-IR luminosity (Burtscher et al. 2015).

angle) are difficult to restrict (see Ramos Almeida et al. 2014). At X-rays, the half-opening angle of the torus is difficult to restrict since it might be linked to the absorption along the LOS (Furui et al. 2016; Baloković et al. 2018). If the origin (in terms of geometrical distribution) of both emissions is the same, the combination of X-ray and mid-IR might help to solve these issues. However, before trying to attempt to a simultaneous fit, the results from independent fits need to be discussed to understand if the same distribution could explain both mid-IR and X-ray continuum emission. In a pilot study, Esparza-Arredondo et al. (2019) showed that this might be the case for the Sy2 IC 5063. However, they tested the smooth gas torus model at X-ray while both smooth and clumpy torus models were tested at mid-IR. The X-ray clumpy gas torus model presented here was not available at the time of that publication. As part of the current work, we included this source again and found that the best combination of models is clumpy at both wavelengths. This result shows the importance of testing several combinations of models.

At mid-IR wavelengths, several works have performed a thorough comparison of the smooth and clumpy models and have discussed the possible issues of each of them (Feltre et al. 2012; Tanimoto et al. 2019). However, only a few works have focused on the comparison of these two distributions of gas at X-ray wavelengths (e.g., Liu & Li 2014; Furui et al. 2016). These works used the same code to create these models, and they froze some parameters in order to obtain better spectral fitting for a few objects. Here, we analyzed a sample of AGN for the first time. Based on their good statistics (χ^2/d.o.f. < 1.2), we can compare the best models chosen to fit the mid-IR and X-ray spectra in 25 out of the 36 AGN (see Table 3). We focused on these 25 AGN, and we refer the reader to Appendix B for a discussion regarding the 11 objects with poor spectral fittings. In the following subsections, we discuss the smooth or clumpy distribution of dust and gas and the complexity of the torus inferred from our results.

7.1. Distribution of gas and dust

Following the Akaike criterion, the absorption variability information, and the possible X-ray and mid-IR model combinations for each source, we found that six sources are consistent with the smooth models at both wavelengths. We also found 14 objects consistent with the clumpy models at both wavelengths. Meanwhile, a combination of the smooth and clumpy models is applicable for 17 of the sources (see Cols. 4 and 5 in Table 6). We note that in some cases, both models are suitable in a given wavelength.

The comparison of clumpy models at both wavelengths was explored recently, using preexisting mid-IR results (Buchner et al. 2019; Ogawa et al. 2020). However, the smooth versus clumpy comparison has never been explored, and it is found as a plausible scenario in this work. These results could suggest a scenario where the gas and dust are not necessarily distributed in the same way for some objects. Indeed, Liu & Li (2014) pointed out that this kind of mismatch might occur when comparing both wavelengths. Absorption variability among AGN has been claimed as a corroboration of the clumpy nature of the absorber at X-rays (e.g., Markowitz et al. 2014). However, Laha et al. (2020) conducted an X-ray spectral variability study of 20 Compton-thin AGN, finding N_H variations in only seven objects (see also Hernández-García et al. 2015, 2016). They found constant N_H over a decade for some objects. This is consistent with our results that some sources fit to a smooth gas torus model at X-rays.

There are several possibilities to explain this mismatch seen for some objects between the distributions of the gas at X-ray and the dust at mid-IR wavelengths: (1) the gas is a smooth distribution associated with the inter-cloud dust medium; or (2) at least part of the gas comes from a smooth distribution associated with the dust-free inner region of the AGN. At mid-IR, Stalevski et al. (2016) developed an AGN dust model assuming a two-phase distribution of dust in a torus-like geometry (see also Siebenmorgen et al. 2015); dust is distributed smoothly and a clumpy distribution is embedded within it. Therefore, with the first option, it is possible that at X-ray wavelengths a two-phases models are more capable of explaining this gas distribution. Unfortunately, these kinds of models are not currently available.

Gas in the dust-free inner region or in both the dust-free and dust torus regions are also possibilities to explain a smooth distribution at X-ray wavelengths and a clumpy distribution at mid-IR wavelengths. These scenarios might nicely explain the high dust-to-gas ratio found in many objects (see Sect. 6 and also Maiolino et al. 2001). Indeed, most of the X-ray reflection models do not impose inner radii in their geometry (e.g., Murphy & Yaqoob 2009), which is naturally done for dust models due to the sublimation radius of the dust.

The stability of this component conformed by gas and dust needs to be explored through dynamical models. These models consider the torus as an axisymmetric obscuring structure that mimics a hydrostatic toroidal distribution that contains gas processed by the accretion disk and expelled outward in a disk wind (see Elitzur & Shlosman 2006 and references therein). In this way, the BLR and torus originate at the inner and outer parts of the outflow, respectively. Other models have radiation-driven obscuring structures that replace the classical torus (e.g., Wada 2012). Recently, Sarangi et al. (2019) showed, through a magneto-hydrodynamic wind model, that this wind naturally produces dust with a distribution that resembles a toroidal shape with sizes matching those obtained from VLA imaging (Carilli et al. 2019). Under this model, both gas and dust are smoothly distributed, with a well-defined distribution of dust temperatures preventing dust from destruction (Sturm et al. 2005; Srinivasan et al. 2017), an issue highlighted in early works (Krolik & Begelman 1988). Thus, the smooth distribution preferred at X-rays is stable from the dynamical point of view.

7.2. Complexity of the torus

The comparison between the X-ray reflector and the dusty torus inferred from mid-IR spectral fitting is quite complex, when including all the available information. To illustrate this, we firstly focused on the 13 objects (six Sy1 and seven Sy2) with good spectral fits at both wavelengths and available information on the variable or non-variable LOS absorption. The rest of the sample is discussed below. Table 6 shows the inferred distribution of the gas and dust (i.e., clumpy or smooth), the covering factor at mid-IR, the half-opening angle of the torus at X-rays and mid-IR, the inclination angle, the number of clouds in the equatorial plane (when the clumpy model is preferred at mid-IR), the optical depth of the dust, and the hydrogen column density of the reflection component at X-rays. We split this sample of 13 objects into groups sharing similar properties on the distribution of gas and dust, absorption variability, mid-IR covering factor, and half-opening angle of the torus:

– Panel 1 of Fig. 7 (e.g., Mrk 1393): Sy1 source with absorption variability, intermediate mid-IR covering factor, and small half-opening angle. A clumpy distribution is preferred

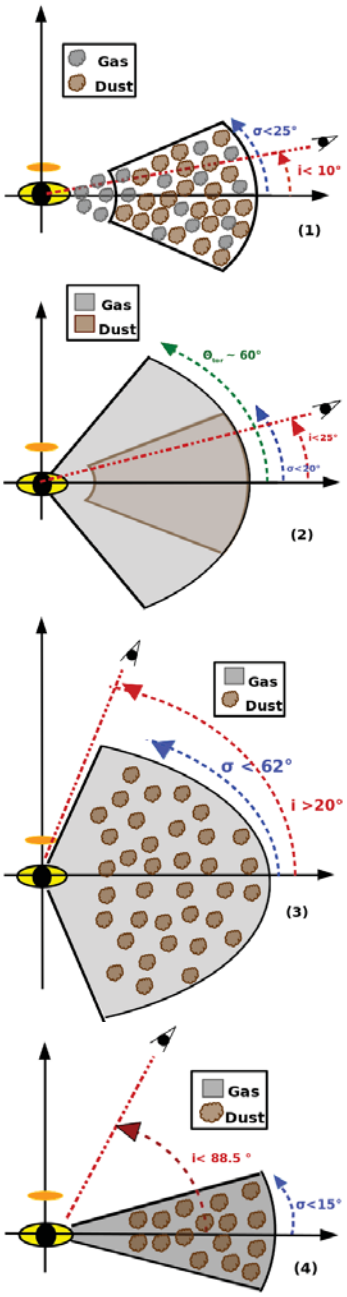

Fig. 7. Illustrations of different gas/dusty tori for some Sy1s in our sample according to the properties gathered in Table 6. The orange and yellow circles show the corona and accretion disk, respectively. The red dashed line shows the LOS (see text for more details).

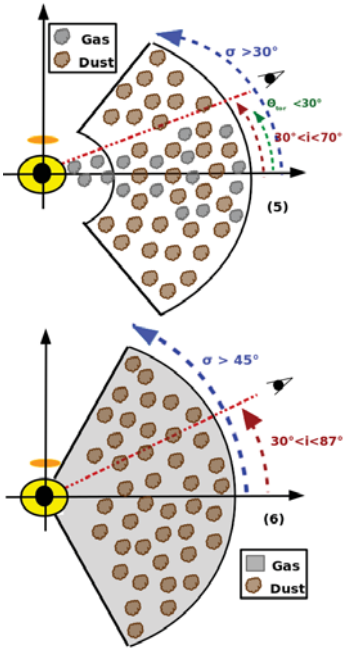

Fig. 8. Illustrations of different gas/dust tori for some Sy2s in our sample according to the properties gathered in Table 6. The orange and yellow circles show the corona and accretion disk, respectively (see text for more details).

for both gas and dust. Interestingly, this object shows many clouds at the equator and low optical depth. This object can be explained with a geometrically thin disk of (a high number of) clumps conformed by dust and gas, where the inner (dust-free) region is filled with these clumps. The low inclination angle toward the structure (measured from the equator) might intercept some clouds close to the central engine producing the absorption variations.

– Panel 2 of Fig. 7 (e.g., PG 0804+761 and PG 1211+143): Sy1 sources without absorption variations, small covering factors, small half-opening angles of the dust, and low-to-intermediate half-opening angles of the gas distribution. A smooth distribution of both dust and gas is preferred for these objects. All the above signatures could be explained with a geometrically thin and smooth dust disk and a geometrically thick and smooth torus of gas, coexisting within the same radii. Interestingly, inclination angles might intercept this thin disk along the LOS, despite its optical classification as Sy1.

– Panel 3 of Fig. 7 (e.g., Mrk 1383 and Mrk 590): Sy1 sources without absorption variability, large covering factors, intermediate-to-high half-opening angles for both gas and dust. The gas is distributed smoothly, while the dust is distributed into clumps. These two objects could be explained with a single geometrically thick torus in which dust is located in clumps while the gas is smoothly distributed.

– Panel 4 of Fig. 7 (e.g., NGC 7213): Sy1 source without absorption variations, low covering factor, and small half-opening angles of the dusty and gas structure. A combination of a smooth distribution of gas and a clumpy distribution of dust is preferred for this object. A geometrically thin disk of gas and dust, where gas is smoothly distributed while clouds hold most of the dust, can explain the observed signatures. The smooth distribution prevents us from observing absorption variability of the source. Furthermore, the inclination angle is consistent with the unobstructed view of the source.

– Panel 5 of Fig. 8 (e.g., NGC 4507, NGC 1052, NGC 4939, and IC 5063): Sy2 sources with absorption variability at X-rays, high covering factors, and half-opening angles at both X-rays and mid-IR consistent with intermediate or high values. A clumpy distribution of both gas and dust is preferred for this group of objects. All the properties described above can be explained with a geometrically thick torus where dust and gas is distributed in clumps. The gas is probably located in both the outer dusty and inner dust-free regions, the latter producing the observed absorption variability. Indeed, the in-

clination angles constrained for these sources are consistent with these clumps being intercepted by the LOS.

– Panel 6 of Fig. 8 (e.g., ESO 138-G1, PKS 2356-61, and NGC 788): Sy2 sources without absorption variability, large covering factors[6], and intermediate or high half-opening angles of both gas and dusty structures. The gas is smoothly distributed, while the dust is located within clumps. A geometrically thick torus of dust and gas is able to explain the observed characteristics of these three objects, where the dust is located in clumps, while the gas is smoothly distributed. Interestingly, these objects are seen at relatively large inclination angles but, in spite of that, the large value of the half-opening angle of the torus prevents a direct view of the accretion disk.

Ten out of the twelve remaining sources without information on the absorption variability might be classified into these groups according to the available information. We included a comment on their plausible classification in Col. 13 of Table 6. For example, among Sy1 sources, Mrk 1392 have similar properties to the source of panel 1 for Sy1 (Fig. 7), such as an intermediate value for the covering factor, small half-opening angle, and many clouds along the equator (N_0). RBS 0770, and two other sources have similar properties to the object of panel 3 of Sy1 (Fig. 7), showing large covering factors and intermediate-to-high half-opening angles. Within the Sy2 class, the properties of UM 146 and three other sources are similar to those observed in the source of panel 5 of Sy2 (Fig. 8), showing large values of the covering factors and intermediate-to-high half-opening angles. The properties of ESO 141-G055 and J05081967+1721483 are different to eatch other and to those observed in other sources; therefore, we are not able to classify them in any of these groups. This suggests that the complexity of these sources might extend even beyond the classes described above. The results presented here are consistent with the current paradigm of AGN in which the accretion disk is surrounded by a plethora of infalling, outflowing, and rotating material, configuring the obscurer we see with the X-ray and mid-IR observations (see Ramos Almeida & Ricci 2017, for a review).

The inclination angles are consistent with the obstructed or unobstructed view of the accretion disk, following the unification theory. However, we did not find a correspondence between different Sy1 and Sy2 groups. For example, the tori of panel 1 of Sy1 (Fig. 7) and panel 5 of Sy2 (Fig. 8) share the same clumpy distribution of dust and gas. However, they differ in their covering factors and half-opening angles, which are larger in Sy2 compared to Sy1. This is also consistent with previous works that have found that Sy2 tori tend to be thicker and therefore intrinsically different to those of Sy1 (e.g., Ramos-Almeida et al. 2011; García-Bernete et al. 2019). Moreover, the optical depths are higher and the number of clouds at the equator of the system is lower in Sy2 compared with Sy1. Thus, the difference between these two groups is beyond the inclination angle toward the system. Even closer resemblance is seen for the torus of panel 3 of Sy1 (Fig. 7) and that in panel 6 of Fig. 8 (Sy2). They show large covering factors and intermediate-to-high half-opening angles. Still, the number of clouds is larger and the optical depth is lower for Sy2 compared with Sy1.

Interestingly, most of these scenarios are also consistent with the existence of gas in a dust-free region. This result is consistent with the recent finding for the Circinus galaxy by Uematsu et al. (2021). Therefore, the reflection component of X-rays might be associated with the same structure producing the dust emission but including gas within the dust sublimation zone. Although we cannot rule out that X-ray and mid-IR wavelengths are tracing different components for some objects, this explanation is particularly appealing for objects where the half-opening widths are consistent for both gas and dust, suggesting a common origin for both dust mid-IR emission and X-ray reflection component.

[6] A large covering factor is found in PKS 2356-61 if it is fit to a clumpy torus at mid-IR, although the smooth model is equally good from the statistical point of view.

8. Conclusions

We studied the $3-70$ keV *NuSTAR* and the $5-30\mu$m *Spitzer*/IRS spectra of a sample of 36 AGN. We restricted the sample to objects dominated by the AGN dust continuum at mid-IR and at least 10% of reflection components contributing to the X-ray spectrum. Furthermore, we excluded objects where disk reflection could contribute to the X-ray spectrum from this analysis. We tested the comparison between smooth and clumpy torus models at both mid-IR and X-ray frequencies. For this, we used the smooth torus model by Baloković et al. (2018) and the clumpy torus model by Buchner et al. (2019) at X-rays. At mid-IR we used analog models by Fritz et al. (2006) and Nenkova et al. (2008a,b).

We find that $\sim 78\%$ of the sample is well reproduced with the smooth model at X-ray wavelengths. At mid-IR wavelengths, $\sim 69\%$ is well fit to clumpy models. Interestingly, there is a very good agreement between the clumpiness or smoothness of the X-ray reflector found in this paper and the existence or lack of variability in the column density along the LOS reported in the literature, respectively.

We were also able to compare the resulting models at both wavelengths for 25 AGN with good spectral fits. We find that at least 50% of the sample could be explained by a clumpy distribution of the dust and a smooth or clumpy distribution of the gas. Moreover, we found that the dust-to-gas ratio is in a range of [0.01-1] times the Galactic ratio. This is consistent with the existence of gas located within the dust-free inner region. Considering all the information compiled in this work, we find at least six different scenarios to explain the torus properties of some sources. Inside these scenarios three gas and dust distributions are possible: clumpy-clumpy, smooth-smooth, and smooth-clumpy. These results show the complexity of the obscuring material in the proximity of AGN.

Acknowledgements. The authors thank the anonymous referee for careful reading and constructive suggestion that improved the paper. This work made use of data from the *NuSTAR* mission, a project led by CalTech, managed by JPL, and funded by NASA. We thank the *NuSTAR* Operations, Software and Calibration teams for support with the execution and analysis of these observations. This research has made use of the *NuSTAR* Data Analysis Software (NuSTARDAS) jointly developed by the ASI Science Data Center (ASDC, Italy) and CalTech. This work is based in part on observations made with the *Spitzer* Space Telescope, which is operated by the Jet Propulsion Laboratory, California Institute of Technology under a contract with NASA. D.E.-A. and N.O.-C. acknowledge support from a CONACYT scholarship. This research is mainly funded by the UNAM PAPIIT projects IN105720 and IA113719 (PI O.G.-M. and PI D.D.). J.M. acknowledges financial support by the Spanish Ministry of Economy and Competitiveness (MEC) under grant no. AYA2016-76682-C3 and from the State Agency for Research of the Spanish MCIU through the "Center of Excellence Severo Ochoa" award to the Instituto de Astrofísica de Andalucía (SEV-2017-0709). C.R.-A. acknowledges financial support from the Spanish Ministry of Science, Innovation and Universities (MCIU) under grant with reference RYC-2014-15779, from the European Union's Horizon 2020 research and innovation programme under Marie Sklodowska-Curie grant agreement No 860744 (BiD4BESt), from the State Research Agency (AEI-MCINN) of the Spanish MCIU under grants "Feeding and feedback in active galaxies" with reference PID2019-106027GB-C4 and "Quantifying the impact of quasar feedback on

galaxy evolution (QSOFEED)" with reference EUR2020-112266. CRA also acknowledges support from the Consejería de Economía, Conocimiento y Empleo del Gobierno de Canarias and the European Regional Development Fund (ERDF) under grant with reference ProID2020010105 and from IAC project P/301404, financed by the Ministry of Science and Innovation, through the State Budget and by the Canary Islands Department of Economy, Knowledge and Employment, through the Regional Budget of the Autonomous Community. I.G.-B. acknowledges support from STFC through grant ST/S000488/1.

References

Almeyda, T., Robinson, A., Richmond, M., et al. 2017, ApJ, 843, 3
Alonso-Herrero, A., Ramos Almeida, C., Mason, R., et al. 2011, ApJ, 736, 82
Alonso-Herrero, A., Pereira-Santaella, M., García-Burillo, S., et al. 2018, ApJ, 859, 144
Antonucci, R. R. J., & Miller, J. S. 1985, ApJ, 297, 621
Arévalo, P., Bauer, F. E., Puccetti, S., et al. 2014, ApJ, 791, 81
Arnaud, K. A. 1996, Astronomical Data Analysis Software and Systems V, 17
Awaki, H., Murakami, H., Leighly, K. M., et al. 2005, ApJ, 632, 793
Ballo, L., Giustini, M., Schartel, N., et al. 2008, A&A, 483, 137
Baloković, M., Brightman, M., Harrison, F. A., et al. 2018, ApJ, 854, 42
Bohlin, R. C., Savage, B. D., & Drake, J. F. 1978, ApJ, 224, 132
Brenneman, L. W., Reynolds, C. S., Nowak, M. A., et al. 2011, ApJ, 736, 103
Brightman, M., & Nandra, K. 2011, MNRAS, 413, 1206
Bruzual, G., & Charlot, S. 2003, MNRAS, 344, 1000
Buchner, J. 2018. [Data set]. Zenodo. http://doi.org/10.5281/zenodo.2211263
Buchner, J., Brightman, M., Nandra, K., et al. 2019, A&A, 629, A16
Burtscher, L., Meisenheimer, K., Tristram, K. R. W., et al. 2013, A&A, 558, A149
Burtscher, L., Orban de Xivry, G., Davies, R. I., et al. 2015, A&A, 578, A47
Burtscher, L., Davies, R. I., Graciá-Carpio, J., et al. 2016, A&A, 586, A28
Carilli, C. L., Perley, R. A., Dhawan, V., et al. 2019, ApJ, 874, L32
Clouse, S., Braatz, J., & Kuo, C.-Y. 2011, APS Four Corners Section Meeting Abstracts, M1.005
Combes, F., García-Burillo, S., Audibert, A., et al. 2019, A&A, 623, A79
Denney, K. D., De Rosa, G., Croxall, K., et al. 2014, ApJ, 796, 134
Done, C., Madejski, G. M., & Życki, P. T. 2000, ApJ, 536, 213
Draine, B. T. 2003, ApJ, 598, 1017
Draine, B. T. 2009, EAS Publications Series, 245
Ebrero, J., Costantini, E., Kaastra, J. S., et al. 2011, A&A, 535, A62
Efstathiou, A., Hough, J. H., & Young, S. 1995, MNRAS, 277, 1134
Elitzur, M., & Shlosman, I. 2006, ApJ, 648, L101
Elitzur, M., & Ho, L. C. 2009, ApJ, 701, L91
Emmanoulopoulos, D., Papadakis, I. E., Epitropakis, A., et al. 2016, MNRAS, 461, 1642
Esparza-Arredondo, D., González-Martín, O., Dultzin, D., et al. 2019, ApJ, 886, 125
Fabian, A. C. 1998, American Institute of Physics Conference Series, 431, 247
Fabbiano, G., Paggi, A., Karovska, M., et al. 2018, ApJ, 855, 131
Fabbiano, G., Siemiginowska, A., Paggi, A., et al. 2019, ApJ, 870, 69
Falocco, S., Larsson, J., & Nandi, S. 2020, A&A, 638, A67.
Feltre, A., Hatziminaoglou, E., Fritz, J., & Franceschini, A. 2012, MNRAS, 426, 120
Fritz, J., Franceschini, A., & Hatziminaoglou, E. 2006, MNRAS, 366, 767
Furui, S., Fukazawa, Y., Odaka, H., et al. 2016, ApJ, 818, 164
Gallimore, J. F., Elitzur, M., Maiolino, R., et al. 2016, ApJ, 829, L7
García-Bernete, I., Ramos Almeida, C., Alonso-Herrero, A., et al. 2019, MNRAS, 486, 4917
García-Burillo, S., Combes, F., Ramos Almeida, C., et al. 2016, ApJ, 823, L12
García-Burillo, S., Combes, F., Ramos Almeida, C., et al. 2019, A&A, 632, A61
Gaspar, G., Díaz, R. J., Mast, D., et al. 2019, AJ, 157, 44
George, I. M., Nandra, K., Fabian, A. C., et al. 1993, MNRAS, 260, 111
Granato, G. L., & Danese, L. 1994, MNRAS, 268, 235
Greenhill, L. J., Booth, R. S., Ellingsen, S. P., et al. 2003, ApJ, 590, 162
Ghisellini, G., Haardt, F., & Matt, G. 1994, MNRAS, 267, 743
González-Martín, O., Masegosa, J., Hernán-Caballero, A., et al. 2017, ApJ, 841, 37
González-Martín, O., Masegosa, J., García-Bernete, I., et al. 2019a, ApJ, 884, 10
González-Martín, O., Masegosa, J., García-Bernete, I., et al. 2019b, ApJ, 884, 10
Guainazzi, M., Fabian, A. C., Iwasawa, K., et al. 2005, MNRAS, 356, 295
Harrison, F. A., Craig, W. W., Christensen, F. E., et al. 2013, ApJ, 770, 103
Hernández-García, L., Masegosa, J., González-Martín, O., et al. 2015, A&A, 579, A90
Hernández-García, L., Masegosa, J., González-Martín, O., et al. 2016, ApJ, 824, 7
Hönig, S. F., Beckert, T., Ohnaka, K., et al. 2006, A&A, 452, 459
Hönig, S. F., Kishimoto, M., Gandhi, P., et al. 2010, A&A, 515, A23
Hönig, S. F., & Kishimoto, M. 2017, ApJ, 838, L20
Hönig, S. F. 2019, ApJ, 884, 171
Ikeda, S., Awaki, H., & Terashima, Y. 2009, ApJ, 692, 608
Impellizzeri, C. M. V., Gallimore, J. F., Baum, S. A., et al. 2019, ApJ, 884, L28
Kammoun, E. S., & Papadakis, I. E. 2017, MNRAS, 472, 3131
Kamraj, N., Harrison, F. A., Baloković, M., et al. 2018, ApJ, 866, 124
Khim, H., & Yi, S. K. 2017, ApJ, 846, 155
Krolik, J. H., & Begelman, M. C. 1988, ApJ, 329, 702
Krongold, Y., Dultzin-Hacyan, D., & Marziani, P. 2003, Revista Mexicana De Astronomia Y Astrofisica Conference Series, 105
Kormendy, J., & Richstone, D. 1995, ARA&A, 33, 581
Kormendy, J., & Ho, L. C. 2013, ARA&A, 51, 511
Koshida, S., Minezaki, T., Yoshii, Y., et al. 2014, ApJ, 788, 159
Krumpe, M., Husemann, B., Tremblay, G. R., et al. 2017, A&A, 607, L9
Laha, S., Markowitz, A. G., Krumpe, M., et al. 2020, ApJ, 897, 66.
Laor, A. 1991, ApJ, 376, 90
Lawrence, A. 1991, MNRAS, 252, 586
Lebouteiller, V., Barry, D. J., Spoon, H. W. W., et al. 2011, ApJS, 196, 8
Leftley, J. H., Tristram, K. R. W., Hönig, S. F., et al. 2018, ApJ, 862, 17
Lira, P., Videla, L., Wu, Y., et al. 2013, ApJ, 764, 159
Liu, Y., & Li, X. 2014, ApJ, 787, 52
Liu, J., Hönig, S. F., Ricci, C., et al. 2019, MNRAS, 490, 4344
Lohfink, A. M., Reynolds, C. S., Miller, J. M., et al. 2012, ApJ, 758, 67
López-Gonzaga, N., Burtscher, L., Tristram, K. R. W., et al. 2016, A&A, 591, A47
Lopez-Rodriguez, E., Fuller, L., Alonso-Herrero, A., et al. 2018, ApJ, 859, 99
Maiolino, R., Marconi, A., & Oliva, E. 2001, A&A, 365, 37
Maiolino, R., Shemmer, O., Imanishi, M., et al. 2007, A&A, 468, 979
Makarov D., Prugniel P., Terekhova N., Courtois H., & Vauglin I. 2014, A&A, 570, A13
Manske, V., & Henning, T. 1998, A&A, 337, 85
Marchesi, S., Ajello, M., Zhao, X., et al. 2019, ApJ, 872, 8
Markowitz, A. G., Krumpe, M., & Nikutta, R. 2014, MNRAS, 439, 1403
Martínez-Paredes, M., Aretxaga, I., Alonso-Herrero, A., et al. 2017, MNRAS, 468, 2
Martínez-Paredes, M., González-Martín, O., Esparza-Arredondo, D., et al. 2020, ApJ, 890, 152
Mason, R. E., Geballe, T. R., Packham, C., et al. 2006, ApJ, 640, 612
Mateos, S., Carrera, F. J., Alonso-Herrero, A., et al. 2016, ApJ, 819, 166
Marziani, P., Sulentic, J. W., Negrete, C. A., et al. 2010, MNRAS, 409, 1033
Murphy, K. D., & Yaqoob, T. 2009, MNRAS, 397, 1549
Nenkova, M., Sirocky, M. M., Ivezić, Ž., et al. 2008, ApJ, 685, 147
Nenkova, M., Sirocky, M. M., Nikutta, R., et al. 2008, ApJ, 685, 160
Netzer, H. 2015, ARA&A, 53, 365
Nicastro, F., Martocchia, A., & Matt, G. 2003, ApJ, 589, L13
Noda, H. & Done, C. 2018, MNRAS, 480, 3898. doi:10.1093/mnras/sty2032
Ogawa, S., Ueda, Y., Tanimoto, A., et al. 2020, arXiv:2011.13931
Oh, K., Yi, S. K., Schawinski, K., et al. 2015, ApJS, 219, 1
Osorio-Clavijo, N., González-Martín, O., Papadakis, I. E., et al. 2020, MNRAS, 491, 29
Papadakis, I. E., Reig, P., & Nandra, K. 2003, MNRAS, 344, 993
Pasetto, A., González-Martín, O., Esparza-Arredondo, D., et al. 2019, ApJ, 872, 69
Patrick, A. R., Reeves, J. N., Porquet, D., et al. 2012, MNRAS, 426, 2522
Pei, Y. C. 1992, ApJ, 395, 130
Pier, E. A., & Krolik, J. H. 1992, ApJ, 401, 99
Piconcelli, E., Bianchi, S., Vignali, C., et al. 2011, A&A, 534, A126
Porquet, D., Reeves, J., Lobban, A., et al. 2017, The X-ray Universe 2017, 180
Porquet, D., Reeves, J. N., Matt, G., et al. 2018, A&A, 609, A42
Ramos Almeida, C., Levenson, N. A., Rodríguez Espinosa, J. M., et al. 2009, ApJ, 702, 1127
Ramos Almeida, C., Levenson, N. A., Alonso-Herrero, A., et al. 2011, ApJ, 731, 92
Ramos Almeida, C., Alonso-Herrero, A., Levenson, N. A., et al. 2014, MNRAS, 439, 3847
Ramos Almeida, C., & Ricci, C. 2017, Nature Astronomy, 1, 679
Reeves, J. N., Lobban, A., & Pounds, K. A. 2018, ApJ, 854, 28
Reynolds, C. S. 2014, Space Sci. Rev., 183, 277
Ricci, C., Trakhtenbrot, B., Koss, M. J., et al. 2017, ApJS, 233, 17
Ricci, C., Trakhtenbrot, B., Koss, M. J., et al. 2017, Nature, 549, 488. doi:10.1038/nature23906
Rieke, G. H. 1978, ApJ, 226, 550
Risaliti, G., Elvis, M., & Nicastro, F. 2002, ApJ, 571, 234
Ronchini, S., Tombesi, F., Vagnetti, F., et al. 2019, A&A, 625, A26.
Rowan-Robinson, M. 1995, MNRAS, 272, 737
Sani, E., Lutz, D., Risaliti, G., et al. 2010, MNRAS, 403, 1246
Sarangi, A., Dwek, E., & Kazanas, D. 2019, ApJ, 885, 126
Schartmann, M., Meisenheimer, K., Camenzind, M., et al. 2008, A&A, 482, 67
Scott, J. E., Kriss, G. A., Lee, J. C., et al. 2004, ApJS, 152, 1
Siebenmorgen, R., Heymann, F., & Efstathiou, A. 2015, A&A, 583, A120

Smith, J. D. T., Draine, B. T., Dale, D. A., et al. 2007, ApJ, 656, 770
Srinivasan, S., Kemper, F., Zhou, Y., et al. 2017, Planet. Space Sci., 149, 56
Stalevski, M., Fritz, J., Baes, M., et al. 2012, Publications de l'Observatoire Astronomique de Beograd, 91, 235
Stalevski, M., Ricci, C., Ueda, Y., et al. 2016, MNRAS, 458, 2288
Sturm, E., Schweitzer, M., Lutz, D., et al. 2005, ApJ, 629, L21
Suganuma, M., Yoshii, Y., Kobayashi, Y., et al. 2006, ApJ, 639, 46
Sulentic, J. W., Marziani, P., & Dultzin-Hacyan, D. 2000, ARA&A, 38, 521
Tanimoto, A., Ueda, Y., Kawamuro, T., et al. 2018, ApJ, 853, 146
Tanimoto, A., Ueda, Y., Odaka, H., et al. 2019, ApJ, 877, 95
Teng, S. H., Brandt, W. N., Harrison, F. A., et al. 2014, ApJ, 785, 19
Tristram, K. R. W., Raban, D., Meisenheimer, K., et al. 2009, A&A, 502, 67
Tombesi, F., Veilleux, S., Meléndez, M., et al. 2017, ApJ, 850, 151
Uematsu, R., Ueda, Y., Tanimoto, A., et al. 2021, arXiv:2103.11224
Ursini, F., Bassani, L., Panessa, F., et al. 2018, MNRAS, 481, 4250
Urry, C. M., & Padovani, P. 1995, PASP, 107, 803
Vestergaard, M., & Peterson, B. M. 2006, ApJ, 641, 689
Wada, K. 2012, ApJ, 758, 66
Walton, D. J., Zoghbi, A., Cackett, E. M., et al. 2013, ApJ, 777, L23
Walton, D. J., Fuerst, F., Harrison, F., et al. 2013, ApJ, 779, 148
Walton, D. J., Brightman, M., Risaliti, G., et al. 2018, MNRAS, 473, 4377
Wang, T. G., Zhou, H. Y., Grupe, D., et al. 2009, AJ, 137, 4002
Wang, J., Xu, D. W., & Wei, J. Y. 2020, ApJ, 901, 1
Wilkes, B. J., Mathur, S., Fiore, F., et al. 2001, ApJ, 549, 248
Woo, J.-H., & Urry, C. M. 2002, ApJ, 581, L5
Yang, G., Boquien, M., Buat, V., et al. 2020, MNRAS, 491, 740
Yaqoob, T. 2012, MNRAS, 423, 3360.
Xu, Y., Baloković, M., Walton, D. J., et al. 2017, ApJ, 837, 21

Appendix A: Disk reflection at X-rays

In order to study the existence of disk reflection emission in our sample, we added the RELXILL to the baseline model used in Eq. 5 (Sect. 3). We used borus02 as the distant reflector component from the torus. Thus, the baseline model is

$$M = zpcfabs \times cutoffpl + (borus02 + relxill) \quad (A.1)$$

We also used an alternative scenario where the disk reflector is affected by the partial covering, which can be written as follows:

$$M = zpcfabs \times (cutoffpl + relxill) + borus02 \quad (A.2)$$

We then statistically compared the best fit obtained using these two baseline models with that obtained without the disk reflection component. When the f-test probability is below 10^{-4} we consider that the disk reflection component is required by the data.

The initial sample includes the 47 AGN with more than 10% of reflection emission (see Sect. 3). Using the baseline model included in Eq. A.1, we found that the disk reflection component is required in 14 out of these 47 AGN. When we used the baseline model included in Eq. A.2, the disk reflection is statistically needed for 12 AGN. Ten objects require reflection irrespective of the baseline model used, another four AGN show signatures of the disk reflection if Eq. A.1 is used, and another two if Eq. A.2 is used.

Among these 16 objects, five of these sources (ESO 103-G035, ESO138-G1, MCG +07-41-03, ESO -097-G013 and NGC 6300) show a resulting model not physically consistent with their type 2 AGN classification. In particular, the model preferred for MCG +07-41-03 is 95% BORUS, 5% RELXILL, and has no intrinsic component (only using Eq. A.1). A similar case is found for ESO 138-G1 where disk reflection is needed only using Eq. A.1 and lack of intrinsic continuum. Meanwhile, the best fits obtained for ESO 103-G035, ESO -097-G013, and NGC 6300 show only RELXILL component without any contribution of BORUS component. In fact, ESO -097-G013 is one of the objects where the disk reflection is only needed when using Eq. A.1, and NGC 6300 requires it only when using Eq. A.2. Arévalo et al. (2014) found that there is an extended reflection component in ESO -097-G013 that might explain the complex behavior without claiming the existence of disk reflection. Indeed, ESO -097-G013 and ESO 103-G035 have already been reproduced with the UXClumpy model by Buchner et al. (2019).

Thus, we excluded the nine Sy1s (FAIRALL 9, Ark,120, NGC 3783, MCG-06-30-15, IC 4329A, NGC 5548, Mrk 841, NGC 6814, and NGC 7314) and two Sy2s (MCG-05-23-16 and IRAS 13197-1627) with significant disk reflection from this analysis. All of them show a contribution to the 3-70 keV of the RELXILL component in the range between ∼15% and 40% and less than ∼5% of the BORUS component (after including disk reflection). Reinforcing this analysis, disk reflection is reported in the literature for eight out of these nine Sy1s (Lohfink et al. 2012; Porquet et al. 2017; Patrick et al. 2012; Brenneman et al. 2011; Walton et al. 2018; Kammoun & Papadakis 2017; Done et al. 2000; Reynolds 2014; Walton et al. 2013; Ebrero et al. 2011). The exception is NGC 5548. We note that, interestingly, among these nine Sy1s, three (NGC 3783, Fairall 9, Mrk 841) require disk reflection using Eq. A.1 but did not require it using Eq. A.2. However, we kept them out of the sample since disk reflection has been reported in the literature for them (see above references). Furthermore, none of the other AGN in our sample have disk reflection reported in the literature.

Appendix B: Poor spectral fits

We found 11 sources (four at X-ray and eight at mid-IR wavelengths) where the resulting fits in one or both wavelengths are bad (χ^2/d.o.f. > 1.2). Figures B.1 and B.2 show the best fit found at X-rays and mid-IR wavelengths, respectively. The *NuSTAR* spectra of Mrk 1018 and PG 1535+547 have fewer than 100 bins in the 3-70 KeV range and the FeKα emission line is not clearly detected. Therefore, a low signal-to-noise ratio might explain the poor fit found. In the case of ESO 428-G014, the spectra have fewer than 80 bins and the N_H value is the lowest obtained through the clumpy baseline model (see Fig. 3, top right panel). Fabbiano et al. (2018) reported the discovery of kilo-parsec extended components in the 3-6 keV hard continuum and FeKα emission line for this source. They concluded that the hard continuum and the FeKα emission line could be associated with circumnuclear clouds and not with a nuclear component (as the torus is), which might explain why we fail to find a good fit with our baseline models.

Regarding the statistically poor mid-IR fits, we found six sources where both baseline models are not able to fit well in the range from $10 - 20\,\mu$m. Interestingly, all of them nicely fit at near-IR wavelengths, an issue that has been reported before for torus models at mid-IR (e.g., Netzer 2015). We note that in the case of MCG +07-41-03, we are not capable of fitting the spectra through any of the tested X-ray and mid-IR baseline models. ESO 097-G013 and NGC 6300 show large residuals for the full mid-IR spectral range. In the case of NGC 6300, we have an ISM contribution when fitting the *Spitzer*/IRS spectra through the clumpy baseline model. Previously radio and near-IR observations of these two sources show evidence that most of the obscuration is associated with water masers or gas outflows, respectively (Greenhill et al. 2003; Gaspar et al. 2019). Therefore, the disk+wind model proposed by Hönig & Kishimoto (2017) might return better fits. However, these models are not available at X-ray wavelengths. The main discrepancies found at mid-IR wavelengths come from the 10 and 20 μm features. These discrepancies might be related to dust particle size and/or composition (Martínez-Paredes et al. 2020).

Appendix C: NH versus inclination angles

We investigated whether the selection of inclination angles, θ_{inc}, could affect the result presented in this work because it is one of the main differences expected between Sy1 and Sy2. However, the difference between the N_H obtained using the smooth (clumpy) baseline model with an inclination angle, θ_{inc}, fixed to 19 (1) and 87 (90) is less than $\log(N_H)$ <0.5 for 95% of the sample. Only Mrk 1392 shows significant disagreement on the N_H (i.e., $\log(N_H) > 0.5$) for each of the models. This source is located outside the one-to-one relation shown in Fig. 3 (top right). Therefore, it shows a disagreement on the column densities obtained for smooth and clumpy models. If the inclination angle of the smooth and clumpy baseline models is fixed to 87 and 90, respectively, Mrk 1392 could be located inside the relationship. However, these inclination angles are not compatible with the source type (Sy1). We conclude that the locus of the sources in Fig. 3 (top right) does not depend on the inclination angle chosen in general.

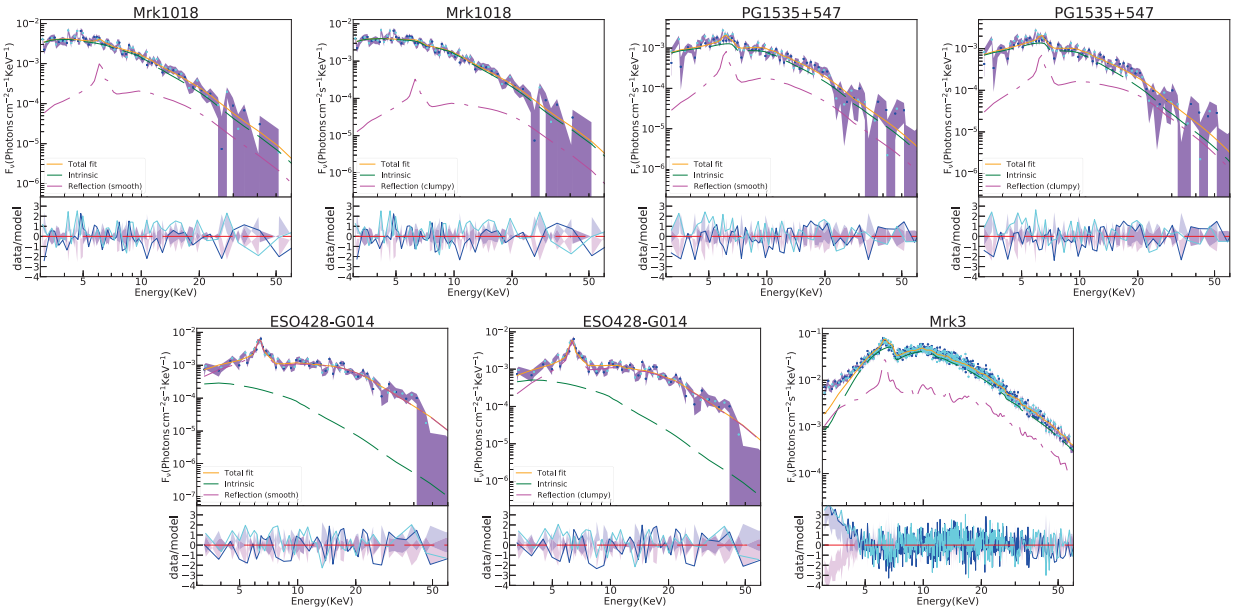

Fig. B.1. Unfolded spectra of Mrk 1018, PG 1535+547, ESO-428-G014, and MCG+07-41-03. The solid orange lines are the best fit obtained from the smooth (top) and clumpy (bottom) baseline models at X-ray wavelengths. *NuSTAR* spectra are displayed with blue and purple solid lines. The green and magenta dotted lines show the the absorbed power law and the reprocessed components, respectively. The lower panels display the residuals between data and the best-fit model.

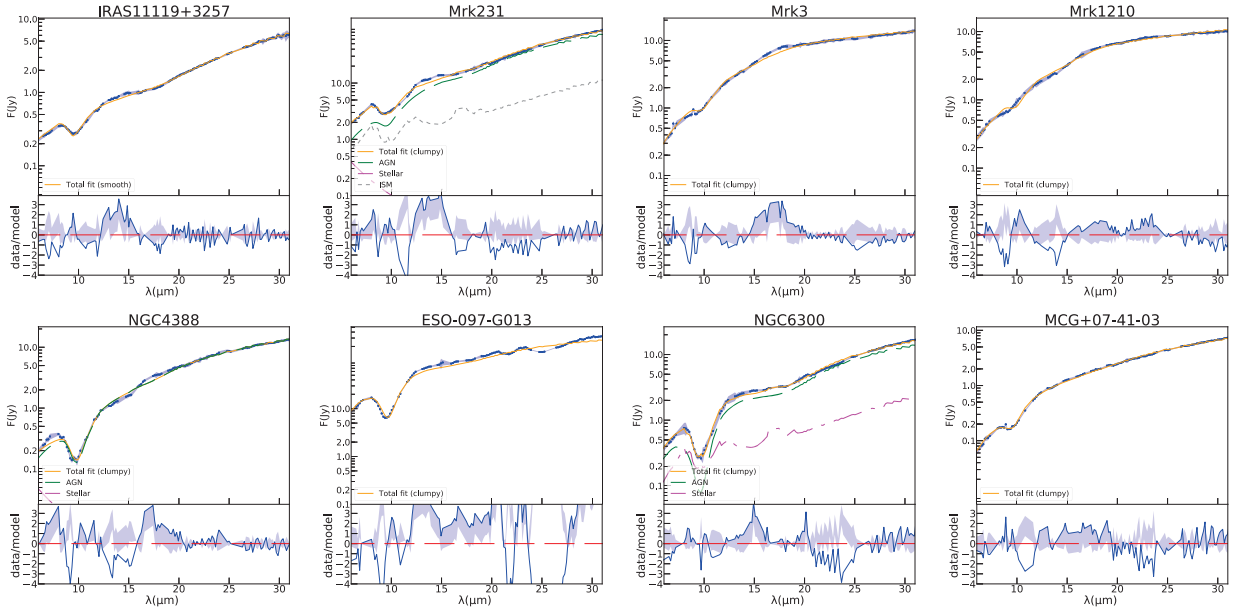

Fig. B.2. Unfolded spectra of I1119+3257,Mrk231,Mrk3,Mrk1210,NGC4388, ESO-097-G013, NGC6300, and MCG+07-41-03. The solid orange lines are the best fit obtained from the smooth baseline model at mid-IR wavelengths. *Spitzer* spectrum is displayed with blue points. The green,pink and gray dotted lines show the AGN, stellar, and ISM components, respectively. The lower panels display the residuals between data and the best-fit model.

Table 6. Comparison between mid-IR and X-ray parameters

Objname	type	N_H	model		Cf		σ	i	N_0	τ_ν	log(NH_{tor})	comment
		variable	X-ray	mid-IR	mid-IR	X-ray	mid-IR		mid-IR		X-ray	
(1)	(2)	(3)	(4)	(5)	(6)	(7)	(8)	(9)	(10)	(11)	(12)	(13)
						Seyfert 1						
Mrk1393	Sy1	Y	Clumpy*	Clumpy	$0.61^{0.79}_{0.47}$	-	<25.3	$10.7^{11.7}_{4.6}$	>14.1	<10.6	$23.9^{24.1}_{23.8}$	
PG0804+761	Sy1	N	Smooth	Smooth	$0.07^{0.11}_{0.02}$	$36.9^{65.6}_{9.1}$	<21.1	<0.1	-	$18.4^{24.6}_{18.0}$	$24.5^{24.7}_{24.3}$	
PG1211+143	Sy1	N	Smooth	Smooth	$0.12^{0.14}_{0.11}$	$64.2^{72.7}_{50.2}$	<20.3	$25.3^{35.3}_{24.0}$	-	>153.9	$24.2^{24.4}_{24.1}$	
Mrk1383	Sy1	N	Smooth	Clumpy	$0.82^{0.93}_{0.54}$	$65.1^{55.1}_{72.2}$	<62.9	>16.8	$3.1^{3.4}_{2.8}$	$75.7^{86.3}_{63.8}$	$24.3^{24.5}_{24.2}$	
Mrk590	Sy1	N	Smooth*	Clumpy	$0.81^{0.94}_{0.51}$	-	>31.7	>55.7	$4.2^{8.2}_{3.5}$	$135.0^{149.2}_{66.3}$	$23.7^{23.8}_{23.7}$	
NGC7213	Sy1	N	Smooth	Clumpy	$0.37^{0.39}_{0.35}$	-	<15.1	<88.5	$7.0^{7.3}_{5.6}$	$55.8^{59.2}_{50.6}$	$22.8^{23.2}_{22.4}$	
						Seyfert 2						
NGC4507	Sy2	Y	Clumpy*	Clumpy	$0.81^{0.91}_{0.51}$	$9.9^{14.2}_{0.6}$	>47.6	>35.3	$3.1^{3.5}_{3.0}$	$70.8^{76.6}_{64.8}$	$23.8^{23.8}_{23.8}$	
NGC1052	Sy2	Y	Clumpy*	Clumpy	$0.87^{0.95}_{0.68}$	$27.8^{60.4}_{0.7}$	>46.6	>51.0	$3.5^{4.6}_{3.3}$	$199.9^{218.0}_{178.6}$	$23.4^{23.4}_{23.3}$	
NGC4939	Sy2	Y	Clumpy*	Clumpy	$0.95^{0.96}_{0.93}$	>21.4	>54.2	<71.7	>8.2	>216.6	$23.7^{23.7}_{23.6}$	
IC5063	Sy2	Y	Clumpy	Clumpy	$0.86^{0.92}_{0.77}$	>16.5	$38.2^{49.7}_{29.9}$	<60.0	>8.8	$95.3^{112.3}_{79.0}$	$23.5^{23.5}_{23.5}$	
ESO138-G1	Sy2	N	Smooth*	Clumpy	$0.95^{0.96}_{0.94}$	$79.4^{80.6}_{78.2}$	>66.8	<87.7	$5.5^{6.1}_{5.2}$	$19.0^{20.1}_{14.6}$	$24.5^{24.6}_{24.5}$	
PKS2356-61	Sy2	N	Smooth	S/C	$0.14^{0.16}_{0.12}$ /$0.8^{0.93}_{0.56}$	-	<21.7/$35.0^{53.1}_{23.4}$	$24.8^{28.2}_{21.3}$ /$40.2^{55.9}_{23.4}$	$5.4^{10.4}_{5.2}$	>204.4/$40.0^{51.0}_{28.3}$	$23.1^{23.2}_{23.0}$	
NGC788	Sy2	N	Smooth	Clumpy	$0.92^{0.96}_{0.81}$	-	>46.8	>28.9	$10.4^{12.1}_{9.6}$	$43.3^{46.5}_{40.6}$	$23.8^{23.9}_{23.8}$	
						Unclassified						
Mrk1392	Sy1	-	Clumpy	Clumpy	$0.52^{0.65}_{0.43}$	$3.0^{7.6}_{0.2}$	<17.9	$6.1^{12.9}_{2.8}$	>13.6	$12.7^{14.3}_{10.8}$	$22.4^{22.4}_{22.4}$	Panel 1 of Fig. 7
RBS0770	Sy1	-	S/C	S/C	$0.11^{0.13}_{0.1}$ /$0.8^{0.93}_{0.52}$	- /$5.4^{7.7}_{2.2}$	<20.4/<57.4	$0.0^{1.9}_{0.0}$ />16.3	$5.0^{6.0}_{3.8}$	$166.4^{181.7}_{155.2}$ /$28.0^{37.5}_{20.9}$	$25.0^{25.2}_{24.7}$ /$22.1^{22.2}_{22.1}$	Panel 3 of Fig. 7
RBS1125	Sy1	-	S/C	Clumpy	$0.77^{0.94}_{0.5}$	- />0.1	<44.5	>4.9	$6.2^{7.3}_{5.7}$	$20.0^{22.4}_{17.1}$	$24.3^{24.4}_{24.1}$ /$24.0^{24.3}_{23.8}$	Panel 3 of Fig. 7
MCG+01-57-016	Sy1	-	S/C	Clumpy	$0.87^{0.95}_{0.67}$	>80.5/$0.3^{0.4}_{0.1}$	$42.6^{67.7}_{29.3}$	<8.5	>6.7	$198.9^{259.6}_{167.8}$	$24.3^{24.9}_{23.9}$ /$22.6^{22.6}_{22.5}$	Panel 3 of Fig. 7
ESO141-G055	Sy1	-	Smooth	S/C	$0.08^{0.14}_{0.07}$ /$0.62^{0.79}_{0.39}$	$59.5^{65.6}_{46.0}$	<21.6/<36.9	$44.7^{47.0}_{40.4}$ />2.7	$3.1^{3.4}_{2.7}$	>215.9/$50.4^{58.6}_{44.1}$	$24.4^{24.6}_{24.3}$	unclassified
UM146	Sy2	-	S/C	Clumpy	$0.92^{0.94}_{0.87}$	- /$1.8^{20.3}_{0.5}$	>55.4	>37.9	$4.8^{5.1}_{4.4}$	$24.7^{28.4}_{22.6}$	$23.3^{23.6}_{23.0}$ /$23.4^{23.5}_{23.0}$	Panel 5 of Fig. 8
NGC1358	Sy2	-	S/C	S/C	$0.42^{0.85}_{0.16}$ /$0.84^{0.95}_{0.56}$	>26.1/<9.6	<58.6/ -	<42.1/<55.6	$7.7^{10.3}_{5.6}$	>53.0/<16.0	$24.2^{24.3}_{24.2}$ /$24.2^{24.3}_{24.2}$	Panel 5 of Fig. 8
IC4518W	Sy2	-	S/C	Clumpy	$0.92^{0.96}_{0.74}$	- /$2.7^{9.7}_{0.3}$	>48.1	>51.5	$8.3^{12.1}_{6.5}$	$27.2^{46.9}_{22.6}$	$23.4^{23.4}_{23.3}$ /$23.3^{23.4}_{23.2}$	Panel 5 of Fig. 8
Mrk78	Sy2	-	S/C	Clumpy	$0.94^{0.96}_{0.82}$	- / -	>55.7	>21.8	>13.9	$53.6^{56.6}_{47.7}$	$23.8^{23.8}_{23.7}$ /$23.8^{23.8}_{23.7}$	Panel 5 of Fig. 8
J05081967+1721483	Sy2	-	Clumpy	Clumpy	$0.83^{0.93}_{0.57}$	>3.3	$53.3^{61.5}_{41.0}$	<75.4	$4.3^{6.7}_{3.1}$	>139.7	$23.5^{23.6}_{23.4}$	Unclassified
ESO103-G35	Sy2	-	Smooth	Clumpy	$0.85^{0.95}_{0.59}$	-	<46.6	>22.7	$8.8^{11.8}_{8.7}$	$46.8^{50.7}_{41.9}$	$24.3^{24.4}_{24.3}$	Panel 6 of Fig. 8
J10594361+6504063	Sy2	-	Smooth	S/C	$0.93^{0.95}_{0.77}$ /$0.96^{0.97}_{0.96}$	-	<22.1/>68.9	$74.6^{78.1}_{71.1}$ /$54.2^{47.5}_{62.1}$	>14.7	>196.7/$20.1^{21.2}_{19.7}$	$22.7^{22.9}_{22.5}$	Panel 6 of Fig. 8

Notes. S/C is included in Col. 4 and 5 when neither of the two models is preferred. Objects marked as "Clumpy*" in Col. 4 are variable at X-rays (denoting a clumpy medium) but preferred at smooth model statistically. In Col. 6 we show the covering factors estimated to mid-IR. In Cols. 8 and 9 we show the half-opening angles using the preferred model at X-ray and mid-IR wavelengths, respectively. Both half-opening angle and inclination angles are measured from the equator of the system to its pole. The optical depth is also converted to the 9.7μm optical depth as $\tau_{9.7\mu m} = 0.042\,\tau_V$.

Table 7. X-ray best-fit results per object and model.

Objname	Baseline model	χ^2/d.o.f.	Parameters								
			θ_{inc} °	$N_{H_{LOS}}$ cm^{-2}	*Cf*	Γ	$\log(N_{H_{tor}})$ cm^{-2}	θ_{tor} °	$\log(f_{intr})$ [3-70] KeV	$\log(f_{refl})$ [3-70] KeV	$\log\left(\frac{f_{refl}}{f_{refl}+f_{intr}}\right)$
(1)	(2)	(3)	(4)	(5)	(6)	(7)	(8)	(9)	(10)	(11)	(12)
Mrk1018	Smooth•	1.21	19.0	24.06*	<0.97	$2.01^{2.12}_{1.91}$	$24.06^{24.43}_{23.79}$	25.63*	$-11.52^{-11.5}_{-11.54}$	$-12.18^{-12.07}_{-12.33}$	-0.75±0.25
	Clumpy•	1.24	90.0	23.7*	$0.43^{0.61}_{0.2}$	$2.16^{2.34}_{1.98}$	$23.7^{23.92}_{22.38}$	28.0*	$-11.5^{-11.49}_{-11.52}$	$-12.47^{-12.25}_{-12.9}$	-1.01±0.57
Mrk590	Smooth	0.98	19.0	23.74*	<0.42	$1.95^{2.0}_{1.9}$	$23.74^{23.8}_{23.66}$	0.0*	$-11.18^{-11.17}_{-11.19}$	$-11.68^{-11.64}_{-11.73}$	-0.62±0.08
	Clumpy	0.98	45.0	23.77*	$0.56^{0.59}_{0.52}$	$2.24^{2.33}_{2.13}$	$23.77^{23.83}_{23.69}$	$6.89^{16.55}_{2.27}$	$-11.2^{-11.19}_{-11.22}$	$-11.68^{-11.63}_{-11.74}$	-0.6±0.1
PG0804+761	Smooth	0.89	19.0	24.47*	<0.38	$1.93^{2.0}_{1.87}$	$24.47^{24.66}_{24.27}$	$53.1^{80.92}_{24.43}$	$-10.8^{-10.79}_{-10.82}$	$-11.48^{-11.4}_{-11.58}$	-0.76±0.17
	Clumpy	0.93	1.0	24.44*	$0.27^{0.37}_{0.15}$	$1.89^{1.97}_{1.82}$	$24.44^{24.65}_{24.13}$	17.6*	$-10.75^{-10.74}_{-10.76}$	$-11.85^{-11.68}_{-12.14}$	-1.13±0.45
RBS0770	Smooth	0.97	45.0	25.02*	$0.19^{0.28}_{0.15}$	$1.91^{1.94}_{1.89}$	$25.02^{25.22}_{24.74}$	84.3*	$-10.33^{-10.32}_{-10.33}$	$-11.11^{-11.06}_{-11.17}$	-0.85±0.11
	Clumpy	0.97	1.0	22.14*	>0.0	$1.94^{1.97}_{1.91}$	$22.14^{22.17}_{22.12}$	$5.42^{7.68}_{2.24}$	$-10.37^{-10.36}_{-10.37}$	$-10.98^{-10.94}_{-11.02}$	-0.70±0.07
I11119+3257	Smooth	1.07	87.0	22.88*	1.0*	$2.42^{2.55}_{2.33}$	$22.88^{23.02}_{22.75}$	84.3*	$-11.9^{-11.86}_{-11.94}$	$-12.61^{-12.46}_{-12.85}$	-0.79±0.36
	Clumpy	1.03	45.0	23.09*	>1.0	$2.84^{2.95}_{2.72}$	$23.09^{23.14}_{23.03}$	$5.99^{7.63}_{4.74}$	$-11.97^{-11.95}_{-11.99}$	$-12.41^{-12.33}_{-12.49}$	-0.57±0.13
PG1211+143	Smooth	0.93	19.0	24.19*	<0.3	$2.16^{2.21}_{2.1}$	$24.19^{24.38}_{24.08}$	$25.8^{39.82}_{17.31}$	$-11.29^{-11.28}_{-11.3}$	$-11.6^{-11.57}_{-11.63}$	-0.48±0.05
	Clumpy	0.98	90.0	23.73*	$0.47^{0.56}_{0.4}$	$2.36^{2.45}_{2.29}$	$23.73^{23.82}_{23.62}$	$28.0^{56.07}_{11.59}$	$-11.24^{-11.23}_{-11.25}$	$-11.87^{-11.82}_{-11.94}$	-0.73±0.11
RBS1125	Smooth	1.04	45.0	24.26*	$0.43^{0.54}_{0.38}$	$2.16^{2.2}_{2.11}$	$24.26^{24.42}_{24.11}$	84.3*	$-11.09^{-11.08}_{-11.11}$	$-11.94^{-11.83}_{-12.11}$	-0.91±0.28
	Clumpy	1.08	1.0	23.99*	$0.41^{0.55}_{0.21}$	$2.23^{2.38}_{2.07}$	$23.99^{24.26}_{23.81}$	>0.07	$-11.11^{-11.09}_{-11.12}$	$-11.94^{-11.81}_{-12.12}$	-0.89±0.30
Mrk231	Smooth	1.09	87.0	23.3*	$0.6^{0.82}_{0.51}$	$1.57^{1.68}_{1.47}$	$23.3^{23.49}_{23.23}$	84.3*	$-11.36^{-11.34}_{-11.38}$	$-12.22^{-12.08}_{-12.43}$	-0.92±0.34
	Clumpy	1.11	90.0	23.37*	$0.71^{0.8}_{0.64}$	$1.78^{1.89}_{1.66}$	$23.37^{23.51}_{23.17}$	>2.18	$-11.4^{-11.38}_{-11.41}$	$-12.1^{-11.99}_{-12.25}$	-0.78±0.24
Mrk1383	Smooth	0.91	19.0	24.34*	<0.4	$2.1^{2.14}_{2.05}$	$24.34^{24.46}_{24.24}$	$24.86^{34.91}_{17.81}$	$-10.82^{-10.81}_{-10.82}$	$-11.26^{-11.23}_{-11.3}$	-0.58±0.06
	Clumpy	0.95	45.0	24.2*	$0.36^{0.43}_{0.28}$	$2.14^{2.2}_{2.09}$	$24.2^{24.2}_{24.14}$	$7.01^{23.28}_{0.01}$	$-10.79^{-10.78}_{-10.79}$	$-11.4^{-11.35}_{-11.46}$	-0.71±0.10
Mrk1392	Smooth	1.02	87.0	25.29*	0.0*	$1.92^{2.0}_{1.85}$	>25.1	84.3*	$-10.98^{-10.97}_{-11.0}$	$-11.33^{-11.28}_{-11.39}$	-0.51±0.10
	Clumpy	0.97	1.0	22.4*	>0.0	$1.99^{2.07}_{1.92}$	$22.4^{22.43}_{22.39}$	$3.03^{7.6}_{0.16}$	$-11.04^{-11.02}_{-11.05}$	$-11.29^{-11.25}_{-11.34}$	-0.45±0.07
Mrk1393	Smooth	1.02	87.0	23.98*	$0.2^{0.4}_{0.01}$	$2.08^{2.17}_{2.0}$	$23.98^{24.12}_{23.89}$	53.1*	$-10.78^{-10.77}_{-10.78}$	$-11.69^{-11.61}_{-11.8}$	-0.97±0.20
	Clumpy	1.03	90.0	23.94*	$0.36^{0.46}_{0.24}$	$2.12^{2.21}_{2.02}$	$23.94^{24.06}_{23.85}$	27.92*	$-10.74^{-10.73}_{-10.75}$	<-12.08	<-1.77
PG1535+547	Smooth•	1.29	19.0	23.85*	$0.78^{0.86}_{0.71}$	$1.97^{2.18}_{1.79}$	$23.85^{23.95}_{23.77}$	9.87*	$-11.75^{-11.72}_{-11.78}$	$-12.28^{-12.18}_{-12.43}$	-0.64±0.22
	Clumpy•	1.27	90.0	23.77*	$0.82^{0.86}_{0.76}$	$2.14^{2.31}_{1.99}$	$23.77^{23.88}_{23.64}$	>0.09	$-11.82^{-11.79}_{-11.85}$	$-12.12^{-12.04}_{-12.23}$	-0.478±0.15
ESO141-G055	Smooth	1.03	19.0	24.39*	0.0*	$1.92^{1.93}_{1.9}$	$24.39^{24.62}_{24.29}$	$30.45^{44.01}_{24.37}$	$-10.29^{-10.29}_{-10.29}$	$-10.9^{-10.89}_{-10.92}$	-0.70±0.03
	Clumpy	1.06	90.0	23.52*	$0.11^{0.13}_{0.07}$	$1.97^{1.99}_{1.96}$	$23.52^{23.66}_{23.23}$	$28.0^{46.64}_{17.71}$	$-10.29^{-10.29}_{-10.29}$	$-10.95^{-10.94}_{-10.97}$	-0.75±0.03
NGC7213	Smooth	0.99	45.0	22.81*	$0.18^{0.46}_{0.10}$	$1.89^{1.93}_{1.87}$	$22.81^{23.20}_{22.35}$	0.0*	$-10.46^{-10.45}_{-10.47}$	$-11.70^{-11.59}_{-11.82}$	-1.26±0.24
	Clumpy	1.01	90.0	23.13*	$0.24^{0.36}_{0.19}$	$1.96^{2.0}_{1.92}$	$23.13^{23.31}_{22.68}$	> 1.05	$-10.46^{-10.45}_{-10.47}$	$-11.84^{-11.65}_{-12.28}$	-1.40±0.56
MCG+01-57-016	Smooth	1.07	19.0	24.34*	<0.22	$1.71^{1.77}_{1.64}$	$24.34^{24.86}_{23.92}$	>9.53	$-10.94^{-10.93}_{-10.95}$	$-11.83^{-11.69}_{-12.05}$	-0.94±0.35
	Clumpy	1.06	1.0	22.55*	$0.51^{0.83}_{0.19}$	$1.82^{1.92}_{1.75}$	$22.55^{22.6}_{22.48}$	$0.29^{0.36}_{0.12}$	$-11.01^{-11.0}_{-11.02}$	$-11.56^{-11.48}_{-11.66}$	-0.66±0.16

Table 7. continued.

Objname	Baseline model	χ^2/d.o.f.	Parameters								
			θ_{inc} °	$N_{H_{LOS}}$ cm^{-2}	*Cf*	Γ	$\log(N_{H_{tor}})$ cm^{-2}	θ_{tor} °	$\log(f_{intr})$ [3-70] KeV	$\log(f_{refl})$ [3-70] KeV	$\log\left(\frac{f_{refl}}{f_{refl}+f_{intr}}\right)$
(1)	(2)	(3)	(4)	(5)	(6)	(7)	(8)	(9)	(10)	(11)	(12)
UM146	Smooth	0.86	87.0	23.34*	>0.48	$1.76^{1.91}_{1.55}$	$23.34^{23.56}_{23.01}$	36.92*	$-11.47^{-11.44}_{-11.51}$	$-11.92^{-11.82}_{-12.03}$	-0.58±0.18
	Clumpy	0.88	1.0	23.45*	$0.77^{0.98}_{0.7}$	$2.2^{2.33}_{1.98}$	$23.45^{23.53}_{23.03}$	$1.82^{20.27}_{0.49}$	$-11.6^{-11.57}_{-11.64}$	$-11.76^{-11.68}_{-11.84}$	-0.38±0.12
NGC788	Smooth	0.9	87.0	23.84*	$0.9^{0.91}_{0.89}$	<1.53	$23.84^{23.87}_{23.82}$	84.3*	$-10.69^{-10.66}_{-10.73}$	$-10.95^{-10.88}_{-11.04}$	-0.45±0.13
	Clumpy	1.0	45.0	23.69*	1.0*	$1.56^{1.63}_{1.46}$	$23.69^{23.76}_{23.61}$	$10.44^{19.92}_{0.17}$	$-10.8^{-10.77}_{-10.83}$	$-10.83^{-10.78}_{-10.89}$	-0.32±0.07
NGC1052	Smooth	1.02	45.0	23.31*	$0.81^{0.84}_{0.79}$	$1.7^{1.74}_{1.66}$	$23.31^{23.36}_{23.25}$	0.0*	$-10.6^{-10.59}_{-10.6}$	$-11.53^{-11.47}_{-11.61}$	-0.99±0.14
	Clumpy	1.02	1.0	23.37*	$0.85^{0.87}_{0.84}$	$1.88^{1.92}_{1.84}$	$23.37^{23.41}_{23.32}$	$27.77^{60.43}_{0.71}$	$-10.64^{-10.64}_{-10.65}$	$-11.32^{-11.28}_{-11.37}$	-0.76±0.08
NGC1358	Smooth	0.93	45.0	24.24*	1.0*	$1.59^{1.7}_{1.51}$	$24.24^{24.28}_{24.21}$	>63.9	$-10.94^{-10.92}_{-10.95}$	$-11.52^{-11.49}_{-11.55}$	-0.68±0.06
	Clumpy	0.94	1.0	24.21*	$0.99^{1.0}_{0.98}$	$1.68^{1.77}_{1.59}$	$24.21^{24.26}_{24.17}$	<9.6	$-11.06^{-11.03}_{-11.09}$	$-11.26^{-11.23}_{-11.3}$	-0.41±0.06
J05081967+1721483	Smooth	1.18	87.0	23.61*	$0.35^{0.45}_{0.19}$	$1.9^{1.98}_{1.8}$	$23.61^{23.7}_{23.53}$	25.76*	$-10.58^{-10.57}_{-10.59}$	$-11.34^{-11.28}_{-11.43}$	-0.83±0.15
	Clumpy	1.15	90.0	23.51*	$0.53^{0.58}_{0.45}$	$2.12^{2.19}_{2.03}$	$23.51^{23.62}_{23.37}$	>3.32	$-10.64^{-10.63}_{-10.65}$	$-11.13^{-11.09}_{-11.19}$	-0.61±0.08
Mrk3	Smooth	0.99	87.0	23.87*	$0.96^{0.96}_{0.96}$	$1.62^{1.63}_{1.61}$	$23.87^{23.87}_{23.86}$	$72.43^{74.51}_{70.58}$	$-9.79^{-9.79}_{-9.8}$	$-10.57^{-10.53}_{-10.63}$	-0.85±0.10
	Clumpy•	1.24	45.0	23.8*	1.0*	$1.63^{1.66}_{1.61}$	$23.8^{23.81}_{23.78}$	$4.83^{7.98}_{2.1}$	$-9.84^{-9.83}_{-9.84}$	$-10.37^{-10.34}_{-10.4}$	-0.64±0.06
ESO428-G014	Smooth•	1.42	19.0	24.38*	<0.99	$2.23^{2.45}_{2.03}$	$24.38^{24.44}_{24.3}$	$13.16^{17.6}_{9.94}$	$-12.82^{-12.68}_{-13.02}$	$-11.2^{-11.18}_{-11.21}$	-0.01±0.01
	Clumpy•	1.48	1.0	20.75*	0.0*	$1.95^{2.0}_{1.88}$	$20.75^{20.82}_{20.67}$	>68.37	$-12.43^{-12.35}_{-12.52}$	$-11.19^{-11.18}_{-11.21}$	-0.02±0.01
Mrk78	Smooth	1.13	45.0	23.78*	$0.91^{0.93}_{0.89}$	<1.55	$23.78^{23.83}_{23.72}$	45.55*	$-10.88^{-10.85}_{-10.91}$	$-11.74^{-11.58}_{-11.99}$	-0.92±0.39
	Clumpy	1.19	90.0	23.77*	$0.92^{0.94}_{0.9}$	$1.5^{1.62}_{1.37}$	$23.77^{23.83}_{23.69}$	1.0*	$-10.88^{-10.85}_{-10.9}$	$-11.88^{-11.61}_{-12.65}$	-1.04±0.76
Mrk1210	Smooth	1.13	45.0	23.45*	$0.88^{0.91}_{0.86}$	$1.53^{1.56}_{1.46}$	$23.45^{23.49}_{23.37}$	0.0*	$-10.29^{-10.28}_{-10.3}$	$-11.18^{-11.09}_{-11.29}$	-0.94±0.20
	Clumpy	1.09	90.0	23.46*	$0.92^{0.94}_{0.9}$	$1.76^{1.8}_{1.71}$	$23.46^{23.51}_{23.41}$	>1.76	$-10.39^{-10.38}_{-10.4}$	$-10.81^{-10.77}_{-10.86}$	-0.56±0.07
J10594361+6504063	Smooth	0.78	45.0	22.72*	>0.18	$1.57^{1.66}_{1.5}$	$22.72^{22.92}_{22.49}$	0.0*	$-11.2^{-11.17}_{-11.24}$	$-11.98^{-11.83}_{-12.21}$	-0.84±0.35
	Clumpy	0.84	45.0	23.15*	>0.46	$1.74^{1.89}_{1.6}$	$23.15^{23.41}_{22.91}$	1.0*	$-11.19^{-11.17}_{-11.21}$	<-12.03	<-1.18
NGC4388	Smooth	1.01	19.0	23.56*	$0.87^{0.89}_{0.86}$	$1.55^{1.59}_{1.51}$	$23.56^{23.59}_{23.52}$	0.0*	$-10.35^{-10.34}_{-10.36}$	$-10.76^{-10.73}_{-10.8}$	-0.55±0.06
	Clumpy	1.14	45.0	23.44*	1.0*	$1.8^{1.87}_{1.78}$	$23.44^{23.48}_{23.42}$	$6.9^{7.99}_{3.11}$	$-10.5^{-10.49}_{-10.52}$	$-10.55^{-10.53}_{-10.57}$	-0.32±0.03
NGC4507	Smooth	0.95	19.0	23.81*	$0.95^{0.96}_{0.95}$	$1.59^{1.59}_{1.58}$	$23.81^{23.82}_{23.81}$	0.0*	$-9.95^{-9.94}_{-9.95}$	$-10.55^{-10.52}_{-10.58}$	-0.7±0.06
	Clumpy	1.09	45.0	23.78*	1.0*	$1.69^{1.72}_{1.66}$	$23.78^{23.8}_{23.76}$	$9.91^{14.15}_{0.58}$	$-10.02^{-10.01}_{-10.03}$	$-10.36^{-10.34}_{-10.38}$	-0.51±0.04
NGC4939	Smooth	0.7	87.0	23.78*	$0.95^{0.96}_{0.94}$	$1.61^{1.65}_{1.58}$	$23.78^{23.8}_{23.76}$	<51.0	$-10.79^{-10.77}_{-10.82}$	$-11.64^{-11.49}_{-11.87}$	-0.9±0.36
	Clumpy	0.75	90.0	23.67*	1.0*	$1.64^{1.77}_{1.56}$	$23.67^{23.72}_{23.63}$	>21.4	$-10.85^{-10.83}_{-10.88}$	$-11.34^{-11.24}_{-11.46}$	-0.61±0.19
ESO-097-G013	Smooth	1.03	45.0	25.01*	$0.98^{0.99}_{0.98}$	$2.55^{2.56}_{2.55}$	$25.15^{25.16}_{25.14}$	$38.46^{38.48}_{38.43}$	$-11.07^{-11.06}_{-11.08}$	$-9.67^{-9.66}_{-9.67}$	-0.02±0.01
	Clumpy•	1.22	1.0	24.82*	$1.0^{1.0}_{0.99}$	$2.54^{2.56}_{2.51}$	$24.82^{24.83}_{24.81}$	$27.76^{33.88}_{13.53}$	$-9.83^{-9.83}_{-9.84}$	$-10.1^{-10.1}_{-10.1}$	-0.43± 0.01
IC4518W	Smooth	1.04	87.0	23.39*	$0.76^{0.94}_{0.69}$	<1.61	$23.39^{23.45}_{23.34}$	84.3*	$-10.6^{-10.57}_{-10.63}$	$-11.36^{-11.2}_{-11.61}$	-0.83±0.38
	Clumpy	1.02	1.0	23.3*	$0.87^{0.92}_{0.81}$	$1.73^{1.81}_{1.63}$	$23.3^{23.4}_{23.2}$	$2.72^{9.68}_{0.34}$	$-10.72^{-10.7}_{-10.74}$	$-11.0^{-10.93}_{-11.08}$	-0.46±0.12
ESO138-G1	Smooth○	0.99	19.0	$23.87^{23.89}_{23.85}$	$0.96^{0.97}_{0.96}$	$2.51^{2.54}_{2.48}$	$24.51^{24.57}_{24.46}$	$10.57^{11.75}_{9.43}$	$-11.16^{-11.13}_{-11.18}$	$-10.97^{-10.94}_{-10.99}$	-0.22±0.03

Table 7. continued.

Objname	Baseline model	χ^2/d.o.f.	Parameters								
			θ_{inc} °	$N_{H_{LOS}}$ cm^{-2}	*Cf*	Γ	$\log(N_{H_{tor}})$ cm^{-2}	θ_{tor} °	$\log(f_{intr})$ [3-70] KeV	$\log(f_{refl})$ [3-70] KeV	$\log\left(\frac{f_{refl}}{f_{refl}+f_{intr}}\right)$
(1)	(2)	(3)	(4)	(5)	(6)	(7)	(8)	(9)	(10)	(11)	(12)
	Clumpy	0.99	90.0	23.76*	$0.88^{0.9}_{0.86}$	$2.23^{2.29}_{2.17}$	$23.76^{23.82}_{23.68}$	$28.07^{80.37}_{15.66}$	$-11.25^{-11.23}_{-11.28}$	$-10.9^{-10.88}_{-10.92}$	-0.16±0.02
NGC6300	Smooth○	0.85	87.0	$23.3^{23.31}_{23.28}$	$0.95^{0.96}_{0.94}$	$1.95^{1.98}_{1.93}$	$24.35^{24.39}_{24.32}$	<60.57	$-10.21^{-10.2}_{-10.21}$	$-10.53^{-10.51}_{-10.55}$	-0.49±0.03
	Clumpy	0.86	90.0	23.18*	>0.93	$1.78^{1.81}_{1.76}$	$23.18^{23.2}_{23.16}$	$28.0^{63.76}_{17.26}$	$-10.19^{-10.18}_{-10.19}$	$-10.56^{-10.54}_{-10.59}$	-0.53±0.04
ESO103-G35	Smooth○	1.04	87.0	$23.46^{23.47}_{23.45}$	$0.93^{0.94}_{0.93}$	$2.07^{2.09}_{2.05}$	$24.34^{24.36}_{24.32}$	0.0*	$-10.14^{-10.14}_{-10.15}$	$-10.46^{-10.45}_{-10.48}$	-0.49±0.02
	Clumpy	1.06	90.0	23.36*	$0.93^{0.94}_{0.92}$	$1.86^{1.88}_{1.84}$	$23.36^{23.38}_{23.34}$	$28.09^{37.01}_{24.86}$	$-10.12^{-10.11}_{-10.12}$	$-10.49^{-10.47}_{-10.5}$	-0.53±0.02
MCG+07-41-03	Smooth	1.12	87.0	22.92*	$0.61^{0.74}_{0.52}$	$1.69^{1.71}_{1.68}$	$22.92^{23.02}_{22.80}$	$36.92^{40.32}_{33.05}$	$-9.83^{-9.82}_{-9.83}$	$-10.68^{-10.66}_{-10.71}$	-0.91±0.05
	Clumpy	1.18	1.0	23.0*	$0.6^{0.7}_{0.57}$	$1.74^{1.77}_{1.71}$	$23.05^{23.14}_{23.00}$	> 7.40	$-9.78^{-9.77}_{-9.80}$	$-11.32^{-11.09}_{-11.93}$	-1.54±0.70
IC5063	Smooth	0.97	19.0	23.49*	$0.88^{0.9}_{0.86}$	$1.62^{1.67}_{1.56}$	$23.5^{23.53}_{23.42}$	0.0*	$-10.29^{-10.28}_{-10.3}$	$-11.04^{-10.98}_{-11.11}$	-0.82±0.12
	Clumpy	0.93	45.0	23.5*	$0.92^{0.94}_{0.91}$	$1.88^{1.92}_{1.82}$	$23.5^{23.54}_{23.46}$	>16.53	$-10.4^{-10.39}_{-10.4}$	$-10.74^{-10.71}_{-10.78}$	-0.51±0.05
PKS2356-61	Smooth	0.92	45.0	23.09*	>0.73	$1.6^{1.67}_{1.54}$	$23.09^{23.17}_{22.98}$	72.4*	$-10.95^{-10.92}_{-10.97}$	$-11.76^{-11.65}_{-11.9}$	-0.87±0.24
	Clumpy	0.99	90.0	23.31*	>0.78	$1.81^{1.92}_{1.67}$	$23.31^{23.4}_{23.23}$	>0.11	$-10.95^{-10.94}_{-10.96}$	$-11.93^{-11.75}_{-12.24}$	-1.02±0.46

Notes. Col. (1): Source name. Col. (2): X-ray baseline model used. The fit obtained using the baseline model with $N_{H_{tor}}$ independent to the $N_{H_{los}}$ and bat fits (χ^2/d.o.f. > 1.2) are marked with white and black dots next to the baseline model name, respectively. Col. (3): Reduced χ^2 (χ^2/d.o.f.). Cols.(4-9): Final parameter values per model (see Table 1). The asterisk next to the value indicate that the parameter is not constrained. Cols.(10-11): Intrinsic continuum and reflection component fluxes. Col. (12): Reflection fraction relative to the total flux. The confidence range of error calculated here is 1 sigma.

Table 8. Mid-IR best-fit results per object and model.

Objname	Baseline model	A/S/I %	χ^2/d.o.f.	E_{B-V}	Parameters					
	Smooth				i	σ	γ	β	Y	$\tau_{9.7}$
	Clumpy				i	N_0	σ	Y	q	τ_ν
(1)	(2)	(3)	(4)	(5)	(6)	(7)	(8)	(9)	(10)	(11)
Mrk1018	Smooth○	87.6/ 12.4/ 0.0	0.69	<0.5	<0.0	<21.4	$5.7^{5.8}_{5.1}$	>-0.0	<10.1	$5.6^{6.4}_{4.8}$
	Clumpy○	88.2/ 11.8/ 0.0	0.46	<0.5	>77.3	$3.3^{4.0}_{2.5}$	<63.4	$19.7^{25.1}_{12.1}$	>2.2	$41.3^{48.2}_{31.7}$
Mrk590	Smooth○●	100.0/ 0.0/ 0.0	1.31	<0.5	$14.9^{17.2}_{12.8}$	<20.2	>6.0	>-0.0	$21.1^{21.3}_{20.7}$	>9.8
	Clumpy○	96.5/ 3.5/ 0.0	0.23	<0.5	>34.3	$4.2^{8.2}_{3.5}$	>31.7	$10.1^{13.6}_{9.6}$	$1.5^{1.6}_{1.3}$	$135.0^{149.2}_{66.3}$
PG0804+761	Smooth○	96.8/ 3.2/ 0.0	0.76	<0.5	<0.1	<21.1	$4.0^{5.03}_{3.97}$	$-0.75^{-0.7}_{-0.85}$	$11.44^{11.55}_{11.35}$	$0.77^{1.03}_{0.76}$
	Clumpy○●	85.6/ 10.4/ 4.0	1.63	<0.5	>76.3	<1.2	<64.4	>40.3	$2.29^{2.35}_{2.23}$	$67.0^{86.8}_{54.8}$
RBS0770	Smooth○	94.7/ 5.3/ 0.0	0.44	<0.5	<1.9	<20.4	>6.0	$-0.2^{-0.1}_{-0.3}$	<10.1	$7.0^{7.6}_{6.5}$
	Clumpy○	93.9/ 6.1/ 0.0	0.47	<0.5	>73.7	$5.0^{6.0}_{3.8}$	<57.4	$10.0^{10.7}_{9.3}$	$1.6^{1.8}_{1.4}$	$28.0^{37.5}_{20.9}$
I11119+3257	Smooth○●	100.0/ 0.0/ 0.0	1.20	$0.3^{0.4}_{0.1}$	<2.5	>59.3	$0.08^{0.12}_{0.05}$	>-0.0	$115.9^{123.9}_{108.4}$	$2.3^{2.4}_{2.2}$
	Clumpy●	62.0/ 6.6/ 31.4	2.54	$0.6^{0.7}_{0.6}$	<0.0	>14.9	$48.1^{49.1}_{47.7}$	$80.0^{81.2}_{78.4}$	$0.2^{0.5}_{0.1}$	$80.0^{82.6}_{77.8}$
PG1211+143	Smooth○	94.9/ 5.1/ 0.0	1.01	<0.5	$25.3^{35.3}_{24.0}$	<20.3	>6.0	$-0.5^{-0.49}_{-0.51}$	<10.2	>6.5
	Clumpy○●	92.9/ 7.1/ 0.0	1.25	<0.5	>84.0	$3.0^{3.4}_{2.9}$	$31.8^{41.7}_{16.1}$	$20.0^{21.2}_{18.9}$	$1.82^{1.89}_{1.76}$	$39.7^{42.6}_{35.3}$
RBS1125	Smooth○●	100.0/ 0.0/ 0.0	1.63	<0.5	$66.5^{68.1}_{51.2}$	$22.6^{32.8}_{21.1}$	$0.25^{0.35}_{0.2}$	$-0.7^{-0.6}_{-0.8}$	<10.1	$6.0^{6.1}_{5.7}$
	Clumpy○	93.5/ 6.5/ 0.0	0.51	<0.5	>85.1	$6.2^{7.3}_{5.7}$	<44.5	$20.9^{23.5}_{19.2}$	$1.1^{1.3}_{1.0}$	$20.0^{22.4}_{17.1}$
Mrk231	Smooth○●	100.0/ 0.0/ 0.0	2.54	$0.5^{0.5}_{0.4}$	<0.0	$35.8^{36.5}_{34.9}$	$1.98^{2.01}_{1.68}$	>-0.0	$117.8^{121.6}_{113.3}$	$2.3^{2.36}_{2.26}$
	Clumpy●	78.0/ 2.2/ 19.8	2.46	$0.9^{1.0}_{0.8}$	<0.0	>14.9	$48.1^{48.6}_{46.2}$	$48.4^{50.9}_{46.8}$	$0.5^{0.51}_{0.37}$	$78.7^{81.0}_{69.1}$
Mrk1383	Smooth○	82.2/ 7.3/ 10.6	0.83	<0.5	<0.0	<20.8	>5.9	>-0.0	$12.4^{12.5}_{12.1}$	$7.1^{7.6}_{6.9}$
	Clumpy○	85.0/ 7.8/ 7.3	0.42	<0.5	>73.2	$3.1^{3.4}_{2.8}$	<62.9	>55.1	>2.4	$75.7^{86.3}_{63.8}$
Mrk1392	Smooth○●	97.9/ 2.1/ 0.0	1.69	<0.5	$16.0^{20.0}_{14.9}$	<20.4	>6.0	>-0.0	$22.2^{23.0}_{21.9}$	>9.6
	Clumpy○	91.7/ 2.4/ 5.8	0.68	<0.5	$83.9^{87.2}_{77.1}$	>13.6	<17.9	$14.1^{15.3}_{13.4}$	<0.1	$12.7^{14.3}_{10.8}$
Mrk1393	Smooth○●	100.0/ 0.0/ 0.0	2.30	<0.5	$65.9^{67.5}_{64.7}$	<20.6	<0.0	>-0.0	<10.1	$6.0^{6.3}_{5.8}$
	Clumpy○	95.4/ 4.6/ 0.0	0.62	<0.5	$79.3^{85.4}_{78.3}$	>14.1	<25.3	$20.0^{20.3}_{17.3}$	$0.7^{0.8}_{0.4}$	<10.6
PG1535+547	Smooth○	83.8/ 8.1/ 8.1	0.19	<0.5	<1.7	<25.4	$3.8^{4.3}_{2.8}$	<-1.0	<10.3	$4.2^{4.8}_{3.2}$
	Clumpy○	87.0/ 7.5/ 5.5	0.58	$0.7^{0.8}_{0.6}$	>83.0	$3.0^{3.1}_{2.7}$	$54.4^{67.8}_{47.4}$	$14.5^{17.3}_{12.5}$	>2.5	$40.1^{41.7}_{38.4}$
ESO141-G055	Smooth○	88.0/ 8.1/ 3.8	0.99	<0.5	$44.7^{47.0}_{40.4}$	<21.6	>5.9	$-0.6^{-0.5}_{-0.7}$	$11.3^{11.5}_{10.9}$	>9.1
	Clumpy○	90.1/ 9.9/ 0.0	0.97	<0.5	>87.3	$3.1^{3.4}_{2.7}$	<36.9	>67.0	$2.11^{2.17}_{2.06}$	$50.4^{58.6}_{44.1}$
NGC7213	Smooth○●	95.6/ 4.4/ 0.0	8.39	<0.5	$24.0^{25.9}_{23.1}$	<20.1	>6.0	>-0.0	$16.1^{16.6}_{15.8}$	>9.9
	Clumpy○	97.0/ 3.0/ 0.0	1.08	$0.8^{0.8}_{0.7}$	<1.5	$7.0^{7.3}_{5.6}$	<15.1	$10.2^{10.6}_{10.0}$	<0.0	$55.8^{59.2}_{50.6}$
MCG+01-57-016	Smooth●	76.0/ 3.7/ 20.3	1.78	<0.5	$15.3^{16.8}_{14.7}$	<21.9	>5.9	>-0.0	$37.3^{38.0}_{36.6}$	>9.0

Table 8. continued.

Objname	Baseline model	A/S/I %	χ^2/d.o.f.	E_{B-V}	Parameters					
	Smooth				i	σ	γ	β	Y	$\tau_{9.7}$
	Clumpy				i	N_0	σ	Y	q	τ_ν
(1)	(2)	(3)	(4)	(5)	(6)	(7)	(8)	(9)	(10)	(11)
	Clumpy	62.2/ 4.7/ 33.1	1.00	<0.5	<81.5	>6.7	$42.6^{67.7}_{29.3}$	$10.6^{12.0}_{9.3}$	<1.5	$198.9^{259.6}_{167.8}$
UM146	Smooth○	100.0/ 0.0/ 0.0	0.92	<0.5	<0.0	$55.4^{57.1}_{49.5}$	>5.4	>-0.1	$36.7^{40.9}_{34.5}$	$3.8^{4.0}_{3.3}$
	Clumpy○	100.0/ 0.0/ 0.0	0.56	$0.8^{0.9}_{0.7}$	>52.1	$4.8^{5.1}_{4.4}$	>55.4	>95.9	$1.26^{1.34}_{1.21}$	$24.7^{28.4}_{22.6}$
NGC788	Smooth○●	100.0/ 0.0/ 0.0	2.45	<0.5	$9.9^{10.1}_{5.5}$	<20.2	$5.64^{5.7}_{5.57}$	>-0.0	$16.8^{17.2}_{16.6}$	>10.0
	Clumpy○	89.8/ 3.7/ 6.5	0.63	<0.5	>61.1	$10.4^{12.1}_{9.6}$	>46.8	$20.0^{23.7}_{17.4}$	>2.4	$43.3^{46.5}_{40.6}$
NGC1052	Smooth○●	95.8/ 4.2/ 0.0	2.53	<0.5	$22.4^{22.9}_{21.7}$	<20.4	>5.9	>-0.0	$27.9^{28.4}_{27.4}$	>9.7
	Clumpy○	82.1/ 5.3/ 12.5	0.79	<0.5	>39.0	$3.5^{4.6}_{3.3}$	>46.6	$10.0^{10.3}_{9.8}$	$1.0^{1.1}_{0.7}$	$199.9^{218.0}_{178.6}$
NGC1358	Smooth○	100.0/ 0.0/ 0.0	0.22	<0.5	<42.1	<58.6	<0.2	<-0.4	$59.4^{94.5}_{35.3}$	>2.2
	Clumpy○	100.0/ 0.0/ 0.0	0.23	$3.4^{3.9}_{2.6}$	<34.4	$7.7^{10.3}_{5.6}$	>15.0	>80.3	$0.9^{1.1}_{0.6}$	<16.0
J05081967+1721483	Smooth○●	81.0/ 0.0/ 19.0	1.66	<0.5	$20.0^{20.4}_{19.5}$	<21.4	$4.17^{4.21}_{4.12}$	<-1.0	$127.5^{133.4}_{121.0}$	$8.5^{8.9}_{8.0}$
	Clumpy	65.3/ 1.9/ 32.8	0.97	$0.7^{0.8}_{0.6}$	<14.6	$4.3^{6.7}_{3.1}$	$53.3^{61.5}_{41.0}$	>95.9	$1.1^{1.2}_{1.0}$	>139.7
Mrk3	Smooth○●	100.0/ 0.0/ 0.0	3.11	<0.5	$10.0^{10.4}_{8.8}$	<20.1	>6.0	>-0.0	$29.5^{29.9}_{29.2}$	>9.9
	Clumpy○●	100.0/ 0.0/ 0.0	1.38	<0.5	$75.5^{88.0}_{74.0}$	>14.3	$42.5^{46.6}_{41.6}$	$20.0^{20.1}_{19.8}$	$0.5^{0.52}_{0.43}$	<10.1
ESO428-G014	Smooth○	100.0/ 0.0/ 0.0	1.02	$0.4^{0.5}_{0.3}$	$9.9^{10.4}_{5.4}$	<27.5	$5.6^{5.8}_{2.7}$	>-0.0	$33.4^{34.0}_{32.8}$	>9.6
	Clumpy○	100.0/ 0.0/ 0.0	0.57	$0.5^{0.6}_{0.4}$	>57.8	>9.8	<26.4	$35.0^{39.4}_{32.2}$	$1.5^{1.6}_{1.3}$	$26.1^{33.3}_{22.1}$
Mrk78	Smooth○●	87.9/ 1.4/ 10.7	1.69	<0.5	$0.8^{4.3}_{0.2}$	<20.7	$5.22^{5.3}_{5.17}$	>-0.0	$30.0^{30.4}_{29.8}$	>9.9
	Clumpy○	82.9/ 3.6/ 13.5	0.82	$0.5^{0.5}_{0.4}$	>68.2	>13.9	>55.7	>48.3	>2.4	$53.6^{56.6}_{47.7}$
Mrk1210	Smooth○●	100.0/ 0.0/ 0.0	2.40	<0.5	$12.5^{13.1}_{12.2}$	<20.1	>6.0	>-0.0	$29.9^{30.1}_{29.7}$	>9.8
	Clumpy○●	100.0/ 0.0/ 0.0	1.21	<0.5	$67.9^{75.2}_{63.2}$	$12.3^{13.1}_{11.5}$	$50.3^{61.9}_{37.8}$	$22.6^{23.1}_{22.0}$	$0.5^{0.51}_{0.33}$	<10.1
J10594361+6504063	Smooth○	100.0/ 0.0/ 0.0	0.24	$0.6^{0.7}_{0.4}$	$74.6^{78.1}_{71.1}$	<22.1	<0.0	>-0.1	<10.6	>8.3
	Clumpy○	83.3/ 6.7/ 10.0	0.22	$0.7^{0.9}_{0.4}$	$35.8^{42.5}_{27.9}$	>14.7	>68.9	$11.0^{11.5}_{10.6}$	<0.0	$20.1^{21.2}_{19.7}$
NGC4388	Smooth○●	83.6/ 0.0/ 16.4	2.35	<0.5	$52.4^{53.2}_{51.3}$	<20.0	<0.0	>-0.1	$30.0^{30.1}_{29.5}$	$7.8^{7.9}_{7.6}$
	Clumpy○●	98.2/ 1.8/ 0.0	1.75	$0.9^{1.0}_{0.8}$	>80.2	$11.4^{11.7}_{11.1}$	>67.0	$52.6^{54.5}_{51.1}$	$0.5^{0.53}_{0.46}$	<10.1
NGC4507	Smooth●	79.6/ 4.1/ 16.4	2.51	<0.5	$12.9^{14.0}_{10.9}$	<20.8	>6.0	>-0.0	$21.1^{21.7}_{20.7}$	$7.3^{7.8}_{6.7}$
	Clumpy○	83.2/ 4.7/ 12.1	0.99	<0.5	>54.7	$3.1^{3.5}_{3.0}$	>47.6	>75.3	$2.0^{2.05}_{1.96}$	$70.8^{76.6}_{64.8}$
NGC4939	Smooth○●	98.7/ 1.3/ 0.0	2.06	<0.5	<0.0	<20.2	>6.0	>-0.0	$32.9^{33.3}_{32.2}$	$7.7^{8.1}_{7.2}$
	Clumpy○	90.9/ 3.3/ 5.9	0.85	<0.5	<18.3	>8.2	>54.2	$10.0^{10.1}_{9.6}$	<0.2	>216.6
ESO-097-G013	Smooth●	72.8/ 0.0/ 27.2	32.01	<0.5	<12.7	<20.1	<0.0	>-0.0	<10.0	$6.8^{6.9}_{6.7}$
	Clumpy○●	100.0/ 0.0/ 0.0	26.71	$2.2^{2.2}_{2.2}$	<13.9	$13.0^{13.5}_{12.3}$	>69.0	>99.3	$2.1^{2.2}_{2.0}$	$23.6^{24.6}_{22.6}$

Table 8. continued.

Objname	Baseline model	A/S/I %	χ^2/d.o.f.	E_{B-V}	Parameters					
	Smooth				i	σ	γ	β	Y	$\tau_{9.7}$
	Clumpy				i	N_0	σ	Y	q	τ_ν
(1)	(2)	(3)	(4)	(5)	(6)	(7)	(8)	(9)	(10)	(11)
IC4518W	Smooth●	74.8/ 0.0/ 25.2	1.37	$1.4^{1.5}_{1.2}$	<1.2	$48.7^{51.8}_{44.2}$	$4.0^{4.1}_{3.8}$	>-0.0	$36.6^{38.7}_{34.5}$	$6.0^{6.2}_{5.8}$
	Clumpy	73.6/ 2.4/ 24.0	0.88	$3.1^{3.3}_{2.9}$	>38.5	$8.3^{12.1}_{6.5}$	>48.1	>96.5	$1.67^{1.74}_{1.59}$	$27.2^{46.9}_{22.6}$
ESO138-G1	Smooth○●	90.5/ 2.1/ 7.3	1.67	<0.5	$11.5^{13.1}_{5.9}$	<20.2	>6.0	>-0.0	$15.0^{15.2}_{14.8}$	>9.6
	Clumpy○	87.7/ 0.0/ 12.3	0.67	$0.8^{0.8}_{0.6}$	<2.3	$5.5^{6.1}_{5.2}$	>66.8	$11.0^{11.3}_{10.9}$	<0.0	$19.0^{20.1}_{14.6}$
NGC6300	Smooth●	75.4/ 0.0/ 24.6	3.73	$2.1^{2.2}_{2.0}$	<0.0	$50.6^{51.9}_{48.2}$	>5.9	>-0.0	$21.1^{21.6}_{20.4}$	>9.7
	Clumpy●	78.8/ 0.0/ 21.2	1.90	$4.3^{4.3}_{4.1}$	<12.0	$10.2^{11.1}_{9.1}$	<32.5	>97.0	$1.78^{1.79}_{1.73}$	>290.0
ESO103-G35	Smooth○●	85.4/ 0.0/ 14.6	3.57	<0.5	$60.0^{60.1}_{59.8}$	<20.0	<0.0	>-0.0	<10.0	$7.4^{7.5}_{7.3}$
	Clumpy○	97.7/ 2.3/ 0.0	0.53	$1.2^{1.3}_{1.2}$	>67.3	$8.8^{11.8}_{8.7}$	<46.6	$28.1^{35.7}_{24.6}$	$2.2^{2.3}_{2.1}$	$46.8^{50.7}_{41.9}$
MCG+07-41-03	Smooth○●	93.9/ 0.0/ 6.1	5.14	$0.3^{0.3}_{0.2}$	<0.0	$22.5^{24.6}_{21.2}$	>6.0	>-0.0	$42.7^{43.2}_{41.8}$	>9.9
	Clumpy○●	100.0/ 0.0/ 0.0	1.48	$1.3^{1.4}_{1.3}$	<14.1	$7.0^{7.8}_{6.5}$	>62.9	>97.3	$1.85^{1.88}_{1.83}$	$177.2^{201.9}_{150.5}$
IC5063	Smooth○●	89.3/ 0.0/ 10.7	2.01	<0.5	<0.4	$23.4^{24.5}_{22.5}$	>6.0	>-0.0	$25.4^{26.1}_{24.7}$	$8.5^{8.8}_{8.0}$
	Clumpy○	93.8/ 0.0/ 6.2	0.61	$0.6^{0.6}_{0.5}$	<30.0	>8.8	$38.2^{49.7}_{29.9}$	$16.4^{18.6}_{14.1}$	$0.8^{1.0}_{0.7}$	$95.3^{112.3}_{79.0}$
PKS2356-61	Smooth○	98.3/ 1.7/ 0.0	0.33	$1.0^{1.1}_{0.9}$	$24.8^{28.2}_{21.3}$	<21.7	>5.8	>-0.0	$27.9^{29.4}_{26.7}$	>8.6
	Clumpy○	100.0/ 0.0/ 0.0	0.31	$1.2^{1.3}_{1.1}$	$49.8^{66.6}_{34.1}$	$5.4^{10.4}_{5.2}$	$35.0^{53.1}_{23.4}$	$18.4^{21.1}_{15.8}$	<0.9	$40.0^{51.0}_{28.3}$

Notes. Col. (1): Source name. Col. (2): Mid-IR baseline model used. Col. (3):Percentage contribution to the $5-30\,\mu m$ waveband per component (A: AGN; S: stellar; and I: Interstellar medium). Col. (4): Reduced χ^2 (χ^2/d.o.f.). Col. (5): Color excess for the foreground extinction. Cols. (6-11): Final parameter values per model (see Table 1). The confidence range of error calculated here is 1 sigma. AGN-dominated spectra in more than 80% and the bad-fits (χ^2/d.o.f. > 1.2) are marked with white and black dots next to the model name, respectively.

Chapter 4

Development of the simultaneous fitting technique

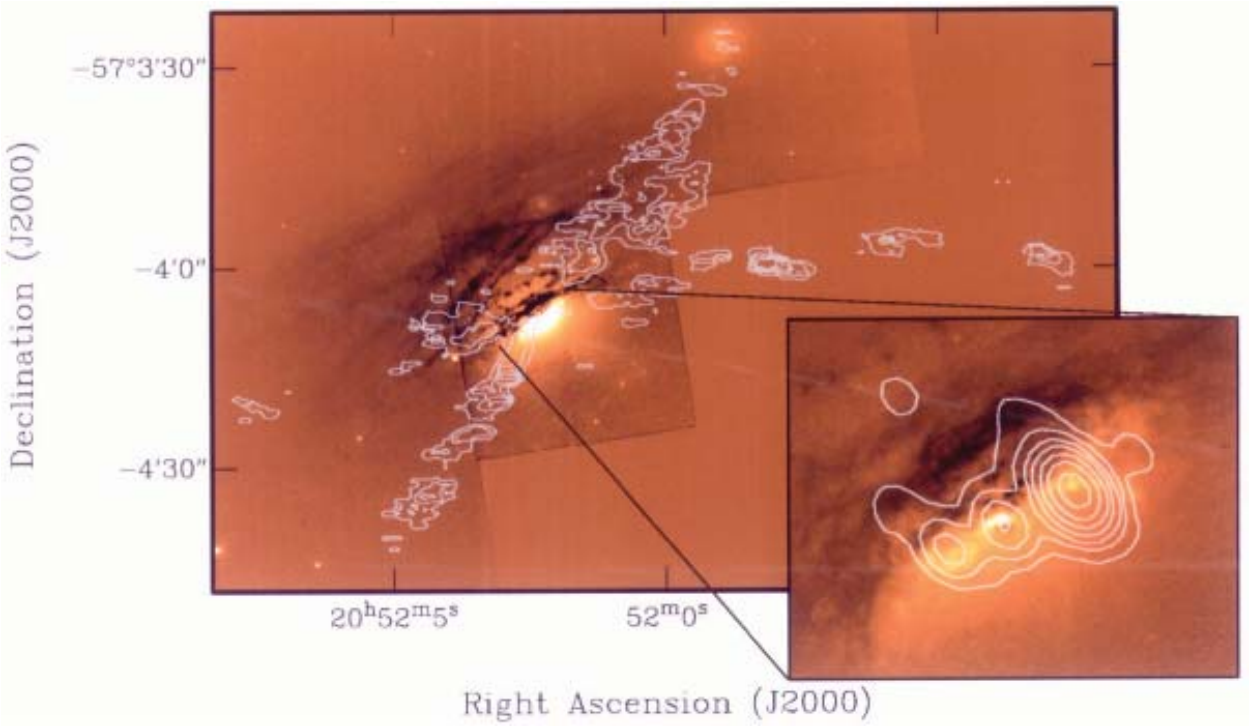

Figure 4.1: Distribution of the high-excitation ionized gas as outlined by the [OIII]λ5007/H_α + [N_{II}] ratio map (contours) superposed on the *HST* image (Morganti et al., 1998)

In this chapter, we explore the possibility that a simultaneous fitting of mid-IR and X-ray data can better restrict the dusty-gas torus parameters. In this part of the work, we used three mid-IR models that assume different distributions of dust: smooth by Fritz et al. (2006), clumpy by Nenkova et al. (2008a), and clumpy torus+wind by Hönig & Kishimoto (2017). Meanwhile, at X-rays, we used the borus02 model by Baloković et al. (2018) which assumes a smooth distribution of the gas. We did not consider the clumpy model at X-rays because this model was not available by the date of this publication. The data used and relevant techniques are included in Chapter 2. We give here a brief overview of the selected target to perform the simultaneous fitting.

The pilot source IC 5063.

IC 5063 is a nearby galaxy ($z \sim 0.0088$, $d \sim 46$ Mpc, Alonso-Herrero et al., 2011) classified as a Sy2 (Véron-Cetty & Véron, 2006). Figure 4.1 shows the optical image of this source. Dust is clearly visible, although a nuclear bright point source, corresponding to the Sy2, is also seen. The bolometric luminosity of this sources is $3.38 \times 10^{44}\,\mathrm{ergs}^{-1}$. This source has the advantage of having both mid-IR and X-ray spectra publicly available. The X-ray spectrum has a strong contribution from the reflection component, including the detection of the FeKα emission line. Furthermore, ground-based mid-IR images are also available to study the isolation of the nuclear source at mid-IR properly. By comparing the *Spitzer* spectrum with high spatial resolution photometric data from ground-based telescopes, we ensured that the spectrum corresponds to the emission of the inner < 100 pc of the nucleus (see Figure 1 in the following paper). All of this makes the data available for IC 5063 ideal for our purposes.

The main result of this investigation is that we demonstrate that our technique can be used to infer the physical properties of the torus, at least when AGN dust dominates the mid-IR emission and the reflection component is significant at X-rays. Smooth distribution of gas and dust, both in a torus-like geometry, is the best combination to explain the spectra, suggesting that the same physical component is responsible for both mid-IR and X-ray components of AGN. As an update on the subject, after publication, Maksym et al. (2020) presented new near-IR and optical observations of IC 5063 using *HST*. They show that this source contains broad radial rays (extending to 11 kpc) from the nucleus. They argue that this shadow might arise from dust scattering from the AGN continuum emission, possibly by a warped torus. This reinforces the existence of a torus in IC 5063.

Author disclosure: This work was developed mostly on my own. Dra. Omaira González-Martín developed the code to convert the mid-IR models and spectra into XSPEC format. Furthermore, she and Dra. Deborah Dultzin reviewed the analysis and discussion of the main results. The other coauthors gave comments in order to improve the final document. This work was published in Astrophysical Journal on November 28, 2019. The electronic version of this publication can be found in the following URL: https://iopscience.iop.org/article/10.3847/1538-4357/ab4ced/pdf

The Astrophysical Journal, 886:125 (14pp), 2019 December 1 https://doi.org/10.3847/1538-4357/ab4ced

Physical Parameters of the Torus for the Type 2 Seyfert IC 5063 from Mid-IR and X-Ray Simultaneous Spectral Fitting

Donaji Esparza-Arredondo[1], Omaira González-Martín[1], Deborah Dultzin[2], Cristina Ramos-Almeida[3,4], Jacopo Fritz[1], Josefa Masegosa[5], Alice Pasetto[1], Mariela Martínez-Paredes[6], Natalia Osorio-Clavijo[1], and Cesar Victoria-Ceballos[1]
[1] Instituto de Radioastronomía y Astrofísica (IRyA-UNAM), 3-72 (Xangari), 8701, Morelia, Mexico; d.esparza@irya.unam.mx
[2] Instituto de Astronomía (IA-UNAM), Mexico city, Mexico
[3] Instituto de Astrofísica de Canarias (IAC), C/Vía Láctea, s/n, E-38205 LaLaguna, Spain
[4] Departamento de Astrofísica, Universidad de La Laguna (ULL), E-38205 La Laguna, Spain
[5] Instituto de Astrofísica de Andalucía (CSIC), Glorieta de la Astronomía s/n E-18008, Granda, Spain
[6] Korea Astronomy and Space Science Institute 776, Daedeokdae-ro, Yuseong-gu, Daejeon 34055, Republic of Korea
Received 2019 July 26; revised 2019 September 25; accepted 2019 October 9; published 2019 November 28

Abstract

In order to understand the diversity of classes observed in active galactic nuclei (AGNs), a geometrically and optically thick torus of gas and dust is required to obscure the central engine depending on the line of sight to the observer. We perform a simultaneous fitting of X-ray and mid-infrared (mid-IR) spectra to investigate whether the same structure could produce both emissions and, if this the case, to obtain better constraints for the physical parameters of the torus. In this case we take advantage of the fact that both emissions show important signatures of obscuration. We used the nearby type 2 active nucleus IC 5063 as a test object. This object is ideal because of the wealth of archival data, including some high-resolution data. It also has a relatively high AGN luminosity that dominates at both X-ray and mid-IR frequencies. We use high spectral resolution *NuSTAR* and *Spitzer/IRS* spectra. The AGN dusty models used several physically motivated models. We found that the combination of the smooth torus models at mid-IR by Fritz et al. and at X-rays by Baloković et al., with the viewing and half-opening angles linked to the same value, is the best choice to fit the spectra at both wavelengths. This allows us to determine all the parameters of its torus. This result suggests that the structure producing the continuum emission at mid-IR and the reflection component at X-ray is the same. Therefore, we prove that this technique can be used to infer the physical properties of the torus, at least when AGN dust dominates the mid-IR emission and the reflection component is significant at X-rays.

Unified Astronomy Thesaurus concepts: Active galactic nuclei (16); Infrared astronomy (786); X-ray astronomy (1810)

1. Introduction

According to the simple unification model of active galactic nuclei (AGNs), a toroidal structure (broadly referred to as the torus) provides the anisotropic obscuration needed to explain the diversity of AGN properties observed across the electromagnetic spectrum (Antonucci 1993; Urry & Padovani 1995). The line of sight (LOS) to the observer with respect to the torus, its geometry, chemical composition, and distribution are key to understanding AGN diversity, perhaps linked to fundamental changes for different AGN classes (Shlosman 2005; Elitzur & Netzer 2016).

This torus absorbs optical/ultraviolot (UV) accretion disk radiation and reemits it at infrared wavelengths (see Netzer 2015; Ramos Almeida & Ricci 2017 for a review). Radiative transfer models based on dust distributed on a toroidal geometry have been proven to be successful in reproducing the infrared spectral energy distribution (SED) of AGNs (e.g., Hatziminaoglou et al. 2008, 2009; Ramos Almeida et al. 2009; Alonso-Herrero et al. 2011; Hönig & Kishimoto 2017). Initially, most researchers used smooth dust distributions with different radial and vertical density profiles for simplicity (e.g., Pier & Krolik 1993; Granato & Danese 1994; Efstathiou & Rowan-Robinson 1995; Schartmann et al. 2005; Fritz et al. 2006). It was later proposed that the dust is most probably arranged in clouds instead of being smoothly distributed (e.g., Krolik & Begelman 1988; Tacconi et al. 1994). The dusty torus has been the subject of several kinds of models that aimed to extract physical (e.g., optical depth) and geometrical (e.g., orientation and size) properties from the SED and, in some cases, interferometric observations. We can divide them into four kinds: smooth (Fritz et al. 2006), clumpy (Nenkova et al. 2008a, 2008b; Hönig et al. 2010; Hönig & Kishimoto 2010), smooth + clumpy (Stalevski et al. 2012; Siebenmorgen et al. 2015), and windy (Hönig & Kishimoto 2017). For the past two decades, adjusting models to IR spectra and broadband SEDs has been the one and only method in the attempt to derive clues on the dust geometry, composition, and geometrical distribution.

Furthermore, signatures of reprocessing emission by the torus in the X-ray band arise primarily from the interaction of X-ray photons with the surrounding gas (Ghisellini et al. 1994; Krolik et al. 1994). The two main features are the neutral iron line around 6.4 keV (FeKα) and the Compton hump peaking at ~10–30 keV. These features have been observed in the X-ray spectra of most AGNs (e.g., Matt et al. 1991; Ricci et al. 2014). Reprocessed continua are known to vary as a function of geometry of the reprocessing material (Nandra & George 1994). It has been suggested that both the Compton hump and the narrow cores of the FeKα emission line in AGNs are likely produced in the torus (see Liu & Wang 2010; Shu et al. 2010; Fukazawa et al. 2016), because it is an ubiquitous component in Seyfert galaxies (Bianchi et al. 2004). Therefore, X-ray spectral fitting to the high-energy continuum emission (above 10 keV) and the FeKα line might provide important information about the torus geometry, cloud distribution, and opacity.

The 100-fold increase in sensitivity in the hard X-ray band (>10 keV) brought by *NuSTAR* (Harrison et al. 2013) made possible for the first time the study of the spectral signatures of the torus. Empirically, spectral models with approximately toroidal geometry have been calculated by Murphy & Yaqoob (2009) (MyTorus), Ikeda et al. (2009), Brightman & Nandra (2011) (BNtorus), Liu & Li (2015) (ctorus), Furui et al. (2016) (MONACO), and Baloković et al. (2018) (borus02). Several of them are currently available to the community.

For this work, we selected the type 2 Seyfert IC 5063 as a test object. This AGN is located at the center of a nearly lenticular galaxy at 46 Mpc (Alonso-Herrero et al. 2011). This galaxy contains a disk with large-scale dust lanes (Morganti et al. 1998), possibly resulting from a merger (Morganti et al. 1998). According to Ichikawa et al. (2015) the bolometric luminosity of IC 5063 is 3.38×10^{44} erg s^{-1}. At X-ray wavelengths, IC 5063 has been observed with *Ginga* (Koyama et al. 1992), *ASCA* (Tanaka et al. 1994), and *ROSAT* (Pfeffermann et al. 1987; Vignali et al. 1997). More recently, IC 5063 was observed at X-ray wavelengths with *NuSTAR* (Baloković et al. 2018; see also M. Baloković 2019, in preparation, for details on the X-ray spectral analyses). At infrared wavelengths, Peeters et al. (2004) observed this source with the *ISO* satellite, determining that it is dominated by the AGN with little evidence of polycyclic aromatic hydrocarbons (PAHs) molecule emission. The dusty torus properties of IC 5063 have been explored through high angular resolution near- and mid-infrared (mid-IR) photometric data (Ramos Almeida et al. 2009, 2011; Alonso-Herrero et al. 2011) and the clumpy models of Nenkova et al. (2008a, 2008b), allowing a direct comparison with our results.

In this paper, we present a new technique to combine X-ray and mid-IR spectral information to make a simultaneous fit to torus models. We demonstrate that our method can successfully constrain the torus parameters and obtain more complete information in both ranges of wavelengths. The X-ray and mid-IR data are presented in Section 2. In Section 3, we give a brief summary of the X-ray and mid-IR models used in this work. Subsequently, the spectral-fitting methodology is shown in Section 4. The main results and discussion, within the framework of our goals, are presented in Sections 5 and 6. Finally, a brief summary and conclusions are given in Section 7.

2. Data

2.1. X-Ray Data

There are several X-ray observations available in the archives of different satellites for IC 5063. However, we need to cover energies above 10 keV because it is the aim of this paper to constrain the reflection component associated with the torus. The *NuSTAR* is the first focusing hard X-ray telescope with high sensitivity.[7] This allows observation with a single mode from ~3 to 79 keV, perfectly suited to study the AGN reflection component. Therefore, we use the hard band spectrum observed with *NuSTAR* (Harrison et al. 2013), including both FPMA and FPMB focal plane modules. *NuSTAR* has observed IC 5063 once (ObsID 60061302002, P.I. Harrison) on 2013 July 8.

NuSTAR data reduction was done using the data analysis software *NuSTARDAS* v.1.4.4 distributed by the High Energy Astrophysics Archive Research Center (HEASARC). The calibrated, cleaned and screened event files were generated using the NUPIPELINE task (CALDB 20160502). A circular region of 1′ radius was taken to extract the source and background spectrum on the same detector and to compute the response files (RMF and ARF files) using the NUPRODUCTS package within *NuSTARDAS*. Finally, we used the GRPPHA task within the FTOOLS to group the spectra with at least 60 counts per bin. The net exposure is 18.4 ksec. We found some cross-calibration issues between the FPMA and FPMB modules, larger below ~3 keV. We used the *NuSTAR* data above 3 keV to avoid them.

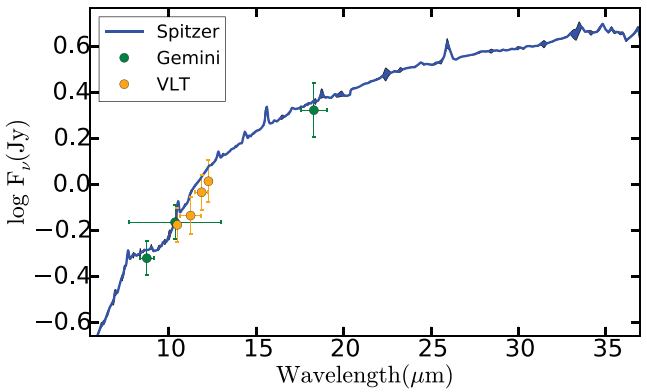

Figure 1. The *Spitzer*/IRS spectrum and photometric data. The orange and green points are measurements from VLT and Gemini, respectively.

2.2. Mid-IR Data

Regarding the IR data, we used the high-resolution *Spitzer*/IRS spectrum downloaded from the CASSIS[8] catalog (the Cornell AtlaS of *Spitzer*/IRS Sources, Lebouteiller et al. 2011). The spectral resolution of *Spitzer*/IRS ($R \sim 60$–130) is similar to that obtained by ground-based observations. The *Spitzer*/IRS spectrum could have a high contribution of galaxy emission due to its relatively low spatial resolution. Note that we could overcome this issue by including stellar libraries to the fit. However, the inclusion of these libraries significantly worsens the estimate of the resulting parameters (González-Martín et al. 2019a, 2019b). In order to investigate this, we compared this spectrum with ground-based high spatial resolution fluxes (see Figure 1). In particular, we compiled VISIR/VLT and T-ReCS/Gemini fluxes in Si2$_{8.73\,\mu m}$, *N*-band$_{10.4\mu m}$, S IV$_{10.5\mu m}$, PAH2$_{11.3\,\mu m}$, NEII_1$_{12.3\,\mu m}$, and Qa$_{18.2\,\mu m}$ filters reported in NED[9] (Hönig et al. 2010; Ramos Almeida et al. 2011). These data provide high spatial resolution fluxes (~100 pc). We found that the *Spitzer*/IRS spectrum shows slightly higher fluxes than the VLT and Gemini photometric data points, although those are well in agreement when ground-based flux calibration uncertainties are taken into account (15% at *N* band and 25% at *Q* band of the flux according to, e.g., Ramos Almeida et al. 2011).

In fact, Asmus et al. (2014) studied the T-ReCS and VISIR images of IC 5063 and found a compact but consistently elongated mid-IR nucleus (FWHM (major axis) ~ 0.52 arcsec ~ 110 pc; P.A. ~ 107°) without any further host emission detected. They found that the direction of this elongation coincides with the extended [O III] line emission. Additionally, Hönig et al. (2010) compares the photometric

[7] https://heasarc.gsfc.nasa.gov/docs/nustar/

[8] http://cassis.astro.cornell.edu/atlas/

[9] https://ned.ipac.caltech.edu/

data with the *Spitzer*/IRS and VISIR spectra extracted over 0.″75 and found that they agree well. Indeed, according to Panuzzo et al. (2011) the continuum of IC 5063 in the low-resolution *Spitzer*/IRS spectrum is dominated by hot dust, most probably coming from the AGN torus. They did not find PAH feature emission, although some forbidden lines were detected. The lack of strong stellar or starburst components makes the *Spitzer*/IRS spectrum of IC 5063 ideal to study the torus parameters throughout the mid-IR spectral fitting.

In order to perform spectral fitting to the data, we converted the mid-IR *Spitzer*/IRS spectrum into XSPEC format using the FLX2XSP task within HEASOFT. This tool reads a text file containing one or more spectra and errors and writes out a standard XSPEC pulse height amplitude (PHA[10]) file and response file. This will allow us to perform X-ray and mid-IR simultaneous fits too.

3. The Mid-IR and X-Ray Models

We give here a brief summary of the characteristics of the models used to fit X-ray and mid-IR spectra. Both wavelengths carry information on the torus-like structure that obscures the accretion disk at certain viewing angles. Both models are produced using radiative transfer codes including the physics required to account for mid-IR and X-ray main continuum features. The mid-IR models include reemission due to dust, while X-ray models mainly include reflection in neutral gas.

3.1. X-Ray Model

The bulk of the AGN emission is produced in the accretion disk and emitted at optical and UV wavelengths. A portion of this emission is reprocessed by a corona of a hot electron plasma close to the accretion disk that scatters the energy in the X-ray bands due to inverse Compton (Netzer 2015; Ramos Almeida & Ricci 2017, and references therein). This comptonization produces one of the three main components of X-ray spectra known as the intrinsic continuum. It is modeled by a power law with a spectral index (Γ) typically around 1.8–2.3 (e.g., Yang et al. 2015). This feature dominates the spectral emission above 2 keV, and it is a distinctive signature of the AGN emission. Some part of this primary emission is absorbed by the torus or the broad-line region, and another is reprocessed by a distant material (e.g., the inner walls of the torus) and gives way to the second most relevant component, called the Compton hump, with a maximum of its emission at $\sim$30 keV (Ricci et al. 2011). The reflection component depends on the shape of the reprocessing material, both its geometry and density (Ghisellini et al. 1994). This structure could be the torus and depends mainly on the geometrical covering factor of the reprocessed material and its average $N_{\rm H}$. The third component is the FeKα emission line, whose origin is the reflection of X-ray photons. The origin of the narrow FeKα line might also be associated with the torus, while the broad FeKα line is thought to originate in the inner parts of the accretion disk (Fabian 1998; Laor 1991). This analysis is based on the hypothesis that the reprocessor is the torus, which seems to be the case for the vast majority of the sources (Matt et al. 1991).

The reflection component of AGN has been studied through different models (e.g., Murphy & Yaqoob 2009; Ikeda et al. 2009; Brightman & Nandra 2011; Liu & Li 2015). In this work, we used a new grid of X-ray spectral templates called the borus02 model as presented by Baloković et al. (2018). These templates were based on BORUS, a radiative transfer code that assumes a toroidal geometry of neutral gas. To generate the borus02 templates, the geometry was simplified as a smoother toroidal distribution of gas. This geometry approximation is represented as a uniform-density sphere with two conical polar cutouts with the opening angle as a free parameter, such as the one employed by Brightman & Nandra (2011) (see also Baloković et al. 2018, for more details).

The borus02 model allows us to explore the following parameters of the torus: (1) the average column density ($N_{\rm H_{tor}}$), (2) the relative abundance of iron ($A_{\rm FeK\alpha}$), and (3) the angular size ($\theta_{\rm tor}$). Additionally, borus02 considered the incident emission in the torus as a power law with index Γ multiplied by an exponential cutoff ($e^{(-E/E_{\rm cut})}$). Finally an additional parameter controls the viewing angle of the torus relative to the observer ($\theta_{\rm inc}$). Figure 2 (top right corner with orange labels) shows the geometry and parameters associated with borus02.

3.2. Mid-IR Model

The dusty torus has been the subject of several AGN models at mid-IR wavelengths that aimed to extract physical properties from the SED. In this work, we used three of these SED grids to fit our mid-IR spectra: smooth (Fritz et al. 2006; Feltre et al. 2012), clumpy (Nenkova et al. 2008a, 2008b), and CAT3D-WIND (Hönig & Kishimoto 2017). These models are based on radiative transfer codes that use different geometrical distributions and compositions of dust. Figure 2 summarizes the geometry assumed for these models. Below we give a short description for each model.

1. Smooth model: This model has a torus-like morphology. It was created by modeling a flared disk created as two concentric spheres, delimiting the inner ($R_{\rm in}$) and the outer ($R_{\rm out}$) radius of the torus with the polar cones removed. It considers graphite grains with radius $a_{\rm G} = 0.05\ \mu$m and sublimation dust temperature of 1500 K to compute the $R_{\rm in}$ (see Equation (5) from Barvainis 1987). It describes the dust density in polar coordinates (see Equation (3) in Fritz et al. 2006) and allows us to explore the following parameters of the torus: (1) the viewing angle of the observer toward the torus ($i_{\rm F06}$), (2) the half-opening angle (σ), (3) the exponent of the logarithmic elevation density distribution (γ), (4) the exponent of the power law of the radial profile of the density distribution (β), (5) the equatorial optical depth at 9.7 μm ($\tau_{9.7}\ \mu$m), and (6) the outer-to-inner radius ratio (Y).
2. Clumpy model: The clumpy model considers a formalism where an AGN is surrounded by a toroidal distribution of dusty clouds. This assumes a standard Galactic composition (of 53% silicates and 47% graphite) of dust. Among them the most extensively used one is the clumpy model of Nenkova et al. (2008b) (although see also Hönig & Kishimoto 2010) due to their large number of SEDs and proven ability to explain the mid-IR emission of low luminous (González-Martín et al. 2017), intermediate luminous (e.g., Ramos Almeida et al. 2009), and high luminous (Martínez-Paredes et al. 2017) AGNs. The model parameters are (1) the viewing angle ($i_{\rm N08}$) with respect to the polar plane, (2) the number of clouds in the equatorial plane of the torus ($N_{0_{\rm N08}}$), (3) the half angular width of the torus (σ), (4) the ratio between the inner and the outer radius ($Y = R_{\rm out}/R_{\rm in}$), (5) the slope of the radial

[10] Engineering unit describing the integrated charge per pixel from an event recorded in a detector.

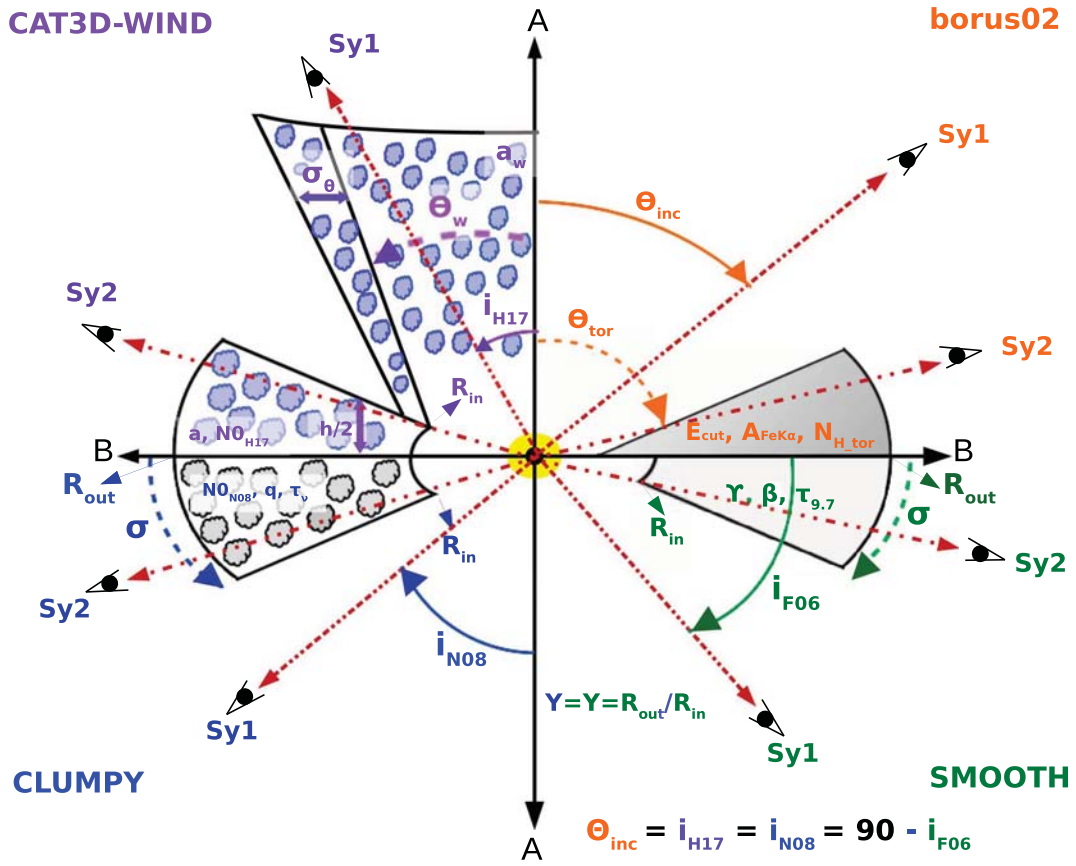

Figure 2. Geometry of the borus02 and the three mid-IR models used in this paper. The borus02 model by Baloković et al. (2018) is shown as a torus cut surface above the equatorial plane and filled-in dark gray gradient. The smooth torus model by Fritz et al. (2006) is shown as a torus cut surface below the equatorial plane and is filled in with light gray. The clumpy torus model by Nenkova et al. (2008b) is shown as a torus cut surface below the equatorial plane filled with gray clouds. The CAT3D-WIND model by Hönig & Kishimoto (2017) is shown as a disk + wind cut surface above the equatorial plane and is filled in with blue clouds. Clouds represent models with clumpy distribution of dust. The parameters for each model are shown with different colors: borus02 (orange), smooth (green), clumpy (blue), and CAT3D-WIND (purple). In all of them we show an example of a view for a Sy1 and a Sy2.

distribution of clouds described by a power law (q), and the optical depth for the individual clouds (τ_ν).

3. CAT3D-WIND model: The CAT3D-WIND model is built upon the hypothesis that the dust around the AGN consists of a geometrically thin disk of optically thick dust clumps and an outflowing wind described by a hollow cone composed by dusty clouds. The near-IR emission up to ~5 μm is due to an inflowing disk in the equatorial plane, while the main contributor to mid-IR emission is the polar dust. The distribution of the dust clouds in the disk is described with the following parameters: (1) the power-law slope (a), (2) the inner radius ($R_{\rm in}$), which denotes the distance from the AGN in units of the sublimation radius, (3) the dimensionless scale height (h) from the midplane of the disk of the vertical Gaussian distribution of clouds in units of the sublimation radius, and (4) the average number of dust clouds ($N_{0_{\rm H17}}$) along the equatorial LOS of the disk. The polar outflow is modeled as a hollow cone with the following parameters: (1) the radial distribution of dust clouds in the wind ($a_{\rm w}$), (2) the half-opening angle of the wind (θ_w), and (3) the angular width (σ_θ). Finally, two further parameters are common to both components, namely, the inclination angle toward the observer ($i_{\rm H17}$) and the ratio between the number of clouds along the cone and $N_{0_{\rm H17}}$ of the disk (fwd). This model considers a standard composition disk (similar to clumpy models) and an outflow composed of large grains.

The SEDs produced by the smooth and the clumpy models are defined by a 0.001–1000 μm wavelength range, and those produced by the CAT3D-WIND model cover a wavelength range between 0.01 and 36,000 μm.

3.3. Derived Quantities

3.3.1. Covering Factor

We calculate the covering factor Cf in both X-ray and mid-IR models. We use the relationship between the Cf and $\theta_{\rm tor}$ given by $Cf = \cos(\theta_{\rm tor})$. Note that this is a simplistic approximation that assumes that the clouds take up most of the torus volume, following the prescription given by Baloković et al. (2018).

We can also calculate the Cf using the mid-IR parameters. To derive the equation of the Cf of the smooth model ($Cf_{\rm F06}$), we take into account the extinction coefficient, the density distribution along the radial and polar distances, the normalization constant, and the β value (see Equation (3) from Fritz et al. 2006). Note that we assumed $\beta = 0$ because this number only has two values in the SED provided (0 or 1), and we obtained a value close to zero for our best fit. For the clumpy model we calculate this Cf ($Cf_{\rm N08}$) using Equation (9) from (Nenkova et al. 2008a) and the angular distribution of clumps (Feltre et al. 2012). A similar equation is

used to calculate the *Cf* for each component (wind and disk) for the CAT3D-WIND model, with the total *Cf* as the sum of the two components. Note that the *Cf* of the wind is calculated as the subtraction of two toroidal structures as in Hönig et al. (2010) with half-opening angles of $\theta_w + \sigma_\theta$ and θ_w. Using our notation for each parameter, these are the equations required to compute *Cf* :

1. Smooth model (case $\beta = 0$):

$$\mathrm{Cf_{F06}} = \frac{\ln(\tau_{9.7})}{\gamma}. \quad (1)$$

2. Clumpy model:

$$\mathrm{Cf_{N08}} = 1 - \int_0^{\pi/2} \cos\beta e^{N_{0_{\mathrm{N08}}} e^{-\beta^2/\sigma^2}} d\beta. \quad (2)$$

3. CAT3D-WIND model:

$$\mathrm{Cf_{H17}} = 1 + \int_0^{\pi/2} \cos\theta e^{N_{0_w} e^{-\theta^2/\theta_w^2}} d\theta - \int_0^{\pi/2} \cos\theta e^{N_{0_w} e^{-\theta^2/(\theta_w+\sigma_\theta)^2}} d\theta - \int_0^{\pi/2} \cos\theta e^{N_{0_d} e^{-\theta^2/\sigma_d^2}} d\theta, \quad (3)$$

where $\sigma_d = \arctan h/2$.

3.3.2. Dust Mass

We also estimate the total dust mass (M_{tor}) using the parameters obtained for each model. This value is obtained from the integration of the density distribution of dust over the volume. We use Equation (9) from Mor et al. (2009) given $q = 2$ for the clumpy model. We follow the equations in Table 1 from Hönig et al. (2010) to compute the mass for the CAT3D-WIND model. We sum up the contributions of the disk and the wind, with the latter obtained as the subtraction of two toroidal distribution with angular width of $\theta_w - \sigma_\theta$ and θ_w. Note that we analytically derive the mass equations assuming $\beta = 0$ for the smooth model and $q = 2$ for the clumpy model because these values are close to the results that we find for our object (see Table 1 and Section 5). Using our notation for each parameter, the equations to compute the total dust mass are

1. Smooth model ($\beta = 0$)

$$M_{\mathrm{tor}}(F06) = \frac{4\pi\tau_{9.7}}{3\kappa\gamma} \frac{(R_{\mathrm{out}}^3 - R_{\mathrm{in}}^3)(1 - e^{-\gamma})}{R_{\mathrm{out}} - R_{\mathrm{in}}}, \quad (4)$$

where κ is the extinction coefficient in the Milky Way.

2. Clumpy model ($q = 2$)

$$M_{\mathrm{tor}}(N_{0_{\mathrm{N08}}}) = 4\pi \sin(\sigma) N_{0_{\mathrm{N08}}} * N R_{\mathrm{in}}^2 Y \frac{Y}{2\log_{10} Y}, \quad (5)$$

where $N = N_{\mathrm{H}} * A_\nu * mH$ is the N_{H} multiplied by the extinction due to dust (obtained from τ_ν and assuming a constant dust-to-gas ratio) times the hydrogen mass in kilograms for a single cloud.

3. CAT3D-WIND model[11]

$$M_{\mathrm{tor}}(\mathrm{H17}) = \frac{N\sqrt{\pi}}{R_{\mathrm{cl;0}}^2} \times (N_{0_w}(f_{(\theta_w - \sigma_\theta)} - f_{\theta_w}) + N_{0_d} f_{\sigma_d}), \quad (6)$$

where f_{θ_0} function is defined as (Hönig et al. 2010)

$$f_{\theta_0} = \theta_0 e^{-\theta_0^2/4} \times \left(\mathrm{Erf}\frac{\pi - i\theta_0^2}{2\theta_0} + \mathrm{Erf}\frac{\pi + i\theta_0^2}{2\theta_0} \right). \quad (7)$$

The constant dust-to-gas ratio relation assumed is $N_{\mathrm{H}} = 1.9 \times 10^{21} * 1.086 * \tau_\nu$ (Bohlin et al. 1978).

4. Spectral Fitting

Spectral fitting is performed using the XSPEC fitting package. XSPEC is a command-driven, interactive, spectral-fitting tool within the HEASOFT[12] software. XSPEC has been used to analyze X-ray data such as *ROSAT*, *ASCA*, *Chandra*, *XMM-Newton*, *Suzaku*, *NuSTAR*, or *Hitomi*. XSPEC allows users to fit data with models constructed from single emission components coming from different mechanisms and/or physical regions. XSPEC already includes a large number of models, but new ones can be incorporated using the ATABLE task. The borus02 templates have been included in XSPEC using this tool. In particular we use the χ^2 statistics (through the standard $\chi_r^2 = \chi^2/\mathrm{dof}$, where dof is the number of degrees of freedom, which is equal to the number of data bins in the spectrum minus the number of free parameters), and we assess the goodness of fit performing a test to reject the null hypothesis that the observed data are drawn from the model. The parameter confidence regions are found by surfaces of constant delta statistic from the best-fit value (ERROR task). Finally, XSPEC also allows us to find simultaneous confidence regions of multiple parameters to study the degeneracy among parameters.

X-ray data and models used in this analysis are already formatted to be used within XSPEC. To use these capabilities for the mid-IR spectra (and simultaneous X-ray and mid-IR fitting), we converted the data (see Section 2) and models (see Section 4.1 below) to XSPEC format.

4.1. Mid-IR Models in XSPEC

We converted the mid-IR models SED libraries to multi-parametric models within the spectral-fitting tool XSPEC as an additive table. The basic concept of a table model in XSPEC format is that the file contains an *N*-dimensional grid of model spectra with each point on the grid calculated for particular values of the *N* parameters in the model. XSPEC will interpolate on the grid to get the spectrum for the parameter values required at that point in the fit. To adapt mid-IR models we first created a one-parameter table (in fits format) associated with all the SEDs using the FLX2TAB task within HEASOFT. Note that each of the SEDs has been interpolated using 5000 steps between the minimum and maximum wavelengths due to the need for equally spaced SEDs. We then wrote a python routine to change the headers associating each SED to a set of parameters. This model has the free parameters described in Section 3.2 plus redshift and normalization. For the clumpy model we were not able to obtain an XSPEC model using the entire SED library due to the unpractical size of the final model (over 100 GB). Instead of $N_0 = [1\text{–}15]$ and $\sigma = [15\text{–}70]$ in steps of 1 and 5, respectively, we slightly constrained the number of clouds and the angular width of the torus to the

[11] Note that these equations are derived from Hönig et al. (2010) assuming $b = 1$ as in Hönig & Kishimoto (2017).

[12] https://heasarc.gsfc.nasa.gov

Table 1
The Best-fit Physical Parameters of the Torus Models for IC 5063

Parameter (1)	bS1 Baseline Model borus02 + Smooth $i_{F06} = 90. - \theta_{inc}$ (2)	bC1 Baseline Model borus02 + Clumpy $i_{N08} = \theta_{inc}$ (3)	bW1 Baseline Model borus02 + CAT3D-WIND $i_{H17} = \theta_{inc}$ (4)	bS2 Baseline Model borus02 + Smooth $i_{F06} = 90. - \theta_{inc}$ (5)
Γ	$1.72 \pm^{0.07}_{0.06}$	$1.74 \pm^{0.06}_{0.07}$	$1.70 \pm^{0.06}_{0.08}$	$1.72 \pm^{0.07}_{0.07}$
$\log(N_{H_{tor}})$	$24.00 \pm^{0.07}_{0.06}$	$23.98 \pm^{0.02}_{0.07}$	$23.90 \pm^{0.11}_{0.08}$	$23.99 \pm^{0.08}_{0.07}$
$\log(N_{H_{los}})$	$23.25 \pm^{0.02}_{0.02}$	$23.25 \pm^{0.01}_{0.03}$	$23.26 \pm^{0.03}_{0.03}$	$23.25 \pm^{0.03}_{0.02}$
θ_{tor}	$60.0 \pm^{2.6}_{4.5}$	$78.3 \pm^{0.4}_{12.4}$	<21.9	$56.0\ (90.-\sigma)$
θ_{inc}	$75.4 \pm^{1.3}_{1.6}$	87.1^{*}	$30.80 \pm^{0.30}_{0.34}$	$75.3 \pm^{1.5}_{1.5}$
σ	$34.1 \pm^{0.8}_{1.9}$	$34.9 \pm^{0.2}_{14.6}$	...	$34.0 \pm^{2.7}_{1.0}$
Y	$14.1 \pm^{0.2}_{0.2}$	>95.6	...	$14.1 \pm^{0.2}_{0.2}$
$\tau_{9.7}$	>9.27	...	...	>9.1
τ_{ν}	...	$49.3 \pm^{0.7}_{3.8}$	50.0^{*}	—
β	0.0	...	1.0^{*}	0.0
$N_{0_{N08}}$ or N_{0_w}	...	$3.67 \pm^{0.03}_{0.20}$	>7.46	—
σ_{θ}	...	...	<7.2	—
θ_w	...	...	>44.6	—
γ, q or aw	>5.7	$2.13 \pm^{0.03}_{0.02}$	<-2.5	>5.6
N_{0_d}	...	...	>9.97	...
a	...	...	> -0.5	...
h	...	...	>0.5	...
fwd	...	...	>0.72	...
χ^2 /dof	681/647	708/647	730/645	682/648
Derived parameters				
R_{in} (pc)	0.23^{*}	0.23^{*}	0.16^{*}	0.23^{*}
R_{out} (pc)	3.40 ± 0.05	>23.9	450^{*}	3.4 ± 0.05
$Cf_{X\text{-ray}}$	$0.50 \pm^{0.04}_{0.07}$	$0.20 \pm^{0.21}_{0.01}$	<0.92	$0.56 \pm^{0.04}_{0.07}$
Cf_{midIR}	>0.4	0.66 ± 0.01	>0.4	>0.4
M_{tor} ($\times 10^5\ M_{\odot}$)	>0.06	>30.3	$<0.2^{**}$	>0.06

Note. Columns 2–4 show the resulting parameters from fits assuming that inclination angles from mid-IR and X-ray models are linked. Column 5 shows the resulting parameters from a fit assuming that inclination and half-opening angles from smooth and borus02 models are linked. The values marked with an asterisk (*) are fixed parameters. **Total mass calculated as the sum of wind and disk masses ($0.03 \times 10^5\ M_{\odot}$ from wind and $0.16 \times 10^5\ M_{\odot}$ from disk). Note that the $Cf_{X\text{-ray}}$ is calculated as $\cos(\theta_{tor})$, while the Cf_{midIR} depends on several parameters according to the mid-IR model chosen (see Section 3.3.1).

ranges $N_0 = [1, 3, 5, 7, 9, 11, 13, 15]$ and $\sigma = [15, 25, 35, 45, 55, 65, 70]$, respectively. This is in order to recover a more transferable model (~6 GB). Note that this does not affect our results because XSPEC interpolates between models to find the best solution.

4.2. The Total Model in XSPEC

We fit the mid-IR and X-ray spectra of IC 5063 following a command sequence in XSPEC:

$$\begin{aligned} &\text{phabs} * (\text{atable}\{\text{borus02}\} + \text{zdust} * \text{zphabs} \\ &\quad * \text{cabs} * \text{cutoffpl}) + \text{zdust} * \text{atable}\{\text{midIR}_{\text{model}}\}, \end{aligned} \quad (8)$$

where phabs is the foreground galactic absorption.[13] The model borus02[14] accounts for the reflection component. The zdust * zphabs * cabs represents the LOS absorption at the redshift of the source. Following the recipe provided by Baloković et al. (2018), we linked the N_H component to the zphabs to take into account for the total extinction along the LOS, including the Compton scattering losses. We realized that these X-ray absorbers are not evaluated at energies below 10^{-4} keV. Therefore, mid-IR and X-ray simultaneous fit requires that the X-ray intrinsic emission be properly absorbed below those energies. For that reason we introduced a *zdust* component to neglect any artificial contribution of this component to mid-IR wavelengths. This model is also used to incorporate foreground extinction at mid-IR wavelengths. We fixed the Ecut parameter to 300.0 keV because our X-ray spectra only cover a wavelength range between 3 and 100 keV. Also, we fixed the $A_{FeK\alpha}$ parameters to the solar value. We varied these parameters on the final fit, but they did not produce any statistical improvement. Finally, the $\text{midIR}_{\text{model}}$ is one of the three mid-IR models described in Section 3.2.

Note that the main advantage of the borus02 template for our analysis is that it allows us to constrain several parameters closely linked to the mid-IR models (see following sections).

5. Fitting Results

5.1. Linking Viewing Angles

We first consider that the only parameter linked between the mid-IR and X-ray models is the viewing angle. Therefore, we linked the mid-IR and X-ray viewing angles to the same value as shown in Figure 2 (i.e., $i_{F06} = 90 - \theta_{inc}$, $i_{N08} = \theta_{inc}$, and

[13] In the case of IC 5063 this value is fixed at 0.067×10^{22} cm^{-2}, obtained by the NH tool within Heasoft.
[14] We used the *borus02_v170323c.fits* file from http://www.astro.caltech.edu/ mislavb/download/.

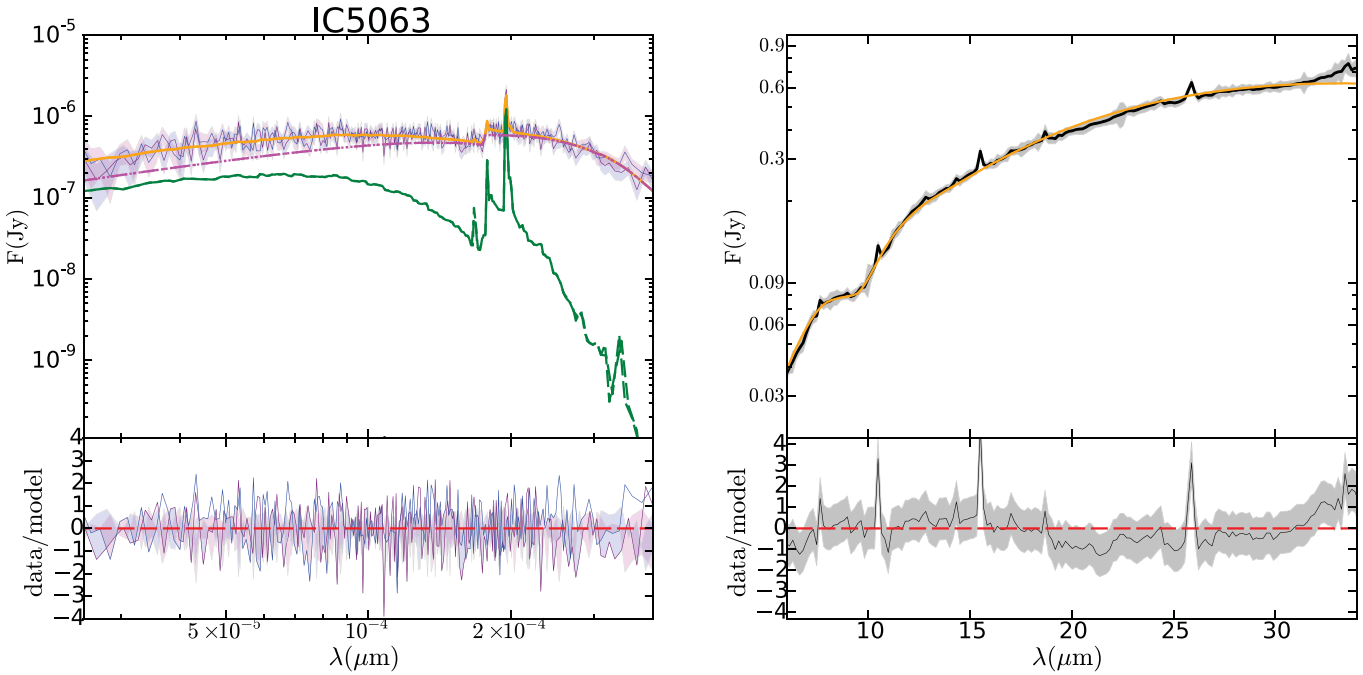

Figure 3. Unfolded spectra of IC 5063. The orange solid lines are the best fit obtained from the bS1 baseline model. Left: *NuSTAR* spectra are displayed with blue and purple solid lines. The magenta and green dotted lines show the the absorbed power law and the reprocessed components, respectively. Right: the *Spitzer*/IRS spectrum is shown with a black solid line. The lower panels display the residuals between data and the best-fit model.

$i_{\rm H17} = \theta_{\rm inc}$). Table 1 shows the resulting values for each parameter after fitting simultaneously the *NuSTAR* spectra using the borus02 model and the *Spitzer*/IRS spectrum with each of the three mid-IR models (smooth torus, clumpy torus, or clumpy wind-disk models in columns 2, 3, and 4, respectively). Hereafter, we refer to these combinations of the borus02 model with either the smooth, clumpy, or CAT3D-WIND model as the bS1, bC1, and bW1 baseline models, respectively.

Regarding the X-ray parameters, we found that (1) the $\log N_{\rm H_{tor}}$ is independent from the mid-IR model selected; (2) the Γ shows slight changes depending on the model; and (3) the $\theta_{\rm tor}$ and $\theta_{\rm inc}$ strongly depend on the mid-IR model used. Note that the viewing angle $\theta_{\rm inc}$ is constrained when using the bS1 and bW1 baseline models, and both angles are consistent with a Sy2.

The bS1 baseline model has four free mid-IR parameters: two are constrained, and the other two (γ and $\tau_{9.7}$) are close to the upper limit defined by the model; β is set to $\beta = 0$, giving better results than $\beta = 1$. Only Y is close to the upper limit among the five free parameters for the bC1 baseline model, because the other free parameters are well constrained. Finally, among the seven free parameters of the bW1 baseline model, five are upper limits and two are lower limits.

While a direct comparison between mid-IR parameters from each model is indeed challenging, we compare some mid-IR parameters among the bS1, bC1, or/and bW1 baseline models, such as the σ, Y, $N_{0_{N08}}(N_{0_w})$, and the power-law indices of the dust radial distributions (q, γ, or aw). In particular, we can compare the bC1 and bS1 baseline models in terms of σ and Y parameters. Similar results are obtained for σ with both models. The bC1 baseline model shows a large value for the Y parameter that implies[15] a torus size > 24 pc, compared with $\sim$3.4 pc for the bS1 baseline model. The latter is in better agreement with more recent works (see references in Ramos Almeida & Ricci 2017). We also computed the number of clouds along the wind using fwd and N_{0_d} parameters ($N_{0_w} = \text{fwd} * N_{0_d}$) for the bW1 baseline model. This number is larger than the number of clouds in the equatorial LOS for the torus obtained for the bC1 baseline model (i.e., $N_{0_{\rm N08}}$). We found that a_w (bW1) is very similar to q (bC1), while γ has a higher value.

We used the reduced χ^2 statistic value to assess the goodness of fit for each model. The χ^2/dof for the bS1, bC1, and bW1 baseline models are reported in Table 1. Note that there are no large differences between the χ^2/dof from these three baseline models, although the bW1 baseline model shows a larger χ^2/dof than the other two baseline models and a slightly better χ^2/dof is obtained with the combination of the borus02 and smooth models (bS1 baseline model). In Figure 3, we show the IC 5063 spectra and the resulting fit using bS1 baseline model. Note that the bS1 baseline model better reproduces the [7–10] μm wavelength range compared with the bC1 and bW1 baseline models (Figures 4 and 5).

We also explored the cases in which the direction of the inclination angle for the mid-IR models can be inversely related to the inclination angle for the X-ray band (i.e., $i_{\rm F06} = \theta_{\rm inc}$, $i_{\rm N08} = 90 - \theta_{\rm inc}$, and $i_{\rm H17} = 90 - \theta_{\rm inc}$). This scenario will represent a reflector neutral gas that fills up the gaps where the mid-IR emitting dust is not present. We also obtained the statistic values for these cases, and we compared them with those obtained above (i.e., direct link between viewing angles reported in Table 1). We found that this interpretation of the viewing angle is worse than that assumed before for the bS1 and bC1 baseline models, obtaining a χ^2/dof of 685/647 and 754/648 (i.e., $\Delta\chi^2$/dof of 4 and 6 compared with those reported in the table), respectively. Interestingly, in the case of the bW1 baseline model, we found that this new link between

[15] Note that the inner radius of both models is set to the same value.

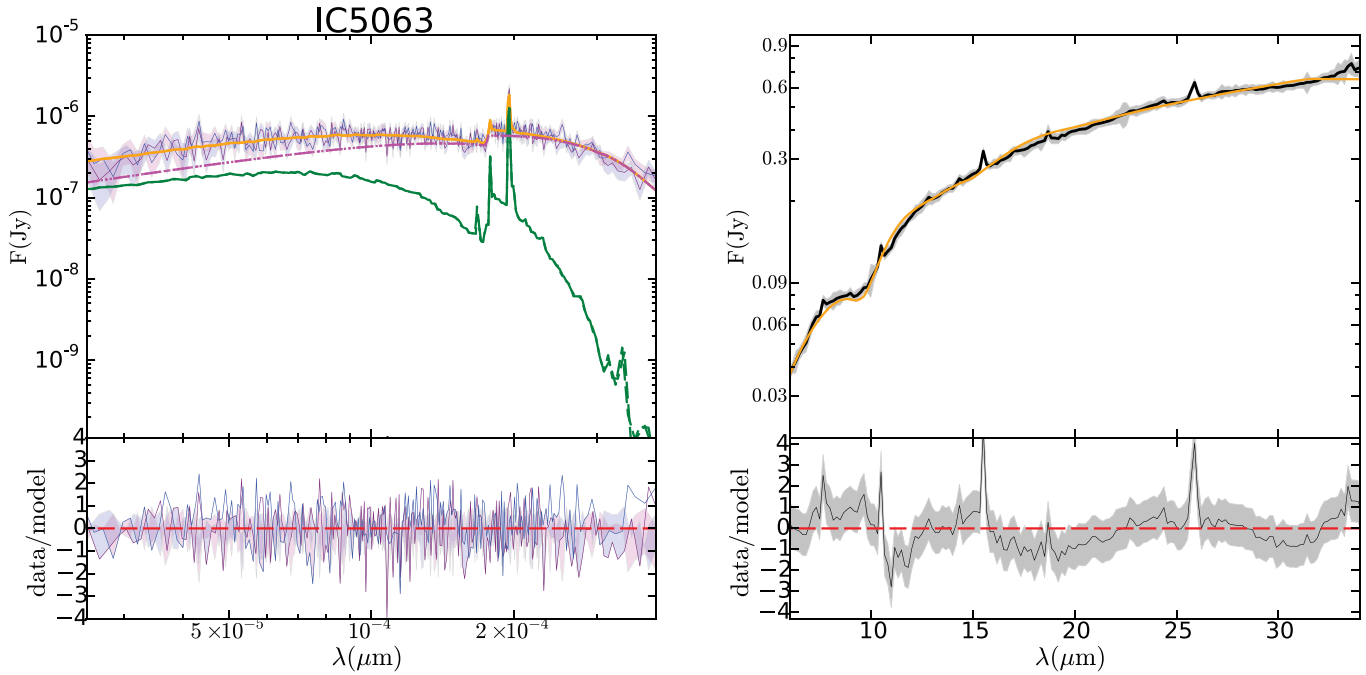

Figure 4. Same as Figure 3 but using the bN1 baseline model.

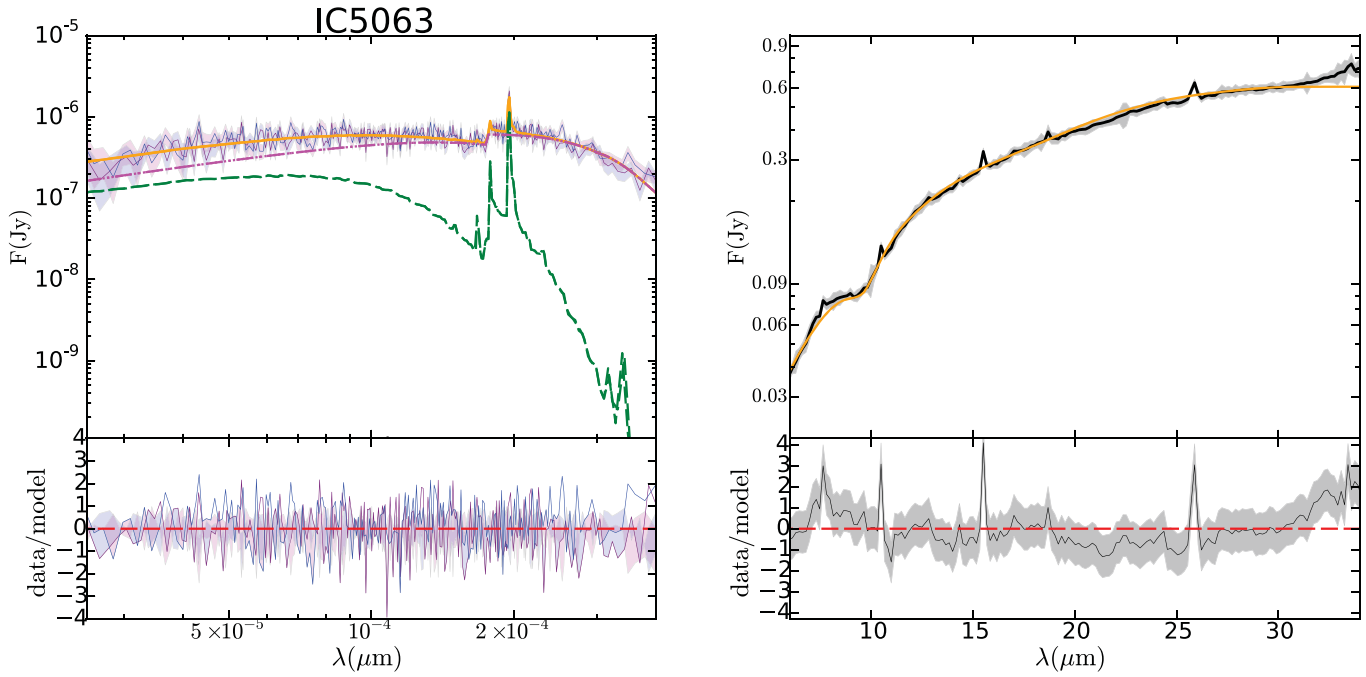

Figure 5. Same as Figure 3 but using the bW1 baseline model.

viewing angles is an improvement, with a χ^2/dof of 718/645 (i.e., $\Delta\chi^2/\mathrm{dof} = -12$).

We reported the covering factors *Cf*s obtained from X-ray models using the bS1, bC1, and bW1 baseline models in Table 1 (quoted as $Cf_{\text{X-ray}}$). Both the bS1 and bC1 baseline models give consistent *Cf*s within error bars, while the bW1 baseline model gives a higher *Cf*. Table 1 also reports the *Cf*s obtained using the mid-IR parameters (denoted as Cf_{midIR}). *Cf*s for different baseline models are consistent with each other. A comparison between $Cf_{\text{X-ray}}$ and Cf_{midIR} shows compatible results for the bS1 and the bW1 baseline models. However, the *Cf* obtained from X-rays is larger than that obtained from the mid-IR for the bC1 baseline model.

Finally, we check for the degeneracy among parameters of the fit. For this purpose we used the best-fit baseline model obtained (i.e., bS1). Figure 6 shows the two-dimensional χ^2 distribution for each free parameter (dotted lines). We found that most parameters are well constrained within the 3σ contours. The most controversial parameter is θ_{tor}, which we cannot yet restrict because it is in the range [10–70] at the 2σ

level. However, note that the σ parameter from the smooth model is constrained and both parameters (σ and $\theta_{\rm tor}$) could be directly linked (see below).

5.2. Linking Both Viewing and Half-Opening Angles

We test here whether we can link both the viewing angle and the half-opening angle in the bS1 baseline model. Conforming to the definitions of the opening angles in the smooth and the borus02 models, the link between both parameters is $\theta_{\rm tor} = 90 - \sigma$. Hereafter, we refer to this new combination as the bS2 baseline model. In column 5 from Table 1 we report the values obtained for the bS2 baseline model.

These new parameters are consistent within the errors to those measured for the bS1 baseline model (reported in Table 1). This is the case even for σ and $\theta_{\rm tor}$. Note that the derived parameters *Cf* (X-ray), *Cf* (mid-IR), and $M_{\rm tor}$ also remain the same compared with the bS1 baseline model. We compared χ^2/dof from the bS1 and bS2 baseline models through the f-test, obtaining a probability 0.37, which is greater than 10^{-4}. Therefore, we discard the hypothesis that a most complex baseline model (bS1) is better to fit the spectra, that is, the simpler baseline model (bS2) is enough to reproduce the data.

We also check the degeneracy among the parameters for the bS2 baseline model. In Figure 6, we show the two-dimensional χ^2 distribution for each combination of parameters when using the bS2 baseline model (solid lines). Note that all parameters are constrained within the 3σ contours. The advantage of linking them is that now the half-opening angle is constrained for both fits. This slightly improves the calculus of the degeneracy of the parameters, showing smoother contours in Figure 6 with no significant spoilage of the parameter restriction.

Other parameters that can be associated are $\log(N_{\rm H_{tor}})$ and τ_ν because both are associated with the density of the medium. However, the relationship between both parameters is not simple. We explore this possibility in the next section.

6. Discussion

In this work, we investigate the properties of the dusty torus of IC 5063, exploring the combination of mid-IR and X-ray spectral fits. We discuss here whether the same structure producing the mid-IR continuum can also describe the reprocessed emission at X-ray wavelengths (Section 6.1), what the resulting torus properties are (Section 6.2), and whether the combination can better constrain the physical parameters of the dusty structure when they are used to fit simultaneously the *Spitzer*/IRS and *NuSTAR* spectra (Section 6.3).

6.1. Link between Mid-IR Continuum and Reprocessed Emission at X-Ray Wavelengths

Our first step to combine the information at both wavelength ranges was to assume that the viewing angle of the torus is the same. For the bS1 and the bC1 baseline models, we found that the best options to link the mid-IR and X-ray viewing angles are $i_{\rm F06} = 90. - \theta_{\rm inc}$ and $i_{\rm N08} = \theta_{\rm inc}$, respectively. These options imply a scenario where dust and gas are in the same location (distributed along the equatorial plane). In the case of a bW1 baseline model, we found that the best option is $i_{\rm H17} = 90. - \theta_{\rm inc}$. This scenario implies that most of mid-IR emission is in the equatorial plane. Therefore, these three baseline models are consistent with the idea that most of the dust producing the mid-IR continuum emission is distributed in the equatorial plane where the torus has historically been located. Furthermore, the X-ray reflector under this scenario is also in the equatorial plane.

We reviewed and compared the reduced χ^2 statistic values for each of the baseline models. From this analysis, we concluded that the best statistic is obtained when using the combination of borus02 (X-ray) and smooth (mid-IR) models (the so-called bS1 baseline model) to fit the spectra at both wavelengths. Even though this baseline model has the best reduced χ^2, it is not capable of restricting the half-opening angle from X-ray ($\theta_{\rm tor}$), but it can restrict the mid-IR half-opening angle (σ). This issue is solved when both viewing and opening angles are linked (bS2 baseline model). We found that all the parameters can be constrained in bS2 baseline model using $\theta_{\rm tor} = 90 - \sigma$. The link between half-opening angles suggests a common origin for both emissions. Indeed, the statistic does not improve if these two parameters are allowed to vary individually. Therefore, the bS2 baseline model, where the viewing and half-opening angles are tied together, is enough to explain the observations at both wavelengths. The fact that the inclination and half-opening angles from the mid-IR and X-ray are directly linked to the same value is consistent with previous results (Farrah et al. 2016). Furthermore, the σ parameter could be related to the opening angle of the ionization cone, which is a tracer of [O III] emission (e.g., García-Bernete et al. 2019). Schmitt et al. (2003) presented the observation of IC 5063 in the [O III] filter from the *Hubble Space Telescope*. They found that this emission is extended and aligned with the radio emission and the host galaxy major axis. These results are similar to those found by Morganti et al. (1998). According to Schmitt et al. (2003) the [O III] emission can be represented by a bicone centered at the nucleus, with an opening angle of $\alpha({\rm cone}) = 60°$, extending for $\sim$2.6 kpc along P.A. $= -65°$ and $\sim$660 pc along the perpendicular direction. Using this measurement of the ionization opening angle, we obtained a free-of-cone half-opening angle of $\alpha(cone - free) \sim 60°$.[16] This suggests the torus occupies a free-of-cone area, although it does not fill it up completely.

The borus02 model is capable of separating the density of the reprocessed material and that of the LOS. This option allows us to explore whether the material that produces the reflection component is different from that producing the obscuration along the LOS (see also Baloković et al. 2018). We tested the scenario in which both $N_{\rm H}$ are linked. We found that $\Delta\chi^2$ increases (χ^2/dof $= 706.15/649$) if we fit the IC 5063 spectra using the bS2 baseline model and we assume that $N_{\rm H_{los}} = N_{\rm H_{tor}}$ (best-fit result in $\log(N_{\rm H}) = 23.25 \pm 0.02$). We compared this χ^2/dof with the bS2 statistic through the f-test, and we obtained a low probability value of 1.91×10^{-6} for the null hypothesis. Therefore, a scenario where these two values are different is statistically preferred. In Figure 7 (left), we show the two-dimensional χ^2 distributions for the $N_{\rm H_{los}}$ versus $N_{\rm H_{tor}}$ parameters when we used the bS2 baseline model. We found that these parameters are not the same at the 3σ level. Therefore, $N_{\rm H_{tor}}$ is larger than $N_{\rm H_{los}}$ beyond parameter degeneracy (see also Table 1). Note that in a scenario where both parameters belong to the same structure it is not feasible that $N_{\rm H_{tor}}$ is larger than $N_{\rm H_{los}}$, as it is in our case (see Table 1), because the former is the average density and the latter decreases with the azimuthal angle. Therefore, the $N_{\rm H_{los}}$ and $N_{\rm H_{tor}}$ parameters measure the $N_{\rm H}$ of different absorbing materials. This

[16] $\alpha({\rm cone - free}) = \frac{180° - \alpha({\rm cone})}{2}$.

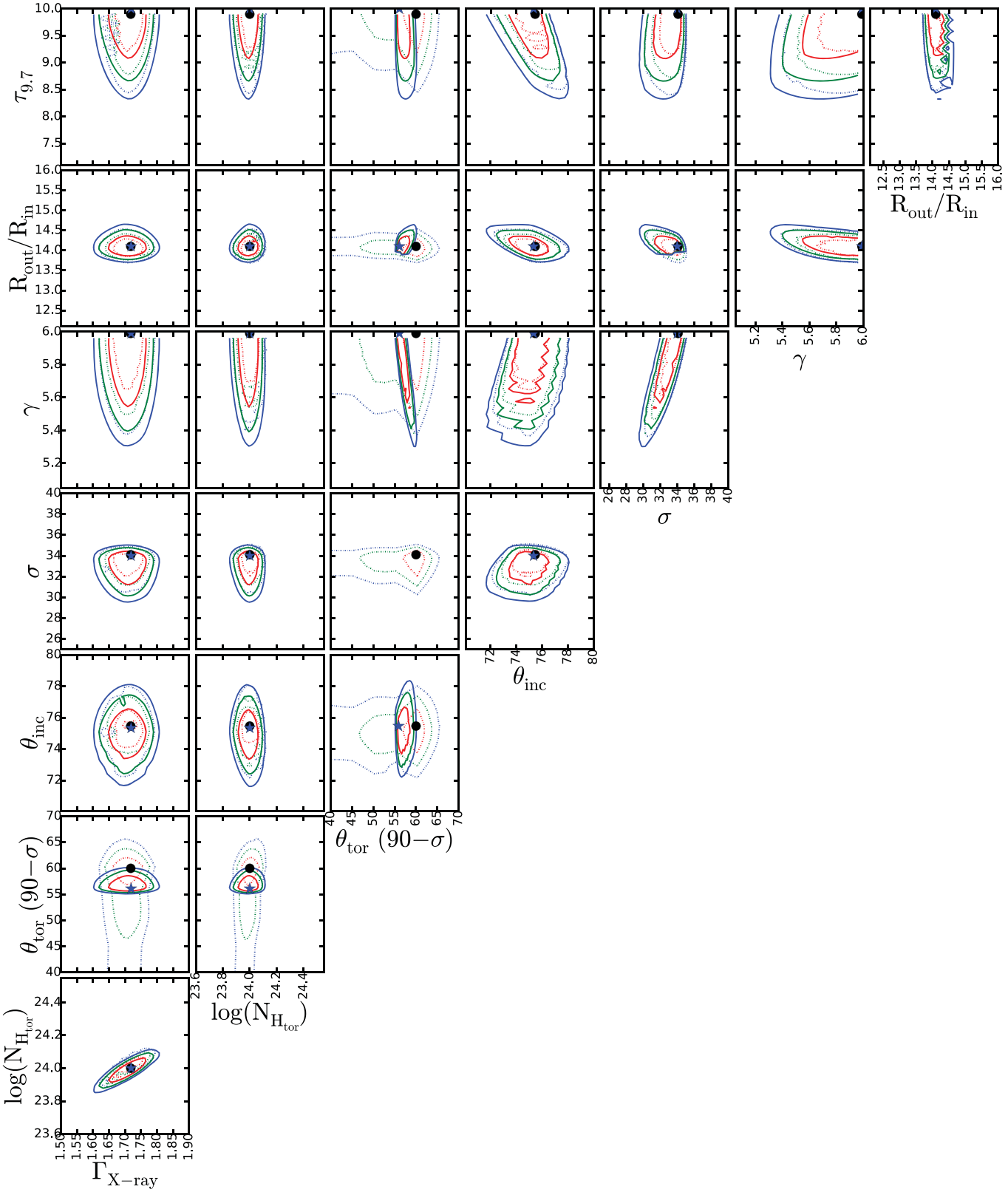

Figure 6. Two-dimensional Δ_{χ^2} contours for the resulting free parameters when we used the bS1 (dotted lines) and the bS2 (solid lines) baseline models to fit IC 5063. The red, green, and blue (dotted and solid) lines show the contours at 1σ, 2σ, and 3σ, respectively. The black circles and blue stars are the resulting values for each parameter using the bS1 and bS2 baseline models, respectively. Notice that these values are reported in columns 2 and 4 of Table 1.

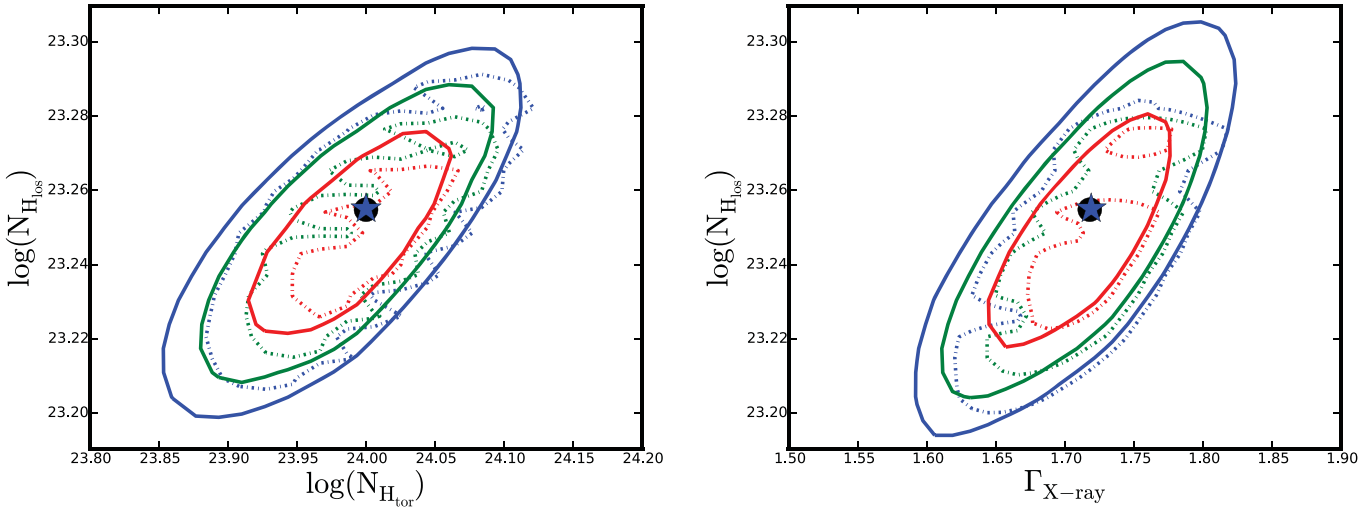

Figure 7. Two-dimensional Δ_{χ^2} contours for the LOS, density profile, and torus $N_{\rm H_{tor}}$ for the bS1 (dotted lines) and bS2 (solid lines) baseline models. The red, green, and blue lines are the 1σ, 2σ, and 3 σ contours. The values reported in Table 1 are shown with a black circle and blue star for the bS1 and bS2 baseline models, respectively.

result is also found by Baloković et al. (2018). As a final caveat on the subject, we found that the $N_{\rm H_{los}}$, $N_{\rm H_{tor}}$, and Γ parameters are partially degenerated. We think that this coupling between parameters is due to the natural degeneracy between obscuration and power-law steepness, where high $N_{\rm H_{los}}$ and low Γ could mimic, at a certain level, low $N_{\rm H_{los}}$ and high Γ (see Figures 7 and 6).

Another way to explore the properties of the torus taking into account the information at both wavelength ranges is through the column density and the optical depth from the X-ray and mid-IR models, respectively. The two parameters are associated with the density of the obscuring material. The link between these parameters is not straightforward because the $N_{\rm H_{tor}}$ is an average measurement of the column density at the inner parts of the torus (where the reflection is produced), while the $\tau_{9.7}$ is a measurement of the equatorial optical depth. We considered the relationship between extinction and column density, assuming a constant dust-to-gas ratio, and the relationship between the optical depth at 9.7 μm and that in V band (Nenkova et al. 2008b; Feltre et al. 2012).[17] Following these considerations and using the values reported in Table 1 for the bS2 baseline model, we obtained a column density of $\log(N_{\rm H_{\tau_{9.7}}}) > 23.65\ {\rm cm}^{-2}$ in the equatorial plane. This value is already consistent with $N_{\rm H_{tor}}$. However, strictly speaking, to compare it with $N_{\rm H_{tor}}$, we must calculate the average column density using the dependence of the density distribution with the azimuthal angle. Nevertheless, the resulting upper limit will always be less restrictive that the $N_{\rm H_{\tau_{9.7}}}$ reported above. On the other hand, we also compare the expected LOS column density from the dust distribution with the actual calculated LOS column density $N_{\rm H_{los}}$ considering the inclination angle and the dust density distribution values from the bS2 baseline model.[18] The resulting value is $\log(N^{\rm los}_{\rm H_{\tau_{9.7}}}) > 23.03$, which is consistent with the $N_{\rm H_{los}}$ value:

Therefore, we were able to find evidence suggesting that the structure that produces the continuum (mid-IR) and the reprocessed (X-ray) emissions is the same. This suggests that the reflection component has its origin in the AGN torus. Indeed, the smooth and the borus02 models individually fitting the mid-IR and X-ray spectra (individual fits reported in Table 2) also show consistent viewing angles and width of the torus, although the $\theta_{\rm tor}$ and $\theta_{\rm inc}$ parameters are better restricted when using the bs2 baseline model. This result has been largely argued in the literature, although we lack observational evidence. Although without simultaneous fitting, Farrah et al. (2016) also look for the similarities on the geometrical distribution resulting from the mid-IR and X-ray spectroscopic analysis of the radio galaxy IRAS 09104+4109. They concluded that both obscurers are consistent with being coaligned, although the viewing angle needed to be fixed to that obtained at mid-IR wavelengths. Bianchi & Guainazzi (2007) suggested that the widespread presence of a Compton reflection component strongly favors a scenario where most of the FeKα emission comes from the torus, and Bianchi et al. (2012) listed reasons why these two components come from a region smaller than 100 pc, associating it with the AGN. One of the strongest arguments in favor of an origin of the reflection component on the torus comes from the FeKα emission line, always attached to the Compton hump. Iwasawa & Taniguchi (1993) reported for the first time an anticorrelation between the strength of the neutral narrow core of the FeKα emission line and the 2–10 keV luminosity (the so-called X-ray Baldwin effect or Iwasawa-Taniguchi effect[19]). Page et al. (2004) have also explored this effect and suggested that a possible explanation is a decrease in the *Cf* of the Compton thick torus when the luminosity increases (see also Boorman et al. 2018). The current work shows one of the first direct evidences of the link between the reflection component and the torus.

6.2. Parameters and Derived Quantities of the Dusty Structure

The dust torus parameters of IC 5063 have been explored using the clumpy model and a Bayesian approach on high-resolution spectra and/or photometry by Ramos Almeida et al. (2011) and

[17] $\tau_{9.7} = 0.042 * \tau_{\nu}$.

[18] We used the following equation to calculate the $N_{\rm H}$ in the LOS derived from the mid-IR optical depth: $N^{\rm inc}_{\rm H_{\tau_{9.7}}}({\rm cm}^{-2}) = \frac{1.086}{0.042} * \tau_{9.7} * 1.9 \times 10^{21} * e^{-\gamma \cos(\theta_{\rm inc})}$. This equation considers the density function (see Equation (3) in Fritz et al. 2006), which depends on $\theta_{\rm inc}$ and γ.

[19] The Baldwin effect is an anticorrelation between the equivalent width and the luminosity found in optical/UV lines.

Table 2
The Best-fit Physical Parameters Using the Borus02 (Top) and the Smooth (Bottom) Models for IC 5063

Parameter	Value
Γ	$1.73\ ^{+0.01}_{-0.07}$
$\log(N_{\rm H_{tor}})$	$24.00\ ^{+0.04}_{-0.04}$
$\log(N_{\rm H_{los}})$	$23.25\ ^{+0.03}_{-0.01}$
$\theta_{\rm tor}$	$59.9\ ^{+2.5}_{-15.4}$
$\theta_{\rm inc}$	$75.5\ ^{+2.6}_{-2.1}$
χ^2/ dof	530/464
$i_{\rm F06}$ $(90.-\theta_{\rm inc})$	$14.9\ ^{+0.4}_{-0.4}$
σ	$34.2\ ^{+2.5}_{-2.2}$
β	0.0
Y	$14.1\ ^{+0.3}_{-0.3}$
$\tau_{9.7}$	>8.9
γ	>5.6
χ^2/ dof	148/181

Alonso-Herrero et al. (2011). The values obtained using our bC1 baseline model, except for $\theta_{\rm inc}$ and q, do not agree with theirs. However, it should also be noted that the statistic obtained for this baseline model is not the best for this source. If we compare their values with the ones from our best baseline model (i.e., bS2) we find the Y and $\theta_{\rm inc}$ are well in agreement with their error ranges. Meanwhile, our σ value is half of their reported value. Indeed, the smooth model accounts for the same dust in a smaller volume compared with the clumpy models (see also González-Martín et al. 2019a, 2019b). As suggested in the literature, the resulting model parameters and derived quantities seem to strongly depend on the model used, wavelength, and/or kind of data (i.e., spectroscopy or photometry). While they mostly rely on near- and mid-IR photometry (with ground-based Q-band spectroscopy), we use spectroscopic data covering the mid-IR and X-ray.

On the other hand, Baloković et al. (2018) fitted the *NuSTAR* spectra of IC 5063 using the borus02 model. Their values of $\Gamma = 1.75$, $\log(N_{\rm H_{tor}}) = 23.3$, $\log(N_{\rm H_{los}}) = 23.9$, and $\theta_{\rm inc} > 52°$ are consistent with our values within 1σ for the individual fits (see Table 2) and those obtained for the bS2 baseline models (see Table 1). The largest discrepancy is found for the $\theta_{\rm tor}$ parameter. Baloković et al. (2018) found $\theta_{\rm tor} < 40°$, which is consistent with the reported value using the individual fit and the bS1 baseline model (see Tables 2 and 1) at 3σ (see Figure 6). However, this value is not consistent with that obtained by the bS2 baseline model. Note that these values are obtained assuming a fixed value by the $N_{\rm H_{tor}}$ parameter. This might explain the discrepancy found and shows the difficulties in restricting the $\theta_{\rm tor}$ using X-ray data alone, reinforcing the need to produce a consistent picture using multiwavelength information.

This issue is also visible in the derived quantities. In the last row of Table 1 we report the dust masses obtained from the mid-IR parameters, which cover a range $(0.06–30.3) \times 10^5\ M_\odot$. Therefore, the dust mass depends on the chosen baseline model to fit the spectra. Despite this, the values are consistent with the ranges reported in other works (Fritz et al. 2006; Mor et al. 2009). Furthermore, Cf is strongly dependent on the baseline model used. Ramos Almeida et al. (2011) compared the properties of a large sample of Sy1 and Sy2 Seyfert tori using the clumpy torus models. They found that the dusty torus in Sy2 is wider than that in Sy1 and is composed of a larger number of clouds with lower optical depth. Our mid-IR covering factors ($Cf_{\rm midIR}$ in Table 1) are consistent with their results (see also Brightman 2015).

We also calculated the $R_{\rm out}$ for each of our baseline models. We find $R_{\rm out} > 23.9$ pc (diameter $\sim 0\farcs2$) and $R_{\rm out} = 3.4$ pc (diameter $\sim 0\farcs03$) when using the bC1 and bS2 baseline models to fit the spectra, respectively. This last $R_{\rm out}$ value is consistent with that reported by Ichikawa & Inayoshi (2017) for IC 5063. Therefore, the selection of the baseline model is crucial to obtain meaningful results for both structural parameters and derived quantities. Additionally, note that only the $R_{\rm out}$ obtained using the bC1 baseline model could be detectable at the best spatial resolution provided by the Atacama Large Millimeter/submillimeter Array (ALMA).[20] However, ALMA data are also sensitive to the radio jet emission, so a proper study of the SED is required to use ALMA data to study the AGN dust (Pasetto et al. 2019). Finally, we suggest that future work test as many models as possible with multiwavelength spectroscopy to try to disentangle which model better reproduces the data before drawing any conclusion on the parameters.

Overall, according to the values of parameters results using the bS2 baseline model, the IC 5063 torus is a compact ($R_{\rm out} \sim 3.4$ pc) and relatively thin ($\sigma \sim 34$) structure. Our bS2 baseline model solution also favors a dust torus in which the density profile only has an azimuthal dependence ($\gamma > 5.6$), that is, a strong decrease in the dust/gas density when the half-opening angle increases.

6.3. About Our Simultaneous Fitting Technique

Apart from simultaneously explaining both mid-IR and X-ray continuum emission, the main advantage of being able to link some parameters from mid-IR and X-ray models is that we can find all of them from the final fit (see Figure 6). Therefore, we can obtain more information and explore the source of obscuration at both wavelengths.

In the case of IC 5063, we found that the best option to fit its spectra is using a combination of the smooth and borus02 models (bS2). A caveat to this result is that these two models may have been our best choice to fit the data due to their geometric similarities. Indeed, both models assume a smooth distribution arranged in a torus-like structure. Nevertheless, these models assume a different density distribution; the borus02 model assumes a uniform density profile for the gas distribution, and the smooth model decreases toward large azimuths and radii. Additionally, the smooth model assumes that a dusty structure is located between an inner and outer radius while gas can reach the accretion disk. Recently, Tanimoto et al. (2019) constructed the XCLUMPY model, which is the radiative transfer of neutral gas at X-rays using the same distribution as the clumpy torus at mid-IR. A combination of the XCLUMPY and clumpy models might also get good results. We can discard this scenario for IC 5063 because the residuals seen at mid-IR for the clumpy model are significantly larger than those reported for the smooth model. However, as we expect different AGNs to be better reproduced with different models, we will explore this possibility using an

[20] The highest spatial resolution obtained with ALMA uses a configuration C43-10 in band 7.

AGN sample in a forthcoming paper (D. Esparza-Arredondo 2019, in preparation).

Finally, a few words on the applicability of this technique to AGN samples. Our technique of simultaneous fitting can be applied to any type of AGN that is not dominated by the host galaxy. The best results could be found when using the high spatial resolution mid-IR spectra and hard (>10 keV) X-ray spectra to ensure a proper decontamination of the host galaxy and a characterization of the reflection component, respectively. The reflection-dominated spectra at X-ray (i.e., with high obscuration toward the LOS) are also better targets. *Spitzer*/IRS spectra can be used as long as the AGN dominates the emission; future *James Webb Space Telescope* observations would be needed otherwise.

7. Conclusions

In this work, we explored whether the X-ray reflection component and the mid-IR continuum of AGNs are linked to the same structure, that is, the so-called AGN torus. Showing that is the case, we also investigate whether the combination of X-ray and mid-IR spectra and different torus models could help us to restrict the torus physical parameters of the nearby Seyfert IC 5063 galaxy. We considered *Spitzer*/IRS and *NuSTAR* spectra for this analysis. We combined the radiative transfer code borus02 at X-ray (Baloković et al. 2018) to describe the X-ray reflection and smooth (Fritz et al. 2006), clumpy (Nenkova et al. 2008b), or CAT3D-WIND (Hönig & Kishimoto 2017) models to describe mid-IR AGN dust to create a set of baseline models. We found that the combination of the borus02 and smooth models is the best choice to fit the spectra from both wavelengths of IC 5063. Moreover, all the parameters of the dusty torus can be constrained if the X-ray and mid-IR inclination and half-opening angles are linked to the same value (bS2 baseline model). This link between parameters suggests that the same structure producing the reflection component is emitting through dust heating at mid-IR. This could be the first time such behavior is confirmed by comparing the expected morphology and obscuring material distributions at both wavelengths. This technique can be used to infer the physical properties of the torus of any AGN that is not dominated by the host galaxy at mid-IR and shows a significant fraction of the reflection component at X-ray.

The authors thank the anonymous referee for careful reading and constructive suggestions that improved the paper. This work made use of data from the *NuSTAR* mission, a project led by CalTech, managed by Jet Propulsion Laboratory, and funded by NASA. We thank the *NuSTAR* Operations, Software and Calibration teams for support with the execution and analysis of these observations. This research has made use of the *NuSTAR* Data Analysis Software (NuSTARDAS) jointly developed by the ASI Science Data Center (ASDC, Italy) and CalTech. This work is based in part on observations made with the *Spitzer Space Telescope*, which is operated by the Jet Propulsion Laboratory, California Institute of Technology, under a contract with NASA. D.E.-A. acknowledges support from a CONACYT scholarship. This research is mainly funded by the UNAM PAPIIT project IA103118 (PI OG-M). M.M.-P. acknowledges support from KASI postdoctoral fellowships. J.M. acknowledges financial support from the research project AYA2016-76682-C3-1-P (AEI/FEDER, UE) and the State Agency for Research of the Spanish MCIU through the Center of Excellence Severo Ochoa award for the Instituto de Astrofísica de Andalucía (SEV-2017-0709). C.R.-A. acknowledges the Ramón y Cajal Program of the Spanish Ministry of Economy and Competitiveness through project RYC-2014-15779 and the Spanish Plan Nacional de Astronomía y Astrofisíca under grant AYA2016-76682-C3-2-P.

ORCID iDs

Donaji Esparza-Arredondo https://orcid.org/0000-0001-8042-9867
Omaira González-Martín https://orcid.org/0000-0002-2356-8358
Cristina Ramos-Almeida https://orcid.org/0000-0001-8353-649X
Jacopo Fritz https://orcid.org/0000-0002-7042-1965
Alice Pasetto https://orcid.org/0000-0003-1933-4636
Mariela Martínez-Paredes https://orcid.org/0000-0002-0088-0103

References

Alonso-Herrero, A., Ramos Almeida, C., Mason, R., et al. 2011, ApJ, 736, 82
Antonucci, R. 1993, ARA&A, 31, 473
Asmus, D., Hönig, S. F., Gandhi, P., Smette, A., & Duschl, W. J. 2014, MNRAS, 439, 1648
Baloković, M., Brightman, M., Harrison, F. A., et al. 2018, ApJ, 854, 42
Barvainis, R. 1987, ApJ, 320, 537
Bianchi, S., & Guainazzi, M. 2007, in AIP Conf. Ser. 924, The Multicolored Landscape of Compact Objects and Their Explosive Origins, ed. T. di Salvo et al. (Melville, NY: AIP), 822
Bianchi, S., Maiolino, R., & Risaliti, G. 2012, AdAst, 2012, 782030
Bianchi, S., Matt, G., Balestra, I., Guainazzi, M., & Perola, G. C. 2004, A&A, 422, 65
Bohlin, R. C., Savage, B. D., & Drake, J. F. 1978, ApJ, 224, 132
Boorman, P. G., Gandhi, P., Baloković, M., et al. 2018, MNRAS, 477, 3775
Brightman, M., Baloković, M., Stern, D., et al. 2015, ApJ, 805, 41
Brightman, M., & Nandra, K. 2011, MNRAS, 413, 1206
Efstathiou, A., & Rowan-Robinson, M. 1995, MNRAS, 273, 649
Elitzur, M., & Netzer, H. 2016, MNRAS, 459, 585
Fabian, A. C. 1998, in AIP Conf. Ser. 431, Accretion Processes in Astrophysical Systems: Some Like it Hot!, ed. S. S. Holt & T. R. Kallman (Melville, NY: AIP), 247
Farrah, D., Baloković, M., Stern, D., et al. 2016, ApJ, 831, 76
Feltre, A., Hatziminaoglou, E., Fritz, J., & Franceschini, A. 2012, MNRAS, 426, 120
Fritz, J., Franceschini, A., & Hatziminaoglou, E. 2006, MNRAS, 366, 767
Fukazawa, Y., Furui, S., Hayashi, K., et al. 2016, ApJ, 821, 15
Furui, S., Fukazawa, Y., Odaka, H., et al. 2016, ApJ, 818, 164
García-Bernete, I., Ramos Almeida, C., Alonso-Herrero, A., et al. 2019, MNRAS, 486, 4917
Ghisellini, G., Haardt, F., & Matt, G. 1994, MNRAS, 267, 743
González-Martín, O., Masegosa, J., García-Bernete, I., et al. 2019a, ApJ, 884, 10
González-Martín, O., Masegosa, J., García-Bernete, I., et al. 2019b, ApJ, 884, 11
González-Martín, O., Masegosa, J., Hernán-Caballero, A., et al. 2017, ApJ, 841, 37
Granato, G. L., & Danese, L. 1994, MNRAS, 268, 235
Harrison, F. A., Craig, W. W., Christensen, F. E., et al. 2013, ApJ, 770, 103
Hatziminaoglou, E., Fritz, J., Franceschini, A., et al. 2008, MNRAS, 386, 1252
Hatziminaoglou, E., Fritz, J., & Jarrett, T. H. 2009, MNRAS, 399, 1206
Hönig, S. F., & Kishimoto, M. 2010, A&A, 523, A27
Hönig, S. F., & Kishimoto, M. 2017, ApJL, 838, L20
Hönig, S. F., Kishimoto, M., Gandhi, P., et al. 2010, A&A, 515, A23
Ichikawa, K., & Inayoshi, K. 2017, ApJL, 840, L9
Ichikawa, K., Packham, C., Ramos Almeida, C., et al. 2015, ApJ, 803, 57
Ikeda, S., Awaki, H., & Terashima, Y. 2009, ApJ, 692, 608
Iwasawa, K., & Taniguchi, Y. 1993, ApJL, 413, L15
Koyama, K., Awaki, H., Iwasawa, K., & Ward, M. J. 1992, ApJL, 399, L129
Krolik, J. H., & Begelman, M. C. 1988, ApJ, 329, 702
Krolik, J. H., Madau, P., & Zycki, P. T. 1994, ApJL, 420, L57

Laor, A. 1991, ApJ, 376, 90
Lebouteiller, V., Barry, D. J., Spoon, H. W. W., et al. 2011, ApJS, 196, 8
Liu, T., & Wang, J.-X. 2010, ApJ, 725, 2381
Liu, Y., & Li, X. 2015, MNRAS, 448, L53
Martínez-Paredes, M., Aretxaga, I., Alonso-Herrero, A., et al. 2017, MNRAS, 468, 2
Matt, G., Perola, G. C., & Piro, L. 1991, A&A, 247, 25
Mor, R., Netzer, H., & Elitzur, M. 2009, ApJ, 705, 298
Morganti, R., Oosterloo, T., & Tsvetanov, Z. 1998, AJ, 115, 915
Murphy, K. D., & Yaqoob, T. 2009, MNRAS, 397, 1549
Nandra, K., & George, I. M. 1994, MNRAS, 267, 974
Nenkova, M., Sirocky, M. M., Ivezić, Ž, & Elitzur, M. 2008a, ApJ, 685, 147
Nenkova, M., Sirocky, M. M., Nikutta, R., Ivezić, Ž, & Elitzur, M. 2008b, ApJ, 685, 160
Netzer, H. 2015, ARA&A, 53, 365
Page, K. L., O'Brien, P. T., Reeves, J. N., & Turner, M. J. L. 2004, MNRAS, 347, 316
Panuzzo, P., Rampazzo, R., Bressan, A., et al. 2011, A&A, 528, A10
Pasetto, A., González-Martín, O., Esparza-Arredondo, D., et al. 2019, ApJ, 872, 69
Peeters, E., Spoon, H. W. W., & Tielens, A. G. G. M. 2004, ApJ, 613, 986
Pfeffermann, E., Briel, U. G., Hippmann, H., et al. 1987, Proc. SPIE, 733, 519
Pier, E. A., & Krolik, J. H. 1993, ApJ, 418, 673
Ramos Almeida, C., Levenson, N. A., Alonso-Herrero, A., et al. 2011, ApJ, 731, 92
Ramos Almeida, C., Levenson, N. A., Rodríguez Espinosa, J. M., et al. 2009, ApJ, 702, 1127
Ramos Almeida, C., & Ricci, C. 2017, NatAs, 1, 679
Ricci, C., Ueda, Y., Paltani, S., et al. 2014, MNRAS, 441, 3622
Ricci, C., Walter, R., Courvoisier, T. J.-L., & Paltani, S. 2011, A&A, 532, A102
Schartmann, M., Meisenheimer, K., Camenzind, M., Wolf, S., & Henning, T. 2005, A&A, 437, 861
Schmitt, H. R., Donley, J. L., Antonucci, R. R. J., et al. 2003, ApJS, 148, 327
Shlosman, I. 2005, The Evolution of Starbursts, 783, 223
Shu, X. W., Yaqoob, T., & Wang, J. X. 2010, ApJS, 187, 581
Siebenmorgen, R., Heymann, F., & Efstathiou, A. 2015, A&A, 583, A120
Stalevski, M., Fritz, J., Baes, M., Nakos, T., & Popović, L. Č. 2012, MNRAS, 420, 2756
Tacconi, L. J., Genzel, R., Blietz, M., et al. 1994, ApJL, 426, 77
Tanaka, Y., Inoue, H., & Holt, S. S. 1994, PASJ, 46, L37
Tanimoto, A., Ueda, Y., Odaka, H., et al. 2019, ApJ, 883, 110
Urry, C. M., & Padovani, P. 1995, PASP, 107, 803
Vignali, C., Comastri, A., Cappi, M., & Palumbo, G. G. C. 1997, MmSAI, 68, 139
Yang, Q.-X., Xie, F.-G., Yuan, F., et al. 2015, MNRAS, 447, 1692

Chapter 5

The AGN obscuration and its evolutionary stages

The dust-gas obscuring structure is key for understanding the shutdown and/or ignition processes in AGN. This is due to its relationship to the feedback process involving the SMBH and the accretion disk. This obscuring structure surrounds the accretion disk and, therefore, has a dominant role in providing it with the material. Such is the case that previous theoretical works have been shown that lack of winds is linked to the low efficiency of the accretion disk. In this chapter, we search for a sample of fading or rising AGN to understand the role of the obscuration component in the evolution of AGN.

We used the AGN scaling relations mentioned in Section 2.3 to explore differences in the energy budget between components. Initially, we considered nearby AGN with the available information at three wavelengths (optical, X-ray, and mid-IR) in the catalogs presented in Section 2.1.3. We then considered the information available at other wavelengths to explore the robustness of our methodology. We further investigate our sources' fading/rising nature using other pieces of evidence reported in the literature. In particular, we compiled mid-IR *Spitzer* spectra to study the AGN dust, and we search for the existence of a jet using archival radio images. We further explored the optical classification using BPT diagrams. Then, we compiled [OIV] emission line fluxes to test the adequacy of the [OIII] as a tracer of the NLR emission and used UV continuum emission to test the X-rays as a tracer of the disk emission (see chapter 2).

We finally compiled a catalog of 88 AGN in the nearby universe that show hints of fading or rising in their activity. Among them, 96% are in the fading state. This result might imply that one-tenth of the AGN duty cycle of activity is spent in the fading phase according to Hopkins et al. (2005). Indeed, the fading phase is expected to last longer than the rising phase. Alternatively, the lack of rising AGN might be a natural consequence of the switching off of the SF and AGN activity at the present time, according to Hopkins (2012). This result is consistent with the fact that the universe had its peaks of AGN activity somewhere in the past and is shutting down at present. Finally, we found that a torus-like geometry was preferred for these sources, which is consistent with these phases.

Author disclosure: This work is the result of an active contribution from all authors. All

contributed to data analysis and drafting of the results. As the first author, my contribution is significantly above the others. Particularly, my contribution to this work consisted in the selection of sources using the X-ray versus [OIII] luminosities relationship, the analysis of the robustness of sample through [OIV] versus [OIII] relationship, the decomposition and fit of *Spitzer* spectra, discussion of results, and redaction of several sections. Among the major contributions, Natalia Osorio Clavijo searched for the candidates through the mid-IR versus X-ray luminosity relationship. She also analyzed *NuSTAR* spectra for several sources that did not have robust measurements of line-of-sight absorption. On the other hand, Omaira González Martín refined the classification and wrote some parts of the paper. César Victoria Ceballos searched for the absorption corrected luminosities of most of the sources. He was also in charge of the morphological classification of galaxies and their environment. Alice Pasetto performed the analysis of the radio images, Ulises Reyes-Amador performed BPT diagrams, and Sinhué Haro-Corzo and Jafet López-Sánchez performed the UV versus X-ray correlations. This work was published in the Astrophysical Journal on December 9, 2020. The electronic version of this publication can be found in the following URL: https://ui.adsabs.harvard.edu/abs/2020ApJ...905...29E/abstract

The Astrophysical Journal, 905:29 (23pp), 2020 December 10 https://doi.org/10.3847/1538-4357/abc425

Active Galactic Nucleus Ghosts: A Systematic Search for Faded Nuclei

Donaji Esparza-Arredondo[1], Natalia Osorio-Clavijo[1], Omaira González-Martín[1], César Victoria-Ceballos[1], Sinhué A. R. Haro-Corzo[2], Omar Ulises Reyes-Amador[1], Jafet López-Sánchez[2], and Alice Pasetto[1]
[1] Instituto de Radioastronomía and Astrofísica (IRyA-UNAM) 3-72 (Xangari), 8701 Morelia, México; d.esparza@irya.unam.mx
[2] Escuela Nacional de Estudios Superiores (ENES-UNAM) 3-72 (Xangari), 8701 Morelia, México
Received 2020 August 27; revised 2020 October 11; accepted 2020 October 21; published 2020 December 9

Abstract

Physical processes such as reignition, enhancement, and fading of active galactic nuclei (AGN) are not entirely understood because the timeline of these events is expected to last many years. However, it is well known that the differences in the energy budget between AGN components, like the optical ionizing region and the mid-infrared (MIR) dust echoes, can be interpreted as a hint of AGN evolution. Here we present a catalog of 88 AGN candidates showing hints of the fading and rising of their activity in the nearby universe. We use AGN scaling relations to select them from an initial sample of 877 candidates using publicly available optical, X-ray, and MIR luminosities. We then use the multiwavelength information to discard sources contaminated with extranuclear emission and those with an X-ray luminosity not well corrected for absorption. We find that 96% of our candidates are fading sources. This result suggests a scenario where the universe had its peak of AGN activity somewhere in the past and is dominated by a fading phase at the present time. Alternatively, the fading phase is longer than the rising phase, which is consistent with galaxy merger simulations. Around 50% of these fading candidates are associated with merging or interacting systems. Finally, we also find the existence of jets in ∼30% of these candidates and that the preferred AGN dust geometry is torus-like instead of wind-like. Our results are compatible with the fading of nuclear activity, expected if they are in an inefficient state.

Unified Astronomy Thesaurus concepts: Active galactic nuclei (16); Catalogs (205); Active galaxies (17); Infrared galaxies (790); X-ray active galactic nuclei (2035)

1. Introduction

Some of the most important questions in the active galactic nucleus (AGN) field are how and why AGN initiate or finish their activity. Understanding this behavior plays a key role in the context of supermassive black hole (SMBH) growth, which is linked to these active phases, and the evolution of the galaxies themselves (see Hopkins & Quataert 2010). Indeed, it is well known that the mass of the SMBH is linked to other properties of galaxies (e.g., Kormendy & Ho 2013).

Despite its importance, little is known about it, with only a brief idea of the AGN ignition/fading process and/or the duration of the AGN phase. Marconi et al. (2004) suggested that this phase should last 10^{7-9} yr spread in small duty cycles of 10^5 yr each (see also Novak et al. 2011; Schawinski et al. 2015; Shulevski et al. 2015). Under this context, the study of AGN duty cycles cannot be done without a proper classification of the stages of the AGN.

It has long been known that some AGN are accompanied by emission line regions both narrow and broad (the so-called NLR and BLR). The NLR is a zone of ionized gas spanning galaxy scales or even larger. Such regions can trace the geometry of the ionizing radiation escaping from the AGN and the host galaxy and, at least implicitly, give hints of the AGN luminosity when this structure was created (Keel et al. 2017). Indeed, the difference in the energy budget between the accretion disk and the NLR can be interpreted as a hint of the AGN evolution. This is what is called the optical ionization echo. In this way, several fading AGN have been discovered by the Galaxy Zoo project (Lintott et al. 2008). A very well-known example of a fading AGN discovered using this method is the Hannys Voorwerp near the spiral galaxy IC 2497 (Lintott et al. 2009; Keel et al. 2012). This object shows an NLR spanning a projected range from 15 to 35 kpc from the galaxy nucleus that should have been produced by an AGN at least 2 orders of magnitude higher in bolometric luminosity than nuclear luminosity. This indicates that the nucleus faded from a QSO-like luminosity to a modest Seyfert/LINER level within 10^5 yr. The AGN showing this scenario have also been reported in the high-redshift universe by the discovery of 14 Lyα blobs with weak AGN activity (e.g., Schirmer et al. 2016).

Extrapolating this line of thought, not only can the NLR trace these echoes of past activity, other components could help to find changes in AGN activity. Mid-infrared (MIR) wavelengths can be used to trace MIR dust echoes because this emission is dominated by the obscuring dust located a few parsecs away from the nucleus (Ramos Almeida & Ricci 2017). Of course, the closer the structure to the accretion disk, the shorter the timescale of the evolution. Thus, in a fading scenario, we would expect the bolometric luminosity required for the NLR to be higher than that required for the AGN dust, with the accretion disk current bolometric luminosity being the lowest among them. This idea has already been applied to the case of Arp 187 showing a clear decline of nuclear activity (with over 10^3 times lower luminosity) in an estimated time lapse of 10^4 yr (Ichikawa et al. 2016, 2019a, 2019b). Ichikawa et al. (2019b) claimed that the nucleus of Arp 187 has already ceased its activity, with its NLR and jet being evidence of the past activity. Despite their importance, very few fading AGN have been reported so far. The largest compilation of them shows ∼20 AGN (see Table 2 presented by Ichikawa et al. 2019b, and references therein). This technique could, in principle, not only detect fading but also rising AGN, i.e., those AGN that show an increased accretion disk bolometric luminosity compared to the MIR dust echoes and optical ionization echoes. Currently, the detection of rising AGN candidates using only the NLR emissions is difficult

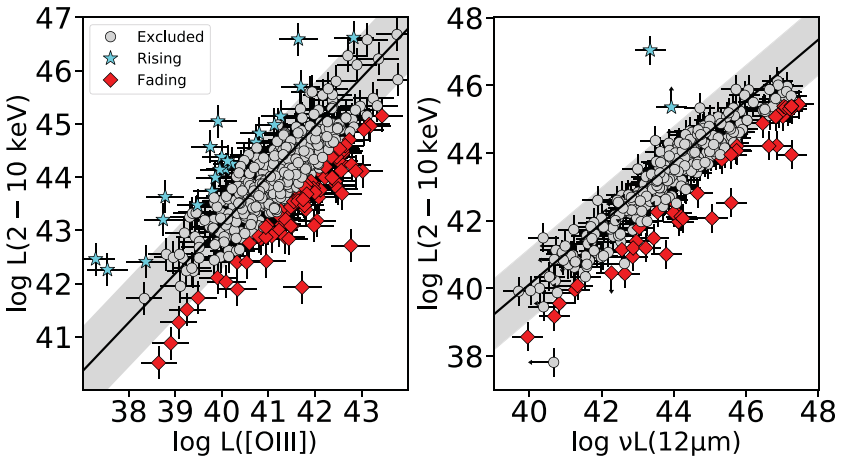

Figure 1. Left: The 2–10 keV X-ray luminosity, L(2–10 keV), vs. the [O III] reddened corrected luminosity, L([O III]) (both in logarithmic scale), for the BASS sample reported by Berney et al. (2015). Right: The 2–10 keV X-ray luminosity, L(2–10 KeV), vs. the MIR 12 μm continuum luminosity, $\nu L(12\ \mu\mathrm{m})$), in logarithmic scales. The black solid line shows the best linear fit using type 1 AGN in the left panel, whereas it shows the relation reported by Gandhi et al. (2009) in the right panel. The gray shaded region indicates the 2σ from the linear relation. Gray circles, cyan stars, and red diamonds show the excluded, AGN rising candidates, and AGN fading candidates, respectively.

because they may be indistinguishable from a lack of gas for ionization echoes (Schawinski et al. 2015). In general terms, fading (rising) AGN show large-scale signatures of a prominent (weak) AGN process and small-scale signatures of a much weaker (stronger) AGN.

The purpose of this paper is to compile a sample of fading and rising AGN candidates using multiwavelength information. The paper is organized as follows. In Section 2, we use individual scaling relations found in AGN to derive an initial sample of candidates using publicly available optical and MIR observations of AGN. This sample is further refined in Section 3, combining accurate measurements of the disk, AGN dust, and NLR for the initial sample. In Section 4, we further explore the robustness of the selection of candidates using all available multiwavelength information. We give a summary and discuss the main results in Section 5. Finally, the main conclusions of the paper are presented in Section 6. Throughout this work, we adopt $H_0 = 67.8\ \mathrm{km\ s^{-1}\ Mpc^{-1}}$ as a cosmological parameter.

2. Scaling Relations and Initial Sample

We look for rising/fading AGN using well-known linear relations between signatures of several AGN components at different wavelengths. This assumes that a relation is found when the involved components are traced by the same bolometric luminosity. Objects showing values out of these relations imply different bolometric luminosities for each component and therefore being candidates for a long-term evolution of the bolometric luminosity for the source.

2.1. The X-ray versus [O III] λ5007 Luminosity Relationship

We considered all sources classified as Seyferts reported by Berney et al. (2015) to explore the relationship between X-ray and [O III] luminosities. This relation is of the form

$$\log L(2\text{–}10\ \mathrm{keV}) = \alpha\ \log L([\mathrm{OIII}])\ +\ \beta. \qquad (1)$$

This relationship is well explored, showing a good behavior from high- to low-luminosity AGN (e.g., Ward et al. 1988; Panessa et al. 2006; González-Martín et al. 2009a). The X-ray luminosity traces the accretion disk associated with the current bolometric luminosity. The L([O III]) traces the NLR with a bolometric luminosity associated with this kiloparsec-scale structure. Note also that the [O III] emission parent ion recombines much more rapidly than almost any other (especially hydrogen recombination, whose timescale can be thousands of years in extended emission line regions (EELRs); Binette & Robinson 1987). Meanwhile, the X-ray emission traces the nuclear source luminosity associated with $\sim 10^{-2}$ pc scale structure or a timescale of $\sim 3 \times 10^{-2}$ yr (Hawkins 2007).

We used the optical and X-ray measurements reported by Berney et al. (2015). Their optical data are taken from the BAT AGN Spectroscopic Survey (BASS) Data Release 1 (Koss et al. 2017). The BASS catalog contains 67.6% of the total AGN detected in the Swift BAT 70 month catalog and has an average redshift of $z = 0.10$. The optical measurements were obtained using a combination of power-law plus Gaussian components to fit the continuum and emission lines, respectively. The flux uncertainty for the [O III] emission line is typically below 0.01%. We use the intrinsic fluxes reported by them, which were corrected for host galaxy extinction using the Balmer decrement (i.e., Hα/Hβ). They corrected for extinction using the narrow Balmer line ratio Hα/Hβ assuming an intrinsic ratio of $R = 3.1$ (e.g., Ferland & Osterbrock 1986) and the reddening curve provided by Cardelli et al. (1989). The 2–10 keV intrinsic fluxes are based on a homogeneous spectral fitting using the best available X-ray data with simultaneous fitting of the 0.2–10 keV band (from XMM-Newton, Chandra, or Swift/XRT) and the 14–195 keV band from Swift BAT (details in Ricci et al. 2017). Our sample contains 579 sources with [O III] and X-ray measurements: one type BL Lac and 55 type 1, 107 type 1.2, 100 type 1.5, 96 type 1.9, and 220 type 2 AGN.

In order to minimize issues due to attenuation and/or obscuration of type 2 AGN, we define the slope and offset of this relationship (Equation (1)) using unobscured type 1 AGN only. The resulting relationship, together with the data, is shown in Figure 1 (left panel). We obtained a slope of $\alpha = 0.92$ and an offset of $\beta = 6.27$, which are consistent with previous results. We selected rising/fading AGN as the sources that are located outside 2σ from this relationship (shaded area in Figure 1). In total, we obtained 113 candidates using this criteria: 23 rising

and 90 fading sources. Among them we found 69 type 1, 43 type 2, and one BL Lac.[3]

2.2. MIR versus X-Ray Luminosity Relationship

The X-ray–versus–MIR luminosity relationship is also a very well-known scaling relation in AGN (Elvis et al. 1978; Glass et al. 1982; Krabbe et al. 2001; Lutz et al. 2004; Ramos Almeida et al. 2007) of the form

$$\log \nu\, L(12\ \mu\mathrm{m}) = \alpha\, \log L(2\text{–}10\ \mathrm{keV}) + \beta. \quad (2)$$

It has been interpreted as a connection between the accretion disk and the dusty torus. Gandhi et al. (2009) reported $\alpha = 1.11 \pm 0.07$ and $\beta = -4.37 \pm 3.08$ using a sample of 42 AGN, with a median $z = 0.1$ and a range of MIR luminosities of $\log(\nu\ L_{12\mu\mathrm{m}}) = [41.4\text{–}44.6]$. Posterior analysis has shown consistent values for these constants (e.g., Asmus et al. 2015). At the typical range scale of the dusty torus of ∼0.3–10 pc, this structure traces the bolometric luminosity of the source roughly from 10 to 30 yr (Lyu et al. 2019). Thus, outliers in this relation might trace changes in shorter timescales than the X-ray–versus–[O III] relation explained above.

We use all of the sources reported in Asmus et al. (2015), which contains a catalog of 253 sources with ground-based MIR photometric data from several observatories (e.g., VIRIS/VLT, T-ReCS/Gemini, CanariCam/GTC, Michelle/Gemini). This sample contains AGN with MIR luminosities of $\log(\nu\ L_{12\mu\mathrm{m}}) = [39.7\text{–}45.7]$ and redshifts lower than $z < 0.4$. Asmus et al. (2014) marked sources as nonreliable for low count rate observations, or AGN classified as Compton-thick obscured sources, for which X-ray observations with XMM-Newton, Suzaku, or NuSTAR were not available at the time of that publication. We do not exclude these sources to avoid losing potential candidates for fading/rising AGN activity. We further investigate the reliability of these candidates in Section 3.

We also added to the analysis the sources reported by Stern (2015), which includes several samples in order to compare with high-luminosity AGN (magnitude in the I band in the range $I[-29.3, -30.2]$) and high-redshift AGN ($1.5 < z < 4.6$). Among these samples, they included the mixed Fifth Data Release Sloan Digital Sky Survey/XMM-Newton Quasar Survey (SDSS DR5; Young et al. 2009), the Serendipitous Extragalactic X-ray Source Identification (SEXSI; Harrison et al. 2003; Eckart et al. 2005, 2006, 2010) sample, the QSO sample from Just et al. (2007), and both Compton-thick and Compton-thin samples using NuSTAR data, with MIR luminosities from WISE, VLT/VISIR, and Spitzer.

Note that the intrinsic (i.e., absorption-corrected) 2–10 keV X-ray luminosities included in these samples are obtained from the literature. We refer the reader to Asmus et al. (2015) and Stern (2015) for further details. We further explore in Section 4 whether the line-of-sight absorption correction is robust, with particular attention to the Compton-thick nature of the sources to provide a more robust list of rising/fading AGN candidates.

Altogether, the sample we explore includes 419 AGN: 224 type 1 AGN, 123 type 2 AGN, 32 LINERS, 37 composite AGN, and three unclassified AGN. Among them, 253 sources come from the sample reported by Asmus et al. (2014) and 166 sources from the sample published by Stern (2015). Figure 1 (right panel) shows the MIR versus X-ray luminosities for the combined sample and the relation found by Gandhi et al. (2009). As in the previous section, we consider as rising/fading candidate AGN those sources outside of this relation at the 2σ level. Note that, although two objects fall out of the relation, they have been excluded from the sample because the MIR luminosity is an upper limit; therefore, they are consistent with being in the relation. In total, we obtained 49 sources: two rising and 47 fading. Among them we found 17 type 1 and 18 type 2 AGN, 10 LINERs, and four composite AGN.

3. AGN Fading/Rising Candidate Sample

In summary, we select a total of 137 fading and 25 rising AGN candidates using the two selection criteria explained in Section 2. Among them, one object was common to both selection criteria. Therefore, our initial sample contains 161 candidates.

However, using only a single criterion is not enough to consider the candidate secure. By definition, AGN are variable sources. These variations are expected to occur throughout the entire electromagnetic spectrum. Inner components, such as the accretion disk, are expected to vary in timescales of hours. Thus, random variations of the disk are expected to occur when compared to the torus or the NLR, without implying a consistent fading/rising scenario. These variations will be reflected in the scaling relations above as scatter. Some of this scatter could be included in our sample of fading/rising candidates. Thus, the three AGN components should show consistent fading/rising behavior of the bolometric luminosity for the AGN to be considered a good candidate. For this reason, we complete our compilation of X-ray, MIR, and [O III] luminosities from the literature. We only use L([O III]) corrected from reddening (mainly from SDSS), and the MIR luminosities are obtained from several catalogs at the 12 μm, using the NASA Extragalactic Database (NED[4]; e.g., Risaliti et al. 1999; Tran 2003; Heckman et al. 2005; Goulding & Alexander 2009; Lamastra et al. 2009; Noguchi et al. 2010; Jin et al. 2012; Berney et al. 2015) as the main search engine. We complete the three luminosities for 110 objects. Among them, 58 are type 1 AGN, and 52 are type 2 AGN.

Although we already had X-ray luminosities for all of the candidates, we took particular care to look for X-ray luminosities fully corrected from obscuration along the line of sight. Indeed, uncorrected luminosities in moderate-to-highly obscured AGN ($N_{\mathrm{H}} > 10^{23}\,\mathrm{cm}^{-2}$) could wrongly locate the object outside the scaling relations. This might overestimate the detection of fading AGN candidates. All of the X-ray measurements used in the previous section are intrinsic luminosities (i.e., corrected from obscuration). However, many of them rely on spectral analysis below 10 keV. This might wrongly estimate the intrinsic luminosity for Compton-thick AGN (with $N_{\mathrm{H}} > 3 \times 10^{24}\,\mathrm{cm}^{-2}$). The X-ray spectra with energies below 10 keV cannot be used to estimate the true value for the obscuration if that is above the Compton-thick limit (Comastri 2004). In order to mitigate this effect, we look for obscuration measurements for all objects, giving priority to the analysis where spectra above 10 keV are considered (e.g., NuSTAR or Suzaku). Most of them were obtained from the Swift BAT 70 month catalog (Ricci et al. 2017). We also checked for signatures of Compton thickness reported in the literature and found N_{H} measurements for all but 35 objects. We also found archival NuSTAR data for 18 out of these 35 objects. The

[3] This source could have errors in the [O III] line flux measurement. It will be discarded in the next section through other criteria.

[4] http://ned.ipac.caltech.edu

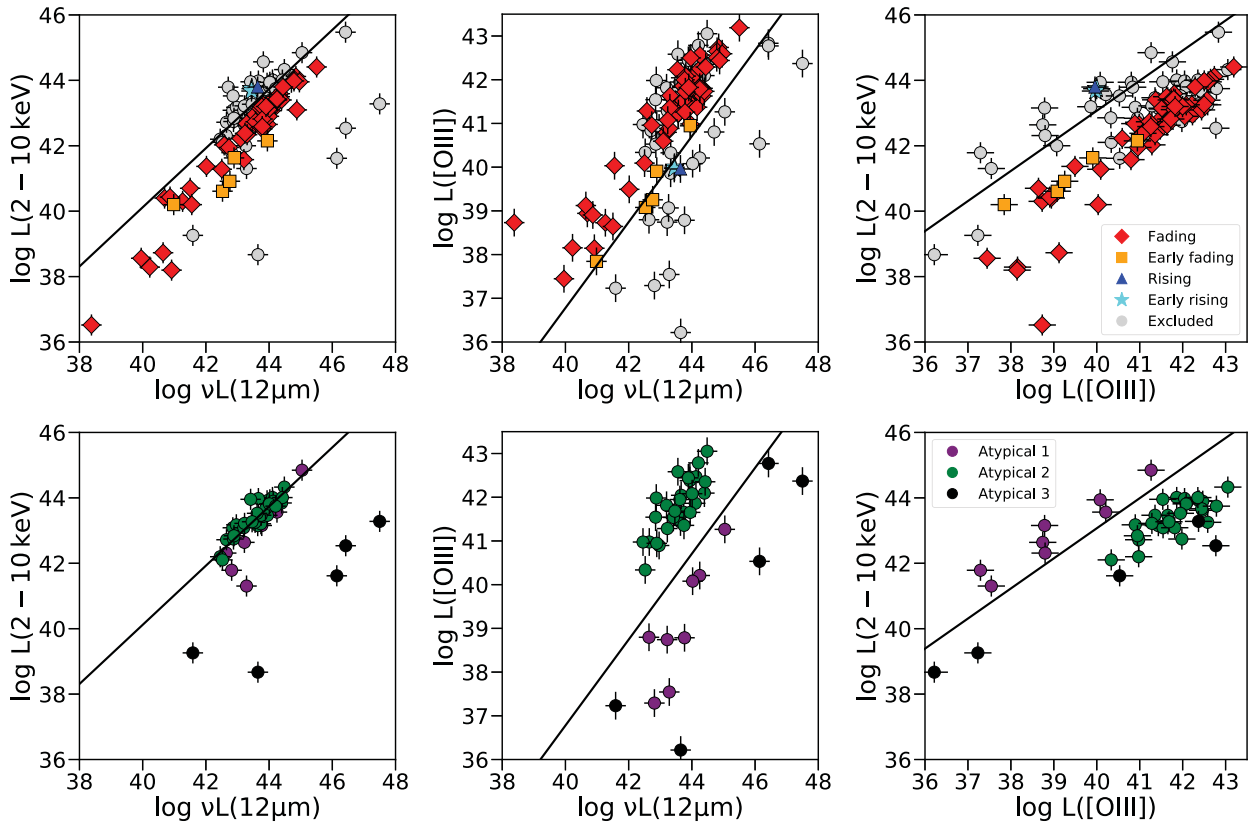

Figure 2. Scaling relations used to confirm (top panels) and reject (bottom panels) the fading and rising candidates: X-ray vs. MIR luminosity (left panels), [O III] vs. MIR luminosity (middle panels), and X-ray vs. [O III] luminosity (right panels). The black solid lines in the left and right panels are those used to select objects in Section 2. The black solid line shown in the middle panel is obtained by combining the MIR–to–X-ray and [O III]–to–X-ray scaling relationships. In the top panels, gray circles are rejected candidates, red diamonds are fading candidates, orange squares are early fading candidates, blue triangles are rising candidates, and cyan stars are early rising candidates. Atypical classification is shown in the bottom panels as purple, green, and black circles for atypical 1, atypical 2, and atypical 3, respectively (see text).

NuSTAR spectra were extracted using standard procedures and fitted to a power-law model with partial covering to estimate the $N_{\rm H}$ and X-ray intrinsic luminosity (see Appendix A for more details).

Figure 2 shows the three scaling relations for our 110 fading/rising candidates: X-ray versus MIR luminosity (left), [O III] versus MIR luminosity (middle), and X-ray versus [O III] luminosity (right). The scaling relations used in Section 2 are shown as a black solid line in the left and right panels. The middle panel shows the expected relation combining the previous two relations. According to the position in this plot, we classify most of the sources into four main categories (see top panels in Figure 2).

1. Fading candidates (red diamonds). The three diagrams show an increase of the bolometric luminosity from the disk toward the torus and NLR (the red line in Figure 3 shows the estimated behavior of the bolometric luminosity for these sources). We found 53 objects belonging to this category.
2. Early fading candidates (orange squares). The object shows an increase of the bolometric luminosity from the disk toward the torus and from the disk toward the NLR. However, the bolometric luminosities obtained for the torus and NLR are consistent with each other (orange line in Figure 3). Five objects belong to this category.
3. Rising candidate (blue triangle). The three diagrams show the object in a consistent decrease of bolometric luminosity from the disk toward the torus and the NLR (blue line in Figure 3). Only one object belongs to this category.
4. Early rising candidates (cyan stars). The object shows a decrease of the bolometric luminosity from the disk toward the torus and from the disk toward the NLR. However, the bolometric luminosities obtained for the torus and NLR are consistent with each other (cyan line in Figure 3). Two objects belong to this category.

We keep early fading/rising candidates in the sample under the interpretation that these objects might be a premature fading/rising of the central source, still not clearly shown in the outskirts of the system. Note that the object is considered above/below the relation with $\Delta\log(L) > 0.2$, which is consistent with the systematic errors in these relations. Table 1 compiles the names and general information of these objects.

Among the 110 objects studied, 49 have been rejected on the basis of unexpected behavior in the set of X-ray, MIR, and [O III] luminosities. Eight of these objects show a monotonic increase or decrease in the luminosities, but this behavior is inconclusive due to $\Delta\log(L) < 0.2$. Therefore, these eight sources are rejected. We classify the 41 remaining sources into three subcategories (see bottom panels in Figure 2).

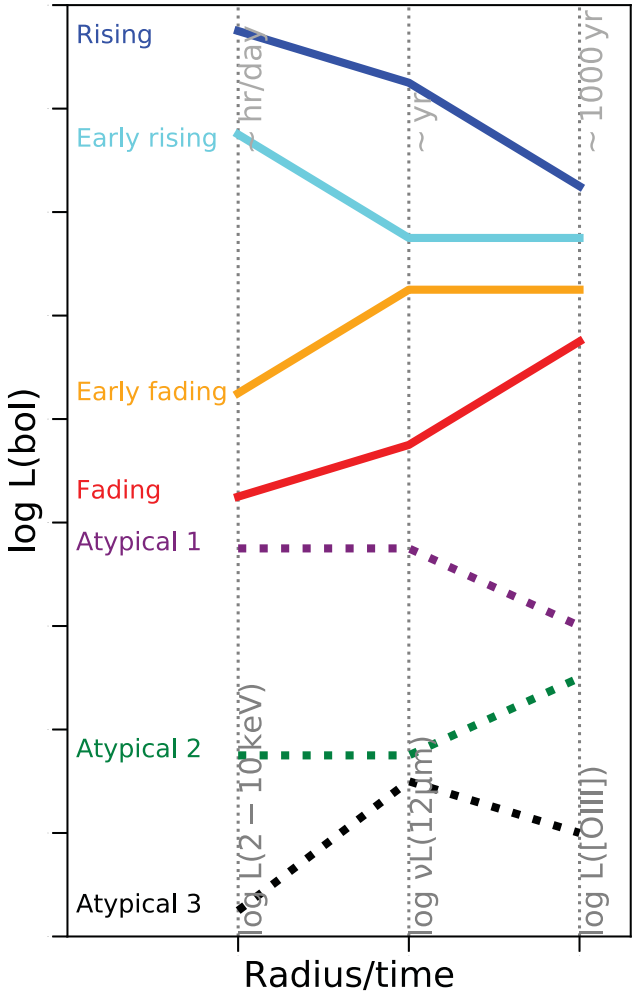

Figure 3. Illustrations of the different types of classified objects according to the bolometric luminosity obtained with X-ray, MIR, and [O III] luminosities (in logarithmic representation). These bolometric luminosities correspond to days, years, and thousands of years (also highlighted in the top horizontal axis of the plot). Fading and rising candidates are shown with solid lines. The behaviors presented for the atypical objects are shown with dashed lines (see text for more details). Axes are in arbitrary units.

1. Atypical 1 (purple circles). Eight objects show a decrease in bolometric luminosity between the disk and the torus and between the disk and the NLR. However, the torus shows similar bolometric luminosity compared to that of the disk, which might be inconsistent with the rising scenario (shown as a purple dotted line in Figure 3).
2. Atypical 2 (green circles). Twenty-eight objects show an increase of the bolometric luminosity associated with the NLR when compared to that of the disk/torus that might indicate a fading of the source. However, there might not be a consistent fading scenario when it comes to the comparison between torus and disk bolometric luminosity (shown as a green dotted line in Figure 3).
3. Atypical 3 (black circles). Five objects show an increase of the bolometric luminosity for the disk compared to that of the torus and for the disk compared to that of the NLR. However, there is a decrease in the bolometric luminosity of the NLR compared to that of the torus, which might be inconsistent with the fading scenario (shown as a black dotted line in Figure 3).

These 41 candidates showing atypical behavior are included in Table 2.

4. Robustness of the Fading/Rising Candidates

We further explore fading, rising, and atypical candidates (102 objects) to investigate the robustness of the methodology using ancillary observations available for the sample.

4.1. AGN Nature and [O III] as Tracer of the NLR

The absence of the accretion disk could be considered an indication of the switching off of the nucleus if the torus and/or NLR are still present. However, it could also indicate that the object does not harbor an AGN, which is a particularly relevant discussion for low-luminosity objects with $L_{\rm bol} < 10^{42}$ erg s^{-1}. Indeed, 23 objects belong to this category among our candidates.

In order to study the AGN nature of these sources, Figure 4 shows the [O III]/Hβ–versus–[N II]/Hα emission line ratios for 84 sources of our sample. This is a well-known AGN diagnostic diagram first explored by Baldwin et al. (1981; details on the construction of this diagram are included in Appendix B.1). We only found one object (Mrk 335, a fading candidate) not consistent with pure AGN according to the limit proposed by Kauffmann et al. (2003). However, this is a well-known and bright AGN from the X-ray point of view (e.g., Parker et al. 2019). Furthermore, six other objects are not consistent with pure AGN according to the demarcation proposed by Kewley et al. (2001). Among them, ESO 137-G034 belongs to atypical 3; 2MASSX J02420381+0510061, Cen A, and NGC 3079 to atypical 1; 2MASSX J14391186 +1415215 to early rising; and 2MASSX J08551746−2854218 to rising. This group is consistent with a composite behavior of the source at optical wavelengths. Interestingly, two out of the three rising candidates are in this latter category. Note that the [O III] line emission could be contaminated by star-forming processes for these seven objects. This would move the objects toward the left in Figure 2 (right) and downward in Figure 2 (middle). However, note that even if it were the case, both early rising and rising objects would still be classified as such, as they would still remain out of the expected correlations in Figure 2. Some of the sources could be affected by lower metallicity than the "standard" ones used to set up the various versions of the Baldwin, Phillips & Telervich (BPT) strong-line diagram, where AGN-ionized gas can masquerade as ionized by stars. Groves et al. (2006) showed that the respective BPT model evaluations may return different metallicity values. If we consider models with 0.25 solar metallicity, all of our sources could be classified as AGN. However, in order to be conservative, we keep the AGN classification as that found when using solar metallicity, which is the most restrictive classification.

Objects classified as atypical 1 (purple circles in Figure 2) tend to locate at lower [O III]/Hβ compared to other AGN in the sample. This is easily explained by large-scale extinction affecting the [O III] line emission (see below and Figure 5). Another reason for the contamination of the [O III] emission might come from tidal tails seen after merging processes that, in addition, can cause scatter in the [O III] scaling laws. However, we find that the vast majority of the sources (∼92%) are located in the AGN area of the plot, supporting the AGN nature of them and the use of [O III] as a tracer of the NLR.

Table 1
Final Sample of Rising/Fading Candidates

Name	R.A.	Decl.	z	νL (12 μm)	L_X	$L_{[O\ III]}$	Candidate Class	Radio Morph.	N_H cm^{-2}	$\log(\nu L_\nu)$ λ2500 Å	Morph.	Env.
(1)	(2)	(3)	(4)	(5)	(6)	(7)	(8)	(9)	(10)	(11)	(12)	(13)
Mrk 335	$00^h06^m19^s52$	$20^d12^m10^s5$	0.0351	44.34	43.5	41.63	Fading	Compact	20.48	44.27	E	⋯
J00430184+3017195	$00^h43^m01^s87$	$30^d17^m19^s6$	0.0441	44.08	43.07	41.77	Fading	⋯	22.30	41.86	⋯	⋯
Mrk 359	$01^h27^m32^s55$	$19^d10^m43^s8$	0.0167	43.29	42.68	40.89	Fading	Compact	20.61	43.04	S0	group
NGC 1068	$02^h42^m40^s71$	-00 d00^{m}47^{s}8	0.0032	43.79	42.82	41.72	Fading	Linear[4]	24.95	43.07	Sb	group
Fornax A	$03^h22^m41^s72$	$-37^d12^m29^s6$	0.0043	41.26	40.3	38.73	Fading	Diffuse[3]	⋯	42.67	S0	pair
IRAS 04124–0803	$04^h14^m52^s67$	-07 d55^{m}39^{s}9	0.0382	44.21	43.27	42.22	Fading	⋯	⋯	43.09	⋯	⋯
Mrk 618	$04^h36^m22^s24$	-10 d22^{m}33^{s}8	0.0356	44.39	43.4	41.73	Fading	Compact	⋯	43.76	SBb	⋯
LEDA 097068	$05^h02^m58^s22$	22 d59^{m}51^{s}8	0.0577	44.79	43.98	42.50	Fading	⋯	⋯	44.27	E	⋯
IRAS 05218–1212	$05^h24^m06^s50$	-12 d09^{m}59^{s}6	0.049	44.26	43.39	42.56	Fading	⋯	⋯	43.44	E	⋯
Mrk 6	$06^h52^m12^s25$	74 d25^{m}37^{s}5	0.0222	43.81	43.25	42.08	Fading	Linear[6]	20.76	42.62	S0-a	pair
Mrk 79	$07^h42^m32^s80$	49 d48^{m}34^{s}7	0.0316	44.25	43.43	41.79	Fading	Linear[6]	⋯	43.75	Sb	⋯
Mrk 10	$07^h47^m29^s13$	60 d56^{m}00^{s}6	0.0292	43.84	43.13	41.53	Fading	Compact	20.53	44.16	SABb	⋯
Mrk 1210	$08^h04^m05^s86$	05 d06^{m}49^{s}8	0.0135	43.72	43.15	41.52	Fading	Compact	23.40	42.31	S?	⋯
IRAS 09149–6206	$09^h16^m09^s39$	$-62^d19^m29^s9$	0.0573	44.96	43.95	42.59	Fading	⋯	$24.19^{+0.05*}_{-0.05}$	44.74	⋯	⋯
Mrk 704	$09^h18^m26^s01$	$16^d18^m19^s2$	0.0292	44.25	43.4	41.83	Fading	Compact	$22.72^{+0.51*}_{-0.07}$	43.63	S0-a	group
M81	$09^h55^m33^s17$	69 d03^{m}55^{s}1	0.0008	41.50	38.8	38.64	Fading	Diffuse[1]	$23.58^{+0.03*}_{-0.03}$	39.94	Sab	triple
3C 234.0	$10^h01^m49^s52$	28 d47^{m}09^{s}0	0.1849	45.50	44.41	43.19	Fading	Linear[7]	23.51	43.98	⋯	⋯
NGC 3227	$10^h23^m30^s58$	19 d51^{m}54^{s}2	0.0043	43.09	42.22	40.59	Fading	Diffuse[1]	20.95	41.03	SABa	pair
ESO 317-G038	$10^h29^m45^s61$	-38 d20^{m}54^{s}8	0.0151	43.20	41.58	40.80	Fading	⋯	23.41	42.37	SBa	⋯
NGC 3379	$10^h47^m49^s59$	12 d34^{m}53^{s}8	0.003	40.22	38.29	38.15	Fading	Compact	⋯	41.68	E	triple
NGC 3521	$11^h05^m48^s58$	-00 d02^{m}09^{s}1	0.0027	40.92	38.20	38.14	Fading	Linear[8]	⋯	42.71	SABb	⋯
ESO 438-G009	$11^h10^m48^s00$	-28 d30^{m}03^{s}8	0.0219	43.95	42.65	40.99	Fading	⋯	$24.51^{+0.46*}_{-0.31}$	43.83	SBab	⋯
NGC 3607†	$11^h16^m54^s64$	18 d03^{m}06^{s}3	0.0032	40.65	38.73	39.12	Fading	Compact	⋯	41.28	E-S0	pair
PG 1138+222	$11^h41^m16^s16$	21 d56^{m}21^{s}8	0.0632	44.44	43.80	42.29	Fading	Compact	⋯	43.40	Sab	⋯
NGC 3982	$11^h56^m28^s13$	55 d07^{m}30^{s}9	0.0048	41.55	40.2	40.03	Fading	Compact	$23.83^{+0.18*}_{-0.20}$	41.90	SABb	group
UGC 07064	$12^h04^m43^s32$	$31^d10^m38^s2$	0.0247	43.78	42.59	41.26	Fading	Diffuse[2]	22.59	42.54	SBb	triple
NGC 4151	$12^h10^m32^s58$	39 d24^{m}20^{s}6	0.0023	42.58	42.03	41.28	Fading	Linear[4]	22.71	42.18	Sab	pair
Mrk 766	$12^h18^m26^s51$	29 d48^{m}46^{s}3	0.0129	43.57	42.73	41.23	Fading	Compact	20.32	42.43	SBa	pair
NGC 4303	$12^h21^m54^s90$	04 d28^{m}25^{s}1	0.0052	38.38	36.52	38.73	Fading	Diffuse[1]	⋯	43.96	Sbc	pair
NGC 4395	$12^h25^m48^s86$	33 d32^{m}48^{s}9	0.0009	40.87	40.43	38.91	Fading	Diffuse[1]	21.04	42.39	Sm	multiple
J123212.3–421745	$12^h32^m11^s83$	$-42^d17^m52^s2$	0.1009	44.85	44.12	42.74	Fading	⋯	⋯	44.46	⋯	⋯
LEDA 170194	$12^h39^m06^s29$	$-16^d10^m47^s1$	0.0360	43.54	42.95	42.23	Fading	⋯	22.76	43.14	S0	⋯
NGC 4736	$12^h50^m53^s06$	41 d07^{m}13^{s}6	0.0011	39.95	38.56	37.45	Fading	Diffuse[1]	⋯	42.37	SABa	group
NGC 4748	$12^h52^m12^s46$	-13 d24^{m}53^{s}0	0.0142	43.30	42.34	41.36	Fading	Compact	⋯	42.87	S?	⋯
NGC 4941	$13^h04^m13^s14$	-05 d33^{m}05^{s}8	0.0040	42.50	41.28	40.09	Fading	Linear[6]	23.72	43.11	SABa	group
NGC 4939	$13^h04^m14^s39$	-10 d20^{m}22^{s}6	0.0105	43.24	42.38	41.08	Fading	Diffuse[1]	23.29	41.46	Sbc	group
MCG-03-34-064	$13^h22^m24^s46$	-16 d43^{m}42^{s}5	0.0199	44.34	43.59	41.80	Fading	Linear[6]	23.80	42.59	S0	
M51a	$13^h29^m52^s71$	$47^d11^m42^s6$	0.0018	40.69	40.4	38.94	Fading	Diffuse[1]	$24.67^{+0.06*}_{-0.06}$	43.01	SABb	pair
ESO 509-G038	$13^h31^m13^s90$	-25 d24^{m}10^{s}0	0.0263	43.78	42.51	41.48	Fading	⋯	$23.90^{+0.07*}_{-0.06}$	43.02	S0-a	⋯
NGC 5283	$13^h41^m05^s76$	67 d40^{m}20^{s}3	0.0103	42.73	41.95	40.96	Fading	Linear[4]	23.15	41.74	S0	⋯
NGC 5273	$13^h42^m08^s34$	35 d39^{m}15^{s}2	0.0038	42.02	41.37	39.49	Fading	Compact	20.59	40.93	S0	pair
Mrk 463	$13^h56^m02^s87$	18 d22^{m}19^{s}5	0.0503	44.88	43.10	42.44	Fading	Linear[9]	23.57	43.74	Sc	⋯
Mrk 477	$14^h40^m38^s10$	53 d30^{m}15^{s}9	0.0377	43.97	43.26	42.50	Fading	Compact	23.52	43.51	S0	pair
IC 4518A	$14^h57^m41^s18$	-43 d07^{m}55^{s}6	0.0163	43.57	42.66	41.22	Fading	⋯	23.36	44.00	Sc	multiple
Mrk 1392	$15^h05^m56^s55$	03 d42^{m}26^{s}3	0.0356	43.98	43.10	41.81	Fading	Compact	$24.63^{+0.16*}_{-0.18}$	43.70	SBcd	group

Table 1
(Continued)

Name	R.A.	Decl.	z	νL (12 μm)	L_X	$L_{[O\ III]}$	Candidate Class	Radio Morph.	N_H cm^{-2}	$\log(\nu L_\nu)$ λ2500 Å	Morph.	Env.
(1)	(2)	(3)	(4)	(5)	(6)	(7)	(8)	(9)	(10)	(11)	(12)	(13)
J15462424+6929102	$15^h46^m24^s33$	69 d29^{m}10^{s}0	0.0376	43.72	43.08	41.86	Fading	Linear[2]	23.49	42.33	⋯	⋯
J16531506+2349431	$16^h53^m15^s05$	23 d49^{m}43^{s}0	0.1031	44.80	44.03	42.65	Fading	Compact	23.27	43.11	E	⋯
Fairall 49	$18^h36^m58^s29$	−59 d24^{m}08^{s}6	0.0201	44.17	43.40	41.37	Fading	⋯	22.03	42.34	E-S0	⋯
J19373299–0613046	$19^h37^m33^s01$	−06 ^{d}13^{m}04^{s}8	0.0103	43.48	42.77	41.44	Fading	⋯	20.85	43.32	E	⋯
MCG+02-57-002	$22^h23^m45^s02$	11 d50^{m}09^{s}0	0.0294	43.31	42.63	41.64	Fading	Diffuse[2]	⋯	43.86	Sb	⋯
Mrk 915	$22^h36^m46^s50$	−12 d32^{m}42^{s}6	0.0239	43.77	43.20	42.00	Fading	Compact	$23.53^{+0.07*}_{-0.09}$	43.79	Scd	triple
MCG+01-57-016	$22^h40^m17^s05$	08 d03^{m}14^{s}1	0.0249	43.87	43.04	41.78	Fading	Compact	⋯	43.72	SBa	⋯
NGC 7469	$23^h03^m15^s62$	08 d52^{m}26^{s}4	0.0139	43.90	43.2	41.82	Fading	Diffuse[4]	20.53	43.13	Sa	pair
NGC 3627	$11^h20^m14^s96$	12 d59^{m}29^{s}5	0.0024	40.98	39.5	37.84	Early fading	Diffuse[1]	$24.26^{+0.67*}_{-0.45}$	43.25	Sb	pair
NGC 4051	$12^h03^m09^s61$	44 d31^{m}52^{s}8	0.0031	42.89	41.63	39.91	Early fading	Diffuse[1]	$24.53^{+0.02*}_{-0.02}$	42.14	SABb	group
M106	$12^h18^m57^s50$	47 ^{d}18^{m}14^{s}3	0.0016	42.53	40.61	39.08	Early fading	Diffuse[5]	23.00	43.10	Sbc	pair
NGC 5033	$13^h13^m27^s47$	36 d35^{m}38^{s}2	0.0028	42.76	40.91	39.25	Early fading	Diffuse[1]	⋯	42.18	Sc	group
NGC 7130	$21^h48^m19^s52$	−34 d57^{m}04^{s}5	0.0161	43.95	42.15	40.95	Early fading	Compact	24.00	43.12	Sa	pair
NGC 1194	$03^h03^m49^s11$	−01 d06^{m}13^{s}5	0.0131	43.44	43.67	39.97	Early rising	Linear[6]	24.33	40.98	S0-a	multiple
J14391186+1415215	$14^h39^m11^s87$	14 ^{d}15^{m}22^{s}0	0.0717	43.45	43.74	40.00	Early rising	⋯	22.40	42.06	E	⋯
J08551746–2854218	$08^h55^m17^s47$	−28 d54^{m}21^{s}4	0.073	43.64	43.80	39.96	Rising	⋯	21.95	43.87	⋯	⋯

Note. The sources removed in Section 5 are marked with a dagger next to the name in column (1). Asterisks alongside the value represent those objects with a wrong column density estimate, for which further analysis was carried out (see Appendix A). Column (11): logarithmic of luminosity (erg s^{-1}) at λ2500 Å. Data are from the NED. References: 1: Condon (1987); 2: Smith et al. (2016); 3: Fomalont et al. (1989); 4: Kukula et al. (1995); 5: Hummel et al. (1985); 6: Schmitt et al. (2001); 7: Hardcastle et al. (1997); 8: Hummel et al. (1987); 9: Ulvestad et al. (1981).

Table 2
Sample of Atypical Candidates

Name	R.A.	Decl.	z	νL (12 μm)	L_X	$L_{[O\ III]}$	Candidate Class	Radio Morph.	N_H cm^{-2}	$\log(\nu L_\nu)$ λ2500 Å	Morph.	Env.
(1)	(2)	(3)	(4)	(5)	(6)	(7)	(8)	(9)	(10)	(11)	(12)	(13)
NGC 612†	$01^h33^m57\overset{s}{.}74$	$-36\ d29^m35\overset{s}{.}7$	0.0301	44.02	43.94	40.08	Atypical 1	Linear[1]	23.99	42.79	S0-a	Multiple
J02420381+0510061†	$02^h42^m03\overset{s}{.}80$	$05\ ^d10^m06\overset{s}{.}1$	0.0711	44.25	43.56	40.21	Atypical 1	⋯	23.50	42.58	⋯	⋯
J04440903+2813003†	$04^h44^m09\overset{s}{.}01$	$28\ ^d13^m00\overset{s}{.}7$	0.0107	43.22	42.64	38.74	Atypical 1	⋯	22.65	43.50	Sb	⋯
PKS 0558–504†	$05^h59^m47\overset{s}{.}38$	$-50\ d26^m52\overset{s}{.}4$	0.1372	45.04	44.85	41.26	Atypical 1	⋯	$25.46^{+1.00*}_{-0.50}$	45.20	⋯	⋯
NGC 3079†	$10^h01^m57\overset{s}{.}80$	$55\ d40^m47\overset{s}{.}2$	0.0036	43.29	41.30	37.54	Atypical 1	Diffuse[2]	25.10	42.66	SBc	Pair
Cen A†	$13^h25^m27\overset{s}{.}62$	$-43\ d01^m08\overset{s}{.}8$	0.00086	42.82	41.79	37.29	Atypical 1	Linear[3]	23.02	42.20	S0	Pair
ESO 097-G013†	$14^h13^m09\overset{s}{.}950$	$-65\ d20^m21\overset{s}{.}20$	0.00094	42.64	42.31	38.80	Atypical 1	⋯	24.40	42.10	Sb	Pair
MCG+04-48-002†	$20^h28^m35\overset{s}{.}06$	$25\ d44^m00\overset{s}{.}0$	0.0139	43.77	43.16	38.78	Atypical 1	⋯	23.86	42.73	Sd	Pair
MCG-07-03-007	$01^h05^m26\overset{s}{.}82$	$-42\ ^d12^m58\overset{s}{.}3$	0.0302	43.75	43.47	41.36	Atypical 2	⋯	24.18	42.21	Sa	⋯
MCG+08-03-018	$01^h22^m34\overset{s}{.}43$	$50\ d03^m18\overset{s}{.}0$	0.0202	43.66	43.98	42.04	Atypical 2	⋯	24.24	41.68	Sc	⋯
NGC 526A	$01^h23^m54\overset{s}{.}39$	$-35\ d03^m55\overset{s}{.}9$	0.0188	43.46	43.27	41.68	Atypical 2	⋯	22.01	42.45	S0	Multiple
NGC 1229	$03^h08^m10\overset{s}{.}79$	$-22\ d57^m38\overset{s}{.}9$	0.0357	43.42	43.96	41.54	Atypical 2	⋯	24.94	44.25	SBbc	Multiple
J03305218+0538253	$03^h30^m52\overset{s}{.}18$	$05\ d38^m25\overset{s}{.}6$	0.046	43.94	43.62	42.46	Atypical 2	Compact	⋯	43.38	⋯	⋯
CGCG 420-015	$04^h53^m25\overset{s}{.}75$	$04\ d03^m41\overset{s}{.}7$	0.0294	44.11	44.01	41.86	Atypical 2	Linear[4]	24.14	43.69	E	⋯
Mrk 3	$06^h15^m36\overset{s}{.}36$	$71\ d02^m15\overset{s}{.}1$	0.0132	43.89	43.67	42.44	Atypical 2	Linear[5]	24.07	42.10	S0	Pair
Mrk 78	$07^h42^m41\overset{s}{.}73$	$65\ ^d10^m37\overset{s}{.}5$	0.037	44.01	43.82	42.08	Atypical 2	Linear[6]	24.11	42.51	⋯	⋯
J09172716–6456271	$09^h17^m27\overset{s}{.}21$	$-64\ d56^m27\overset{s}{.}1$	0.0859	43.94	43.91	42.38	Atypical 2	⋯	21.41	44.02	⋯	⋯
ESO 374-G044	$10^h13^m19\overset{s}{.}91$	$-35\ d58^m57\overset{s}{.}7$	0.0284	43.95	43.47	41.65	Atypical 2	⋯	23.71	43.83	Sab	⋯
NGC 3393	$10^h48^m23\overset{s}{.}46$	$-25\ d09^m43\overset{s}{.}4$	0.0138	42.87	42.74	41.98	Atypical 2	Linear[4]	24.50	42.08	SBa	Group
ESO 265-G023	$11^h20^m48\overset{s}{.}01$	$-43\ ^d15^m50\overset{s}{.}4$	0.0565	44.40	43.84	42.09	Atypical 2	⋯	⋯	44.26	E	Pair
Mrk 1310	$12^h01^m14\overset{s}{.}36$	$-03\ d40^m41\overset{s}{.}1$	0.0191	42.65	42.72	40.98	Atypical 2	⋯	$<20^*$	42.91	E	⋯
Mrk 205	$12^h21^m44\overset{s}{.}22$	$75\ ^d18^m38\overset{s}{.}8$	0.0708	44.13	43.90	42.47	Atypical 2	Compact	$23.69^{+0.09*}_{-0.13}$	44.53	⋯	⋯
J12313717–4758019	$12^h31^m37\overset{s}{.}16$	$-47\ d58^m02\overset{s}{.}0$	0.028	43.64	43.15	41.43	Atypical 2	⋯	20.59	43.64	SABb	⋯
NGC 4507	$12^h35^m36\overset{s}{.}63$	$-39\ d54^m33\overset{s}{.}3$	0.0117	43.62	43.53	41.95	Atypical 2	⋯	23.95	43.59	Sab	Group
ESO 323-32	$12^h53^m20\overset{s}{.}32$	$-41\ d38^m08\overset{s}{.}3$	0.0160	42.96	43.18	40.90	Atypical 2	⋯	24.79	43.86	S0-a	Group
Mrk 783	$13^h02^m58\overset{s}{.}84$	$16\ d24^m27\overset{s}{.}5$	0.067	44.42	44.01	42.35	Atypical 2	Compact	20.78	44.10	E	⋯
NGC 5135	$13^h25^m44\overset{s}{.}06$	$-29\ d50^m01\overset{s}{.}2$	0.0148	43.22	43.22	41.28	Atypical 2	Ambig.[**]	$24.38^{+0.07*}_{-0.08}$	43.21	Sab	Pair
Mrk 266SW	$13^h38^m17\overset{s}{.}31$	$48\ ^d16^m32\overset{s}{.}0$	0.0287	42.45	42.2	40.98	Atypical 2	⋯	$<20^*$	44.06	Sab	Pair
TOLOLO 00113	$13^h54^m15\overset{s}{.}41$	$-37\ d46^m33\overset{s}{.}2$	0.0508	44.21	43.75	42.79	Atypical 2	⋯	22.91	43.34	⋯	⋯
NGC 5643	$14^h32^m40\overset{s}{.}74$	$-44\ ^d10^m27\overset{s}{.}9$	0.0026	42.52	42.10	40.34	Atypical 2	Linear[7]	25.40	43.20	Sc	⋯
MCG-01-40-001	$15^h33^m20\overset{s}{.}71$	$-08\ d42^m01\overset{s}{.}9$	0.0227	43.56	43.25	42.58	Atypical 2	⋯	22.73	43.50	Sb	⋯
CGCG 367-009	$16^h19^m19\overset{s}{.}26$	$81\ d02^m47\overset{s}{.}6$	0.0230	42.85	43.09	41.54	Atypical 2	⋯	23.02	43.47	⋯	⋯
NGC 6232	$16^h43^m20\overset{s}{.}24$	$70\ d37^m57\overset{s}{.}1$	0.0148	42.89	42.84	40.95	Atypical 2	⋯	24.94	42.72	Sa	Group
LEDA 214543	$16^h50^m42\overset{s}{.}73$	$04\ d36^m18\overset{s}{.}0$	0.0322	43.20	43.09	41.82	Atypical 2	⋯	22.58	42.21	E	⋯
J21090996–0940147	$21^h09^m09\overset{s}{.}97$	$-09\ d40^m14\overset{s}{.}7$	0.0265	43.74	43.21	41.66	Atypical 2	⋯	21.20	43.40	S0	⋯
J21140128+8204483	$21^h14^m01\overset{s}{.}18$	$82\ d04^m48\overset{s}{.}3$	0.084	44.48	44.33	43.05	Atypical 2	Linear[8]	$23.56^{+0.15*}_{-0.39}$	44.70	⋯	⋯
NGC 253†	$00^h47^m33\overset{s}{.}12$	$-25\ ^d17^m17\overset{s}{.}6$	0.0008	41.59	39.26	37.23	Atypical 3	Diffuse[2]	$<20^*$	46.53	SABc	Group
NGC 3628†	$11^h20^m16\overset{s}{.}97$	$13\ d35^m22\overset{s}{.}9$	0.0028	43.65	38.67	36.22	Atypical 3	Diffuse[2]	$23.38^{+0.26*}_{-1.22}$	42.63	SBb	Group
ESO 137-G034†	$16^h35^m14\overset{s}{.}11$	$-58\ d04^m48\overset{s}{.}1$	0.0077	46.42	42.54	42.77	Atypical 3	⋯	24.30	43.22	SABa	Group
ESO 234-G050†	$20^h35^m57\overset{s}{.}88$	$-50\ ^d11^m32\overset{s}{.}1$	0.0087	46.14	41.62	40.53	Atypical 3	⋯	23.08	42.39	E	⋯
ESO 234-IG063†	$20^h40^m15\overset{s}{.}74$	$-51\ d25^m47\overset{s}{.}1$	0.05395	47.50	43.28	42.37	Atypical 3	⋯	23.41	43.91	⋯	Multiple

Note. Columns as in Table 1. References: 1: Morganti et al. (1993); 2: Condon (1987); 3: Burns et al. (1983); 4: Schmitt et al. (2001); 5: Ulvestad & Wilson (1984); 6: Ulvestad et al. (1981); 7: Morris et al. (1985); 8: Lara et al. (2001). **The source NGC 5135 is classified as ambiguous in Ulvestad & Wilson (1989); indeed, from the image, we could not identify a clear sign of linear or diffuse features.

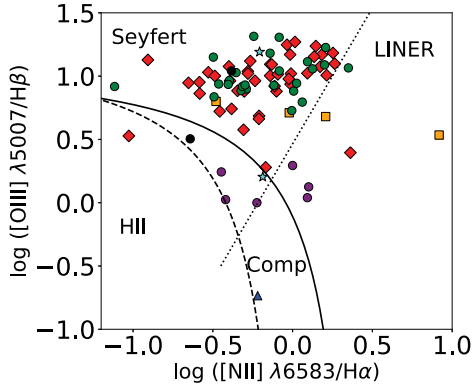

Figure 4. The [O III]/Hβ vs. [N II]/Hα emission line ratios. The solid line shows the upper limit for star-forming galaxies (or H II galaxies) proposed by Kewley et al. (2001). The dashed line is the lower limit for AGN according to Kauffmann et al. (2003). The dotted line marks the separation between pure LINERs from Seyferts from Kauffmann et al. (2003). The symbols and color code are the same as in Figure 2.

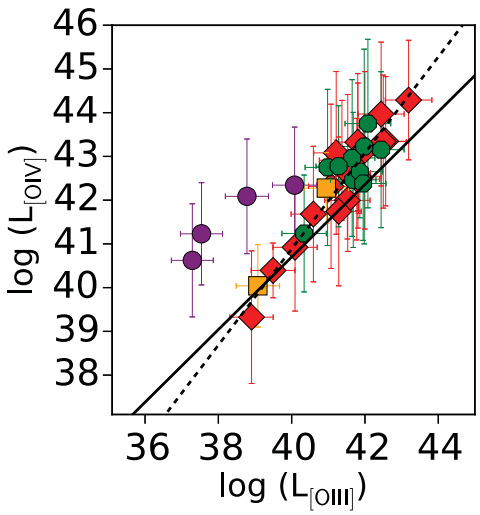

Figure 5. Shown is [O III] at 5007 Å luminosity, $L_{[\mathrm{O\ III}]}$, vs. [O IV] at 25.9 μm luminosity, $L_{[\mathrm{O\ IV}]}$. The black solid line represents the relationship found by Dicken et al. (2014; $\log(L_{[\mathrm{O\ IV}]}) = 0.83\ \log(L_{[\mathrm{O\ III}]}) + 7.5$), and the dashed line represents the best fit to our data ($\log(L_{[\mathrm{O\ IV}]}) = 1.09\ \log(L_{[\mathrm{O\ III}]}) - 3.03$). The symbols and color code are the same as in Figure 2.

We can also compare the [O III] with other tracers of the NLR to look for wrong estimates of the NLR bolometric luminosity. Figure 5 shows the L([O IV])–versus–L([O III]) relation. Details of the [O IV] flux measurements are given in Appendix B.2. We show the relation found for broad-line radio galaxies (BLRGs) by Dicken et al. (2014; black solid line). We also show the linear relation found using objects belonging to the fading category (black dashed line). Fading, early fading, and atypical 1 categories are consistent with the relation found for BLRGs. Interestingly, the four atypical 1 objects (namely, NGC 612, NGC 3079, MCG +04-48-002, and Cen A) tend to show an excess of L([O IV]) compared to L([O III]). This indicates that the [O III] emission might be suffering from extinction ([O IV] emission is much less likely to suffer dust extinction than the optical forbidden lines). Indeed, all of them show column densities at X-rays with values $N_{\mathrm{H}} > 10^{23}$ cm^{-2}, and one of them is well within the Compton-thick regime. According to this, the L([O III]) might be a factor of 10–100 higher for the atypical 1 candidates (as Figure 5 suggests). Therefore, they will move closer to the expected linear relations for AGN, and we can safely remove atypical 1 from the raising/fading candidates.

4.2. X-Ray Luminosity as a Proxy of the Accretion Disk Bolometric Luminosity

Here we explore whether the X-ray luminosity is a good tracer of the disk component by comparing it with optical/UV continuum emission where the peak of the disk luminosity occurs. For that purpose, we compiled from NED the optical/UV continuum luminosity, $\log L_\nu(2500\ \text{Å})$, for the 102 candidates (see column (11) in Tables 1 and 2). We estimated the flux at 2500 Å through an extrapolation available optical and UV flux with NED. Figure 6 (left) shows $\log L_\nu(2500\ \text{Å})$ versus $\log(L_\nu(2\ \text{keV}))$. Tananbaum et al. (1979) defined a relationship between the rest-frame monochromatic luminosity of the form $\alpha_{\mathrm{ox}} = 0.38\ \log(L_\nu(2\ \text{keV})/L_\nu(2500\ \text{Å}))$, which links the accretion disk emission to that of the hot corona emission. The upper allowed limit for this ratio is $\alpha_{\mathrm{ox}} = -2.5$ (green dashed line in Figure 6, left panel) for high-luminosity AGN (Martocchia et al. 2017). We also include, for comparison purposes, as blue, cyan, and magenta dots, the data and their best fit for high- (Just et al. 2007), intermediate- (Steffen et al. 2006), and low-luminosity AGN (Xu 2011), respectively.

Figure 6 (right) also shows the distribution of α_{ox} as a function of extinction-corrected 2500 Å monochromatic luminosity, $\log L_\nu(2500\ \text{Å})$. The black solid line is our best-fit regression curve. In the left panel, this linear relation is described by $\alpha_{\mathrm{ox}} = -0.12\ \log L_\nu(2500\ \text{Å}) + 2.04$, consistent with Equation (4) from Xu (2011). Similar to the left panel, we also include the linear regression found by Xu (2011), Just et al. (2007), and Steffen et al. (2006). Although a large number of objects are consistent with previously found relations, they show a wide range of α_{ox} in a narrow luminosity range.

We find an average $\alpha_{\mathrm{ox}} = -1.37$. The ranges of $\log L_\nu(2500\ \text{Å})$ and $\log L_\nu(2\ \text{keV})$ partially overlap with the sample presented by Xu (2011). Furthermore, the linear fit to our data (black solid line in Figure 6, left) is $\log L_\nu(2\ \text{keV}) = (0.65 \pm 0.15)$, $\log L_\nu(2500\ \text{Å}) + (6.01 \pm 4.24)$, which is quite similar to that found from Xu (2011; see their Equation (2)). In our sample, 96% of the objects are consistent with the linear relation found. Interestingly, the two early rising candidates tend to locate above the linear relation (Figure 6, left) and flat slopes (Figure 6, right). These flat slopes might indicate a fundamental change of the accretion process, which might be associated with the rising scenario. However, it could also be interpreted as an overestimate of the accretion disk luminosity when using the X-ray emission. This would put these two objects back into the general correlations in Figure 2. Under this interpretation, these two objects might not be good rising candidates after all. This X-ray emission sometimes has a nonnegligible contribution from reprocessed material that should not be taken into account for the intrinsic disk luminosity. This could explain the slight excess of X-ray luminosity compared to the UV luminosity. Unfortunately, a detailed analysis of the intrinsic and reprocessed X-ray emission is not possible for these two sources due to the lack of high-energy X-ray spectra. Only objects with high column densities reaching the Compton-thick regime are expected to have a large contribution of the reflection component. This is indeed the case for NGC 1194, one of the two early rising candidates.

Four sources are significantly below the $\log L_\nu(2500\ \text{Å})$–versus–$\log L_\nu(2\ \text{keV})$ relation, with values below $\alpha_{\mathrm{ox}} = -2.5$

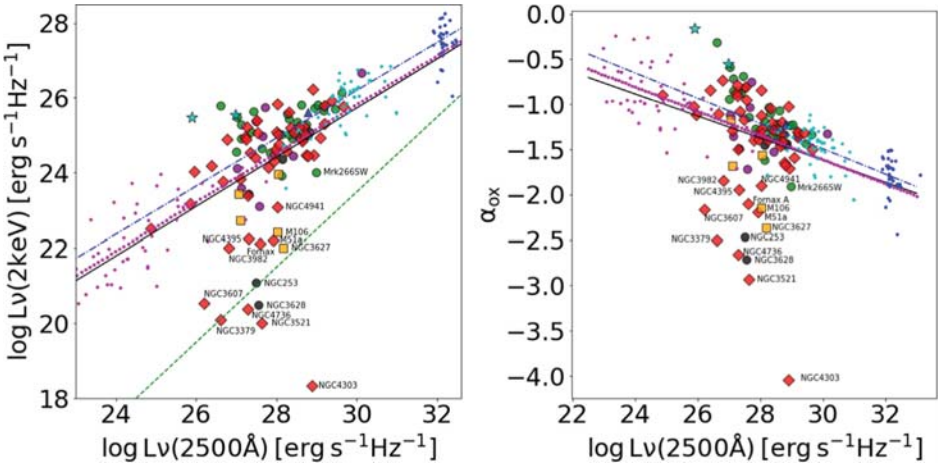

Figure 6. Left: relationship between log L_ν(2500 Å) and log L_ν(2 keV) for fading/rising and atypical candidates. Right: relationship between α_{ox} and log L_ν(2500 Å). The black solid line in both panels shows the best fit for our sample. Blue, cyan, and magenta dots represent the high- (Just et al. 2007), intermediate- (Steffen et al. 2006), and low-luminosity (Xu 2011) AGN data.

(namely, NGC 3521, NGC 4303, NGC 4736, and NGC 3628). González-Martín et al. (2009b) classified NGC 3628 as non-AGN at X-rays based on Chandra extended morphology, the lack of the iron Kα emission line, and no radio jet found. Therefore, the extreme $\alpha_{ox} \sim -2.5$ found for NGC 3628 could be due to the lack of AGN at the center. However, we analyzed the NuSTAR spectrum of NGC 3628 (see Appendix A), finding a spectrum consistent with a mildly obscured AGN. Note, however, that this is a rather simplistic analysis, and a reflection component has not been taken into account. The inclusion of such a component might lead to different results. Indeed, N. Osorio-Clavijo et al. (2020, in preparation) analyzed a sample of AGN at X-rays accounting for a reflection component. They find a significant contribution of this component for this source without obscuration. González-Martín et al. (2009b) also classified NGC 4736 as an AGN showing a compact X-ray, UV, and optical morphology and a jet contributing to the radio emission. Indeed, we also found a jetlike structure in NGC 3521, while we classified the other three as diffuse emission (see discussion and Appendix C). The BPT diagram in Figure 4 confirms the AGN nature of NGC 3521, NGC 4303, and NGC 4736 (there are no available data for NGC 3628). An alternative explanation for the extreme discrepancy between L_ν(2500 Å) and L_ν(2 keV) in these four sources is that the X-ray luminosity is not well corrected from absorption along the line of sight. We compiled the column densities (and computed them in some cases; see Appendix A), preferring those where X-ray spectra include hard X-ray photons above 10 keV. The distribution of N_H is reported in Figure 7. The wrong estimate of the N_H might explain the locus in Figure 6 for NGC 3521, NGC 4303, and NGC 4736 because no spectra above 10 keV are available for these three objects, and such an energy range is necessary to discard that the sources are in the Compton-thick regime. Therefore, spectra in the UV region and above >10 keV with Suzaku, NuSTAR, or future X-ray facilities are needed to confirm the fading nature of these three sources. It is certainly not the case for NGC 3628, where we correct the spectrum from its absorption thanks to NuSTAR (see Appendix A).

Although the other sources are within the standard range of $-2.5 < \alpha_{ox} < -1.5$, it is evident that the scatter is large for Fornax A, M51a, NGC 3379, NGC 3607, NGC 3627, Mrk 266SW, NGC 253, NGC 3982, M106, NGC 4395, and NGC 4941 being well below the X-ray-versus-UV linear relation. The BPT diagram confirms the AGN nature of M106, NGC 4395, and NGC 4941, but there are no available data for the others. Among them, NGC 253, M51a, Mrk 266SW, and NGC 3982 are known AGN (see NED). Based on X-ray observations, González-Martín et al. (2009b) classified NGC 3379, NGC 3607, and NGC 3627 as non-AGN. Interestingly, these three sources are right on the limit of $\alpha_{ox} = -2.5$ (green dashed line in Figure 6). Among these three objects, we find that NGC 3627 is consistent with a Compton-thick AGN using newly reported NuSTAR data, although the data are poor (see Table 3). No absorption measurements are reported for Fornax A or NGC 3379. Among the other eight sources, we found that four objects (M51a, NGC 3982, M106, and NGC 4941) show absorption above $N_H > 10^{23}$ cm^{-2}, while three (NGC 253, Mrk 266SW, and NGC 4395) do not seem to be obscured. No information is found for NGC 3607. Terashima et al. (2002) analyzed the X-ray ASCA spectrum of NGC 3607 and did not find evidence that this source could be classified as an AGN. In fact, Terlevich & Forbes (2002) suggested that the X-ray emission of this source may be linked to stellar processes (see also Flohic et al. 2006). Therefore, we will discard this source. For the others, therefore, it is not clear to us that obscuration might be responsible for a wrong estimation of the intrinsic luminosity of the disk. If that is ruled out, an intrinsic different accretion disk emission might be the reason for such low α_{ox}. Indeed, this has been argued for low-luminosity AGN, for which it has been proposed that the accretion disk might be intrinsically different. The most accepted model for these objects is a disk that heats and turns into an optically thin, geometrically thick inefficient accretion disk (i.e., an advection-dominated accretion flow, ADAF; Narayan & Yi 1995).

5. Summary and Discussion

The aim of this paper is to provide a catalog of candidates for fading and rising AGN in the nearby universe using multiwavelength observations. For this purpose, we started with the 579 and 419 AGN with [O III] and MIR continuum fluxes from Berney et al. (2015) and Asmus et al. (2015) and Stern (2015), respectively (121 objects in common). In both samples, we restricted to objects with $z < 0.04$. Altogether, the initial

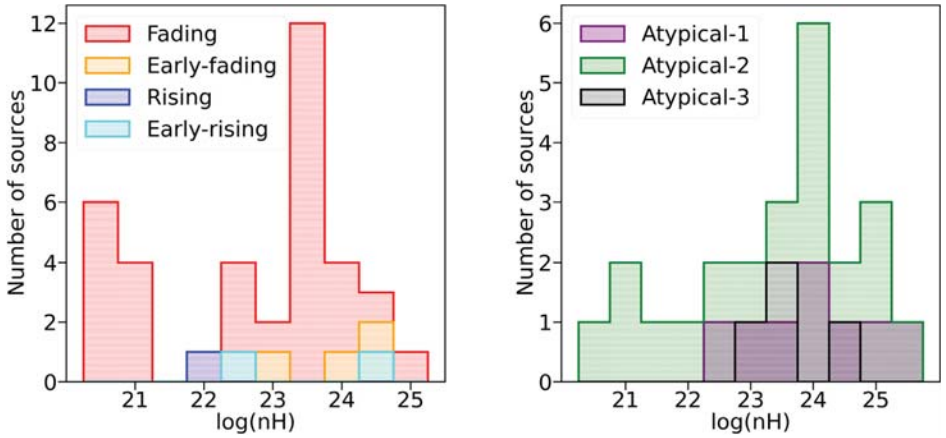

Figure 7. Histograms of hydrogen column densities, $N_{\rm H}$, observed at X-rays for fading/rising AGN (left) and atypical AGN (right). It includes 37 fading, 4 early fading, 2 early rising, 1 rising, 23 atypical 2, 4 atypical 3, and 8 atypical 1.

Table 3
Spectral Fit for Those Objects with Available NuSTAR Observations

Name	χ^2/dof	Γ	log $N_{\rm H}$] [cm^{-2}]	log $L_{(2-10])\ keV}$ [erg s^{-1}]
(1)	(2)	(3)	(4)	(5)
PKS 0558–504*	220.99/270	$2.16^{+0.03}_{-0.02}$	$25.46^{+1.00}_{-0.50}$	$44.76^{+0.19}_{-0.19}$
NGC 253	769.88/449	$2.44^{+0.01}_{-0.02}$	...	$39.58^{+0.01}_{-0.01}$
IRAS 09149–6206	1324.1/1015	$1.95^{+0.02}_{-0.02}$	$24.19^{+0.05}_{-0.05}$	$44.28^{+0.01}_{-0.01}$
Mrk 704	400.8/342	$1.49^{+0.05}_{-0.03}$	$22.72^{+0.51}_{-0.07}$	$43.32^{+0.11}_{-0.11}$
M81	1422.1/1323	$2.11^{+0.02}_{-0.02}$	$23.58^{+0.03}_{-0.03}$	$40.693^{+0.003}_{-0.003}$
ESO 438-G009	105.6/137	$1.84^{+0.08}_{-0.06}$	$24.51^{+0.46}_{-0.31}$	$42.78^{+0.04}_{-0.04}$
Mrk 1392	220.71/198	$1.84^{+0.05}_{-0.04}$	$24.63^{+0.16}_{-0.18}$	$43.36^{+0.03}_{-0.03}$
Mrk 915	470.71/493	$1.87^{+0.06}_{-0.06}$	$23.53^{+0.07}_{-0.09}$	$43.11^{+0.02}_{-0.02}$
NGC 4051	2177.02/1619	$1.85^{+0.01}_{-0.01}$	$24.53^{+0.02}_{-0.02}$	$43.563^{+0.003}_{-0.003}$
NGC 3982	51.25/42	$3.06^{+1.27}_{-0.76}$	$23.83^{+0.18}_{-0.20}$	$41.12^{+1.06}_{-1.06}$
ESO 509-G038	250.34/243	$2.12^{+0.10}_{-0.11}$	$23.90^{+0.07}_{-0.06}$	$43.34^{+0.05}_{-0.05}$
J21140128 +8204483	188.20/196	$1.96^{+0.11}_{-0.11}$	$23.56^{+0.15}_{-0.39}$	$44.49^{0.07}_{-0.07}$
Mrk 1310	300.03/285	$1.77^{+0.02}_{-0.02}$	...	$42.89^{+0.01}_{-0.01}$
Mrk 205	278.9/297	$2.14^{+0.10}_{-0.10}$	$23.69^{+0.09}_{-0.13}$	$44.24^{+0.04}_{-0.04}$
Mrk 266SW	51.6/52	$1.08^{+0.15}_{-0.15}$	...	$41.84^{+0.09}_{-0.09}$
NGC 5135	77.8/52	$1.25^{+0.17}_{-0.18}$	$24.38^{+0.07}_{-0.08}$	$39.98^{+0.13}_{-0.13}$
NGC 3627	60.59/67	$2.57^{+0.45}_{-0.21}$	$24.26^{+0.67}_{-0.45}$	<40.20
NGC 3628	65.58/69	$2.44^{+0.29}_{-0.24}$	$23.38^{+0.26}_{-1.22}$	$40.14^{+0.41}_{-0.41}$
M51	170.35/166	$1.78^{+0.09}_{-0.09}$	$24.67^{+0.06}_{-0.06}$	$40.23^{+0.04}_{-0.04}$

Note. Column (1) is the object name; column (2) is the statistics, χ^2/dof; column (3) is the photon index; column (4) is the column density in units of cm^{-2}; and column (5) is the intrinsic luminosity in the 2–10 keV band.

sample contains 877 nearby AGN, all of them with available X-ray luminosity.

The hypothesis behind this multiwavelength comparison is that each luminosity is tracing a different component: the X-ray continuum is a tracer of the disk emission, MIR is a tracer of the AGN dusty torus, and [O III] is a tracer of the NLR emission. Since each of them occupy a different spatial scale, they might trace recent (up to ∼3000 yr) changes in the bolometric luminosity of the system. This allowed us to select fading or rising candidates as those out of the known linear relations between X-ray versus [O III] and X-ray versus MIR luminosities (see Section 2). Using this technique, we selected 161 AGN fading/rising candidates.

We complemented [O III], MIR, and X-ray luminosities (corrected from obscuration along the line of sight) for 110 of these candidates to study the monotonic behavior of the AGN activity. Among them, we discarded eight sources because they were close to 2σ from the linear relations in Figure 1, leaving 102 candidates. We found that (1) 53 objects are consistent with a fading scenario (called fading), (2) five objects only show this fading scenario in the comparison between the X-ray and MIR luminosity but not when comparing MIR and [O III] luminosities (called early fading), (3) one object shows a monotonic increase of the bolometric luminosity between the three wavelengths (called rising), and (4) two objects show an increase of the bolometric luminosity between X-ray and MIR luminosity but consistent values with the linear relation between MIR and [O III] luminosity (called early rising). We further explored more complex behaviors named atypical 1, atypical 2, and atypical 3, with 8, 28, and 5 objects belonging to these categories, respectively (see Section 3 and Figure 3).

We also explored the robustness of the selection using available optical emission line diagnostics, MIR spectra, and UV continuum luminosity (see Section 4). Through these comparisons, we ruled out six sources belonging to the category atypical 1 because the L[O III] could be attenuated due to dust, and a proper correction of the luminosity might discard them as fading candidates. Moreover, we also excluded from our statistics the other two objects belonging to the group atypical 1 because they do not show a consistent rising or fading scenario. We also discarded NGC 3607 due to previous evidence that the nuclear emission could be associated with stellar processes. These seven sources are marked with daggers next to the name in all tables. Although their nature might indicate abrupt changes in the disk luminosity, due to the complex behavior of the group atypical 3 (black dotted line in Figure 3), we do not further discuss them here. However, the group called atypical 2 is kept within the fading candidates

because they might be in a late stage of the fading phase (see below). Therefore, our bona fide sample includes 88 candidates (52 fading, 28 atypical 2, 5 early fading, 1 rising, and 2 early rising).

5.1. Comparison with Reported Candidates and Caveats

Previously reported dying AGN are Arp 187 (Ichikawa et al. 2019a) and NGC 7252 (Schweizer et al. 2013), while fading AGN are IC 2497 (Józsa et al. 2009), the Teacup Galaxy (also known as SDSS J143029.88+133912.0; Keel et al. 2012), Mkn 1498, NGC 5252, NGC 5972, SDSS J151004.01+074037.1, SDSS J220141.64+115124.3, UGC 7342, and UGC 11185 (Keel et al. 2017). We find that three (namely, Mkn 1498, UGC 11185, and NGC 5252) of these 11 sources were initially included among our samples in Section 2 (see also Hernández-García et al. 2019). However, none of the three are classified as fading AGN according to our criteria. They are selected by Keel et al. (2012) for having ionized cones of over 10 kpc; therefore, all of them show extended NLR. Thus, the first caveat in this methodology is that we might be missing fading type 2 AGN because the NLR emission is too extended to be included in the [O III] fluxes presented in this work. However, note that 38 of the fading candidates are type 2 AGN (47% of the sample), while 42 are type 1 AGN (53%), as reported in the last column in Tables 4 and 5. Thus, we are not missing all type 2 AGN but probably only those with a very extended NLR.

Another caveat of this classification is that the accretion disk or the NLR signatures might be obscured (and not properly corrected) in our X-ray or [O III] luminosity. However, we have used [O IV] emission line luminosity, finding that, apart from the so-called atypical 1 class, where the [O III] might be attenuated, the [O III] and [O IV] emission lines seem to behave as expected in AGN (see Figure 5).

Furthermore, we also explored X-ray–versus–UV continuum correlations to search for candidates highly obscured in X-rays. The obtained correlations of $\log(L_\nu(2500\,\text{Å}))$ versus $\log(L_\nu(2\,\text{keV}))$ and $\alpha_{\rm ox}$ versus $\log(L_\nu(2500\,\text{Å}))$ are in agreement with previous work (Just et al. 2007; Xu 2011). Thus, we rule out a wrong estimate of the intrinsic disk luminosity for the overall sample. However, the scatter of the sources is obvious and nonnegligible, with four extreme objects having $\alpha_{\rm ox} < -2.5$ and 11 sources having $-2.5 < \alpha_{\rm ox} < -1.5$. However, even for those sources, we did not find indications of a wrong estimate of $N_{\rm H}$. Figure 7 shows the distribution of $N_{\rm H}$ when available for fading/rising AGN (left) and atypical AGN (right). Most of our sources are classified as obscured sources in X-rays (i.e., $N_{\rm H} > 10^{22}\,{\rm cm}^{-2}$). These measurements are taken from Swift/BAT or NuSTAR observations, ensuring that, even for Compton-thick AGN (i.e., with $N_{\rm H} > 3 \times 10^{24}\,{\rm cm}^{-2}$), the X-ray luminosity is properly corrected from this attenuation.

We are capable of measuring recent (last ∼3000 yr for fading/rising and ∼30 yr for early fading/rising) luminosity changes. Another caveat to bear in mind is that large-amplitude disk continuum variations might result in similar rising/fading of the nuclear signatures compared to the luminosity of the NLR or the dusty structure, as the ones presented here. However, particularly for the fading and rising candidates, this change must be sustained for a long period of time to produce a consistently decreasing/increasing behavior in their luminosity. Indeed, in changing-look AGN, such long-term disk-related changes have long been discussed (Matt et al. 2003). Despite a systematic search for changing-look QSO candidates at distances beyond our parent samples (Graham et al. 2017; Rumbaugh et al. 2018; MacLeod et al. 2019), a few dozen Seyfert galaxies are known to have changed their optical spectral type. Here we present a compilation of objects belonging to this category: NGC 3516 (Collin-Souffrin et al. 1973), NGC 7603 (Tohline & Osterbrock 1976; Kollatschny et al. 2000), NGC 4151 (Penston & Perez 1984), Fairall 9 (Kollatschny & Fricke 1985), NGC 2617 (Shappee et al. 2014), Mrk 590 (Denney et al. 2014), HE 1136–2304 (Parker et al. 2016), 1ES 1927+654 (Trakhtenbrot et al. 2019), IRAS 23226–3843 (Kollatschny et al. 2020), SDSS J095209.56+214313.3 (Komossa et al. 2008), Mrk 1018 (Noda & Done 2018), and ESO 121-G006 (Annuar et al. 2020). Interestingly, only NGC 4151 is classified here as a fading candidate, while seven (Fairall 9, NGC 3516, NGC 4151, NGC 7613, HE 1136–2304, Mrk 590, and Mrk 1018) of these 11 were included within the 877 sources analyzed in the initial sample of this paper. Based on dynamical, thermal, and viscous timescales, Ichikawa et al. (2019b) suggested that the luminosity changes in dying and changing-look AGN are likely based on the different physical mechanisms of the accretion disk. While changing-look AGN might be associated with thermal timescales corresponding to the disk cooling, dying AGN are more likely associated with the viscous timescale of the accretion process. To investigate whether some of these candidates are indeed changing-look AGN or have persistent fading/rising of their AGN activity, follow-up observations are needed. This can allow us to study the long-term variations in order to try to characterize the plausible disappearance of broad lines within a few years through optical spectroscopy (as, for instance, Lawrence 2018).

5.2. AGN Components

Additional support for the fading stage of these sources comes from the analysis of the AGN components. Here we explore the AGN dust and jet. To study the AGN dust, we compiled Spitzer/IRS spectra available for 31 AGN discussed here[5] (see Tables 4 and 5). We decompose the spectra into AGN dust and circumnuclear contributors (i.e., stellar and interstellar medium). For the AGN dust, we use a set of five available models in the literature (see Appendix B.2 for more details). Among the 22 objects where the AGN dust dominates (15 classified as fading, one as early fading, and six as atypical 2), the torus-like morphology is preferred against the disk wind in our sample, with only three objects preferring the latter (five if we add two that are equally fitted with either a torus-like geometry or the disk+wind model). This result is opposite to that found for nearby AGN by González-Martín et al. (2019), where the largest percentage of good fits is obtained for the clumpy disk+wind model by Hönig & Kishimoto (2017).

The AGN radio lobes are also analyzed to look for AGN aging through the study of the kinematic jet age of the radio lobes (e.g., Ichikawa et al. 2019b). Although we leave the kinematic jet age estimates for a subsequent analysis, we explore here whether these jets, as long-standing signatures of past activity, are present within our sample of candidates. We found that among all sources with available radio images (a total of 61 available radio images and 55 within the secure sample of fading/rising of activity), the percentage of clear linear sources is ∼31%. We characterized the radio morphology of fading, rising, and atypical objects (see column (9) in Tables 1 and 2) after looking for radio images in the literature (see Appendix C

[5] We compiled 38 Spitzer/IRS spectra; 31 of them are classified within the fading/rising and atypical 2 classes.

for more details). This percentage is very large, considering that the percentage of local AGN showing powerful radio jets has been measured to be of the order of 0.1% (rising to 10% for high-redshift quasars; Blandford et al. 2019). Moreover, considering that half of the compact sources could show a linear morphology (hence, the presence of a radio jet) after performing deeper and more sensitive radio observations, this percentage of radio jets within our sample should be considered as a lower limit. This suggests that relativistic jets are produced in the center of a large portion of these (mostly) AGN fading candidates.

Both the lack of outflows and the presence of radio jets are expected in the fading phase of nuclear activity, at least in the context of BH X-ray binaries. When they enter into a burst, they evolve into two distinct states along their duty cycle, known as hard and soft states. The hard state occurs at the beginning and end of the burst, while the soft state is associated with the most efficient accretion rate along the burst. In the soft state, there is a weak or nonexistent core jet and a strong accretion disk wind. On the other hand, the hard state is associated with a powerful, quasi-steady jet linked to the initial rise and fade of the transient event (Fender & Belloni 2012; Fender & Muñoz-Darias 2016, and references therein). Therefore, in both the rising and fading stages of the duty cycle, jets are expected, and winds/outflows are lacking.

Further support for the lack of winds and the launch of jets within the low-accretion AGN state comes from theory. During this stage, SMBHs may switch to a different accretion mode, characterized by a corona of low accretion rate and low radiative efficiency (radiatively inefficient accretion flow models, RIAFs; Narayan 2005). Thus, the geometrically thin and optically thick disk might not be present in this AGN stage. The funnels in the geometrically thick toroidal RIAFs are invoked as a plausible mechanism for collimating the jet (Nagar et al. 2002). Furthermore, under the wind model, a minimal accretion rate is required to produce a minimal column density to detect the outflows (Elitzur & Netzer 2016). Therefore, the lack of dusty winds in our sample might be the manifestation of the lack of accretion power to sustain the wind/outflow activity. Note, however, that our sample covers a wide range in X-ray luminosity, indicating that this might not be as simple as a luminosity threshold. Indeed, theoretical studies show that the existence of these winds might rely on the particular configuration of the wind (Elitzur & Ho 2009; Elitzur & Netzer 2016). Our results are consistent with this framework.

5.3. Implications for the Duty Cycle of AGN

Altogether, we found 85 fading candidates (including fading, early fading, and atypical 2) and three rising candidates among the 877 nearby analyzed sources. Most of them are Seyfert nuclei, with only eight LINERs (see Tables 4 and 5). Thus, we find ∼10% (∼0.3%) of fading (rising) AGN in the local universe. Statistically speaking, this might imply that one-tenth of the AGN duty cycle of activity (∼10 Myr) is spent in this fading phase (Hopkins et al. 2005). This cycle can be explained as the activation of the nuclear accretion toward the SMBH due to a merger process or strong disk instabilities. Interestingly, roughly half of the sample (40 of these 88 sources) are associated with pairs, groups, or systems with multiple objects (e.g., galaxy clusters). Thus, we would expect to see a prevalence for elliptical galaxies. However, among these 41 sources, we do not see a preference for any morphological type (12 elliptical/S0/irregulars and 28 spiral galaxies).

Under the merger event, the gas supplied will be 100 times larger than that needed to efficiently feed the SMBH. Thus, the rising phase is expected to happen quickly. This might explain the very few objects found in the rising phase in this analysis. Then, the SMBH growth continues while gas suppliers start to skimp, until the gas is depleted and the duty cycle ends (Hopkins 2012). Thus, the fading phase is expected to last longer than the rising phase, as statistically found in this paper.

Alternatively, the lack of rising AGN in our sample might be a natural consequence of the switching off of the star formation and AGN activity at the present time as a result of gas-rich mergers that occurred in the past (Hopkins et al. 2008). The star formation rate density peaked approximately 3.5 Gyr after the Big Bang, at $z \sim 2$ (known as cosmic noon), and declined exponentially at later times (see Madau & Dickinson 2014, for a review). Studies at higher redshift might help to corroborate this hypothesis by studying the fraction of rising and fading AGN at the peak of the star-forming activity.

If the fading phase is long enough, we might expect to see different stages along it. Interestingly, we could see at least three categories: early fading, fading, and atypical 2. Most of these sources are classified as AGN in the BPT diagram (see Figure 4) and they are also placed in the [O IV]-versus-[O III] emission line luminosity relation (see Figure 5). Therefore, we neglect extinction to be affecting these three classes. The fading AGN category contains 52 AGN showing a monotonic increase of AGN bolometric luminosity, with a lower value for the disk and larger values for the torus and NLR. Five objects belong to the early fading class, showing a disk bolometric luminosity lower than that inferred from the torus/NLR but with a torus and NLR with compatible bolometric luminosity. We think that in these five sources, the fading of the nuclear activity is more recent than that of AGN fading candidates, so the outer parts of the AGN have not yet adjusted to the current fading of the AGN accretion disk (here called "early fading"). Moreover, 28 objects belonging to the category atypical 2 are consistent with a late fading phase, where the disk and torus are consistent with the same bolometric luminosity but the NLR still reflects a larger bolometric luminosity.

Interestingly, these three classes of sources show slightly different average bolometric luminosities of the disk. To illustrate this, Figure 8 shows the histogram of X-ray luminosity for these three categories. The early fading, fading, and atypical 2 (late fading) classes show different average disk luminosities, where atypical 2 shows the lowest luminosity, fading candidates show intermediate luminosity, and early fading candidates show the highest. This is also consistent with the idea that these three classes are indeed stages of the same evolutionary track toward the AGN activity switching off.

6. Conclusions

We have found a bona fide sample of 88 candidates (out of 877 AGN) of rising or fading of the AGN activity in the nearby universe using AGN scaling relations. In particular, we explored the MIR–versus–X-ray and [O III]–versus–X-ray relations. We selected fading/rising candidates out of these relations. We also used multiwavelength information (mainly optical BPT, the UV luminosity, and the MIR spectrum) to explore sources contaminated by extranuclear emission, X-ray

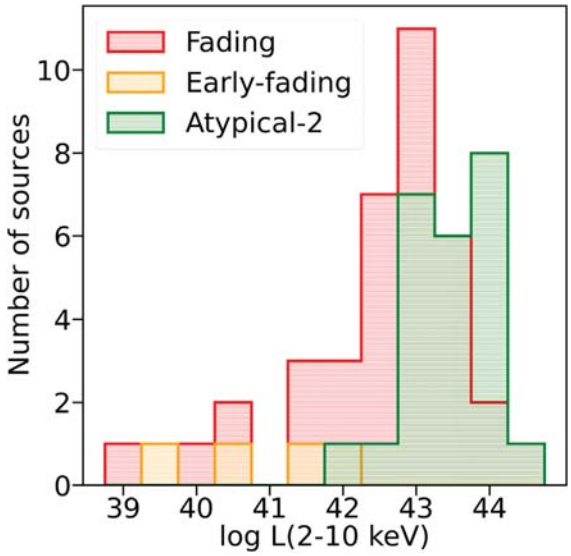

Figure 8. Histogram of 2–10 keV X-ray luminosity, L(2–10 keV), for the fading, early fading, and atypical 2 candidates.

luminosity not well corrected from absorption in highly obscured AGN, and non-AGN-powered sources.

Around 10% of our initial sample presents a fading/rising scenario. Furthermore, the vast majority of these candidates (∼96%) are fading sources. This may be explained if the universe had its peak of activity in the past and is currently dominated by the AGN activity switching off. Alternatively, this might indicate that the fading phase is longer than the rising phase. The current sample of fading candidates might be missing type 2 AGN because the NLR emission is extended. The large-amplitude disk continuum variations might also result in a similar rise/fade of the nuclear signatures compared to the luminosity of the NLR or the dusty structure, perhaps including some changing-look AGN. Follow-up observations are needed in order to confirm these candidates.

We found that these (mostly) fading candidates are placed within merging or interacting systems. We also found that among our sample, ∼31% of our AGN had clear evidence for the existence of a linear radio source (jet), which is higher than that estimated in the nearby universe. Moreover, we also found a prevalence of AGN dust associated with torus-like geometries rather than outflows. The lack of outflows and the presence of radio jets are expected in the fading phase of nuclear activity. In fact, King et al. (2011) suggested that large-scale outflows may persist for as long as 100 Myr after a powerful AGN episode fades (see also Zubovas & King 2014).

We thank to the anonymous referee for useful comments. This research has made use of the NASA/IPAC Extragalactic Database (NED), which is operated by the Jet Propulsion Laboratory, California Institute of Technology, under contract with the National Aeronautics and Space Administration. This work is based in part on observations made with the Spitzer Space Telescope, which is operated by the Jet Propulsion Laboratory, California Institute of Technology, under a contract with NASA. This research is mainly funded by UNAM PAPIIT projects IA103118 and IN105720 (PI: O.G.-M.). D.E.-A., N.O.-C., C.V.-C., and O.U.R.-A. acknowledge support from CONACYT scholarships.

Appendix A
NuSTAR Archival Observations

We find in the sample, that 35 objects do not present a reliable obscuration measurement (those marked with an asterisk or ellipsis in column (10) in Tables 1 and 2). Out of these 35, we searched the NuSTAR archive and found observations for 18 objects: PKS 0558–504, NGC 253, IRAS 09149–6206, Mrk 704, M81, ESO 438-G009, Mrk 1392, Mrk 915, NGC 4051, NGC 3982, ESO 509-G038, J21140128+8204483, Mrk 1310, Mrk 205, Mrk 266SW, NGC 5135, NGC 3627, and NGC 3628. We extracted the spectra using standard procedures by using the analysis software NuSTARDAS v.1.4.4 with a 60″ extraction radius in all cases.

We fit the spectra with a single power law with a partial covering absorber, accounting for Galactic absorption as well. We find significant absorption in all but three sources (for which column (4) in Table 3 is marked with an ellipsis). In the case of NGC 252, Mrk 704, and NGC 5135, we also add the Fe Kα line at 6.4 keV. In Table 3, we show the values found for $N_{\rm H}$, Γ, and intrinsic luminosity in the 3–10 keV band in all cases.

Appendix B
Multiwavelength Diagnostic

B.1. Optical Diagnostic

To create the BPT diagrams (Baldwin et al. 1981), we compile the reddened corrected fluxes' available measurements of the [O III] 5007 Å, [N II] 6583 Å, Hβ, and Hα emission lines presented in the Swift BAT 70 month catalog (Koss et al. 2017). In Tables 4 and 5, we include these optical emission line fluxes for the accepted fading/rising and atypical candidates, respectively.

B.2. Infrared Diagnostic

We convert IRS/Spitzer spectra into X-ray spectral fitting package XSPEC (Arnaud 1996) format using the FLX2XSP task within HEASOFT.[6] Following the technique developed by González-Martín et al. (2009a), we fit each spectrum using four baseline models:

$$M_1 = zdust \times \text{AGN dust}, \quad \text{(B1)}$$

$$M_2 = zdust \times \text{AGN dust} + \text{Stellar}, \quad \text{(B2)}$$

$$M_3 = zdust \times \text{AGN dust} + \text{ISM}, \quad \text{(B3)}$$

and

$$M_4 = zdust \times \text{AGN dust} + \text{ISM} + \text{Stellar}, \quad \text{(B4)}$$

where the zdust, ISM, and Stellar components are the foreground extinction by dust grains (Pei 1992), interstellar medium (Smith et al. 2007), and stellar populations of 10^{10} yr and solar metallicity (Bruzual & Charlot (2003)), respectively. Finally, the AGN dust corresponds to the smooth model by Fritz et al. (2006), clumpy model by Nenkova et al. (2008a, 2008b) and Hönig & Kishimoto (2010), two-phase (clumpy and smooth) torus models by Stalevski et al. (2016), and clumpy disk wind model by Hönig & Kishimoto (2017) designed to describe the IR AGN emission. We compute the χ^2 statistics throughout the analysis to find the absolute minimum for each parameter as

[6] https://heasarc.gsfc.nasa.gov

Table 4
Fluxes for Fading/Rising Candidates (Same as Table 1)

Name	Optical				MIR					Classification
	$F_{H\beta}$	$F_{[O\ III]}$	$F_{H\alpha}$	$F_{[N\ II]}$	$\log(L_{[O\ IV]})$	Model	AGN/Stellar/ISM	χ^2_r	$E(B-V)$	
	[10^{-15} W m^{-2}]				[erg s^{-1}]		[%]			
(1)	(2)	(3)	(4)	(5)	(6)	(7)	(8)	(9)	(10)	(11)
Mrk 335	82 ± 15.7	276.2 ± 6.5	243.4 ± 6.9	22.9 ± 2.6	⋯	⋯	⋯	⋯	⋯	S1.2
J00430184+3017195	25.8	91.5 ± 2.7	⋯	⋯	⋯	⋯	⋯	⋯	⋯	S2
Mrk 359	22.2 ± 1	122.4 ± 0.1	108.6 ± 2.2	45 ± 1	⋯	⋯	⋯	⋯	⋯	S1.5
NGC 1068	2208.7 ± 13.5	27677.7 ± 32.8	6497.5 ± 3.7	11935 ± 8	⋯	⋯	⋯	⋯	⋯	S2
Fornax A	⋯	⋯	⋯	⋯	⋯	⋯	⋯	⋯	⋯	L2
IRAS 04124–0803	32.9 ± 10.4	441.8 ± 3.3	369.7 ± 0.8	45.8 ± 0.9	⋯	⋯	⋯	⋯	⋯	S1
Mrk 618	37.1 ± 5.8	195.4 ± 3.7	117.1 ± 7.2	40.9 ± 2	⋯	⋯	⋯	⋯	⋯	S1
LEDA 097068	22.2 ± 17.5	392.7 ± 17	655.1 ± 24.1	604.1 ± 19.2	⋯	⋯	⋯	⋯	⋯	S1
IRAS 05218–1212	6.5 ± 0.1	85.5 ± 0.3	39.4 ± 0.8	21.4 ± 0.5	43.4 ± 1.5	H17	85.8/0.0/14.2	0.36	<0.5	S1
Mrk 6	161.5 ± 11.4	1482.8 ± 21	608.9 ± 3.3	354 ± 3.4	⋯	⋯	⋯	⋯	⋯	S1.5
Mrk 79	55.2 ± 4.8	556.2 ± 4.6	185.3 ± 7.4	133.9 ± 7.5	⋯	⋯	⋯	⋯	⋯	S1.2
Mrk 10	13.8 ± 6	171.1 ± 0.7	62.4 ± 1.3	45.2 ± 1.2	42.6 ± 1.8	N08	94.3/5.7/0.0	0.31	<0.5	S1.2
Mrk 1210	73.6 ± 0.2	803 ± 0.3	173.1 ± 0.6	90.8 ± 0.1	42.1 ± 1.0	H17	81.8/1.7/16.5	1.83	<0.5	S1
IRAS 09149–6206	48.3 ± 127	505.9 ± 104.1	26.3 ± 4.2	13.8	⋯	⋯	⋯	⋯	⋯	S1
Mrk 704	37.7 ± 5.7	337.7 ± 6.2	94.4 ± 16.8	24.6 ± 10.9	⋯	⋯	⋯	⋯	⋯	S1.2
M81	107.4	266.8 ± 6.8	200 ± 25.4	460.6 ± 19.3	⋯	⋯	⋯	⋯	⋯	L1.8
3C 234.0	15 ± 0.1	160.7 ± 0.1	56.7 ± 0.3	16.8 ± 0.1	44.24 ± 1.3	F06	92.2/2.9/5.0	0.37	<0.5	S1
NGC 3227	78.6 ± 3.5	932.5 ± 4.1	386.5 ± 3.2	574.3 ± 6.6	41.7 ± 1.6	N08	51.0/3.3/45.7	1.29	<0.5	S1.5
ESO 317-G038	8.3 ± 0.2	122.8 ± 0.3	91.8 ± 0.6	88.6 ± 0.6	⋯	⋯	⋯	⋯	⋯	S2
NGC 3379	⋯	⋯	⋯	⋯	⋯	⋯	⋯	⋯	⋯	L2
NGC 3521	⋯	⋯	⋯	⋯	⋯	⋯	⋯	⋯	⋯	L2
ESO 438-G009	39.7 ± 0.9	75.5 ± 0.3	211.5 ± 2.6	143.3 ± 1.8	⋯	⋯	⋯	⋯	⋯	S1.5
NGC 3607[†]	⋯	⋯	⋯	⋯	⋯	⋯	⋯	⋯	⋯	L2
PG 1138+222	27.5 ± 0.3	200.4 ± 0.4	136.9 ± 4.3	35.8 ± 1.7	⋯	⋯	⋯	⋯	⋯	S1
NGC 3982	⋯	⋯	⋯	⋯	⋯	⋯	⋯	⋯	⋯	S2
UGC 07064	12.1	126.7 ± 0.2	59 ± 0.2	57.6 ± 0.2	⋯	⋯	⋯	⋯	⋯	S1.9
NGC 4151	812.2 ± 302	10035.9 ± 66.4	3067 ± 25.6	2270.7 ± 24.4	41.7 ± 1.8	N08	95.9/4.1/0.0	0.98	<0.5	S1.5
Mrk 766	61.3 ± 2.4	463.8 ± 1.1	209.6 ± 1.7	104.3 ± 0.5	⋯	⋯	⋯	⋯	⋯	S1.5
NGC 4303	⋯	⋯	⋯	⋯	⋯	⋯	⋯	⋯	⋯	S2
NGC 4395	37.7 ± 0.2	333.5 ± 0.2	149.1 ± 0.2	33.2 ± 0.1	39.3 ± 1.5	N08	72.7/4.0/23.4	0.69	<0.5	S1.8
J123212.3–421745	11.3 ± 7.5	216.2 ± 11.9	82.7 ± 0.6	2.8 ± 0.9	⋯	⋯	⋯	⋯	⋯	S1.5
LEDA 170194	65.7 ± 0.1	568 ± 0.1	611.6 ± 0.1	593.9 ± 0.2	⋯	⋯	⋯	⋯	⋯-	S2
NGC 4736	⋯	⋯	⋯	⋯	⋯	⋯	⋯	⋯	⋯	S2
NGC 4748	70.1 ± 1.2	531.3 ± 1.1	297.1 ± 1.2	235.5 ± 1.1	⋯	⋯	⋯	⋯	⋯	S1
NGC 4941	29 ± 0.2	294.7 ± 0.4	119.2 ± 0.6	194.8 ± 0.6	40.9 ± 1.5	N08	100.0/0.0/0.0	0.44	$0.7^{0.8}_{0.6}$	S2
NGC 4939	32.5 ± 0.3	479.5 ± 0.9	148.8 ± 0.6	226.6 ± 0.9	42.3 ± 1.8	N08	90.7/3.3/6.0	0.85	<0.5	S2
MCG-03-34-064	65.4 ± 0.5	996.5 ± 1.5	129.2 ± 0.7	231.3 ± 0.9	43.3 ± 1.6	⋯	Circumnuclear contribution	⋯	⋯	S1.8
M51a	⋯	⋯	⋯	⋯	⋯	⋯	⋯	⋯	⋯	S2
ESO 509-G038	13.7 ± 0.6	195.1 ± 0.5	49.8 ± 0.8	67.9 ± 1	⋯	⋯	⋯	⋯	⋯	S1
NGC 5283	40.5 ± 0.8	385 ± 0.7	139.4 ± 0.1	131.9 ± 0.2	⋯	⋯	⋯	⋯	⋯	S2
NGC 5273	5.9 ± 0.2	101.9 ± 0.4	27.1 ± 0.1	37.9 ± 0.3	40.2 ± 0.5	F06	100.0/0.0/0.0	0.23	<0.5	S1.9
Mrk 463	60.5	463.5 ± 0.2	141.3 ± 0.3	63.8 ± 0.1	43.9 ± 1.6	S16	83.3/4.4/12.3	0.70	$0.1^{0.2}_{0.0}$	S2
Mrk 477	95.1 ± 0.2	953.9 ± 0.3	294.9 ± 0.7	96 ± 0.4	43.3 ± 1.5	⋯	Circumnuclear contribution	⋯	⋯	S1
IC 4518A	35.1 ± 0.4	292.6 ± 0.2	160.9 ± 0.3	124.1 ± 0.2	43.07 ± 1.9	⋯	Circumnuclear contribution	⋯	⋯	S2

Table 4
(Continued)

Name	Optical				MIR					Classification
	$F_{H\beta}$	$F_{[O\ III]}$	$F_{H\alpha}$	$F_{[N\ II]}$	$\log(L_{[O\ IV]})$	Model	AGN/Stellar/ISM	χ^2_r	$E(B-V)$	
		$[10^{-15}$ W m$^{-2}]$			[erg s^{-1}]		[%]			
(1)	(2)	(3)	(4)	(5)	(6)	(7)	(8)	(9)	(10)	(11)
Mrk 1392	11.3 ± 0.5	210.4 ± 0.3	90.6 ± 0.9	93.8 ± 0.8	43.0 ± 1.73	N08	91.7/2.4/5.9	0.68	<0.5	S1.8
						H17	77.5/1.5/21.0	0.67	<0.5	
J15462424+6929102	20.5 ± 0.3	215.9 ± 0.1	66 ± 0.1	81.7 ± 0.1	⋯	⋯	⋯	⋯	⋯	S1.9
J16531506+2349431	13.7 ± 0.1	163.4 ± 0.1	53.9 ± 0.2	21.5 ± 0.1	⋯	⋯	⋯	⋯	⋯	S2
Fairall 49	55.1 ± 0.3	267.1 ± 0.3	334.5 ± 0.7	206.3 ± 0.6	42.96 ± 1.4	N08	66.4/6.1/27.5	1.21	<0.5	S2
J19373299–0613046	125.5 ± 55.1	1153.4 ± 8.3	479.3 ± 2.3	194.3 ± 1.1	⋯	⋯	⋯	⋯	⋯	S1
MCG+02-57-002	57.3 ± 1.3	215.8 ± 0.5	512.6 ± 1.5	252.5 ± 1.3	⋯	⋯	⋯	⋯	⋯	S1.5
Mrk 915	72.3 ± 0.6	761.1 ± 0.7	263.8 ± 1.9	179.6*e*.15 ± 2.5	43.1 ± 1.7	N08	75.1/4.1/20.8	0.48	<0.5	S1
MCG+01-57-016	40.9 ± 1.4	422.3 ± 1	131.7 ± 0.5	106.4 ± 0.7	42.5 ± 1.3	N08	62.2/4.7/33.1	1.00	<0.5	S1.8
NGC 7469	252.3 ± 10.2	1159.5 ± 8.8	920.7 ± 5.1	565.9 ± 3.8	42.5 ± 0.84	⋯	Circumnuclear contribution	⋯	⋯	S1.2
NGC 3627	⋯	⋯	⋯	⋯	⋯	⋯	⋯	⋯	⋯	S2
NGC 4051	49.1 ± 38.3	310 ± 6.2	448.3 ± 1.7	148.4 ± 0.5	⋯	⋯	⋯	⋯	⋯	S1.5
M106	52.3 ± 1.5	179.2 ± 0.6	13.1 ± 2.1	108.5 ± 1.4	40.0 ± 0.9	N08	86.1/2.5/11.4	0.25	$0.5^{0.6}_{0.5}$	L1.9
NGC 5033	8.1 ± 0.2	38.8 ± 0.3	48.9 ± 0.6	78.8 ± 1.1	⋯	⋯	⋯	⋯	⋯	S1.9
NGC 7130	30.3 ± 0.3	155.5 ± 0.5	119.7 ± 1	114 ± 0.7	42.2 ± 0.8	⋯	Circumnuclear contribution	⋯	⋯	L1.9
NGC 1194	1.9	29.5 ± 0.3	16.6 ± 0.1	10.3 ± 0.1	⋯	⋯	⋯	⋯	⋯	S1.9
J14391186+1415215	0.5	0.8	2	1.3	⋯	⋯	⋯	⋯	⋯	S1
J08551746–2854218	3.8 ± 0.2	0.7 ± 0.1	4.8 ± 0.1	2.9	⋯	⋯	⋯	⋯	⋯	S2

Note. Column (1): source name. Columns (2)–(5): optical fluxes obtained from Swift BAT 70 month catalog (Ricci et al. 2017) that were used in the BPT diagram (Figure 4). All fluxes are in units of 10^{-15} W m^{-2}. Column (6): [O IV] luminosity. Columns (7)–(10): best-fit results per object. Column (7): models used to fit the data (F06: Fritz et al. 2006; N08: Nenkova et al. 2008; S16: Stalevski et al. 2016; H17: Hönig & Kishimoto 2017). Column (8): percentage contribution to the 5–30 μm wave band per component (A: AGN; S: stellar; I: ISM). Column (9): reduced χ^2 (χ^2/dof). Column (10): color excess for the foreground extinction $E(B-V)$. Column (11): classification retrieved from Hyperleda, NED, and, in a few cases, Ichikawa et al. (2017).

Table 5
Fluxes for Atypical Candidates (Same as Table 2)

Name	Optical				MIR					Classification
	$F_{H\beta}$	$F_{[O\ III]}$	$F_{H\alpha}$	$F_{[N\ II]}$	$\log(L_{[O\ IV]})$	Model	AGN/Stellar/ISM	χ^2_r	$E_{(B-V)}$	
		$[10^{-15}$ W m$^{-2}]$			[erg s^{-1}]		[%]			
(1)	(2)	(3)	(4)	(5)	(6)	(7)	(8)	(9)	(10)	(11)
NGC 612†	3	5.9 ± 0.3	6.5 ± 0.8	6.5 ± 0.4	42.3 ± 1.3	⋯	Circumnuclear contribution	⋯	⋯	S2
J02420381+0510061†	1.4 ± 0.1	1.4 ± 0.3	7.7	4.6	⋯	⋯	⋯	⋯	⋯	S2
J04440903+2813003†	2.1 ± 0.1	2.3 ± 0.2	10.1 ± 0.1	12.5 ± 0.1	⋯	⋯	⋯	⋯	⋯	S2
PKS 0558–504†	3.5 ± 1.1	3.7 ± 0.5	41.8 ± 0.4	15.9 ± 0.5	⋯	S16	84.2/4.6/11.1	0.46	<0.5	S1
NGC 3079†	0.6	0.8 ± 0.1	6.9 ± 0.2	8.7 ± 0.2	41.2 ± 1.2	⋯	Circumnuclear contribution	⋯	⋯	L2
Cen A†	⋯	⋯	⋯	⋯	40.6 ± 1.3	⋯	Circumnuclear contribution	⋯	⋯	S2
ESO 097-G013†	⋯	⋯	⋯	⋯	⋯	⋯	Circumnuclear contribution	⋯	⋯	S2
MCG+04-48-002†	0.8	1.4 ± 0.1	23.5 ± 0.1	8.4 ± 0.2	42.0 ± 1.2	⋯	Circumnuclear contribution	⋯	⋯	S2
MCG-07-03-007	6.4 ± 0.7	107.7 ± 6.4	42.6 ± 7	68.6 ± 8.9	⋯	⋯	⋯	⋯	⋯	S2
MCG+08-03-018	81.7 ± 0.4	1153.6 ± 0.2	236.6 ± 0.1	75.4 ± 0.1	⋯	⋯	⋯	⋯	⋯	S2
NGC 526A	54.1 ± 0.2	594.8 ± 0.9	147.7 ± 0.3	121.9 ± 0.3	42.4 ± 1.5	H17	100.0/0.0/0.0	0.20	$0.3^{0.4}_{0.3}$	S1.5
						H10	94.8/5.2/0.0	0.29	$0.3^{0.4}_{0.2}$	
NGC 1229	13.8 ± 0.1	116.7 ± 0.4	44.1 ± 0.1	33.7 ± 0.3	⋯	⋯	⋯	⋯	⋯	S2
J03305218+0538253	70.9 ± 5.5	587.1 ± 3.6	363 ± 3.1	27.8 ± 1.6	⋯	⋯	⋯	⋯	⋯	S1
CGCG 420-015	33.9 ± 0.2	361.5 ± 0.4	90.9 ± 0.1	40.2 ± 0.1	42.7 ± 1.1	H17	84.5/0.0/15.5	0.38	$0.0^{0.1}_{0.0}$	S2
Mrk 3	600.3 ± 4	6853.8 ± 3.7	1049.2 ± 2.8	1401.2 ± 1.8	43.1 ± 1.8	⋯	Circumnuclear contribution	⋯	⋯	S2
Mrk 78	25.6 ± 0.1	388.2 ± 0.3	185.3 ± 7.4	133.9 ± 7.5	43.7 ± 1.9	N08	82.9/3.6/13.5	0.82	$0.5^{0.5}_{0.4}$	S2
J09172716–6456271	15.2 ± 0.4	131.7 ± 0.1	39.5 ± 0.9	13.6 ± 0.5	⋯	⋯	⋯	⋯	⋯	S2
ESO 374-G044	12.2	247.2 ± 0.5	72.1 ± 0.3	59.4 ± 0.2	42.9 ± 1.7	H17	87.6/0.0/12.4	1.00	<0.0	S2
						N08	97.2/2.8/0.0	1.14	<0.5	
NGC 3393	291.4 ± 6.9	2557.2 ± 11	464 ± 1.4	491.5 ± 1.6	43.2 ± 2.2	N08	82.3/2.0/15.8	0.99	<0.5	S2
ESO 265-G023	23.8	163.3 ± 0.6	23 ± 0.9	7.4 ± 0.9	⋯	⋯	⋯	⋯	⋯	S1
Mrk 1310	11.6 ± 0.2	107.1 ± 0.3	46.8 ± 0.5	18.8 ± 0.2	⋯	⋯	⋯	⋯	⋯	S1
Mrk 205	29.5 ± 16	244.2 ± 12.1	365.6 ± 12.2	177.2 ± 30	⋯	⋯	⋯	⋯	⋯	S1
J12313717–4758019	19.1 ± 0.5	151.3 ± 0.2	74.1 ± 0.4	38 ± 1.2	⋯	⋯	⋯	⋯	⋯	S1
NGC 4507	341.2 ± 1.4	2902.1 ± 2.6	648.9 ± 6.8	326.5 ± 2	42.4 ± 1.3	N08	83.2/4.7/12.1	0.99	<0.5	S2
ESO 323-32	11.3	131.2 ± 0.2	24.9 ± 0.3	55.7 ± 0.6	⋯	⋯	⋯	⋯	⋯	L2
Mrk 783	23.9 ± 5.4	205.7 ± 0.9	192.2 ± 1.6	75.9 ± 0.3	⋯	⋯	⋯	⋯	⋯	S1.5
NGC 5135	⋯	⋯	⋯	⋯	42.8 ± 1.4	⋯	Circumnuclear contribution	⋯	⋯	S2
Mrk 266SW	⋯	⋯	⋯	⋯	42.7 ± 1.8	⋯	Circumnuclear contribution	⋯	⋯	L2
TOLOLO 00113	87 ± 0.3	996.1 ± 1.3	⋯	⋯	⋯	⋯	⋯	⋯	⋯	S1.9
NGC 5643	48.9 ± 0.7	635.4 ± 0.6	194.3 ± 0.3	240.9 ± 0.5	41.2 ± 1.3	⋯	Circumnuclear contribution	⋯	⋯	S2
MCG-01-40-001	4.7	25.1 ± 0.4	2021.6 ± 11.4	1997.7 ± 10.4	⋯	⋯	⋯	⋯	⋯	S2
CGCG 367-009	37.6 ± 0.6	286.3 ± 1.1	273.4 ± 0.6	277.6 ± 1.2	⋯	⋯	⋯	⋯	⋯	S2
NGC 6232	28.5 ± 0.1	177.7	72.9	83.8 ± 0.1	⋯	⋯	⋯	⋯	⋯	S2
LEDA 214543	22.8	279.9 ± 1.3	265.1 ± 3.6	420.5 ± 2.6	⋯	⋯	⋯	⋯	⋯	S2
J21090996–0940147	36.1 ± 2.3	277.4 ± 1.9	144.2 ± 27.4	68.5 ± 4.9	⋯	⋯	⋯	⋯	⋯	S1.2
J21140128+8204483	31.8 ± 10.7	655.8 ± 179.6	255.1 ± 5.3	145.7 ± 3.7	⋯	⋯	⋯	⋯	⋯	S1

Table 5
(Continued)

Name	Optical				MIR					Classification
	$F_{H\beta}$	$F_{[O\ III]}$	$F_{H\alpha}$	$F_{[N\ II]}$	$\log(L_{[O\ IV]})$	Model	AGN/Stellar/ISM	χ^2_r	$E_{(B-V)}$	
		$[10^{-15}$ W m$^{-2}]$			[erg s^{-1}]		[%]			
(1)	(2)	(3)	(4)	(5)	(6)	(7)	(8)	(9)	(10)	(11)
NGC 253[†]	...	...	...	...	...	...	...	...	...	S2
NGC 3628[†]	...	...	...	...	...	...	Circumnuclear contribution	...	...	L2
ESO 137-G034[†]	3409 ± 66.4	41158.5 ± 78.1	...	...	...	...	...	...	...	S2
ESO 234-G050[†]	61.4 ± 0.3	196.2 ± 0.6	161.3 ± 0.6	36.8 ± 0.3	...	...	...	...	...	S2
ESO 234-IG063[†]	30.6 ± 0.2	336.1 ± 0.7	72.5 ± 0.3	30 ± 0.3	...	...	...	...	...	S2

Note. Column descriptions are the same as in Table 4.

the best fit. We then use f-statistics to test whether the inclusion of the stellar (Equation (B2)), ISM (Equation (B3)), and/or stellar+ISM (Equation (B4)) components significantly improves the simpler model when the F-test probability is below 10^{-4}. If several models describe the data equally well (according to the χ^2 statistics and using the Akaike criteria (see Equations (5)–(7) by Emmanoulopoulos et al. 2016)), we include both models as a feasible representation of the data. We provide good spectral fitting ($\chi^2/\mathrm{dof} < 1.3$) for all but one object (Mrk 1210).

The range that covers the Spitzer spectra allows us to measure the [O IV] line. Therefore, we compiled the [O IV] fluxes at 25.9 μm for the 38 objects observed with Spitzer and available at the Combined Atlas of Sources with Spitzer IRS Spectra (CASSIS[7]). We compute the emission line flux by fitting a Gaussian above the continuum. Tables 4 and 5 include the [O IV] luminosities, when available, for accepted and atypical candidates, respectively. Among them, 2, 19, 10, 1, and 6 are early fading, fading, atypical 2, atypical 3, and atypical 1, respectively.

Appendix C
Radio Morphology

We search the radio images available in the literature of the 102 sources considered in Section 3. Among the 61 bona fide candidates, we found radio images for 46 targets, while for the remaining 15, no radio images were available. Among the 41 atypical candidates, we found only 15 radio images. All of the radio data we collected have been obtained using the Jansky Very Large Array (JVLA) at different frequencies from low-frequency *L* band (1.4 GHz) to high-frequency *K* band (22 GHz) and using different configurations of the interferometer array. Therefore, the angular resolution of the images ranges in a broad interval from tens to 1″. We are aware that this huge range of available angular resolutions of the different observations could result in an uncertain morphological classification (e.g., extended emission that could be resolved out at higher angular resolution); new radio observations with an equal observational setup for all sources would be appropriate to eliminate this uncertainty. Therefore, we suggest taking this classification as a first hint. The classification we adopted is described as follows.

1. Compact source: a pointlike object with unresolved radio emission.
2. Linear source: an object showing elongated, jetlike features.
3. Diffuse source: an object showing extended, rounded emission features.

The morphological classification and the relative references for the linear and diffuse images are available in column (9) in Tables 1 and 2. The images found in the literature for the linear and diffuse sources are collected in Figures 9 and 10.

[7] https://cassis.sirtf.com

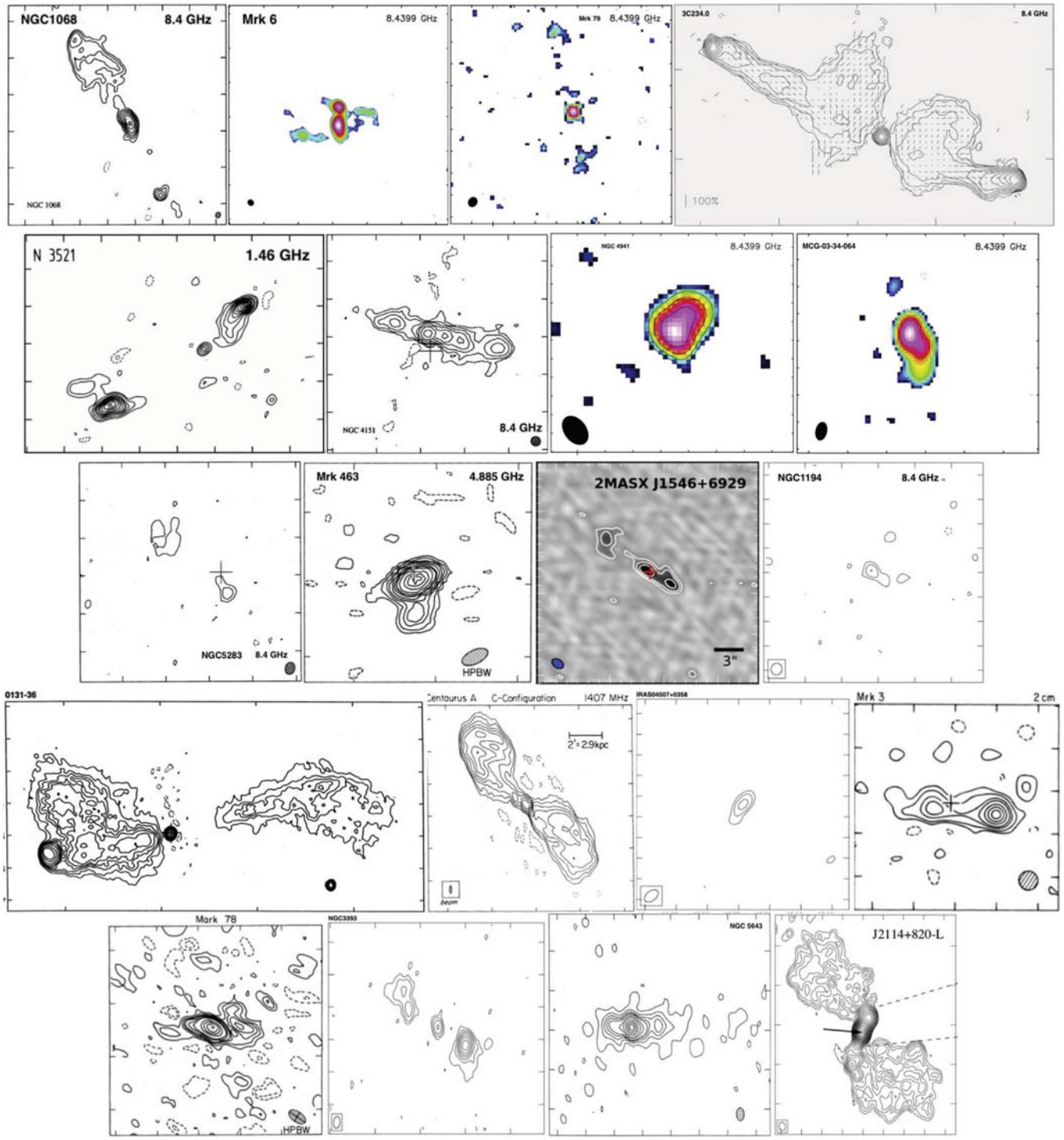

Figure 9. Images of the objects classified as linear among the bona fide and atypical sources. All of the data are JVLA images at different angular resolutions; references are reported in Table 1.

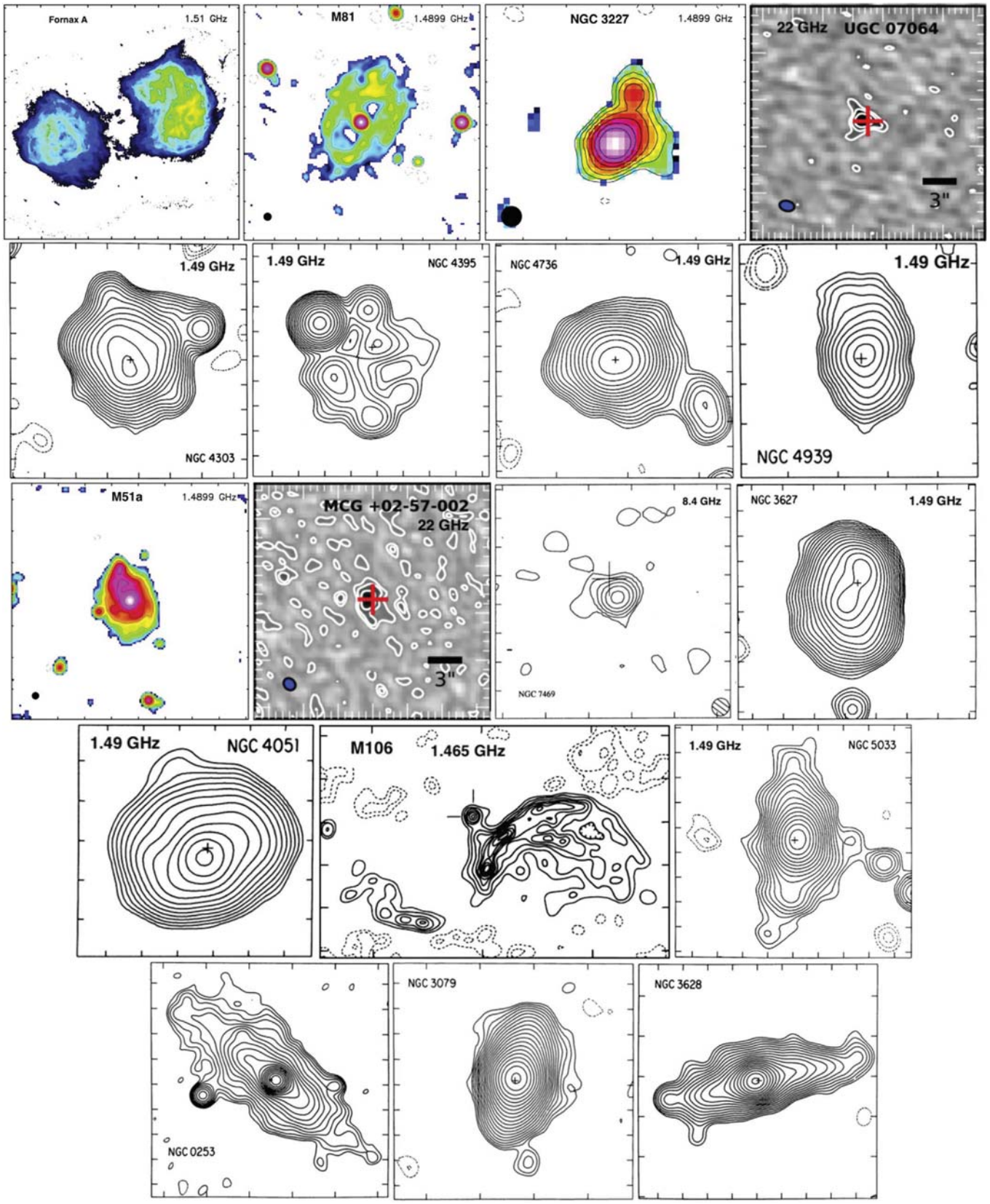

Figure 10. Images of the objects classified as diffuse among the bona fide and atypical sources. All of the data are JVLA images at different angular resolutions; references are reported in Table 2.

ORCID iDs

Donaji Esparza-Arredondo https://orcid.org/0000-0001-8042-9867
Natalia Osorio-Clavijo https://orcid.org/0000-0002-3467-8077
Omaira González-Martín https://orcid.org/0000-0002-2356-8358
César Victoria-Ceballos https://orcid.org/0000-0001-5625-7815
Sinhué A. R. Haro-Corzo https://orcid.org/0000-0001-9385-4176
Omar Ulises Reyes-Amador https://orcid.org/0000-0001-7707-7389
Jafet López-Sánchez https://orcid.org/0000-0001-8298-8582
Alice Pasetto https://orcid.org/0000-0003-1933-4636

References

Annuar, A., Alexander, D. M., Gandhi, P., et al. 2020, MNRAS, 497, 229
Arnaud, K. A. 1996, in ASP Conf. Ser. 101, Astronomical Data Analysis Software and Systems V, ed. G. H. Jacoby & J. Barnes (San Francisco, CA: ASP), 17
Asmus, D., Gandhi, P., Hönig, S. F., Smette, A., & Duschl, W. J. 2015, MNRAS, 454, 766
Asmus, D., Hönig, S. F., Gandhi, P., Smette, A., & Duschl, W. J. 2014, MNRAS, 439, 1648
Baldwin, J. A., Phillips, M. M., & Terlevich, R. 1981, PASP, 93, 5
Berney, S., Koss, M., Trakhtenbrot, B., et al. 2015, MNRAS, 454, 3622
Binette, L., & Robinson, A. 1987, A&A, 177, 11
Blandford, R., Meier, D., & Readhead, A. 2019, ARA&A, 57, 467
Bruzual, G., & Charlot, S. 2003, MNRAS, 344, 1000
Burns, J. O., Feigelson, E. D., & Schreier, E. J. 1983, ApJ, 273, 128
Cardelli, J. A., Clayton, G. C., & Mathis, J. S. 1989, ApJ, 345, 245
Collin-Souffrin, S., Alloin, D., & Andrillat, Y. 1973, A&A, 22, 343
Comastri, A. 2004, in Compton-Thick AGN: The Dark Side of the X-Ray Background, ed. A. J. Barger (Dordrecht: Kluwer Academic), 245
Condon, J. J. 1987, ApJS, 65, 485
Denney, K. D., De Rosa, G., Croxall, K., et al. 2014, ApJ, 796, 134
Dicken, D., Tadhunter, C., Morganti, R., et al. 2014, ApJ, 788, 98
Eckart, M. E., Laird, E. S., Stern, D., et al. 2005, ApJS, 156, 35
Eckart, M. E., McGreer, I. D., Stern, D., Harrison, F. A., & Helfand, D. J. 2010, ApJ, 708, 584
Eckart, M. E., Stern, D., Helfand, D. J., et al. 2006, ApJS, 165, 19
Elitzur, M., & Ho, L. C. 2009, ApJL, 701, L91
Elitzur, M., & Netzer, H. 2016, MNRAS, 459, 585
Elvis, M., Maccacaro, T., Wilson, A. S., et al. 1978, MNRAS, 183, 129
Emmanoulopoulos, D., Papadakis, I. E., Epitropakis, A., et al. 2016, MNRAS, 461, 1642
Fender, R., & Belloni, T. 2012, Sci, 337, 540
Fender, R., & Muñoz-Darias, T. 2016, Lecture Notes in Physics, 905 (Berlin: Springer), 65
Ferland, G. J., & Osterbrock, D. E. 1986, ApJ, 300, 658
Flohic, H. M. L. G., Eracleous, M., Chartas, G., Shields, J. C., & Moran, E. C. 2006, ApJ, 647, 140
Fomalont, E. B., Ebneter, K. A., van Breugel, W. J. M., & Ekers, R. D. 1989, ApJL, 346, L17
Fritz, J., Franceschini, A., & Hatziminaoglou, E. 2006, MNRAS, 366, 767
Gandhi, P., Horst, H., Smette, A., et al. 2009, A&A, 502, 457
Glass, I. S., Moorwood, A. F. M., & Eichendorf, W. 1982, A&A, 107, 276
González-Martín, O., Masegosa, J., García-Bernete, I., et al. 2019, ApJ, 884, 11
González-Martín, O., Masegosa, J., Márquez, I., & Guainazzi, M. 2009a, ApJ, 704, 1570
González-Martín, O., Masegosa, J., Márquez, I., Guainazzi, M., & Jiménez-Bailón, E. 2009b, A&A, 506, 1107
Goulding, A. D., & Alexander, D. M. 2009, MNRAS, 398, 1165
Graham, M. J., Djorgovski, S. G., Drake, A. J., et al. 2017, MNRAS, 470, 4112
Groves, B. A., Heckman, T. M., & Kauffmann, G. 2006, MNRAS, 371, 1559
Hardcastle, M. J., Alexander, P., Pooley, G. G., & Riley, J. M. 1997, MNRAS, 288, 859
Harrison, F. A., Eckart, M. E., Mao, P. H., Helfand, D. J., & Stern, D. 2003, ApJ, 596, 944
Hawkins, M. R. S. 2007, A&A, 462, 581
Heckman, T. M., Ptak, A., Hornschemeier, A., & Kauffmann, G. 2005, ApJ, 634, 161
Hernández-García, L., Panessa, F., Bassani, L., et al. 2019, MNRAS, 489, 4049
Hönig, S. F., & Kishimoto, M. 2010, A&A, 523, A27
Hönig, S. F., & Kishimoto, M. 2017, ApJL, 838, L20
Hopkins, P. F. 2012, MNRAS, 420, L8
Hopkins, P. F., Hernquist, L., Cox, T. J., & Kereš, D. 2008, ApJS, 175, 356
Hopkins, P. F., Hernquist, L., Martini, P., et al. 2005, ApJL, 625, L71
Hopkins, P. F., & Quataert, E. 2010, MNRAS, 407, 1529
Hummel, E., Pedlar, A., van der Hulst, J. M., & Davies, R. D. 1985, A&AS, 60, 293
Hummel, E., van der Hulst, J. M., Keel, W. C., & Kennicutt, R. C. J. 1987, A&AS, 70, 517
Ichikawa, K., Kawamuro, T., Shidatsu, M., et al. 2019b, ApJL, 883, L13
Ichikawa, K., Ricci, C., Ueda, Y., et al. 2017, ApJ, 835, 74
Ichikawa, K., Ueda, J., Bae, H.-J., et al. 2019a, ApJ, 870, 65
Ichikawa, K., Ueda, J., Shidatsu, M., Kawamuro, T., & Matsuoka, K. 2016, PASJ, 68, 9
Jin, C., Ward, M., & Done, C. 2012, MNRAS, 422, 3268
Józsa, G. I. G., Garrett, M. A., Oosterloo, T. A., et al. 2009, A&A, 500, L33
Just, D. W., Brandt, W. N., Shemmer, O., et al. 2007, ApJ, 665, 1004
Kauffmann, G., Heckman, T. M., Tremonti, C., et al. 2003, MNRAS, 346, 1055
Keel, W. C., Lintott, C. J., Maksym, W. P., et al. 2017, ApJ, 835, 256
Keel, W. C., Lintott, C. J., Schawinski, K., et al. 2012, AJ, 144, 66
Kewley, L. J., Dopita, M. A., Sutherland, R. S., Heisler, C. A., & Trevena, J. 2001, ApJ, 556, 121
King, A. R., Zubovas, K., & Power, C. 2011, MNRAS, 415, L6
Kollatschny, W., Bischoff, K., & Dietrich, M. 2000, A&A, 361, 901
Kollatschny, W., & Fricke, K. J. 1985, A&A, 146, L11
Kollatschny, W., Grupe, D., Parker, M. L., et al. 2020, A&A, 638, A91
Komossa, S., Zhou, H., Wang, T., et al. 2008, ApJL, 678, L13
Kormendy, J., & Ho, L. C. 2013, ARA&A, 51, 511
Koss, M., Trakhtenbrot, B., Ricci, C., et al. 2017, ApJ, 850, 74
Krabbe, A., Böker, T., & Maiolino, R. 2001, ApJ, 557, 626
Kukula, M. J., Pedlar, A., Baum, S. A., & O'Dea, C. P. 1995, MNRAS, 276, 1262
Lamastra, A., Bianchi, S., Matt, G., et al. 2009, A&A, 504, 73
Lara, L., Cotton, W. D., Feretti, L., et al. 2001, A&A, 370, 409
Lawrence, A. 2018, NatAs, 2, 102
Lintott, C. J., Schawinski, K., Keel, W., et al. 2009, MNRAS, 399, 129
Lintott, C. J., Schawinski, K., Slosar, A., et al. 2008, MNRAS, 389, 1179
Lutz, D., Maiolino, R., Spoon, H. W. W., & Moorwood, A. F. M. 2004, A&A, 418, 465
Lyu, J., Rieke, G. H., & Smith, P. S. 2019, ApJ, 886, 33
MacLeod, C. L., Green, P. J., Anderson, S. F., et al. 2019, ApJ, 874, 8
Madau, P., & Dickinson, M. 2014, ARA&A, 52, 415
Marconi, A., Risaliti, G., Gilli, R., et al. 2004, MNRAS, 351, 169
Martocchia, S., Piconcelli, E., Zappacosta, L., et al. 2017, A&A, 608, A51
Matt, G., Guainazzi, M., & Maiolino, R. 2003, MNRAS, 342, 422
Morganti, R., Killeen, N. E. B., & Tadhunter, C. N. 1993, MNRAS, 263, 1023
Morris, S., Ward, M., Whittle, M., Wilson, A. S., & Taylor, K. 1985, MNRAS, 216, 193
Nagar, N. M., Falcke, H., Wilson, A. S., & Ulvestad, J. S. 2002, A&A, 392, 53
Narayan, R. 2005, Ap&SS, 300, 177
Narayan, R., & Yi, I. 1995, ApJ, 452, 710
Nenkova, M., Sirocky, M. M., Ivezić, Ž., & Elitzur, M. 2008b, ApJ, 685, 147
Nenkova, M., Sirocky, M. M., Nikutta, R., Ivezić, Ž, & Elitzur, M. 2008a, ApJ, 685, 160
Noda, H., & Done, C. 2018, MNRAS, 480, 3898
Noguchi, K., Terashima, Y., Ishino, Y., et al. 2010, ApJ, 711, 144
Novak, G. S., Ostriker, J. P., & Ciotti, L. 2011, ApJ, 737, 26
Panessa, F., Bassani, L., Cappi, M., et al. 2006, A&A, 455, 173
Parker, M. L., Komossa, S., Kollatschny, W., et al. 2016, MNRAS, 461, 1927
Parker, M. L., Longinotti, A. L., Schartel, N., et al. 2019, MNRAS, 490, 683
Pei, Y. C. 1992, ApJ, 395, 130
Penston, M. V., & Perez, E. 1984, MNRAS, 211, 33P
Ramos Almeida, C., Pérez García, A. M., Acosta-Pulido, J. A., & Rodríguez Espinosa, J. M. 2007, AJ, 134, 2006
Ramos Almeida, C., & Ricci, C. 2017, NatAs, 1, 679
Ricci, C., Trakhtenbrot, B., Koss, M. J., et al. 2017, ApJS, 233, 17
Risaliti, G., Maiolino, R., & Salvati, M. 1999, ApJ, 522, 157

Rumbaugh, N., Shen, Y., Morganson, E., et al. 2018, ApJ, 854, 160
Schawinski, K., Koss, M., Berney, S., & Sartori, L. F. 2015, MNRAS, 451, 2517
Schirmer, M., Malhotra, S., Levenson, N. A., et al. 2016, MNRAS, 463, 1554
Schmitt, H. R., Ulvestad, J. S., Antonucci, R. R. J., & Kinney, A. L. 2001, ApJS, 132, 199
Schweizer, F., Seitzer, P., Kelson, D. D., Villanueva, E. V., & Walth, G. L. 2013, ApJ, 773, 148
Shappee, B. J., Prieto, J. L., Grupe, D., et al. 2014, ApJ, 788, 48
Shulevski, A., Morganti, R., Barthel, P. D., et al. 2015, A&A, 583, A89
Smith, J. D. T., Draine, B. T., Dale, D. A., et al. 2007, ApJ, 656, 770
Smith, K. L., Mushotzky, R. F., Vogel, S., Shimizu, T. T., & Miller, N. 2016, ApJ, 832, 163
Stalevski, M., Ricci, C., Ueda, Y., et al. 2016, MNRAS, 458, 2288
Steffen, A. T., Strateva, I., Brandt, W. N., et al. 2006, AJ, 131, 2826
Stern, D. 2015, ApJ, 807, 129
Tananbaum, H., Avni, Y., Branduardi, G., et al. 1979, ApJL, 234, L9
Terashima, Y., Iyomoto, N., Ho, L. C., & Ptak, A. F. 2002, ApJS, 139, 1
Terlevich, A. I., & Forbes, D. A. 2002, MNRAS, 330, 547
Tohline, J. E., & Osterbrock, D. E. 1976, ApJL, 210, L117
Trakhtenbrot, B., Arcavi, I., MacLeod, C. L., et al. 2019, ApJ, 883, 94
Tran, H. D. 2003, ApJ, 583, 632
Ulvestad, J. S., & Wilson, A. S. 1984, ApJ, 278, 544
Ulvestad, J. S., & Wilson, A. S. 1989, ApJ, 343, 659
Ulvestad, J. S., Wilson, A. S., & Sramek, R. A. 1981, ApJ, 247, 419
Ward, M. J., Done, C., Fabian, A. C., Tennant, A. F., & Shafer, R. A. 1988, ApJ, 324, 767
Xu, Y.-D. 2011, ApJ, 739, 64
Young, M., Elvis, M., & Risaliti, G. 2009, ApJS, 183, 17
Zubovas, K., & King, A. R. 2014, MNRAS, 439, 400

Chapter 6

Summary and discussion

Previous studies at near-IR, mid-IR, and sub-mm wavelengths tried to constrain the physical parameters of the torus (e.g. Ramos Almeida et al., 2014; Gallimore et al., 2016; García-Burillo et al., 2016; Lopez-Rodriguez et al., 2018). However, observations at these wavelengths might be contaminated by stellar light (Ramos Almeida et al., 2014), diffuse dust emission from the ISM (Mason et al., 2006), or synchrotron emission (Pasetto et al., 2019). The smooth and clumpy models have been tested in large samples of AGN using infrared SEDs and have found differences in the torus parameters between type-1 and type-2 AGN (e.g. Ramos-Almeida et al., 2009; Ramos Almeida et al., 2011; García-Bernete et al., 2019) and even a dependency with the AGN luminosity (González-Martín et al., 2017, 2019b). However, obtaining the full set of parameters for these models has been difficult so far, partially due to the lack of spectral coverage and nuclear isolation that current observations have (Ramos Almeida et al., 2014; González-Martín et al., 2019b).

Meanwhile, at X-ray wavelengths, several models have also been developed in the last decades to try to understand the reflection component, which is also associated, in most cases, with the obscuring structure (Liu & Li, 2015; Buchner et al., 2019). As for the infrared continuum, the reflection components at X-rays depend on the shape (geometry and density) of the reprocessing material (e.g. Ghisellini et al., 1994; Nenkova et al., 2008a). Thus, comparing spectra and models in both bands helps to infer the properties of the AGN torus, otherwise unreachable for the vast majority of the AGN due to the small scales involved. Still, X-ray data modeling is complicated due to the spectral resolution of current observations and simplification of models. The understanding of the obscuring material has made great progress through these works, but there is still a long way to go. For instance, only a few works have compared these models with data in an effort to constrain the model parameters for a handful of objects (e.g. Liu & Li, 2015; Furui et al., 2016; Baloković et al., 2018).

Only very recently, some works combine mid-IR and X-ray observations and models either by the SED fitting of photometric points for large collections of objects (Yang et al., 2020) or by combining previously reported mid-IR results with newly developed X-ray spectral fitting (Ogawa et al., 2021). In the next years, we will have access to new technology

allowing better isolation of the nucleus at mid-IR (e.g., *JWST*) and high spectral resolution at X-rays (e.g., *Athena*). Therefore, new techniques to harness the full potential of these observations are mandatory. The ultimate goal of this thesis is to *contribute to the resolution of mysteries associated with the obscuring structure of AGN*. For this, we used a multi-wavelength approach which allowed us to combine the most recent developments at each wavelength, such as models and observations obtained with modern technology.

This thesis started with the goal of understanding the complexity of the obscuring structure in AGN. In this study, we incorporated the maximum number of sources possible where AGN dust dominates at mid-IR, and the reflection component dominates at X-ray wavelengths. It is broadly accepted that the bulk of the torus emission is re-radiated throughout dust heating at mid-IR wavelengths (Ramos Almeida & Ricci, 2017). It is also widely accepted at X-rays that the X-ray reflection component comes from a distant neutral obscurer that reflects part of the X-ray intrinsic continuum coming from a corona (which is reprocessed emission from the disc). Both the mid-IR AGN continuum and X-ray reflection component are assumed to be powered by the obscurer that produces the AGN type dichotomy. However, a proper confrontation of the results from both wavelengths was still missing. Thus, our aim was to make a more realistic picture of the obscurer by combining, for the first time, the results coming from both wavelengths.

In parallel to our investigation, Ogawa et al. (2021) confronted the clumpy torus model developed at X-rays with previously reported results at mid-IR wavelengths for a sizable sample of objects. These recent results are commented below, although they did not include a homogeneous analysis of the mid-IR spectra (since these results are taken from literature). They only cover the comparison on the clumpy torus model. Our aim was also to investigate the smooth torus model and produce a homogeneous analysis at both wavelengths. For this purpose, a sample of 36 nearby AGN was chosen, and spectral data were fit using the most recent smooth and clumpy models available to date; i.e., a torus geometry with the distribution being smooth at mid-IR (Fritz et al., 2006), smooth at X-rays (Baloković et al., 2018), clumpy at mid-IR (Nenkova et al., 2008b), and clumpy at X-rays (Buchner et al., 2019). Note that sources where the AGN dust continuum is dominating the *Spitzer* spectra are selected to ensure a better determination of the parameters of the models throughout the spectral fitting. Furthermore, we also focus on X-ray spectra where the reflection component significantly contributes to the *NuSTAR* spectra used in this analysis because this component contains the relevant information to derive the parameters of the gaseous torus. Finally, we also remove from the analysis objects where this reflection component might be contaminated from disk reflection since it would add complexity to the interpretation of the results.

The dust and gas parameters were partially obtained for each source through these individual fits (Esparza-Arredondo et al., 2021). Note that a simultaneous fit is required to restrict the parameters fully, as shown in this work (this is further discussed below but see Esparza-Arredondo et al., 2019). However, we extracted important results from this analysis regarding the diversity of gas and dust distributions of the obscuring structure. We learned

that three distributions of gas and dust are possible: smooth-smooth, smooth-clumpy, and clumpy-clumpy (being the former the distribution of the gaseous X-ray torus and the latter that of the dusty mid-IR torus). Interestingly, whenever the absorption variation analysis has been performed in our objects, mostly from Laha et al. (2020), it nicely matches with the resulting smooth or clumpy distribution found from our spectral fitting analysis. This reinforces the results obtained at X-rays in this work.

One of the key results is that we found for the first time the smooth-clumpy combination (smooth at X-rays and clumpy at mid-IR), which can describe ∼80% of the AGN. This possible mismatch that can occur when these two wavelengths are compared was already pointed out by Liu & Li (2015). We analyzed two possible explanations for this combination: 1) the gas is a smooth distribution located between the dusty clouds, or 2) at least part of the gas comes from a smooth distribution associated with the dust-free inner region AGN. This second explanation could also explain the low dust-to-gas ratio for the torus found in many objects of our sample. This latter result on the dust-to-gas ratio of the torus has already been reported in early results (see also Maiolino et al., 2001). Furthermore, Buchner et al. (2019) already reported the need for an additional component to the X-ray reflection probably due to material in the BLR (i.e., the inner dust-free region) at least for the few objects tested. From a dynamic point of view, this distribution is possible and even required for a long-lived structure (see works by Elitzur & Shlosman, 2006; Wada, 2012; Sarangi et al., 2019; Ogawa et al., 2021).

It is also worth mentioning that dust and gas conform to a complex structure that varies almost by the object. Ogawa et al. (2021) very recently reported the comparison between the clumpy torus model results reported in the literature at mid-IR wavelengths with the new implemented clumpy model at X-rays (Tanimoto et al., 2019). Although the smooth torus models were not included in their analysis and the mid-IR analysis recalls in previous non-homogeneous results, they already pinpointed that different half opening angles of the torus are found. Indeed, we found at least six scenarios explaining the observed properties of some sources, where dust and gas partially overlap (see Figure 7 in Esparza-Arredondo et al., 2021, Chapter 3). Moreover, type-1 AGN shows intrinsic different configurations compared to type-2 AGN, in contradiction with the unification scheme (Antonucci & Miller, 1985; Urry & Padovani, 1995). This is consistent with the current paradigm of AGN, where a complex diversity of clouds are expected to contribute to the AGN obscuration within tens to hundreds of parsecs around the accretion disk (for a recent review on the subject, see Ramos Almeida & Ricci, 2017). This is also consistent with evolutionary theories (Krongold et al., 2003a,b) where the obscurer should go throughout phases linked to the evolution of the galaxies (perhaps through galaxy mergers, Hopkins and Quataert , 2010).

In many objects, the distribution of gas and dust can be linked; in particular for objects where the half-opening widths are consistent and suggest a common origin to both emissions or at least to the vast majority of this emission. We developed a simultaneous fitting technique under the hypothesis that mid-IR continuum emission and X-ray reflection emis-

sion might share a link. This technique consisted of using the mid-IR and X-ray models to fit both wavelengths simultaneously. We investigated whether the combination of different models could help us restrict the torus physical parameters through this simultaneous fit. This technique allowed us to combine the common information of both wavelengths, such as the values of the half-opening and inclinations angles. There is no similar effort in the literature so far actually to combine these spectral wavelengths. Perhaps the closest effort is made by Yang et al. (2020) where they made an upgrade to the CIGALE code to include an X-ray module to perform AGN SED fitting. However, this code aims to provide rough estimates on the contribution of each component for high-redshift AGN. Thus, it is not meant to study the parameter space of the torus itself.

Our technique was tested for the first time in the pilot source IC 5063 source (Esparza-Arredondo et al., 2019). We found that a combination of the smooth models was the best choice to fit the spectra from both wavelengths. Additionally, the link between half-opening and inclination angle values of both wavelengths allowed us to constrain all physical torus parameters. This link between angles is consistent with the idea that most of the IR emission is in the equatorial plane and that there exists a common origin with the X-ray reflection emission. Previous comparisons of opening angles determined independently from X-ray and mid-IR data agree with this behavior (Brightman et al., 2015; Farrah et al., 2016; Baloković et al., 2018).

According to this result, the torus of IC 5063 is a compact and relatively thin structure in which there is a strong decrease in the dust/gas density when the half-opening angle increases. The parameters obtained for this source are consistent with those found in previous works (e.g. Fritz et al., 2006; Ramos Almeida et al., 2011; Ichikawa et al., 2017). This is not the first work that attempts to understand whether the half-opening and viewing angles between wavelengths concur (e.g., Farrah et al., 2016). Still, it is the first to use a straightforward approach to link the spectra obtained from these two wavelengths simultaneously.

When we developed this work, only the smooth torus model at X-rays was available. This gives the idea of how fast this field is growing. However, it did not allow us to test this model in 2019 when this work got published. Interestingly, the spectral fitting to both smooth and clumpy models at both wavelengths for IC5063 (reported in our sample, see Esparza-Arredondo et al. 2021) showed a clumpy-clumpy combination is preferred for this source. Simultaneous fitting using the clumpy torus models at both wavelengths is still lacking (and planned for future work, see Chapter 7). Furthermore, more complexity in the models is argued to be needed at both X-rays and mid-IR wavelengths. The former because the current X-ray models are still too simplistic compared to mid-IR models. Indeed, some geometries, such as winds, are only barely tested at X-rays while they are better explored at mid-IR (Ramos Almeida & Ricci, 2017). Also, at mid-IR, as claimed when comparing with extensive collections of objects, there may be room for improvement in modeling. This, perhaps, by trying with different dust compositions and grain size distributions different from that of the ISM Galaxy (González-Martín et al., 2019b; Martínez-Paredes et al., 2020).

Finally, we also explored the role of the obscuration component depending on the evolutionary stage of the AGN activity. Mainly, we studied the ignition and shut-down processes in AGN. Despite its importance, little is known about it, with only a brief idea of the AGN ignition/fading processes and/or the duration of the AGN phase. Marconi et al. (2004) suggested that this phase should last 10^{7-9} years spread in short duty cycles of 10^5 years each (Novak et al., 2011; Schawinski et al., 2015; Shulevski et al., 2015). Under this context, the study of AGN duty cycle cannot be done without a proper classification of the stages of the AGN.

The difference in the energy budget between the accretion disk and the NLR can be interpreted as a hint on the AGN evolution. This is what is called the optical ionization echo. In this way, several fading AGN have been discovered by the Galaxy Zoo project (Lintott et al., 2008). A very well-known example of a fading AGN found using this method is Hanny's Voorwerp near the spiral galaxy IC 2497, where the extended NLR indicates a fading of the current AGN activity several orders of bolometric luminosities (Lintott et al., 2009; Keel et al., 2012). Other components could help to find changes in the AGN activity. In particular, mid-IR dust echoes can also help catch objects in these evolutionary stages using the distant AGN torus. This idea has already been applied to the case of Arp 187 showing an evident decline of the nuclear activity in an estimated lapse of time of 10,000 years, where the AGN has possibly ceased its activity (Ichikawa et al., 2016, 2019b).

We created a new sample of 88 AGN candidates that show hints of fading or rising in their activity from a parent sample of more than 877 AGN in the nearby universe. We used a multi-wavelength approach thanks to the fact that a different AGN component dominates each wavelength. The methodology applied to find these fading and rising candidates is as follows. First, we used the AGN scaling relations: [OIII] versus X-ray, mid-IR versus X-ray, and [OIII] versus mid-IR to select these candidate sources, as those AGN falling far from these relations. Then, we complemented the information for all sources and discarded those close to 2σ from the linear relations to find consistent fading or rising behaviors. We created four main categories according with the position of sources at these relationships: 1) *Fading*, *Early fading*, *Rising*, and *Early rising*. Additionally, we created three subcategories of objects showing complex behaviours (see Figure 3 in Chapter 5): *Atypical 1*, *Atypical 2*, and *Atypical 3*. Our next step was to explore the robustness of the selection using available tools, such as optical emission-line diagnostic diagrams, MIR spectra, and UV continuum luminosity. According to this analysis, our 88 sources are classified as 52 fading, 28 atypical 2, five early fading, one rising, and two early risings.

We found that $\sim 10\%$ of AGN in the local universe were fading, which might be consistent with the expectation that one-tenth of the AGN duty cycle of activity (~ 10 Myr) is spent in this fading phase (Hopkins et al., 2005). Meanwhile, we only found a few rising AGN. This could have two main explanations: 1) This stage is very short due to the amount of gas supplying that it is enough to efficient feedback of both AGN during merging event (Hopkins, 2012) or 2) the current stage of our universe, where SF and AGN activity is switching off

(Hopkins et al., 2008).

We also explored the existence of radio lobes and the morphology of AGN dust. Previous works used measures of radio lobes to calculate the aging of AGN (e.g. Ichikawa et al., 2019b). We explored these lobes as long-standing signatures of the past activity. We found that $\sim 31\%$ of sources have these lobes. This percentage is huge, considering that the percentage of local AGN showing powerful radio jets has been measured to be of the order of 0.1% (rising to 10% for high-redshift quasars, see Blandford et al., 2019).

To investigate the dust among our selected fading AGN, we fitted the mid-IR spectra of the 31 candidates with available *Spitzer* spectra with five mid-IR AGN dust models. Interestingly, we found that most of our sources preferred a torus-like rather than a disk-wind geometry. This is consistent with a fading phase because the production of wind requires more energy. This is consistent with other studies that find that lower luminosity AGN are commonly fitted with torus-like geometries, contrary to powerful AGN that need the inclusion of dust in the wind (González-Martín et al., 2019b). The existence of jets and the lack of winds/outflows in the rising and fading stages of the duty cycles are consistent with the switch off of the AGN duty cycle (e.g. King et al., 2011; Fender & Belloni, 2012; Fender & Muñoz-Darias, 2016). This shows how important is the study of the evolution of these AGN components to understand how this process occurs.

This thesis is an honest attempt to unveil the properties of AGN obscuration by developing new techniques and the use of all available information in large collections of AGN. We have just conquered the tip of the iceberg by showing the complexity of the AGN obscuration material and its plausible dependence on the evolutionary stage of nuclear activity.

Chapter 7

Future Work

The results and tools obtained in this thesis are promising for future advances in the AGN field. In this last chapter, we mention some of the forthcoming investigations that could be developed based on this work in the following years.

The simultaneous fitting technique could be applied to the sample of AGN created by Esparza-Arredondo et al. (2021) to constrain the physical parameters of their tori. This will allow us to restrict the parameters of the torus, which has been hard to obtain from previous mid-IR or X-ray studies. The combination of these two wavelengths will subsequently allow us to study whether the toroidal properties change with the type of AGN activity (e.g., bolometric luminosity, accretion rate, or BH mass). Furthermore, these results could be compared with those related to the circumnuclear environment, like the star-formation rate reported in previous works (e.g. Esparza-Arredondo et al., 2018), under the hypothesis that the AGN obscurer evolves with the host galaxy.

The simultaneous fitting technique could also be improved in the following aspects.

- **Incorporation of X-ray clumpy torus model.** Currently, the simultaneous fitting code only considers the smooth model at X-ray because the clumpy model was not available when our work on IC 5063 was developed in 2019. It is necessary to add this model to test the combinations that include it. Esparza-Arredondo et al. (2021) found that the complexity of the gas and dust distribution allows for clumpy-clumpy, smooth-smooth, and smooth-clumpy combinations. This needs to be taken into account to perform this new simultaneous fitting. Furthermore, our pilot source (IC 5063) was included in these individual fits and revealed that the best combination is clumpy-clumpy. In contrast, a simultaneous fit showed that a smooth-smooth combination was the best option (Esparza-Arredondo et al., 2018). The inclusion of this new model allows us to compare and choose the best combination of models.

- **Incorporation of X-ray reflection disk model.** Twelve sources show that the reflection component at X-rays is partially associated with the accretion disk. This could be analyzed using a modification of the simultaneous fitting procedure such that it also considers a contribution from a disk reflection model. For that purpose, new

data at soft X-rays (perhaps using *XMM-Newton* or *Chandra*) is needed to disentangle disk from torus reflection since disk reflection has significative signatures at soft X-rays from the ionized plasma that can better distinguish this contribution from the torus reflection. Furthermore, this new data need to be simultaneously fit to avoid issues due to the intrinsically variable nature of these sources.

- **Incorporation of soft X-rays.** Although *NuSTAR* data are unique to track the reflection component thanks to the high energies above 10 keV, these data are only sensitive to relatively large absorption due to the lack of spectra below 3 keV. The inclusion of soft X-rays in the analysis will also help to improve the resulting absorption measurements when the column density is low.

- **Further investigation on the covering factors.** As shown in chapter 3, the covering factors estimated from X-rays in type-1 Seyferts are somehow misleading, probably due to other components contributing to the soft X-rays rather than the scattered light from the intrinsic continuum (which is how we infer the covering factor). An investigation about how to estimate the covering factor of Seyfert 1 is necessary, probably also adding soft X-rays.

- **New and more realistic models at both X-rays and mid-IR wavelengths.** As shown in this work, X-ray models are simpler and less realistic than mid-IR models. Indeed, the disk-wind model was not tested for our sample due to the lack of similar models at X-rays. X-ray radiative transfer codes like REFLEX could be used to add new models that could help us to investigate further complexity in the data. Although in some advantage, the mid-IR models always rely on the ISM dust composition and grain size distributions. New modeling allowing to change these aspects is desirable for a better comprehension of the nature of the torus. This could be done with the radiative transfer code SKIRT.

Alternatively, this work could continue to develop to the understanding of the AGN activity. An observational proposal to *NuSTAR* could be submitted to observe the fading AGN candidates. These spectra could be fit individually to try to understand the accretion state and obscurer properties. This sample could be used in combination with current *Spitzer* spectra to characterize the obscurer in these sources. Furthermore, this work can also be extended with future *JWST* data for fainter AGN (either lower-luminosity of more distant sources). Thus, the tools developed in this work are a new promising endeavor.

Appendices

Appendix A

Coevolution between AGN and host galaxy

The infrared wavelengths are also good tools to study SF in the close proximity of the AGN. The advantage of using SF tracers, in this range, is that they are not contaminated by AGN emission. We will study good traces of the SF in the proximity of the AGN radiation field, to use them to understand the plausible coevolution between AGNs and their host galaxies.

In the mid-IR wavelengths, we can analyze emission lines which are produced by different components of AGNs and/or nuclear SF in the host galaxy. Particularly, we can observe the emission of the Polycyclic Aromatic Hydrocarbons (PAHs) that trace SF (e.g. Peeters et al., 2004; Esquej et al., 2014). The PAHs are molecules in space that contain 20-100 carbon and hydrogen atoms, which are heated a high temperatures due to younger B stars (Peeters et al., 2004). The PAHs emission has been observed in the nuclear region close to the AGN (González-Martín et al., 2013; Alonso-Herrero et al., 2014). Diamond-Stanic et al. (2009) found a strong correlation between nuclear SF at scales of kilo-parsecs using the 11.3μm PAH and 24μm continuum emission in Seyfert galaxies. Other authors have found that PAHs emission is weak or lacking in Sy1 (e.g. Mason et al., 2007). This lack of PAHs could be related to the destruction of the molecules responsible of their emission by the radiation field of the AGN.

These works are based on a comparison of nuclear and circumnuclear SF, using the nuclear spectrum of ground-based telescopes (i.e., with the best spatial resolution available) and the circumnuclear spectra from satellites (i.e., with low spatial resolution, e.g. Esquej et al., 2014). Only, some studies do a detailed analysis of circumnuclear emission using different radial apertures centered in the AGN (e.g. Alonso-Herrero et al., 2014).

At the same range of wavelengths, we can study the [SIV] line emission at 10.5μ m. This line arises from ions with an ionization potential of 35 eV. It has been observed in different objects, such as planetary nebulae, HII galactic regions, and ULIRGS (Rank et al., 1970; Holtz et al., 1971; Gillett et al., 1972). In the case of AGNs, the origin of this line is controversial. Some works suggest that this line is produced in the SF regions and/or NLR (Pereira-Santaella et al., 2010; Groves et al., 2008).

This work includes some results obtained during my masters' studies which were expanded in the following months with data from PIRATAS collaboration. This work was submitted to APJ for publication during my first year of Ph.D.

Author disclosure: This work was developed mostly on my own. Dra. Omaira González-Martín and Dra. Deborah Dultzin helped me to development of the discussion and drafting of this work. The other coauthors gave comments in order to improve the final document. This work was published in Astrophysical Journal on May 30, 2018. The electronic version of this publication can be found in the following URL: https://ui.adsabs.harvard.edu/abs/2018ApJ...859..124E/abstract

The Astrophysical Journal, 859:124 (33pp), 2018 June 1 https://doi.org/10.3847/1538-4357/aabcbc

Circumnuclear Star Formation and AGN Activity: Clues from Surface Brightness Radial Profile of PAHs and [S IV]

Donaji Esparza-Arredondo[1], Omaira González-Martín[1], Deborah Dultzin[2], Almudena Alonso-Herrero[3,4,5], Cristina Ramos Almeida[6,7], Tanio Díaz-Santos[8], Ismael García-Bernete[6], Mariela Martinez-Paredes[1], and Jose Miguel Rodríguez-Espinosa[6,7]

[1] Instituto de Radioastronomía y Astrofísica, Universidad Nacional Autónoma de México, Campus Morelia, Apartado Postal 3-72, 58090, Morelia, Michoacán, México; d.esparza@crya.unam.mx
[2] Instituto de Astronomía, Universidad Nacional Autónoma de México, Apartado Postal 70-264, 04510, CDMX, México
[3] Centro de Astrobiología (CAB, CSIC-INTA), ESAC Campus, E-28692 Villanueva de la Cañada, Madrid, Spain
[4] Department of Physics, University of Oxford, Oxford OX1 3RH, UK
[5] Department of Physics and Astronomy, University of Texas at San Antonio, San Antonio, TX 78249, USA
[6] Instituto de Astrofísica de Canarias (IAC), C/Vía Láctea, s/n, E-38205 La Laguna, Spain
[7] Departamento de Astrofísica, Universidad de La Laguna, E-38206 La Laguna, Tenerife, Spain
[8] Núcleo de Astronomía de la Facultad de Ingeniería, Universidad Diego Portales, Av. Ejercito Libertador 441, Santiago, Chile
Received 2017 June 16; revised 2018 April 4; accepted 2018 April 5; published 2018 May 30

Abstract

We studied the circumnuclear mid-IR emission in a sample of 19 local active galactic nuclei (AGNs) with high spatial resolution spectra using T-ReCS (Gemini) and CanariCam (GTC), together with *Spitzer*/IRS observations. We measured the flux and the equivalent width for the 11.3 μm PAH feature and the [S IV] line emission as a function of galactocentric distance. This allowed us to study the star formation (SF) at subkiloparsec scales from the nucleus for a large sample of nearby AGNs. The [S IV] line emission could be tracing the AGN radiation field within a few thousand times the sublimation radius (R_{sub}), but it often peaks at distances greater than 1000 R_{sub}. One possibility is that the SF is contributing to the [S IV] total flux. We found an 11.3 μm PAH emission deficit within the inner few tens of parsecs from the AGN. This deficit might be due to the destruction of the molecules responsible for this feature or the lack of SF at these distances. We found a sensible agreement in the expected shift of the relation of the AGN bolometric luminosity and the SF rate. This indicates that numerical models attributing the link between AGN activity and host galaxy growth to mergers are in agreement with our data, for most inner galaxy parts.

Key words: galaxies: active – galaxies: evolution – galaxies: nuclei

1. Introduction

The understanding of the coevolution of active galactic nuclei (AGNs) and the host galaxy has been one of the greatest challenges in astronomy in the past decades. Several studies have discovered correlations between the mass of the supermassive black hole (SMBH), the mass of the bulge (Magorrian et al. 1998; Tremaine et al. 2002; Marconi & Hunt 2003; McConnell & Ma 2013), and the bulge velocity dispersion (Kormendy & Richstone 1995; Ferrarese & Merritt 2000). However, the physical connection between these observational properties is still unclear. The study of SMBH accretion and circumnuclear[9] star formation (SF) can be the key. Some authors propose that the gas that moves toward the center is responsible for both the growth of the SMBH and the enhancement of SF (Sanders et al. 1988; Barnes & Hernquist 1991; Storchi-Bergmann et al. 2001). Other works suggest that quenching of SF is due to AGN feedback (Silk & Rees 1998; Vollmer & Davies 2013, and references therein).

Numerical simulations propose a scenario where large-scale processes can be related to small-scale phenomena close to the nucleus (e.g., Kawakatu & Wada 2008; Hopkins & Quataert 2010; Neistein & Netzer 2014; Gutcke et al. 2015; Volonteri et al. 2015). According to these studies, major mergers and even tidal interactions produce perturbations that can be correlated with the accretion of the SMBH and SF (Krongold et al. 2002). Other authors propose a scenario in which the radiation field of the SMBH is able to stop the SF, imposing a balance between the two (e.g., Wu et al. 2009).

The study of the neighborhood of AGNs is very complex because the classic indicators of SF such as the ultraviolet (UV) continuum, Paα, and Hα emission line are easily contaminated by the powerful AGN emission (Alonso-Herrero et al. 2014, and references therein). However, the mid-infrared (MIR) wavebands are a powerful tool to disentangle SF and AGN contributions (e.g., Dultzin-Hacyan et al. 1990; González-Martín et al. 2013; Alonso-Herrero et al. 2014). Recently, new MIR spectroscopic data have provided opportunities to quantify the SF close (<1 kpc) to the AGN (e.g., Esquej et al. 2014; Ruschel-Dutra et al. 2017). The polycyclic aromatic hydrocarbon (PAH) emission features at 3.3, 6.2, 7.7, 8.6, and 11.3 μm contribute to MIR flux. The PAHs are composed of 20–100 atoms of carbon and hydrogen (Millar & Williams 1993). These features are powerful tools to study SF on the vicinity of AGNs. These molecules have been studied in different objects associated with dust and gas including evolved stars, reflection nebulae, Orion bars, and star-forming regions (Gillett et al. 1973; Cohen et al. 1986; Aitken & Roche 1984). It is known that the PAH emissions are good tracers of young and massive stars (i.e., recent circumnuclear SF activity). In particular, starburst galaxies show a good correlation between the strength of the PAH and the IR luminosity, indicating that they are good tracers of SF (Brandl et al. 2006).

[9] We considered circumnuclear scales at distances less than 1 kpc.

Among these PAH features, the 11.3 μm PAH feature has the advantage of being isolated (i.e., not blended) from others and is observable with ground-based telescopes (i.e., with enough spatial resolution to disentangle the contribution of the few tenths of parsecs from the nucleus in nearby galaxies). Indeed, the 11.3 μm PAH emission feature has been used in several works to study the SF in the vicinity of AGNs (e.g., Diaz-Santos et al. 2010). Recently, Esquej et al. (2014) computed the SF rate (SFR) from this feature and compared it with the AGN accretion rate. They confronted this relation with coevolution models elaborated by Hopkins & Quataert (2010). They found a good agreement between observations and theoretical models for physical scales of $\sim$100 pc. Recently, Ruschel-Dutra et al. (2017) have analyzed the circumnuclear SF in a sample of 15 AGNs in order to investigate the validity of the same relation. They found that SF luminosities are correlated with the bolometric luminosity of the AGN (for objects with $L_{\rm bol,AGN} \geqslant 10^{42}$ erg s^{-1}).

The PAH features have been studied in the vicinity of the AGNs of many galaxies. Some authors claim that these molecules are destroyed by the strong AGN radiation field (Voit 1992; Wu et al. 2009; Diaz-Santos et al. 2010). Siebenmorgen et al. (2004) and Ruschel-Dutra et al. (2014) have found evidence in favor of this destruction of PAHs in AGNs. Supporting this, the correlation between the strength of the PAH features and the IR luminosity appears to be absent or weak in AGNs (Weedman et al. 2005). If this were the case, the PAH emission feature could not be used as a tracer of SF in AGNs. In a more recent paper, it has been suggested that PAH emission might not be a good tracer of the SF within 1 kpc around an AGN (Jensen et al. 2017).

Against it, Alonso-Herrero et al. (2014) concluded that at least those molecules responsible for the 11.3 μm PAH feature survive in the nuclear environment as close as 10 pc from the nucleus for their sample of six local AGNs (see also Esquej et al. 2014; Ramos Almeida et al. 2014). They propose that material in the dusty tori, nuclear gas disk, and/or host galaxies of AGNs is likely providing the column density necessary to protect the PAH molecules from the AGN radiation field.

Here we investigate whether the 11.3 μm PAH can be used (and at which scales) as a tracer of SF, and we use it to get some clues about the coevolution between the AGN and its host galaxy. For that purpose we have compiled a sample of high spatial resolution spectra (8–13 μm) of local AGNs observed with T-ReCS in the Gemini South observatory and CanariCam on the 10.4 m Gran Telescopio CANARIAS (GTC). This allowed us to study the SF at different scales from the nucleus for a large sample of sources. The coverage of these spectra will also allow us to analyze the origin of the [S IV] line emission at 10.5 μm. The [S IV] line arises from ions with an ionization potential of 35 eV. It has been proposed as an indicator of the AGN isotropic luminosity since it might come from the narrow-line region (NLR; Dasyra et al. 2011). However, high spatial resolution MIR spectra indicate that this emission is not resolved at 100 pc scales, against its NLR origin (Hönig et al. 2008). The [S IV] line emission at 10.5 μm could also be related to star-forming regions (Pereira-Santaella et al. 2010). Our high spatial resolution spectra are very well suited to understand the origin of the [S IV] line emission.

The main goal of this work is to address three questions: (1) the origin of [S IV] line emission, (2) the goodness of the 11.3 μm PAH feature as a tracer of SF in the vicinity of AGNs, and (3) the connection between SF and AGN activity. The paper is organized as follows: Section 2 presents our sample and the data reduction. Section 3 presents the analysis of the spectra. Sections 4 and 5 provide a discussion of the main results in the framework of our goals. Finally, a brief summary is given in Section 6. Throughout this work, we assumed a ΛCDM cosmology with $\Omega_\Lambda = 0.73$, $\Omega_{\rm M} = 0.27$, and $H_0 = 70$ km s^{-1} Mpc^{-1}.

2. Sample Selection and Data Reduction

2.1. Sample

Our sample consists of 19 local AGNs with ground-based *N*-band (i.e., 8–13 μm) spectra available. All spectra have been observed with ground-based telescopes. These sources are taken from the samples of González-Martín et al. (2013) and Alonso-Herrero et al. (2016), which contain 22 and 45 local AGNs, respectively. We have only included AGNs showing extended emission. We considered the source as extended if we can detect emission of the 11.3 μm PAH feature or [S IV] line in more than three circumnuclear apertures (see Section 3 for a detailed explanation on the aperture extraction procedure).

This sample is the largest reported where high-resolution studies have been done in the vicinity of AGNs. However, note that this sample is not complete in any sense. Table 1 shows the main observational details of the sample. Fifteen objects are type 2 Seyferts (Sy2), and four are type 1 Seyferts (Sy1). Our sample covers a range of X-ray luminosity (absorption corrected) of $L(2\text{–}10\,{\rm keV}) \sim 5 \times 10^{39}$–$4 \times 10^{43}$ erg s^{-1}. The range of X-ray luminosity covers classical Seyfert galaxies and low-luminosity AGNs ($<10^{42}$ erg s^{-1}). The Appendix contains a short review of the published information on star-forming regions around these objects, when available.

Eleven objects were observed with the Thermal-Region Camera Spectrograph (T-ReCS; Telesco et al. 1998; De Buizer & Fisher 2005) located in the 8.1 m Gemini South Telescope and published by González-Martín et al. (2013) (and references therein). The slit width used for the spectroscopy results in a spatial resolution in the range of $\sim$20–250 pc (see Column (9) in Table 1). The rest of the sources in our sample were obtained with CanariCam (Telesco et al. 2003) in the 10.4 m Gran Telescopio CANARIAS (GTC) and were published by Alonso-Herrero et al. (2016). For these eight sources the slit width used for the spectroscopy results in a spatial resolution in the range of $\sim$50–160 pc. The angular and spectral resolutions for both instruments (T-ReCS and CanariCam) are within an average of FWHM $\sim$ 0.3 arcsec and $R \sim 100$, respectively. Note that these spectral resolutions are not high enough to examined the width of the [S IV] line. Indeed, all the [S IV] emission lines reported here have a width compatible with the instrumental spectral resolution.

We have included the *Spitzer*/IRS spectral data downloaded from the CASSIS[10] catalog (the Cornell AtlaS of *Spitzer*/IRS Sources; Lebouteiller et al. 2011) to study larger regions in each galaxy. Note that the spectral resolution of *Spitzer*/IRS ($R \sim 60$–130) is similar to that obtained by our ground-based observations. CASSIS provides flux-calibrated nuclear spectra associated with each observation. The *Spitzer* spectra are not available for four of the sources in our sample (NGC 931, NGC 1320, NGC 4569, and NGC 7465). In four additional

[10] http://cassis.astro.cornell.edu/atlas/

Table 1
General Properties of Sample

Object	Type	D (Mpc)	L_x [A] log(L(2–10 keV))	M_{BH} [B] log($M/M_\odot$)	Instrument	P.A. (deg)	Scale Factor	Slit Width (Nuclear) (arcsec/pc)	*Spitzer* Slit Width (arcsec/pc)	Radius (in/out) (pc/pc)	R_{subl} (pc)	logd_{25} log(0.1 arcmin)	Ref.
(1)	(2)	(3)	(4)	(5)	(6)	(7)	(8)	(9)	(10)	(11)	(12)	(13)	(14)
NGC 931	Sy1	49.4	43.3 (c)	8.3 (I)	CanariCam	80	–	0.52/124.5	–	93.4/242.8	0.24	1.39	2
Mrk 1066	Sy2	51.7	42.9 (a)	7.0 (I)	CanariCam	315	1.23	0.52/130.3	3.7/927.3	87.9/440.3	0.09	1.08	2,4
NGC 1320	Sy2	37.7	42.5 (c)	7.2 (I)	CanariCam	315	–	0.52/95.0	–	149.7/406.4	0.03	1.27	2
NGC 1386	Sy2	16.2	41.6 (a)	7.4 (I)	T-ReCS	0	1.17	0.31/24.4	3.7/291.1	31.8/88.3	0.02	1.55	1
NGC 1808	Sy2	11.5	39.7 (a)	6.7 (II)	T-ReCS	45	1.35	0.35/19.6	3.7/207.2	27.6/62.8	0.002	1.73	1
NGC 2992	Sy1.8	31.6	41.9 (c)	7.7 (I)	CanariCam	30	0.4	0.52/79.7	3.7/566.8	59.7/741.2	0.03	1.47	2
NGC 3081	Sy2	32.5	42.5 (b)	7.1 (II)	T-ReCS	0	0.96	0.65/102.4	3.7/582.9	63.6/205.0	0.06	1.43	1
”	”	”	”	”	”	350	0.92	”	”	91.9/205.1	”	”	
NGC 3227	Sy1.5	21.8	42.1 (c)	7.6 (I)	CanariCam	0	0.64	0.52/54.9	3.7/391.0	74.2/205.6	0.04	1.60	2
NGC 3281	Sy2	21.8	43.2 (a)	7.9 (II)	T-ReCS	315	0.61	0.35/77.6	3.7/820.0	109.4/248.6	0.14	1.49	1,4
NGC 4253*	Sy1	55.4	42.5 (c)	6.8 (III)	CanariCam	285	0.75	0.52/139.6	–	94.2/408.3	0.06	0.95	2
NGC 4569	Sy2	12.6	39.4 (e)	7.8 (IV)	CanariCam	30	–	0.52/31.7	–	19.1/285.9	0.004	1.96	2
NGC 5135*	Sy2	58.6	43.1 (b)	7.3 (II)	T-ReCS	30	1.33	0.70/199.0	–	89.3/1033.5	0.13	1.38	1,3
NGC 5643	Sy2	16.9	42.6 (b)	7.4 (II)	T-ReCS	80	0.68	0.35/28.7	3.7/303.1	55.2/106.6	0.07	1.72	1
IC 4518W*	Sy2	69.6	42.6 (b)	7.5 (V)	T-ReCS	5	1.22	0.70/236.3	–	166.7/560.6	0.07	1.10	1,3
IC 5063*	Sy2	48.6	42.9 (c)	7.7 (I)	T-ReCS	303	1.33	0.65/153.1	–	95.2/306.7	0.09	1.43	1,5
NGC 7130	Sy2	69.2	42.9 (a)	7.6 (II)	T-ReCS	348	1.35	0.70/234.7	3.7/1240.7	135.4/496.6	0.09	1.19	1,3
NGC 7172	Sy2	33.9	42.7 (a)	7.7 (II)	T-ReCS	60	0.57	0.35/57.5	3.7/608.0	95.8/228.6	0.08	1.44	1,6
NGC 7465	Sy2	27.2	41.4 (d)	7.6 (VI)	CanariCam	330	–	0.52/68.6	–	46.3/200.6	0.03	1.03	2
NGC 7582	Sy2	22.5	42.6 (b)	7.1 (II)	T-ReCS	0	0.39	0.70/76.4	3.7/403.6	53.8/396.6	0.07	1.84	1

Notes. Column (1): source name. Column (2): type of sources according to González-Martín et al. (2013) or Alonso-Herrero et al. (2016). Column (3): distances calculated from redshift obtained from observations for $\Omega_\Lambda = 0.73$, $\Omega_M = 0.27$, and $H_0 = 70$ km s^{-1} Mpc^{-1}. Column (4): X-ray luminosity. Column (5): BH mass. Column (6): instrument used by each object. Column (7): position angle. Column (8): scale factor between T-ReCS/CanariCam and *Spitzer* spectra. The mark "*" is used to identify the sources where we do not use the *Spitzer* spectra. Column (9): Slit width for nuclear spectra. Column (10): slit width for *Spitzer* spectra. Column (11): minimum and maximum radius used for the extended profiles (T-ReCS or CanariCam). Column (12): sublimation radius. Column (13): isophotal diameter. Column (14): references where the observations were originally published: (1) González-Martín et al. 2013; (2) Alonso-Herrero et al. 2016; (3) Diaz-Santos et al. 2010; (4) Sales et al. 2011; (5) Young et al. 2007; (6) Roche et al. 2007.

[A] The references for the X-ray results are (a) González-Martín (2018), (b) González-Martín et al. (2013), (c) Liu et al. (2014), (d) O'Sullivan et al. (2001), (e) Ho et al. (2001).

[B] The BH mass is calculated using the relation with the stellar velocity dispersion. References: (I) Woo & Urry (2002), (II) Esquej et al. (2014), (III) Woo et al. (2015), (IV) Mason et al. (2015), (V) Alonso-Herrero et al. (2013), (VI) Dudik et al. (2005).

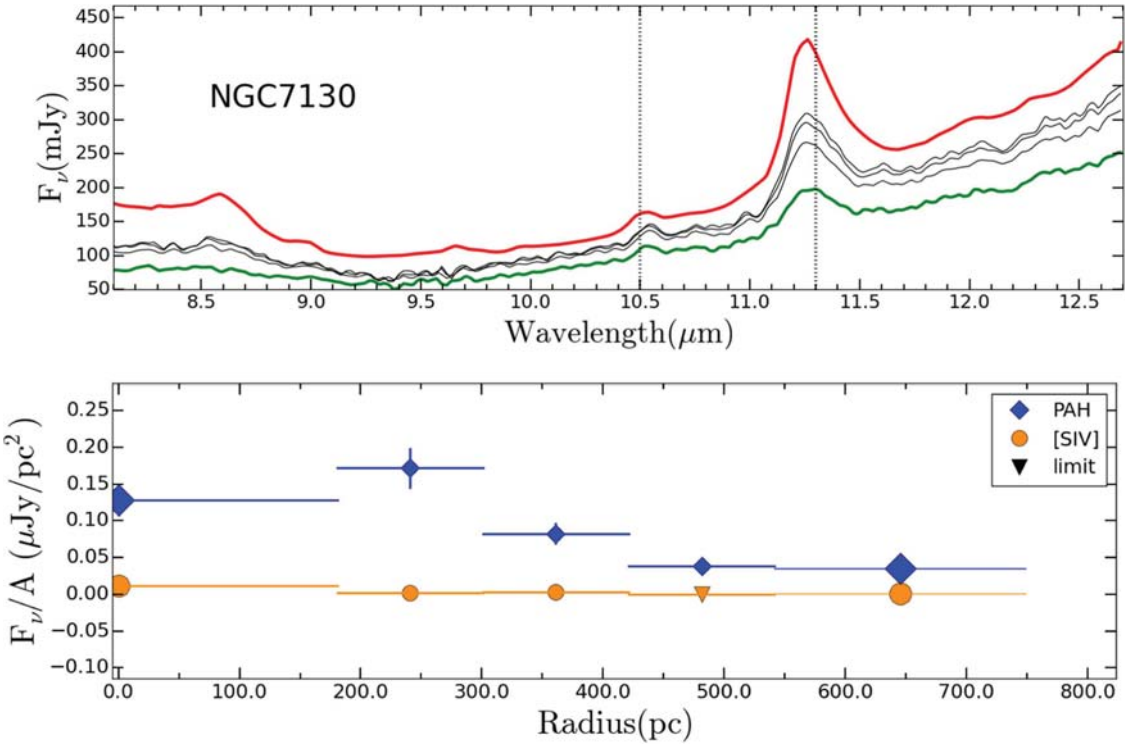

Figure 1. Top: extracted spectra at different scales for NGC 7130. The red line is the spectrum obtained by *Spitzer*, and the green and black lines correspond to the nuclear spectrum and extended-aperture spectra, respectively. The dotted lines show the PAH feature and [S IV] line emissions. Bottom: surface brightness radial profiles in units of μJy/pc^2 for NGC 7130. We first extracted the flux at the radius of each aperture, and then we subtracted that of all inner apertures to get the flux of a ring. The radial profile for 11.3 μm PAH emission is presented with blue diamonds, while the radial profile for [S IV] line emission is shown with orange circles (the triangles are limit values). The larger symbols (diamonds or circles) correspond to the nuclear and *Spitzer* spectra, respectively. The rest of the symbols represent the measurements for the extended apertures.

sources we did not use the *Spitzer* data because the emission of the ground-based data extends up to the spatial resolution of *Spitzer* data. Therefore, these observations do not add extra information to our ground-based data. Thus, we included *Spitzer*/IRS spectra for 11 of the objects; Column (10) in Table 1 shows the *Spitzer* radius spectra when we used them in the analysis.

González-Martín et al. (2013) and Alonso-Herrero et al. (2016) focused their analyses on the nuclear emission. Also focusing on the central region, four sources have been observed with VISIR/VLT and reported by Hönig & Kishimoto (2010). Furthermore, the MIR extended emission of some of our sources has been studied individually before. Three of our sources (NGC 5135, IC 4518W, and NGC 7130) were studied by Diaz-Santos et al. (2010). They studied the extended emission of different features, including the 11.3 μm and the [S IV] line, and they compared it with the *Spitzer* spectra. Mrk 1066 was analyzed by Ramos Almeida et al. (2014) and Alonso-Herrero et al. (2014) to study the survival of the responsible molecules for the 11.3 μm PAH feature in the close vicinity of an AGN. García-Bernete et al. (2015) studied the extended emission of NGC 2992 up to $\sim$3 kpc, finding that PAH features might indicate that the bulk of this extended emission is dust heated by SF. Esquej et al. (2014) compared nuclear with larger apertures (using *Spitzer* spectra) in 12 of our sources to study the correlation between SFR through the 11.3 μm PAH feature and AGN accretion. These works will be compared with our results throughout this paper.

2.2. Data Reduction

The data have been reduced using the RedCan pipeline (González-Martín et al. 2013). RedCan is a fully automated pipeline that was designed to efficiently exploit CanariCam data. Due to the similarities between CanariCam and T-ReCS low spectral resolution data, this pipeline can analyze successfully both sets of observations considered in this paper. RedCan is able to produce flux-calibrated images and 1D spectra. The main input is an ASCII file, which contains an observation list. The reduction process basically consists of eight steps: (1) identification of files, (2) flat-fielding, (3) stacking, (4) image flux calibration, (5) wavelength calibration, (6) trace determination, (7) spectral extraction, and (8) spectral flux calibration and the combination of spectra. Within these steps, the subtraction of the sky background and rejection of bad images are also included. Flux calibration is performed by observing standard stars taken immediately before or after the target.

Spitzer/IRS spectra provided by CASSIS are already reduced. However, observations using data from both short–low and long–low spectra modules suffer from mismatches due to telescope pointing inaccuracy or due to a different spatial resolution of the IRS orders. This is not corrected in the final products given by CASSIS. Still, in this work it is not necessary to correct these mismatches, because we only considered one spectrum (SL1). This spectrum only covers a range between 7.5 and 15 μm. Finally, the spectra are shifted to the rest frame according to the distances of the objects (see Column (3) in Table 1).

Table 2
Integrated Fluxes and EWs for the Nuclear and *Spitzer* Spectra

Object	Fluxes (10^{-13} erg s^{-1} cm^{-2})				EW (10^{-3} μm)			
	$PAH_{11.3\ \mu m}$		$[S\ IV]_{10.5\ \mu m}$		$PAH_{11.3\ \mu m}$		$[S\ IV]_{10.5\ \mu m}$	
	Nuclear	*Spitzer*	Nuclear	*Spitzer*	Nuclear	*Spitzer*	Nuclear	*Spitzer*
NGC 931	<2	–	13 ± 2	–	<1	–	10 ± 2	–
Mrk 1066	82 ± 12	264 ± 40	<0.1	11 ± 2	118 ± 18	158 ± 25	<0.2	19 ± 3
NGC 1320	7 ± 2	–	6 ± 1	–	9 ± 3	–	7 ± 1	–
NGC 1386	<0.3	16 ± 2	17 ± 3	23 ± 4	<1	14 ± 2	28 ± 5	26 ± 4
NGC 1808	154 ± 24	1176 ± 178	<0.1	<7	107 ± 16	167 ± 26	<0.3	<2
NGC 2992	<6	160 ± 25	4 ± 1	10 ± 2	<22	149 ± 25	17 ± 3	19 ± 4
NGC 3081	<0.2	6 ± 2	10 ± 4	29 ± 12	<1	9 ± 2	23 ± 12	39 ± 6
NGC 3081	<0.1	6 ± 1	12 ± 4	29 ± 10	<0.1	9 ± 3	26 ± 8	38 ± 14
NGC 3227	32 ± 5	176 ± 29	10 ± 2	9 ± 3	41 ± 6	119 ± 21	13 ± 2	11 ± 3
NGC 3281	<0.3	<12	10 ± 2	18 ± 5	<0.4	<13	15 ± 2	30 ± 6
NGC 4253	22 ± 3	–	5 ± 1	–	37 ± 6	–	9 ± 1	–
NGC 4569	32 ± 5	–	<0.02	–	115 ± 18	–	<0.1	–
NGC 5135	14 ± 2	–	9 ± 1	–	40 ± 6	–	28 ± 5	–
NGC 5643	5 ± 1	74 ± 11	10 ± 2	15 ± 2	12 ± 2	110 ± 17	29 ± 5	37 ± 6
IC 4518W	<0.1	–	<0.1	–	<0.3	–	<0.2	–
IC 5063	<7	–	9 ± 1	–	<3	–	5 ± 1	–
NGC 7130	39 ± 6	145 ± 22	4 ± 1	6 ± 1	74 ± 11	132 ± 20	12 ± 2	14 ± 2
NGC 7172	<0.5	33 ± 5	2.1 ± 0.4	5 ± 1	<1	70 ± 11	25 ± 4	24 ± 4
NGC 7465	14 ± 2	–	<0.1	–	54 ± 9	–	<0.3	–
NGC 7582	8 ± 1	182 ± 28	<0.1	6 ± 1	27 ± 4	177 ± 28	<0.1	23 ± 4

Note. The symbol "–" indicates that *Spitzer* spectra were not available.

Table 3
PAH and [S IV] Fluxes

Object	Fluxes (10^{-13} erg s^{-1} cm^{-2})							
	$PAH_{11.3\ \mu m}$				$[S\ IV]_{10.5\ \mu m}$			
	100 pc	200 pc	500 pc	700 pc	100 pc	200 pc	500 pc	700 pc
NGC 931	–	–	–	–	21 ± 3	35 ± 6	40 ± 6	–
Mrk 1066	–	160 ± 25	267 ± 41	273 ± 42	–	9 ± 1	12 ± 2	13 ± 2
NGC 1320	–	–	–	–	7 ± 1	8 ± 1	11 ± 2	–
NGC 1386	–	–	–	–	24 ± 4	24 ± 4	–	–
NGC 1808	486 ± 74	1065 ± 161	–	–	–	–	–	–
NGC 2992	–	–	–	–	11 ± 2	13 ± 2	20 ± 3	–
NGC 3081	–	–	–	–	17 ± 3	28 ± 6	–	–
NGC 3081	–	–	–	–	16 ± 3	27 ± 5	–	–
NGC 3227	80 ± 12	121 ± 18	–	–	9 ± 2	12 ± 2	–	–
NGC 3281	–	–	–	–	–	14 ± 2	–	–
NGC 4253	43 ± 7	60 ± 9	64 ± 10	–	6 ± 1	9 ± 1	13 ± 2	–
NGC 4569	307 ± 47	396 ± 61	–	–	–	–	–	–
NGC 5135	4 ± 1	17 ± 3	60 ± 9	88 ± 13	13 ± 2	21 ± 3	32 ± 5	34 ± 5
NGC 5643	26 ± 4	74 ± 11	–	–	13 ± 2	15 ± 2	–	–
IC 4518W	–	–	–	–	–	7 ± 1	10 ± 2	10 ± 2
IC 5063	–	–	–	–	–	15 ± 2	–	–
NGC 7130	–	65 ± 10	90 ± 14	145 ± 22	–	5 ± 1	6 ± 1	6 ± 1
NGC 7172	5 ± 1	11 ± 2	33 ± 5	–	5 ± 1	5 ± 1	5 ± 1	–
NGC 7465	35 ± 5	44 ± 7	–	–	–	–	–	–
NGC 7582	26 ± 4	56 ± 9	179 ± 27	181 ± 28	–	–	–	–

Note. These measurements have been obtained from interpolation at different distances from the nucleus (see text). Note that the symbol "–" indicates that we do not consider the measurement because the interpolated value is within nuclear radii or at larger radii than our outer radius for the sources.

3. Spectral Analysis

Nuclear spectra were first extracted as point-like sources using RedCan pipeline. These spectra show photometric errors typically of 11% in flux for all objects (Alonso-Herrero et al. 2016). We used these spectra as the nuclear component of our radial profile.

Then, in order to analyze the change in the spectrum at different distances from the nucleus and to study the circumnuclear emission, we have divided the spatial axis of the spectra into apertures at different radii. Thus, each aperture gives the spectrum of the extended emission within this radius, together with the nuclear component. The maximum radius is determined as the largest one where extended emission can be

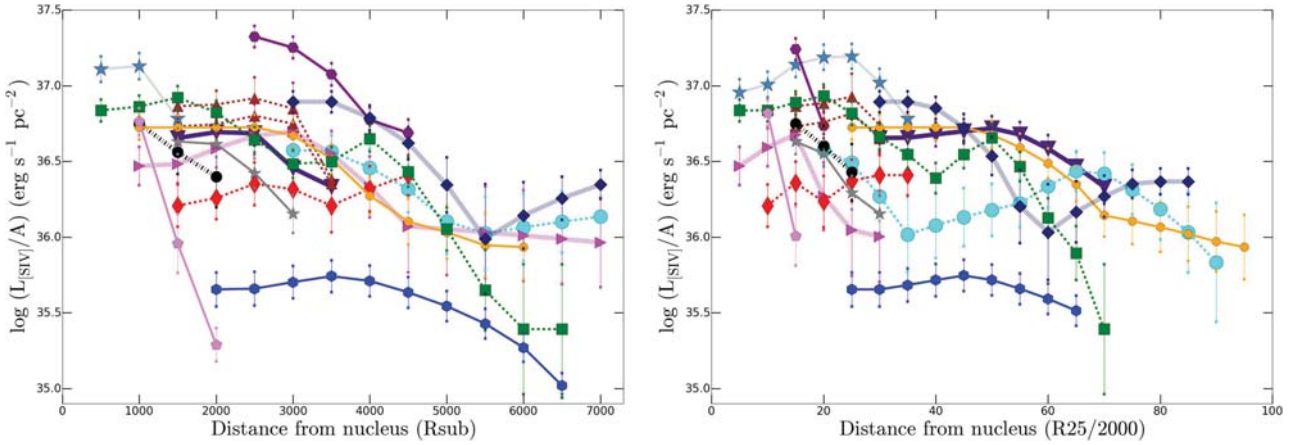

Figure 2. Left: luminosity of the [S IV] line as a function of distance from the nucleus in units of the sublimation radius. Right: luminosity of the [S IV] line as a function of the distance from the nucleus in units of the isophotal radius divided by 2000 for each galaxy. In both figures, the symbols are measurements at fixed distances. The different lines link all the measurements for each object: (1) NGC 931 (steel blue stars), (2) Mrk 1066 (indigo triangles pointing down), (3) NGC 1320 (cyan circles), (4) NGC 1386 (purple hexagons), (5) NGC 2992 (magenta triangles pointing right), (6) NGC 3081 (brown triangles pointing down), (7) NGC 3227 (red thin diamonds), (8) NGC 3281 (black circles), (7) NGC 4253 (orange octagons), (8) NGC 5135 (green squares), (9) NGC 5643 (violet pentagons), (10) IC 4518W (navy blue diamonds), (11) IC 5963 (gray stars), and NGC 7130 (blue hexagons).

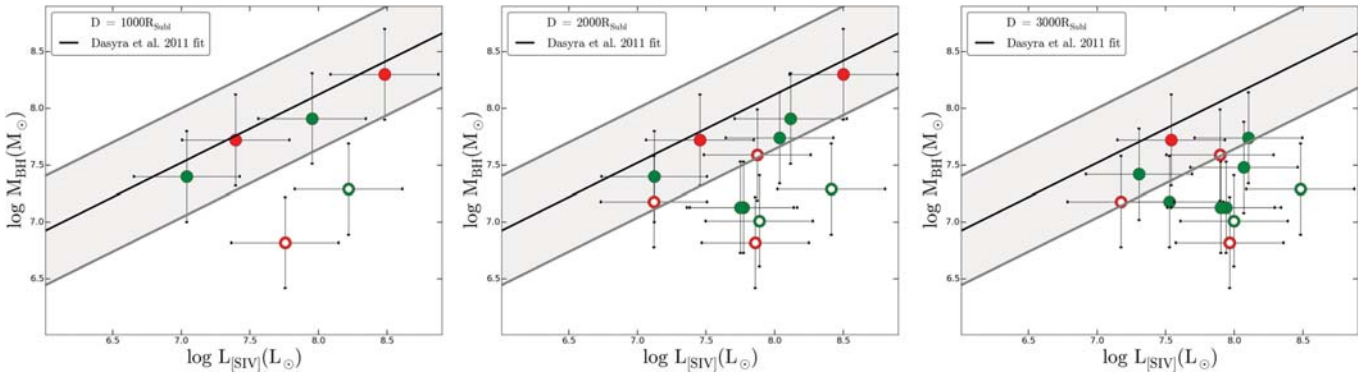

Figure 3. [S IV] line emission luminosity vs. M_{BH} at $1000R_{sub}$, $2000R_{sub}$, and $3000\ R_{sub}$. The white circles are sources where SF regions were previously reported at these spatial scales. The Sy1 and Sy2 are shown as red and green circles, respectively. The relation found by Dasyra et al. (2011) is shown as a black solid line in all panels.

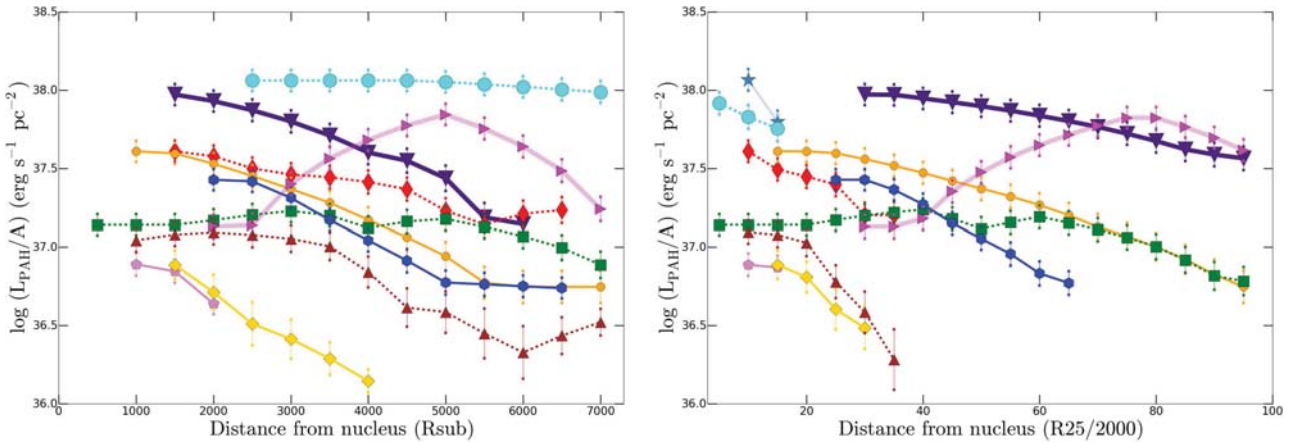

Figure 4. Left: luminosity of the 11.3 μm PAH as a function of distance from the nucleus in units of the sublimation radius. Right: luminosity of the 11.3 μm PAH as a function of the distance from the nucleus in units of the isophotal radius divided by 2000 for each galaxy. In both figures, the symbols are measurements at fixed distances. The different lines link all the measurements for each object: (1) Mrk 1066 (indigo triangles pointing down), (2) NGC 1808 (steel blue stars), (3) NGC 3227 (red thin diamonds), (4) NGC 4253 (orange octagons), (5) NGC 4569 (cyan circles), (6) NGC 5135 (green squares), (7) NGC 5643 (violet pentagons), (8) NGC 7130 (blue hexagons), (9) NGC 7172 (gold diamonds), (10) NGC 7465 (magenta triangles pointing right), and (11) NGC 7582 (brown triangles pointing up).

seen in the 2D spectra. The aperture increments are fixed to 4 pixels because this matches the FWHM of the average point-spread function in our observations. The extraction has been done using the extended source mode provided by RedCan. The minimum radius of the apertures is calculated as the first aperture where the 12 μm continuum flux is greater (or equal)

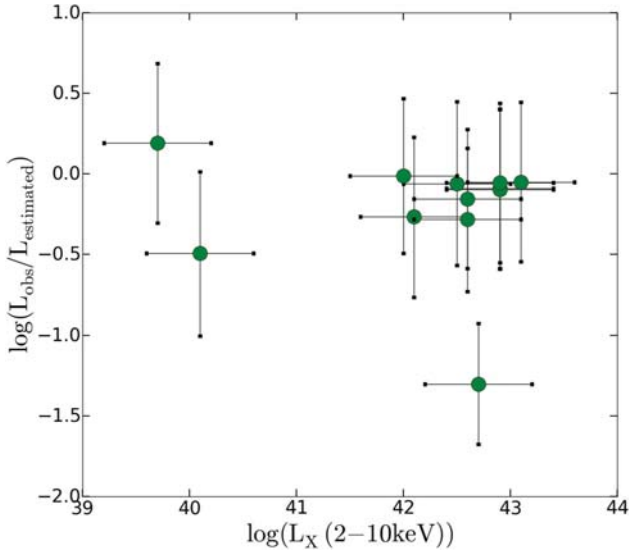

Figure 5. X-ray luminosity vs. PAH luminosity deficit (see text). This deficit is measured as the ratio between the observed and the expected one. The expected PAH luminosity expected is estimated as the linear extrapolation to the center of the radial profile within 200 pc.

than the nuclear continuum flux.[11] Table 1 (Column (11)) reports the minimum (i.e., nuclear component extracted as point-like source) and maximum radius used for the extended profiles in units of pc. We are tracing minimum (maximum) extensions of ∼20 pc (∼1 kpc) in the spatial direction of the 2D spectra.

Since we use T-ReCS/CanariCam and *Spitzer*/IRS spectra together, we have studied the flux cross-calibration from both instruments, for which we have measured the 12 μm continuum flux. We computed a 12 μm radial continuum profile including both T-ReCS/CanariCam and *Spitzer* fluxes (see Section 3.2 for more details about radial profiles). Then, we investigated whether the *Spitzer* flux follows the extrapolation of the T-ReCS/CanariCam radial profile. We found that *Spitzer* spectra (in the sources where it was used) do not extrapolate naturally from the radial distribution observed in high spatial resolution spectra. In five cases, the 12 μm continuum flux for *Spitzer* data is higher than that of ground-based spectra, and in the other six cases, it is lower. A larger integrated *Spitzer* flux than that predicted by the extrapolation of the ground-based spectra is expected because they cover a different area although mapping the same aperture (3.7×3.7 arcsec^2 and slit width $\times$ 3.7 arcsec^2 for *Spitzer* and ground-based data, respectively). Lower integrated *Spitzer* flux is most certainly due to flux calibration uses in the ground-based spectra due to the highly variable sky. In order to correct this cross-calibration problem, we implemented a recalibration of the T-ReCS/CanariCam data for each source. This calibration was implemented as a scaled value for each source as the difference between the extrapolation of the fluxes given in the T-ReCS/CanariCam radial profiles and the *Spitzer* flux at 12 μm. We then multiply the T-ReCS/CanariCam fluxes by this value (see Column (8) in Table 1). Note that the scaled value is not within the reported error range for the *Spitzer* or T-ReCS/CanariCam data. However, the correction applied is in general very small ($|F_{12\ \mu m}(T - ReCS/CanariCam)/F_{12\ \mu m\ (Spitzer)}| \sim 1.3$).

In Figure 1 (bottom) we show NGC 7130 as an example of the data presented in this paper. This example clearly shows the PAH feature at 11.3 μm and the [S IV] line in 10.5 μm. A similar figure for each object in our sample is included in the Appendix.

3.1. PAH Feature and [S IV] Line Measurements

There are several methods to measure the fluxes of the PAH features. The best approach depends on the spectrum characteristics. For instance, PAHFIT (Smith et al. 2007) and DecompIR (Mullaney et al. 2011) are able to measure the PAH features and are very useful when the spectra are highly contaminated by their host galaxy emission. However, they require a wide spectral coverage in order to produce satisfactory results—larger than that of the T-ReCS or CanariCam spectra presented here (see Esquej et al. 2014). Instead, we followed the procedure described by Alonso-Herrero et al. (2014) and Esquej et al. (2014) to measure the flux and the equivalent width (EW). They use the method described by Hernán-Caballero & Hatziminaoglou (2011), which is well suited for limited wavelengths (case of [S IV] line) or weak PAHs. Their method sets a local continuum by interpolating from two narrow bands (i.e., 10.7–10.9 μm and 11.7–11.9 μm) at both sides of the PAH feature or at both sides of the [S IV] line emission (i.e., 10.35–10.40 μm and 10.65–10.75 μm). Note that we selected these continuum ranges individually according to the particularities of each spectrum. This was done to optimize the measurement of the bands according to the natural width of the PAH feature. After subtracting the underlying continuum, residual data were fitted using a Gaussian profile. We compared the fluxes obtained from the Gaussian fit and the direct integration in the case of the nuclear spectra. The discrepancy in the flux between the two methods for the nuclear spectrum is on average less than 3% and 7% for the PAH feature and the [S IV] line, respectively.

Then, the EW of the lines is measured by dividing the integrated flux by the interpolated continuum flux at the center. The uncertainties are obtained by Monte Carlo simulation using the calculated dispersion around the flux measurements. We have applied a smoothing to the high spatial resolution spectra to improve the signal-to-noise ratio of the features. This smoothing was applied to the data using the average of three near spectral bins. The smoothing causes a peak dilution, which could dilute the emission lines if they are less than three points. Nevertheless, the lines that we studied are broad; therefore, we do not expect to have any significant effect on the results (see Alonso-Herrero et al. 2014, for more details on the smoothing technique). Table 2 shows integrated fluxes and EW measurements from each emission obtained with the nuclear and *Spitzer*/IRS spectra.

3.2. Surface Brightness Radial Profiles

We create surface brightness and EW radial profiles[12] for each object. We first extracted the flux at the radius of each aperture, and then we subtracted that of all inner apertures to get the flux of a ring. When the subtracted measurement was

[11] The nuclear continuum is extracted as a point source using the trace of the standard star (see González-Martín et al. 2013, for more details).

[12] We use the term "radial profile" for referring to the surface brightness radial profiles.

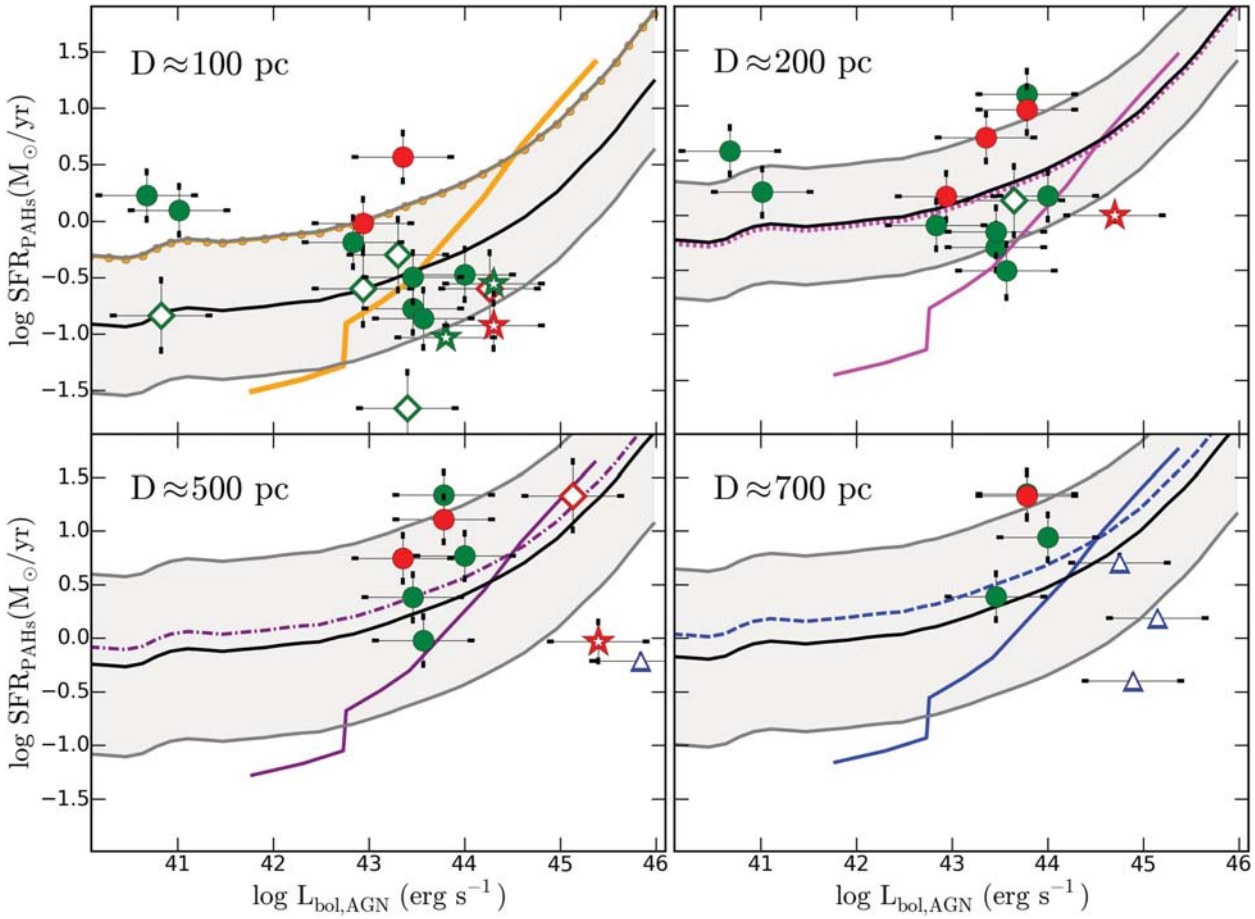

Figure 6. SFR vs. bolometric AGN luminosity at different distances. Each panel corresponds to the integrated SFR_{PAHs} for the 100, 200, 500, and 700 pc apertures, respectively. The QSO observations from Martinez-Paredes et al. (submitted) are shown as blue triangles. The Seyfert galaxies from Esquej et al. (2014), Ruschel-Dutra et al. (2017), and our work are shown as starts, diamonds, and circles, respectively. The Sy1 and Sy2 are shown as red and green circles, respectively. The dashed and solid lines in all panels correspond with the correlations proposed by Neistein & Netzer (2014) as a function of radius shifted using the predictions given by Hopkins & Quataert (2010) (see text). The dashed line is the simulated SFR value for a given $L_{bol,\ AGN}$, and the solid line corresponds to the average $L_{bol,\ AGN}$ for a given value of SFR according to Neistein & Netzer (2014). The black solid line and the shaded area in each panel show the average and standard deviation of the best shift to the relation predicted by Neistein & Netzer (2014), respectively.

Table 4
Comparison with Models by 11.3 μm PAH

Distance	Theory	Measurement	
		Mean	σ
100 pc	1.00	1.09	0.60
200 pc	1.06	0.88	0.70
500 pc	1.23	0.91	0.75
700 pc	1.35	0.95	0.80

Note. For the PAH feature, we have computed the observed shift for the relation as the average and standard deviation of the relation predicted by Neistein & Netzer (2014). For more information see Section 5.2.

lower than 3σ, we considered it as a limit. We then divided each value by its respective area to correct for different aperture radii. In the case of the nucleus, the area is computed with the radius of the unresolved emission times the slit width. For the rest of the apertures, the area is calculated as the slit width times increment radius for the aperture (i.e., 2 pixels; see Table 1, Column (7)).

Figure 1 (bottom) shows the radial profile for the PAH feature at 11.3 μm (blue diamonds) and [S IV] line emission at 10.5 μm (orange circles). The Appendix includes the radial profiles for the full sample (see Figures 7–26).

In order to analyze the behavior of the two emission features across the full sample, we calculated the integrated flux at fixed physical scales: 100, 200, 500, and 700 pc. The measurements were calculated from a linear interpolation between the nearest points. Notice that we do not take into account the nuclear measurement to compute these values at a fixed distance. These measurements are reported in Table 3. We report measurements only when our radial profile includes these distances.

4. The Origin of the [S IV] Line Emission

The [S IV] is an emission line typically observed in the planetary nebula, H II regions, and ULIRGs (Rank et al. 1970; Holtz et al. 1971; Gillett et al. 1972), as well as AGNs. The origin of the nuclear [S IV] line emission is controversial in the case of AGNs. It can be produced in the NLR and therefore can be a good tracer of gas ionized by the AGNs (Dasyra et al. 2011). However, it can also be related to star-forming regions owing to its relatively low excitation potential (Diaz-Santos et al. 2010; Pereira-Santaella et al. 2010).

Diaz-Santos et al. (2010) studied four LIRG-type objects, finding that half of the [S IV] line emission flux comes from the nucleus. Our sample has three objects in common with theirs (NGC 5135, IC 4518W, and NGC 7130). For NGC 5135 they found that ∼40% of [S IV] line emission integrated flux comes from the nuclear spectrum. Fairly consistent with that, we find that the nuclear spectrum contributes ∼35% to the integrated flux of this emission line. They found that the [S IV] nuclear flux in IC 4518W is smaller than the emission in the integrated spectrum by ∼22%. We also agree that there is an excess of [S IV] emission at 0.5 arcsec (∼200 pc), which is unrelated to the excess of 11.3 μm PAH emission. Diaz-Santos et al. (2010) suggested that this emission is associated with the central AGN. In NGC 7130 we found that 70% of the [S IV] flux comes from the nuclear spectrum, while Diaz-Santos et al. (2010) found that the [S IV] nuclear emission corresponds to 50% of the total flux. In both IC 4518W and NGC 7130, star-forming regions near the nucleus have been found (see the Appendix). Based on the *Spitzer* observations, Pereira-Santaella et al. (2010) could not conclude whether the [S IV] line emission is related to star-forming regions for this object owing to poor data quality. However, they found that extended emission of the [S IV] line can be attributed to star-forming regions, using Pα and Hα images for the other three objects of their sample.

We explored the luminosity of the [S IV] emission line ($L_{[\mathrm{S\ IV}]}$) in the AGN environment by studying the radial profiles of $L_{[\mathrm{S\ IV}]}/L_{\mathrm{Edd}}$ as a function of the sublimation radius (R_{sub}; Nenkova et al. 2008). The latter was computed as

$$R_{\mathrm{sub}} \simeq 0.4\left(\frac{L}{10^{45}\ \mathrm{erg^{-1}}}\right)^{1/2}\left(\frac{1500\ \mathrm{K}}{T_{\mathrm{sub}}}\right)^{2.6}\ \mathrm{pc}, \quad (1)$$

where is assumed to be $T_{\mathrm{sub}} = 1400$ K.

We interpolated the given values of $L_{[\mathrm{S\ IV}]}$ to obtain measurements at the following distances from the nucleus: (1000, 2000, 3000, 4000, 5000, 6000, 7000)R_{sub}. This allowed us to compare the $L_{[\mathrm{S\ IV}]}$ at the same spatial scales. Figure 2 (left) shows the radial profiles of the $L_{[\mathrm{S\ IV}]}$ as a function of R_{sub} using the new measurements for the 13 AGNs in our sample where we detected the [S IV] emission line in more than two apertures. The number of values included in the radial profiles varies owing to the minimum and maximum distances from the nucleus that we can trace. In general, the radial profiles in Figure 2 (left) show a chaotic behavior. It might be plausible that these profiles strongly depend on the gas suppliers around each AGN, adding scatter to the expected behavior. The proper comparison between available gas around AGNs and the [S IV] emission needs to be studied prior to any further conclusions. Figure 2 (right) shows the radial profiles of the [S IV] line as a function of isophotal radius (R_{25}) of the galaxy.[13] We found a similar chaotic behavior.

Dasyra et al. (2011) used the [Ne V], [O IV], [Ne III], and [S IV] line emissions to study the kinematics of the NLR. They concluded that the M_{BH} and the gas velocity dispersion are related to the luminosity of these emission lines originating in the NLR. We studied the relationship between M_{BH} and the luminosity of the [S IV] line emission ($L_{[\mathrm{S\ IV}]}$) to interpret the origin of the line. Figure 3 shows this relation at 1000R_{sub}, 2000R_{sub}, and 3000R_{sub} for the sources where we detected the [S IV] line emission at these scales. The solid line corresponds to the Dasyra et al. (2011) relation:

$$\log(M_{\mathrm{BH}}) = 0.6 \times \log(L_{[\mathrm{S\ IV}]}) + 3.32. \quad (2)$$

This relation is based on the best fit for their AGN sample using *Spitzer*/IRS spectra and considering that the [S IV] line emission only comes from the NLR. The rms scatter computed for this relation is 0.48 dex (shaded area in Figure 3). For a few sources without significant SF, the [S IV] line fluxes follow the Dasyra et al. (2011) relation at scales of ∼1000R_{sub}. However, the sources move away from the relation with increasing distance from the nucleus. This result could be interpreted as H II regions, planetary nebulae, or blue compact dwarfs contributing to the sulfur excitation, along with the AGNs (Groves et al. 2008).

Even if the nuclear [S IV] line emission could arise from photoionization by the AGNs in some of our sources, it could be strongly suppressed by dust because it is inside the broad 9.7 μm silicate absorption feature (Pereira-Santaella et al. 2010). Therefore, it could not be an isotropic measurement of the AGN luminosity. Moreover, the obscuration of the internal parts of the AGN by the dusty torus could also play a major role in the [S IV] line emission attenuation. This could be the case for NGC 7172, showing a large value of the 9.7 μm optical depth ($\tau_{9.7\ \mu\mathrm{m}} = 1.9$; González-Martín et al. 2013). Indeed, a very weak detection of the [S IV] line emissions has been found for this object. We have considered the possibility that attenuation is affecting the [S IV] line emission in the inner parts. We found a deficit between nuclear and the first apertures in five sources (see the Appendix). We have compiled the nuclear $\tau_{9.7\ \mu\mathrm{m}}$ from González-Martín et al. (2013) and Alonso-Herrero et al. (2016), but we did not find any relation between the $\tau_{9.7\ \mu\mathrm{m}}$ and the deficit on the [S IV] line emission flux. Also, Dasyra et al. (2011) found that this obscuration does not significantly affect the relative flux of MIR lines. In summary, in 6 of the 13 sources we did not observe a common decrease in the radial profile, as we would expect if this line were caused by AGN photoionization.

4.1. The [S IV] Emission Line versus the 11.3 μm PAH Feature

The [S IV] emission line could be produced by star-forming regions. If this is the case, we would expect a close resemblance between the [S IV] and PAH radial profiles at these radii.

We compared nine sources where the radial profiles of both the PAH feature and the [S IV] line show more than one measurement at different distances from the nucleus. In all sources, the radial profile for both emissions shows a complex behavior. In six[14] of these nine sources it is clear that the behaviors of the radial profiles of both emissions are not related to each other at any distance. Even with that, it could be the case that the star-forming regions traced by the 11.3 μm PAH feature are not the same as those that give origin to the [S IV] emission in the majority of the sources. A plausible explanation is that both emissions are tracing different stages of SF and thus different degrees of ionizing fluxes. Ideally, to distinguish the type of stars that contribute to the [S IV] line emission, high spatial resolution images of [S IV] line emission, together with

[13] The isophotal diameter of a galaxy is the decimal logarithm of the length of the projected major axis of a galaxy at isophotal level 25 mag arcsec^{-2} in the *B* band. See http://leda.univ-lyon1.fr/leda/param/logd25.html.

[14] NGC 2992, NGC 3227, NGC 5135, NGC 5643, NGC 7172, NGC 7465.

other tracers of SF related to different stages of the SF activity, would be needed.

5. The Behavior of the PAH Emission Feature

In this section, we review the plausible dilution/destruction of PAHs in the innermost parts of the AGN (Section 5.1), and we use PAHs as tracers of SF to study the coevolution of the AGN and its host galaxy (Section 5.2).

5.1. On the Dilution/Destruction of the Nuclear PAHs

The relation between the strength of the PAHs and IR luminosity is weak or absent in galaxies with AGNs (Siebenmorgen et al. 2004; Weedman et al. 2005). An important implication of this is that PAHs might not be used as star-forming tracers in the surroundings of the nucleus because they can be destroyed by the AGN radiation field (Siebenmorgen et al. 2004). The AGN can directly modify PAH grain size distribution and even serve as the excitation source for some PAH emission (Genzel et al. 1998; Laurent et al. 2000; Smith et al. 2007). On the other hand, PAHs could survive because they are shielded from the AGN radiation (Goulding et al. 2012). Even more extremely, PAH could be induced by the AGN radiation field (Jensen et al. 2017). Diamond-Stanic & Rieke (2010) found that the 6.2, 7.7, and 8.6 μm PAH features are suppressed with respect to the 11.3 μm PAH feature in local Seyferts. They speculate that destruction of these features might be related to the fact that they are produced by the smallest aromatic molecules and, therefore, more easily destroyed. Following this argument, the molecules responsible for 11.3 μm PAH emission could survive because they are more difficult to destroy. Already from *IRAS* data, it was pointed out that the emission at the 12 μm band fits very well the predictions that follow from the emission modeling of transiently heated PAH molecules (Dultzin-Hacyan et al. 1990). More recently, Diamond-Stanic & Rieke (2012) found a correlation between the nuclear SF ($<$1 kpc) and SMBH accretion rate, where the nuclear SF is traced by the PAH at 11.3 μm aromatic feature.

We detected the PAH feature at 11.3 μm in 15 out of the 19 objects in our sample ($\sim$90% of our sources), and 10 of these sources show nuclear PAHs ($\sim$58% of our sample). The 11.3 μm PAH feature was measured in more than one aperture in 11 objects along the radial profiles.[15] We found that in eight sources (except NGC 5643, NGC 7172, and NGC 7582) the nuclear EW of the PAH is larger than the one found in the first aperture.[16]

In Figure 4, we show the radial profiles of the $L_{11.3\ \mu\mathrm{m\ PAH}}$ as a function of R_{sub} (left) and $R_{25}/2000$ (right). This figure is similar to Figure 2 from the previous section. We observed a complex behavior. Increments and decrements at different distances were found.

Regarding the 11.3 μm PAH, nuclear fluxes are larger than those of the first aperture only in NGC 1808 and NGC 5135. The unresolved nucleus shows lower flux than the first-aperture PAH flux in most of our cases (7 out of 12, i.e., 60%). When observed, this decrement is seen within $\sim$100 pc. Note that in many cases we do not see a decrease in the radial profile (as, e.g., in NGC 7582), but a drop between the nuclear and the first aperture (e.g., NGC 7172). Therefore, this decrement could be affecting even lower spatial scales. The explanations of this decrement are (1) PAH dilution by AGN continuum,[17] (2) PAH destruction by the radiation field, (3) lack of the inner SF, and (4) the existence of a nuclear ring. In the following we discuss these four possibilities.

Alonso-Herrero et al. (2014) suggested that the apparent decrease in the EW of the PAH feature is an effect of the dilution of the PAH feature by the strong continuum of the AGN in the nuclear apertures. They indeed recovered an increase on the nuclear PAH flux toward the center in their sample of six local AGNs. Meanwhile, the EW of the PAH feature showed an apparent decrease. We have not found a similar behavior in any of our objects, but we only have one object in common with their analysis (MRK 1066). They computed the radial profile in isolated apertures at different distances from the nucleus. In our analysis, we have extracted spectra centered at the nucleus with different radii. Thus, each of our apertures includes the nuclear emission. In order to study the radial profile, we subtracted the previous inner aperture scaled to the area (see Section 3). This way, we avoided the dilution due to this effect. Thus, dilution cannot play a role in the lack of nuclear PAHs in the sources analyzed here.

Siebenmorgen et al. (2004) suggested that the suppression of PAH emission near the AGN may be due to the destruction of PAHs by the strong radiation field of the AGN. If this is the case, we would expect a relation between the PAH luminosity deficit and the X-ray luminosity as a tracer of the AGN bolometric luminosity. The stronger the AGN radiation field, the larger the nuclear PAH deficit. We have measured the PAH luminosity deficit from our radial profiles as the ratio between the expected and the observed one. We have estimated the expected nuclear PAH luminosity in two ways: (1) as the linear extrapolation of the radial profile within 200 pc, and (2) as the maximum of PAH emission within 200 pc. Figure 5 shows the deficit obtained by extrapolation versus the X-ray luminosity. We do not find a relation between the PAH deficit and the AGN X-ray luminosity. Thus, from our data we have not found observational support for the destruction of the PAH features due to the AGN radiation field. However, we cannot rule out this hypothesis since more sensitive and better-resolution observations are needed. For instance, higher spatial resolution spectra could help pinpoint the distance from the nucleus at which the PAH emission starts to show this deficit. In this sense it might be possible that the relation is missing owing to a poor estimate of the PAH luminosity deficit.

Of course, a natural explanation of this inner deficit in the PAH feature is that there is a lack in SF toward the center. This is supported by the scenario in which the high-velocity winds or AGN-driven massive molecular outflows could be able to quench the surrounding SF (Cicone et al. 2014; McAlpine et al. 2015; Wylezalek & Zakamska 2016). Another possible explanation for this deficit in PAHs in internal parts can be related to the dust/gas distribution, which is ring-like rather than disk-like at the center (e.g., Ohsuga & Umemura 1999; Yankulova 1999). In order to corroborate this, other measurements of the nuclear tracers of the SF must be compared with

[15] Another four objects of the sample show emission only in one aperture (NGC 1386, NGC 2992, NGC 3081, and IC 4518W). The other four sources do not show detection of the 11.3 μm PAH feature.

[16] Note that we do not take into account IC 4518W because the measurements at distances $<$400 pc are only upper limits.

[17] We refer to dilution as a decrease in equivalent width from the PAH feature due to the strength of the AGN continuum.

our PAH nuclear fluxes, isolating nuclear and circumnuclear emission.

5.2. Hints on the Coevolution of the AGN and Its Host Galaxy

Hopkins & Quataert (2010) and Neistein & Netzer (2014) have explored the correlation between BH accretion rate and the SFR through hydrodynamic simulations and semianalytic models, respectively. Hopkins & Quataert (2010) predicted the relation between BH accretion rate and SFR at different galactic scales. Their simulations start with a major galaxy merger of isolated bar-(un)stable disk galaxies. They found that nuclear SF is more coupled to AGNs than the global SFR of the galaxy. Neistein & Netzer (2014) developed similar simulations including advection-dominated accreting flow to account for the accretion processing low-luminosity AGNs. They observed a lack of correlation between SFR and AGN luminosity (related to BH accretion rate) at $z < 1$ and $L_{\rm bol,AGN} < 10^{44}\,{\rm erg\,s^{-1}}$ (see also Rosario et al. 2012). They justified this possible lack of correlation as follows: (1) secular SF is perhaps not associated with BH accretion, or (2) BH accretion rate and SFR could be delayed, removing any correlation (see also Hopkins 2012). They also found that AGNs with low or intermediate luminosity might be associated with minor merger events.

In this work we compare Hopkins & Quataert (2010) and Neistein & Netzer (2014) predictions with our results. We derived nuclear and circumnuclear SFRs using the PAH 11.3 μm feature luminosities ($L_{11.3\,\mu{\rm m}}$) and applying the relation derived in Shipley et al. (2016) (using *Spitzer* measurements of 105 galaxies):

$$\log {\rm SFR}\ (M_\odot\ {\rm yr^{-1}}) = (-44.14 \pm 0.08) + (1.06 \pm 0.03) \log L_{11.3\,\mu{\rm m}}({\rm erg\ s^{-1}}). \quad (3)$$

The uncertainties in the derived SFRs using Equation (3) are typically 0.14 dex (see Shipley et al. 2016, for full details). As a caveat on the use of the PAH as a tracer of SF, Jensen et al. (2017) recently found that the slopes of the radial profile of the PAH emission are very similar, with a strength proportional to the AGN luminosity. They argue that this might imply that a compact emission source is required to explain the common slopes. Both an AGN and a nuclear star cluster are possible sources of PAH heating/excitation. Although we obtain in general a decrease of the PAH flux with the radius, a more complex behavior (with a deficit at the nuclear and peaks of emission on top of a general decrease) is observed in most of our sources, indicating in situ PAH heating.

This is not the first time such a comparison has been done. Esquej et al. (2014) used a sample of 29 nuclear spectra to explore the same relation between SFR and BH accretion rate. They compared their data with the relations obtained by Hopkins & Quataert (2010), and they concluded that predictions for distances (D) <100 pc reproduce their data well. We have seven sources in common with their sample.[18] Our measurements show slightly higher SFR compared to theirs (factor of 2), perhaps due to a different methodology for defining the continuum around the PAH feature. Ruschel-Dutra et al. (2017) also analyzed the presence of circumnuclear SF in a sample of 15 AGNs using MIR images (with two filters centered at the 11.3 μm PAH features and at the adjacent continuum, respectively). They compared their data with the correlation presented by Neistein & Netzer (2014). They concluded that SFR is correlated with bolometric AGN luminosity ($L_{\rm bol,AGN}$) for objects with $L_{\rm bol,AGN} \geqslant 10^{42}\,{\rm erg\,s^{-1}}$, while the low-luminosity AGN has larger SFR for their $L_{\rm bol,AGN}$.

Compared to previous works, our analysis has the advantage that it allows us to explore the SFR at different subkiloparsec scales from the nucleus. We calculate the $L_{\rm bol,AGN}$ from X-ray luminosities (reported in Table 1, Column (4)) using the relation $L_{\rm bol,AGN} = {\rm kL(2–10\,keV)}$, where the bolometric correction (k) depends on L(2–10 keV) itself with a fourth-order polynomial (see Marconi et al. 2004). In Figure 6, we present the relation between $L_{\rm bol,AGN}$ and ${\rm SFR_{PAHs}}$ integrated at different distances from the nucleus. Each panel corresponds to integrated ${\rm SFR_{PAHs}}$ for the 100, 200, 500, and 700 pc apertures, respectively. Note that this plot includes the 12 sources where we measure the 11.3 μm PAH feature (the integrated fluxes density are reported in Table 3). The number of sources varies for each plot depending on the resolution and spatial scale of the extended emission for each spectrum. Furthermore, Sy1 and Sy2 are shown as red and green circles, respectively. We also include the measurements for QSOs from Martinez-Paredes et al. (submitted; triangles), as well as Seyferts from Esquej et al. (2014; stars) and Ruschel-Dutra et al. (2017; diamonds).

Two of our objects (NGC 1808 and NGC 4569) are in the range of low luminosities ($L_{\rm bol,AGN} < 10^{42}\,{\rm erg\,s^{-1}}$). Hopkins & Quataert (2010) predictions are not able to reproduce these low-efficiency objects. Ruschel-Dutra et al. (2017) suggest that the low-luminosity AGNs have high circumnuclear SF. However, our objects with high luminosity have similar or higher SFRs. Neistein & Netzer (2014) presented two correlations: (1) the average SFR value for a given $L_{\rm bol,AGN}$ in their models, and (2) the average of $L_{\rm bol,AGN}$ for a given value of total SFR. Indeed, the first relation flattens toward low luminosities, as seen by our two low-luminosity AGNs. In Figure 6, we show these relations shifted as predicted by Hopkins & Quataert (2010) for different apertures (dashed and solid lines with different colors in each panel):

$${\rm SFR_{PAHs}}(R < 100\ {\rm pc}) = {\rm SFR_{PAHs}}(<10\ {\rm pc}) - 1.0, \quad (4)$$

$${\rm SFR_{PAHs}}(R < 1\ {\rm kpc}) = {\rm SFR_{PAHs}}(<10\ {\rm pc}) - 1.52, \quad (5)$$

$${\rm SFR_{PAHs}}({\rm total}) = {\rm SFR_{PAHs}}(<10\ {\rm pc}) - 2.52. \quad (6)$$

These relations have been computed using Equations (15)–(18) in Hopkins & Quataert (2010). Note that scatter in these relations is significant. In general terms, these relations have the form

$${\rm SFR_{PAHs}}(R < Rs) = {\rm SFR_{PAHs}}(<10\ {\rm pc}) - B(Rs), \quad (7)$$

where $B(Rs)$ is a constant that depends on the physical scale. We have interpolated the given values to obtain the expected shifts on the physical scales derived from our analysis (reported in the second column of Table 4).

In order to compare predictions with models, we have computed the observed shift to this relation as the average and standard deviation of the relation predicted by Neistein & Netzer (2014) and our data points. These shifts are reported in

[18] NGC 1808, NGC 3227, NGC 5135, NGC 5643, NGC 7130, NGC 7172, and NGC 7582.

the third and fourth columns of Table 4. This correlation and standard deviations are shown as the black solid line and shaded area in each panel, respectively.

Note that the results shown in Figure 6 could be affected by the following errors: (1) The systematic offset due to the use of different SFR tracers. The dispersion from the correlation used to calculate the SFR from the 11.3 μm PAH feature is similar to that obtained by other tracers. We have taken into account this dispersion in the error bars in Figure 6. (2) Timescale for the SF. According to Neistein & Netzer (2014), a necessary condition for agreement between data and model is that the correct timescale for both SF and AGN activity is adopted. The models are constrained to calculate the SFR average using only the SF in the last 150 Myr. We have calculated the SFR using the 11.3 μm PAH as a tracer. This feature is usually associated with B stars (Peeters et al. 2004). (3) Calculation errors in the $L_{\rm bol,AGN}$. In the models the $L_{\rm bol,AGN}$ depends on the accretion mass, while in our data it depends on the X-ray luminosity, which might vary up to one order of magnitude. In Figure 6, we have already included this uncertainty in the error bars.

We found a sensible agreement between the theoretical relations proposed by Neistein & Netzer (2014) shifted according to Hopkins & Quataert (2010) and our data, for most inner galaxy parts. This result is of interest, as, in the simulated objects, major mergers with tidal events have been deemed responsible for both the SF and BH feeding.

6. Summary and Conclusions

In this paper, we present a sample of 19 local AGNs observed with ground-based T-ReCS/Gemini and CanariCam/GTC spectra. We complemented these observations with available *Spitzer*/IRS spectra. We have studied the surface brightness radial profile of the 11.3 μm PAH feature and the [S IV] line emission. According to the results of this research, we tried to answer the following three questions:

(1) What is the origin of the [S IV] line emission in the nuclear region?

The contribution to the [S IV] line emission is not circumnuclear. Instead, it often peaks at distances greater than $1000R_{\rm Sub}$ from the nucleus. We have not found a relation between the surface brightness radial profiles of the [S IV] line and the PAH feature at different distances from the nucleus. If the PAH is a good tracer of SF, we speculate that the [S IV] line emission could be tracing SF with different ages than those traced by the PAH feature.

(2) How good is the 11.3 μm PAH feature as a tracer of SF in the vicinity of the AGN?

We found a PAH flux deficit closer to the AGN as compared with larger apertures (toward the inner $\sim$100 pc). This deficit cannot be related to dilution by the AGN continuum. We have not found observational support for the destruction of PAH features due to the AGN radiation field. Intrinsic lack of SF toward the center is also a plausible explanation.

(3) What can we say about the connection between SF and AGN activity?

We found a sensible agreement between the expected shift in the $L_{\rm bol,AGN}$–SFR theoretical relation proposed by Neistein & Netzer (2014), Hopkins & Quataert (2010), and our observations, for most inner galaxy parts.

The authors thank the anonymous referee for careful reading and constructive suggestion that improved the paper. This scientific publication is based on observations made with the Gran Telescopio CANARIAS (GTC), installed at the Spanish Observatorio del Roque de los Muchachos of the Instituto de Astrofísica de Canarias on the island of La Palma. This work is based in part on observations made with the *Spitzer Space Telescope*, which is operated by the Jet Propulsion Laboratory, California Institute of Technology, under a contract with NASA. D.E.-A. and O.G.-M. acknowledge support from grant IA100516 and IA103118 PAPIIT DGAP UNAM. D.D. and D.E.-A. acknowledge support through grants IN108716 from PAPIIT, UNAM, and 221398 from CONACyT. D.E.-A. acknowledges support from a CONACYT scholarship. A.A.-H. acknowledges support from the Spanish Ministry of Economy and Competitiveness through the Plan Nacional de Astronomía y Astrofísica under grant AYA2015-64346-C2-1-P, which is party funded by the FEDER program. C.R.-A. acknowledges the Ramón y Cajal Program of the Spanish Ministry of Economy and Competitiveness through project RYC-2014-15779 and the Spanish Plan Nacional de Astronomía y Astrofisíca under grant AYA2016-76682-C3-2-P. T.D.-S. acknowledges support from ALMA-CONICYT project 31130005 and FONDECYT regular project 1151239.

Appendix
Catalog of Spectra and Reported Nuclear Star-forming Regions

NGC 931 (Mrk 1040) is a barred galaxy (Sbc) with an Sy1 nucleus. Ward & Wilson (1978) found that this galaxy interacts with a satellite galaxy located 10 kpc from NGC 931. We did not find records of SF in other works at the scales traced with our observations.

Mrk 1066 is a starburst galaxy with an Sy2 nucleus. Ramos Almeida et al. (2014) found star-forming knots at $\sim$400 pc of the galaxy center, after subtracting the AGN component. Alonso-Herrero et al. (2014) suggest that close to the center ($\sim$125 pc) the near-IR lines are dominated by the AGN processes.

NGC 1320 is an edge-on galaxy with an Sy2 nucleus. This source is a "warm galaxy" with a relatively high IR luminosity (De Robertis & Osterbrock 1986). We did not find records of SF in other works at the scales traced with our observations.

NGC 1386 is an edge-on spiral galaxy with an Sy2 nucleus. Ruschel-Dutra et al. (2014) found that the 11.3 μm PAH feature is more pronounced at distances $\sim$100 pc from the nucleus. They also found that the [S IV] line emission is only detected in the nucleus at distances $<$100 pc. Our observations are in agreement with these results. Optical studies show evidence of heavy obscuration (Weaver et al. 1991; Storchi-Bergmann et al. 1996; Rossa et al. 2000).

NGC 1808 is an inclined spiral galaxy with an Sy2 nucleus and a prominent starburst (Veron-Cetty & Veron 1985; Krabbe et al. 1994). Yuan et al. (2010) considered the possibility that the nucleus is an H II region. Asmus et al. (2014) found that star-forming regions dominate the MIR emission within $\sim$200 pc.

NGC 2992 is an inclined spiral galaxy (de Vaucouleurs et al. 1991) and located in the interacting system Arp 245. The nucleus of this source is classified as an Sy1.9 in the optical. However, in other works it is classified as Sy1.5 or Sy2 (Gilli et al. 2000; Trippe et al. 2008). Gilli et al. (2000) suggested that

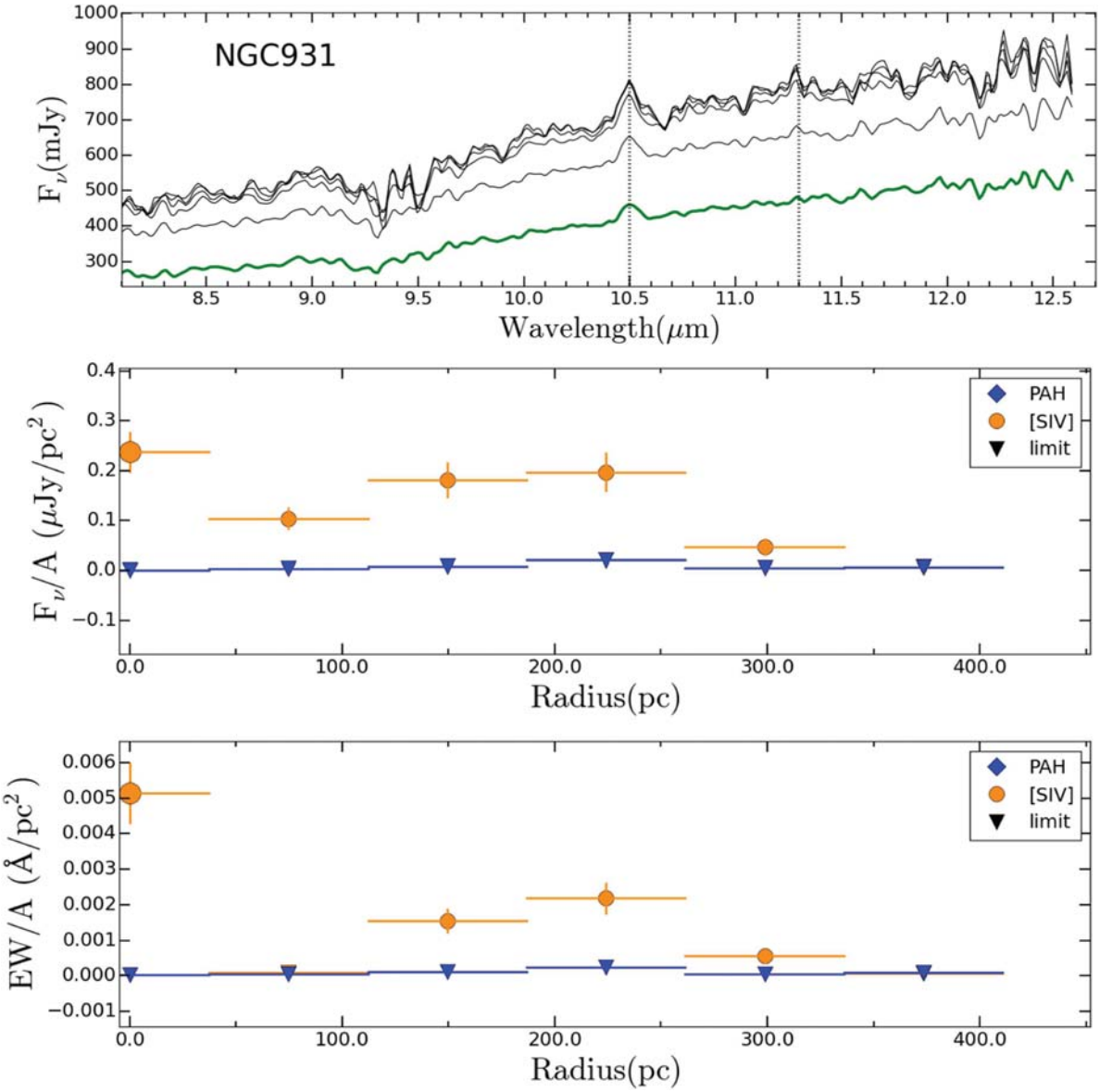

Figure 7. Top panel: extracted spectra at different scales for NGC 931. The green and black lines correspond to the nuclear spectrum and extended aperture spectra, respectively. The dotted lines show the PAH feature and [S IV] line emissions. Middle and bottom panels: surface brightness and EW radial profiles, respectively. The radial profiles for 11.3 μm PAH emission are presented with blue diamonds, while radial profiles for [S IV] line emission are shown with orange circles (the triangles are limits values). The larger circle corresponds to [S IV] emission in the nuclear spectrum. The vertical line marks the 200 pc distance from the center.

the IR variations were probably caused by a retriggered AGN. García-Bernete et al. (2015) found that the starburst component dominates the MIR emission, while the AGN component dominates at higher wavelengths ($\lambda > 15$ μm).

NGC 3081 is a low-inclination barred spiral galaxy with an Sy2 nucleus (Phillips et al. 1983; Asmus et al. 2014). However, Moran et al. (2000) reported a type 1 optical spectrum in polarized light. Weaver et al. (2010) found that the *Spitzer* spectrum exhibits a weak absorption by silicate at 10 μm, a weak PAH emission, and prominent forbidden emission lines. However, Asmus et al. (2014) concluded that the MIR emission is mostly due to the AGN.

NGC 3081: (see above).

NGC 3227 is a low-inclination barred spiral galaxy. This source is in interaction with NGC 3226. The nucleus is classified as Sy1.5, and it is surrounded by circumnuclear starburst (Véron-Cetty & Véron 2010). Rodríguez-Ardila & Viegas (2003) and Davies et al. (2006) found star-forming regions at ∼70 pc from the nucleus. Asmus et al. (2014) also found that the MIR emission is dominated by star-forming regions (at arcsecond scale).

NGC 3281 is a highly inclined spiral galaxy with an Sy2 nucleus (Véron-Cetty & Véron 2010). Ramos Almeida et al. (2009) and Sales et al. (2011) presented observations of this source with T-ReCS with the broad N and Qa bands. They found that the spectrum of NGC 3281 shows only a very deep silicate absorption at 9.7 μm and some forbidden emission lines (e.g., [S IV] at 10.5 μm). They conclude that NGC 3281 is a heavily obscured source, due to concentrated dust within a radius of 200 pc.

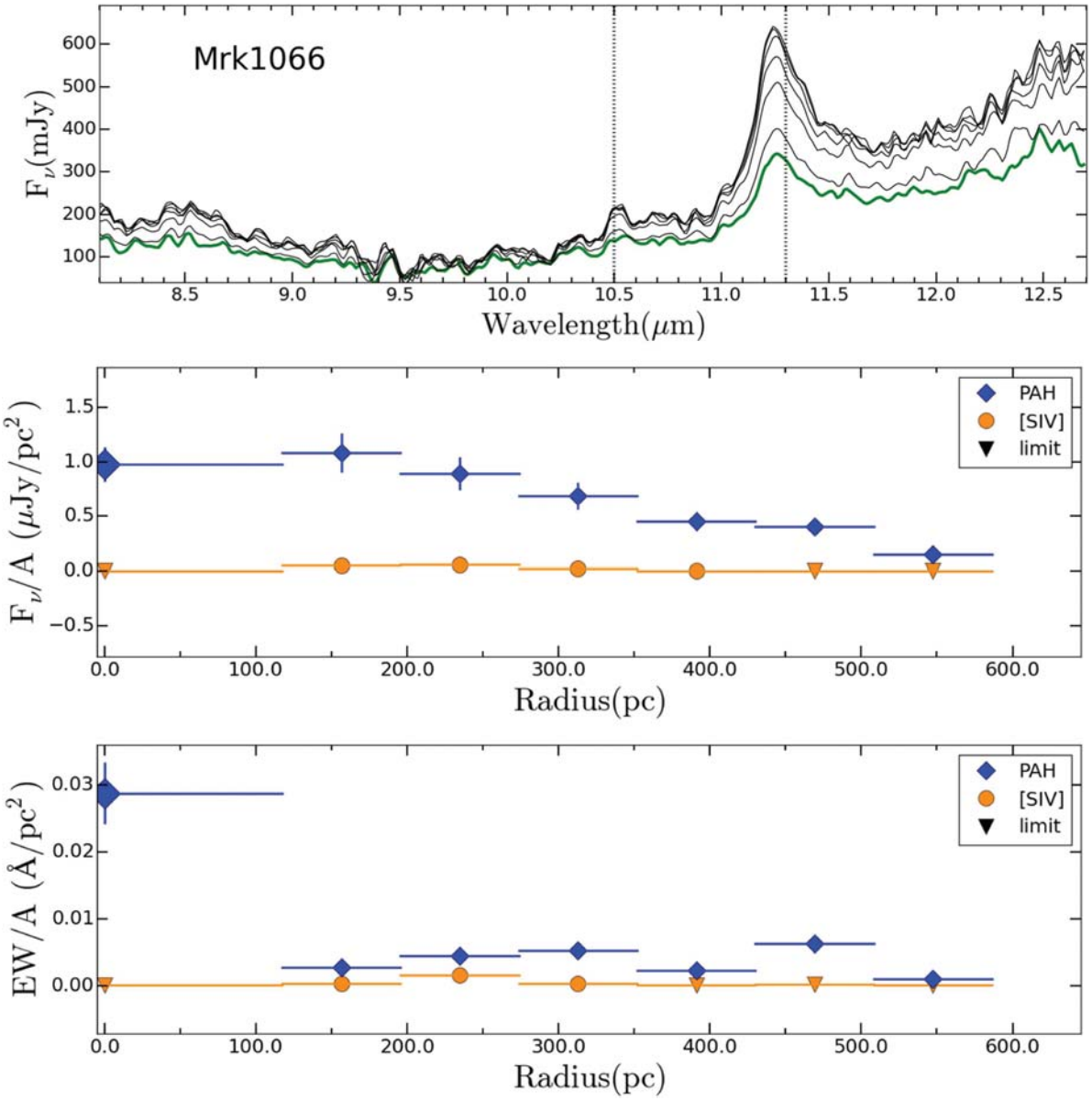

Figure 8. Extracted spectra and radial profiles for Mrk 1066; same description as in Figure 7.

NGC 4253 (Mrk 766) is a barred spiral galaxy (SBa) with an Sy1 nucleus. The *HST* images of this source show some irregular dust filaments around the nucleus (Malkan et al. 1998). Rodríguez-Ardila et al. (2005) studied the near-IR spectrum and found permitted, forbidden, and high-ionization lines. Furthermore, Rodríguez-Ardila & Viegas (2003) found emission in the 3.3 μm PAH feature located 150 pc from the nucleus. They considered that this emission is a signature of starburst activity.

NGC 4569 is the most massive, spiral, late-type, and gas-poor galaxy in the Virgo Cluster (van den Bergh 1976). This source shows strong Balmer absorption lines, which could be indicating SF in the last 1.5 Gyr (Ho et al. 2003). Dale et al. (2006) and Mason et al. (2015) also suggested recent and/or ongoing SF activity based on the detection of PAH emission at MIR.

NGC 5135 is an infrared-luminosity, face-on barred spiral galaxy. The nucleus is classified as an Sy2 (Véron-Cetty & Véron 2010), and it is surrounded by a banana-shaped circumnuclear SF (González Delgado et al. 1998; Bedregal et al. 2009). The inner and outer radii of the SF emission are located at ∼300 and ∼750 pc from the nucleus, respectively.

NGC 5643 is a face-on barred spiral galaxy with an Sy2 nucleus (Véron-Cetty & Véron 2010). The IRAC and MIPS images show a compact MIR nucleus embedded within the spiral-like host emission (Asmus et al. 2014). Moreover, the arcsecond-scale MIR spectral energy distribution (SED) is significantly affected by SF (e.g., Shi et al. 2006; Goulding & Alexander 2009).

IC 4518W is a spiral galaxy with an Sy2 nucleus (Véron-Cetty & Véron 2010). Diaz-Santos et al. (2010) and Asmus et al. (2014) found that the SF contribution at subarcsecond resolution is probably minor in its nucleus. Diaz-Santos et al. (2010) found [S IV] line emission at ∼265 pc toward the north of the nucleus. They suggested that this emission could be related to the NLR.

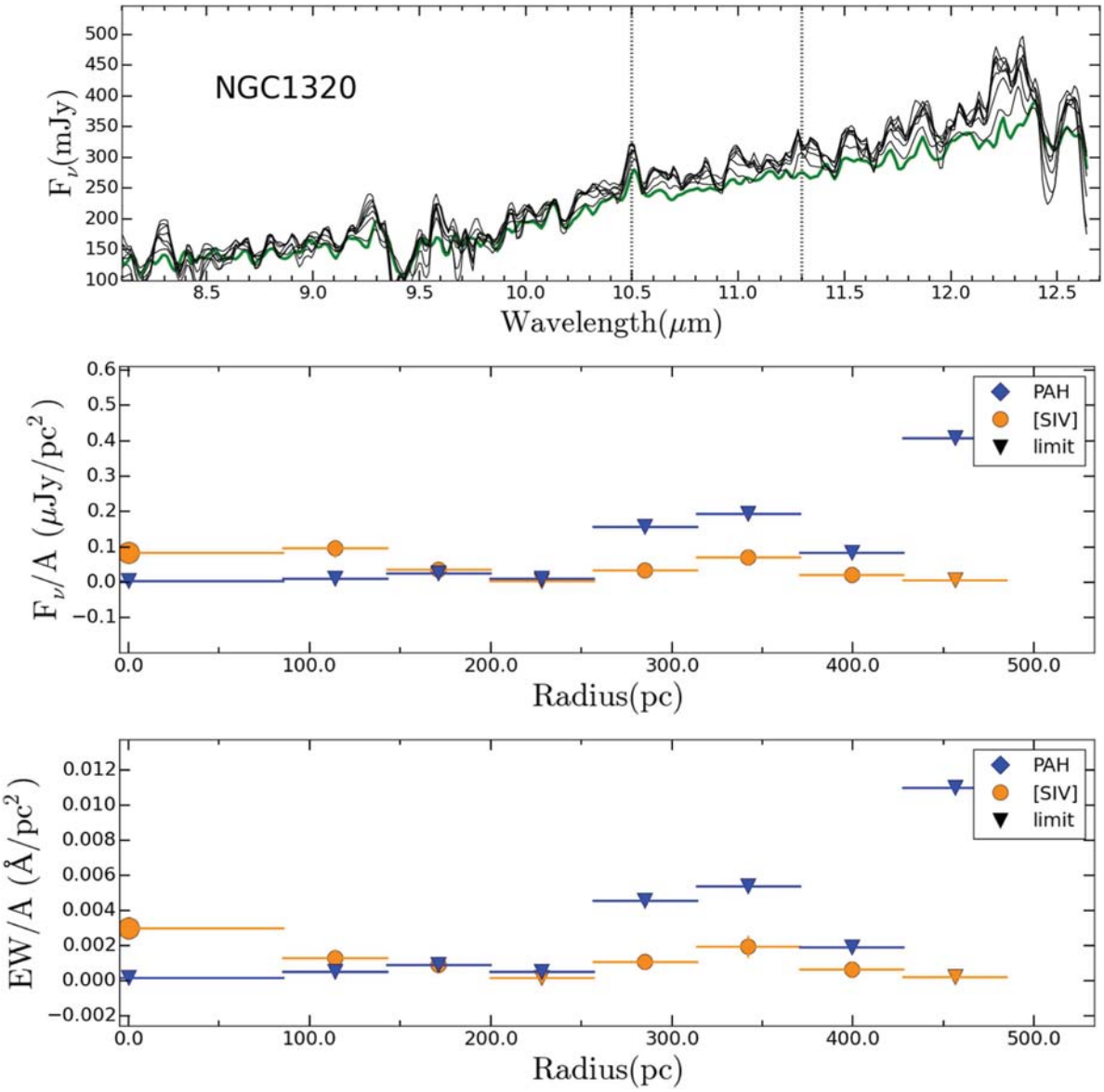

Figure 9. Extracted spectra and radial profiles for NGC 1320; same description as in Figure 7.

IC 5063 is a peculiar galaxy with both spiral and elliptical properties with an Sy2 nucleus (Kewley et al. 2001). Colina et al. (1991) proposed that IC 5063 is a remnant of a recent merger, while Martini et al. (2003) speculated that the nuclear obscuration might be caused by foreground dust lanes. We did not find records of SF in other works at the scales traced by our observations.

NGC 7130 is a peculiar low-inclination spiral galaxy with an Sy1.9 nucleus. A compact starburst is located at the center, and it is extended over ∼300 pc (González Delgado et al. 1998; Levenson et al. 2005). Wu et al. (2009) and Alonso-Herrero et al. (2012) found that the arcsecond-scale MIR SED indicates obscured AGN emission with a high SF contribution. Asmus et al. (2014) also concluded that the nuclear MIR SED is presumably still affected by significant SF emission.

NGC 7172 is an edge-on lenticular galaxy with an Sy2 nucleus (Véron-Cetty & Véron 2010). Smajić et al. (2012) found a prominent dust lane projected along the nucleus. The arcsecond-scale MIR SED might be affected by significant SF (Wu et al. 2009; Gallimore et al. 2010). However, Asmus et al. (2014) concluded that the nuclear MIR SED is free of SF contamination.

NGC 7465 is a spiral galaxy with an Sy2 nucleus. This source is part of a group of nine interacting galaxies (Haynes 1981). The dominant stellar population in the nuclear region of NGC 7465 corresponds to stars between K3 III and M3 III types, according to the relative absorption band measurements (Ramos Almeida et al. 2009).

NGC 7582 is a highly inclined barred spiral galaxy with an obscured nucleus. The nuclear spectrum has been studied as a composition between AGN and starburst (Veron et al. 1997). The AGN is surrounded by a powerful SF disk (major-axis diameter ∼400 pc) and a dust lane crossing over the nucleus (Morris et al. 1985; Riffel et al. 2009). Asmus et al. (2014) concluded that the starburst dominates the total MIR emission.

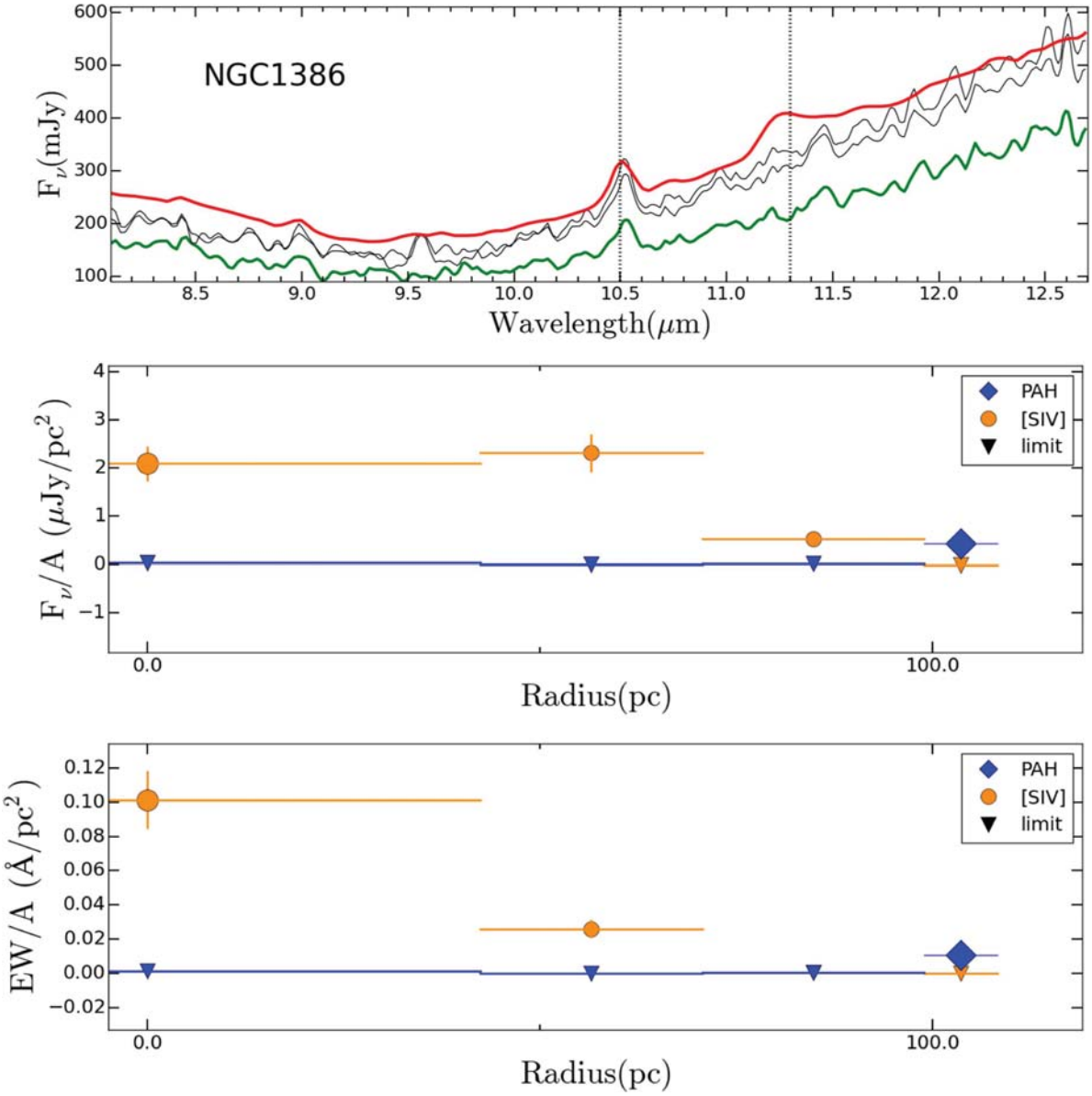

Figure 10. Extracted spectra and radial profiles for NGC 1386; same description as in Figure 7.

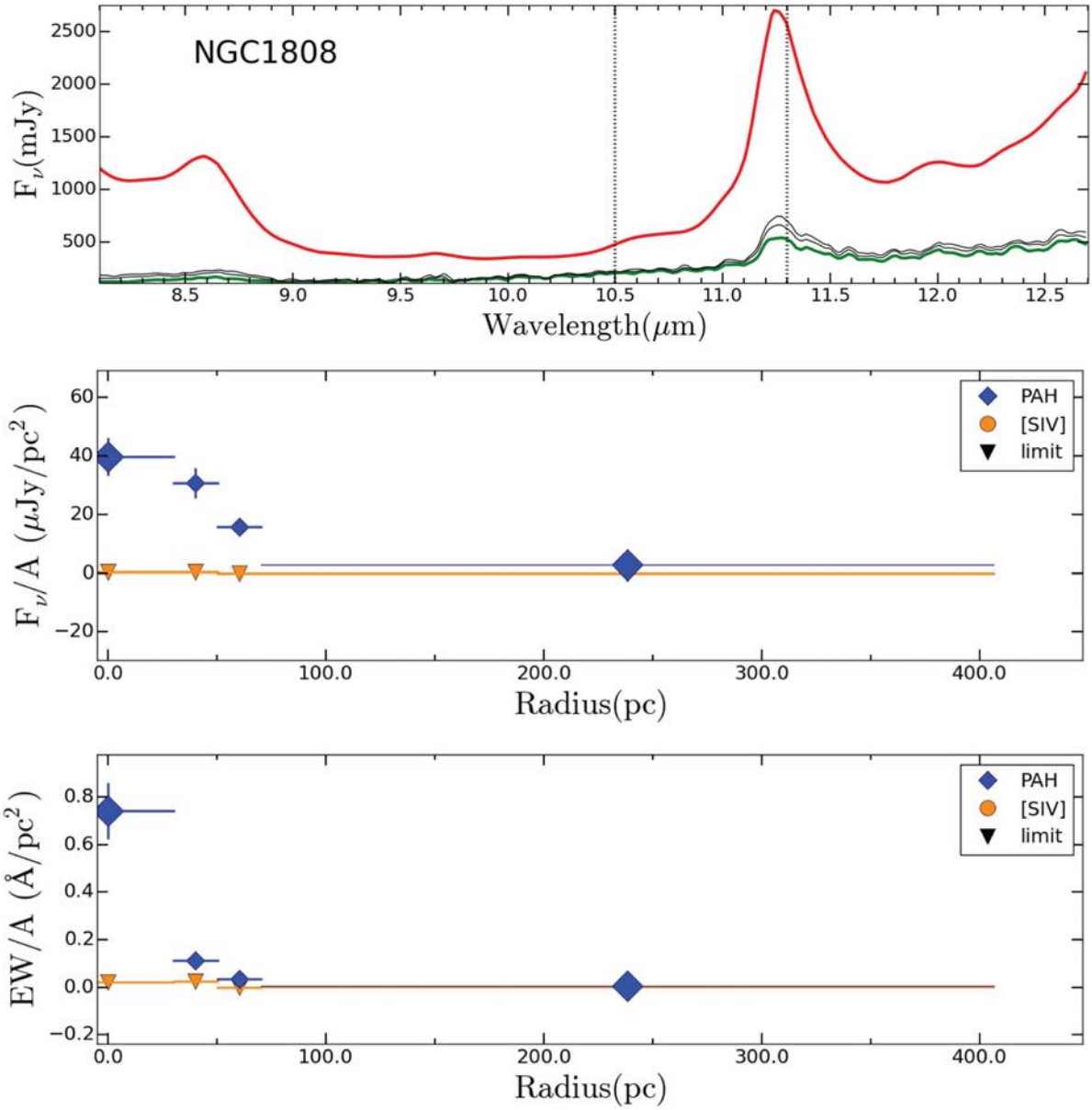

Figure 11. Extracted spectra and radial profiles for NGC 1808; same description as in Figure 7.

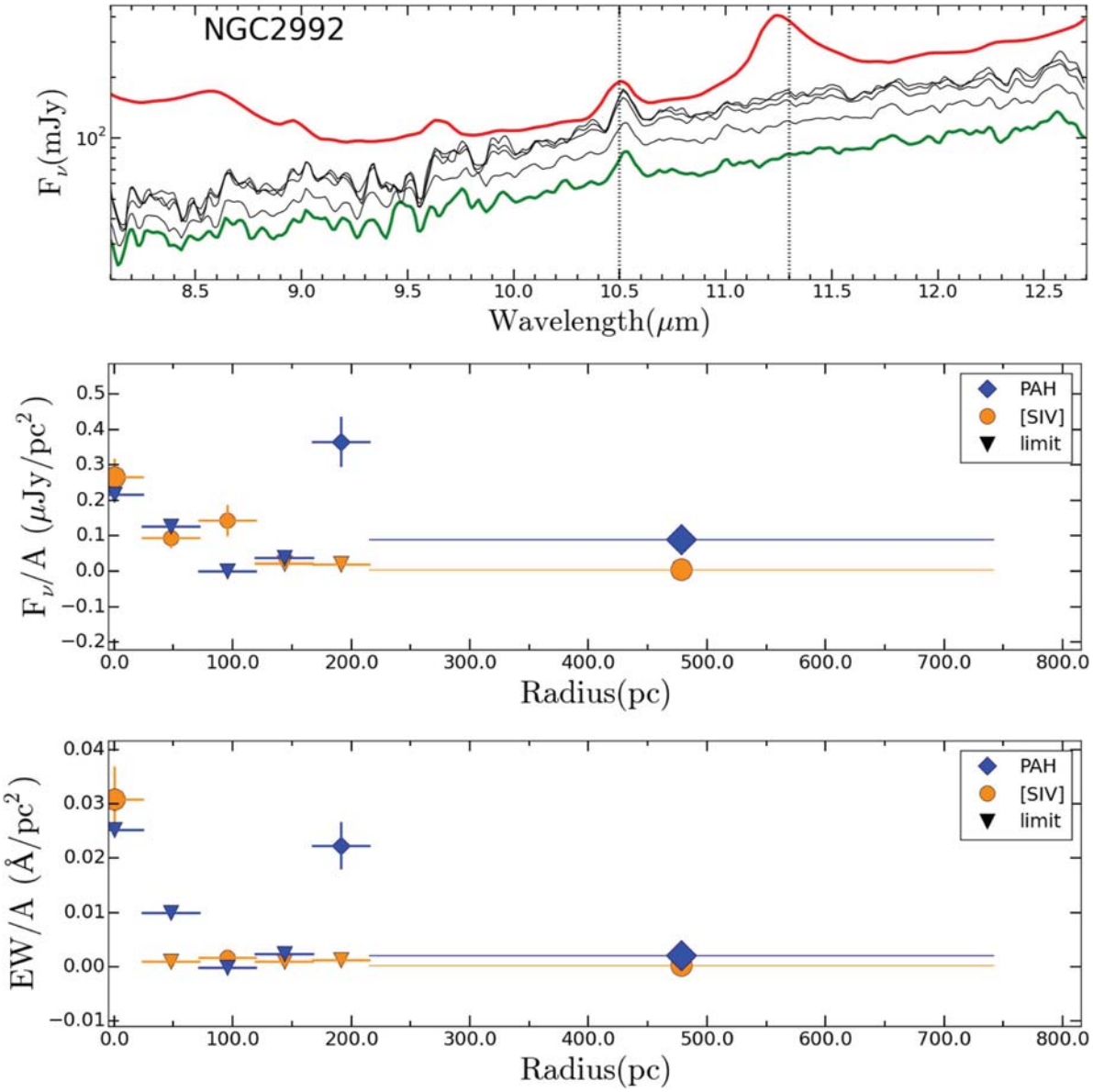

Figure 12. Extracted spectra and radial profiles for NGC 2992; same description as in Figure 7.

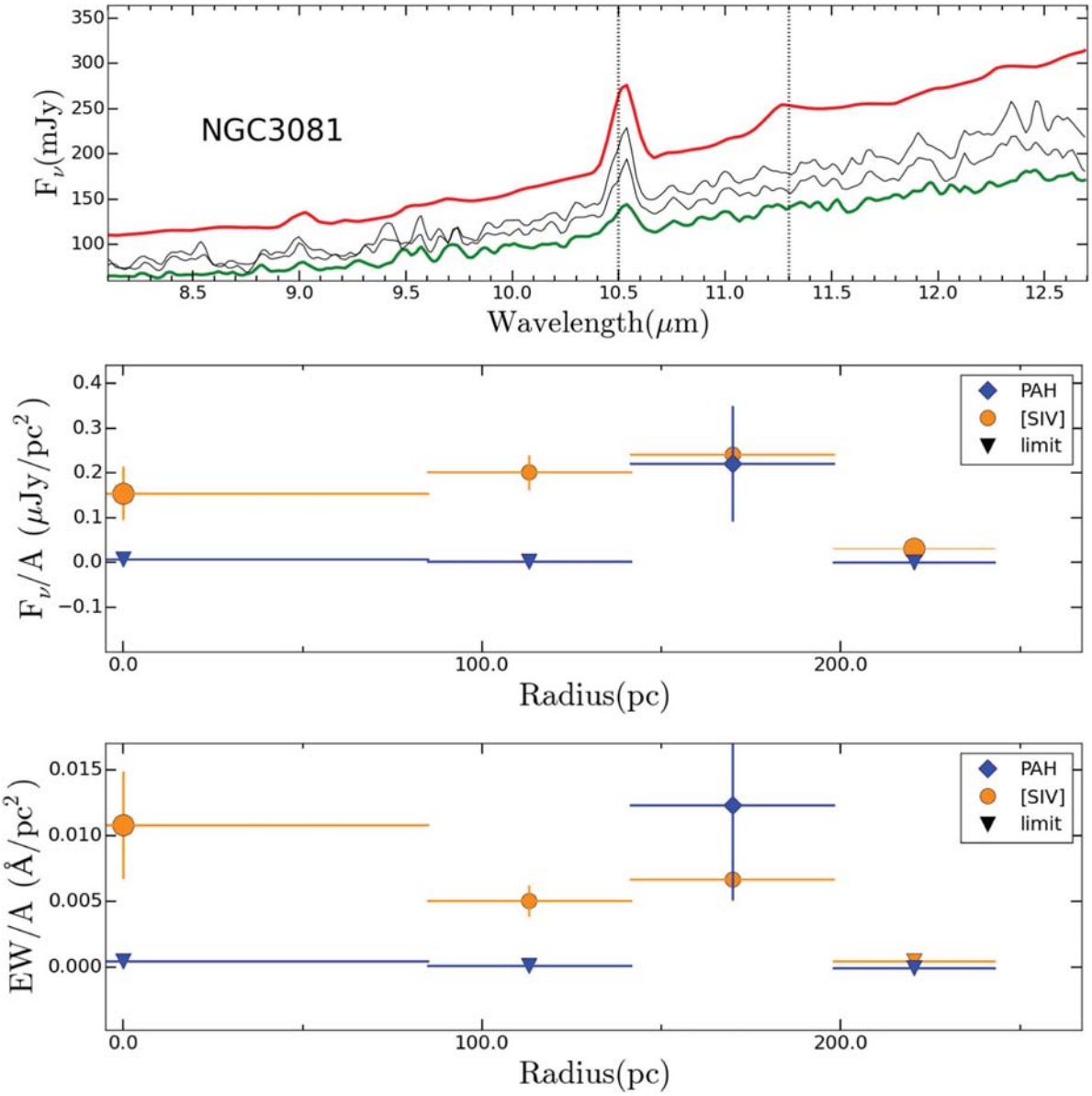

Figure 13. Extracted spectra and radial profiles for NGC 3081 with PA = 0°; same description as in Figure 7.

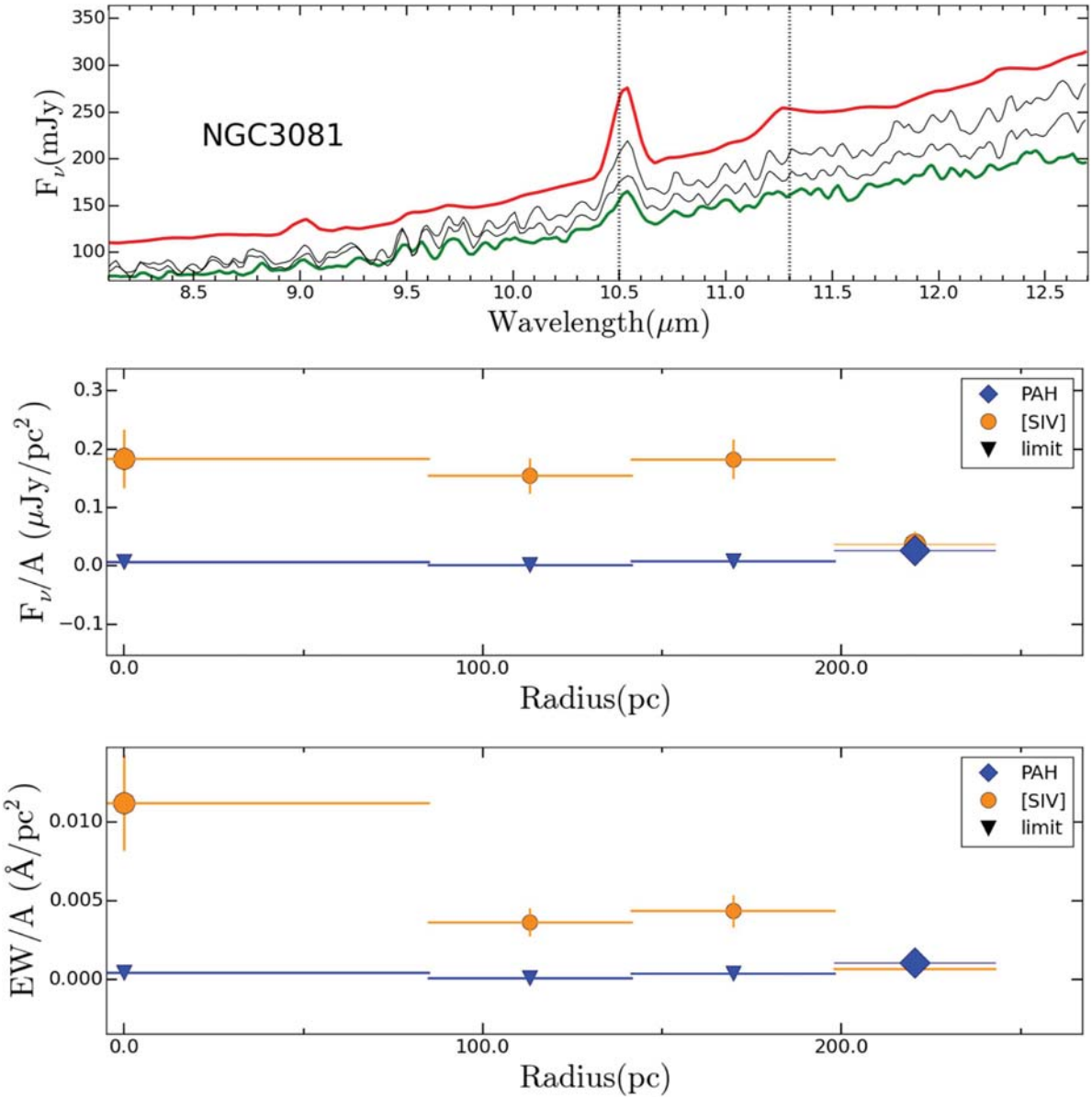

Figure 14. Extracted spectra and radial profiles for NGC 3081 with PA = 350°; same description as in Figure 7.

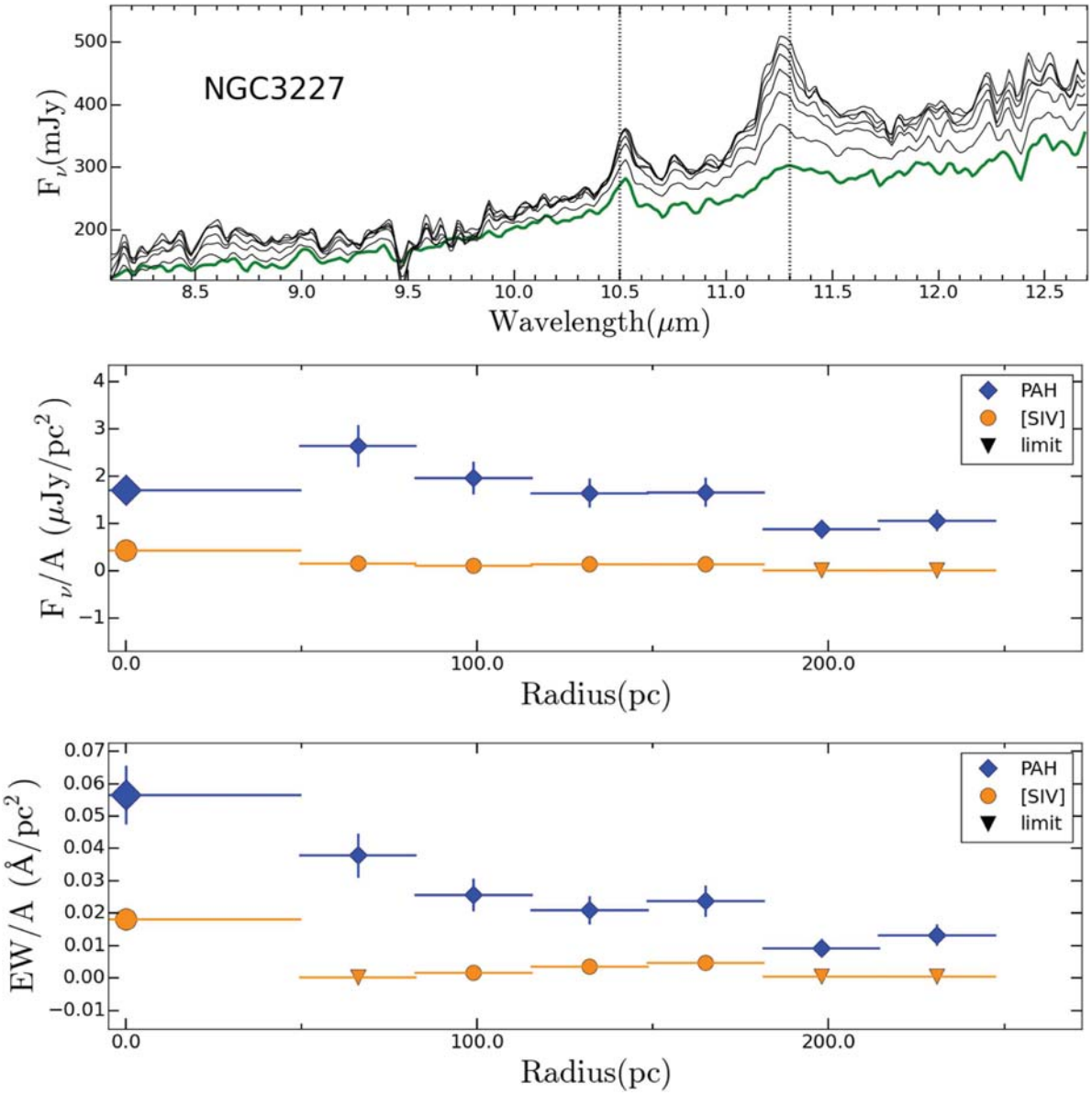

Figure 15. Extracted spectra and radial profiles for NGC 3227; same description as in Figure 7.

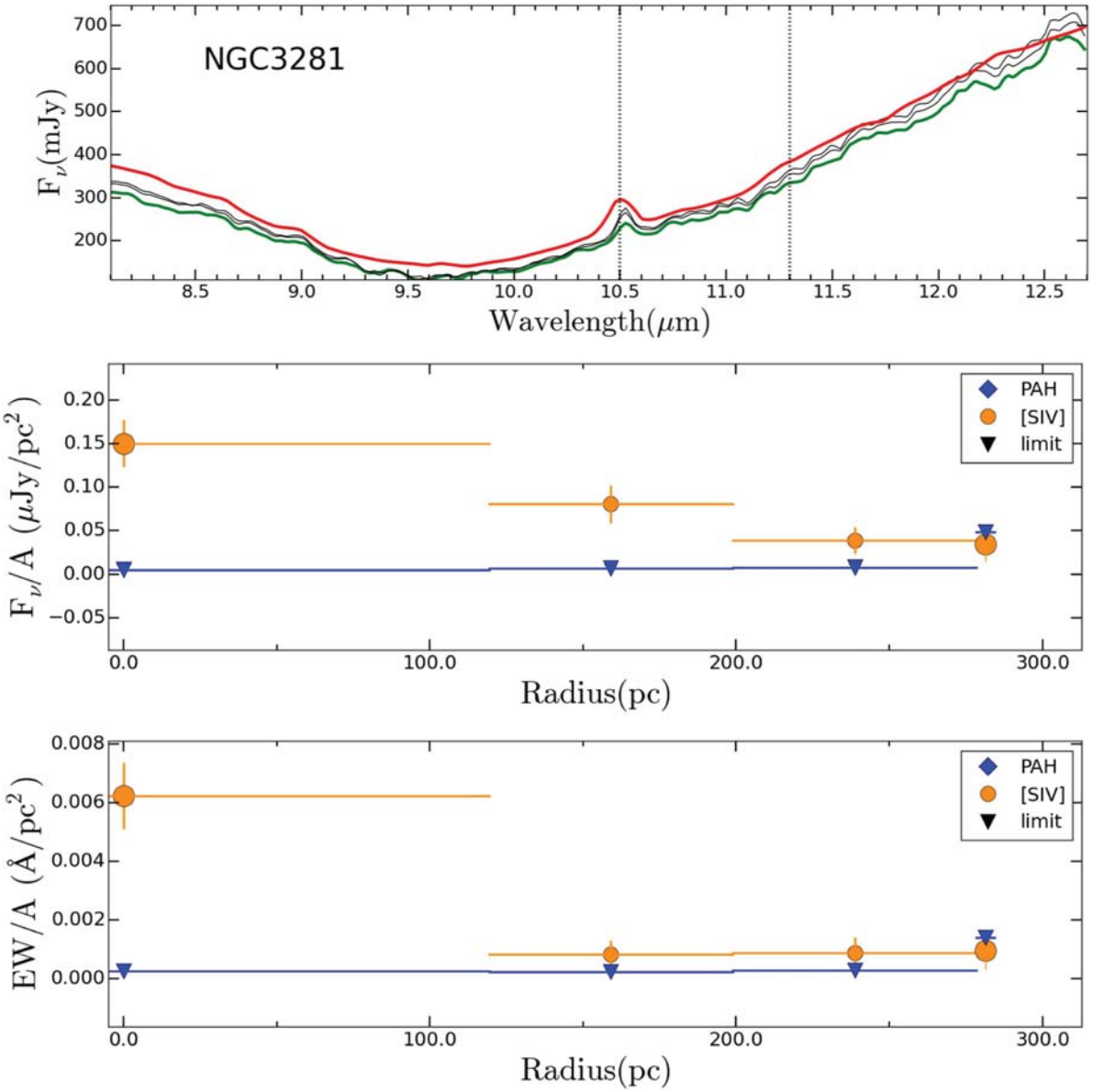

Figure 16. Extracted spectra and radial profiles for NGC 3281; same description as in Figure 7.

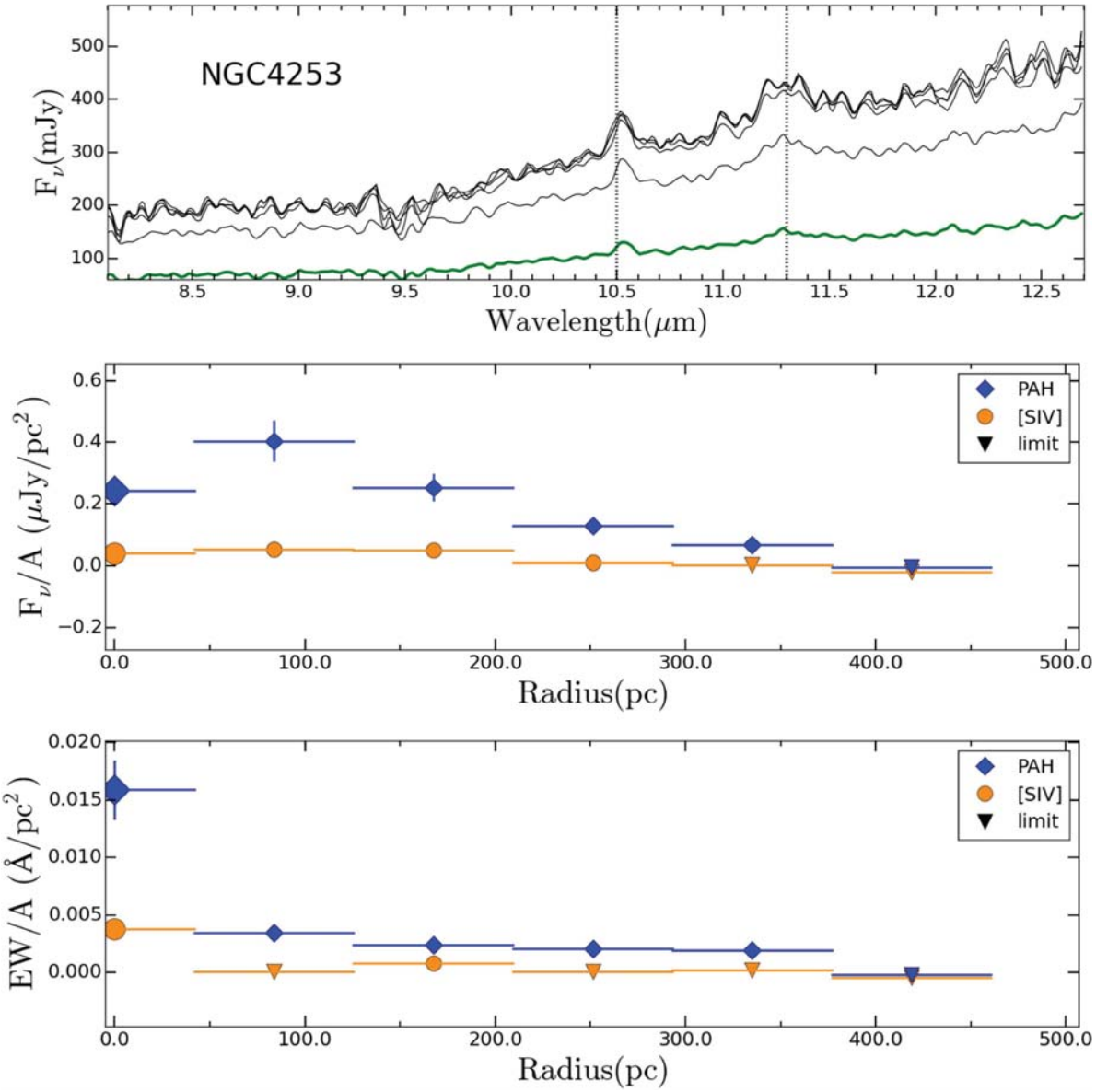

Figure 17. Extracted spectra and radial profiles for NGC 4253; same description as in Figure 7.

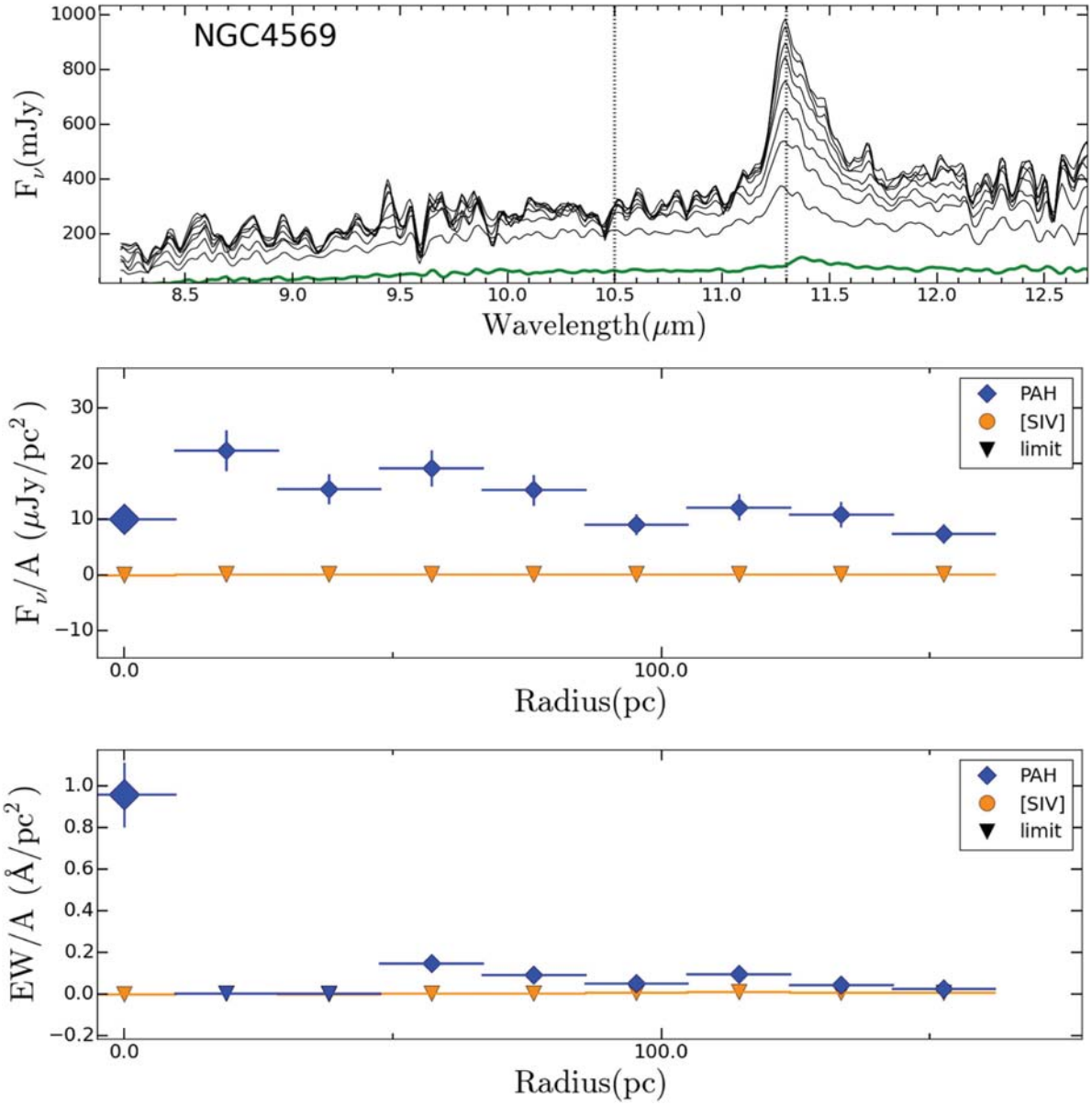

Figure 18. Extracted spectra and radial profiles for NGC 4569; same description as in Figure 7.

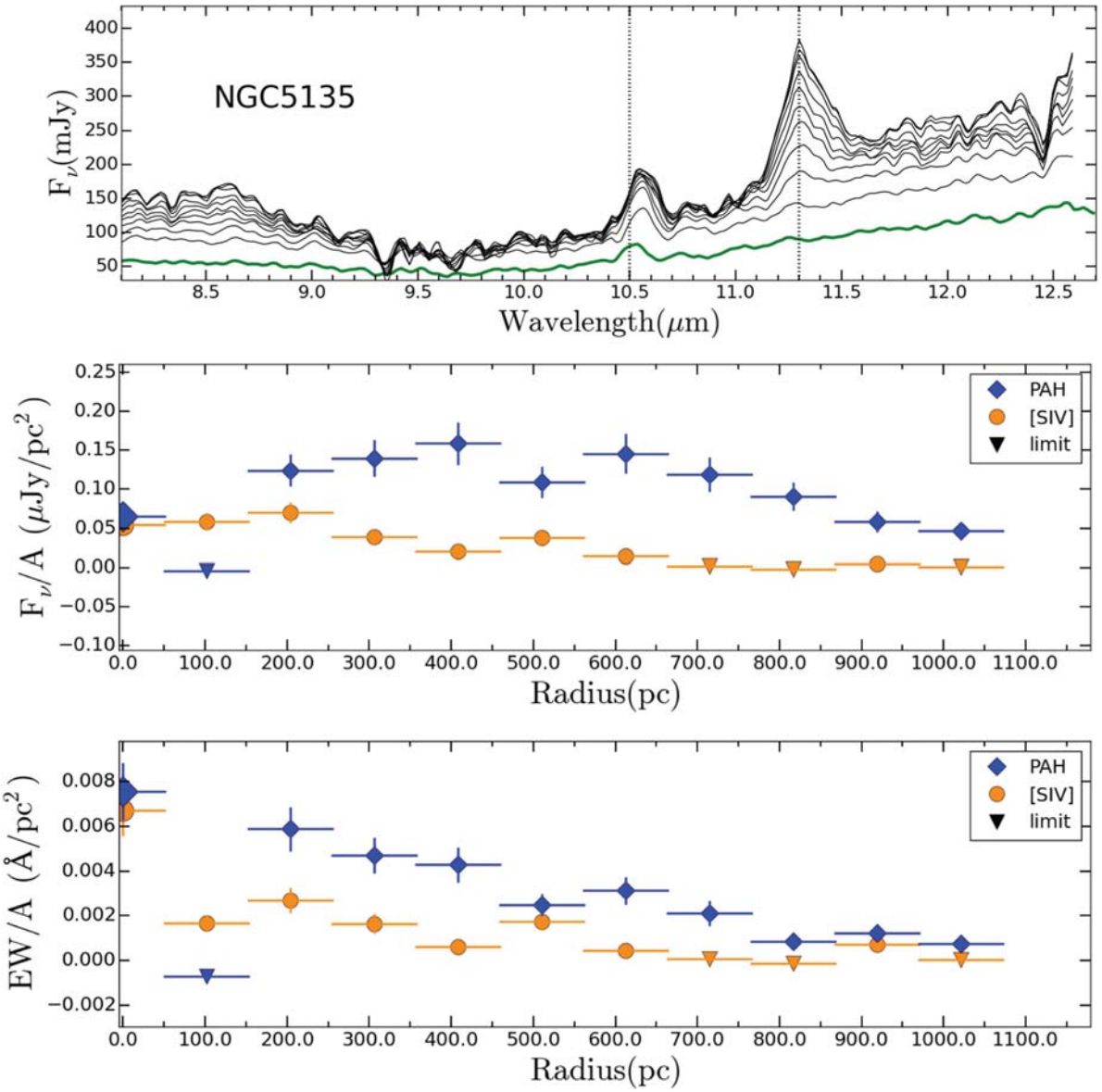

Figure 19. Extracted spectra and radial profiles for NGC 5135; same description as in Figure 7.

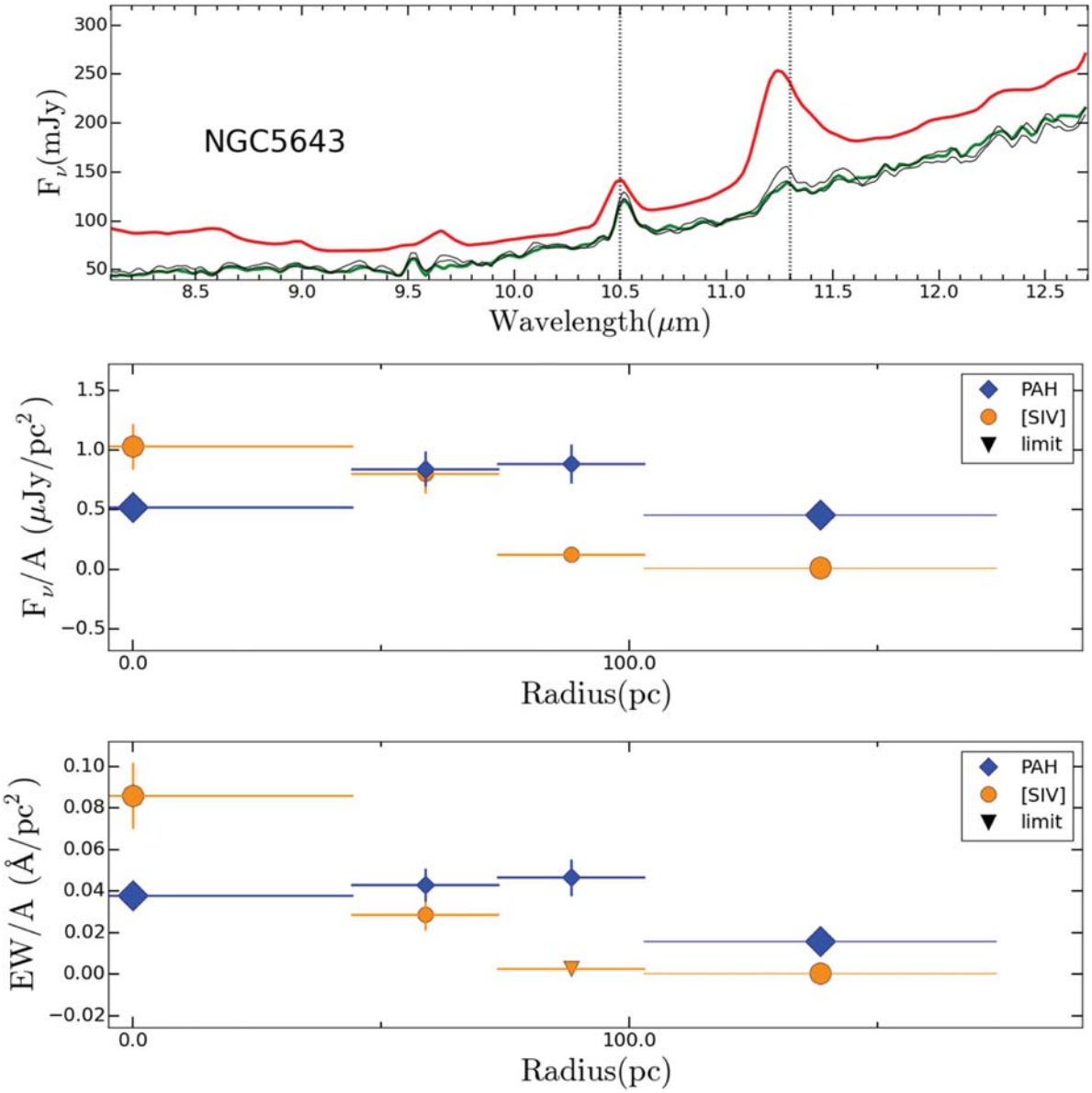

Figure 20. Extracted spectra and radial profiles for NGC 5643; same description as in Figure 7.

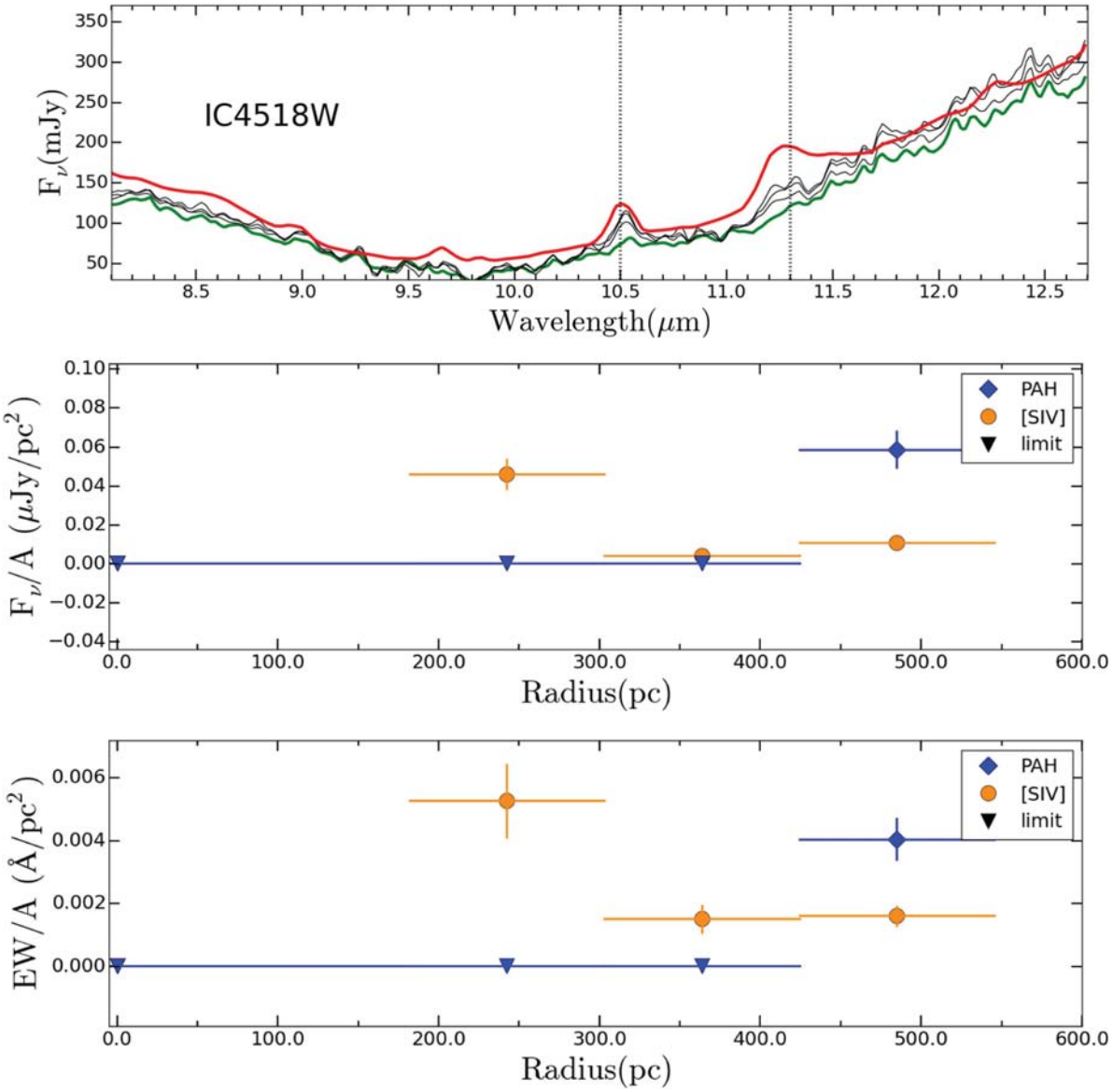

Figure 21. Extracted spectra and radial profiles for IC 4518W; same description as in Figure 7.

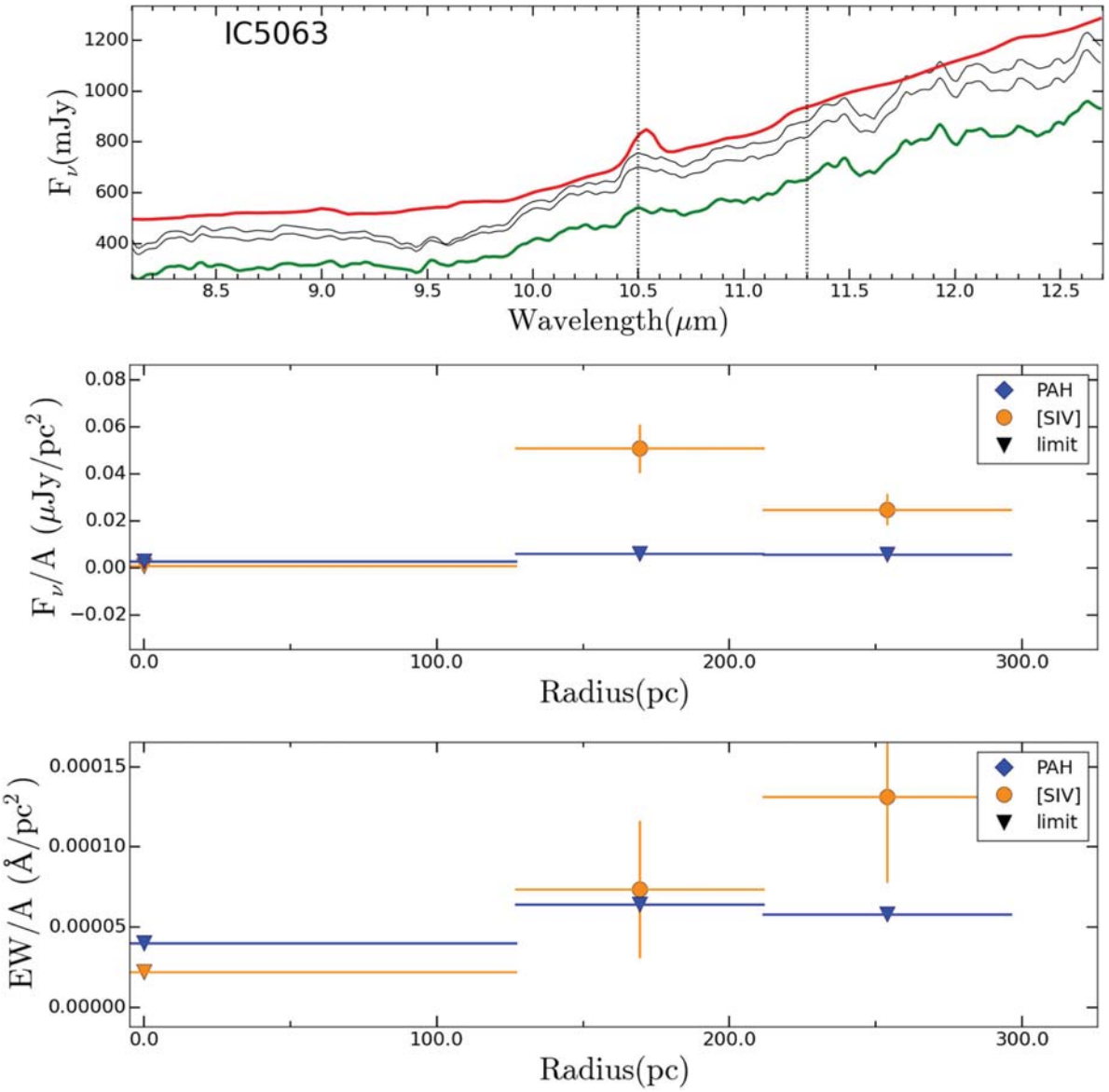

Figure 22. Extracted spectra and radial profiles for IC 5063; same description as in Figure 7.

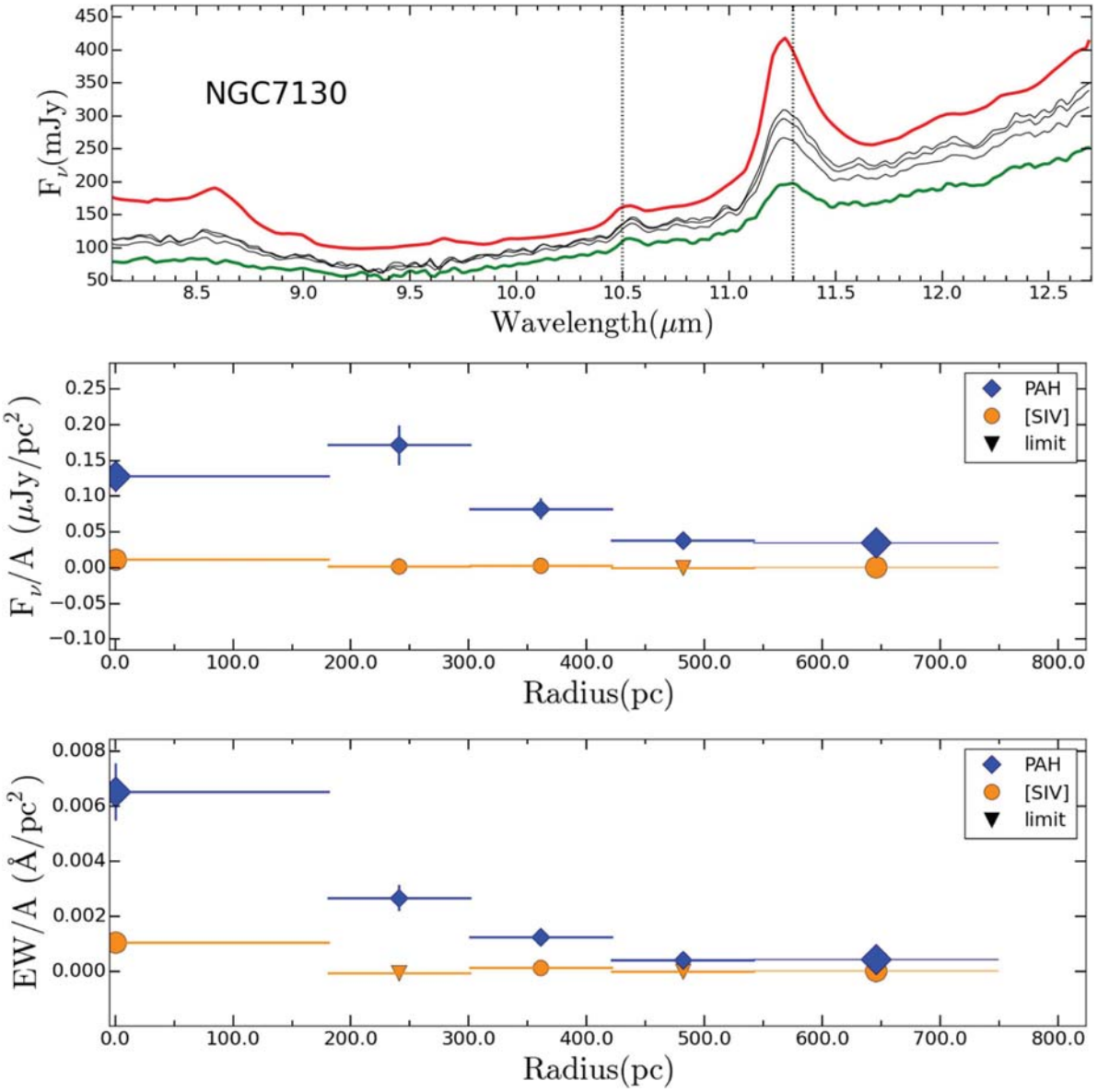

Figure 23. Extracted spectra and radial profiles for NGC 7130; same description as in Figure 7.

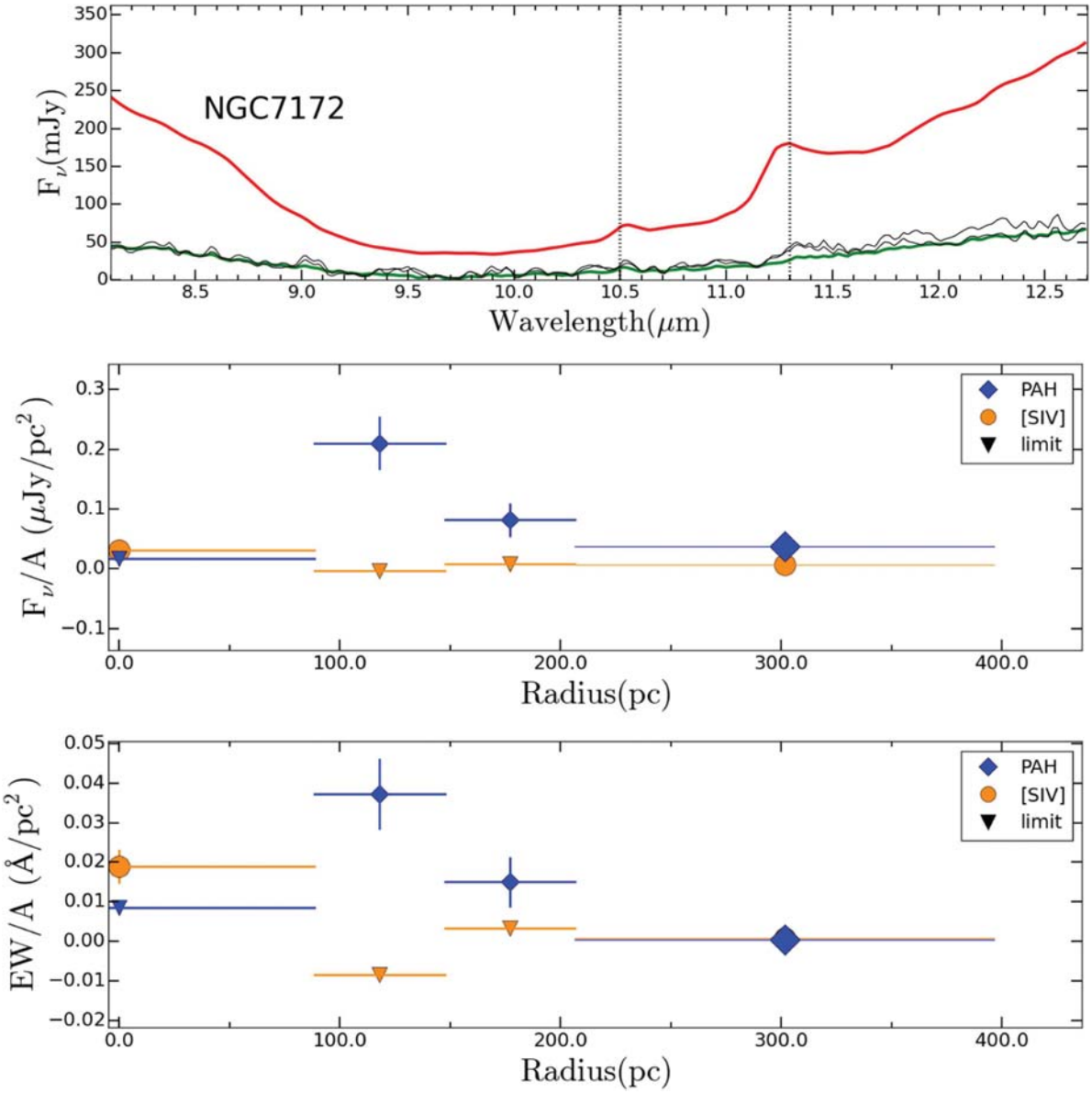

Figure 24. Extracted spectra and radial profiles for NGC 7172; same description as in Figure 7.

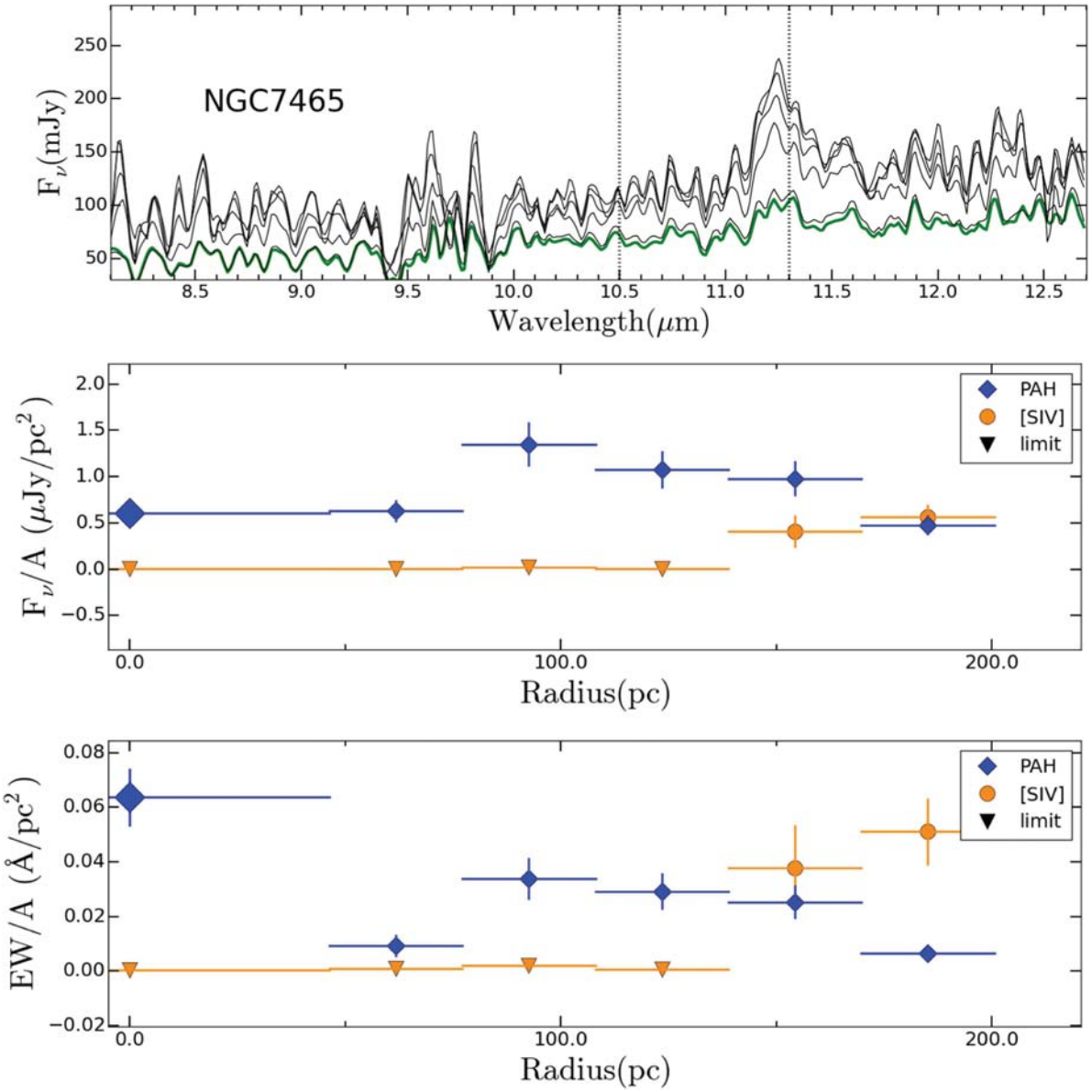

Figure 25. Extracted spectra and radial profiles for NGC 7465; same description as in Figure 7.

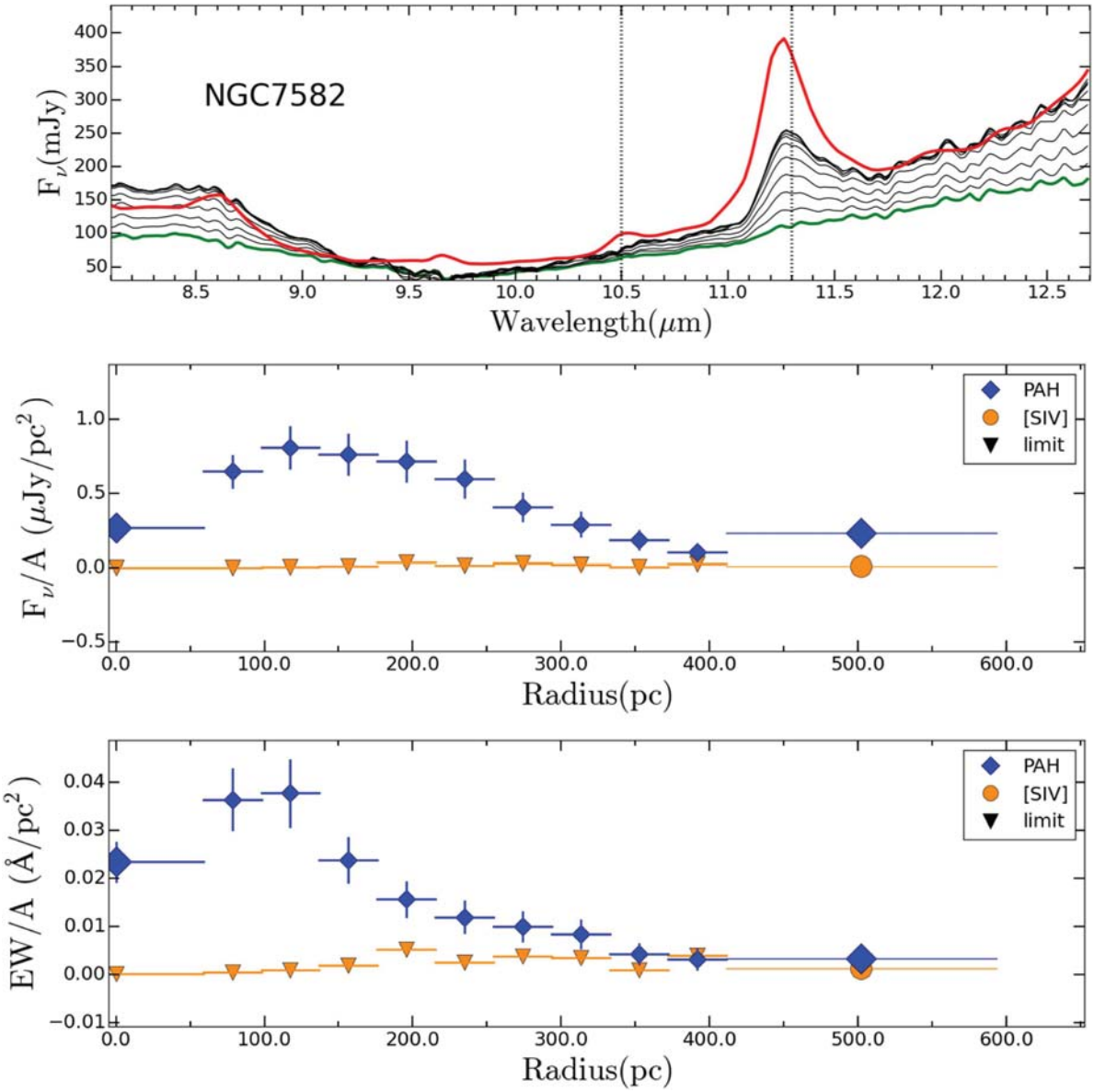

Figure 26. Extracted spectra and radial profiles for NGC 7582; same description as in Figure 7.

ORCID iDs

Donaji Esparza-Arredondo https://orcid.org/0000-0001-8042-9867
Omaira González-Martín https://orcid.org/0000-0002-2356-8358
Almudena Alonso-Herrero https://orcid.org/0000-0001-6794-2519
Cristina Ramos Almeida https://orcid.org/0000-0001-8353-649X
Tanio Díaz-Santos https://orcid.org/0000-0003-0699-6083
Jose Miguel Rodríguez-Espinosa https://orcid.org/0000-0002-0674-1470

References

Aitken, D. K., & Roche, P. F. 1984, MNRAS, 208, 751
Alonso-Herrero, A., Esquej, P., Roche, P. F., et al. 2016, MNRAS, 455, 563
Alonso-Herrero, A., Pereira-Santaella, M., Rieke, G. H., et al. 2013, ApJ, 765, 78
Alonso-Herrero, A., Pereira-Santaella, M., Rieke, G. H., & Rigopoulou, D. 2012, ApJ, 744, 2
Alonso-Herrero, A., Ramos Almeida, C., Esquej, P., et al. 2014, MNRAS, 443, 2766
Asmus, D., Hönig, S. F., Gandhi, P., Smette, A., & Duschl, W. J. 2014, MNRAS, 439, 1648
Barnes, J. E., & Hernquist, L. E. 1991, ApJL, 370, L65
Bedregal, A. G., Colina, L., Alonso-Herrero, A., & Arribas, S. 2009, ApJ, 698, 1852
Brandl, B. R., Bernard-Salas, J., Spoon, H. W. W., et al. 2006, ApJ, 653, 1129
Cicone, C., Maiolino, R., Sturm, E., et al. 2014, A&A, 562, A21
Cohen, M., Allamandola, L., Tielens, A. G. G. M., et al. 1986, ApJ, 302, 737
Colina, L., Sparks, W. B., & Macchetto, F. 1991, ApJ, 370, 102
Dale, D. A., Smith, J. D. T., Armus, L., et al. 2006, ApJ, 646, 161
Dasyra, K. M., Ho, L. C., Netzer, H., et al. 2011, ApJ, 740, 94
Davies, R. I., Thomas, J., Genzel, R., et al. 2006, ApJ, 646, 754
De Buizer, J., & Fisher, R. 2005, High Resolution Infrared Spectroscopy in Astronomy, 84
De Robertis, M. M., & Osterbrock, D. E. 1986, ApJ, 301, 98

de Vaucouleurs, G. et al. (ed.) 1991, Third Reference Catalogue of Bright Galaxies, Vol. I: Explanations and References, Vol. II: Data for Galaxies Between 0^h and 12^h, Vol. III: Data for Galaxies Between 12^h and 24^h (New York: Springer), 2091
Diamond-Stanic, A. M., & Rieke, G. H. 2010, ApJ, 724, 140
Diamond-Stanic, A. M., & Rieke, G. H. 2012, ApJ, 746, 168
Diaz-Santos, T., Alonso-Herrero, A., Colina, L., et al. 2010, ApJ, 711, 328
Dudik, R. P., Satyapal, S., Gliozzi, M., & Sambruna, R. M. 2005, ApJ, 620, 113
Dultzin-Hacyan, D., Masegosa, M. J., & Moles, M. 1990, A&A, 238, 28
Esquej, P., Alonso-Herrero, A., González-Martín, O., et al. 2014, ApJ, 780, 86
Ferrarese, L., & Merritt, D. 2000, ApJL, 539, L9
Gallimore, J. F., Yzaguirre, A., Jakoboski, J., et al. 2010, ApJS, 187, 172
García-Bernete, I., Ramos Almeida, C., Acosta-Pulido, J. A., et al. 2015, MNRAS, 449, 1309
Genzel, R., Lutz, D., Sturm, E., et al. 1998, ApJ, 498, 579
Gillett, F. C., Forrest, W. J., & Merrill, K. M. 1973, ApJ, 183, 87
Gillett, F. C., Merrill, K. M., & Stein, W. A. 1972, ApJ, 172, 367
Gilli, R., Maiolino, R., Marconi, A., et al. 2000, A&A, 355, 485
González Delgado, R. M., Heckman, T., Leitherer, C., et al. 1998, ApJ, 505, 174
González-Martín, O. 2018, arXiv:1803.05925
González-Martín, O., Rodríguez-Espinosa, J. M., Díaz-Santos, T., et al. 2013, A&A, 553, A35
Goulding, A. D., & Alexander, D. M. 2009, MNRAS, 398, 1165
Goulding, A. D., Alexander, D. M., Bauer, F. E., et al. 2012, ApJ, 755, 5
Groves, B., Nefs, B., & Brandl, B. 2008, MNRAS, 391, L113
Gutcke, T. A., Fanidakis, N., Macciò, A. V., & Lacey, C. 2015, MNRAS, 451, 3759
Haynes, M. P. 1981, AJ, 86, 1126
Hernán-Caballero, A., & Hatziminaoglou, E. 2011, MNRAS, 414, 500
Ho, L. C., Feigelson, E. D., Townsley, L. K., et al. 2001, ApJL, 549, L51
Ho, L. C., Filippenko, A. V., & Sargent, W. L. W. 2003, ApJ, 583, 159
Holtz, J. Z., Geballe, T. R., & Rank, D. M. 1971, ApJL, 164, L29
Hönig, S. F., & Kishimoto, M. 2010, A&A, 523, A27
Hönig, S. F., Smette, A., Beckert, T., et al. 2008, A&A, 485, L21
Hopkins, P. F. 2012, MNRAS, 420, L8
Hopkins, P. F., & Quataert, E. 2010, MNRAS, 407, 1529
Jensen, J. J., Hönig, S. F., Rakshit, S., et al. 2017, MNRAS, 470, 3071
Kawakatu, N., & Wada, K. 2008, ApJ, 681, 73
Kewley, L. J., Heisler, C. A., Dopita, M. A., & Lumsden, S. 2001, ApJS, 132, 37
Kormendy, J., & Richstone, D. 1995, ARA&A, 33, 581
Krabbe, A., Sternberg, A., & Genzel, R. 1994, ApJ, 425, 72
Krongold, Y., Dultzin-Hacyan, D., & Marziani, P. 2002, ApJ, 572, 169
Laurent, O., Mirabel, I. F., Charmandaris, V., et al. 2000, A&A, 359, 887
Lebouteiller, V., Barry, D. J., Spoon, H. W. W., et al. 2011, ApJS, 196, 8
Levenson, N. A., Weaver, K. A., Heckman, T. M., Awaki, H., & Terashima, Y. 2005, ApJ, 618, 167
Liu, T., Wang, J.-X., Yang, H., Zhu, F.-F., & Zhou, Y.-Y. 2014, ApJ, 783, 106
Magorrian, J., Tremaine, S., Richstone, D., et al. 1998, AJ, 115, 2285
Malkan, M. A., Gorjian, V., & Tam, R. 1998, ApJS, 117, 25
Marconi, A., & Hunt, L. K. 2003, ApJL, 589, L21
Marconi, A., Risaliti, G., Gilli, R., et al. 2004, MNRAS, 351, 169
Martini, P., Regan, M. W., Mulchaey, J. S., & Pogge, R. W. 2003, ApJS, 146, 353
Mason, R. E., Rodríguez-Ardila, A., Martins, L., et al. 2015, ApJS, 217, 13
McAlpine, K., Prandoni, I., Jarvis, M., et al. 2015, Advancing Astrophysics with the Square Kilometre Array (AASKA14), 83
McConnell, N. J., & Ma, C.-P. 2013, ApJ, 764, 184
Millar, T. J., & Williams, D. A. 1993, Sci, 262, 1462
Moran, E. C., Barth, A. J., Kay, L. E., & Filippenko, A. V. 2000, ApJL, 540, L73
Morris, S., Ward, M., Whittle, M., Wilson, A. S., & Taylor, K. 1985, MNRAS, 216, 193
Mullaney, J. R., Alexander, D. M., Goulding, A. D., & Hickox, R. C. 2011, MNRAS, 414, 1082
Neistein, E., & Netzer, H. 2014, MNRAS, 437, 3373
Nenkova, M., Sirocky, M. M., Nikutta, R., Ivezić, Ž., & Elitzur, M. 2008, ApJ, 685, 160
O'Sullivan, E., Forbes, D. A., & Ponman, T. J. 2001, MNRAS, 328, 461
Ohsuga, K., & Umemura, M. 1999, ApJL, 521, L13
Peeters, E., Spoon, H. W. W., & Tielens, A. G. G. M. 2004, ApJ, 613, 986
Pereira-Santaella, M., Alonso-Herrero, A., Rieke, G. H., et al. 2010, ApJS, 188, 447
Phillips, M. M., Charles, P. A., & Baldwin, J. A. 1983, ApJ, 266, 485
Ramos Almeida, C., Alonso-Herrero, A., Esquej, P., et al. 2014, MNRAS, 445, 1130
Ramos Almeida, C., Levenson, N. A., Rodríguez Espinosa, J. M., et al. 2009, ApJ, 702, 1127
Rank, D. M., Holtz, J. Z., Geballe, T. R., & Townes, C. H. 1970, ApJL, 161, L185
Riffel, R. A., Storchi-Bergmann, T., Dors, O. L., & Winge, C. 2009, MNRAS, 393, 783
Roche, P. F., Packham, C., Aitken, D. K., & Mason, R. E. 2007, MNRAS, 375, 99
Rodríguez-Ardila, A., Contini, M., & Viegas, S. M. 2005, MNRAS, 357, 220
Rodríguez-Ardila, A., & Viegas, S. M. 2003, MNRAS, 340, L33
Rosario, D. J., Santini, P., Lutz, D., et al. 2012, A&A, 545, A45
Rossa, J., Dietrich, M., & Wagner, S. J. 2000, A&A, 362, 501
Ruschel-Dutra, D., Pastoriza, M., Riffel, R., Sales, D. A., & Winge, C. 2014, MNRAS, 438, 3434
Ruschel-Dutra, D., Rodríguez Espinosa, J. M., González Martín, O., Pastoriza, M., & Riffel, R. 2017, MNRAS, 466, 3353
Sales, D. A., Pastoriza, M. G., Riffel, R., et al. 2011, ApJ, 738, 109
Sanders, D. B., Soifer, B. T., Elias, J. H., et al. 1988, ApJ, 325, 74
Shi, Y., Rieke, G. H., Hines, D. C., et al. 2006, ApJ, 653, 127
Shipley, H. V., Papovich, C., Rieke, G. H., Brown, M. J. I., & Moustakas, J. 2016, ApJ, 818, 60
Siebenmorgen, R., Krügel, E., & Spoon, H. W. W. 2004, A&A, 414, 123
Silk, J., & Rees, M. J. 1998, A&A, 331, L1
Smajić, S., Fischer, S., Zuther, J., & Eckart, A. 2012, A&A, 544, A105
Smith, J., Draine, B., Dale, D., et al. 2007, ApJ, 656, 770
Storchi-Bergmann, T., González Delgado, R. M., Schmitt, H. R., Cid Fernandes, R., & Heckman, T. 2001, ApJ, 559, 147
Storchi-Bergmann, T., Rodriguez-Ardila, A., Schmitt, H. R., Wilson, A. S., & Baldwin, J. A. 1996, ApJ, 472, 83
Telesco, C. M., Ciardi, D., French, J., et al. 2003, Proc. SPIE, 4841, 913
Telesco, C. M., Pina, R. K., Hanna, K. T., et al. 1998, Proc. SPIE, 3354, 534
Tremaine, S., Gebhardt, K., Bender, R., et al. 2002, ApJ, 574, 740
Trippe, M. L., Crenshaw, D. M., Deo, R., & Dietrich, M. 2008, AJ, 135, 2048
van den Bergh, S. 1976, ApJ, 206, 883
Veron, P., Goncalves, A. C., & Veron-Cetty, M.-P. 1997, A&A, 319, 52
Veron-Cetty, M.-P., & Veron, P. 1985, A&A, 145, 425
Véron-Cetty, M.-P., & Véron, P. 2010, A&A, 518, A10
Voit, G. M. 1992, MNRAS, 258, 841
Vollmer, B., & Davies, R. I. 2013, A&A, 556, A31
Volonteri, M., Capelo, P. R., Netzer, H., et al. 2015, MNRAS, 452, L6
Ward, M. J., & Wilson, A. S. 1978, A&A, 70, L79
Weaver, K. A., Meléndez, M., Mushotzky, R. F., et al. 2010, ApJ, 716, 1151
Weaver, K. A., Wilson, A. S., & Baldwin, J. A. 1991, ApJ, 366, 50
Weedman, D. W., Hao, L., Higdon, S. J. U., et al. 2005, ApJ, 633, 706
Woo, J.-H., & Urry, C. M. 2002, ApJ, 579, 530
Woo, J.-H., Yoon, Y., Park, S., Park, D., & Kim, S. C. 2015, ApJ, 801, 38
Wu, Y., Charmandaris, V., Huang, J., et al. 2009, ApJ, 701, 658
Wylezalek, D., & Zakamska, N. L. 2016, MNRAS, 461, 3724
Yankulova, I. M. 1999, A&A, 344, 36
Young, S., Packham, C., Mason, R. E., Radomski, J. T., & Telesco, C. M. 2007, MNRAS, 378, 888
Yuan, T.-T., Kewley, L. J., & Sanders, D. B. 2010, ApJ, 709, 884

Appendix B

Catalogue spectral fittings

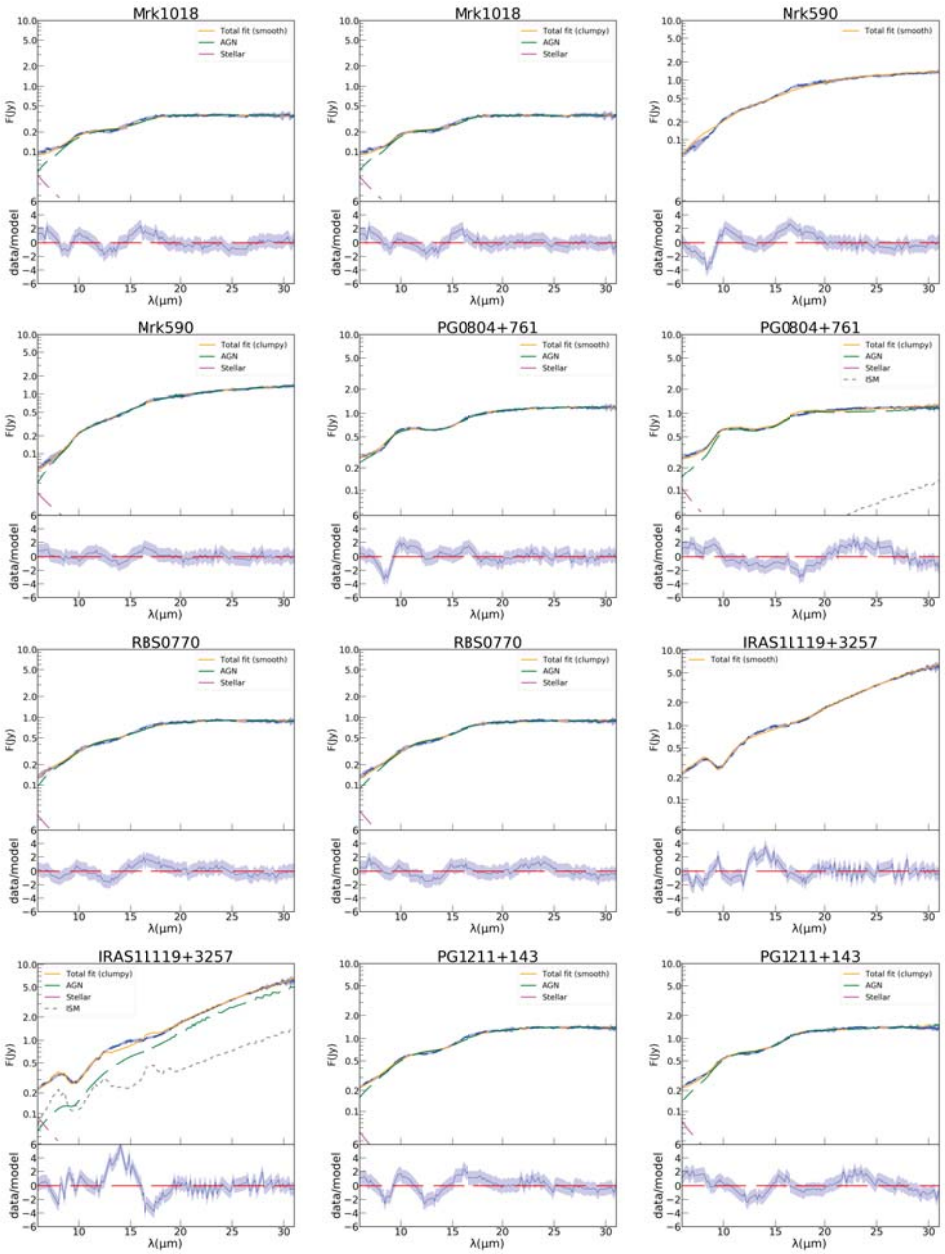

Figure B.1: Spectral fits of mid-IR Seyfert 1 data.

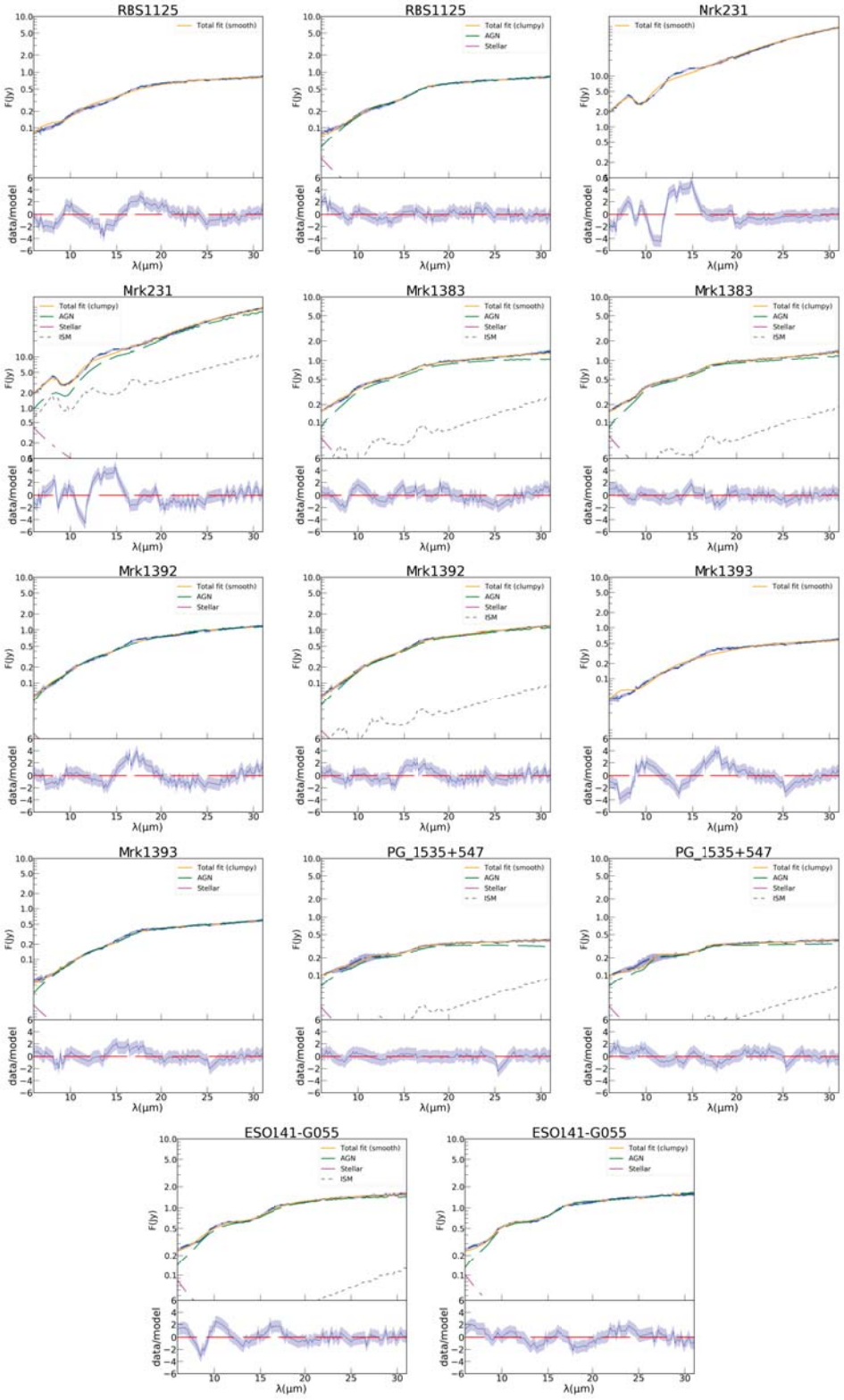

Figure B.2: Spectral fits of mid-IR Seyfert 1 data.

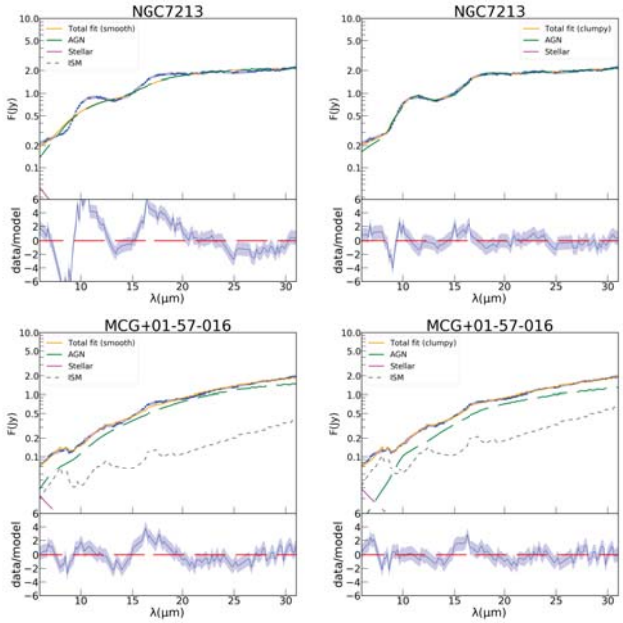

Figure B.3: Spectral fits of mid-IR Seyfert 1 data.

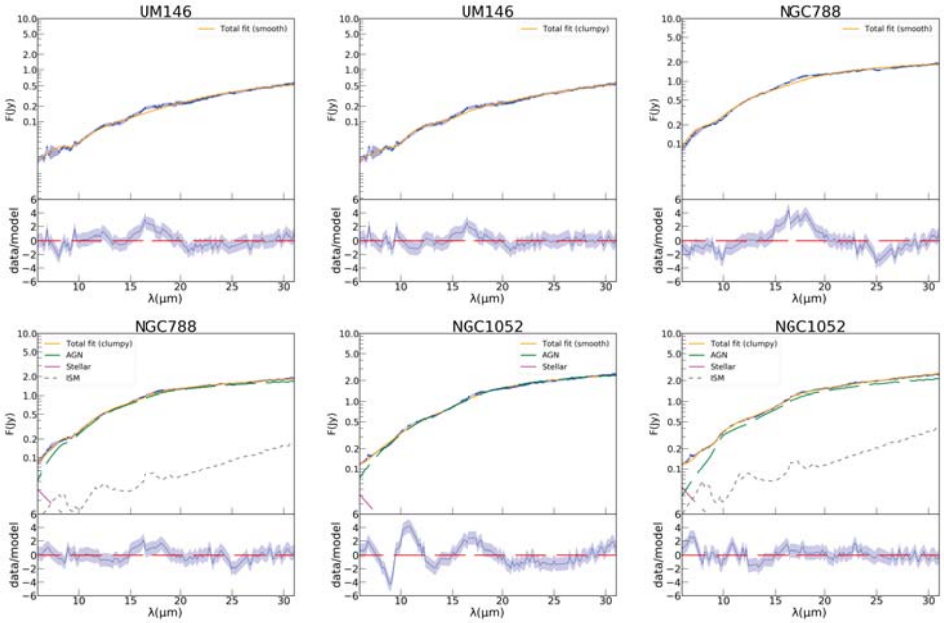

Figure B.4: Spectral fits of mid-IR Seyfert 2 data.

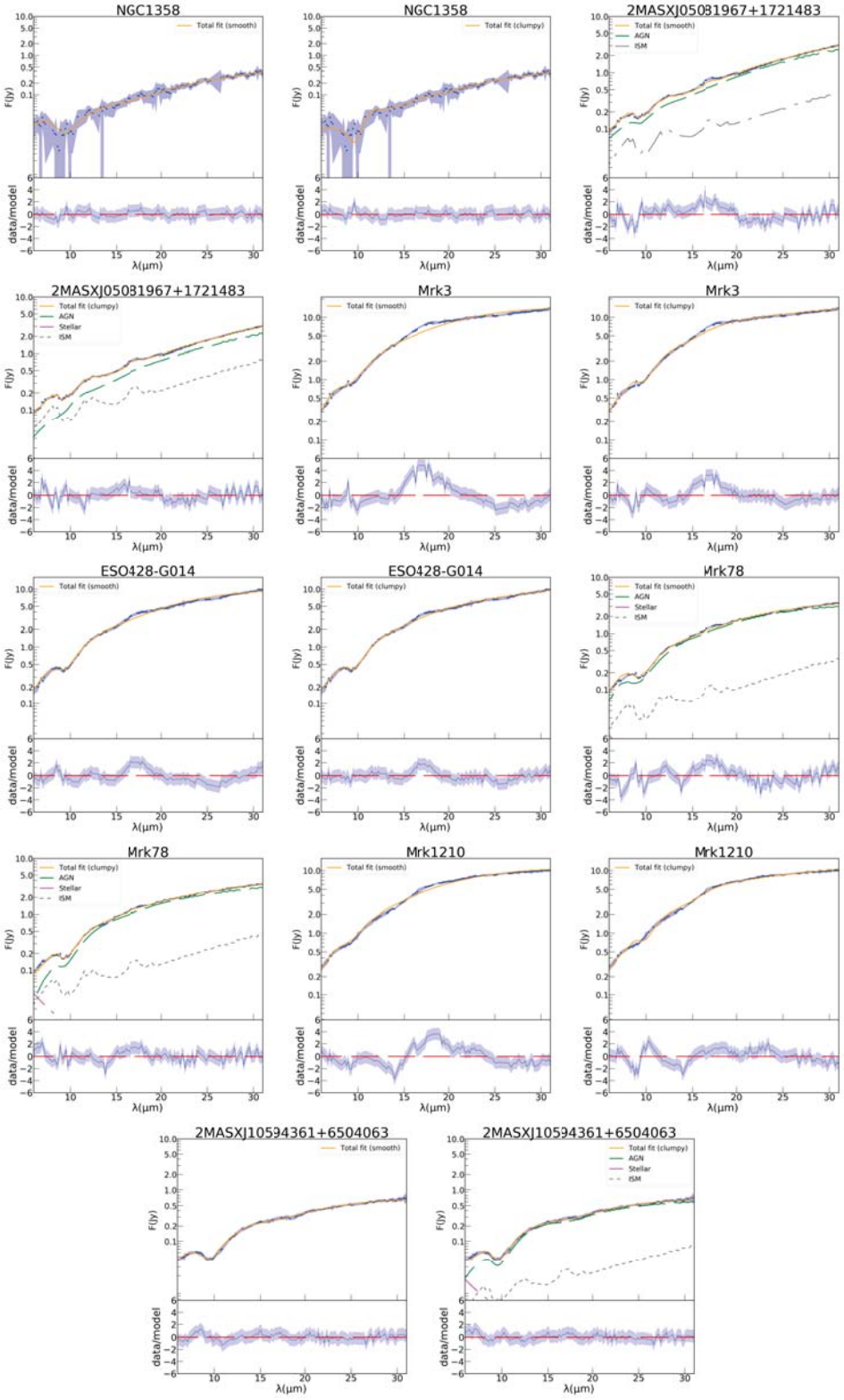

Figure B.5: Spectral fits of mid-IR Seyfert 2 data.

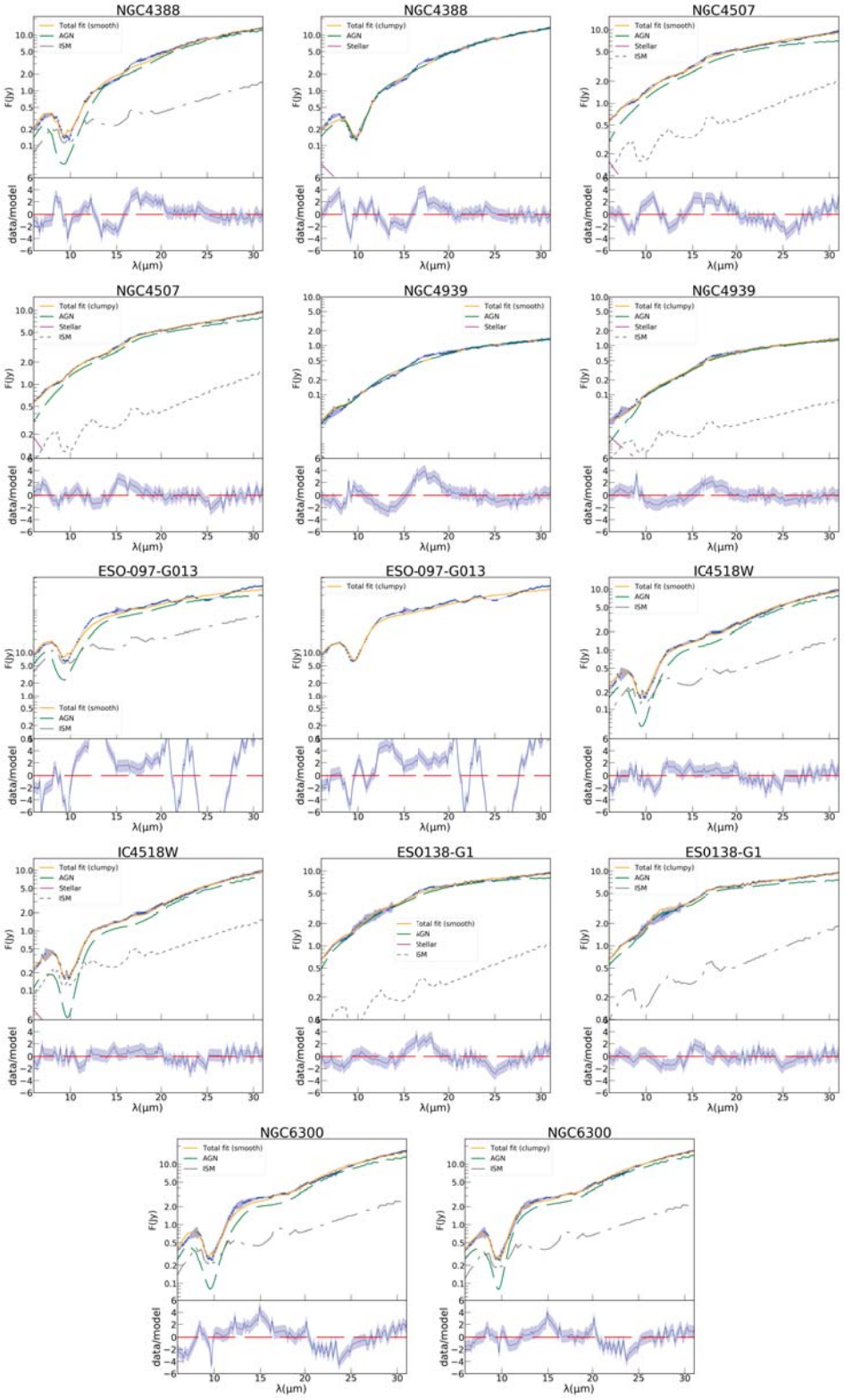

Figure B.6: Spectral fits of mid-IR Seyfert 2 data.

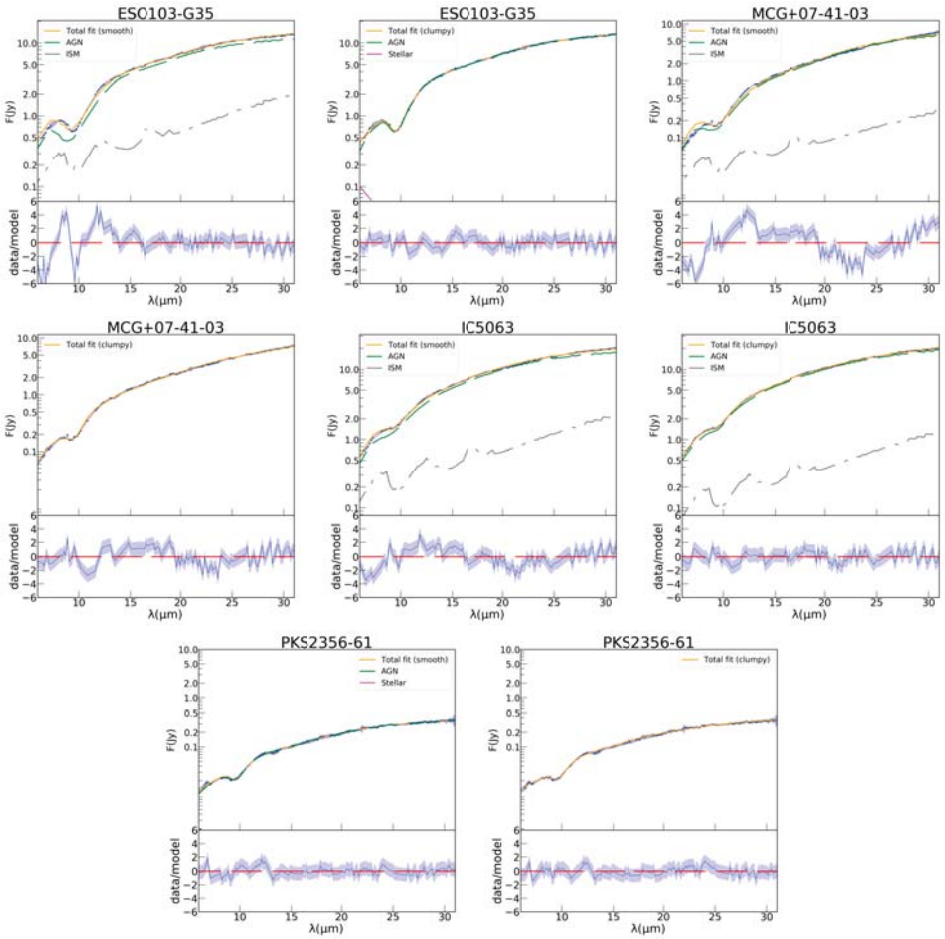

Figure B.7: Spectral fits of mid-IR Seyfert 2 data.

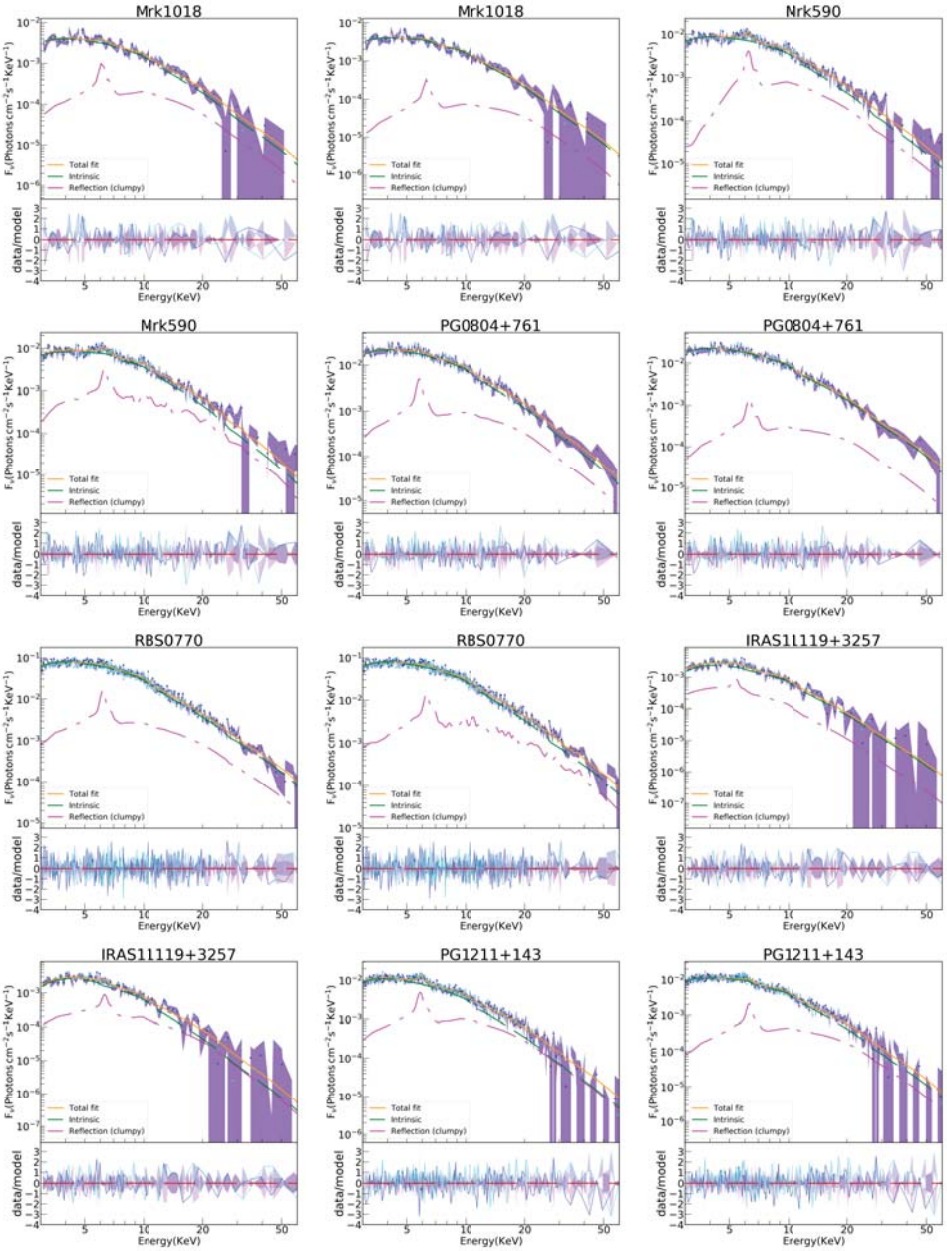

Figure B.8: Spectral fits of X-ray Seyfert 1 data.

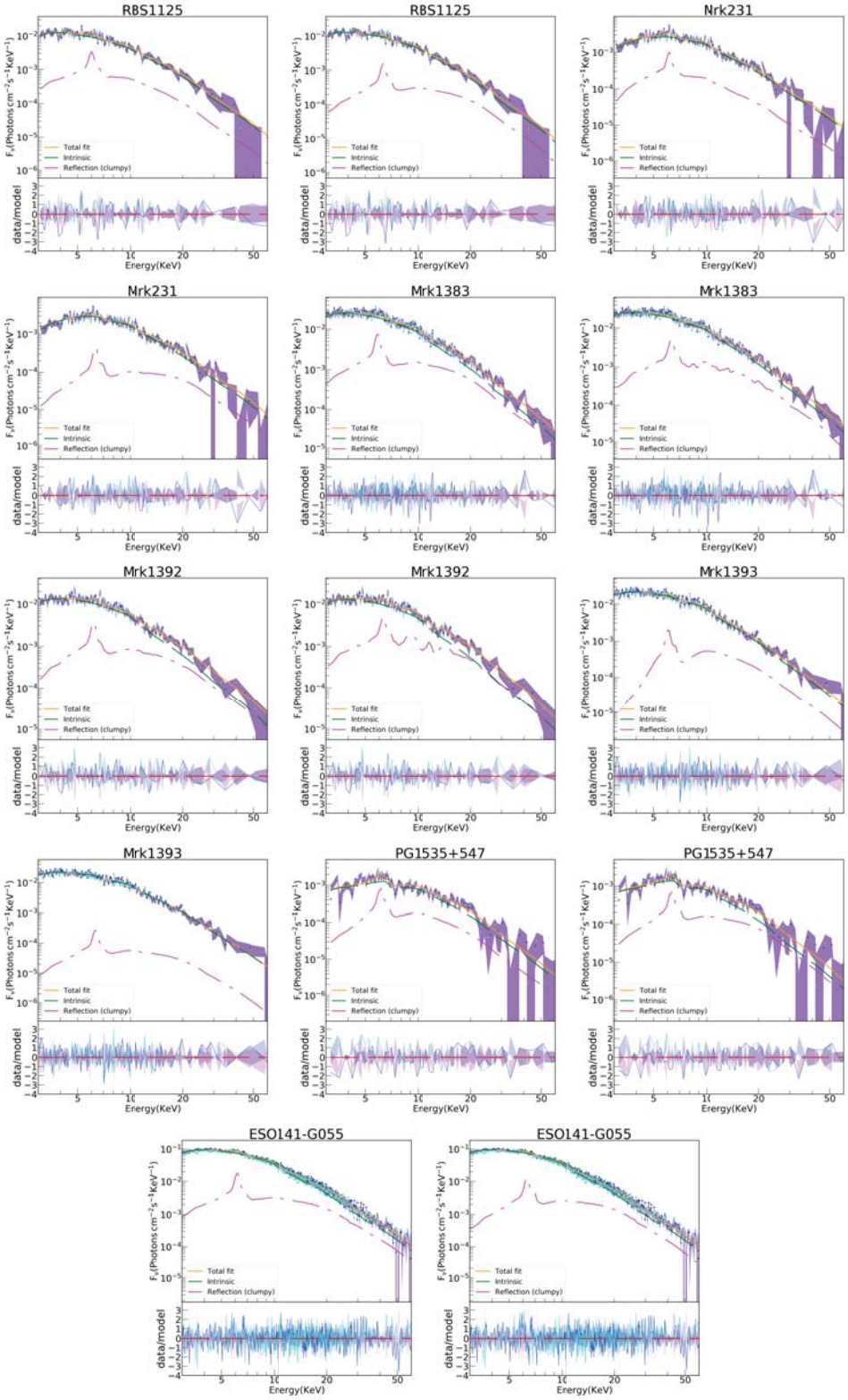

Figure B.9: Spectral fits of X-ray Seyfert 1 data.

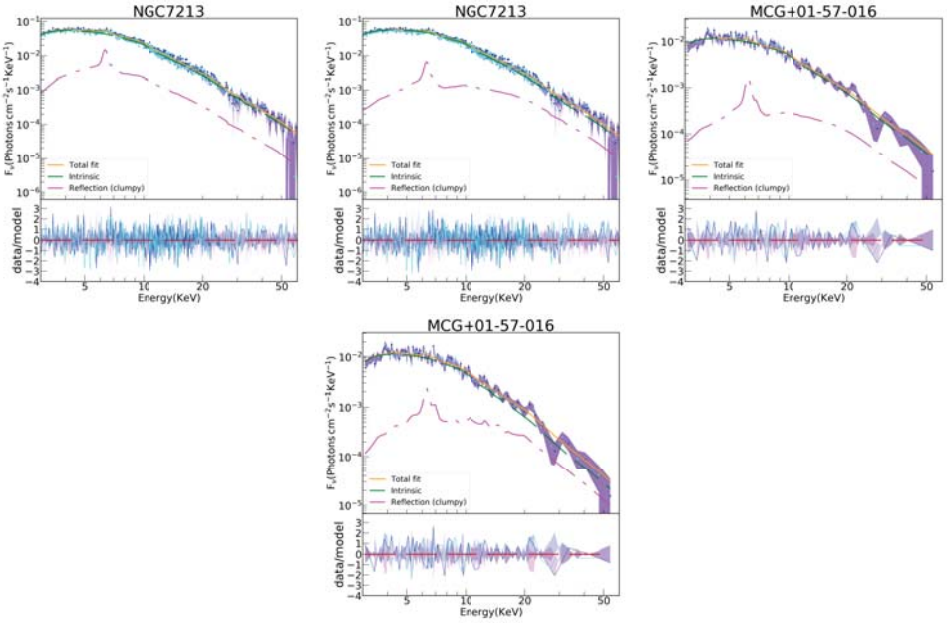

Figure B.10: Spectral fits of X-ray Seyfert 2 data.

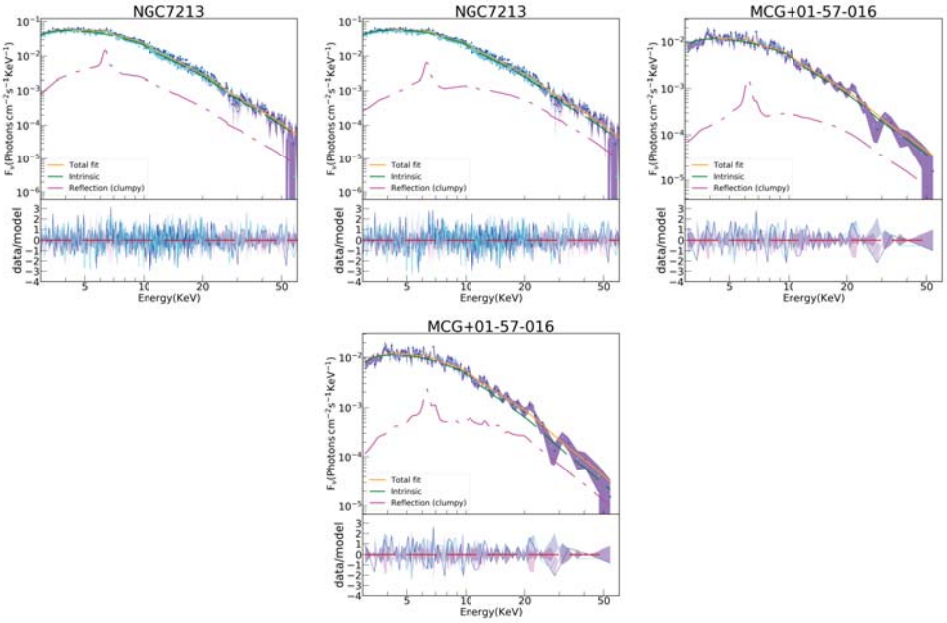

Figure B.11: Spectral fits of mid-IR Seyfert 2 data.

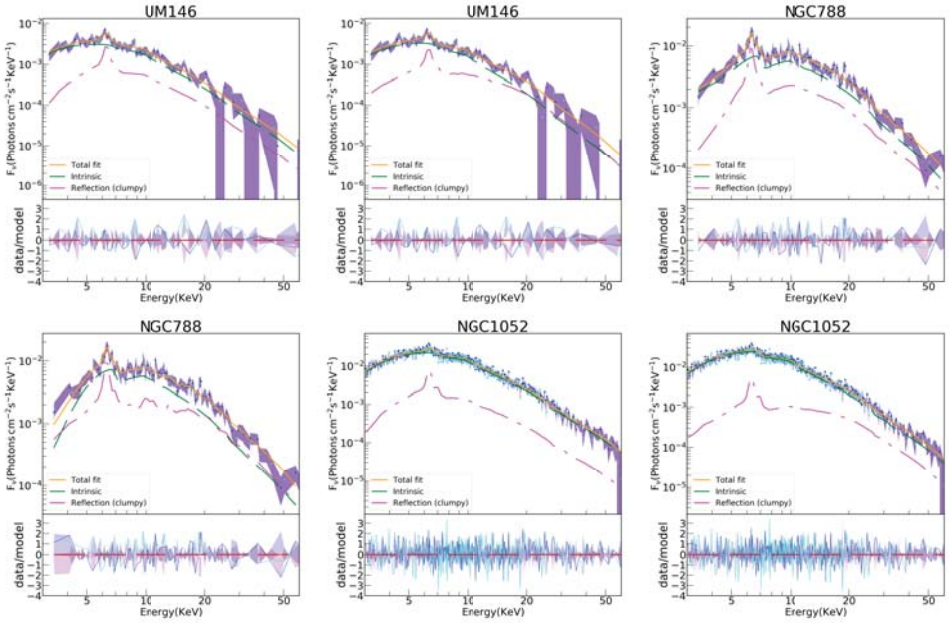

Figure B.12: Spectral fits of X-ray Seyfert 2 data.

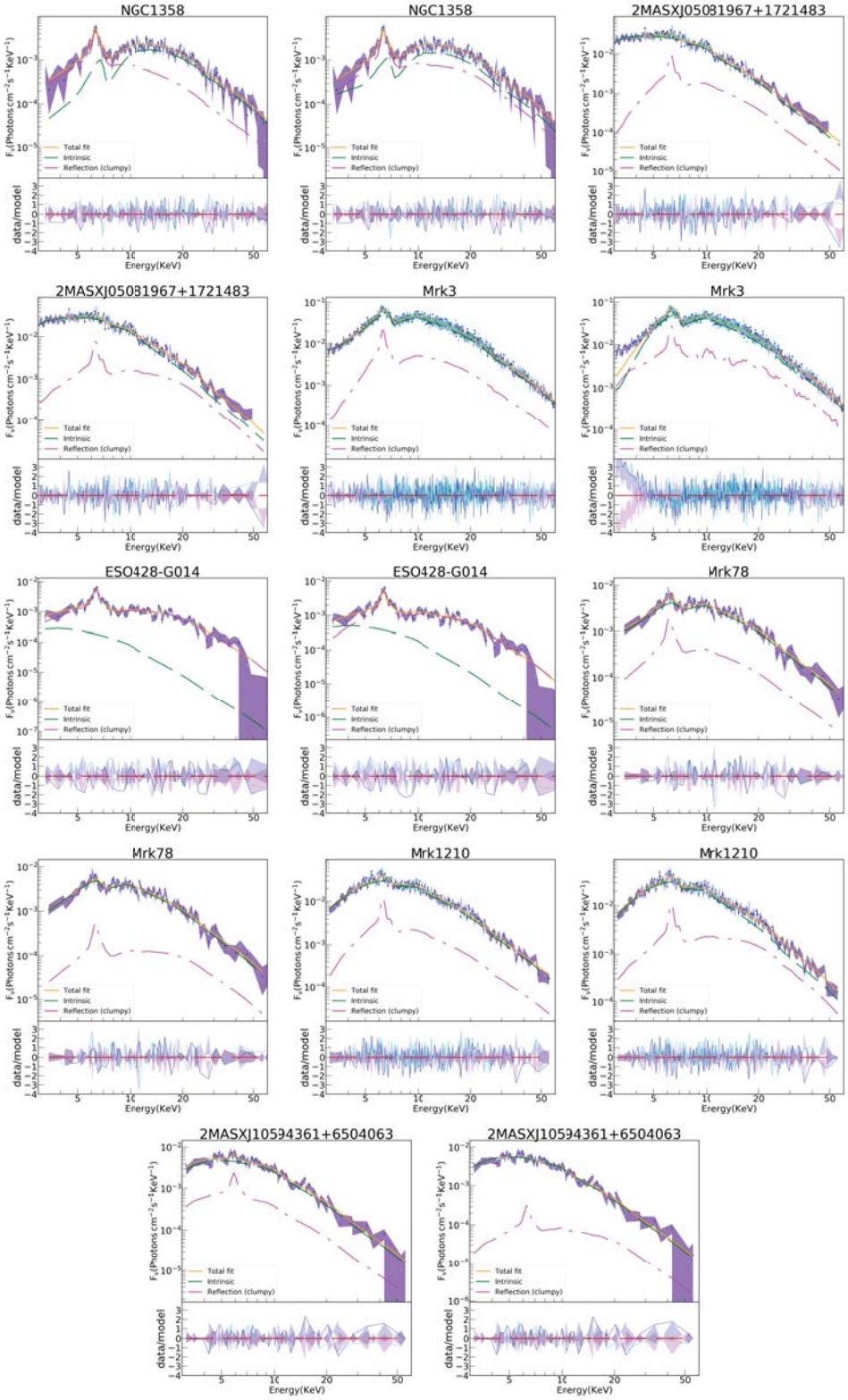

Figure B.13: Spectral fits of X-ray Seyfert 2 data.

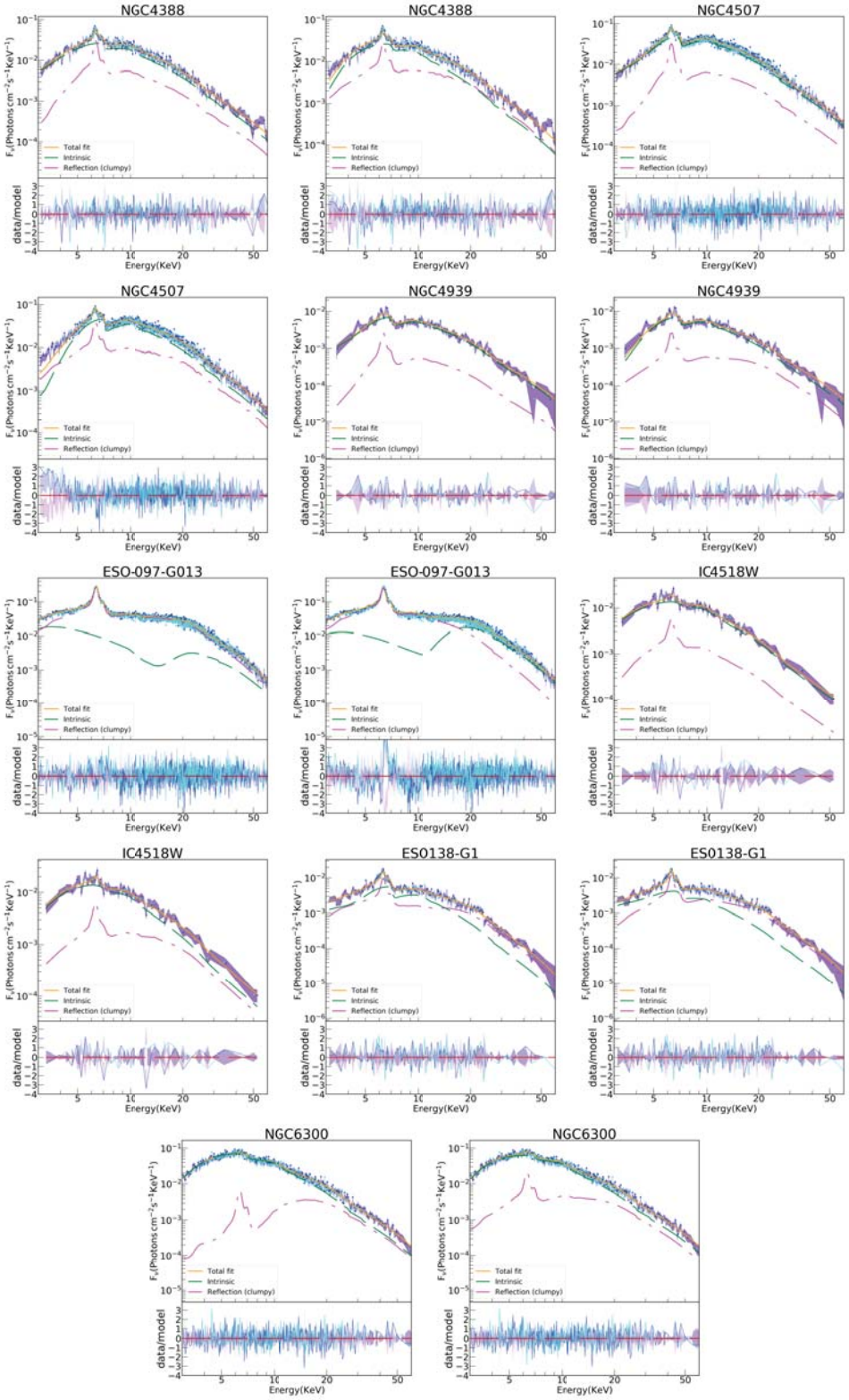

Figure B.14: Spectral fits of X-ray Seyfert 2 data.

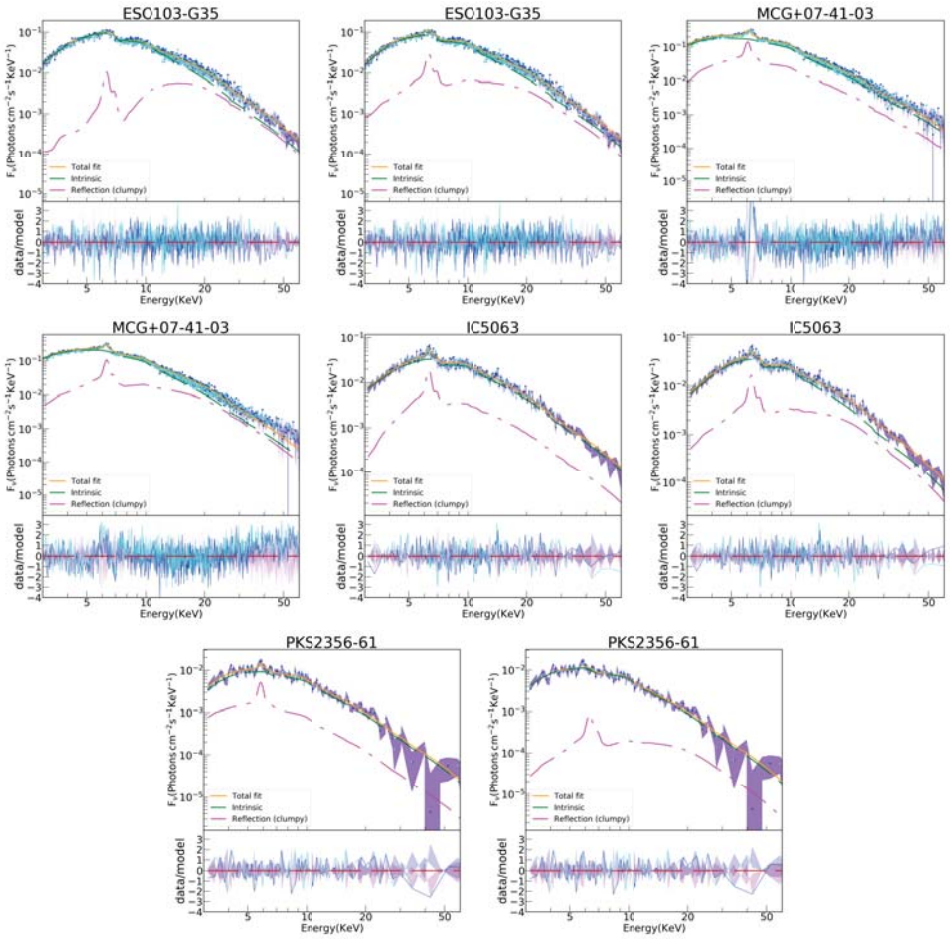

Figure B.15: Spectral fits of X-ray Seyfert 2 data.

Bibliography

Abramowicz, M. A. & Fragile, P. C. 2013, Living Reviews in Relativity, 16, 1.

Alam, S., Albareti, F. D., Allende Prieto, C., et al. 2015, ApJS , 219, 12.

Alexander, T. & Netzer, H. 1997, MNRAS , 284, 967

Alonso-Herrero, A., Ramos Almeida, C., Mason, R., et al. 2011, ApJ , 736, 82

Alonso-Herrero, A., Ramos Almeida, C., Esquej, P., et al. 2014, MNRAS , 443, 2766

Antonucci, R. R. J. & Cohen, R. D. 1983, ApJ , 271, 564

Antonucci, R. R. J., & Miller, J. S. 1985, ApJ , 297, 621

Asmus, D., Hönig, S. F., Gandhi, P., et al. 2014, MNRAS , 439, 1648.

Asmus, D., Gandhi, P., Hönig, S. F., et al. 2015, MNRAS , 454, 766.

Awaki, H., Koyama, K., Inoue, H., et al. 1991, PASJ , 43, 195

Baldwin, J. A., Phillips, M. M., & Terlevich, R. 1981, PASP , 93, 5

Ballo, L., Braito, V., Della Ceca, R., et al. 2004, ApJ , 600, 634

Baloković, M., Brightman, M., Harrison, F. A., et al. 2018, ApJ , 854, 42

Bañados, E., Venemans, B. P., Mazzucchelli, C., et al. 2018, Nature , 553, 473

Barcons, X. & Athena Science Study Team 2011, AAS/High Energy Astrophysics Division #12

Barr, E. S. 1961, Infrared Physics, 1, 1,IN1,3,IN3

Bassani, L., Dadina, M., Maiolino, R., et al. 1999, ApJS , 121, 473

Bauer, F. E., Arévalo, P., Walton, D. J., et al. 2015, ApJ , 812, 116

Barr, P., White, N. E., Sanford, P. W., et al. 1977, MNRAS , 181, 43P.

Becklin, E. E. & Neugebauer, G. 1969, ApJL , 157, L31

Beckmann, V. & Shrader, C. R. 2012, Active Galactic Nuclei, ISBN-13: 978-3527410781. 350 pages. Wiley-VCH Verlag GmbH, 2012

Bennett, A. S. 1962, MmRAS , 68, 163

Bentz, M. C., Denney, K. D., Grier, C. J., et al. 2013, ApJ , 767, 149

Berney, S., Koss, M., Trakhtenbrot, B., et al. 2015, MNRAS , 454, 3622

Bianchi, S., Maiolino, R., & Risaliti, G. 2012, Advances in Astronomy, 2012, 782030

Blandford, R., Meier, D., & Readhead, A. 2019, ARA&A , 57, 467

Bradt, H. V., Swank, J. H., & Rothschild, R. E. 1990, Advances in Space Research, 10, 297.

Brandt, W. N., Fabian, A. C., Nandra, K., et al. 1994, MNRAS , 271, 958.

Brightman, M., & Nandra, K. 2011, MNRAS , 413, 1206

Boella, G., Butler, R. C., Perola, G. C., et al. 1997, A&AS , 122, 299

Böhm, A., Wisotzki, L., Bell, E. F., et al. 2013, A&A , 549, A46

Bond, P. 2000, Encyclopedia of Astronomy and Astrophysics, 1957. *https* : *//sites.astro.caltech.edu/ george/ay*20*/ir − telescopes.pdf*

Boissay, R., Ricci, C., & Paltani, S. 2016, A&A , 588, A70

Brenneman, L. W. & Reynolds, C. S. 2006, ApJ , 652, 1028

Brightman, M., Baloković, M., Stern, D., et al. 2015, ApJ , 805, 41

Buchner, J. 2018. [Data set]. Zenodo. http://doi.org/10.5281/zenodo.2211263

Buchner, J., Brightman, M., Nandra, K., et al. 2019, A&A , 629, A16

Bundy, K., Bershady, M. A., Law, D. R., et al. 2015, ApJ , 798, 7

Burrows, D. N., Hill, J. E., Nousek, J. A., et al. 2005, Space Sci. Rev. , 120, 165.

Burtscher, L., Meisenheimer, K., Tristram, K. R. W., et al. 2013, A&A , 558, A149

Capellupo, D. M., Wafflard-Fernandez, G., & Haggard, D. 2017, ApJL , 836, L8

Civano, F., Elvis, M., Lanzuisi, G., et al. 2010, ApJ , 717, 209

Czerny, B., Hryniewicz, K., Nikołajuk, M., et al. 2011, MNRAS , 415, 2942

Conselice, C. J. 2014, ARA&A , 52, 291

Crenshaw, D. M. & Kraemer, S. B. 1999, ApJ , 521, 572.

Dauser, T., Garcia, J., Parker, M. L., et al. 2014, MNRAS , 444, L100

Dasyra, K. M., Ho, L. C., Netzer, H., et al. 2011, ApJ , 740, 94.

Detweiler, S. 1980, ApJ , 239, 292

Diamond-Stanic, A. M., Fan, X., Brandt, W. N., et al. 2009, ApJ , 699, 782.

Dicken, D., Tadhunter, C., Morganti, R., et al. 2014, ApJ , 788, 98.

DiPompeo, M. A., Hickox, R. C., Carroll, C. M., et al. 2018, ApJ , 856, 76

Done, C., Gierliński, M., & Kubota, A. 2007, A&A Rev. , 15, 1

Done, C., Jin, C., Middleton, M., et al. 2013, MNRAS , 434, 1955

Doeleman, S. S., Weintroub, J., Rogers, A. E. E., et al. 2008, Nature , 455, 78

Draine, B. T., Dale, D. A., Bendo, G., et al. 2007, ApJ , 663, 866.

Ebrero, J., Kaastra, J. S., Kriss, G. A., et al. 2016, A&A , 587, A129

Edge, D. O., Shakeshaft, J. R., McAdam, W. B., et al. 1959, MmRAS , 68, 37

Elitzur, M., & Shlosman, I. 2006, ApJL , 648, L101

Elitzur, M. 2012, ApJL , 747, L33

Elitzur, M., Ho, L. C., & Trump, J. R. 2014, MNRAS , 438, 3340

Elvis, M., Maccacaro, T., Wilson, A. S., et al. 1978, MNRAS , 183, 129.

Emmanoulopoulos, D., Papadakis, I. E., Epitropakis, A., et al. 2016, MNRAS , 461, 1642

Esin, A. A., McClintock, J. E., & Narayan, R. 1997, ApJ , 489, 865

Esparza-Arredondo, D., González-Martín, O., Dultzin, D., et al. 2018, ApJ , 859, 124

Esparza-Arredondo, D., González-Martín, O., Dultzin, D., et al. 2019, ApJ , 886, 125.

Esparza-Arredondo, D., Osorio-Clavijo, N., González-Martín, O., et al. 2020, ApJ , 905, 29.

Esparza-Arredondo, D, González-Martín, O., Dultzin, D., et al. 2021, å,

Esquej, P., Alonso-Herrero, A., González-Martín, O., et al. 2014, ApJ , 780, 86

Falcke, H., Körding, E., & Markoff, S. 2004, A&A , 414, 895

Falcke, H. & Markoff, S. B. 2013, Classical and Quantum Gravity, 30, 244003

Falomo, R., Bettoni, D., Karhunen, K., et al. 2014, MNRAS , 440, 476

Fanaroff, B. L. & Riley, J. M. 1974, MNRAS , 167, 31P

Farrah, D., Baloković, M., Stern, D., et al. 2016, ApJ , 831, 76

Fath, E. A. 1909, Lick Observatory Bulletin, 149, 71

Feltre, A., Hatziminaoglou, E., Fritz, J., & Franceschini, A. 2012, MNRAS , 426, 120

Fender, R. & Belloni, T. 2012, Science, 337, 540.

Fender, R. & Muñoz-Darias, T. 2016, Lecture Notes in Physics, Berlin Springer Verlag, 65.

Ferrarese, L., & Merritt, D. 2000, ApJL , 539, L9

Fish, V. L., Doeleman, S. S., Beaudoin, C., et al. 2011, ApJL , 727, L36

Fosbury, R., De Breuck, C., Mainieri, V., et al. 2007, arXiv e-prints, arXiv:0708.1378

Fritz, J., Franceschini, A., & Hatziminaoglou, E. 2006, MNRAS , 366, 767

Furui, S., Fukazawa, Y., Odaka, H., et al. 2016, ApJ , 818, 164

Gabor, J. M., Impey, C. D., Jahnke, K., et al. 2009, ApJ , 691, 705

Gallimore, J. F., Elitzur, M., Maiolino, R., et al. 2016, ApJL , 829, L7

Gandhi, P., Horst, H., Smette, A., et al. 2009, A&A , 502, 457.

García, J., Dauser, T., Lohfink, A., et al. 2014, ApJ , 782, 76

García-Bernete, I., Ramos Almeida, C., Alonso-Herrero, A., et al. 2019, MNRAS , 486, 4917

García-Burillo, S., Combes, F., Ramos Almeida, C., et al. 2016, ApJL , 823, L12

García-Burillo, S., Combes, F., Ramos Almeida, C., et al. 2019, A&A , 632, A61

Garcia-Burillo, S., Alonso-Herrero, A., Ramos Almeida, C., et al. 2021, arXiv:2104.10227

Gebhardt, K., Bender, R., Bower, G., et al. 2000, ApJL , 539, L13

Ghisellini, G., Haardt, F., & Matt, G. 1994, MNRAS , 267, 743

Giacconi, R., Gursky, H., Paolini, F. R., et al. 1962, PRL , 9, 439.

Giacconi, R., Gursky, H., & Waters, J. R. 1964, Nature , 204, 981.

Giacconi, R., Kellogg, E., Gorenstein, P., et al. 1971, ApJL , 165, L27.

Giacconi, R., Bechtold, J., Branduardi, G., et al. 1979, ApJL , 234, L1.

Gillett, F. C., Merrill, K. M., & Stein, W. A. 1972, ApJ , 172, 367

Glass, I. S., Moorwood, A. F. M., & Eichendorf, W. 1982, A&A , 107, 276

Gralla, S. E., Lupsasca, A., & Strominger, A. 2018, MNRAS , 475, 3829

Greenstein, J. L. 1963, Nature , 197, 1041

Goddi, C., Falcke, H., Kramer, M., et al. 2017, International Journal of Modern Physics D, 26, 1730001-239

Graham, M. J., Djorgovski, S. G., Drake, A. J., et al. 2017, MNRAS , 470, 4112

Grogin, N. A., Conselice, C. J., Chatzichristou, E., et al. 2005, ApJL , 627, L97

González-Martín, O., Masegosa, J., Márquez, I., Guainazzi, M., & Jiménez-Bailón, E. 2009, A&A , 506, 1107

González-Martín, O., Rodríguez-Espinosa, J. M., Díaz-Santos, T., et al. 2013, A&A , 553, A35

González-Martín, O., Masegosa, J., Hernán-Caballero, A., et al. 2017, ApJ , 841, 37

González-Martín, O., Masegosa, J., García-Bernete, I., et al. 2019a, ApJ , 884, 10

González-Martín, O., Masegosa, J., García-Bernete, I., et al. 2019b, ApJ , 884, 10

Goulding, A. D., & Alexander, D. M. 2009, MNRAS , 398, 1165

Greenstein, J. L., & Schmidt, M. 1964, ApJ , 140, 1

Groves, B., Nefs, B., & Brandl, B. 2008, MNRAS , 391, L113

Grupe, D., Komossa, S., Leighly, K. M., et al. 2010, ApJS , 187, 64

Guainazzi, M., Matt, G., & Perola, G. C. 2005, A&A , 444, 119

Guerras, E., Mediavilla, E., Jimenez-Vicente, J., et al. 2013, ApJ , 764, 160

Gültekin, K., Richstone, D. O., Gebhardt, K., et al. 2009, ApJ , 698, 198

Gunn, J. E. 1971, ApJL , 164, L113

Gunn, J. E., Siegmund, W. A., Mannery, E. J., et al. 2006, AJ , 131, 2332

Guo, H., Sun, M., Liu, X., et al. 2019, ApJL , 883, L44.

Haardt, F., Maraschi, L., & Ghisellini, G. 1994, ApJL , 432, L95

Halpern, J. P. 1984, ApJ , 281, 90.

Hao, H., Elvis, M., Civano, F., et al. 2010, ApJL , 724, L59

Hao, C.-N., Kennicutt, R. C., Johnson, B. D., et al. 2011, ApJ , 741, 124

Haardt, F., & Maraschi, L. 1991, ApJL , 380, L51

Hao, L., Spoon, H. W. W., Sloan, G. C., et al. 2005, ApJL , 625, L75

Harrison, C. 2014, Ph.D. Thesis

Harrison, F. A., Craig, W. W., Christensen, F. E., et al. 2013, ApJ , 770, 103.

Hatziminaoglou, E., Hernán-Caballero, A., Feltre, A., et al. 2015, ApJ , 803, 110

Hayes, M. J. C., Culhane, J. L., & Burnell, S. J. B. 1980, MNRAS , 192, 1P.

Heckman, T. M., Ptak, A., Hornschemeier, A., et al. 2005, ApJ , 634, 161

Hernán-Caballero, A., Alonso-Herrero, A., Hatziminaoglou, E., et al. 2015, ApJ , 803, 109.

Heusler, M. 1996, Helvetica Physica Acta, 69, 501

Hickox, R. C. & Alexander, D. M. 2018, ARA&A , 56, 625

Holtz, J. Z., Geballe, T. R., & Rank, D. M. 1971, ApJL , 164, L29

Hönig, S. F., Kishimoto, M., Gandhi, P., et al. 2010, A&A , 515, A23

Hönig, S. F., & Kishimoto, M. 2010, A&A , 523, A27

Hönig, S. F., & Kishimoto, M. 2017, ApJL , 838, L20

Hopkins, P. F., Hernquist, L., Martini, P., et al. 2005, ApJL , 625, L71

Hopkins, P. F., Hernquist, L., Cox, T. J., et al. 2008, ApJS , 175, 356

Hopkins, P. F. and Quataert, E., 2010 , MNRAS , 407, 1529

Hopkins, P. F. 2012, MNRAS , 420, L8.

Ho, L. C., Filippenko, A. V., & Sargent, W. L. W. 1997, ApJS , 112, 315

Hubble, E. P. 1926, ApJ , 64, 321

Hutsemékers, D., Agís González, B., Marin, F., et al. 2020, A&A , 644, L5.

Ichikawa, K., Packham, C., Ramos Almeida, C., et al. 2015, ApJ , 803, 57

Ichikawa, K., Ueda, J., Shidatsu, M., et al. 2016, PASJ , 68, 9.

Ichikawa, K., Ricci, C., Ueda, Y., et al. 2017, ApJ , 835, 74

Ichikawa, K., Ueda, J., Bae, H.-J., et al. 2019, ApJ , 870, 65

Ichikawa, K., Kawamuro, T., Shidatsu, M., et al. 2019, ApJL , 883, L13

Ichimaru, S. 1977, ApJ , 214, 840

Ikeda, S., Awaki, H., & Terashima, Y. 2009, ApJ , 692, 608

İkiz, T., Peletier, R. F., Barthel, P. D., et al. 2020, A&A , 640, A68.

in't Zand, J. J. M., Bozzo, E., Qu, J., et al. 2019, Science China Physics, Mechanics, and Astronomy, 62, 29506.

Inoue, H. 1989, Two Topics in X-Ray Astronomy, Volume 1: X Ray Binaries. Volume 2: AGN and the X Ray Background, 1, 783

Jansen, F., Lumb, D., Altieri, B., et al. 2001, A&A , 365, L1.

Jarrett, T. H., Cohen, M., Masci, F., et al. 2011, ApJ , 735, 112

Jiang, L., Fan, X., Brandt, W. N., et al. 2010, Nature , 464, 380

Jones, D. H., Read, M. A., Saunders, W., et al. 2009, MNRAS , 399, 683

Johnson, H. L. 1960, Lowell Observatory Bulletin, 5, 17

Just, D. W., Brandt, W. N., Shemmer, O., et al. 2007, ApJ , 665, 1004.

Kauffmann, G., Heckman, T. M., Tremonti, C., et al. 2003, MNRAS , 346, 1055

Kaspi, S., Smith, P. S., Netzer, H., et al. 2000, ApJ , 533, 631

Keel, W. C., Irby, B. K., May, A., et al. 2005, ApJS , 158, 139

Keel, W. C., Chojnowski, S. D., Bennert, V. N., et al. 2012, MNRAS , 420, 878.

Kellermann, K. I., Sramek, R. A., Schmidt, M., et al. 1994, AJ , 108, 1163

Kerr, R. P. 1963, PRL , 11, 237

Kewley, L. J., Dopita, M. A., Sutherland, R. S., et al. 2001, ApJ , 556, 121

Kewley, L. J. & Dopita, M. A. 2002, ApJS , 142, 35

Kewley, L. J., Groves, B., Kauffmann, G., et al. 2006, MNRAS , 372, 961

Kewley, L. J., Maier, C., Yabe, K., et al. 2013, ApJL , 774, L10

Kleinmann, D. E. & Low, F. J. 1970, ApJL , 159, L165.

Kristian, J. 1973, ApJL , 179, L61

Koss, M., Trakhtenbrot, B., Ricci, C., et al. 2017, ApJ , 850, 74

Kormendy, J. & Richstone, D. 1995, ARA&A , 33, 581

Kormendy, J., & Ho, L. C. 2013, ARA&A , 51, 511

Krabbe, A., Böker, T., & Maiolino, R. 2001, ApJ , 557, 626

Krolik, J. H., & Begelman, M. C. 1988, ApJ , 329, 702

Krongold, Y., Dultzin-Hacyan, D., & Marziani, P. 2003, Active Galactic Nuclei: From Central Engine to Host Galaxy, 523

Krongold, Y., Nicastro, F., Brickhouse, N. S., et al. 2003, ApJ , 597, 832

Koulouridis, E. 2014, A&A , 570, A72

Lacy, M. & Sajina, A. 2020, Nature Astronomy, 4, 352.

Laha, S., Markowitz, A. G., Krumpe, M., et al. 2020, ApJ , 897, 66.

LaMassa, S. M., Cales, S., Moran, E. C., et al. 2015, ApJ , 800, 144

LaMassa, S. M., Heckman, T. M., Ptak, A., et al. 2010, ApJ , 720, 786.

King, A. R., Zubovas, K., & Power, C. 2011, MNRAS , 415, L6.

Laor, A. 1991, ApJ , 376, 90

Leahy, D. A. & Creighton, J. 1993, MNRAS , 263, 314

Lebouteiller, V., Barry, D. J., Spoon, H. W. W., et al. 2011, ApJS , 196, 8.

Li, K. J., Gao, P. X., Zhan, L. S., et al. 2008, MNRAS , 391, L34.

Lintott, C. J., Schawinski, K., Slosar, A., et al. 2008, MNRAS , 389, 1179.

Lintott, C. J., Schawinski, K., Keel, W., et al. 2009, MNRAS , 399, 129

Liu, B. F. & Meyer-Hofmeister, E. 2001, A&A , 372, 386.

Liu, Y., & Li, X. 2015, MNRAS , 448, L53

Loeb, A. 2007, PRL , 99, 041103

Liu, J., Hönig, S. F., Ricci, C., et al. 2019, MNRAS , 490, 4344

Lopez-Rodriguez, E., Fuller, L., Alonso-Herrero, A., et al. 2018, ApJ , 859, 99

López-Gonzaga, N., Burtscher, L., Tristram, K. R. W., et al. 2016, A&A , 591, A47

Lusso, E., Comastri, A., Vignali, C., et al. 2010, A&A , 512, A34

Lutz, D., Maiolino, R., Spoon, H. W. W., et al. 2004, A&A , 418, 465

Lyutyj, V. M., Oknyanskij, V. L., & Chuvaev, K. K. 1984, Soviet Astronomy Letters, 10, 335

Madejski, G., Done, C., & Życki, P. 2001, Advances in Space Research, 28, 369.

Magorrian, J., Tremaine, S., Richstone, D., et al. 1998, AJ , 115, 2285

Maiolino, R., Marconi, A., & Oliva, E. 2001, A&A , 365, 37

Makino, F. & ASTRO-C Team 1987, Astrophys. Lett. , 25, 223

Maksym, W. P., Schmidt, J., Keel, W. C., et al. 2020, ApJL , 902, L18

Marconi, A., Oliva, E., van der Werf, P. P., et al. 2000, A&A , 357, 24

Marconi, A., Risaliti, G., Gilli, R., et al. 2004, MNRAS , 351, 169

Marinucci, A., Matt, G., Bianchi, S., et al. 2015, MNRAS , 447, 160

Markarian, B. E. 1967, Astrofizika, 3, 55

Martínez-Paredes, M., González-Martín, O., Esparza-Arredondo, D., et al. 2020, ApJ , 890, 152.

Mason, R. E., Geballe, T. R., Packham, C., et al. 2006, ApJ , 640, 612

Mason, R. E., Levenson, N. A., Packham, C., et al. 2007, ApJ , 659, 241

Matt, G., Guainazzi, M., Frontera, F., et al. 1997, A&A , 325, L13

Marshall, F. J. & Clark, G. W. 1984, ApJ , 287, 633

Matt, G., Perola, G. C., & Piro, L. 1991, A&A , 247, 25

Matt, G., Guainazzi, M., & Maiolino, R. 2003, MNRAS , 342, 422

Mateos, S., Carrera, F. J., Alonso-Herrero, A., et al. 2016, ApJ , 819, 166

McConnell, N. J. & Ma, C.-P. 2013, ApJ , 764, 184

McHardy, I. M., Koerding, E., Knigge, C., et al. 2006, Nature , 444, 730

Meléndez, M., Kraemer, S. B., Armentrout, B. K., et al. 2008, ApJ , 682, 94.

Merloni, A., Heinz, S., & di Matteo, T. 2003, MNRAS , 345, 1057

Merloni, A., Dwelly, T., Salvato, M., et al. 2015, MNRAS , 452, 69

Mitchell, R. J. & Culhane, J. L. 1977, MNRAS , 178, 75P

Mitsuda, K., Bautz, M., Inoue, H., et al. 2007, PASJ , 59, S1.

Miyoshi, M., Moran, J., Herrnstein, J., et al. 1995, Nature , 373, 127

Monier, E. M., Mathur, S., Wilkes, B., et al. 2001, ApJ , 559, 675.

Morganti, R., Oosterloo, T., & Tsvetanov, Z. 1998, AJ , 115, 915.

Murphy, K. D., & Yaqoob, T. 2009, MNRAS , 397, 1549

Nandra, K. & George, I. M. 1994, MNRAS , 267, 974.

Nagoshi, S., Iwamuro, F., Wada, K., et al. 2021, PASJ , 73, 122.

Narayan, R., Mahadevan, R., & Quataert, E. 1998, Theory of Black Hole Accretion Disks, 148

Narayan, R., SÄ dowski, A., Penna, R. F., et al. 2012, MNRAS , 426, 3241

Nenkova, M., Sirocky, M. M., Ivezić, Ž., & Elitzur, M. 2008, ApJ , 685, 147-159

Nenkova, M., Sirocky, M. M., Nikutta, R., Ivezić, Ž., & Elitzur, M. 2008, ApJ , 685, 160-180

Netzer, H., Kaspi, S., Behar, E., et al. 2003, ApJ , 599, 933

Netzer, H. 2013, The Physics and Evolution of Active Galactic Nuclei, by Hagai Netzer, Cambridge, UK: Cambridge University Press, 2013

Netzer, H. 2015, ARA&A , 53, 365

Neugebauer, G. & Leighton, R. B. 1969, NASA SP, Washington: NASA, 1969

Nicastro, F., Martocchia, A., & Matt, G. 2003, ApJL , 589, L13

Novak, G. S., Ostriker, J. P., & Ciotti, L. 2011, ApJ , 737, 26

Oke, J. B. 1963, Nature , 197, 1040

Ogawa, S., Ueda, Y., Tanimoto, A., et al. 2021, ApJ , 906, 84

Oppenheimer, J. R., & Volkoff, G. M. 1939, Physical Review, 55, 374

Osterbrock, D. E. 1977, ApJ , 215, 733

Osterbrock, D. E. 1978, Proceedings of the National Academy of Science, 75, 540

Padovani, P., Alexander, D. M., Assef, R. J., et al. 2017, A&A Rev. , 25, 2

Page, M. J. 1998, MNRAS , 298, 537

Pancoast, A., Brewer, B. J., & Treu, T. 2011, ApJ , 730, 139

Panessa, F., Bassani, L., Cappi, M., et al. 2006, A&A , 455, 173

Pasetto, A., González-Martín, O., Esparza-Arredondo, D., et al. 2019, ApJ , 872, 69

Peeters, E., Spoon, H. W. W., & Tielens, A. G. G. M. 2004, ApJ , 613, 986

Penston, M. V. & Perez, E. 1984, MNRAS , 211, 33P.

Pereira-Santaella, M., Alonso-Herrero, A., Rieke, G. H., et al. 2010, ApJS , 188, 447

Pérez-Beaupuits, J. P., Spoon, H. W. W., Spaans, M., et al. 2011, A&A , 533, A56

Peterson, B. M. 1993, PASP , 105, 247

Peterson, B. M. 2014, Space Sci. Rev. , 183, 253

Pier, E. A., & Krolik, J. H. 1992, ApJ , 401, 99

Piotrovich, M. Y., Gnedin, Y. N., Natsvlishvili, T. M., et al. 2017, Ap&SS , 362, 231

Pogge, R. W. 1988, ApJ , 328, 519

Predehl, P., Sunyaev, R. A., Becker, W., et al. 2020, Nature , 588, 227.

Prieto, M. A., Pérez García, A. M., & Rodríguez Espinosa, J. M. 2001, A&A , 377, 60

Raban, D., Jaffe, W., Röttgering, H., et al. 2009, MNRAS , 394, 1325

Ramos Almeida, C., Pérez García, A. M., Acosta-Pulido, J. A., et al. 2007, AJ , 134, 2006

Ramos Almeida, C., Levenson, N. A., Rodríguez Espinosa, J. M., et al. 2009, ApJ , 702, 1127

Ramos Almeida, C., Levenson, N. A., Alonso-Herrero, A., et al. 2011, ApJ , 731, 92

Ramos Almeida, C., Alonso-Herrero, A., Levenson, N. A., et al. 2014, MNRAS , 439, 3847

Ramos Almeida, C. & Ricci, C. 2017, Nature Astronomy, 1, 679

Rank, D. M., Holtz, J. Z., Geballe, T. R., & Townes, C. H. 1970, ApJL , 161, L185

Reynolds, C. S. 1997, MNRAS , 286, 513

Reynolds, C. S. 2012, ApJL , 759, L15

Reynolds, C. S. 2019, Nature Astronomy, 3, 41

Ricci, C., Trakhtenbrot, B., Koss, M. J., et al. 2017, Nature , 549, 488

Risaliti, G. & Elvis, M. 2004, Supermassive Black Holes in the Distant Universe, 187.

Risaliti, G., Harrison, F. A., Madsen, K. K., et al. 2013, Nature , 494, 449

Rodriguez Espinosa, J. M., Rudy, R. J., & Jones, B. 1987, ApJ , 312, 555

Rontgen, W. K. 1896, Science, 3, 726

Rowan-Robinson, M. 1977, ApJ , 213, 635

Ruan, J. J., Anderson, S. F., Eracleous, M., et al. 2019, ApJ , 883, 76

Smith, J. F. & Courtier, G. M. 1976, Proceedings of the Royal Society of London Series A, 350, 421

Sandage, A. 1964, ApJ , 139, 416

Sanders, D. B., Soifer, B. T., Elias, J. H., et al. 1988, ApJ , 325, 74.

Sanders, D. B., & Mirabel, I. F. 1996, ARA&A , 34, 749

Sarangi, A., Dwek, E., & Kazanas, D. 2019, ApJ , 885, 126

Schawinski, K., Koss, M., Berney, S., et al. 2015, MNRAS , 451, 2517

Schmidt, M. 1963, Nature , 197, 1040

Schwarzschild, K. 1916, Abh. Konigl. Preuss. Akad. Wissenschaften Jahre 1906,92, Berlin,1907, 1916, 189

Seyfert, C. K. 1943, ApJ , 97, 28

Scott, A. E., Stewart, G. C., & Mateos, S. 2012, MNRAS , 423, 2633

Serlemitsos, P. J., Becker, R. H., Boldt, E. A., et al. 1976, NASA Special Publication, 67

Shakura, N. I. & Sunyaev, R. A. 1973, A&A , 500, 33

Shapovalova, A. I., Popović, L. Č., Burenkov, A. N., et al. 2010, A&A , 509, A106

Shi, Y., Rieke, G. H., Hines, D. C., et al. 2006, ApJ , 653, 127

Shulevski, A., Morganti, R., Barthel, P. D., et al. 2015, A&A , 583, A89

Siebenmorgen, R., Haas, M., Krügel, E., et al. 2005, A&A , 436, L5.

Siebenmorgen, R., Heymann, F., & Efstathiou, A. 2015, A&A , 583, A120

Silk, J., & Rees, M. J. 1998, A&A , 331, L1

Simpson, C. 2005, MNRAS , 360, 565.

Sirocky, M. M., Levenson, N. A., Elitzur, M., et al. 2008, ApJ , 678, 729

Slipher, V. M. 1917, The Observatory, 40, 304

Stalevski, M., Ricci, C., Ueda, Y., et al. 2016, MNRAS , 458, 2288.

Strateva, I. V., Brandt, W. N., Schneider, D. P., et al. 2005, AJ , 130, 387

Steffen, A. T., Barger, A. J., Cowie, L. L., et al. 2003, ApJL , 596, L23

Stern, D., Assef, R. J., Benford, D. J., et al. 2012, ApJ , 753, 30

Stern, D. 2015, ApJ , 807, 129.

Sturm, E., Lutz, D., Tran, D., et al. 2000, A&A , 358, 481

Tanaka, Y., Inoue, H., & Holt, S. S. 1994, PASJ , 46, L37

Tanaka, Y., Nandra, K., Fabian, A. C., et al. 1995, Nature , 375, 659

Tanimoto, A., Ueda, Y., Odaka, H., et al. 2019, ApJ , 877, 95

Toba, Y., Oyabu, S., Matsuhara, H., et al. 2014, ApJ , 788, 45

Tran, H. D., Osterbrock, D. E., & Martel, A. 1992, AJ , 104, 2072

Tran, H. D. 2001, ApJL , 554, L19

Tran, H. D. 2003, ApJ , 583, 632. doi:10.1086/345473

Tremaine, S., Gebhardt, K., Bender, R., et al. 2002, ApJ , 574, 740

Tristram, K. R. W., Burtscher, L., Jaffe, W., et al. 2014, A&A , 563, A82

Truemper, J. 1982, Advances in Space Research, 2, 241.

Tueller, J., Mushotzky, R. F., Barthelmy, S., et al. 2008, ApJ , 681, 113

Turner, T. J. & Pounds, K. A. 1989, MNRAS , 240, 833

Ueda, Y., Akiyama, M., Ohta, K., et al. 2003, ApJ , 598, 886

Ueda, Y., Hashimoto, Y., Ichikawa, K., et al. 2015, ApJ , 815, 1.

Urry, C. M., & Padovani, P. 1995, PASP , 107, 803

Veilleux, S. & Osterbrock, D. E. 1987, ApJS , 63, 295

Veilleux, S., Goodrich, R. W., & Hill, G. J. 1997, ApJ , 477, 631

Véron-Cetty, M.-P. & Véron, P. 2006, A&A , 455, 773

Wada, K. 2012, ApJ , 758, 66

Walker, H. J. 2000, Astronomy and Geophysics, 41, 10.

Ward, M. J., Done, C., Fabian, A. C., et al. 1988, ApJ , 324, 767

Weisskopf, M. C., Aldcroft, T. L., Bautz, M., et al. 2003, Experimental Astronomy, 16, 1.

Wheeler, J. A. 1968, American Scientist, 56, 1

Wilkes, B. 1999, Quasars and Cosmology, 162, 15

Wu, Y., Charmandaris, V., Huang, J., et al. 2009 , ApJ , 701, 658

XRISM Science Team 2020, arXiv:2003.04962

Xie, Y., Li, A., & Hao, L. 2017, ApJS , 228, 6

Xu, Y.-D. 2011, ApJ , 739, 64

Yaqoob, T. 1997, ApJ , 479, 184.

Yaqoob, T. 2012, MNRAS , 423, 3360.

Yang, G., Boquien, M., Buat, V., et al. 2020, MNRAS , 491, 740.

Young, M., Elvis, M., & Risaliti, G. 2010, ApJ , 708, 1388

Zajaček, M., Tursunov, A., Eckart, A., et al. 2019, Journal of Physics Conference Series, 1258, 012031

Zhang, X.-G. 2021, MNRAS , 500, L57.

Zwicky, I. F. 1964, ApJ , 140, 1467